Flight Mechanics/ Estimation Theory Symposium 1995

1995121342

Flight Mechanics/ Estimation Theory Symposium 1995

Kathy R. Hartman, Editor
*Goddard Space Flight Center
Greenbelt, Maryland*

National Aeronautics and
Space Administration

**Scientific and Technical
Information Branch**

1995

FOREWORD

The papers presented here have been derived primarily from speakers' summaries of talks presented at the Flight Mechanics/Estimation Theory Symposium held May 16-18, 1995 at the Goddard Space Flight Center. For completeness, abstracts are included for those papers which were presented but unavailable at the time of printing. Papers included in this document are presented as received from the authors with little or no editing.

CONTENTS

SESSION 4

SESSION 5

SESSION 6

FLIGHT MECHANICS/ESTIMATION THEORY SYMPOSIUM

MAY 16-18, 1995

SESSION 1

Analysis of Filter Tuning Techniques for Sequential Orbit Determination*

N95- 27764

T. Lee, C. Yee, and D. Oza
Computer Sciences Corporation
Lanham-Seabrook, Maryland, USA 20706

Abstract

This paper examines filter tuning techniques for a sequential orbit determination (OD) covariance analysis. Recently, there has been a renewed interest in sequential OD, primarily due to the successful flight qualification of the Tracking and Data Relay Satellite System (TDRSS) Onboard Navigation System (TONS) using Doppler data extracted onboard the Extreme Ultraviolet Explorer (EUVE) spacecraft. TONS computes highly accurate orbit solutions onboard the spacecraft in realtime using a sequential filter. As the result of the successful TONS-EUVE flight qualification experiment, the Earth Observing System (EOS) AM-1 Project has selected TONS as the prime navigation system. In addition, sequential OD methods can be used successfully for ground OD. Whether data are processed onboard or on the ground, a sequential OD procedure is generally favored over a batch technique when a realtime automated OD system is desired.

Recently, OD covariance analyses were performed for the TONS-EUVE and TONS-EOS missions using the sequential processing options of the Orbit Determination Error Analysis System (ODEAS). ODEAS is the primary covariance analysis system used by the Goddard Space Flight Center (GSFC) Flight Dynamics Division (FDD). The results of these analyses revealed a high sensitivity of the OD solutions to the state process noise filter tuning parameters. The covariance analysis results show that the state estimate error contributions from measurement-related error sources, especially those due to the random noise and satellite-to-satellite ionospheric refraction correction errors, increase rapidly as the state process noise increases. These results prompted an in-depth investigation of the role of the filter tuning parameters in sequential OD covariance analysis.

This paper analyzes how the spacecraft state estimate errors due to dynamic and measurement-related error sources are affected by the process noise level used. This information is then used to establish guidelines for determining optimal filter tuning parameters in a given sequential OD scenario for both covariance analysis and actual OD. Comparisons are also made with corresponding definitive OD results available from the TONS-EUVE analysis.

1. Introduction

This paper presents the results of a study to examine the sensitivity of sequential orbit determination (OD) errors to the filter tuning parameters. The results are obtained primarily from covariance analyses performed to assess the navigation performance of the Tracking and Data Relay Satellite (TDRS) System (TDRSS) Onboard Navigation System (TONS) for two spacecraft missions—the Extreme Ultraviolet Explorer (EUVE) and the Earth Observing System (EOS). TONS is a sequential OD system based on the extended Kalman filter. It is capable of computing highly accurate orbit solutions onboard the spacecraft in realtime and processing TDRSS forward-link one-way Doppler measurements. The feasibility of the TONS navigation method was successfully demonstrated on the flight qualification experiment performed in conjunction with the EUVE mission (Reference 1). As a result of this success, the EOS Project has selected TONS as the prime navigation system for the EOS AM-1 mission.

A sequential OD system using a Kalman filter is normally tuned to prevent it from diverging. Filter divergence can occur when the terms in the covariance matrix approach zero, which in turn causes the computed Kalman gain to approach zero. Since the Kalman gain determines how much emphasis to place on the measurements in updating the filtered state, the filter will ignore any new measurement as the Kalman gain approaches zero, resulting in filter divergence. One way of preventing the filter from diverging is to add a certain level of process noise to the system model to account for the unmodeled error contributions. The addition of process noise prevents the covariance matrix terms from approaching zero, thereby preventing

the Kalman gain from approaching zero. The choice of the appropriate level of process noise is largely heuristic and depends to a large extent on what is known about the unmodeled state parameters. More detailed information about filter tuning can be found in Reference 2. Generally, the larger the process noise levels added to the covariance matrix, the larger the Kalman gain will become, thus placing more emphasis on the measurement information than on the dynamic state model in updating the filtered state. One consequence of this approach is that, as the applied process noise level increases, the contribution from any measurement-related error is likely to be magnified while the contribution from the dynamic error sources is likely to decrease. The choice of optimum filter tuning parameters therefore involves selecting optimum process noise levels in such a way that the combined contribution of the dynamic and measurement-related error sources to the OD errors is minimized.

The covariance analysis results are obtained using the Orbit Determination Error Analysis System (ODEAS) (Reference 3). ODEAS is a general-purpose linear error analysis tool used at the Goddard Space Flight Center (GSFC) Flight Dynamic Division (FDD) to support various missions. On the basis of a tracking scenario and the expected accuracies of the orbital dynamic models and measurement process, ODEAS provides the magnitudes and characteristics of the errors that can be expected in an OD process. In this study, such covariance analysis results are used to identify those error sources that are most sensitive to the process noise level variation and to illustrate how the optimum OD solutions are achieved by controlling the process noise level within the ODEAS framework.

Section 2 of this paper describes the analysis methods used in this study and details the results obtained; Section 3 gives a summary of the study and summarizes the conclusions.

2. Analysis Methods and Results

Covariance analyses were performed for the EUVE and EOS PM-1 spacecraft. In both cases, sequential error analysis simulations were performed by processing 2 days worth of tracking data. The EUVE spacecraft is in a near-circular orbit at a nominal altitude of 520 kilometers and an inclination of 28.5 degrees. The tracking data distribution used for the EUVE study is taken from the actual tracking data around January 17, 1993. The tracking data consisted of 23 tracking passes of one-way forward-link TDRSS Doppler data with pass lengths ranging from 2 to 40 minutes distributed over the 2-day timespan. The EOS PM-1 spacecraft will be in a near-circular frozen orbit at a nominal altitude of 705 kilometers, with an inclination of 98.2 degrees. The tracking data consist of 20 minutes of one-way forward-link TDRSS Doppler data per EOS orbit, which amounts to 29 tracking passes during the 2-day timespan. The EOS PM-1 spacecraft was selected for study rather than EOS AM-1 because previous error analysis results (Reference 4) indicated that the OD error contributions from the ionospheric refraction effects were found to be larger for EOS PM-1 than for EOS AM-1.

Two types of error analysis simulations were performed. In the first case, the orbital state of the TDRSS-user spacecraft (EUVE or EOS) is estimated together with the frequency bias of the ultrastable oscillator (USO) used for onboard frequency reference and the atmospheric drag coefficient. In the second case, the drag coefficient is treated as a considered error source instead of being estimated.

Throughout this study, the sequential filter was tuned using a process noise algorithm based on a linear variance growth model. In this model the process noise variance is assumed to grow linearly with time elapsed between measurements (Reference 3). The process noise computed is added to the propagated error covariance, which is used in computing the Kalman gain matrix. Brief descriptions of the ODEAS gain matrix computation and the time and measurement update algorithm for the covariance matrices are presented below. Using the notations of Reference 3, the time-updated covariance matrix, $P(t_i-)$, and the measurement updated covariance matrix, $P(t_i)$, at a measurement time t_i, are given by

$$P(t_i-) = \phi(t_i, t_{i-1}) P(t_{i-1}) \phi^T(t_i, t_{i-1}) + Q_i \qquad (1)$$

$$P(t_i) = (I - K_i \Omega_i) P(t_i-)(I - K_i \Omega_i)^T + K_i R K_i^T \qquad (2)$$

4

where $\phi(t_i, t_{i-1})$ denotes the state transition function and K_i the Kalman gain matrix. The gain matrix, K_i, is defined in terms of R, the measurement noise variance (MNV), Ω_i, the measurement partial derivative matrix, and $P(t_i-)$, the time updated covariance matrix, as follows:

$$K_i = P(t_i-)\Omega_i^T \left(R + \Omega_i P(t_i-)\Omega_i^T\right)^{-1} \qquad (3)$$

The matrix Q_i on the right-hand side of Equation (1) represents the process noise. The ODEAS linear growth process noise model defines Q_i as follows:

$$Q_i \equiv D \cdot (t_i - t_{i-1}) \qquad (4)$$

The quantity D in the above equation is a diagonal matrix with the variance growth rate of solve-for parameters as diagonal elements. For the nonorbital solve-for parameters such as the clock drift, an additional restriction is imposed such that the computed process noise level, Q_i, does not exceed the respective *a priori* variance. In the present study, D is assumed to be of a special form in which the only nonzero elements are those associated with the user spacecraft velocity components and the clock drift parameter. It is further assumed that the three velocity variance growth rates are the same: that is, a single variance growth rate parameter, designated here as Qdot, is assigned for all three velocity components. The characteristic behavior of the state estimate errors due to major error sources are investigated when the process noise level is varied by specifying different values for the velocity variance growth rate and the MNV parameters. In this paper, the name Qdot will be used to denote the velocity variance growth rate. The value of MNV is obtained by squaring the measurement noise standard deviation (MNSD) specified for the tracking measurements. The variance growth rates for the estimated clock drift (frequency bias) and the drag coefficient (when the drag is estimated) are not varied.

Given below is a description of the methods and results of the EUVE and EOS PM-1 studies, followed by a brief comparison of the EUVE and EOS filter tuning results and a description of the covariance analysis versus the actual OD results.

2.1 EUVE Study

The methods and results of the EUVE filter tuning analysis are presented below.

EUVE Methods

The major error sources included in the EUVE covariance analysis are summarized in Table 1. The measurement-related error sources included are the measurement noise specified by the MNSD, TDRS ephemeris errors, and satellite-to-satellite tracking (SST) ionospheric refraction errors. The major dynamic error sources included are the atmospheric drag and gravity errors. Orbital errors due to the gravity model uncertainties are computed using the Goddard Earth Model-T3 (GEM-T3) standard errors in the ODEAS uncorrelated error model approach (UEMA) (Reference 2). The EUVE results presented here are based on solutions in which the drag coefficient error is included as a considered error source.

Table 1. Major Error Sources Included in the EUVE Analysis

Error Sources	3σ Errors	Notes
Measurement noise	0.001 meter/second and 0.01 meter/second	TDRS one-way range-rate measurements
TDRS ephemeris errors	5 meters, 30 meters, 40 meters in the radial, cross-track, and along-track (HCL) directions	For both TDRS-East and TDRS-West
Ionospheric refraction errors	100% of measurement delay	Bent ionospheric model
Drag coefficient error	30% (when considered)	Harrirs-Priester model with $F_{10.7} = 122 \times 10^{-22}$ watts/meter^3/hertz
Geopotential errors	GEM-T3 30 × 30 sigmas	ODEAS UEMA model

The sensitivities of the solution errors to the process noise level applied are studied with two groups of error analysis solutions, referred to as the Group A and Group B solutions and defined as follows:

- Group A solutions are obtained using an MNSD of 0.001 meter/second, while the Qdot value is varied from zero to 1.0×10^{-9} meter^3/second^2 (a total of six solutions obtained using six different Qdot values given by 0.0, 1.0×10^{-13}, 1.0×10^{-12}, 1.0×10^{-11}, 1.0×10^{-10}, and 1.0×10^{-9} meter^3/second^2).

- Group B solutions are obtained using an MNSD of 0.01 meter/second and the same set of Qdot values used for the Group A solutions. Note that the MNSD values used in Group B solutions are 10 times that of Group A solutions.

EUVE Results

The variation of the covariance analysis solutions with respect to the process noise levels may be better characterized in terms of their statistical properties. The root-mean-square (RMS) position errors and their standard deviations (SDs) are summarized in Table 2, together with their maximum and minimum values. The proportionality of the error magnitudes to the Qdot values used is clearly demonstrated in this table. This table also suggests two simple relations that hold between the Group A and Group B solutions. The first relation is that for solutions obtained without filter tuning, the RMS values and standard deviations are proportional to the MNSD values used (see the last column of Table 1). Note that the Group B results are 10 times the corresponding Group A results, which is the same ratio as the ratio of the MNSD values used for the two groups of solutions. This relation is expected because normally the orbital errors due to the random noise in the steady state period are almost entirely due to the measurement noise.

Table 2. Random Noise Contributions to EUVE Position Errors

Error Statistics	Velocity Filter Tuning Parameter (Qdot) (meter^2/sec^3)					
	1.0×10^{-9}	1.0×10^{-10}	1.0×10^{-11}	1.0×10^{-12}	1.0×10^{-13}	0.0
Group A Solution Statistics (meters) MNSD = 0.001 meter/second						
RMS	5.8936	3.6452	2.3136	1.2901	0.7462	0.4387
SD	3.9215	2.4453	1.5499	0.7336	0.2756	0.0719
Maximum	24.6185	14.8740	11.2404	5.2263	1.9792	0.6270
Minimum	1.5354	0.9985	0.5951	0.4437	0.3591	0.2841
Group B Solution Statistics (meters) MNSD = 0.01 meter/second						
RMS	23.1428	12.9020	7.4623	5.2429	4.5294	4.3873
SD	15.5054	7.3367	2.7562	1.0732	0.7302	0.7191
Maximum	112.4479	52.2718	19.7915	8.1712	6.2792	6.2699
Minimum	5.9508	4.4371	3.5907	3.2023	2.9438	2.8409

A close examination of Table 2 suggests a second relation between the Group A and Group B solutions obtained using finite Qdot values. This relation indicates that the orbital error statistics associated with a Group B solution are approximately 10 times those of the Group A solution that is obtained with a Qdot value that is 100 times smaller than the one used for the Group B solution. For example, the RMS and SD values of the Group B solution obtained using a Qdot value of 1.0×10^{-11} are 10 times those of the Group A solution obtained using a Qdot value of 1.0×10^{-13}. These two solutions can be characterized as having the same Qdot-to-MNV ratio. The MNV value is obtained by squaring the MNSD value. The Group A solutions used an MNV of 1.0×10^{-6} meter^2/second^2, whereas the Group B solutions used an MNV value of 1.0×10^{-4} meter^2/sec^2. This gives a Qdot-to-MNV ratio of 1.0×10^{-7} (in units of 1/second) in the case of the two sample solutions. The first relation described above can be considered as a special case of this second relation because the solutions obtained without filter tuning can be characterized as having a zero Qdot-to-MNV ratio. Thus, Group B solutions can be obtained from Group A solutions obtained using the same Qdot-to-MNV ratios (by multiplying the latter with the ratio of the MNSD values used). This second relation is not as obvious as the first one, but it too can be verified using the ODEAS filter tuning algorithm described earlier.

The very structure of Equations (1) through (3) implies two things in the steady-state region:

- The matrix defined as the covariance matrix divided by MNV is determined by the Qdot-to-MNV ratio only.
- The Kalman gain matrix is determined only by the Qdot-to-MNV ratio as well.

Since the random noise conributions are derived from the covariance matrix, the results summarized in Table 2 are totally consistent with the first of these two asserions. The second property states that the gain matrix is entirely determined by the Qdot-to-MNV ratio only. Figure 2 verifies this assertion numerically. This figure shows the x-components of two gain matrices obtained using the same Qdot-to-MNV ratio in the steady-state region. The vertical axis represents the x-components of the gain matrices expressed in units of meters/(meters/second). Both gain matrices were obtained using a Qdot-to-MNV ratio of 1.0×10^{-6}. The x-components of the two gain matrices are seen to be almost identical. Since the error budgets due to systematic error sources are determined by the gain matrix only, this implies that all orbital error contributions from the measurement-related and dynamic error sources will be determined only by the Qdot-to-MNV ratio as well. As such an example of the dynamical error contributions, the EUVE position errors due to the atmospheric drag error are summarized in Table 3. Similar behavior is observed for position error contributions from the other systematic error sources considered.

The results summarized in Tables 2 and 3 show that, as the process level (or equivalently, the Qdot-to-MNV ratio) increases, the orbital errors due to the measurement-related error sources generally increase while those due to the dynamical error sources decrease. These features are expected from the theoretical considerations mentioned earlier. It should be noted that the SDs of these orbital errors have similar trends. The orbital errors due to the SST ionospheric refraction errors and those due to the atmospheric drag errors were found to be most sensitive to the process noise level changes. The gravity model uncertainty is usually one of the major dynamical error sources, contributing approximately 25 meters to the position errors for the EUVE OD solutions examined here. However, as discussed earlier, the orbital errors due to the gravity model uncertainties were found to be relatively insensitive to the Qdot-to-MNV ratio.
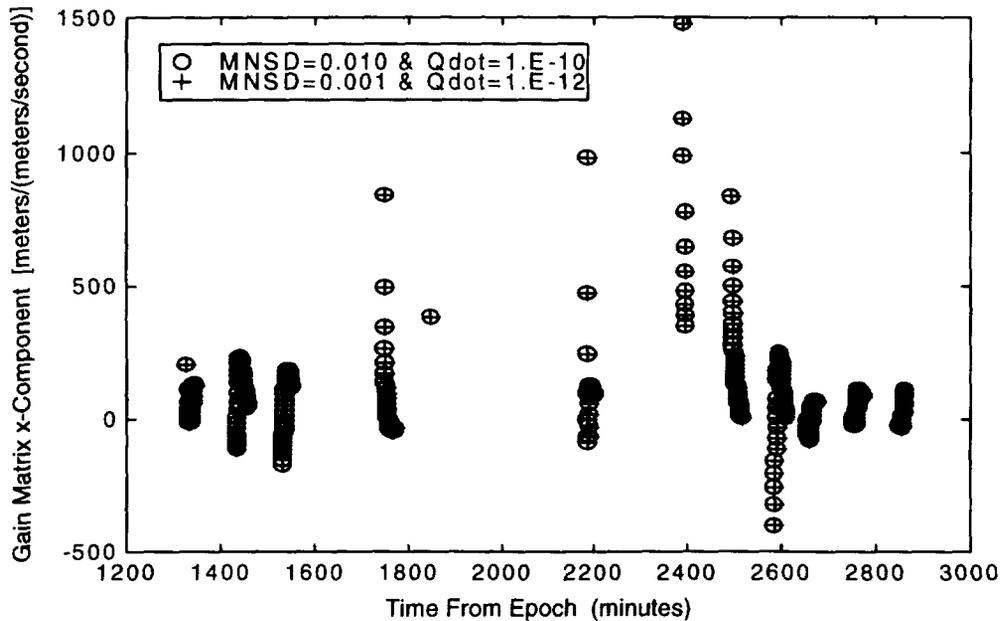
Figure 2. Behavior of x-Components of Gain Matrices

Table 3. Atmospheric Drag Error Contributions to EUVE Position Errors

Error Statistics	Velocity Filter Tuning Parameter (Qdot) (meter^2/second^3)					
	1.0×10^{-9}	1.0×10^{-10}	1.0×10^{-11}	1.0×10^{-12}	1.0×10^{-13}	0.0
Group A Solution Statistics (meters) MNSD = 0.001 meter/second						
RMS	1.2681	1.3643	1.9223	3.4975	6.5251	137.8619
SD	2.5499	2.8581	3.8017	4.7522	6.8147	67.5221
Maximum	21.6648	22.0163	27.8274	36.8109	45.1079	275.8270
Minimum	0.1824	0.0666	0.2418	0.6395	0.9928	20.1890
Group B Solution Statistics (meters) MNSD = 0.01 meter/second						
RMS	1.9223	3.4975	6.5251	12.6430	30.5039	137.8630
SD	3.8017	4.7522	6.8147	9.9910	15.9932	67.5224
Maximum	27.8273	36.8109	45.1079	52.7269	76.9703	275.8284
Minimum	0.2418	0.6395	0.9928	1.5085	9.6304	20.1892

The RMS position errors discussed above without the contribution from the gravity model uncertainty are summarized in Table 4. This table shows that Case 3 which uses the Qdot-to-MNV ratio of 1.0×10^{-8}, gives the optimum solution for both Group A and Group B solutions. The random noise contribution does not play a significant role in either group of solutions. The consider error contributions, especially those due to the SST ionospheric refraction and the drag model uncertainties, determine the optimum filter tuning parameters in the EUVE results presented here.

Table 4. EUVE RMS Position Errors Versus Qdot-to-MNV Ratio

Cases Studied		Group A Solutions (MNSD = 0.001 meter/second)			Group B Solutions (MNSD = 0.01 meter/second)		
Case No.	Qdot-to-MNV Ratio	Consider[a] Errors	Random Noise	Total	Consider[a] Errors	Random Noise	Total
1	0.0	156.2926	0.4387	156.2932	156.2937	4.3873	156.3552
2	1.0×10^{-9}	45.4391[b]	0.4529[b]	45.4413	45.4391	4.5295	45.6643
3	1.0×10^{-8}	34.5827[b]	0.5243[b]	34.5867	34.5827	5.2429	34.9779
4	1.0×10^{-7}	36.8580	0.7462	36.8655	36.8576	7.4623	37.6055
5	1.0×10^{-6}	63.8592	1.2901	63.8722	63.8540	12.9020	65.1444
6	1.0×10^{-5}	127.4191	2.3136	127.4401	127.4037	23.1428	129.4886
7	1.0×10^{-4}	203.2214	3.6452	203.2541	203.2214[c]	36.4523[c]	206.4647
8	1.0×10^{-3}	310.2432	5.8936	310.2992	310.2432[c]	58.9364[c]	315.7916

a: Consider columns: These columns include systematic error contributions from TDRS ephemeris errors, SST ionospheric refraction errors (100%), gravity errors, and the drag errors (30% of C_D). Consider contributions for Case 1 are mostly from the drag errors, and those for Case 8 are mostly from the SST ionospheric refraction errors.

b: These results are obtained from the corresponding Group B solutions.

c: These results are obtained from the corresponding Group A solutions.

To see the influence of the ionospheric refraction and drag errors in determining the optimum Qdot-to-MNV ratio, four series of solutions were constructed in which different magnitudes of the ionospheric refraction and drag errors were assumed. The total RMS position errors based on the Group B solutions are shown in Figure 3. The x-axis of the graph indicates the case number defined in the first column of Table 4. The solid curve represents the results given in the last column of Table 4.

The solution curves split into two groups at each end of the graph. The splits at the right-hand side of the graph are due to the different ionospheric refraction errors assumed, and those at the left-hand side of the graph are due to the different

amount of drag errors assumed. Note that high SST ionospheric refraction errors and low drag errors increase the optimum value of the Qdot-to-MNV ratio. The optimum value for the Qdot-to-MNV ratio remains at 1.0×10^{-8} (Case 3) for three of the solution series, and it changed to 1.0×10^{-7} (Case 4) for the solutions represented by the broken line, which were obtained assuming high drag errors (30 percent) and more moderate ionospheric refraction errors (50 percent). Given the error sources and their relative strengths, the optimum Qdot-to-MNV ratios lie somewhere between 1.0×10^{-7} and 1.0×10^{-9} (Cases 2, 3, and 4). Since different spacecraft missions will have different relative magnitudes of the measurement-related errors (especially the SST ionospheric refraction errors) and the dynamical errors (especially the drag errors), this range of optimum Qdot-to-MNV ratios will vary from spacecraft mission to spacecraft mission. It should also be noted that, in the case of the results presented above for EUVE, the range of the optimum values of the Qdot-to-MNV ratio may have been somewhat underestimated because the gravity error contributions are not included. Inclusion of the gravity error contributions will increase the optimum Qdot-to-MNV ratio, especially when the SST ionospheric refraction errors are small.
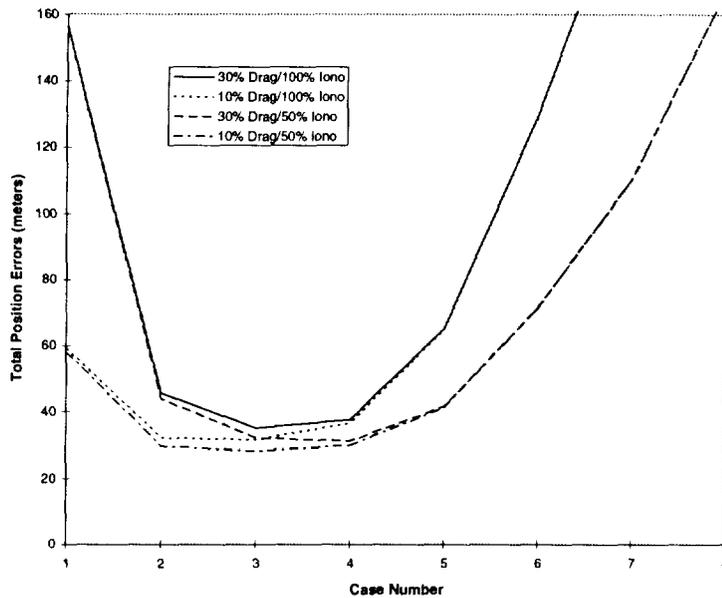
Note: Four series of solutions are shown in this graph. The case number (x-axis) indicates the Qdot-to-MNV ratio used as defined in Table 4. All four series of solutions were obtained using an MNSD of 0.01 and assuming different amounts of the atmospheric drag and ionospheric refraction errors on the SST links.

Figure 3. Influence of Drag and SST Ionospheric Refraction Errors on the Determination of Optimum Filter Tuning Parameters

When the drag coefficient is estimated, it practically eliminates the drag-related errors. Although solar flux uncertainties will still contribute to the drag error, the drag estimation process absorbs most of the solar flux errors, leaving only a small residual effect as the drag-related error contribution to the orbital error. This may be due to the limited nature of the ODEAS drag error modeling, which, for example, could not take the atmospheric effects associated with the geomagnetic storms into account. Assuming a 30-percent solar flux error, this residual solar flux uncertainty contributes less than 5 meters (3.5 meters RMS) to the orbital position errors. This drag contribution is reduced by using a finite Qdot-to-MNV ratio, but the effect is too small to counteract the sizable increase in the measurement-related error contributions, especially those due to the SST ionospheric refraction errors. Thus, it is not surprising to see that the minimum total position error was achieved with no filter tuning when the drag coefficient is estimated. This means that the optimum Qdot-to-MNV ratio for the EUVE OD scenario studied here will be smaller than the smallest finite ratio (1.0×10^{-9}) included in the study.

2.2 EOS PM-1 Study

The methods and results of the EOS PM-1 filter tuning analysis are presented below.

EOS PM-1 Methods

The major error sources included for the EOS PM-1 analysis are shown in Table 5. These error models are somewhat different from those used for the EUVE analysis. In particular, the TDRS ephemeris errors and the daily solar flux levels used for the EOS PM-1 analysis are much higher than than those used for the EUVE analysis. The EOS errror models were selected to simulate a different physical and operational environments.

Table 5. Major Error Sources Included in the EOS PM-1 Analysis

Error Sources	3σ Errors	Notes
Measurement noise	0.00118 meter/second	TDRS one-way range-rate measurements
TDRS ephemeris errors	66 meters, 60 meters, and 120 meters in the HCL directions	For both TDRS-East and TDRS-West
Ionospheric refraction errors	100% of measurement corrrection	Bent ionospheric model
Drag coefficient error	30% (when considered)	Harris-Priester model with $F_{10.7} = 250 \times 10^{-22}$ watts/meter^2/hertz
Geopotential errors	GEM-T3 30 × 30 sigmas	ODEAS UEMA model

Table 6 provides a description of two series of error analysis solutions. In the first series, designated as Series C, the EOS spacecraft state was estimated together with the USO frequency bias used for the onboard frequency reference. The atmospheric drag coefficient error was treated as a considered error source, together with the TDRS ephemeris uncertainties, gravitational potential uncertainties, and other standard error sources. The filter was tuned by applying process noise on the spacecraft velocity and the USO frequency bias. To assess how filter tuning affects the OD errors, various velocity process noise levels were applied in terms of velocity variance growth rates ranging from 5×10^{-15} meter^2/second^3 to 5×10^{-9} meter^2/second^3. This corresponds to Qdot-to-MNV ratios ranging from 5.0×10^{-9} to 5.0×10^{-3}. In all simulations, the USO frequency bias process noise level was set at a variance growth rate of 1.0×10^{-6} nanosecond^2/second^3.

Table 6. Two Series of Covariance Analysis Simulations

Simulation Case	Solve-for Parameters	Qdot-to-MNV Ratio	Velocity Variance Growth Rate for Filter Tuning
C1	EOS State, USO Bias	5×10^{-9}	5×10^{-15}
C2		5×10^{-7}	5×10^{-13}
C3		5×10^{-5}	5×10^{-11}
C4		5×10^{-3}	5×10^{-9}
D1	EOS state, USO bias, and drag coefficient	0.0	0.0
D2		5×10^{-9}	5×10^{-15}
D3		5×10^{-7}	5×10^{-13}
D4		5×10^{-5}	5×10^{-11}
D5		5×10^{-3}	5×10^{-9}

In the second series, designated as Series D, the EOS spacecraft state was estimated together with the USO frequency bias and the drag coefficient. Again, to assess the effects of filter tuning on the OD errors, various velocity process noise levels were employed with variance growth rates ranging from 0.0 (for no filter tuning) to 5×10^{-9} meter^2/second^3. This corresponds to Qdot-to-MNV ratios ranging from 0.0 to 5.0×10^{-3}. No process noise was applied to the drag coefficient or the USO frequency bias.

A daily $F_{10.7}$ solar flux level of 250×10^{-22} watts/meter^2/hertz was assumed for the Harris-Priester atmospheric density calculations throughout the analysis. Note that for Series C the drag coefficient was treated as a considered error source with an *a priori* uncertainty of 30 percent, and the effect of the daily solar flux uncertainty was not modeled. In Series D, the drag coefficient was solved for together with the EOS state, thereby eliminating the direct contribution of this error source on the OD error. However, to account for the residual effect of atmospheric-drag-related error contribution on the OD error, an *a priori* uncertainty of 30 percent in the daily solar flux was assumed. In all error analysis simulations, tracking schedules with favorable TDRSS tracking geometries were selected. A favorable TDRSS tracking geometry is realized by selecting tracking passes with high rates of change in the Doppler data during a tracking pass. This can be achieved when the orbit orientations of TDRS and EOS PM-1 are such that the angle between the TDRS vector and the EOS PM-1 orbit normal vector is close to 90 degrees. The maximum Doppler rate is achieved when this angle is 90 degrees.

EOS PM-1 Results

Table 7 summarizes the error analysis results obtained for simulation Series C. The results include the maximum and RMS position error contributions from various error sources after 1 day of tracking. The maximum position errors range from 66 meters to 604 meters (3σ), and the RMS position errors range from 32 meters to 378 meters (3σ), depending on the process noise levels used. The results show that the EOS total position error reaches a minimum for simulation C3, which uses a process noise level of 5.0×10^{-11} meter^2/second^3 (corresponding to a Qdot-to-MNV ratio of 5.0×10^{-5}). Major error sources include the ionospheric refraction from TDRS to EOS tracking links, the atmospheric drag, the TDRS ephemeris uncertainties, and the gravity potential uncertainties.

*Table 7. RMS Position Error Contributions From Various Error Sources
After 1 Day of Tracking*

Statistical Quantity	Simulation Case	3σ Position Errors (meters)						
		Total	Drag	Gravity	TDRS Ephemeris	Ionospheric Effect via TDRS-5	Ionospheric Effect via TDRS-4	Noise
Maximum	C1*	603.96	603.52	21.18	18.59	12.67	10.34	1.71
	C2*	191.99	190.71	15.24	20.36	16.53	13.65	1.92
	C3**	66.09	40.35	16.08	29.12	58.56	21.36	3.22
	C4**	137.74	21.33	24.02	125.15	118.81	20.13	5.49
RMS	C1*	377.67	377.11	15.82	9.96	6.84	4.46	1.13
	C2*	133.00	131.67	11.50	10.17	8.79	5.54	1.34
	C3**	31.74	17.27	10.47	13.93	18.07	8.04	2.27
	C4**	52.49	8.26	11.09	41.69	26.81	8.84	3.64

* Filter does not stabilize within 2 days of tracking

** Filter stabilizes after 1 day of tracking

Again, as was observed with the EUVE results, Table 7 shows that as the process noise level increases the RMS position errors resulting from the dynamic error sources (such as gravity and atmospheric drag uncertainties) decrease, while those due to measurement-related error sources (such as ionospheric refraction, TDRS ephemeris uncertainties, and measurement noise) increase. In simulation C1, using a velocity process noise level of 5×10^{-15} meter^2/second^3, the atmospheric drag uncertainty was a major error source, causing the EOS position error to increase to 604 meters after 1 day of tracking. However, with an increased velocity process noise level of 5×10^{-11} meter^2/second^3, as in simulation C3, the contribution

from the atmospheric drag uncertainty was substantially reduced, causing the EOS position errors to stabilize at less than 50 meters (3σ) after about 1.5 days of tracking. However, in this case, the OD error contribution from SST ionospheric refraction was magnified, causing it to become one of the major error sources.

Table 8 summarizes the error analysis results obtained for simulation Series D. In this series, the atmospheric drag coefficient is estimated, not considered. The results include the maximum and RMS position error contributions from various error sources after 1 day of tracking. The maximum position errors range from 36 meters to 140 meters, and the RMS position errors range from 22 meters to 57 meters, depending on the filter-tuning approach used. The results show that the total position error reaches a minimum for simulation Case D2 (i.e., using a velocity variance growth rate of 5×10^{-15} meter^2/second^3, corresponding to a Qdot-to-MNV value of 5×10^{-9}). Major error sources include the gravity potential, the ionospheric refraction effect on the TDRS-5 to EOS tracking link, and the TDRS ephemeris uncertainties.

**Table 8.   Maximum and RMS Position Errors Contributed From Various Error Sources
After 1 Day of Tracking**

Statistical Quantity	Simulation Case	3σ Position Errors (meters)						
		Total	Gravity	Solar Flux	TDRS Ephemeris	Ionospherice Effect via TDRS-5	Ionospheric Effect via TDRS-4	Noise
Maximum	D1**	58.09	19.87	9.18	55.55	3.79	3.74	0.29
	D2**	34.48	17.35	11.96	23.08	22.45	17.27	2.45
	D3**	35.76	16.18	13.74	23.25	23.89	17.16	2.46
	D4**	65.64	16.81	13.99	30.85	61.20	20.64	3.28
	D5*	139.41	23.72	7.72	126.59	120.47	20.06	5.87
RMS	D1**	30.49	13.68	4.77	26.49	2.27	2.06	0.19
	D2**	21.61	12.75	5.31	10.43	11.26	7.35	1.64
	D3**	21.89	11.94	5.74	10.57	11.35	7.12	1.66
	D4**	27.29	10.67	6.28	14.53	18.38	7.87	2.35
	D5*	56.77	10.78	3.39	47.55	27.04	9.03	3.70

* Filter does not stabilize within 2 days of tracking

** Filter stabilizes after 1 day of tracking

Again, looking at the RMS values, the EOS position errors resulting from the dynamic error sources, such as the gravity potential, decrease as the process noise level increases. The reverse trend is true for measurement-related error sources, such as the ionospheric refraction. An exception is the EOS position error contribution from TDRS ephemeris uncertainties when filter tuning is not applied (simulation D1). The RMS position error contributed by this error parameter is found to be larger in simulation case D1, where no process noise is applied, than those obtained in cases D2, D3, or D4, where certain process noise levels are applied. The exact cause for the result obtained in case D1 is not known and will require additional analysis. The other simulation cases, D2 through D5, followed the expected trend.

In case D1, where no process noise is applied, the position error stabilizes at less than 60 meters after 1 day of tracking. With some amount of process noise (Case B2 with a process noise level of 5×10^{-15} meter^2/second^3), the position error further decreases to less than 40 meters. However, any further increase in process noise levels causes the EOS position error to increase once again. For Case D5, the EOS position error does not reach a steady-state condition within 2 days of tracking. This is due to the fact that by using a relatively large process noise level, the filter behavior is now controlled primarily by the information provided by each measurement rather than by the cumulative memory provided by the filtered state, causing the orbital error to fluctuate with measurement information.

The EOS PM-1 results summarized above demonstrate that the process noise applied for filter tuning can significantly affect the orbit determination error contributions from various error sources in different ways. It was shown that, in general, the EOS position errors resulting from dynamic error sources, such as gravity potential and atmospheric drag, decrease as the process noise level increases. The reverse trend was found to be true for measurement-related error sources, such as

ionospheric refraction and TDRS ephemeris uncertainty. These findings are consistent with the theoretically expected trend noted earlier.

For Series C, the maximum position errors ranged from 67 to 604 meters, and the corresponding RMS position errors ranged from 32 meters to 378 meters, depending on the filter-tuning approach used. Optimum filter tuning was achieved using a Qdot value of 5.0×10^{-11} meter^2/second^3 (corresponding to a Qdot-to-MNV ratio of 5.0×10^{-5}). Major error sources include ionospheric refraction from the TDRS-5 to EOS tracking link, atmospheric drag, solar flux, and TDRS ephemeris and gravity potential uncertainties. For Series D, the maximum position errors ranged from 36 meters to 140 meters, and the RMS position errors ranged from 22 meters to 57 meters, depending on the filter-tuning approach used. Optimum filter tuning was achieved using a Qdot value of 5.0×10^{-15} meter^2/second^3 (corresponding to a Qdot-to-MNV ratio of 5.0×10^{-9}). Optimum process noise levels were found to be smaller than those used in Series C because of the smaller dynamic error contributions in this series. Major error sources include gravity, ionospheric refraction effect on the TDRS-5 to EOS tracking link, and TDRS ephemeris uncertainties.

2.3 Comparison of EUVE and EOS Filter Tuning Results

The optimum Qdot-to-MNV ratios found for EOS are larger than those found for EUVE solutions by approximately two orders of magnitude. For EUVE, the optimum Qdot-to-MNV ratio ranged from 1.0×10^{-7} to 1.0×10^{-9} when the drag coefficient was not estimated. The corresponding value for the EOS solutions was 5.0×10^{-5}. This is, of course, due to the significantly different conditions under which EOS and EUVE solutions were obtained, especially the different relative error magnitudes of the atmospheric drag and the SST ionospheric refraction uncertainties assumed for the two cases. The EOS solutions were obtained with relatively small SST ionospheric refraction errors and large drag errors, whereas the EUVE solutions were obtained with large SST ionospheric refraction errors and moderate drag errors. This can be seen from Table 4 (EUVE summary) and Table 7 (EOS Series C summary). In addition, the omission of the gravity error contributions and large irregular gaps in the tracking schedule will also cause the optimum Qdot-to-MNV ratios to move toward a smaller value in the case of the EUVE OD scenarios examined here.

2.4 Covariance Analysis Versus Actual Orbit Determination Results

Some actual sequential OD results are available from a recent TONS-EUVE OD analysis report (Reference 1). The solutions presented in that study were obtained using an MNSD value of 0.1 hertz, which corresponds to approximately 0.015 meter/second (in range-rate units). The process noise model used by the TONS sequential OD system is the so-called physically connected process noise model (References 5 and 6), which differs in many respects from the linear growth model used in the present study. The value of 0.1 hertz (≈ 0.015 meter/second) used for MNSD appears to be somewhat high, i.e., one-tenth of this value would be more realistic. However, attempts to use a smaller MNSD value and a proportionately smaller process noise level led to solutions in which good measurements were edited out, probably because such an OD process generates less filter-predicted measurement noise variance, the square-root of which is used for the measurement editing. Therefore, for real OD solutions, it may be acceptable and even desirable to use MNSD values larger than those used in a covariance analysis.

In general, covariance analysis cannot properly address the question of measurement editing. However, an order-of-magnitude estimate of the MNSD value to be used for actual OD solutions may be obtained by computing the prefit root-sum-square (RSS) contributions to the measurement residuals due to all measurement-related error sources. The RMS error of the range-rate measurements due to these error sources may be used for this purpose. For example, in the case of the EUVE OD arc studied here, the ionospheric refraction errors and the TDRS ephemeris errors are the major measurement-related error sources. The RMS values of the measurement errors due to these error sources are found to be 0.011 and 0.0055 meter/second, respectively. These values were obtained after excluding approximately 7 percent of the measurements for which the ionospheric refraction corrections exceeded 0.0505 meter/second. The RSS of these two values and a realistic MNSD value of 0.0014 meter/second give an adjusted MNSD of 0.012 meter/second, which is very close to the MNSD of 0.1 hertz (≈ 0.015 meter/second) used in the actual EUVE OD solutions. The final results for such an MNSD value will depend on other measurement-related error contributions not considered in this example.

A direct application of the results obtained using the ODEAS filter tuning process to the TONS sequential OD solutions is not possible, because in TONS the process noise model used is the physically connected process noise model, which is rather

different from the linear growth model implemented in ODEAS. However, an achievable OD accuracy predicted using the ODEAS model can still be compared to some extent with the corresponding solutions obtained using the TONS model. In the case of EUVE, Group B solutions presented in Table 4 can be used for this purpose. The EUVE total RMS position accuracy achievable is approximately 35 meters (see Group B Case 3 results in Table 4). However, a number of small adjustments are needed for this. First, the random noise contribution has to be adjusted, because the EUVE actual OD solutions were obtained using an MNSD of 0.015 meter/second instead of 0.01 meter/second that was used for the Group B solutions in Table 4. Second, the Group B solutions summarized in Table 4 were obtained with the atmospheric drag error considered, whereas the TONS OD solutions for EUVE were obtained with the drag coefficient solved. Assuming that contributions from other error contributions remain approximately the same when the drag is estimated, the adjusted total RMS error remains approximately the same as 35 meters. As a measure of the TONS-EUVE OD accuracy, Reference 1 reports an RMS total position difference of 30 to 35 meters between the TONS-EUVE OD solutions and the definitive EUVE solutions obtained using the Goddard Trajectory Determination System (GTDS) (Reference 1, Figure 5-3).

The results for EOS PM-1 presented earlier can be similarly adjusted to be applicable to actual OD solutions. It is reasonable to assume that the EOS-TONS OD solutions will be obtained by solving for the drag coefficient and using an MNSD of 0.015 meter/second (0.1 hertz) as was done in the EUVE TONS OD experiment. Then, the results of EOS PM-1 simulation Series D (Table 8) can be used, with adjusted random noise contribution. As discussed earlier, the scale factor for adjustment can be obtained as the ratio of the MNSD values used in actual OD and covariance analysis. This scale factor is computed to be 12.7 (i.e., 0.015/0.00118). The adjusted RMS random noise contributions are 2.42, 20.84, 21.10, and 29.87 meters, respectively, for Cases D1 through D4. Combining these with systematic error contributions, the adjusted total RMS (3σ) positions errors for Cases D1 through D4 are given by 30.58, 29.98, 30.36, and 40.39 meters, respectively. As a result, the first three simulation results are all very close to each other, but simulation D2 remains the optimum case.

3. Summary and Conclusions

A study of filter tuning techniques has been performed using the ODEAS sequential analysis capabilities. The EUVE and EOS results presented in this paper are based on processing 2 days of tracking data. The tracking data distribution for EUVE was taken from the actual EUVE tracking near January 17, 1993; for the EOS tracking data distribution, approximately 20 minutes of tracking per EOS orbit was assumed. In most of the simulation cases, the filter solutions were found to reach steady-state solutions after approximately 1 day of measurement processing. The filter tuning process was based on the ODEAS linear growth model in which the velocity variance growth rate was used to specify the process noise level.

The results demonstrated that the process noise applied for filter tuning can significantly affect the orbit determination errors contributed from various error sources in different ways. It was shown that, in general, the spacecraft position errors contributed from dynamic error sources, such as gravity and atmospheric drag uncertainties, decrease as the process noise level increases. The reverse trend was found to be true for measurement-related error sources, such as satellite-to-satellite ionospheric refraction correction uncertainties, TDRS ephemeris uncertainties, and random noise effects. The choice of optimum filter-tuning parameters, therefore, involves selecting the process noise variance growth rates in such a way that the combined contribution of the dynamic and measurement-related error sources to the OD errors is minimized. It was found that a parameter formed by taking the ratio of the Qdot value to the MNV is convenient for characterizing the statistical properties of the state estimate errors, where Qdot is the velocity variance growth rate used to specify the process noise level. MNV is the square of the MNSD specified for the tracking measurements. This parameter is referred to as the Qdot-to-MNV ratio.

OD solutions obtained using different filter tuning parameters can be characterized in terms of the Qdot-to-MNV ratio and the MNSD value used for each filter tuning simulation case. Characteristic properties of these solutions in terms of the filter tuning parameters are as follows:

• After the filter reaches steady state, state estimate errors due to all systematic (measurement-related and dynamic) error sources are essentially determined by the Qdot-to-MNV ratio only and are independent of the MNSD value used. Steady-state random noise contributions obtained using the same Qdot-to-MNV ratio and different MNSD values are proportional to the MNSD values used.

• Measurement-related error contributions increase and dynamic error contributions decrease as the Qdot-to-MNV ratio increases.

- Magnitudes of the SST ionospheric refraction correction errors and the atmospheric drag-errors were found to play important roles in determing the optimum filter tuning parameters. This means that the larger the magnitudes of the SST ionospheric refraction correction errors, the smaller the optimum Qdot-to-MNV ratio becomes; and the larger the magnitudes of the atmospheric drag-related errors, the larger the optimum ratio becomes.

- An estimated position accuracy of approximately 34 meters can be achieved for EUVE by solving for the drag coefficient, using an MNSD value of 0.015 meter, and setting the Qdot-to-MNV ratio to a value less than 1.0×10^{-9}. When the drag coefficient error is considered, a similar minimum position error can be achieved by using the same MNSD value and a Qdot-to-MNV ratio of 1.0×10^{-8}.

- For the EOS OD scenario, in which the drag coefficient is estimated and an MNSD of 0.015 meters is used, a total position accuracy of approximately 30 meters is achievable using a Qdot-to-MNV ratio of 5.0×10^{-9}. When the drag coefficient error is considered, a position accuracy of approximately 42 meters is achievable using a Qdot-to-MNV ratio of 5.0×10^{-5}.

The optimum Qdot-to-MNV ratio varies with the spacecraft orbital characteristics, tracking scenarios, and estimation parameter set selected. The properties summarized above can be used to reduce the number of simulation cases required for sequential error analysis, as there is no need to vary both Qdot and MNSD values. It is sufficient to generate one series of solutions using different Qdot-to-MNV ratios with a fixed MNSD value. Then, results based on a different MNSD value can easily be obtained from those already available by appropriately scaling the random noise contributions.

References

1. Goddard Space Flight Center, Flight Dynamics Division, 553-FDD-94/001R0UD0, *Tracking and Data Relay Satellite System (TDRSS) Onboard Navigation System (TONS) Experiment Final Report*, G. M. Horstkamp et al., prepared by Computer Sciences Corporation, March 1994.

2. A. Gelb et al., *Applied Optimal Estimation*, MIT Press: Cambridge, Massachusetts, 1974.

3. Goddard Space Flight Center, Flight Dynamics Division, 554-FDD-90/029R2UD0, *Orbit Determination Error Analysis System (ODEAS) Mathematical Specifications*, Revision 2, T. Lee and C. Yee (CSC), prepared by Computer Sciences Corporation, September 1993.

4. Stanford Telecommunications, TR93135, *Earth Observing System (EOS) Supplementary Analyses of Navigation Performance Using the TDRSS Onboard Navigation System (TONS)*, M. A. Lorenz et al., September 1993.

5. Goddard Space Flight Center, Flight Dynamics Division, 553-FDD-93/030R1UD0, *Tracking and Data Relay Satellite System (TDRSS) Onboard Navigation System (TONS) Flight Software Recommended Algorithms*, Revision 1, A. C. Long et al. (CSC), prepared by Computer Sciences Corporation, December 1993.

6. J. Wright, "Sequential Orbit Determination With Auto-Correlated Gravity Modeling Errors," *Journal of Guidance and Control*, Vol. 4, 1981, p. 304.

Evaluation and Modeling of Autonomous Attitude Thrust Control for the Geostationary Operational Environmental Satellite (GOES)-8 Orbit Determination*

W. Forcey and C. R. Minnie
Computer Sciences Corporation
Lanham-Seabrook, Maryland, USA

R. L. DeFazio
Goddard Space Flight Center
Greenbelt, Maryland, USA

Abstract

The Geostationary Operational Environmental Satellite (GOES)-8 experienced a series of orbital perturbations from autonomous attitude control thrusting before perigee raising maneuvers. These perturbations influenced differential correction orbital state solutions determined by the Goddard Space Flight Center (GSFC) Goddard Trajectory Determination System (GTDS). The maneuvers induced significant variations in the converged state vector for solutions using increasingly longer tracking data spans. These solutions were used for planning perigee maneuvers as well as initial estimates for orbit solutions used to evaluate the effectiveness of the perigee raising maneuvers.

This paper discusses models for the incorporation of attitude thrust effects into the orbit determination process. Results from definitive attitude solutions are modeled as impulsive thrusts in orbit determination solutions created for GOES-8 mission support. Due to the attitude orientation of GOES-8, analysis results are presented that attempt to absorb the effects of attitude thrusting by including a solution for the coefficient of reflectivity, C_R. Models to represent the attitude maneuvers are tested against orbit determination solutions generated during real-time support of the GOES-8 mission.

The modeling techniques discussed in this investigation offer benefits to the remaining missions in the GOES NEXT series. Similar missions with large autonomous attitude control thrusting, such as the Solar and Heliospheric Observatory (SOHO) spacecraft and the INTELSAT series, may also benefit from these results.

Introduction

The Geostationary Operational Environmental Satellite (GOES)-8 spacecraft was launched on April 13, 1994, at 06:04:02 Universal Time Coordinated (UTC). The nominal maneuver plan called for a series of six orbital maneuvers to place the spacecraft on-station in geosynchronous orbit. The first three of these maneuvers were designed to place the spacecraft in its approximate geosynchronous orbit by increasing the perigee height. Each maneuver, scheduled to be performed at apogee, are called apogee motor firings (AMF). The remaining three maneuvers, the apogee adjust maneuver (AAM) and dual trim motor firings (TMF), produced final corrections to circularize the orbit and place GOES-8 at its assigned longitude.

Actual mission support deviated from the intended nominal maneuver plan. During AMF-1, a maneuver abort was called because of excessive flange temperatures on the main satellite thruster (MST). Subsequently, a new sequence of 5 AMF maneuvers was developed for the transfer phase. The only difficulty with this scenario occurred during AMF-3, when a premaneuver abort was called due to problems with the Attitude and Orbital Control Electronics (AOCE) system, a subsystem responsible for the autonomous control of the attitude.

The MST used for AMF thrusting is part of the GOES Attitude and Orbit Control System (AOCS). The AOCS includes 12 attitude control thrusters, paired throughout the spacecraft, to provide maneuverability in the pitch, roll, and yaw directions. Figure 1 provides a graphical representation of the attitude control thruster locations. The attitude thrusters in Figure 1 represent thruster pairs designed to rotate the spacecraft around a specific body axis (2/3, yaw; 4/5, pitch; 6/7, roll).

PRECEDING PAGE BLANK NOT FILMED
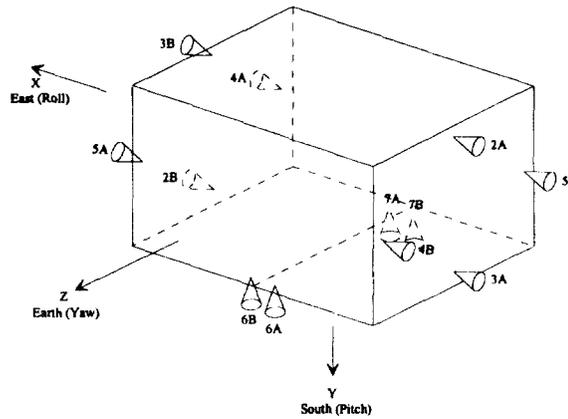
**Figure 1. GOES-8 AOCS Attitude
Thruster Configuration**

In the GOES-8 ascent phase, closed-loop attitude control is performed exclusively with thrusters as actuators. Attitude control is monitored through gyro and sensor output. A particular attitude maneuver is accomplished by an uplink command with unbalanced outputs; the AOCS responds to these offsets by initiating attitude thrust control to match the offset configuration. Once the GOES-8 spacecraft arrived on-station, control of these processes converted from thruster control to momentum wheel control.

Before each AMF maneuver during the ascent phase, attitude control thrusting was completed to configure the spacecraft for the subsequent maneuver. This control thrusting served a number of purposes, most important to 3-axis stabilize the spacecraft and orient the MST for proper delta-V placement during orbit maneuvers. These attitude maneuvers were performed at much smaller thrust levels than the AMF series of maneuvers. Ideally, these maneuvers would incur no net effects on the orbital trajectory, provided thruster pairs operated with balanced force levels and exact alignment. In reality, however, the thrusters are not perfectly balanced, and some misalignment occurs, producing orbital perturbations. This paper describes the best method to treat these autonomous maneuvers for the GOES-8 spacecraft.

The attitude "control box" is defined as the closed-loop tolerance for autonomous attitude control enlisted for a particular orientation. The size of the control box is dependent on the particular mode of attitude control and the requirements for certain sensors. For GOES-8, the control box size was considered large; in fact, real-time support encountered error margins within the same order of magnitude as the size of the control box. In Table 1, the control box sizes are presented referenced to the orientation of the body axes.

Table 1. GOES-8 Attitude Control Box Limits

Attitude Mode	Pitch (deg)	Roll (deg)	Yaw (deg)
Sun Acquisition	+/- 3.00	-	+/- 3.00
Roll Earth Acquisition	+/- 3.00	+/- 0.50	+/- 3.00
Pitch Earth Acquisition	+/- 1.00	+/- 0.50	+/- 1.00
Stationkeeping Mode	+/- 0.25	+/- 0.25	+/- 0.25

The results from real-time orbit determination support of the GOES-8 mission indicate that low-thrust forces did exist due to autonomous attitude control. These perturbations affected orbital state solutions and induced variations in the predicted spacecraft ephemerides for a sequence of solutions that were generated as the satellite approached the next orbit maneuver. The effects of autonomous attitude control are inherently difficult to model, given the imprecise nature of the timeline of events. The concepts included in this analysis evolve into separate topics to discuss possible models: (1) the dynamic representation of these effects by solving for the coefficient of solar radiation pressure and (2) the representation of discrete attitude maneuvers with impulsive thrusts.

Nominal Orbit Determination Results

Orbit determination support for the GOES-8 mission was provided by the Flight Dynamics Facility (FDF) at Goddard Space Flight Center (GSFC). The nominal support scenario for the transfer phase called for a series of the Goddard Trajectory Determination System (GTDS) batch least squares differential correction (DC) solutions to be generated before and following AMF maneuver. Each solution solved only for the epoch state vector. In the hour before an AMF maneuver was to begin, a DC solution termed the best estimated trajectory (BET) was completed to determine the most accurate orbital state before AMF burn ignition. The BET is used as an a priori for AMF thrust estimation solutions (discussed in detail later in this paper) immediately following a maneuver. The methodology involving thrust estimation yields the best available initial state estimate for postmaneuver recovery solutions. The BET solution is also employed as a tool for postmaneuver recalibration of maneuver planning products generated for each orbit maneuver. With these applications in mind, the BET accuracy is considered vital to the general support provided around orbit maneuvers. The orbital states created with the BET are also expected to have stabilized before AMF ignition. This stabilization did not occur during actual mission support; orbital state solutions leading up to a particular AMF maneuver showed significant variations approaching the formulation of the BET. It was theorized that the attitude maneuvers were the cause for this condition.

To illustrate this premise, orbit determination solutions for two premaneuver AMF cases were generated using range and Doppler observations from several tracking stations. The first case, AMF-2, was chosen due to the increase in premaneuver attitude activity prompted by the AMF-1 abort. The second case, AMF-4, was selected because this maneuver had the largest delta-V burn magnitude. In periods before these AMF maneuvers, successive orbital state solutions were completed to furnish updated vectors for acquisition data in support of the National Aeronautics and Space Administration (NASA) and Deep Space Network (DSN) antennae and to provide the foundation for maneuver planning. These series of orbital state solutions exhibited the trends suggesting an increase in attitude control thrusting activity.

The noticeable trends relating to the possibility of attitude control thrusting include increases in solve-for semimajor axis (SMA) values and large differences in ephemeris comparisons for overlapping definitive solutions. In Table 2, both parameters are presented for AMF-2 and AMF-4. The epochs for all solutions were placed near the end of the tracking data span of the specific solution. The designations for solutions (i.e., A8, P15) represent the naming conventions for each segment of the GOES mission; "A" represents the segment before AMF-2 ignition, and "P" represents the phasing orbit segment before AMF-4 ignition. The numerical values represent successive updates in the orbital state determination as a function of time.

Table 2. GOES-8 AMF Premaneuver Orbital State Solution Characteristics

Solution Name	Epoch	ΔSMA (m) at epoch	Stan. Dev. of solved-for SMA (m)	Maximum ephemeris comparison difference (m)
AMF-2				
A8	940418 : 0400	298.7	0.1492	
				5,635.3
A9	940418 : 1600	-17.5	0.4336	
				3,723.3
BET	940418 : 2220	80.3	0.2768	
AMF-4				
P15	940422 : 1900	-6.9	0.3810	
				5,032.3
P17	940423 : 0800	35.4	0.2708	
				3,742.2
P19	940423 : 1439	213.5	0.5038	
				2,824.9
BET	940423 : 1708	272.9	2.3481	

For both AMF-2 and AMF-4, the solution characteristics for the SMA and ephemeris comparisons do not stabilize as the tracking data spans approach the ignition time. Instead, AMF-2 delta SMA values at the epochs vary by as much as 300 meters (m), while maintaining a maximum definitive ephemeris consistency of 3,700 to 5,700 m. The same is true for AMF-4, as delta SMA values increase with solutions approaching burn ignition and definitive ephemeris comparisons range from 2,800 to 5,000 m. The consistent rise in SMA is counterintuitive to the effects of normal perturbative forces (i.e., atmospheric drag, solar radiation pressure), prompting the notion that an unmodeled perturbative force was influencing the solution quality. The

random nature of delta SMA values for AMF-2 and the ephemeris comparisons for AMF-4 implies that the perturbative force varied in magnitude throughout the timespans represented in the solutions, leading to the idea that autonomous attitude control thrusting is the possible source for these irregular trends.

To confirm the effects of attitude control thrusting, a definitive outline of AMF-2 premaneuver attitude control events was compiled. Attitude events were culled from mission support for the 6-hour period leading up to AMF-2 ignition and including the initial period following the completion of the maneuver. In Table 3, the largest attitude control events are listed, noting the orientation affected and the purpose of the maneuver.

Table 3. GOES-8 Pre-AMF-2 Attitude Control Maneuvers

Maneuver	Time (UTC)	Description
1	4/18/94, 18:08:00	DSS Pitch Bias : Capture Earth while maintaining sun sensor coverage
2	4/18/94, 18:53:00	DSS Yaw Bias Command : Cool MST thruster flange temperatures
3	4/18/94, 19:55:00	DSS Pitch Bias Command : Maintain Earth coverage through calibrations
4	4/18/94, 20:39:00	Pitch Earth acquisition
5	4/18/94, 22:06:00	Yaw Reorientation : Ensure AMF-2 delta-V in correct direction
-	-	Stationkeeping Mode : High thruster activity
6	4/18/94, 22:34:00	AMF-2 commences
-	-	Sun Acquisition : Return to normal Sun acquisition mode

DSS = digital Sun sensor

The attitude control thrusting outlined in Table 3 reflects possible events that could influence orbital state solutions. While only discrete events are listed, the effects of stationkeeping within a 0.25 deg control box cannot be neglected. To enhance the representation of the events listed in Table 3, Figure 2 depicts the relative position of these events in the GOES orbital plane, based on true anomaly. This figure also shows the orientation of the Sun and spacecraft. The -X axis is generally in the direction of the Sun and the +Z axis is generally in the direction of the Earth. The event designations correlate with the listing provided in Table 3.
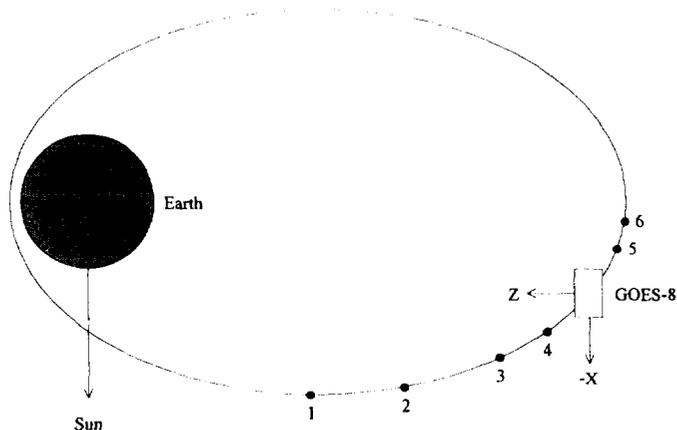
Figure 2. Representation of GOES-8 Attitude Maneuvers Within the Orbital Plane Frame of Reference

The discrete events listed in Table 3 should be visible through the examination of residuals from the DC process. These residuals would reflect instantaneous perturbative effects from range and/or range rate tracking system measurements, ruling out equipment anomalies. The strongest indication of attitude control events came from range rate residuals generated within

the BET solution. In Figure 3, the residuals for the final iteration of the BET definitive period before AMF-2 are presented for range rate tracking data measurements from the DS61 (Madrid) 34-meter DSN site. The a priori vector for this DC solution was provided by the A9 solution, created less than 2 hours before the BET. Figure 3 represents only a portion of the tracking data included for the BET solution. Additional tracking data were received from other sites, but this portion was chosen due to the clear representation of attitude effects.
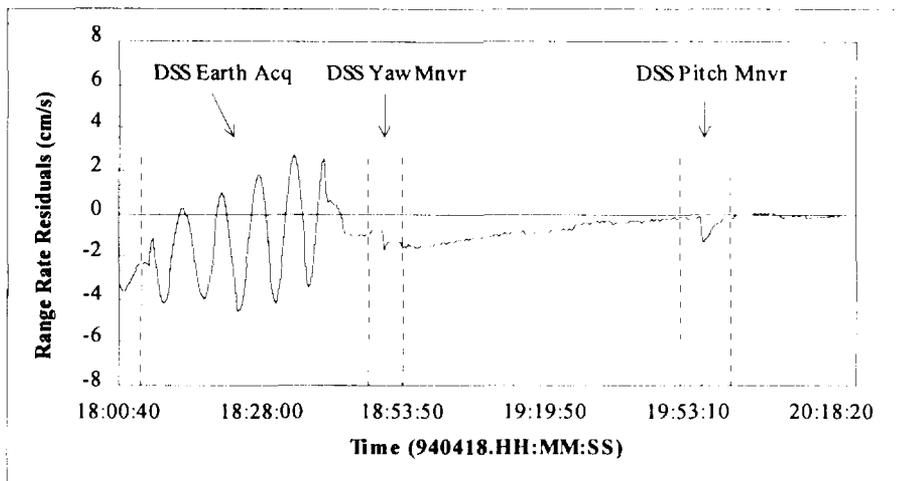
Figure 3. GOES-8 Pre-AMF-2 Final Iteration Range Rate Residuals
From Madrid (Nominal Solution)

Within the timeframe provided by the DS61 tracking data pass, the distinct effects of three attitude control maneuvers are recognized. Each residual disturbance apparent in Figure 3 correlates to an attitude control maneuver as outlined in Table 3. The first maneuver, the DSS Earth Acquisition, is a series of small burns performed to stabilize the spacecraft in 3-axis mode through Earth acquisition, hence the periodic motion of the residuals as the spacecraft oscillates in pitch. The last two maneuvers, the DSS Yaw Bias and the DSS Pitch Bias, perform secular rotations for the purposes summarized in Table 3. Because of the lack of tracking data over the period encompassing the remaining maneuvers, no residuals were generated for these events. A similar timespan of tracking was simultaneously received from the tracking station at Wallops Island, Virginia. The residuals generated from this tracking data directly correlate to events displayed in Figure 3, ruling out possible anomalies in equipment at the respective tracking stations.

With the results from AMF-2 in mind, a similar procedure was completed for the period before AMF-4. Figure 4 depicts the pre-AMF-4 residual region for the same relative time period as AMF-2. Comparable regions of residual disturbances exist between Figures 4 and 3.
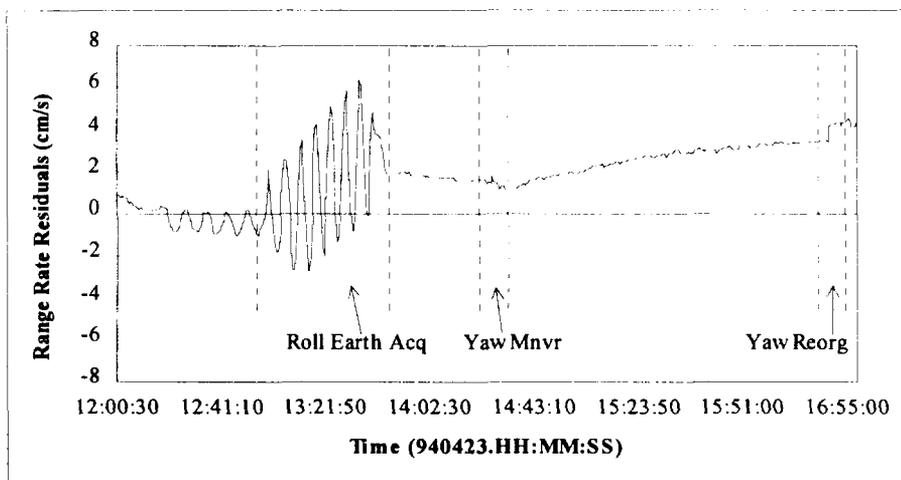
Figure 4. GOES-8 Pre-AMF-4 Final Iteration Range Rate Residuals
From Madrid (Nominal Solution)

21

The residual disturbances found in Figure 4 can be traced to a listing of the confirmed attitude events before AMF-4. Table 4 lists the discrete attitude events that correlate to the occurrences presented in Figure 4. These results establish the constant scenario of attitude control thrusting that has been confirmed for each AMF maneuver.

Table 4. GOES-8 Pre-AMF-4 Attitude Control Maneuvers

Maneuver	Time (UTC)	Description
1	4/23/94, 13:45:36	Roll Earth acquisition complete
2	4/23/94, 14:29:12	Pre-Yaw Maneuver : Cool MST flange
3	4/23/94, 15:34:36	Pitch Earth acquisition
4	4/23/94, 16:54:14	Yaw Reorientation : Place spacecraft in attitude to perform AMF-4 delta-V
5	4/23/94, 16:58:18	Pitch Reorientation : Small burn for pitch orientation
-	-	Stationkeeping Mode : High thruster activity
6	4/23/94, 17:22:58	AMF-4 commences
-	-	Sun Acquisition : Return to normal Sun acquisition mode

The attitude control events presented in Tables 3 and 4 are not the only contributing elements to the overall autonomous attitude control effect. As mentioned previously, the tight attitude control box in place during stationkeeping mode elicits a high degree of attitude thrusting activity. The effects of attitude control are also not limited to the period of time immediately before an AMF maneuver. While not at the same magnitude as pre-AMF activity, attitude thrust control effects were experienced throughout the mission. The effects subsided with the conversion of attitude control to momentum wheels.

With the recognition of autonomous attitude control effects on orbital state solutions comes the question concerning the modeling of these effects. For this analysis, two approaches are assessed: dynamic solar radiation pressure modeling (i.e., solving for C_R) and impulsive thrust modeling.

Orbit Determination Results That Include a Solution for C_R

One possible approach to modeling the perturbative effects of the attitude thrust control is using dynamic solar radiation pressure force modeling. This modeling approach is appropriate for this investigation because GOES-8 attitude is Sun-referenced (Figure 2) and most residual delta-V will be applied along the Sun or anti-Sun pointing vector. The GTDS software includes the capability to solve for C_R in the DC process. The mathematical equation governing the relationship between C_R and the acceleration due to solar radiation pressure is as follows:

$$\ddot{\overline{R}}_{SR} = \nu\, P_s\, R_{sun}^2 \frac{C_R A_{Ref}}{m} \frac{\overline{R}_{sv}}{R_{sv}^3} \tag{1-1}$$

where $\ddot{\overline{R}}_{SR}$ = acceleration due to solar radiation pressure

ν	=	Eclipse factor ($0 < \nu < 1$)
P_s	=	Constant (solar flux at 1 AU / speed of light)
A_{Ref}	=	Spacecraft cross-sectional area
m	=	Spacecraft mass
R_{sun}	=	Earth - Sun vector
R_{sv}	=	GOES-8 - Sun vector

The solar radiation pressure force acts along the Sun-spacecraft vector. The physical limitations of C_R range from 0 to 2 (with 0 representing a body with no momentum transfer due to photons and 2 representing a completely reflective body). During the early phases of the GOES-8 mission, solving for C_R was avoided due to the relatively high eccentricity of the orbit [e = 0.738 (pre-AMF-2)] and the smaller values of SMA. The high eccentricity requires the satellite to travel within two separate regions in which different perturbative forces are significant; at perigee, the satellite experiences a higher magnitude of atmospheric drag, while at apogee, solar radiation pressure is significant. This method does, however, have some advantages. Without the benefit of other solve-for parameters, a solve-for C_R corrects for any and all existing perturbations on the spacecraft that have similar characteristics to that of the force due to solar radiation pressure.

22

During real-time orbit determination support, modeling of solar radiation pressure was limited to the use of a nominal value of C_R in the integration of the satellite equations of motion. For the GOES mission, this value was determined to be 1.5 (Reference 1). Testing of C_R solve-for solutions commenced with analysis of the AMF-4 premaneuver scenario. The solution scenario presented through results in Table 2 were reevaluated through dynamic solar radiation modeling. In each case, the coefficient of reflectivity was solved for in addition to the orbital state. The resulting ephemeris was then compared to the corresponding nominal ephemeris from mission support as well as common intervals of the prior ephemeris, which solved for C_R. These results appear below in Table 5.

Table 5. GOES-8 Pre-AMF-4 C_R Solve-for Results

Solution	Epoch	C_R	C_R Stan Dev	Maximum Ephemeris Position Difference (m)	
				C_R and Nominal Solutions	Successive C_R Solutions
P15	4/22/94 : 1900	28.049	0.0144	2,564.6	
					3,506.7
P17	4/23/94 : 0800	30.190	0.0276	588.6	
					251.9
P19	4/23/94 : 1200	22.440	0.1280	632.5	
					13,771.5
BET	4/23/94 : 1708	-25.824	0.0670	4,108.9	

From the results in Table 5, the influence of indeterminate perturbative forces outside of solar radiation pressure can be established. The solve-for values of C_R range far above the nominal value of 1.5 and exceed the constraints that define the physical application of the solar radiation effects. To quantify the exact perturbative acceleration attributed to solar radiation pressure, the relationship presented in Equation (1) can be used. Table 6 presents accelerations that were generated using the solve-for values of C_R outlined in Table 5 in conjunction with Equation (1).

Table 6. GOES-8 Accelerations Due to Solar Radiation
Pressure for Pre-AMF-4 Solutions

Solution	Solve-for value of C_R	Acceleration from C_R model (m/s^2)
P15	28.049	9.99e-07
P17	30.190	1.07e-06
P19	22.440	8.00e-07
BET	-25.824	9.20e-07

The nominal range of accelerations attributed to solar radiation pressure lies between 5.0e-08 to 5.0e-09 m/s^2 (Reference 2), taken from a random distribution of satellite missions previously launched into orbit. The results obtained from solutions created for GOES-8 are at least one full order of magnitude greater than the nominal range. This discrepancy indicates that solving for C_R is compensating for perturbations beyond solar radiation pressure. This is substantiated by premission covariance analysis, in which attitude thrusting was modeled with an acceleration magnitude of approximately 1.45e-06 m/s^2 (Reference 1). This value, with nominal solar radiation pressure effects included, corresponds to within 20 to 30 percent of the solve-for values for solar radiation pressure force acceleration from real-time mission support. Given the large disparity between predicted and actual values for solar radiation accelerations, the conclusion that attitude effects are distinctly perturbing the orbital trajectory can be established.

A counterpoint to the notion that attitude effects are the primary reason for the large solve-for values of C_R lies in the possible effects of atmospheric drag. Inspection of the orbital elements for the pre-AMF-4 period suggests that drag will not influence the use of C_R. In this phase of the GOES-8 mission, the apogee height was approximately 49,000 km, and the perigee height 13,660 km. Within this region, drag effects are presumed minimal. This assumption was reinforced through tests that solved for the effects of drag.

Beyond the recognition of distinct perturbative effects, the introduction of C_R as a modeling tool for attitude control effects stabilized the results of the DC process in orbit determination solutions. The DC process generates a number of statistics regarding the convergence quality of an orbital state solution. One set of these statistics involves the tracking data residual

quality. For GOES-8, the two major tracking data types were Universal Ranging (URAN) and Universal Range Doppler Format (URDF). In analyzing the standard deviation, σ, and the root-mean-square (RMS) of these residuals, the quality of the respective tracking data fits can be interpreted. In Table 7, the residual standard deviations are presented for the nominal solutions and those that solve for C_R.

Table 7. GOES-8 Tracking Data Residual Standard Deviations for Pre-AMF-4 Orbital State Solutions

Solution	Nominal Solution				C_R Solve-for Solution			
	URAN σ (m)	URAN RMS	URDF σ (cm/s)	URDF RMS	URAN σ (m)	URAN RMS	URDF σ (cm/s)	URDF RMS
P15	04.861	0.228	1.572	0.186	1.604	0.080	0.167	0.017
P17	02.588	0.130	0.944	0.108	1.067	0.083	0.163	0.016
P19	02.890	0.145	0.777	0.078	2.014	0.101	0.336	0.034
BET	22.780	1.134	4.371	0.447	3.798	0.190	0.938	0.094

From the results in Table 7, initial conclusions can be drawn concerning the positive effects of solving for C_R. In each solution, there is a substantial reduction in the standard deviation for the residuals of the respective data types. Standard deviation values for URAN tracking decrease by an average of 60 percent, while the URDF standard deviation values fall by an average of 80 percent. In addition to this study of residual tracking results, some insight can be gained through the analysis of the final orbital state correction produced in the DC process. For each solution leading up to AMF-4 ignition, the difference in the converged orbital state (Cartesian position) between the C_R-modeled and nominal solution increases. These state corrections range in magnitude from 424.3 m for the P15 solution to 4,863.8 m for the BET solution. This suggests an increase in the perturbative effects modeled through the C_R solve-for method. In addition, standard deviation results from the orbit determination solutions reveal improved tracking data fits produced with the C_R solve-for method. Table 8 displays these results for pre-AMF-4 orbit determination solutions.

Table 8. GOES-8 Pre-AMF-4 Orbital State Statistics

Solution	Standard Deviation of Total Position (m)		Reduction in Average Standard deviation (%)
	Nominal Solution	Solve-for C_R Solution	
P15	03.633	01.027	71.731
P17	01.787	01.063	40.487
P19	03.226	02.081	35.484
BET	27.327	13.527	50.500

The results in Table 8 again indicate that a perturbing force is inducing effects on DC solutions. With the assistance of dynamic C_R modeling, the solutions appear to produce a better representation of the observations. Similar results were generated for pre-AMF-2 solutions.

These DC process results can also be analyzed through representation of the tracking data residuals. In Figure 5, the residuals from a dynamic C_R-modeled solution are displayed over approximately the same timespan as Figure 3. As with the nominal orbit determination solutions, only Doppler residuals are presented because they are more sensitive to the attitude maneuvers. One interesting characteristic of Figure 5 is the instantaneous variations that exist in the residuals, most notably during the roll Earth acquisition sequence.

24
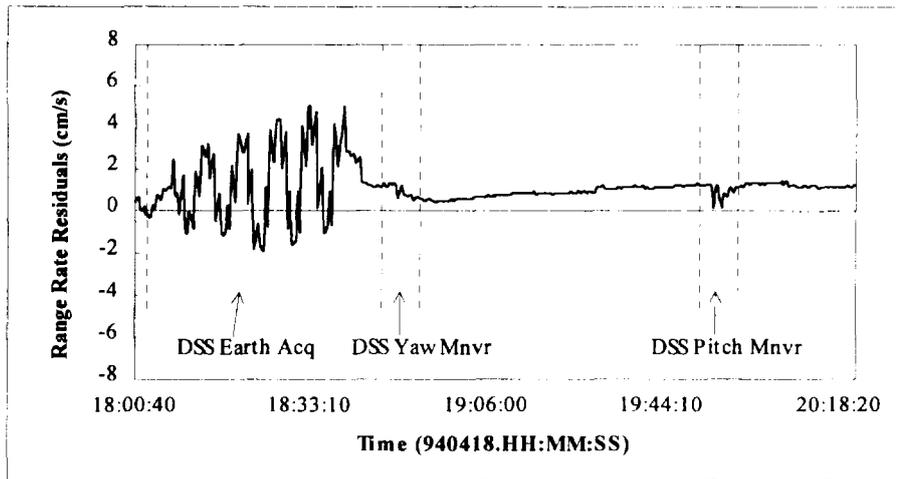
Figure 5. GOES-8 Pre-AMF-2 BET Final Iteration Range Rate Residuals From Madrid (C_R Modeled Solution)

The overall use of dynamic solar radiation pressure modeling has proven to be effective in mitigating the effects of autonomous attitude thrust control for GOES-8. One of the most convincing arguments for its use appeared after the autonomous attitude thruster control ceased. In orbital state solutions following the transition of momentum control to wheels, C_R values stabilized from the 20 to 30 range to steady values in the 1.2 to 1.4 range. These values are comparable to predicted estimates generated during premission analysis (Reference 1).

Orbit Determination Results that Model Attitude Maneuvers as Impulsive Thrusts

Impulsive thrust modeling presents a second possible method for approximating the effects of attitude control thrusting. In this method, discrete events in the series of attitude control maneuvers before the AMF burns are treated as impulsive maneuvers. The impulsive thrust model (ITM) used in GTDS requires the user to define one or more impulsive delta-Vs that are added to the state vector calculated at the maneuver epoch. This process requires knowledge of the attitude of the spacecraft and the orientation of the attitude thrusters relative to the body centered coordinate system shown in Figure 1.

The first test of modeling the attitude maneuvers as impulsive thrusts involved a procedure that simply propagated the state vector from the BET of the nominal solution. This propagation process included adding the impulsive delta-Vs at the appropriate times. This initial test did not involve orbit determination but simply propagation that includes impulsive thrusts to represent attitude maneuvers. This process allows an immediate evaluation of the effects of the approximated attitude maneuvers on the SMA. The delta SMA results from actual orbit determination solutions are presented in Table 2.

This procedure was carried out for both AMF-2 and AMF-4 with the delta-Vs outlined in Tables 3 and 4, with the exception of the roll Earth acquisition sequence. The nature of this specific maneuver should involve modeling with a time history and is, therefore, not appropriately represented by an impulsive thrust. Table 9 presents the results of the changes in several of the Keplerian parameters due to the inclusion of the impulsive representation of the attitude control maneuvers. The values represent Keplerian parameters before the initial modeled attitude maneuver relative to the Keplerian parameters following the completion of the final modeled attitude maneuver.

Table 9. Keplerian Element Variations Due to Impulsive Attitude Events for AMF-2 and AMF-4

Impulse (m/s)	ΔSMA (km)	ΔSMA/SMA	Δecc	Δecc/ecc	Δinc (deg)	Δinc/inc
AMF-2						
10	273.6179	0.0097	-0.0109	-0.0145	-0.0119	-0.0005
1	26.9363	0.0010	-0.0011	-0.0015	0.0049	0.0002
.1	2.7235	9.66e-05	-0.0001	-0.0002	0.0067	0.0003
.01	0.3067	1.09e-05	-3.73e-05	-5.06e-05	0.0068	0.0003
AMF-4						
10	377.3714	0.0120	-0.0144	-0.0255	-0.1239	-0.0111
1	36.8620	0.0012	-0.0015	-0.0026	-0.0134	-0.0012
.1	3.4763	0.0001	-0.0002	-0.0004	-0.0021	-0.0002
.01	0.1443	4.61e-06	-8.50e-05	-0.0002	-0.0010	-8.74e-05

The changes in SMA noted in Table 9 indicate that the attitude control maneuvers produce an orbit-raising effect. This correlates to the information presented in Table 2 from real-time mission support. While the full complement of pre-AMF attitude control maneuvers is not included in the ephemeris created with the impulsive thrusts, the results lead to the conclusion that attitude thrusting can provide changes in the orbital parameters that are comparable to results generated during the GOES-8 mission.

The implementation of this concept would best occur while the BET is being created. With possible attitude effects modeled in this solution, the most accurate orbital state before the orbit maneuver is achieved. However, the concept of autonomous thrust control promises difficulty with implementation of this scheme. As mentioned previously in this paper, the stationkeeping mode immediately before orbit burn ignition produces non-orbit neutral attitude effects that cannot be distinguished discretely.

A better method of representing the attitude maneuvers is to include the impulsive thrusts in the generation of the trajectory that is used to estimate a best-fit orbit state as part of a DC solution. This procedure was applied to the pre-AMF-4 solution. The residuals associated with this solution are shown in Figure 5, over the same time period as presented in Figure 3.
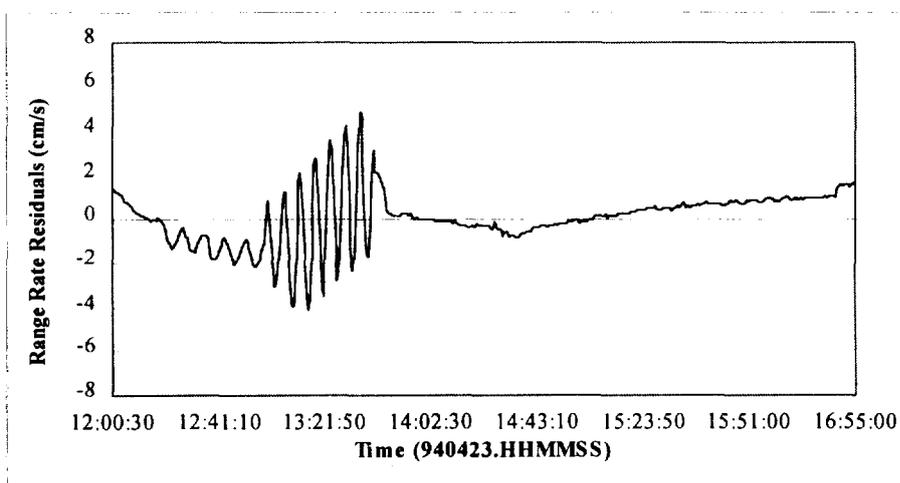
*Figure 6. GOES-8 Pre-AMF-4 Final Iteration Range Rate Residuals
From Madrid (Impulse Modeling)*

In Figure 6, positive effects from the introduction of impulse modeling can be distinguished. There is a clear reduction in the residual size when comparing the results from Figure 6 with those presented in Figure 4. While the unmodeled roll Earth acquisition sequence remains in the same residual magnitude range, the residuals encompassing the modeled attitude maneuvers decrease. Given the use of batch least squares approximations in the DC process, the success of this methodology would appear as a general decrease in the residual magnitudes.

The above discussion has indicated that the use of impulsive modeling can characterize the effects of attitude thrust control. The single drawback to using these methods of representing the attitude maneuvers results from the inability to model the high frequency of autonomous attitude thrusting occurring in the stationkeeping mode.

Thrust Estimation

With analysis completed on several treatments of attitude thrust control, these ideas were implemented for a real time orbit determination scenario. During mission support, one FDF requirement is to provide real-time postmaneuver orbit determination solutions as quickly as possible. Generally, the amount of tracking data available in the allotted period following a maneuver is insufficient to generate accurate orbital states. Two techniques are incorporated to overcome the limitations on the amount of tracking data and the time available to obtain a postmaneuver solution. First, constraints are placed on the a priori values of SMA and mean anomaly. This implies the need for the best possible estimate for the constrained parameters, hence the need for the BET. Second, the GTDS allows for the use of a maneuver thrust model (MTM)

that patterns the effects of an orbit maneuver. Instead of applying an impulsive delta-V, this model incorporates time-dependent nominal accelerations applied to the spacecraft by control thrusters throughout the execution of an orbit maneuver.

During mission support, a General Maneuver Program (GMAN) file is created to represent the nominal thrust acceleration for each AMF maneuver. The GTDS solves for a spacecraft orbital state using tracking data before, during, and after the maneuver with the accelerations due to the maneuver read from the GMAN file. During operational support, the GMAN predicted acceleration file for a particular maneuver is created before the completion of the BET. Therefore, any discrepancies that exist between the BET and the orbital state used to create the GMAN burn file would possibly reflect on the accuracy of thrust estimation.

To estimate differences in the nominal thrust model and that indicated by a solution from tracking data before, during, and after the maneuver period, a perturbative solve-for exists within GTDS modeling capabilities. The thrust coefficient, C_T, is a scaling factor for the nominal thrust model and compensates for disparities that exist between the GMAN burn file and the orbital state corrections reflected by tracking data. Table 10 presents results taken from thrust estimation solutions utilizing a priori vectors created with dynamic C_R models and the nominal support case.

Table 10. Thrust Coefficient Solve-for Values for AMF-2 and AMF-4

A Priori Vector	Thrust Coefficient (C_T)	
	AMF-2	AMF-4
Nominal	-0.01387	-0.006439
C_R	-0.01377	-0.006088

The reduction in C_T for AMF-2 and AMF-4 is 0.72 percent and 5.4 percent. In the process of completing thrust estimation, an ephemeris using the GMAN burn file is created that models the maneuver period. Comparisons were generated using the C_R modeled thrust ephemeris and the nominal thrust ephemeris. For AMF-4, the delta-r value between the ephemerides before the maneuver was nearly constant at 4.1 km, which is approximate to the converged orbital state difference of 4.9 km exhibited between the C_R and nominal DC solution. Postmaneuver comparisons, however, revealed that the delta-r values between the two ephemerides rose to 32 km after 12 hr, and 51 km after 24 hr. These comparisons were repeated for the AMF-2 maneuver scenario; the results revealed a constant premaneuver comparison of 2.5 km, along the same order as the 2.4-km comparison generated in C_R BET testing. The postmaneuver comparisons for AMF-2 reached a magnitude of 6.0 km after 24 hr. These results reveal the effects that small discrepancies in C_T can produce given large-scale delta-v values for AMF maneuvers.

Summary

This paper has analyzed the effect of autonomous attitude control maneuvers on orbit determination of the GOES-8 spacecraft during the early orbit phase of the mission. Neglecting these attitude maneuvers can lead to relatively poor orbit determination results, while attempting to model them is inherently difficult due to the unknown characteristics of many of the individual maneuvers.

The design of the spacecraft and mission resulted in delta-v from attitude maneuvers to lie mostly on the Sun-to GOES-8 vector. This specific feature permits a simplified procedure for modeling the autonomous maneuvers by solving for the coefficient of radiation pressure to help absorb the accelerations due to the maneuvers.

The analysis has been divided into four cases. First, "nominal" orbit solutions have been obtained by ignoring all maneuvers and generating an orbit solution from range and Doppler tracking data from the Madrid, Wallops Island, and Canberra ground sites. Second, orbit solutions have been created from the same tracking data but these include a solution for the coefficient of radiation pressure to help absorb the effects of the attitude maneuvers. Third, orbit solutions have been generated that model most of the autonomous maneuvers as impulsive thrusts. Finally, solutions were generated that assume a finite burn period with a nominal magnitude and direction for a perigee raising maneuver, but they estimate a scale factor for the magnitude of the maneuver.

Conclusions

Attitude maneuvers for the early orbit phase of GOES-8 produced a significant effect on the real-time mission orbit determination solutions. The analysis in this investigation has shown the following characteristics.

Case 1. Solutions that do not model attitude maneuvers (nominal solutions)

> a. A series of solutions leading up to the BET indicate an increase in the converged SMA of the GOES-8 orbit. This suggest the existence of an unmodeled perturbation.

> b. The trends in the residual patterns of these solutions also indicate the existence of an unmodeled perturbation.

Case 2. Solutions that solve for the coefficient of radiation pressure

> c. These solutions produced solved-for values of C_R (20 to 30) that greatly exceed the nominal limits for this parameter (0 to 2). This further substantiates the existence of an unmodeled perturbation.

> d. The standard deviation of the residuals for solutions that solve for C_R are nearly an order of magnitude smaller than for the corresponding nominal solutions in Case 1.

> e. The RMS for the solved-for orbital state components are substantially smaller than those of the nominal solutions.

Case 3. Solutions that model attitude maneuvers as impulsive thrusts

> f. Modeling attitude maneuvers as impulsive thrusts and adding the corresponding instantaneous velocity increments to an orbit propagation (not an orbit determination solution) produced increases in the SMA of the GOES-8 orbit. This further substantiates the idea that the attitude maneuvers produced unmodeled perturbations in the nominal solutions.

> g. Orbit determination solutions that include a modeling of the attitude maneuvers as impulsive thrusts produce the smallest RMS and standard deviation of residuals with no significant deviation from a zero mean.

Case 4. Solutions that solve for the magnitude of the perigee raising maneuver

> h. Comparing thrust-modeled ephemerides based on varying a priori vectors (nominal, C_R) produced sizable position differences that correlated with orbital state correction discrepancies.

> i. Small changes in C_T produced by using C_R-modeled a priori vectors created substantial postmaneuver differences in ephemeris comparisons with nominal thrust solutions.

Recommendations

The results of this investigation suggest that a decision will need to made concerning which methodology should be endorsed to model autonomous attitude maneuvers for spacecraft with similar characteristics to GOES-8. The best fit to the tracking data results from solutions that model the attitude maneuvers in the orbit determination process. If, however, impulsive thrust modeling is not a software option, then solving for C_R produces a distinct improvement in the orbit solutions for spacecraft with an attitude orientation similar to that of GOES-8. Both techniques render superior orbit fits to solutions that ignore the existence of the attitude maneuvers.

Acknowledgments

28

References

1. Computer Sciences Corporation, "Report on Error Analysis for the Transfer Orbit Phase of the Geostationary Operational Environmental Satellite (GOES) (memorandum)," A. Schanzle, J. Rovnak, and D. Oza, August 1993

2. Goddard Space Flight Center, Flight Dynamics Division, FDD/552-89/001, *Goddard Trajectory Determination System (GTDS) Mathematical Theory (Revision 1)*, A. C. Long, J. O. Cappellari, C. E. Velez, and A. J. Fuchs, July 1989

3. A. Milani, A. M. Nobili, and P. Farinella, *Non-Gravitational Perturbation and Satellite Geodesy*, A. Hilger, 1987

4. F. P. J. Rimrott, *Introductory Orbit Dynamics*, Vieweg, 1989

Differenced Range Versus Integrated Doppler (DRVID) Ionospheric Analysis of Metric Tracking in the Tracking and Data Relay Satellite System (TDRSS)*

M. S. Radomski
Computer Sciences Corporation
Lanham-Seabrook, Maryland, USA 20706

C. E. Doll
National Aeronautics and Space Administration
Goddard Space Flight Center
Greenbelt, Maryland, USA 20771

Abstract

The Differenced Range (DR) Versus Integrated Doppler (ID) (DRVID) method exploits the opposition of high-frequency signal versus phase retardation by plasma media to obtain information about the plasma's corruption of simultaneous range and Doppler spacecraft tracking measurements. Thus, DR Plus ID (DRPID) is an observable independent of plasma refraction, while actual DRVID (DR minus ID) measures the time variation of the path electron content independently of spacecraft motion.

The DRVID principle has been known since 1961. It has been used to observe interplanetary plasmas, is implemented in Deep Space Network tracking hardware, and has recently been applied to single-frequency Global Positioning System user navigation. This paper discusses exploration at the Goddard Space Flight Center (GSFC) Flight Dynamics Division (FDD) of DRVID synthesized from simultaneous two-way range and Doppler tracking for low Earth-orbiting missions supported by the Tracking and Data Relay Satellite System (TDRSS).

The paper presents comparisons of actual DR and ID residuals and relates those comparisons to predictions of the Bent model. The complications due to the pilot tone influence on relayed Doppler measurements are considered. Further use of DRVID to evaluate ionospheric models is discussed, as is use of DRPID in reducing dependence on ionospheric modeling in orbit determination.

Introduction

This paper describes preliminary investigations of the Differenced Range (DR) Versus Integrated Doppler (ID) (DRVID) technique. DRVID uses the bandwidth of the coherent ranging signal to extract information about ionospheric delays from the comparison of simultaneous range and nondestruct Doppler observations, much as dual-frequency tracking compares two range or two Doppler observations. The idea is not new (Reference 1), but its application in the Goddard Space Flight Center (GSFC) Flight Dynamics Division (FDD) is. This investigation explores the quality and other properties of DRVID comparisons made using Tracking and Data Relay Satellite (TDRS) System (TDRSS) and Ground Network (GN) tracking data available at the GSFC Flight Dynamics Facility (FDF).

The paper is organized in sections that describe, respectively, the physical basis of DRVID, the analysis techniques, the results, and the conclusions of the investigation.

DRVID Background

The TDRSS or Unified S-Band (USB) two-way range observation is given by

$$R = \tfrac{1}{2}\left[R_L + I_L + T_L + D_L + E_L\right] \tag{1}$$

where

R_L = long path length, i.e., the round-trip distance to the user (a spacecraft or a ground transponder of the Bilateration Ranging Transponder System (BRTS)) and back via a relaying TDRS (if using TDRSS).

I_L, T_L, D_L = respective biasing effects of ionospheric, tropospheric, and residual transponder delays on signal propagation. D_L is constant during a tracking contact; any actual time variation in system delays is classified as belonging to E_L, below.

E_L = effect of other measurement errors, such as extraction error and noise (including unbiased effects of ionospheric scintillation).

R = total observation obtained by multiplying a measured round-trip time by the velocity of light, dividing by 2, and subtracting nominal user-transponder delay effects.

Successive range measurements can be differenced to synthesize the differenced range (DR)

$$DR = \Delta R \tag{2}$$

where Δ in Equation (2) and throughout this paper signifies differencing across the Doppler count interval corresponding to a contemporaneous Doppler observation.

Coherent nondestruct two-way Doppler observations measure finite differences of R_L by comparing the number of carrier wave fronts arriving in a Doppler count interval, ΔT, with the number transmitted in the same time span. If the Integrated Doppler (ID) is defined as

$$ID = -\frac{c\Delta T}{2A}D \tag{3}$$

where c is the velocity of light, A is the user-transmit frequency, D is the nondestruct Doppler observation, and ΔT is the Doppler count interval; then ID is a differenced observation

$$ID = \Delta r \tag{4}$$

of the phase-measured range

$$r = \tfrac{1}{2}\left[R_L - I_L + T_L + D_L + e_L + b\left(R_S - I_S + T_S + D_S + e_S\right)\right] + C_r \tag{5}$$

The quantities on the right-hand side of Equation (5) are defined as follows:

• The constant C_r is arbitrary, because r can only be defined by partial summation of Δr; summed integrated Doppler (SID) observations measure r within a constant.

• The quantity D_L is the transponder phase delay effect (a constant, by definition, so that $\Delta D_L = 0$). In principle, this may differ from D_L in Equation (1) due to frequency dependence in the transponder delays. Any difference is time independent and is subsumed into the integration constant C_r.

• The error e_L is the phase-measurement error, differing from E_L because the Doppler extraction hardware is distinct from the range extraction hardware. The noise components within e_L and E_L are presumed independent.

• The quantities subscripted S correspond to those subscripted L but apply to the short path, or the return-link pilot round-trip loop of TDRSS observations rather than to the long relay round-trip. The short path goes from the receiving terminal to the TDRS and directly back, arriving simultaneously with the relayed signal. These quantities appear because the frequency translations applied to the signal by the relay are derived from the Doppler-shifted pilot tone broadcast by the receiving station.

- The quantity b is the ratio of the pilot frequency, B, to A. This ratio, constant for any given tracking contact, is about 5 for S-band single-access (SA) observations, about -1 for multiple-access (MA) observations, and 0 for non-TDRSS observations.

The negative sign before I_L and I_S in Equation (5) is a consequence of the inverse-square frequency dependence of the signal delays caused by the free-electron plasma of the ionosphere. This is in contrast to the nearly frequency-independent delays T_L and T_S caused by the bound electrons of the neutral troposphere. Because the frequencies of the links between the TDRS and the ground terminal are K-band (11 to 15 gigahertz), I_S is negligible compared with I_L, and the latter is dominated by the contribution of the S-band legs connecting the user to the TDRS.

Ground Network (GN)

For nonrelay tracking, the pilot term is absent. It is then possible to synthesize from simultaneous range and Doppler tracking the two data types (setting $b=0$):

$$DRPID \equiv \tfrac{1}{2}(DR + ID) = \tfrac{1}{2}\Delta\left[R_L + T_L + \tfrac{1}{2}(e_L + E_L)\right] \tag{6}$$

$$DRVID \equiv \tfrac{1}{2}(DR - ID) = \tfrac{1}{2}\Delta\left[I_L + \tfrac{1}{2}(E_L - e_L)\right] \tag{7}$$

The first of these is ionospherically unbiased, and the second is spacecraft independent. Note that the DRPID measurement set is equivalent to the measurement set obtained by calculating ΔI_L from Equation (7) and applying it to either DR or ID.

The DRPID dataset may be free of ionospheric bias but otherwise combines the worst features of the range and Doppler datasets. It has the noise of the range differences, yet shares with the Doppler data their lack of range zero-set information. The former problem can be ameliorated by summing the DRPID data, which filters the noise. This summed DRPID data (SDRPID) has about half as much noise as the original range data but still lacks zero-set information for each pass. This is crucial for orbit determination of a geosynchronous spacecraft, such as a TDRS, which requires unbiased range information to determine the east-west position. For a low Earth-orbiting (LEO) spacecraft, the necessity of solving for a range bias for each pass is not necessarily a heavy burden.

Orbit determination using the SDRPID data, discarding the SDRVID, avoids ionospheric error but may increase total error (see the above paragraph). It has been suggested (Reference 2) to reuse the original low-noise, approximately ionospherically corrected Doppler dataset together with SDRPID. This makes sense if the original Doppler frequencies are not summed. The white frequency-noise ionospheric error model implicit in this Doppler treatment corresponds to a random-walk error model for I_L. This is more realistic than white I_L noise given the correlated nature of error in modeling I_L. The sensitivity of orbit estimation using uncorrelated-error assumptions to the ionospheric frequency shift may thus be less than that to the corresponding range error.

DRVID (Equation (7)) data are themselves of no direct use for orbit determination, but they contain information about the ionospheric biases. Spacecraft and tropospheric effects, as well as other systematic errors common to pulse-delay and phase-delay measurement, cancel in the DRVID subtraction. DRVID is a measurement (with error from $(E_L - e_L)$) of the ionospheric Doppler correction. Summed DRVID data (SDRVID) measures the range correction (modulo an arbitrary constant bias for each pass). DRVID information can help validate ionospheric correction algorithms and models of ionospheric error.

The summed form of DR ± ID is most useful for the current purposes. The noise of DR ± ID measurements is dominated by that of the DR component, with correlations implied by its origin as successive differences of independent range measurements. Summing removes the effect of these correlations, if the resulting sequence is treated as biased. The correlation induced by summing the Doppler component is much smaller. In fact, the Dopplers may be *less* correlated in summed form, since the Doppler count is a coherent phase measurement (Reference 3). In addition, the Bent model for the ionospheric correction (used in the Goddard Trajectory Determination System (GTDS)) provides I_L, from which ΔI_L is calculated for Doppler correction. The comparison between real and modeled ionospheric corrections is thus more straightforward in summed DRVID than in the unsummed form.

Orbit determination accuracy benefits passively from the DRVID principle, since estimation processes implicitly compare the range and Doppler data. The sign opposition of the I_L terms in Equations (1) and (5) is effective whether or not the user deliberately exploits it. Under certain idealized conditions of symmetry in the treatment of the range and Doppler

measurement streams, there is automatically no effect of the ionosphere on orbit determination (except as it may affect data selection). These conditions are the following:

1. The ranges are converted into DR or the Dopplers are partially summed to SID.
2. If the latter, both a range bias and a Doppler-sum bias are solved for.
3. The weights of the range and SID (or DR and ID) are equal in the diagonal weight matrix.
4. The range- and Doppler-derived measurements are accepted and edited in matched pairs.

Under these conditions, a formal transformation of the range- and Doppler-derived measurements into their sum and difference (DR ± ID or their partial sums) leaves their covariance matrix diagonal. (This formal transformation is only a device of mathematical proof and need not be implemented in the numerical solution methods.) Equations (6) and (7) show that the normal equations then decouple into ionospheric and spacecraft sectors. Not only would ionospheric error have no effect on the orbit determination, but a large number of ionospheric variables (potentially as many as the number of observation pairs) may be solved for without impact, except possibly through editing, on the orbit determination sector. Enforcing conditions 1 through 4 is a way of achieving DRPID-only (or SDRPID-only) orbit estimation passively.

The above conditions (particularly the first) are not those under which orbit determination is normally performed (although the second alternative in condition 1 *should* be the norm if Doppler phase noise dominates frequency noise). Nor are these conditions optimal, because range noise is far greater than Doppler noise, even when the latter is summed. Furthermore, it may not be desirable to discard the range zero-set information by differencing or bias-solution. However, the above theorem shows that the measurement information already existing in standard two-way range and Doppler measurements is adequate to support the solution for multiple parameters of a flexible ionospheric model. If the DRPID data are considered to be the result of correcting the Doppler measurement ionospherically using a noisy DRVID-measured correction, then estimating a multiparameter ionospheric model in each pass is one way of smoothing out the influence of the range noise on the Doppler correction. The advantage of this is its seamless integration with existing estimation methodologies and its potential applicability to real-world nonsymmetric estimation.

TDRSS User

For TDRSS (including BRTS) applications, the pilot effects on the Doppler observation complicate the picture:

$$DRPID = \tfrac{1}{2}\Delta\left[R_L + T_L + \tfrac{1}{2}(e_L + E_L) + \frac{b}{2}(R_S + T_S + e_S)\right] \tag{8}$$

$$DRVID = \tfrac{1}{2}\Delta\left[I_L + \tfrac{1}{2}(E_L - e_L) - \frac{b}{2}(R_S + T_S + e_S)\right] \tag{9}$$

The pilot term (the term on the right-hand side of these equations that is multiplied by $b/2$) plays no different role in Equation (8) than in Equation (4) (with Equation (5)). TDRSS measurement analysis has always required a relay trajectory model. Orbit determination with DRPID measurements is qualitatively the same as with Doppler measurements, except that the ionospheric correction is unneeded, the noise is greater, and the pilot coefficient is half as big. DRPID (or SDRPID) orbit determination can still be implemented passively by enforcing conditions 1 through 4 (see above) for symmetric treatment of range and Doppler measurements; however, the following fifth condition must be added:

5. The variables affecting R_S (e.g., the TDRS state) are excluded from the state vector; otherwise orbit variables will be influenced by the (purely formal) DRVID sector (Equation (9)).

The use of DRVID as an ionospheric measurement is affected by the presence in the DRVID Equation (9) of the relay spacecraft degrees of freedom absent in Equation (7). For LEO DRVID, the time scales for variation of the ionospheric terms (10–1000 seconds) are much shorter that those of the pilot terms (fractions of a day). With a model of the TDRS trajectory, correction can be made for the effect of the pilot terms on what may still be regarded as an ionospheric measurement (with a new error source). Equations (1) through (9) apply to observed measurements (O), calculated measurements (C), and observed-minus-corrected (O-C) residuals in an estimation process. In GTDS differential correction (DC) processing, calculated TDRSS measurements take account of the pilot term using a relay trajectory model. The O-C version of Equation (9) has a pilot term coming only from *errors* in the relay trajectory and pilot models. DRVID analysis of O-C residuals is a convenient way of taking advantage of the pilot-loop modeling that is part of the DC processing of TDRSS observations.

The error in modeling the pilot term depends on the accuracy of the TDRS orbit model and the tropospheric delay model. Only the changing part of the error is significant. For LEO user passes that are not too long, an error estimate as an average range rate is appropriate, since these TDRS-associated quantities change slowly. The "wet" component (the most variable part) of the one-way

34

tropospheric delay can change as much as 5 centimeters in an hour (Reference 4) at zenith. Therefore, for a tracking contact of length τ, the buildup of tropospheric error in SDRVID is

$$\tfrac{1}{4}\delta T_S \leq \tfrac{1}{4}\cdot\left(0.05 \text{ meter/hour}\right)\cdot\tau\cdot\left(\sin E\right)^{-1}\cdot 2 \approx \tau\cdot\left(0.14 \text{ meter/hour}\right) \tag{10}$$

at elevations, E, around 10 degrees. The TDRS orbit uncertainty is dominated by the along-track and cross-track components, but the effect of these is reduced geometrically by a factor of the ratio of the TDRSS orbital radius to the Earth radius, making the effect of radial uncertainty comparable. Assuming a 50-meter uncertainty, the peak error is approximately

$$\tfrac{1}{4}\delta R_S \approx \tfrac{1}{4}\cdot\left(50 \text{ meters}\right)\cdot 2\pi\,\frac{\tau}{\tau_T}\cdot\frac{R_E}{R_T}\cdot 2\cdot 2 \approx \tau\cdot\left(2 \text{ meters/hour}\right) \tag{11}$$

where τ_T is the TDRS orbital period (1 day), R_E is the Earth radius (6400 kilometers), and R_T is the TDRS orbital radius (42000 kilometers). One factor of 2 accounts for the addition of the radial error to the contribution of along-track and cross-track error and the other accounts for the round-trip. A somewhat smaller estimate is obtained from typical root-mean-square (RMS) BRTS residuals of less than 10 meters in the TDRS orbit solutions (e.g., Reference 5),

$$\tfrac{1}{4}\delta R_S \leq \tfrac{1}{4}\cdot\left(10 \text{ meters}\right)\cdot 2\pi\,\frac{\tau}{\tau_T} \leq \tau\cdot\left(0.7 \text{ meter/hour}\right) \tag{12}$$

Perhaps much of the orbit error in Equation (11) is in the direction to which R_S is insensitive. This is reasonable since local BRTS measurements (those for which the BRTS transponder is near the ground terminal antenna) account for half of the observations in the TDRS orbit estimation process. Thus, Equation (12) provides the more realistic error estimate, despite its inclusion of the S-band ionospheric error that should be nearly absent from the K-band pilot error. These error estimates must be multiplied by b to gauge their impact on measuring $I_L/2$. This brings the SA error to 3 meters per hour.

Bilateration Ranging Transponder System (BRTS)

A somewhat different analysis is required for DRVID analysis of BRTS tracking. Here, nothing is gained by eliminating the user degrees of freedom while leaving the relay degrees of freedom to be modeled—the two are the same. Using Equation (9) to investigate I_L is no better than using Equation (1). The accuracy of both analyses is limited by knowledge of TDRS-to-terminal nonionospheric delays, R_{SL}, T_{SL}, and E_{SL}. Modeling of the short and long loops is a single problem. Remote BRTS transponder tracking is not useful for DRVID analysis without simultaneous local-transponder or direct observations (through the K-band Telemetry, Tracking and Command (TT&C) channel at the Second TDRSS Ground Terminal (STGT)) to supply the TDRS-to-terminal range information.

Local BRTS measurements, however, present new possibilities for DRVID analysis with less pilot-loop error than TDRSS-user DRVID. The proximity of the tracked BRTS transponder to the ground terminal antenna guarantees that R_S and T_S are close to half of their long-path counterparts. Redefining ID for this case as

$$ID_B \equiv -\frac{c\,\Delta T}{2A + bA}\,D \tag{13}$$

yields

$$ID_B = \Delta r_B \tag{14}$$

with a revised phase-range, r_B, (ignoring the short-path K-band ionospheric effect, I_S,) given by

$$r_B \equiv \frac{1}{2}\left[\begin{array}{l}\left(R_L + T_L + D_L + e_L\right) - \frac{2}{2+b}I_L + \ldots \\[2mm] + \frac{2b}{2+b}\left(R_S - \tfrac{1}{2}R_L + T_S - \tfrac{1}{2}T_L + D_S - \tfrac{1}{2}D_L + e_S - \tfrac{1}{2}e_L\right)\end{array}\right] + C_r' \tag{15}$$

This reformulated phase range, as with the original user phase range, differs from the range measurement of Equation (1) by the constant multiplying the ionospheric effect, instrumental differences (e_L versus E_L), and a pilot term that now includes only the differences between the short path and half the long path.

DRVID is also redefined for this case so as to extract the one-way ionospheric effect from comparison of DR and ID_B as follows:

$$DRVID_B \equiv \frac{2+b}{4+b}(DR - ID_B)$$

$$= \tfrac{1}{2}\Delta\left[I_L + \frac{2+b}{4+b}(E_L - e_L) - \frac{2b}{4+b}(R_S - \tfrac{1}{2}R_L + T_S - \tfrac{1}{2}T_L + e_S - \tfrac{1}{2}e_L)\right] \tag{16}$$

DRPID does not benefit from or need any reformulation for local or remote BRTS tracking, but it does, of course, have a relationship to ID_B different from that to ID:

$$DRPID \equiv \tfrac{1}{2}\left[DR + (1 + \tfrac{1}{2}b)ID_B\right] \tag{17}$$

Pilot error for O-C analysis of DRVID for local BRTS tracking comes from lack of knowledge of the difference between the short path and half the long path. This is nonzero both because of the separation, δx_B, between the ground terminal and the BRTS transponder and because of the slight difference between the forward- and return-link portions of the long path. The former contribution is proportional to the TDRS angular uncertainty as seen from the ground site,

$$\tfrac{1}{2}\delta(R_S - \tfrac{1}{2}R_L) \lesssim \tfrac{1}{2} \cdot \frac{50 \text{ meters}}{R_T} \cdot \delta x_B \cdot 2 \leq 0.006 \text{ meter} \tag{18}$$

where the upper bound applies even for the 5-kilometer separation between the STGT (not used in the present work) and the BRTS site at the original White Sands Ground Terminal (WSGT). (Since there is no geometrical limitation to BRTS pass lengths, the assumption of short tracking contacts is inapplicable; therefore, the factor $2\pi\,v/v_T$ in Equations (10) through (12) is absent for calculation of the total variation over a TDRS orbit.) The latter effect is negligible ($\sim10^{-4}$ meter) if typical RMS BRTS Doppler residuals (~0.010 hertz) are at all representative of knowledge of the TDRS orbit. The tropospheric refractive delay, per passage through the atmosphere, must be essentially the same for the long and short loops when the receive/transmit antenna and the BRTS transponder are as close together (0.6 kilometer (km)) as WSGT and the local BRTS site, WHSJ. For STGT and WHSJ, the possibility of meteorological differentials between the two sites exists. If, for example, the TDRS-to-BRTS legs pass through a spherical cloud of water vapor at 20°C (that the other legs miss) with a 1-inch peak rain capacity, the following DRVID error results:

$$\tfrac{1}{2}\delta(T_S - \tfrac{1}{2}T_L) \leq 0.15 \text{ meter} \tag{19}$$

based on a water-vapor refractivity of 87×10^{-6} and density of 15grams/meter^3 at, for example, a 20-millibar partial pressure (86-percent humidity) (Reference 6). This entails about 3 hours worth of the zenith delay change, cited as a "not unusual" maximum rate by Reference 4, and so is presumably quite infrequent. These error estimates must be multiplied by $[4b/(2+b)]$ (about 0.7 for MA and 1.1 for SA) to gauge their impact on $I_L/2$.

Analysis Techniques

The O-C residuals were collected for a variety of tracking systems (USB (30-foot dish) and TDRSS), spacecraft (LEO and geosynchronous), and time periods, primarily in the last solar maximum timeframe (as shown in Table 1 given on the next page). All the TDRSS observations used WSGT. Residuals were calculated both without and with (except for TOPEX) ionospheric corrections derived from the Bent model with historical solar flux measurements. Tropospheric corrections were always applied. Doppler residuals were converted to ID (Equation (3)) and summed (to SID, i.e., the summed integrated Doppler). (The initial value of the partial sum was chosen so that the mean over each pass matched the mean range residual.) Comparison of the range residuals with the SID residuals was carried out graphically, for both ionospherically corrected and uncorrected residuals, and by subtraction as SDRVID.

Tracking data were obtained from archives of the FDF primary operational 60-byte database in the form of range (converted from raw light-delay time) and Doppler (converted from raw Doppler count) observations. Residuals against observation and trajectory models of a GTDS O-C run on the FDF IBM mainframe computers were captured to full 8-byte floating-point precision. Data on O, C, O-C, time, ionospheric correction, and validity flagging were downloaded to a DOS personal computer (PC), where they were analyzed and graphed using commercial plotting software, principally MATLAB. Full-precision capture was necessary (and sufficient) to reduce to insignificance the truncation error involved in summing long series of ID values. Some raw Doppler count data were analyzed to check that this procedure was accurate (to 10^{-8} cycles) for even the longest passes (5000 seconds).

Only standard operational techniques were employed for trajectory and observation modeling (except for the addition of ionospheric corrections). The desire was only to obtain residuals that were small enough to make interesting features visible in a plot, at the level of a few centimeters, without hiding physically interesting phenomena or introducing artifacts. The user spacecraft trajectory and observation modeling errors appear equally in range (R) and SID residuals and do not affect the comparison. This is not so for the TDRS degrees of freedom, because of their effect on the short pilot path. It would have been desirable to use special methods and solutions for the relay modeling, but this was not done due to time limitations. All relay orbits for TDRSS-user analysis were obtained from operational Permanent TDRS Orbit Files (PTOFs), except in the case of TOPEX, for which special orbit files were available (Reference 7). The pilot-tone error estimates given in the previous section reflect this decision.

Ionospheric corrections included the spacecraft-to-spacecraft legs (TDRSS-user tracking) and the S-band ground-to-space legs (BRTS and GN). These were calculated by a GTDS enhancement called GATFITR, which adds the calculation of the spacecraft-to-spacecraft legs using Gaussian integration, as described in Reference 8.

The source of user spacecraft orbital elements varied in this study (see Table 1, column 7). The original intention was to use elements from operational solutions, and this was followed for those spacecraft for which Table 1 describes the elements source as Ops. In three cases (indicated by Corr DC in the Elements Source column of Table 1), orbital elements were obtained from special DCs employing Bent-model ionospheric corrections. Special DC results (ionospherically uncorrected), which were already available for TOPEX (Reference 6), were used for this spacecraft, as noted in Table 1.

Ideally, the definition of a tracking pass, for purposes of this analysis, should be a period of continuous coherency in two-way range and Doppler tracking. In general, therefore, the interval between two successive Doppler observations should be equal to the Doppler count interval of the latter, usually 10 seconds. However, interpolation of a few Doppler residuals to cover a

Table 1. Spacecraft and Tracking Periods for DRVID Analysis

Spacecraft *	Tracking			Orbit			10.7-Centimeter Solar Flux (10^{-22} watts/meter^2/hertz)	
	Dates	Source	Passes	Semimajor Axis (km)	Inclination (degrees)	Elements Source **	365-Day Mean	Daily
TDRS-1	05/15/89	BRTS	1	42164	3.7	Corr DC	214	183
TDRS-1	12/01–12/02/91	BRTS	3	42166	5.9	Ops	193	172
TDRS-3	10/08/91	DS17/46	6	42054	0.2	Corr DC	201	179
ERBS	10/02/91	BDA3	1	6966	57.0	Corr DC	201	221
HST	10/18/91	TDRSS	11	6984	28.5	Ops	198	158
GRO	10/18/91	TDRSS	8	6816	28.5	Ops	198	158
TOPEX	10/13–10/15/92	TDRSS	20	7721	66.0	Uncr DC	131	106

* ERBS = Earth Radiation Budget Satellite; HST = Hubble Space Telescope; GRO = Gamma Ray Observatory; TOPEX = Ocean Topography Experiment

** Ops = Operational solution elements; Corr DC = ionospherically corrected DC elements; Uncr DC = ionospherically uncorrected DC elements

brief period of loss of Doppler coherency was employed in a few cases. For the very shortest gaps (30 seconds or less, as in TOPEX passes 7 and 13 and in GRO pass 5), residuals were simply zeroed. To cover gaps of 99 and 110 seconds in two long TDRS-1 passes, polynomials were fitted to residuals on either side of the gaps, and the fit values were used inside the gaps. In all cases, the number of interpolated residuals was sufficiently small that any error would have small visible impact on the SID residual plot for the pass.

Results

DRVID Pass Analysis

Table 2 summarizes the results for SDRVID residuals corrected (column 6) and uncorrected (column 7) by Bent-model ionospheric corrections. The correlation coefficient between the ionospherically uncorrected SDRVID residuals and the Bent

model expectation (for $I_L/2$) is given in column 8. High-frequency noise amplitude is estimated for corrected SDRVID residuals by piecewise polynomial fitting using degrees up to 15 with two segments per pass (column 9). The Bent-model relief (column 10) is defined as the difference between the maximum and minimum values of the modeled $I_L/2$. It is a measure of how distinctly the ionosphere is predicted to be visible in DRVID.

Since reproducing 50 plots of R and SID and 50 of SDRVID in this paper is impractical, a Bent model score, subjectively summarizing the general agreement between the plots and the expectations of the Bent model, is assigned in the last column of this table. The meaning of these scores is as follows:

A = reasonable success, qualitatively and quantitatively
B = at least some features qualitatively reproduced
C = success; of marginal significance (ionospheric behavior not strong)
D = ionospheric behavior insignificant relative to uncertainties
E = failure; of marginal significance (ionospheric behavior not strong)
F = qualitative and quantitative failure of Bent model

Figure 1 summarizes some of the results presented in Table 2. The difference between the RMSs of the uncorrected and corrected SDRVID residuals, respectively, is plotted against the Bent-model relief. The straight line shows the relationship between these two quantities that would hold for I_L linear versus time. The success of the Bent model is mixed. The ionospheric model is more successful, in general, the stronger the ionospheric effect is expected to be. In 7 of 10 passes with 2 meters or more of ionospheric relief, the Bent model improves SDRVID residuals, while it degrades them significantly in only one.

The results for each spacecraft are discussed below. Figures 2 through 13 cited in these discussions are given at the end of this Results section.

Hubble Space Telescope (HST) Results

The main emphasis in this work was on TDRSS-user tracking; the HST passes, which are MA with substantial ionospheric effects, give the best examples of this. Figures 2 and 3 show the DRVID comparisons for the fifth HST pass. The plot of R and SID residuals given in Figure 2 clearly shows the mirror image behavior expected from ionospheric transients, most strongly in the uncorrected data (compare range (+) with SID (solid line)). The persistence of a smaller amount of mirror image discrepancy in the corrected data (compare range (o) to SID (dashed line)) shows the imperfect effectiveness of Bent-model correction at removing ionospheric effects. Recall that the arbitrary constant in the definition of SID has been adjusted to null out the mean difference with R. The adjustment of the constant was performed independently for corrected and uncorrected data. The comparison of the uncorrected SDRVID residuals in Figure 3 (+) with the Bent-model for $I_L/2$ (biased to zero mean for comparison with SDRVID and plotted as a solid line) displays this model's success until the end of the pass, where it plateaus spuriously and then fails to reproduce the largest effects. The differences between these two equal the corrected SDRVID residuals (shown as o in Figure 3), which are therefore not reduced quite to zero, especially near the end of the pass. This pass exemplifies the score of A for the Bent model—good, but not great, agreement.

The third HST pass (Figures 4 and 5) exemplifies its B score. The Bent model agrees qualitatively with the uncorrected SDRVID residuals, correctly showing large increases at the wings, but undercorrects the beginning of the pass while overcorrecting the end. There is only a modest improvement in the RMS of the corrected SDRVID residuals.

The zigzags (covering up to 2 meters and 300 seconds) in both sets of SDRVID residuals in Figure 5 are, of course, absent from the Bent model. Examination of Figure 4 shows that these zigzags are present only in the range data and not in the Doppler (down to about 3 percent of the expected magnitude). They are therefore not ionospheric phenomena, which would cause mirror-image features in both R and SID. Neither are they from user spacecraft motion or modeling, which would produce parallel features in both R and SID. Nor are they solely short-path effects, which would appear in Doppler measurements, not ranges. Since this is an MA pass, with the ratio $b = -0.93$, the common effects of the TDRS-to-ground-terminal range on the short and long paths cancel down to the 7-percent level in Doppler but not in range observations. A likely cause would be one that affects only the TDRS range to ground (although 3-percent rather than 7-percent, attenuation is needed). TDRS spacecraft motion would likely affect both the range to the ground and to the user. The zigzags are too large to be a tropospheric effect or a ground antenna motion effect. These zigzags are seen only in this pass and remain unexplained, but they are certainly not ionospheric in origin.

Table 2. SDRVID Analysis Results

| Pass ID	Tracking Source	Start Time (UTC)*	Elapsed Time (seconds)	Observation Count	Uncorrected RMS (meters)	Corrected RMS (meters)	Correlation With Bent Model	Noise Estimate (meters)	Bent Model Relief (meters)	Bent Model Score
TDRS-1 1989										
1	MA	16:45:10	6290	608	0.358	0.561	−0.44	0.23	1.27	E
TDRS-1 1991										
1	MA	05:09:40	1219	114	0.301	0.297	0.15	0.28	0.16	D
2	MA	12:45:40	2490	250	0.273	0.311	−0.16	0.25	0.38	D
3	MA	27:14:40	2480	249	0.527	0.410	0.80	0.28	0.54	C
All				613	0.400	0.352				
TDRS-3 1991										
1	DS17	06:06:00	4380	439	0.480	0.493	−0.03	0.48	0.35	D
2	DS46	07:21:50	3130	314	0.353	0.374	0.11	0.35	0.58	E
3	DS17	08:16:30	3450	346	0.456	0.455	0.05	0.44	0.04	D
4	DS46	09:16:50	1930	194	0.415	0.414	0.09	0.43	0.21	D
5	DS17	09:51:30	23080	2307	1.103	1.021	0.90	0.46	6.53	B
6	DS17	17:03:30	2250	226	0.556	0.486	0.49	0.44	1.01	C
All				3826	0.903	0.842				
ERBS 1991										
1	BDA3	16:32:10	500	51	2.904	1.140	0.92	0.66	9.22	A
GRO 1991										
1	SA	01:17:30	1100	111	7.274	2.856	0.95	0.15	24.17	A
2	SA	04:36:20	1160	117	1.980	2.024	0.25	0.21	3.58	B
3	SA	07:34:00	1660	167	1.466	0.935	0.92	0.24	2.67	B
4	SA	10:52:50	1670	168	3.756	1.886	0.96	0.27	8.47	B
5	SA	13:25:10	630	64	0.780	0.643	0.66	0.25	0.67	F
6	SA	15:53:30	1640	165	0.712	0.432	0.81	0.23	1.68	A
7	SA	19:49:20	1590	160	0.969	1.662	0.35	0.27	7.65	F
8	SA	21:41:20	1050	106	1.161	1.122	0.33	0.22	1.78	F
All				1058	2.982	1.610				
HST 1991										
1	MA	00:46:20	820	83	0.392	1.075	−0.89	0.09	1.91	F
2	MA	02:27:50	830	84	1.362	0.758	0.85	0.09	5.65	B
3	MA	06:33:10	2530	254	1.046	0.640	0.81	0.12	5.78	B
4	MA	08:32:00	840	85	0.244	0.223	0.46	0.13	0.26	D
5	MA	10:02:10	2570	258	2.110	0.609	0.96	0.12	6.44	A
6	MA	12:01:00	490	50	0.356	0.219	0.88	0.13	1.25	A
7	MA	13:51:50	1010	102	0.844	0.877	−0.08	0.12	0.71	F
8	MA	15:22:50	840	85	0.473	0.432	0.46	0.14	1.27	B
9	MA	18:02:50	830	84	0.157	0.133	0.67	0.08	0.56	C
10	MA	19:45:00	1340	135	0.250	0.226	0.46	0.10	0.67	C
11	MA	21:53:00	420	43	0.403	0.471	−0.64	0.12	0.37	E
All				1263	1.163	0.603				
TOPEX 1992										
1	SA	00:46:30	2300	231	0.303			0.22		D
2	SA	03:01:40	1690	170	0.318			0.22		D
3	SA	04:59:30	2300	231	0.253			0.21		D
4	SA	06:57:30	2300	231	0.242			0.23		D
5	SA	09:10:30	2240	225	0.269			0.21		D
6	SA	10:51:40	2290	230	0.325			0.21		D
7	MA	12:25:10	2260	225	0.222			0.11		D
8	MA	14:29:30	2180	219	0.148			0.06		D
9	SA	17:16:30	2300	231	0.325			0.28		D
10	MA	18:21:30	2300	231	0.113			0.07		D
11	SA	20:34:30	1460	147	0.276			0.25		D
12	SA	22:21:10	2200	221	0.307			0.27		D
13	SA	27:25:40	1690	169	0.272			0.23		D
14	SA	29:22:30	2300	231	0.266			0.24		D
15	SA	31:21:40	2290	230	0.308			0.27		D
16	SA	33:33:30	2300	231	0.333			0.28		D
17	SA	35:22:30	2300	231	0.259			0.26		D
18	MA	36:50:20	1760	177	0.154			0.06		D
19	MA	38:51:10	2320	233	0.169			0.12		D
20	MA	63:14:20	1970	198	0.140			0.08		D
All				4292	0.259					

* UTC = coordinated universal time

39
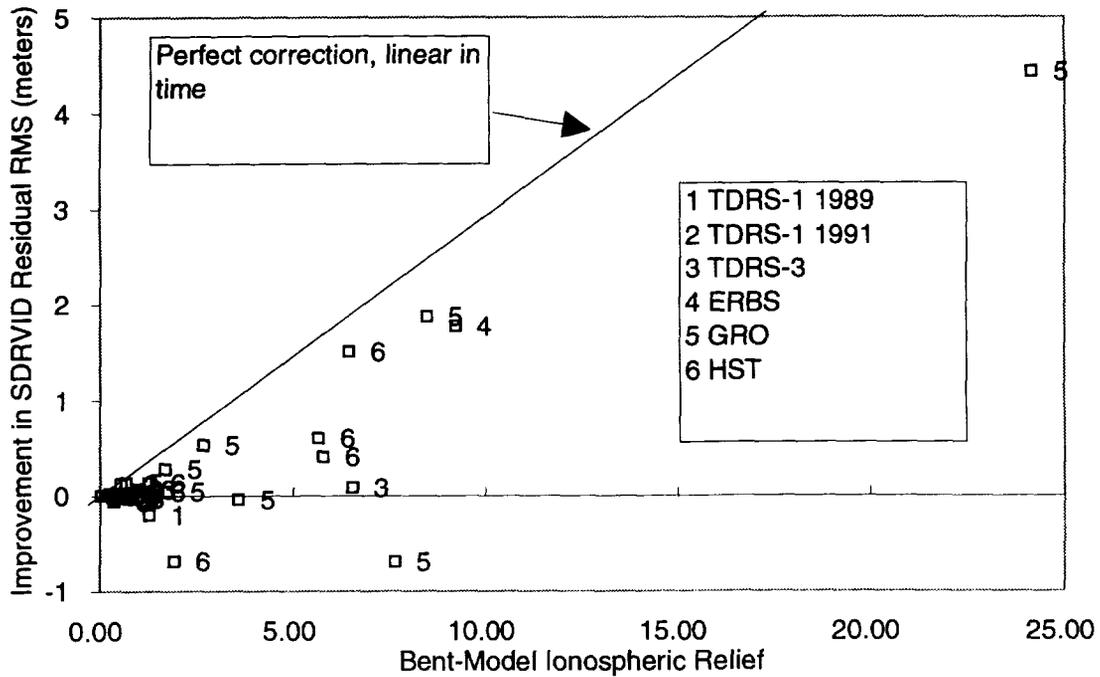
Figure 1. **Improvement in RMS Residuals of SDRVID Due to**
Ionospheric Correction by the Bent Model

The first HST pass exemplifies its F score for the ionospheric model. Table 2 shows corrections tripling the RMS residual of SDRVID, despite a moderate amount of Bent-model relief. The SDRVID data of Figure 6 show why: the model ionospheric corrections decline by almost 2 meters while the measurements increase by almost a meter, for a 3-meter discrepancy. Pilot loop error can account for perhaps a tenth of this (Equation (12)). The Bent model is entirely wrong for this pass. (The plot of R and SID for this pass is omitted since it is unrevealing.)

Gamma Ray Observatory (GRO) Results

Because the GRO passes are all SA, somewhat more caution is needed in interpreting them because potential pilot errors may exceed 3 meters per hour. For example, Figure 7 for the second GRO pass shows the expected mirror-image discrepancies between R and SID not to be at all ameliorated by ionospheric correction. The plot of SDRVID for the pass (Figure 8) displays measured ionospheric features that are present in the Bent model but not quantitatively reproduced. Pilot loop errors at the 3-meters-per-hour level, as indicated by Equation (12) for SA, would not remove the discrepancy, but 25 meters per hour (in the central section only) would help. This would require 24-hour TDRS orbit error levels in the vicinity of 120 meters (along-track or cross-track) or 20 meters (radial), somewhat larger than typical.

The first GRO pass (Figure 9), on the other hand, provides a significant success for the SDRVID method, as well as for the Bent model, which predicts the one-way ionospheric delay to vary from 3.7 meters to 27.9 meters during the pass. At least 24.6 meters of delay at the end of the pass is confirmed by the SDRVID measurements, since the effect must be positive at the beginning of the pass. This includes TDRS line-of-sight elevations down to –3.6 degrees (relative to the local GRO horizontal plane). Even with a cutoff at +5 degrees elevation, 13.1 meters of delay are predicted at the end of the pass and at least 17.1 meters are observed. The RMS SDRVID residual is reduced from over 7 to under 3 meters, despite the model's imperfections in not ramping up soon enough or fast enough. This is one of few passes where unsummed DRVID measurements are significant and large. The average two-way Doppler ionospheric effect over a 200-second period (at the relatively high elevations of 15 to 26 degrees) is here *measured* at 0.58 ± 0.08 hertz (3.8 ± 0.5 centimeters per second). (The 3σ error estimates assume 1σ SDRVID noise of 0.25 meters.) Still higher rates are seen at negative elevations.

Ocean Topography Experiment (TOPEX) Results

The TOPEX results are generally uninformative, given the low levels of variation in the ionospheric delay both expected and observed. TOPEX tracking at this time was evidently geometrically selected to avoid significant ionospheric effects, and solar activity had declined from its peak. The last pass shows a half-meter step function (rise time about one minute) in the range residuals accompanied by a coincident Doppler peak with no more that 10 percent of the expected magnitude.

Earth Radiation Budget Satellite (ERBS) Results

The sole GN pass analyzed for a LEO spacecraft, ERBS, is another success (Figure 10) for the Bent model (this time applied to the ground-to-space line of sight). The fit of SDRVID to the model is excellent and the corrected residuals are uniformly small. As for all ground tracking of LEO spacecraft, the time variation of the correction is largely geometrically determined, while geophysical variation is often important in TDRSS passes for LEO users. A geometrical "cosec model", proportional to the cosecant of the elevation of the line of sight at the point where it attains 300 km altitude, is plotted in Figure 10 to illustrate this point. (The cosec model is normalized to the Bent model at their common minimum.)

Tracking and Data Relay Satellite (TDRS) Results

The success of the ERBS GN analysis makes the unsatisfactory results displayed (Figure 11) for the fifth TDRS-3 pass puzzling, in contrast. The ionospheric correction for geosynchronous spacecraft varies chiefly due to change of the ionospheric state, not due to geometry as for LEO spacecraft. Long passes are therefore needed to demonstrate the DRVID effect. This is really the only geosynchronous spacecraft pass collected that was long enough (over 6 hours) to accumulate major ionospheric variation. Nine-point averages of SDRVID residuals are plotted to reduce clutter and noise. The Bent model correction is too variable by a factor of two in this pass. In fact, one-half of the Bent model (dashed line in Figure 11) is an excellent fit to the data, but this is apparently coincidental. Strenuous, but futile, efforts were made to locate a factor of 2 error in our analysis of this pass. The Bent model implementation used here is, moreover, exactly the same one as produced the success for ERBS.

Given the disappointing results for TDRS-3 above, it is not surprising that the analysis of the necessarily shorter BRTS passes was not a great success. Only a single pass was located as long as the 1.75-hour TDRS-1 event in 1989 (Figure 12). Other shorter passes (see Table 2) did not display enough ionospheric variation for definitive analysis. Although the Bent model dictates that the 1989 pass should have participated in the steep morning (local time) increase in ionospheric effect (Figure 13), the measurements suggest that the diurnal peak had already passed.

Conclusions

Mirror-image transients in range and SID residuals for LEO TDRSS users (e.g., Figures 2 and 7) are clearly related to the Bent model for the ionospheric effect (e.g., Figures 3 and 8) qualitatively and sometimes quantitatively. This demonstrates the existence of the DRVID effect in TDRSS tracking. More importantly, it demonstrates that quantitative measurements of ionospheric effects can be synthesized from ordinary TDRSS coherent tracking. The noise level for measurement of variation in one-way ionospheric range corruption is one-half the range noise, i.e., 6 to 14 centimeters for MA and 15 to 28 centimeters for SA (see Table 2). Systematic errors are 1 to 2 meters per hour of pass length (Equations (11) and (12)) for MA and 5 times that level for SA, but they can be reduced if special care is employed in TDRS orbit modeling. The potential utility in critical evaluation of existing and future ionospheric correction models is evident.

To make full use of this potential, certain transient behaviors in range data that are not reflected in Doppler observations must be understood. These have been observed in the GRO and TOPEX MA ranges at time scales of 1 second to a few hundred seconds and amplitudes of 0.5 to 2 meters. They are caused neither by the ionosphere nor by user spacecraft motion. Even if these transients have a purely instrumental origin, a greater understanding of them will aid in the interpretation of DRVID comparisons.

Comparison of R and SID residuals is also a potential tracking data quality evaluation tool. The range transients mentioned above, for example, are too small to have been considered significant without the SID comparison.

Quite large ionospheric corruption of tracking measurements has been observed (not predicted or modeled) in this study to have occurred during the last solar maximum. Range effects were at least 24.6 meters, over 17 meters of which occurred above 5 degrees in TDRS elevation in a GRO pass. Average ionospheric frequency shifts of 0.6 hertz over a 200-second period at elevations above 15 degrees were also observed in this pass.
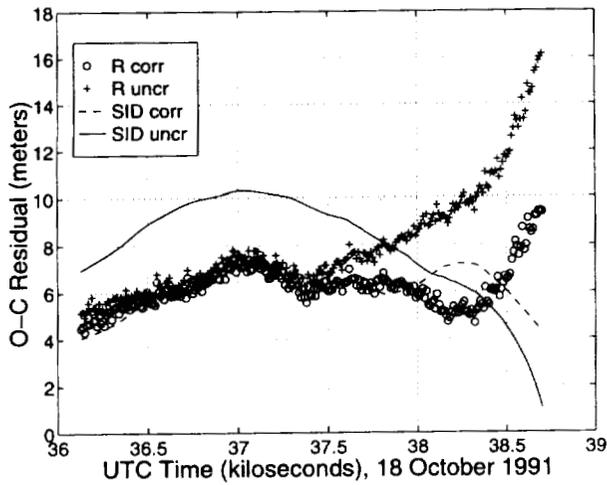
Figure 2. Range and SID Residuals for the Fifth HST Pass
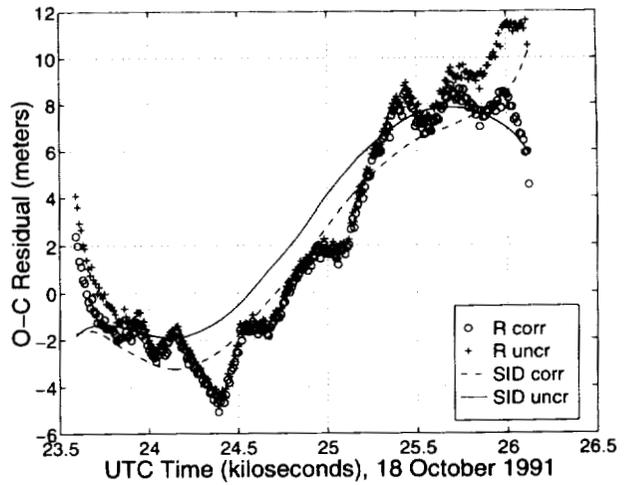
Figure 4. Range and SID Residuals for the Third HST Pass
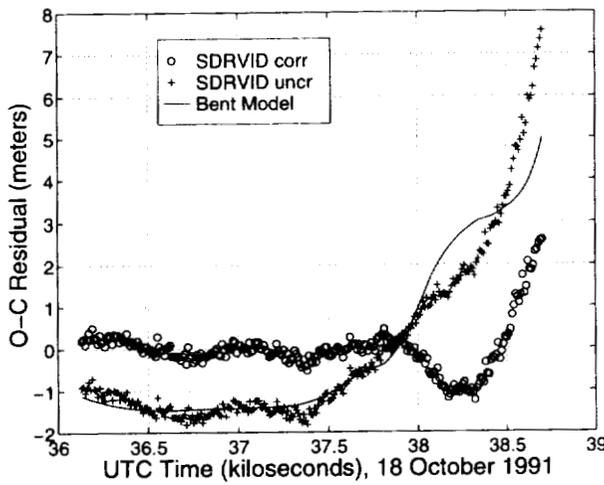
Figure 3. SDRVID Residuals for the Fifth HST Pass
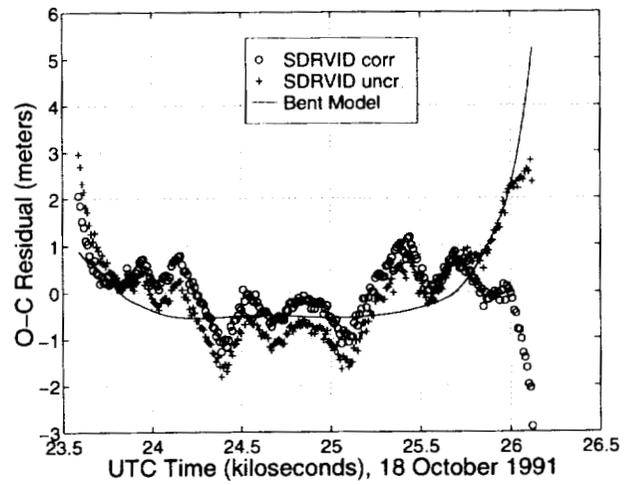
Figure 5. SDRVID Residuals for the Third HST Pass
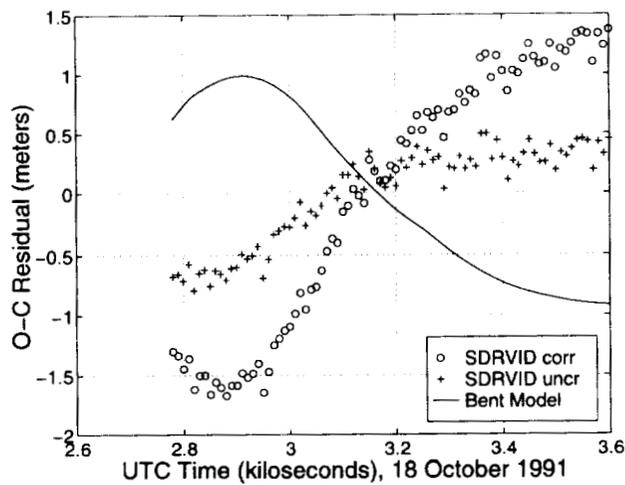
Figure 6. SDRVID Residuals for the First HST Pass

42
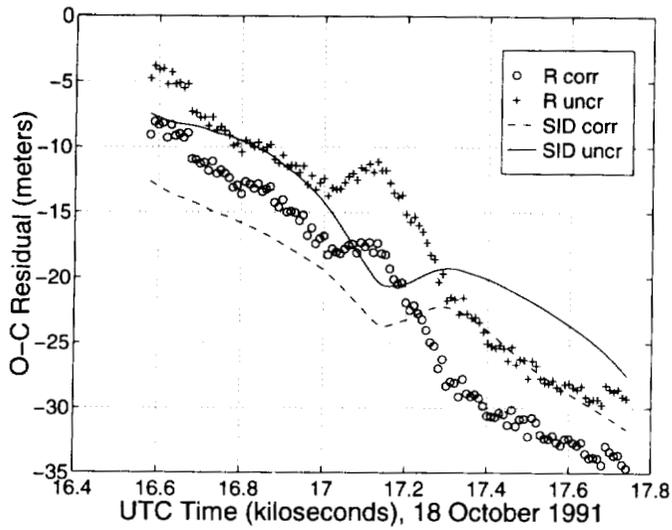
Figure 7. Range and SID Residuals for the Second GRO Pass
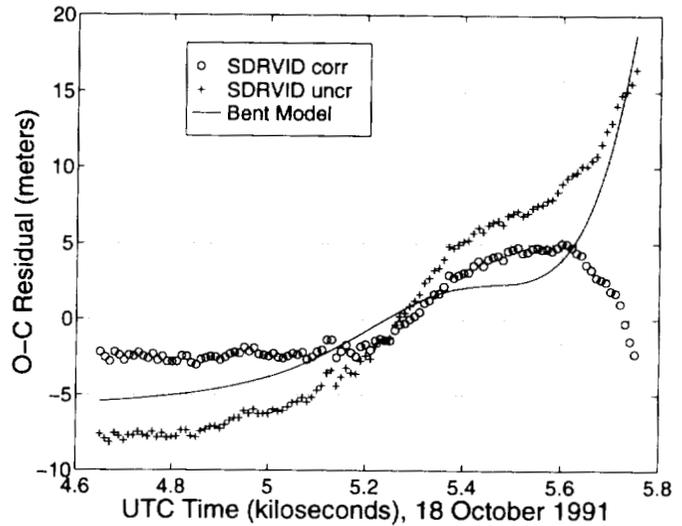
Figure 9. SDRVID Residuals for the First GRO Pass
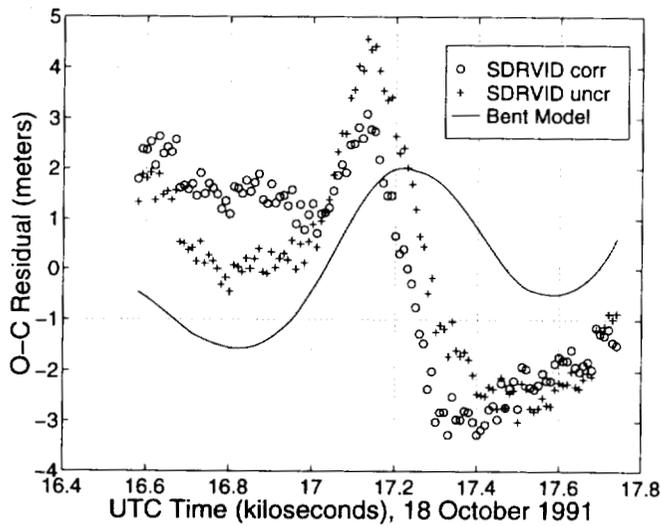
Figure 8. SDRVID Residuals for the Second GRO Pass
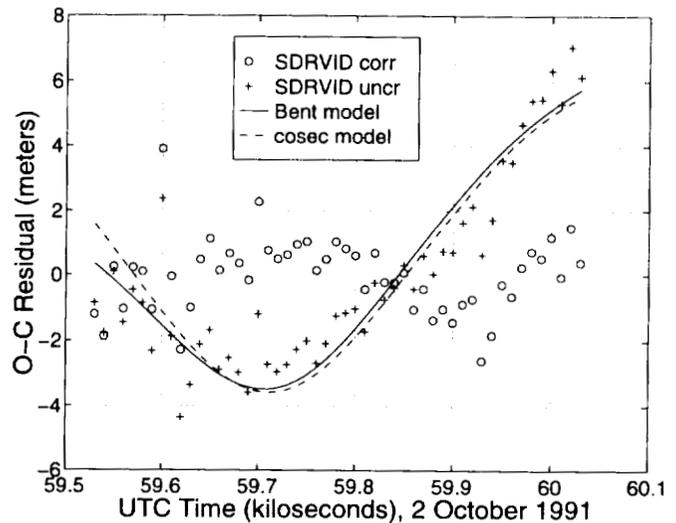
**Figure 10. SDRVID Residuals for the ERBS Pass**

43
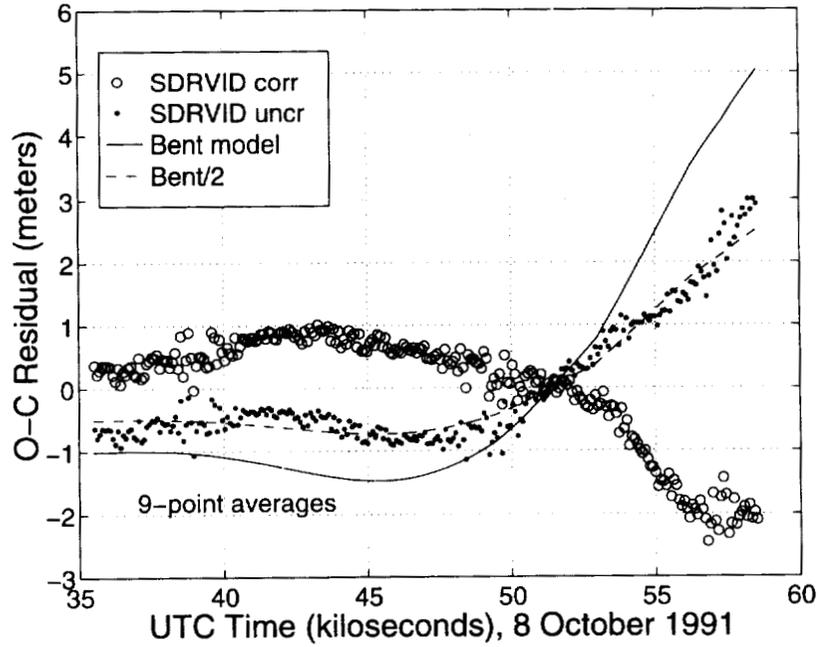
**Figure 11.** Nine-Point Average SDRVID Residuals for the Fifth TDRS-3 Pass
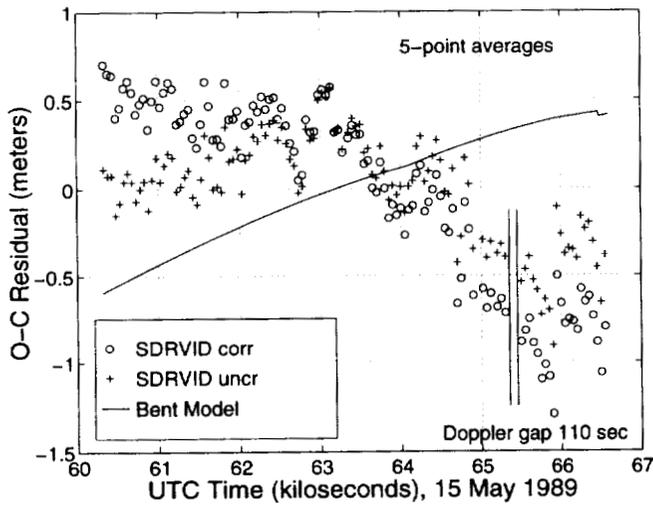
Figure 12. Five-Point Average SDRVID Residuals for the 1989 TDRS-1 Pass
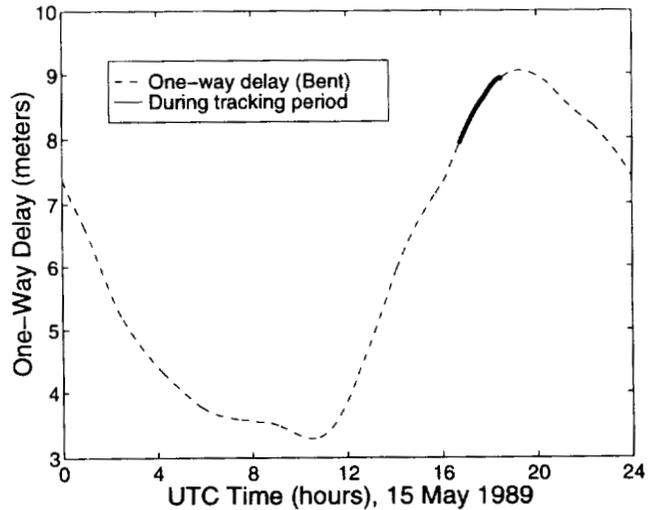

Figure 13. Diurnal Dependence of One-Way Ionospheric Range delay in the Bent Model

Ionospheric corrections for observations of geosynchronous spacecraft change slowly as does the ionosphere itself. Very long tracking passes are therefore required for significant observation of these changes using DRVID. In the only two passes (one a GN and one a BRTS pass) where obviously significant changes occurred, the Bent model performed poorly. It is puzzling how the same correction algorithm can produce accurate variations with geometry at a particular time of day (as the Bent model for USB tracking did for our ERBS pass) and yet overestimate by 100 percent the diurnal time variation at a particular geometry (as it did for the TDRS-3 pass), unless the former success is coincidental.

It appears that useful DRVID analysis of TDRS spacecraft will require specially requested long tracking passes. One or a few 24-hour White Sands BRTS passes (for each of TDRS-East and TDRS-West) would reveal much about ionospheric modeling of these crucial ground-to-space links. Since the night-time ionosphere is relatively quiescent, DRVID measurement of a complete cycle of the diurnal ionospheric delay variations translates into knowledge of the delay with relatively little bias uncertainty. Simultaneous continuous tracking of the remote transponders would permit the same sort of information to be extracted for those paths. The burden on the TDRSS, monopolizing one or even two (of only three) forward S-band services per TDRS for a whole day, would be considerable.

DRPID data is unbiased by the ionosphere and presents possibilities for self-correcting orbit determination with little or no dependence on ionospheric modeling. Possible tracking selections for LEO user orbit determination include DRPID-only, SDRPID-only, and SDRPID + Doppler. The first of these is of interest primarily because it can be implemented very easily in existing software systems for evaluation. TDRS orbit determination with TT&C tracking plus remote-transponder DRPID or SDRPID is a remote possibility that should also be evaluated.

It is possible that the best way to use the DRVID principle in orbit estimation is to solve for several ionospheric correction parameters per pass while still using conventional range and Doppler observations. The influence of these parameters under least-squares minimization will tend to resolve the conflicts between range and Doppler information that are caused by the opposite signs of I_L in Equations (1) and (4). Perhaps a set of phenomenological ionospheric correction models can be found that covers all the various geometrical relationships between the line of sight and the ionosphere (vertically moving, horizontally moving, and stationary). If the number of ionospheric parameters per pass can, with fidelity to the DR-ID data, be kept small relative to the number of observations, what is effectively DRPID or SDRPID orbit determination need not import overwhelming range-difference noise onto the Doppler dataset. If this set of models furthermore realistically correlates the time-dependent shape of the ionospheric correction with its zero point, as is possible for nonlinear models that (like the real ionosphere) yield positive-definite delays, then even some of the undifferenced absolute range information may be preserved.

References

1. P. F. MacDoran, "A First-Principles Derivation of the Differenced Range Versus Integrated Doppler (DRVID) Charged-Particle Calibration Method," *Space Programs Summary 37-62*, Vol. II, March 1970.

2. J. Teles, Computer Sciences Corporation, private communication, September 1994.

3. Goddard Space Flight Center, X-572-80-26, *Tracking and Data Relay Satellite System (TDRSS) Range and Doppler Tracking System Observation Measurement and Modeling*, P. B. Phung, V. S. Guedeney, and J. Teles, September 1980.

4. T. P. Yunck, "Coping With the Atmosphere and Ionosphere in Precise Satellite and Ground Positioning," *Environmental Effects on Spacecraft Positioning and Trajectories*, IUGG Geophysical Monograph 73, Vienna, 1991.

5. Computer Sciences Corporation, 554-FDD-91/097, SEAS(550)/IM-91/034(51-443), *Tracking and Data Relay Satellite (TDRS) Orbit Determination With Amended Ionospheric Refraction Corrections*, M. Radomski, May 1991.

6. E. K. Smith and S. Weintraub, "The Constants in the Equation of Atmospheric Refractive Index at Radio Frequencies," *Proceedings of the I.R.E.*, Volume 41, pp. 1035–1037, August 1953.

7. C. E. Doll, G. D. Mistretta, R. C. Hart, D. H. Oza, D. T. Bolvin, C. M. Cox, M. Nemesure, D. J. Niklewski, and M. V. Samii, "Improved Solution Accuracy for TDRSS-Based TOPEX/Poseidon Orbit Determination," Proceedings of the *Flight Mechanics/Estimation Theory Symposium 1994*, NASA Conference Publication 3265, May 1994.

8. Computer Sciences Corporation, CSC/TM-87/6710, Analysis Report 87005, "A Model for Assessing the Tracking Measurement Refraction Effect on TDRSS User Orbit Determination," *Operational Orbit Techniques Compendium of Analysis Reports*, M. Radomski, December 1987.

Kepler Equation Solver

F. Landis Markley
Guidance and Control Branch, Code 712
NASA Goddard Space Flight Center
Greenbelt, MD 20771

Abstract

Kepler's Equation is solved over the entire range of elliptic motion by a fifth-order refinement of the solution of a cubic equation. This method is not iterative, and requires only four transcendental function evaluations: a square root, a cube root, and two trigonometric functions. The maximum relative error of the algorithm is less than one part in 10^{18}, exceeding the capability of double-precision computer arithmetic. Roundoff errors in double-precision implementation of the algorithm are addressed, and procedures to avoid them are developed.

Introduction

Numerical solution of the two-body problem for orbital motion is heavily dependent on efficient solution of Kepler's Equation

$$M = E - e \sin E \tag{1}$$

for the eccentric anomaly E in terms of the eccentricity e and mean anomaly M [1, 2]. Most methods involve choosing a starting formula and then improving this using an iterative refinement method. Many of these methods have difficulties in the critical region where eccentricity is close to one and mean anomaly is close to zero; some iterative methods even fail to converge in this region [3]. There have been several comparisons of numerical methods for solving Kepler's Equation, with conflicting claims for the accuracy and efficiency of the various algorithms [3-8].

This paper presents a new algorithm using a starting formula resulting from solution of a cubic equation based on a Padé approximation to the sine function. This starting formula has smaller errors than any previously considered [3-8]. A single application of a fifth-order method is used to refine the starting estimate, rather than iteration of a lower-order method to satisfy a convergence criterion. The latter procedure would require at least two more trigonometric function evaluations, and perhaps many more. Odell and Gooding, among others, have emphasized the advantages of refinement using a fixed number of iterations [3]. As pointed out by Mikkola [7], such a method is not really iterative, but is actually a direct solution of Kepler's Equation to the desired accuracy.

The method has errors that are less than the least significant bit of double-precision floating-point numbers over the entire range of elliptic motion, $0 \le e \le 1$. The limit of unit eccentricity is not really elliptic motion, and the solution of Kepler's Equation is not useful there, but the eccentricity can be arbitrarily close to this limit. We present a derivation of the algorithm and display contour plots of its errors as functions of the eccentricity and eccentric anomaly. Numerical problems arising in double-precision implementation of the algorithm are also discussed and resolved.

Starting Formula

Our method starts with a Padé approximation for $\sin E$, depending on a parameter α :

$$\sin E \approx \sigma(\alpha, E) \equiv \frac{6\alpha - (\alpha - 3)E^2}{6\alpha + 3E^2} E. \tag{2}$$

It is assumed that E and M have been reduced by multiples of 2π to have absolute value less than or equal to π. The Taylor series expansion of this approximation at $E = 0$ is

$$\sigma(\alpha, E) = E - \frac{E^3}{6} + \frac{E^5}{12\alpha} - \dots \ . \tag{3}$$

This expansion is exact through terms of order E^3, which is crucial for good performance in the critical region with e near unity and M near zero. The series is exact through terms of order E^5 for $\alpha = 10$, and the approximation for $\sin E$ is exact at $E = \pm \pi$ for $\alpha = 3\pi^2/(\pi^2 - 6) = 7.65$. The precise specification of the parameter α for our method will be considered below.

Substitution of equation (2) into Kepler's Equation gives the cubic equation

$$[3(1-e) + \alpha e]E^3 - 3ME^2 + 6\alpha(1-e)E - 6\alpha M = 0. \tag{4}$$

Defining

$$d \equiv 3(1-e) + \alpha e \tag{5}$$

and

$$z \equiv dE \tag{6}$$

and multiplying through by d^2 gives the standard form for the cubic equation [9]

$$z^3 + a_2 z^2 + a_1 z + a_0 = 0, \tag{7}$$

with

$$a_2 = -3M, \tag{8a}$$

$$a_1 = 6\alpha d(1-e), \tag{8b}$$

and

$$a_0 = -6\alpha d^2 M. \tag{8c}$$

We define the auxiliary quantities

$$q \equiv a_1/3 - a_2^2/9 = 2\alpha d(1-e) - M^2 \tag{9}$$

and

$$r \equiv (a_1 a_2 - 3a_0)/6 - a_2^3/27 = 3\alpha d(d - 1 + e)M + M^3 \tag{10}$$

and note that equation (7) has a unique real root if $q^3 + r^2 > 0$. It is not difficult to see that this

48

condition is satisfied for all positive α, which covers the range of interest, except in the case that $e = 1$ and $M = 0$, in which case the root $z = 0$ is threefold degenerate. In any case, the desired root of equation (7) is given by

$$z = s_1 + s_2 - a_2/3 = s_1 + s_2 + M \tag{11}$$

where

$$s_1 \equiv \left(r + \sqrt{q^3 + r^2} \right)^{\frac{1}{3}} \tag{12a}$$

and

$$s_2 \equiv \left(r - \sqrt{q^3 + r^2} \right)^{\frac{1}{3}}. \tag{12b}$$

The accurate evaluation of equation (11) for small M requires cancellations between s_1 and s_2. We avoid this numerical problem by employing a trick attributed to Karl Stumpff by Battin [2]. Write

$$s_1 + s_2 = \frac{(s_1 + s_2)(s_1^2 - s_1 s_2 + s_2^2)}{s_1^2 - s_1 s_2 + s_2^2} = \frac{s_1^3 + s_2^3}{s_1^2 - s_1 s_2 + s_2^2} = \frac{2r}{s_1^2 - s_1 s_2 + s_2^2}. \tag{13}$$

We next multiply the numerator and denominator by

$$w \equiv \left(|r| + \sqrt{q^3 + r^2} \right)^{\frac{2}{3}} \tag{14}$$

and use the fact that $s_1 s_2 = -q$ to simplify this expression. The absolute value of r is used in equation (14) to avoid cancellations of positive and negative quantities. Inserting the result into equation (11) and using equation (6) gives the first-order solution to Kepler's equation

$$E_1 = \frac{1}{d}\left(\frac{2rw}{w^2 + wq + q^2} + M \right) \tag{15}$$

Since r is proportional to M as the latter quantity goes to zero, this expression does not depend on cancellations in that limit. The solution is singular when both $e = 1$ and $M = 0$ simultaneously, but this is not of concern since equation (1) shows that $E = 0$ whenever $M = 0$. Thus a numerical solution of Kepler's Equation is unnecessary in this case.

This solution is the starting formula for our algorithms. It requires two transcendental function evaluations; the square root and cube root in equation (14). The cube root actually involves two transcendental function evaluations if it is implemented as a logarithm and an exponential.

Specification of α

The criterion for choosing α is the minimization of the relative errors in the starting formula. These errors are computed on a grid of 201 values of e between 0 and 1 and 251 values of E between 0 and π. The exact value of M is calculated at each grid point from equation (1), and then E_1 is obtained from equation (15). The relative error at each grid point is then

$$error = (E_1 - E)/E. \tag{16}$$

These errors were computed using quadruple precision floating point numbers with 112 bits in the mantissa. The contours of constant errors for $\alpha = 10$ and $\alpha = 3\pi^2/(\pi^2 - 6)$ are shown in Figures 1 and 2, respectively. The contours are linearly spaced with an increment of 0.001 between contours. The errors in Figure 1 are all negative, with a minimum value of -0.040. The errors in Figure 2 are all positive and significantly smaller in magnitude, having a maximum value of 0.013. The errors in both figures are monotonically increasing functions of the eccentricity, which suggests that an optimal α could be found by minimizing the errors for eccentricity equal to unity.
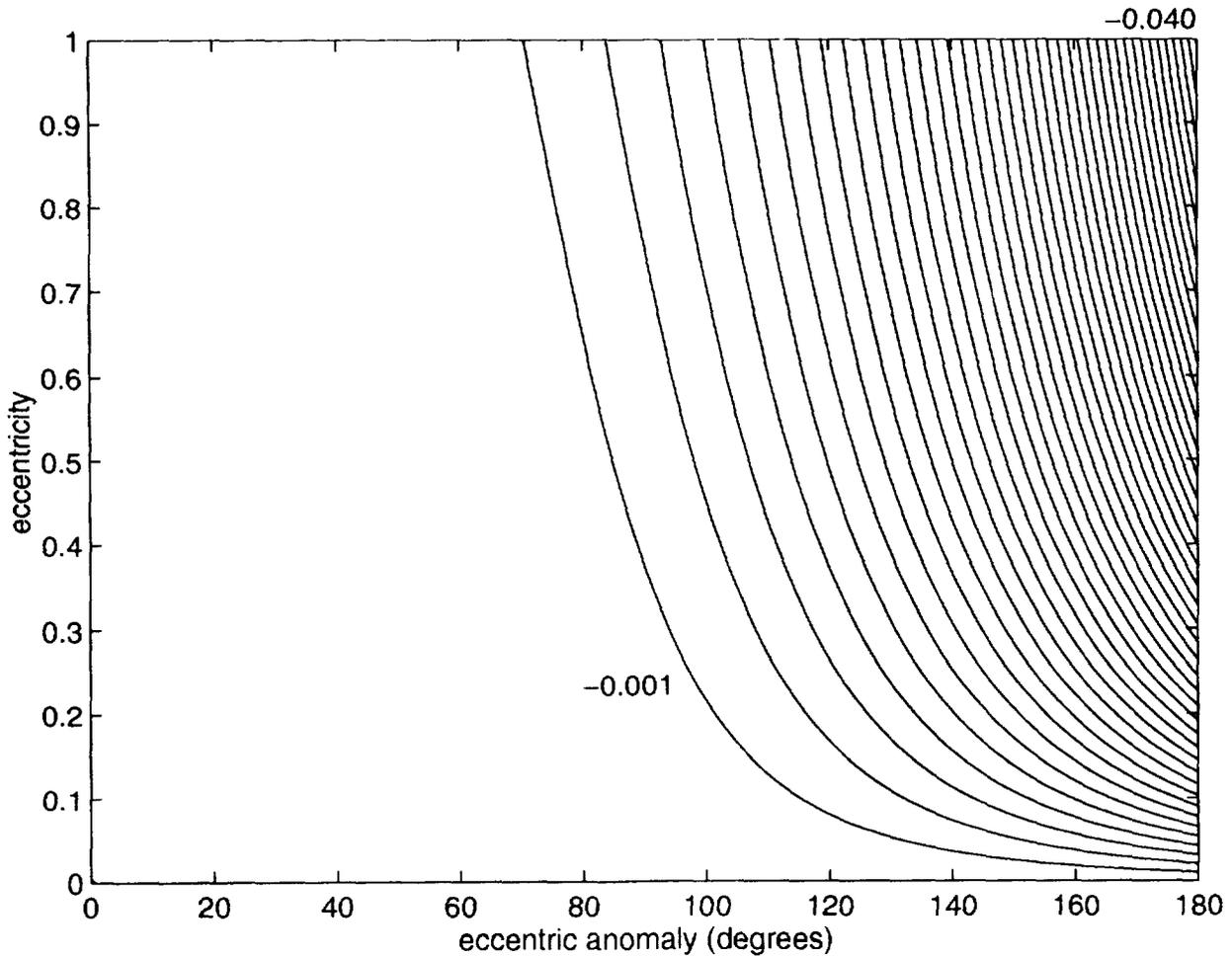
Figure 1. Relative Errors in Starting Formula E_1 for $\alpha = 10$
Equal-error contours with 0.001 linear contour spacing

It is not necessary that α be a constant parameter; we can choose it to be a function of e and M. Equation (2) would be exact if α could be chosen to satisfy

$$\alpha_{\text{ideal}} = \frac{3E^2(E - \sin E)}{E^3 - 6(E - \sin E)} \ . \tag{17}$$

This equation clearly not useful as it stands, since E is not known until Kepler's Equation has been solved. However, it is possible to find a usable function $\alpha(e, M)$ that is a good approximation to equation (17). The right side of this equation is an even function of E, and so $\alpha(e, M)$ must be an even function of M. It is also useful to choose a form that takes the value $\alpha = 3\pi^2/(\pi^2 - 6)$ when $E = M = \pm \pi$, since this will assure the continuity of the solutions over the extended range of these variables outside $[- \pi, \pi]$. This is not really important, since we intend to refine the result to the full accuracy of machine arithmetic, but Figure 2 shows that this condition is likely to lead to a good starting formula.
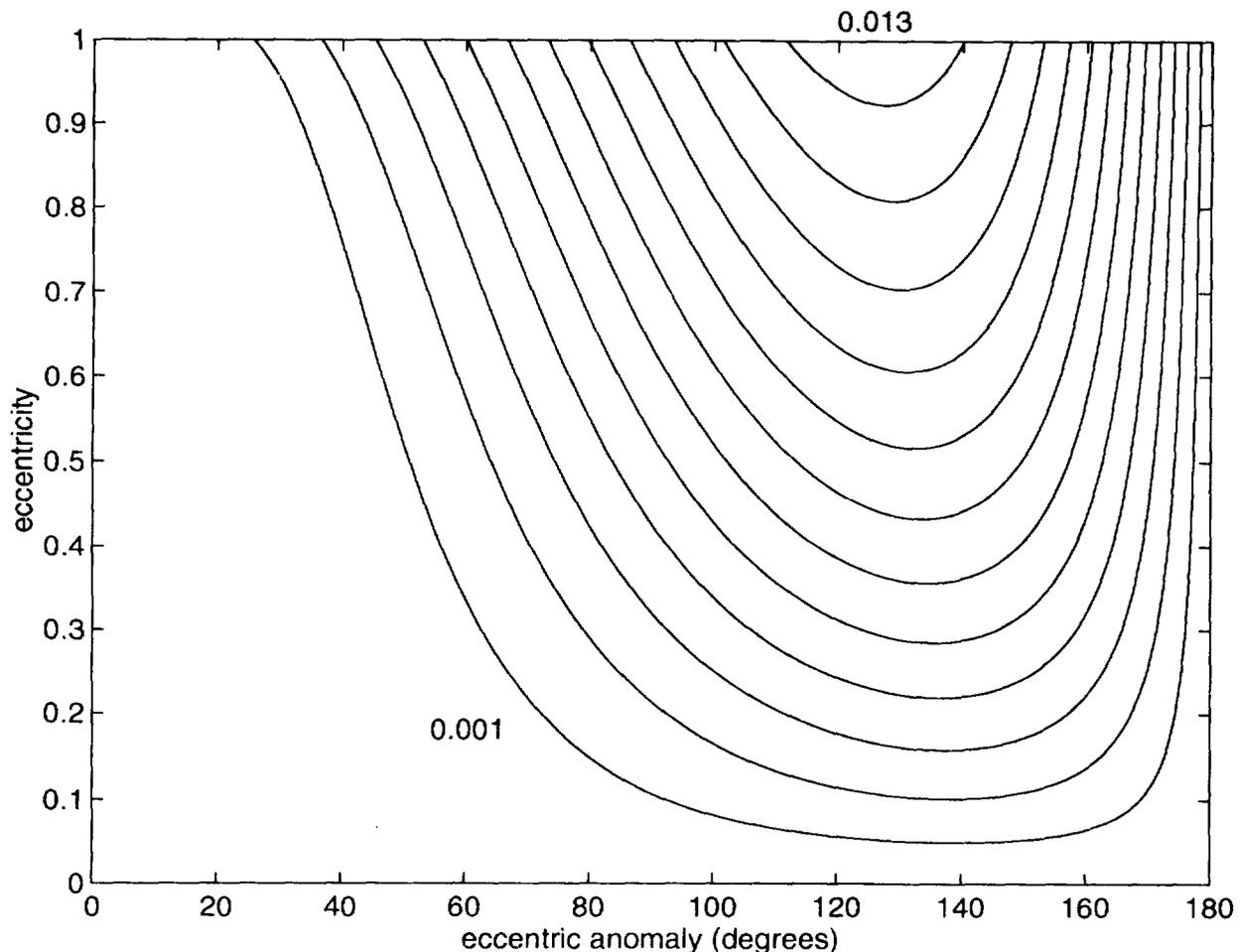
Figure 2. Relative Errors in Starting Formula E_1 for $\alpha = 3\pi^2/(\pi^2 - 6)$
Equal-error contours with 0.001 linear contour spacing

As discussed above, it is most important to find an accurate form for $\alpha(e,M)$ on the boundary $e = 1$. Figure 3 shows α_{ideal} and the straight line fit

$$\alpha(1,M) = \frac{3\pi^2 + 0.8\pi(\pi - |M|)}{\pi^2 - 6} \quad , \tag{18}$$

where M is given by equation (1) with $e = 1$. This formula can be extended to all eccentricities by noting that equations (17) and (18) are functions of E and M, respectively. We obtain the correct dependence of the slope of the straight line at the right end point by making use of

$$\left.\frac{\partial M}{\partial E}\right|_{E=\pi} = 1 + e. \tag{19}$$

The resulting approximation for all eccentricities and mean anomalies is given by

$$\alpha(e,M) = \frac{3\pi^2 + 1.6\pi(\pi - |M|)/(1+e)}{\pi^2 - 6} \quad . \tag{20}$$
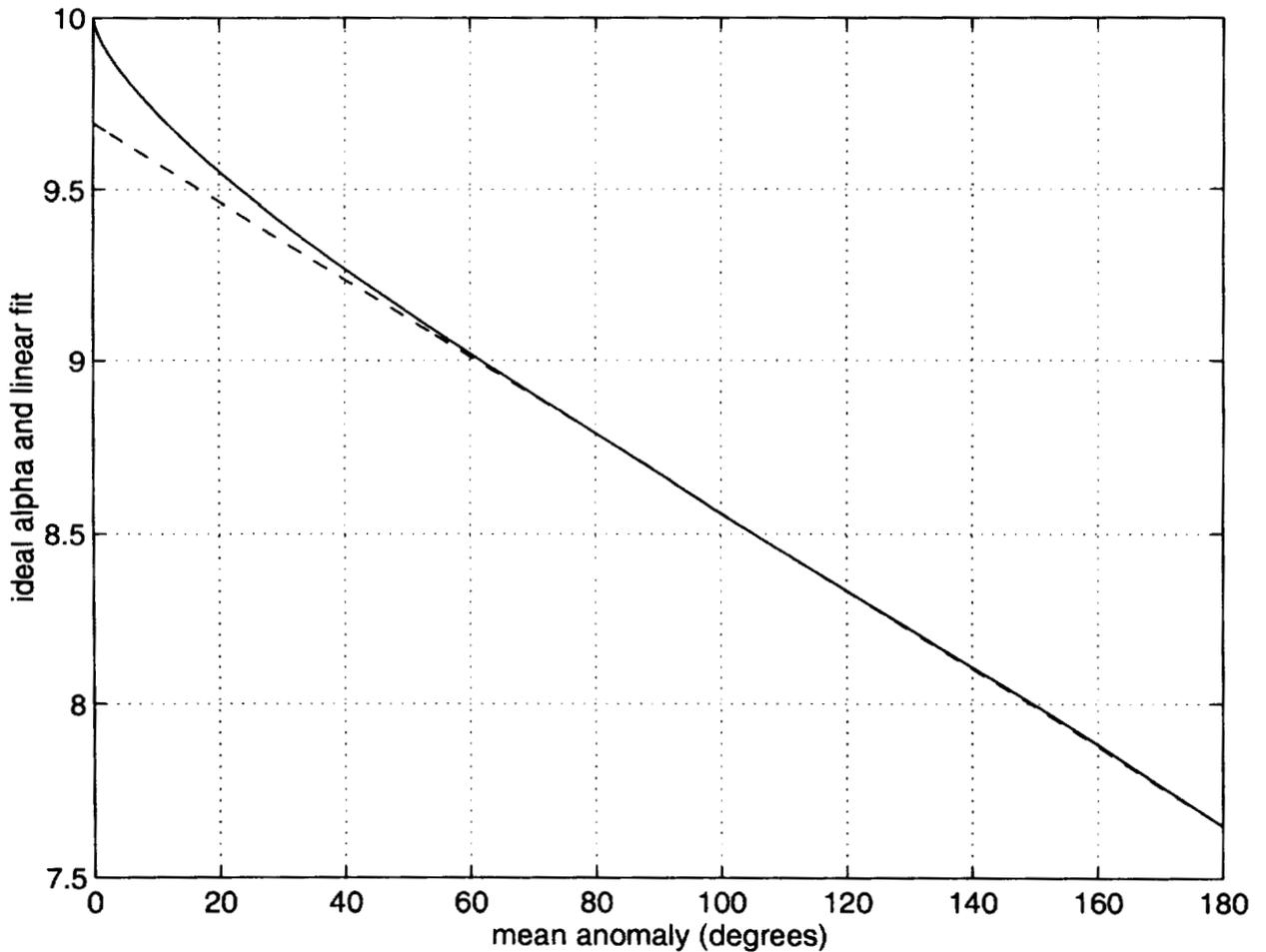
Figure 3. The Parameter α_{ideal} (solid curve) and Straight Line Fit (dotted line)

Our starting formula is given by the solution of the cubic for this form of α. The error contours for this starting formula are shown in Figure 4, with linear contour spacing of 2×10^{-5}. This is fifty times finer than the spacing of the contours in Figures 1 and 2. The values of these errors are between -2.3×10^{-4} and 2.8×10^{-4}, which are smaller than the errors of any other starting formula known to the author. The starting formula does involve a fair amount of computation, but Mikkola [7] has also proposed a starting formula that requires solution of a cubic equation and has maximum errors seven times as large as those of the method proposed here.

Refinement

The iterative refinements are based on finding roots of polynomial approximations of

$$f(E) = E - e\sin E - M. \tag{21}$$

The aim of this paper is to find a computational method yielding errors are smaller than the least significant bit of double-precision floating point numbers with 52 bits in the mantissa, which is
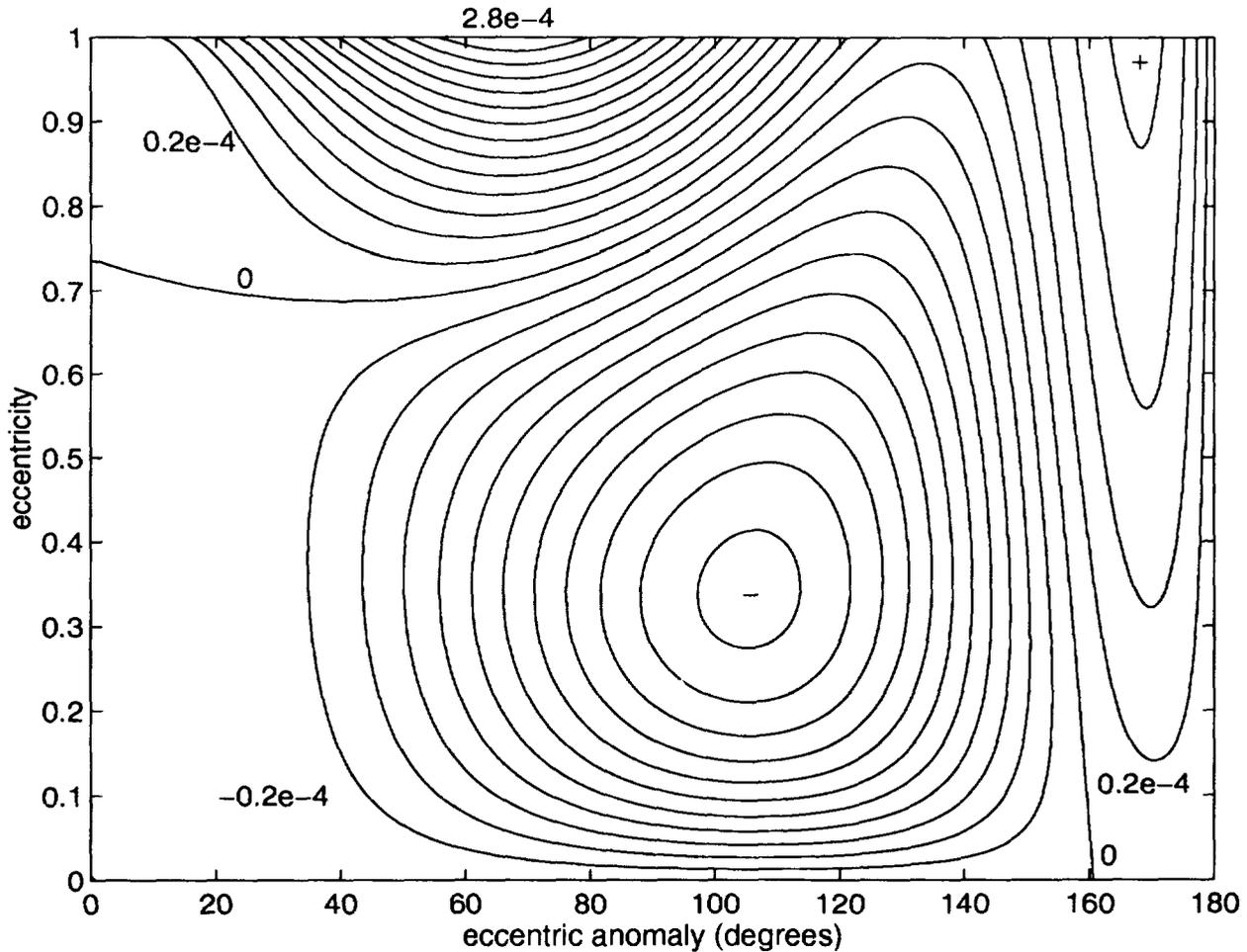
Figure 4. Relative Errors in Starting Formula E_1 for α Given by Equation (20)
Equal-error contours with 2×10^{-5} linear contour spacing

about 10^{-16}. A fifth-order refinement of the starting formula is expected to have relative errors less of $(2.8 \times 10^{-4})^5 = 1.7 \times 10^{-18}$, which is adequate to achieve double-precision accuracy. The third-order (Halley) and higher-order corrections are given by

$$\delta_3(E) = -\frac{f(E)}{f'(E) - \frac{1}{2}f(E)f''(E)/f'(E)}, \tag{22}$$

$$\delta_4(E) = -\frac{f(E)}{f'(E) + \frac{1}{2}\delta_3(E)f''(E) + \frac{1}{6}\delta_3^2(E)f'''(E)}, \tag{23}$$

and

$$\delta_5(E) = -\frac{f(E)}{f'(E) + \frac{1}{2}\delta_4(E)f''(E) + \frac{1}{6}\delta_4^2(E)f'''(E) + \frac{1}{24}\delta_4^3(E)f''''(E)}, \tag{24}$$

where the subscripts denote the order of the correction. The required partial derivatives are:

$$f'(E) = 1 - e\cos E, \tag{25}$$

$$f''(E) = e\sin E. \tag{26}$$

$$f'''(E) = e\cos E = 1 - f'(E), \tag{27}$$

and

$$f''''(E) = -e\sin E = -f''(E). \tag{28}$$

where the second forms of equations (27) and (28) are used to avoid additional trigonometric function evaluations. The fifth-order refined estimate is given by

$$E_5 = E_1 + \delta_5(E_1). \tag{29}$$

The equal-error contours of E_5 are plotted in Figure 5 with logarithmic spacing of the contours, which is to say that the errors on adjacent contours differ by a factor of ten. The zero contour is not plotted because of numerical roundoff; this contour is not significant since the magnitude of the errors is more important than their sign. The magnitude of the relative errors is less than 10^{-24} over large areas of the figure, and the maximum error magnitude over the entire range of elliptic motion is 7.35×10^{-19}. This is about half the naive prediction based on the order of the correction employed. This method requires only two trigonometric function evaluations in addition to the transcendental function evaluations need to solve the cubic equation for the starting formula.

Numerical Considerations

The errors of our method are smaller than the least significant bit of double-precision floating point numbers. Special care must be taken when this method is actually implemented in double-precision arithmetic, however. A naive implementation yields unacceptably large errors exceeding 5×10^{-14}. Plotting error contours shows that all errors with magnitudes in excess of 5×10^{-16} are in the region $e > 0.75$ and $E < 45°$. This effect was discussed by Odell and Gooding [3], who attribute it to cancellations in the computation of $f(E)$ and $f'(E)$ by equations (21) and (25),

54
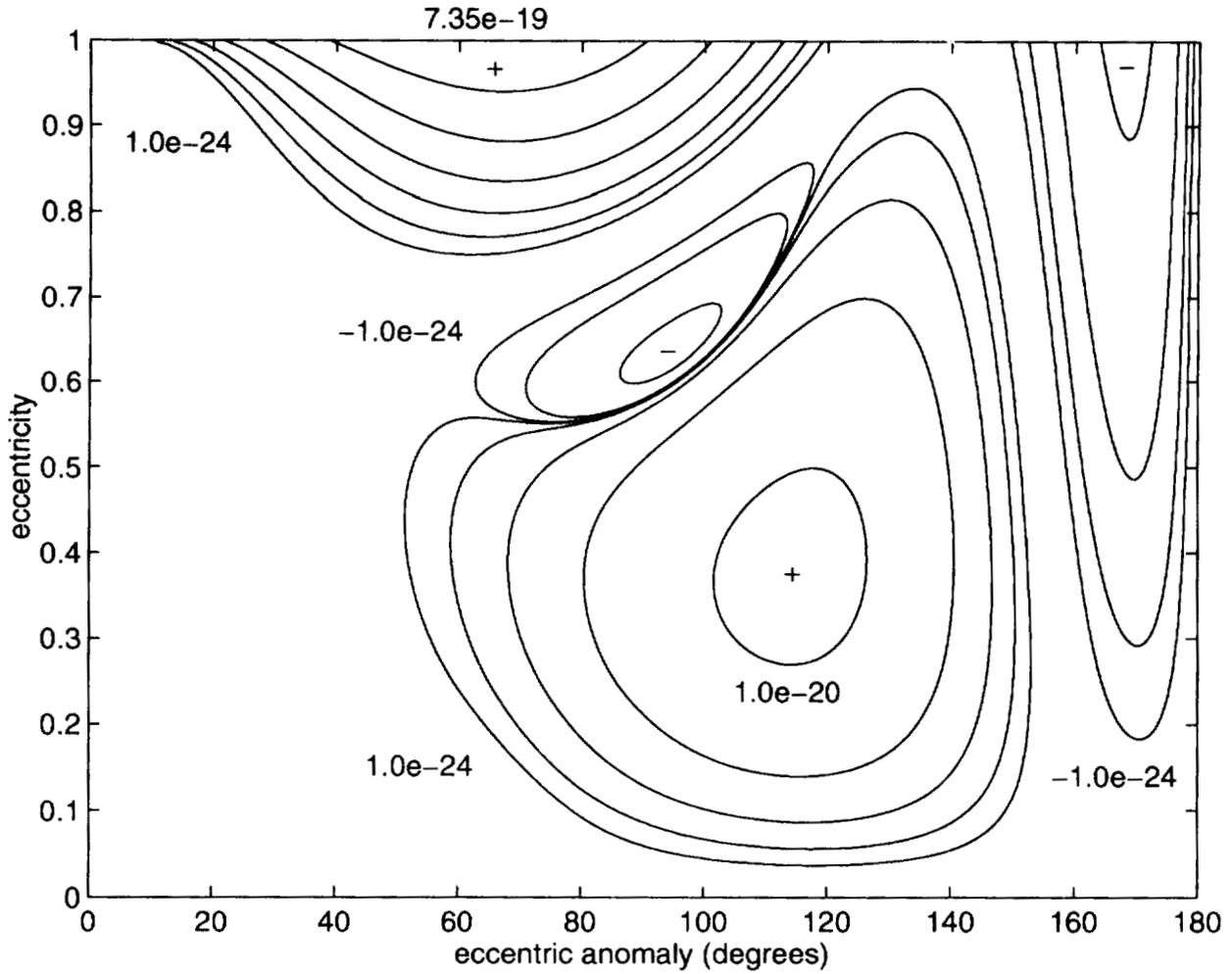
Figure 5. Relative Errors in Refined Eccentric Anomaly E_9
Equal-error contours with $\times 10$ logarithmic contour spacing

respectively. The solution to this problem is to modify the computation of these quantities. The revision to the first derivative computation is straightforward; equation (25) is replaced by

$$f'(E) = 1 - e + 2e \sin^2(E/2).$$ (30)

The fix to equation (21) is not so simple. The method employed here is to replace equation (21) by the equivalent form

$$f(E) = M^*(e, E) - M,$$ (31)

where

$$M^*(e, E) \equiv E - e \sin E$$ (32)

outside the range $e > 0.5$ and $E_1 < 1$ radian. Inside this range, $M^*(e, E)$ is given by the Padé approximant:

$$M^*(e, E) \equiv (1 - e)E + eE^3 \frac{numerator}{denominator},$$ (33)

55

with

$$numerator \equiv -1.7454287843856404 \times 10^{-6} E^6 + 4.1584640418181644 \times 10^{-4} E^4$$
$$- 3.0956446448551138 \times 10^{-2} E^2 + 1 \tag{34a}$$

and

$$denominator \equiv 1.7804367119519884 \times 10^{-8} E^8 + 5.9727613731070647 \times 10^{-6} E^6$$
$$+ 1.0652873476684142 \times 10^{-3} E^4 + 1.1426132130869317 \times 10^{-1} E^2 + 6. \tag{34b}$$

The second derivative is computed as

$$f''(E) = E - M^*(e, E) \tag{35}$$

over the entire range of eccentricity and eccentric anomaly. The third and fourth derivatives are computed as usual. No additional transcendental function evaluations are required by these fixes, although the Padé approximant is probably more expensive to evaluate than the sine function.

The resulting double precision implementation of the algorithm has relative errors less than 4×10^{-16} over the entire range of elliptic motion. Inspection of a plot of the error contours revealed no systematic pattern, confirming that the errors are due solely to unavoidable machine arithmetic roundoff.

Discussion

The algorithm developed in this paper has been shown to have errors well within the inherent limitations of double-precision computer arithmetic, over the entire range of elliptic orbital motion. Among algorithms with this property, this method is at least as efficient as any proposed previously, requiring only four transcendental function evaluations: a square root, a cube root, and two trigonometric functions. The method is singular only when the eccentricity is unity and the mean anomaly is simultaneously zero. There are two reasons why it is never necessary to solve Kepler's Equation in this case: first, unit eccentricity is not really elliptic motion, and second, the eccentric anomaly is known to be zero when the mean anomaly is zero, making numerical solution unnecessary. Special procedures to handle double-precision roundoff errors near this singular point have been developed and tested. The resulting algorithm is well suited for implementation in orbit propagation systems.

References

[1] Peter Colwell, *Solving Kepler's Equation Over Three Centuries*, Willman-Bell, Richmond, VA (1993)

[2] Richard H. Battin, *An Introduction to the Mathematics and Methods of Astrodynamics*, American Institute of Aeronautics and Astronautics, New York (1987)

[3] A. W. Odell and R. H. Gooding,"Procedures for Solving Kepler's Equation," Celestial Mechanics, **38** (1986) pp 307-334

[4] J. M. A. Danby and T. M. Burkardt, "The Solution of Kepler's Equation, I," Celestial Mechanics, **31** (1983) pp 95-107

[5] T. M. Burkardt and J. M. A. Danby , "The Solution of Kepler's Equation, II," Celestial Mechanics, **31** (1983) pp 317-328

[6] J. M. A. Danby, "The Solution of Kepler's Equation, III," Celestial Mechanics, **40** (1987) pp 303-312

[7] Seppo Mikkola, "A Cubic Approximation for Kepler's Equation," Celestial Mechanics, **40** (1987) pp 329-334

[8] L. G. Taff and T. A. Brennan, "On Solving Kepler's Equation," Celestial Mechanics and Dynamical Astronomy, **46** (1989) pp 163-176

[9] Milton Abramowitz and Irene A. Stegun, *Handbook of Mathematical Functions*, Dover, New York (1965)

Accurate Orbit Determination Strategies for the Tracking and Data Relay Satellites*

D. H. Oza, D. T. Bolvin, J. M. Lorah, and T. Lee
Computer Sciences Corporation (CSC)
Lanham-Seabrook, Maryland, USA

C. E. Doll
Goddard Space Flight Center (GSFC)
Greenbelt, Maryland, USA

Abstract

The National Aeronautics and Space Administration (NASA) has developed the Tracking and Data Relay Satellite (TDRS) System (TDRSS) for tracking and communications support of low Earth-orbiting satellites. TDRSS has the operational capability of providing 85-percent coverage for TDRSS-user spacecraft. TDRSS currently consists of five geosynchronous spacecraft and the White Sands Complex (WSC) at White Sands, New Mexico. The Bilateration Ranging Transponder System (BRTS) provides range and Doppler measurements for each TDRS. The ground-based BRTS transponders are tracked as if they were TDRSS-user spacecraft. Since the positions of the BRTS transponders are known, their radiometric tracking measurements can be used to provide a well-determined ephemeris for the TDRS spacecraft.

For high-accuracy orbit determination of a TDRSS user, such as the Ocean Topography Experiment (TOPEX)/Poseidon spacecraft, high-accuracy TDRS orbits are required. This paper reports on successive refinements in improved techniques and procedures leading to more accurate TDRS orbit determination strategies using the Goddard Trajectory Determination System (GTDS). These strategies range from the standard operational solution using only the BRTS tracking measurements to a sophisticated iterative process involving several successive simultaneous solutions for multiple TDRSs and a TDRSS-user spacecraft. Results are presented for GTDS-generated TDRS ephemerides produced in simultaneous solutions with the TOPEX/Poseidon spacecraft. Strategies with different user spacecraft, as well as schemes for recovering accurate TDRS orbits following a TDRS maneuver, are also presented. In addition, a comprehensive assessment and evaluation of alternative strategies for TDRS orbit determination, excluding BRTS tracking measurements, are presented.

1.0 Introduction

This paper assesses the accuracy achievable using various techniques for performing Tracking and Data Relay Satellite (TDRS) orbit determination using the Goddard Trajectory Determination System (GTDS), which is an operational batch least–squares orbit determination system, and the Orbit Determination Error Analysis System (ODEAS) covariance analysis system, both used within the Goddard Space Flight Center (GSFC) Flight Dynamics Division (FDD).

The TDRS System (TDRSS) is a geosynchronous relay satellite network, which currently consists of five geosynchronous spacecraft and the White Sands Complex (WSC) located at White Sands, New Mexico. Three of the five TDRSs (TDRS–East, TDRS–West, and TDRS–Spare, located at 41 degrees, 174 degrees, and 62 degrees west longitude, respectively) actively support tracking of TDRSS–user spacecraft. One of the remaining TDRSs (located at 275 degrees west longitude) is used only for satellite communications, while the other TDRS (located at 46 degrees west longitude) is being reserved for future use. TDRSS can provide 85– to 100–percent coverage, depending on spacecraft altitude. The Bilateration Ranging Transponder System (BRTS) provides range and Doppler tracking measurements of the TDRSs for TDRS orbit determination.

Currently, the operational accuracy requirement for TDRS orbit determination is 600 meters (3σ), which is driven by Space Transportation System (STS) support. The TDRS orbit accuracy requirements for other currently supported FDD missions are less strict. Current operational procedures at FDD produce TDRS orbits accurate to 150 meters (3σ). For future mission support, however, the TDRS orbit determination accuracy requirements will become more stringent. For example, the upcoming Earth Observing Satellite (EOS) AM-1 accuracy requirement for TDRS orbits is 75 meters (3σ), which is not met by current operational TDRS orbit determination solutions. This requirement raises the need to develop improved technical approaches and procedures.

Previous FDD precision orbit determination analysis results indicated that TDRS orbit determination errors are a significant error source in TDRSS-user orbit determination (Reference 1). To obtain high-accuracy TDRSS-user orbits, new methods are needed that improve and refine TDRS orbit determination accuracy over the current operational support procedure.

The current operational method for determining TDRS orbits uses the radiometric ranging measurements acquired through BRTS. For standard support, only the range measurements are used over 42-hour arcs to determine position, velocity, a solar pressure coefficient, and a range measurement bias in a separate solution for each TDRS. Previous analysis (Reference 2) demonstrated that a dramatic improvement in overlap consistencies, reducing them from the 40- to 50-meter level for a separate solution for TDRS to the 20- to 30-meter level, was possible by performing simultaneous TDRSs/TDRSS-user orbit determination using a low-Earth orbiting TDRSS-user satellite. Since this earlier analysis in 1990, the force modeling used at the FDD has improved significantly, most notably after the launch of TOPEX. With better force modeling for a low-Earth orbiting TDRSS-user, which will reduce dynamic errors, it is expected that in a simultaneous solution the TDRS orbit accuracy can be improved compared to the earlier analysis. This concept is further developed and exploited in the current analysis.

A variety of innovative techniques for enhancing TDRS orbit determination accuracy, most of which involve the generation of a series of simultaneous TDRSs/TDRSS-user orbit solutions to calibrate the TDRSS range measurement biases, are developed and analyzed. In this study, the TDRSS users investigated are the Ocean Topography Experiment (TOPEX)/Poseidon, Earth Radiation Budget Satellite (ERBS), and Landsat-4 spacecraft. It is important to note that, just as TDRS orbit accuracy affects TDRSS-user orbit determination accuracy, TDRSS-user accuracy also affects TDRS orbit accuracy when performing simultaneous TDRS/TDRSS-user orbit determination. Since TDRSS-user orbit determination error is normally dominated by geopotential and atmospheric drag errors, higher altitude spacecraft such as TOPEX/Poseidon will significantly reduce these detrimental effects on TDRS orbit determination and provide more accurate estimates of the TDRS orbits. Therefore, the simultaneous TDRS/TDRSS-user solutions using the lower-altitude ERBS and Landsat-4 spacecraft are not expected to provide as accurate TDRS orbits as those determined using TOPEX/Poseidon. For completeness, the accuracy of the current FDD TDRS operational orbit determination procedure is also assessed. Because of the future support load expected of each TDRS and the frequent TDRS maneuvers required to maintain stationkeeping, additional analysis is performed to develop methods for improving the accuracy of TDRS postmaneuver solutions using extremely short TDRS postmaneuver data spans.

Because of the potential cost associated with replacing the aging BRTS transponders, analysis is also performed to create and assess a number of alternative techniques for performing TDRS orbit determination without the use of BRTS tracking measurements. These new, innovative methods utilize a variety of tracking sources, including the new Second TDRSS Ground Terminal (STGT) tracking, telemetry and command (TT&C) tracking measurements. Alternative TDRS orbit determination strategies, including those that make use of Global Positioning System (GPS) technology, are also addressed. For the strategies, an orbit determination accuracy assessment is not performed through data reduction, but estimates of the accuracy achievable for the TDRS orbit determination are obtained by covariance analysis error estimates using ODEAS. Estimates of the errors on the TDRS orbit states are generated using realistic error sources, and the results are evaluated.

Based on the TDRS orbit determination solutions, short- and long-term orbit predictions are routinely generated by the FDD for use in planning and scheduling spacecraft activities. As the orbit determination accuracy requirements become more stringent, so too will the prediction accuracy requirements. However, the effects of the improved TDRS orbit determination techniques on orbit prediction, though important, are beyond the scope of this investigation and will not be addressed here.

The GTDS batch least–squares orbit determination and ODEAS covariance analysis procedures and evaluation methods used are presented in Section 2.0. An accuracy assessment of the precision TDRS solutions using improved techniques in GTDS is contained in Section 3.0. Section 4.0 discusses the results of strategies for performing TDRS orbit determination that include BRTS tracking measurements and addresses the postmaneuver recovery of TDRS orbit solutions. Section 5.0 describes the results of TDRS orbit determination strategies that exclude BRTS tracking measurements. Section 6.0 provides the conclusions and recommendations of this study.

2.0 Analysis Methodology

This section describes the tracking measurements and analysis procedures used in this study and the methods for assessing the analysis results.

2.1 Strategies and Tracking Measurements

Table 1 summarizes the various TDRS orbit determination techniques analyzed and evaluated in this study. It also includes a general description of the tracking measurements used for each type of orbit determination solution. For some analyses, additional measurement types were added. These additional measurement types are described below.

Table 1. Summary of TDRS Orbit Determination Strategies and Tracking Measurements

Orbit Determination Solution Concept	Solution Description	Tracking Measurement Description
BRTS (Current Baseline)	Using existing BRTS for TDRS-only orbit determination	BRTS range measurements for TDRSs
BRTS + User	Using existing BRTS for simultaneous TDRS + user orbit determination	BRTS range measurements for TDRSs; TDRSS range and two-way Doppler for TDRSS-user
BRTS + K-band	Using STGT K-Band TT&C range measurements and remote BRTS for TDRS-only orbit determination	BRTS and TT&C range measurements for TDRSs
TDRS Ground Network (GN)	Using GN tracking of TDRS for TDRS-only orbit determination	GN range and two-way range-rate measurements for TDRSs
K-band + user	Using STGT K-Band TT&C range measurements and simultaneous TDRS + user orbit determination	TT&C range measurements for TDRSs; TDRSS range and two-way Doppler measurements for TDRSS-user
TDRS GN + User	Using GN tracking of TDRS and simultaneous TDRS + user orbit determination	GN range and two-way range-rate measurements for TDRSs; TDRSS range and two-way Doppler for TDRSS-user
User GN + User TDRSS	Using simultaneous TDRS + user orbit determination with GN and TDRSS tracking of user	GN range and two-way range-rate and TDRSS range and two-way Doppler measurements for TDRSS-user

Tracking measurements from a variety of sources were used in this study. TDRSS tracking measurements for the GTDS orbit determination solutions were obtained primarily from TDRS-4 and TDRS-5, though, for some analyses, tracking measurements from TDRS-6 were used. These measurements consist of two-way Doppler and range measurements of the user spacecraft via each TDRS, except when the user spacecraft was TOPEX, when one-way return Doppler measurements were also included. BRTS two-way range measurements were used for the TDRSs and, for the TDRS-4 postmaneuver recovery analysis, BRTS two-way Doppler and White Sands antenna azimuth-elevation angle measurements were also included. TT&C range measurements were used for some of the TDRS orbit determination covariance analyses. For GN tracking of the user spacecraft, two-way range and two-way range-rate measurements were used.

BRTS tracking coverage of each TDRS spacecraft typically consists of twelve to fifteen 5-minute passes per day. TT&C tracking of the TDRSs is nearly continuous. In covariance analysis, we used a tracking schedule comparable to that for BRTS. The TDRS tracking of the TOPEX spacecraft consisted of an average of 10 passes of one-way return Doppler measurements and 11 passes of two-way range and Doppler measurements per day, with the average pass lasting 40 minutes. TDRSS tracking of the ERBS spacecraft typically consisted of 12 tracking passes per day, with each pass averaging 10 minutes in duration. The GN tracking of ERBS consisted of an average of two 10-minute passes per day. For Landsat-4, each TDRSS pass lasted 5 to 20 minutes, with approximately 6 to 7 passes per day.

2.2 Orbit Determination Methods and Modeling

This section describes the orbit determination methods and modeling used to generate the batch least-squares GTDS solutions and the batch least-squares covariance analysis results.

2.2.1 Orbit Determination

Batch least-squares solutions were generated and analyzed for a number of TDRSS-supported spacecraft for the TOPEX Cycle 5 and Cycle 21 timespans. Cycle 5 is the fifth 10-day TOPEX groundtrack repeat cycle and covers the period from 17:32 hours universal time coordinated (UTC) on November 1, 1992, through 21:33 hours UTC on November 11, 1992. Cycle 21 is the 21st 10-day TOPEX groundtrack repeat cycle and covers the period from 09:08 hours UTC on April 9, 1993, through 11:06 hours UTC on April 19, 1993. These periods were selected because they contained minimal TOPEX spacecraft attitude perturbations and minimal TDRS spacecraft orbit and attitude maneuvers. The batch least-squares estimation algorithm used

by GTDS for this analysis is the same as that used for operational navigation support of the TDRSs by the GSFC FDF. The procedure used for operational support includes using the BRTS range measurements and solving for the TDRS spacecraft state, the solar radiation pressure coefficient, and the White Sands ground antenna range measurement bias. The modeling and state estimation parameters used for this analysis have been modified and enhanced to provide more accurate results and to take advantage of modeling and techniques not currently in operational use. The standard technique developed for obtaining more accurate TDRS orbit solutions using GTDS, referred to as the analytic calibration of biases (ACB) technique, involves performing a series of simultaneous TDRSs/TDRSS-user solutions to calibrate a set of relative range measurement biases for each source of range measurement error in the TDRSS. Because this technique was developed using the TOPEX/Poseidon spacecraft as the TDRSS-user, the ACB method will be presented in this section in terms of the TOPEX modeling and measurement types. For other TDRSS users, such as ERBS and Landsat-4, the modeling and measurement types will vary slightly, but the basic ACB technique is the same. The slight deviations in the standard ACB technique, as well as the deviations to the standard force modeling and parameters to suit other TDRSS users, will be described later in the results sections. The TOPEX and TDRS ACB standard force modeling and parameters used in this study are provided in Table 2. Any deviations for special runs are noted where applicable.

Table 2. Standard Parameters and Options Used in the GTDS Solutions

Orbit Determination Parameter or Option	GTDS Values*	
	TOPEX	TDRSs
Estimated parameters	Orbital state, thrust coefficients, coefficient of solar radiation pressure (C_R), USO bias and drift	Orbital state, coefficient of solar radiation pressure (C_R), spacecraft transponder delay, BRTS transponder delays
Integration type	Cowell 12th order	Cowell 12th order
Coordinate system of integration	Mean-of-J2000.0	Mean-of-J2000.0
Integration step size (seconds)	60 seconds	600 seconds
Tracking measurements	TDRSS two-way Doppler TDRSS one-way return Doppler TDRSS two-way range	BRTS two-way range
Measurement span	See text	See text
Data rate	1 per minute	1 per 20 seconds
Differential correction (DC) convergence parameter	0.00005	0.00005
Editing criterion	3σ	3σ
Ionospheric editing criterion	Central angle greater than 79.48 degrees	-
Measurement weight sigmas	Doppler: 10 millihertz Range: 1.5 meters	2 meters
Satellite area model	Variable mean area model	Constant, 40 meters^2
Satellite mass	2417.2 kilograms	TDRS-5: 1973.1 kilograms TDRS-4: 1853.6 kilograms
Geopotential model	70 x 70 JGM-2	20 x 20 JGM-2
Atmospheric density model	Jacchia-Roberts	N/A
Solar and lunar ephemerides	DE-200	DE-200
Coefficient of drag (C_D)	2.3 applied	N/A
Ionospheric refraction correction Ground-to-spacecraft Spacecraft-to-spacecraft	Yes No (central angle edit instead)	Yes N/A
User-spacecraft antenna offset correction	Constant radial, along-track, cross-track	No
Tropospheric refraction correction	Yes	Yes
Polar motion correction	Yes	Yes
Solid Earth tides	Yes	Yes
Ocean tides	No	No
Plate motion	No	No
Earth radiation pressure	No	No

*JGM = Joint Gravity Model; N/A = not applicable

62

The simultaneous TDRS/TDRSS-user solution arcs used in this analysis were selected to avoid all TDRS maneuvers and angular momentum unloads, wherever possible, while maintaining the longest possible data spans. Previous analysis has shown that longer TDRS/TDRSS-user data arcs provide more accurate solutions. In addition, central angle editing was used to mitigate the effects of ionospheric refraction on the TDRS–to–TDRSS-user tracking link. All measurements with a central angle larger than 79.5 degrees were excluded to eliminate all measurements below the TDRSS-user local horizon.

The ACB technique estimates, in a methodical manner, a set of relative range measurement biases for each source of range measurement error within the TDRSS. In the standard ACB technique, a total of six solutions are generated. The first five solutions are simultaneous TDRSs/TDRSS-user solutions used to obtain the best possible TDRS trajectories. The final solution is a TDRSS-user-only solution that uses the best estimated TDRS trajectories determined from the previous simultaneous solutions.

The first solution determines, through analysis of BRTS range residuals, which BRTS transponders have range biases relative to the TDRSS range measurements for the TDRSS-user. The second solution estimates a "pseudo" TDRSS-user transponder delay through the estimation and differencing of BRTS and TDRSS-user range measurement biases. The next three solutions determine the best possible TDRS orbits using the information obtained from the first two simultaneous solutions and iteratively estimating the BRTS, "pseudo" TDRSS-user and TDRSs transponder delays. The final solution is a TDRSS-user-only solution using the TDRSs' trajectories obtained from the final iterative simultaneous solution.

The details of the standard ACB technique, using TOPEX as the TDRSS user, are described below:

Solution (1):

Purpose:	Solution (1) determines which BRTS transponders appear to have biases in the range tracking measurements relative to the TDRSS range measurements of TOPEX, which is accomplished through examination and analysis of the BRTS range residuals resulting from the solution. This information will be used in Solution (3).
Solution Type:	Simultaneous TOPEX/TDRSs
Tracking Measurements:	BRTS range measurements for the TDRSs and TDRSS range and two-way and one-way return Doppler for TOPEX
Range-Measurement-Related Parameters:	Estimate range measurement biases on the TOPEX range measurements at the White Sands ground antennas.

Solution (2):

Purpose:	Solution (2) determines a "pseudo" TOPEX transponder delay. This information will be used in Solution (3).
Solution Type:	Same as Solution (1)
Tracking Measurements:	Same as Solution (1)
Range Measurement-Related Parameters:	Estimate range measurement biases on the TOPEX range measurements at the White Sands ground antennas. Estimate range measurement biases on the BRTS range measurements at the White Sands ground antennas. Determine the pseudo TOPEX transponder delay by differencing the BRTS range bias and the TOPEX range bias for each White Sands ground antenna, and then averaging these differences to obtain a single average White Sands ground antenna range bias. This average White Sands ground antenna bias serves as an approximation for the TOPEX transponder delay.

Solution (3a):

Purpose: Solutions (3a), (3b), and (3c) use the information from Solution (1) and Solution (2) to obtain the best possible TDRS orbits for use in Solution (4). Solution (3a) is the first iteration for estimating the best possible TDRS orbits.

Solution Type: Same as Solution (1)

Tracking Measurement: Same as Solution (1)

Range Measurement-Related Parameters: Estimate the BRTS transponder delays for the "biased" BRTS transponders identified in Solution (1). Apply the average White Sands ground antenna bias (pseudo TOPEX transponder delay) determined in Solution (2) to each White Sands ground antenna. Estimate the TDRS transponder delays for each TDRS.

Solution (3b):

Purpose: Solution (3b) is second step in the iterative process to obtain the best possible TDRS orbits.

Solution Type: Same as Solution (1)

Tracking Measurements: Same as Solution (1)

Range Measurement-Related Parameters: Apply the BRTS transponder delays determined in Solution (3a) to the corresponding "biased" BRTS transponders. Estimate the White Sands ground antenna biases (pseudo TOPEX transponder delay) for each White Sands ground antenna. Apply the TDRS transponder delays determined in Solution (3a) to the corresponding TDRS.

Solution (3c):

Purpose: Solution (3c) is the final step in the iterative process to obtain the best possible TDRS orbits.

Solution Type: Same as Solution (1)

Tracking Measurements: Same as Solution (1)

Range Measurement-Related Parameters: Same as Solution (3a), except apply the individual White Sands ground antenna biases (pseudo TOPEX transponder delay) determined in Solution (3b) to each corresponding White Sands ground antenna.

Solution (4):

Purpose: Solution (4) uses the TDRS orbits obtained from Solution (3c) to determine the best possible
Solution Type: TOPEX-Only

Tracking Measurements: TDRSs two-way and one-way return Doppler for TOPEX

Range Measurement-Related Parameters: Not applicable. Range measurements eliminated to minimize the effect of TOPEX range measurement bias modeling errors on the TOPEX trajectory

The ACB procedure is schematically depicted in Figure 1.

2.2.2 Covariance Analysis

Batch least-squares covariance analysis using ODEAS was performed to analyze the accuracy of a number of alternative TDRS orbit determination strategies. These strategies exclude the use of BRTS tracking measurements and utilize several other tracking measurements types. The force and error models used for the covariance analysis mimic the parameters that would typically be used for TDRS orbit determination and are provided in Table 3.

Table 3. Landsat-4 and TDRS Error Sources and Associated 3σ Uncertainties

| Parameter or Option	3σ Uncertainty		
GM (Earth)	$GMx(3x10^{-8})$		
Earth Gravity Field	300% of $(JGM2 - JGM2_{clone})$ (70x70)		
Drag Coefficient for Landsat-4	Estimated		
Solar Radiation Pressure Coefficient	30% for Landsat-4 2% for each TDRS		
Solar Flux	5% for 0-24 hours and 15% for 24-34 hours		
Station Position	3 meters each local tangent x, y, and z		
Tropospheric Refraction	45%		
Ionospheric Refraction	100%		
Measurements	Noise-σ	Weight-σ	Bias
Landsat-4 TDRSS two-way Range-Rate (meters/sec)	$2.82x10^{-3}$	$3.2765x10^{-2}$	0
Landsat-4 TDRSS two-way Range (meters)	1.5	10	7
BRTS two-way Range (meters)	1.5	30	7
TT&C two-way Range (WHSK↔TDRS) (meters)	1.5	30	3
GN two-way Range for TDRS (meters)	3	40	30
GN two-way Range for Landsat-4 (meters)	1.5	20	15
GN two-way Range-Rate for Landsat-4 (meters/sec)	0.001	0.1	0

N/A = not applicable
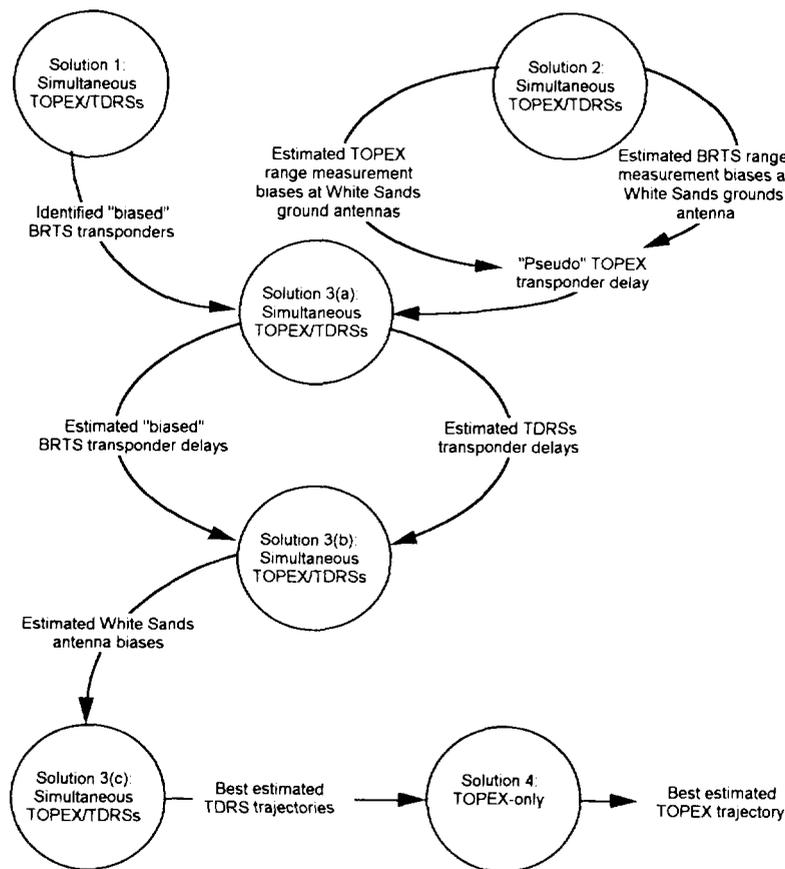
**Figure 1. A Schematic of the ACB Procedure**

3.0 Precision TDRS Orbit Determination Results

The accuracy of the TDRS orbit determination solutions generated in this study is assessed through comparisons with high-accuracy TDRS precision orbit ephemerides (POEs) generated by the Precision Orbit Determination (POD) team, using the Geodynamics (GEODYN) System, within the Space Geodesy Branch located at GSFC. The TDRS POEs are generated using the high-precision TOPEX/Poseidon POEs as an input measurement type to the TDRS orbit determination process. The TDRS POEs are estimated to be accurate to within 3 meters in total position based on preliminary covariance analysis results as well as analysis results using the TOPEX POEs (Reference 3). The definitive orbit determination requirements for the TOPEX/Poseidon POEs include a maximum 39–centimeter (3σ) radial position error. The availability of the independent orbit determination solutions generated by the Space Geodesy Branch provides a unique opportunity to evaluate the accuracy of the orbit determination systems used by the FDD for operational navigation and analysis support.

Using the standard ACB method described in Section 2.2.1 with the TOPEX spacecraft as the TDRSS user, 5-day TOPEX, TDRS-4, and TDRS-5 orbit determination solutions were generated covering the period 00:00 hours UTC on November 7, 1992, through 00:00 hours UTC on November 12, 1992, which corresponds to the latter portion of TOPEX Cycle 5. The TDRS ephemerides were compared at 10-minute intervals with the corresponding TDRS-4 and TDRS-5 POEs in orbit plane coordinates.

The root-sum-square (RSS) position differences between the Cycle 5 TDRS-4 GTDS solution (3c) and the corresponding POE are shown in Figure 2. The root-mean-square (RMS) of the RSS position difference is 4.3 meters, with a maximum difference of 9.4 meters. The RMS differences in the radial, along-track, and cross-track components are 1.2, 3.4, and 2.4 meters, respectively. The RSS position differences between the Cycle 5 TDRS-5 GTDS solution (3c) and the corresponding POE are shown in Figure 3. The RMS of the RSS position difference is 3.6 meters, with a maximum difference of 8.8 meters. The RMS differences in the radial, along-track, and cross-track components are 1.4, 2.8, and 1.9 meters, respectively.

Additional TDRS-4 and TDRS-5 GTDS solutions using the ACB technique with TOPEX were generated within the Cycle 5 timespan and compared with the corresponding TDRS POEs. TDRS-4, TDRS-5, and TOPEX solutions were generated for a 5-day period extending from 00:00 hours UTC on November 4, 1992, through 00:00 hours UTC on November 9, 1992, corresponding to the middle portion of TOPEX Cycle 5. The RMS of the RSS position differences between the GTDS ephemerides and the TDRS POEs were 11.2 meters for TDRS-4 and 11.2 meters for TDRS-5, somewhat larger than the previous 5-day results. The reason for the degraded comparison results for TDRS-5 is the inclusion of tracking measurements following a TDRS-5 momentum unload, which were edited in the previous 5-day solution. Previous analysis shows that inclusion of the postmomentum wheel unload tracking measurements can degrade solution accuracy. The reason for the degraded TDRS-4 solution is still under investigation.
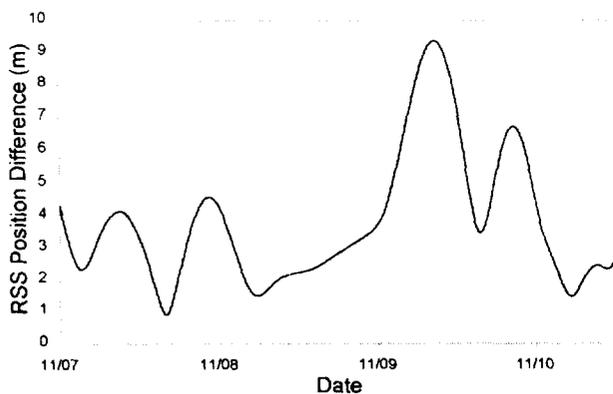

Figure 2. Position Differences Between TDRS-4 POE and GTDS TDRS-4 Ephemerides
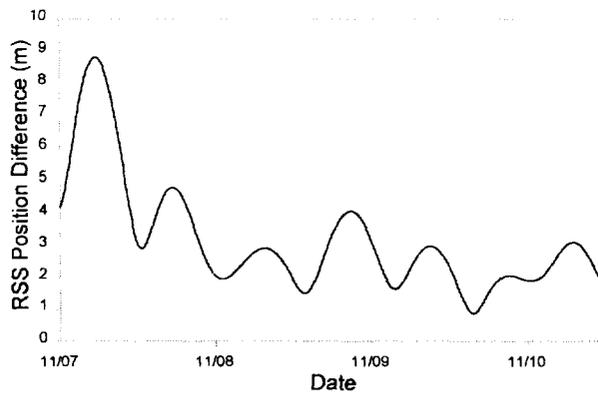
Figure 3. Position Difference Between TDRS-5 POE and GTDS TDRS-5 Ephemerides

66

Longer 7-day TDRS-4, TDRS-5, and TOPEX solutions were also generated for a period extending from 00:00 hours UTC on November 4, 1992, through 00:00 hours UTC on November 11, 1992. The RMS of the RSS position differences were 15.1 meters for TDRS-4 and 11.3 meters for TDRS-5. It is believed that the cumulative effects of the TDRS-4 and TDRS-5 momentum wheel unloads are the cause of the less favorable ephemeris comparison results compared with the 5-day solutions.

4.0 Strategies for TDRS Orbit Determination Solutions

This section discusses several strategies for obtaining high-accuracy TDRS trajectories from simultaneous solutions from the ERBS and Landsat-4 spacecraft. Section 4.1 presents the results for the ERBS and Landsat-4 spacecraft using the standard ACB method described in Section 2.2.1. The accuracy of these trajectories is assessed by parallel comparisons with high-accuracy TDRS POE trajectories described in Section 3.0. A "quick-look" approach for determining TDRS trajectories using Landsat-4 is presented in Section 4.2. Section 4.3 describes several scenarios for accurately determining the postmaneuver trajectory of a TDRS spacecraft within 2 hours of its maneuver.

4.1 ERBS and Landsat-4 Cycle 5 ACB Results

The measurements for the ERBS and Landsat-4 spacecraft ACB runs came from a 6-day timespan from November 4, 1992, through November 10, 1992. These dates were chosen so that the solution arc overlaps with the TDRS POE solution arc. During this time, ERBS and Landsat-4 were being tracked by TDRS-4 and TDRS-5. This study uses the TDRSS two-way range and Doppler measurements, as well as the two-way BRTS range measurements. The comparison of the resulting TDRS trajectories with the TDRS POEs can be seen in Table 4. Also included in this table for comparison purposes are the results from the TOPEX analysis described in Section 3.0. Note that the TDRS-5 trajectory is consistently better than the TDRS-4 trajectory. This is as expected, since the geometry of the three BRTS stations tracking TDRS-5 is better than the geometry of the two stations tracking TDRS-4.

Table 4. Comparison of Various TDRS-4 and TDRS-5 Trajectories
With the TDRS POEs

Spacecraft	TDRS-5 RMS in meters)	TDRS-4 (RMS in meters)
TOPEX 5-day	3.6	4.3
ERBS	12.190	44.876
Landsat-4	13.476	30.810

4.2 Landsat-4 Cycle 5 "Quick-Look" Results

A "quick-look" solution would be very attractive for use in an operational environment as long as the accuracy of the resulting TDRS trajectories remained high. There is the added benefit of obtaining trajectories for several TDRSs at a time. The "quick-look" scenario is a pared down version of the standard ACB method. It consists of a single simultaneous solution with a user spacecraft and two TDRS spacecraft corresponding to step 3(a) of the standard ACB method. The first ACB step can be skipped by assuming that the same BRTS ground transponders are biased with respect to the TDRSS-user range measurement type; the transponder delay for each of these "biased" BRTS stations is estimated. The second ACB method step consists of finding the relative biases between the TDRSS-user range measurements and the BRTS range measurements. This step can be skipped by assuming there is a typical value for the relative bias and using that value in the single simultaneous solution. This section presents results from this quick-look scenario for the Landsat-4 spacecraft.

The Landsat-4 quick-look analysis covers the same timespan and uses the same measurement types as the ACB analysis. A value of 17.83 meters from a previous ACB solution with the ERBS is used as the relative bias between the TDRSS-user range and the BRTS range measurement types. The resulting TDRS-4/5 accuracies are 72.1 meters and 20.5 meters RMS. The ACB method yields relative bias values of 5.4 meters and 3.1 meters for TDRS-4 and TDRS-5, respectively; this generates a TDRS trajectory accuracy of 30.8 meters for TDRS-4 and 13.5 meters for TDRS-5. The difference between the ACB and quick-look trajectories is 53.5 meters for TDRS-4 and 12.9 meters for TDRS-5. Because of this sensitivity of the TDRS trajectories to the input relative bias, this quick-look method should be studied in greater detail before adopting it for routine use.

4.3 TDRS-4 Cycle 5 Postmaneuver Recovery Results

Occasionally, it is necessary to maneuver a TDRS to ensure that it remains within its designed stationkeeping window. The goal is to develop methods and procedures using 2 hours of postmaneuver tracking measurements from the maneuvered TDRS to recover the trajectory of a maneuvered TDRS to better than 600 meters to satisfy current requirements and to better than 75 meters (3σ) for future requirements.

The analysis reported in this section focuses on the time immediately following a TDRS-4 maneuver on November 4, 1992. The tracking measurement span used is 01:00 to 03:00 UTC, where 01:00 UTC is just after the TDRS-4 maneuver burnout. The strategy is to try a variety of cases, concentrating on simultaneous solutions with a TDRSS-user spacecraft and a second, nonmaneuvering TDRS. Both spacecraft have good solutions, which will help constrain the solution for the maneuvering TDRS. There is the additional benefit of being able to use longer measurement arcs for these latter two spacecraft.

This study uses TDRS-5 and TOPEX for the second TDRS and the TDRSS-user spacecraft, respectively. The various scenarios, the measurement types used, and the results of comparing the TDRS-4 trajectory with the high-accuracy TDRS-4 POE are shown in Table 5. The 40-hour and 5-day timespans for TDRS-5 and TOPEX start earlier and end at the same time as the TDRS-4 arc. The 40-hour arc is used to approximate the arc length used in operational TDRS solutions, while a 5-day arc gives the best solutions in a standard ACB analysis with TOPEX. The BRTS-only TDRS-4 solution uses the setup for normal operational TDRS orbit determination. The remaining solutions were all generated in a single simultaneous solution that corresponds to solution 3(a) of the standard ACB procedure, treating TDRS-4 and TDRS-5 the same except for the length of the measurement arcs. The previous TOPEX/TDRSs simultaneous solution 1 and solution 2 analysis results were used as input to the solution 3(a) generated in the current analysis. Because none of the nominal cases were close to the 75-meter (3σ) goal, some "nonnominal" runs were investigated, where TDRS-5 and TDRS-4 were treated differently. TDRS-5 followed the normal procedure, while for TDRS-4, more types of measurements were added, and the parameter set estimated was different.

Note that case D1 (the first attempt at a nonnominal solution) is close to the 75-meter (3σ) goal. Several refinements improve the numbers slightly. Also note that excellent results can be obtained for the shorter timespans in case C1. An interesting note is that the estimated values for the TDRS-4 solar reflectivity coefficient (C_R) were generally between 3 and 9 for most of the nonnominal solutions, whereas, the expected value is around 1 to 1.5. Normally, this solution would be considered questionable, but the excellent agreement with the POE lends confidence to its accuracy.

The results of this analysis show that it is possible to meet the 600-meter (3σ) goal using standard ACB methods and the 75 meter (3σ) goal using slightly modified ACB procedures. To further improve the accuracy of TDRS orbit determination solutions following a maneuver, it is recommended that a three-dimensional thrust scaling algorithm be implemented into GTDS. With this enhancement, both premaneuver and postmaneuver tracking measurements can be processed in a single orbit determination arc to scale an input nominal thrust profile in three separate components.

5.0 Alternative TDRS Orbit Determination Strategies Without BRTS

Section 5.1 presents a summary of the orbit determination and error analysis results for TDRS orbit determination strategies that exclude BRTS tracking measurements. Section 5.2 describes the details of orbit determination analysis using GN tracking measurements of the TDRSS-user spacecraft instead of BRTS tracking measurements for the TDRSs. Additional alternative TDRS orbit determination strategies described by other authors are presented in Section 5.3.

Table 5. Summary of Postmaneuver Recovery Results

Case	Solution Type	Measurement Types	Orbit Determination Arc Lengths	Total RMS (m) of compare with TDRS-4 POE
A	TDRS-4 only	BRTS range for TDRS-4	2-hours	12102.08
B	Standard ACB: TOPEX/TDRS-4/TDRS-5 simultaneous	BRTS range for TDRS-4 and TDRS-5; TDRS-4 range and two-way Doppler for TOPEX; TDRS-5 range and two-way and one-way Doppler for TOPEX	TDRS-4: 2 hours TDRS-5: 2 hours TOPEX: 2 hours	2188.03
C	Standard ACB: TOPEX/TDRS-4/TDRS-5 simultaneous	BRTS range for TDRS-4 and TDRS-5; TDRS-4 range and two-way Doppler for TOPEX; TDRS-5 range and two-way and one-way Doppler for TOPEX	TDRS-4: 2 hours TDRS-5: 40 hours TOPEX: 40 hours	258.05
C1	Same as C, except for TDRS-4: 1. Estimate user range bias for White Sands antenna 2. Do not estimate BRTS transponder delays 3. Change integration stepsize from 600 to 180 seconds	Same as C	Same as C	19.79
D	Standard ACB: TOPEX/TDRS-4/TDRS-5 simultaneous	BRTS range for TDRS-4 and TDRS-5; TDRS-4 range and two-way Doppler for TOPEX; TDRS-5 range and two-way and one-way Doppler for TOPEX	TDRS-4: 2 hours TDRS-5: 5 days TOPEX: 5 days	149.18
D1	Same as D, except for TDRS-4: 1. Estimate user range bias for White Sands antenna 2. Do not estimate BRTS transponder delays 3. Change integration stepsize from 600 to 180 seconds	Same as D	Same as D	27.54
D2	Same as D1, except do not estimate TDRS-4 transponder delay	Same as D, except add White Sands azimuth-elevation angle tracking measurements	Same as D	23.42

5.1 TDRS Orbit Determination Error Analysis Results

Orbit determination error analysis was undertaken to investigate and evaluate alternative TDRS orbit determination strategies without the use of BRTS tracking measurements. Table 6 summarizes the orbit determination error analysis results for TDRS orbit determination strategies that exclude BRTS tracking measurements. The table includes a brief description of the technique, the estimated 3σ accuracy of the resulting solutions, and the major error sources associated with the estimated solution accuracy. For the error analysis, all simultaneous TDRS/TDRSS-user solutions were 34-hours long and used

Landsat-4 as the TDRSS user. The Landsat-4 tracking measurement distribution was the same as that currently used for operational support. The major error sources for both Landsat-4 and the TDRSs are provided in Table 3. The major strengths and weaknesses for practical application of each strategy in Table 6 have been discussed elsewhere (Reference 4).

Table 6. Alternative Technical Approaches That Exclude BRTS

Technique	Description	3σ RSS Accuracy	Basis of Accuracy Statement	Primary Error Contributors
TDRS GN	Use of GN tracking of TDRS for TDRS-only orbit determination	164 meters (TDRS-4) 125 meters (TDRS-5)	Mean 3σ error from covariance analysis using 30 meter GN range bias assumed TDRS-4 tracked by Madrid and Ascension TDRS-5 tracked by Goldstone and Canberra	Measurement biases: 123 meters for TDRS-4; 85 meters for TDRS-5
K-band + User TDRSS	Use of STGT K-Band TT&C range data and simultaneous TDRS+user orbit determination	67 meters (TDRS-4) 57 meters (TDRS-5)	Mean 3σ error from covariance analysis of simultaneous Landsat-4 and TDRS orbit determination based on a 10 meter two-way range bias for K-Band TT&C	Tropospheric refraction: 35 meters for TDRS-4; 38 meters for TDRS-5
TDRS GN + User TDRSS	Use of GN tracking of TDRS and simultaneous TDRS+user orbit determination	73 meters (TDRS-4) 74 meters (TDRS-5)	Mean 3σ error from covariance analysis using 30 meter GN range bias TDRS-4 tracked by Madrid and Ascension TDRS-5 tracked by Goldstone and Canberra	Measurement biases: 38 meters for TDRS-4; 41 meters for TDRS
User GN + User TDRSS	Use of simultaneous TDRS+user orbit determination with GN tracking of user	84 meters (TDRS-4) 81 meters (TDRS-5)	Mean 3σ error from covariance analysis No BRTS No direct tracking of TDRS-4 and TDRS-5 are used	Measurement biases: 45 meters for TDRS-4; 44 meters for TDRS-5

Among the strategies that eliminate the BRTS tracking measurements, the "K-band + user" approach is the most attractive for meeting the future accuracy requirement of 75 meters (3σ). Figure 4 shows the dependence of the 1σ TDRS orbit determination position error on the K-Band TT&C range uncertainty when using the K-band + user approach. The dominant error source in the TDRS position is tropospheric refraction, which is the leading contributor to the 16- to 17-meter error when there was no range data uncertainty. The additional position errors resulting from the range data uncertainty are linear in nature. An 18- to 19-meter two-way TT&C range data bias (9 to 9.5 meters one-way) will permit TDRS orbit determination accuracies of 150 meters (3σ). TDRS orbit determination accuracies of 75 meters (3σ) are possible if the two-way uncertainty is 7 to 7.5 meters (3.5 to 4 meters one-way).

TDRS orbit determination analysis was performed using the available TT&C tracking measurements from December 1994 and January 1995. These results were not included since the quality of the tracking measurements during this period were not yet at expected operational support levels.

5.2 TDRS/User-GN Orbit Determination Analysis Results

This section reports on the orbit determination analysis undertaken to study the feasibility of using tracking of a TDRSS-user spacecraft from GN stations to replace BRTS measurements in determining TDRS orbits in simultaneous solutions. For this study, the user spacecraft was ERBS. The timespan covered is 22:00 hours UTC on April 10, 1993, through 22:00 hours UTC on April 15, 1993, during which there was good GN tracking of ERBS. This corresponds to the middle part of Cycle 21 for TOPEX.

The method used for generating the TDRSs/ERBS simultaneous solutions using GN measurements is performed in three steps, analogous to the ACB method. The BRTS measurements are replaced by GN range and range-rate measurements from Wallops Island, Goldstone, and Merritt Island. Additionally, TDRSS two-way range and Doppler are used, but no TDRSS one-way Doppler. Furthermore, the GN measurements are downweighted 50 percent from nominal, i.e., the range measurement weight is increased from 20 to 30 meters while the range-rate measurement weight is changed from 10 to 15 cm/sec. In the first step, the ground stations whose range measurements are biased relative to the TDRSS range measurements are identified. In the second step, the ERBS transponder delay is directly estimated, in contrast to the standard ACB case where the relative biases between different range types are determined. In the third step, the user transponder delay from step 2 is applied, while the TDRS transponder delays are estimated (as they are in the standard ACB scenario). Nominally, only

those ground stations whose range measurements are biased relative to the TDRSS range measurement type (determined in step 1) have their range biases estimated. However, more accurate results are obtained when the range biases for all the GN tracking stations are estimated.
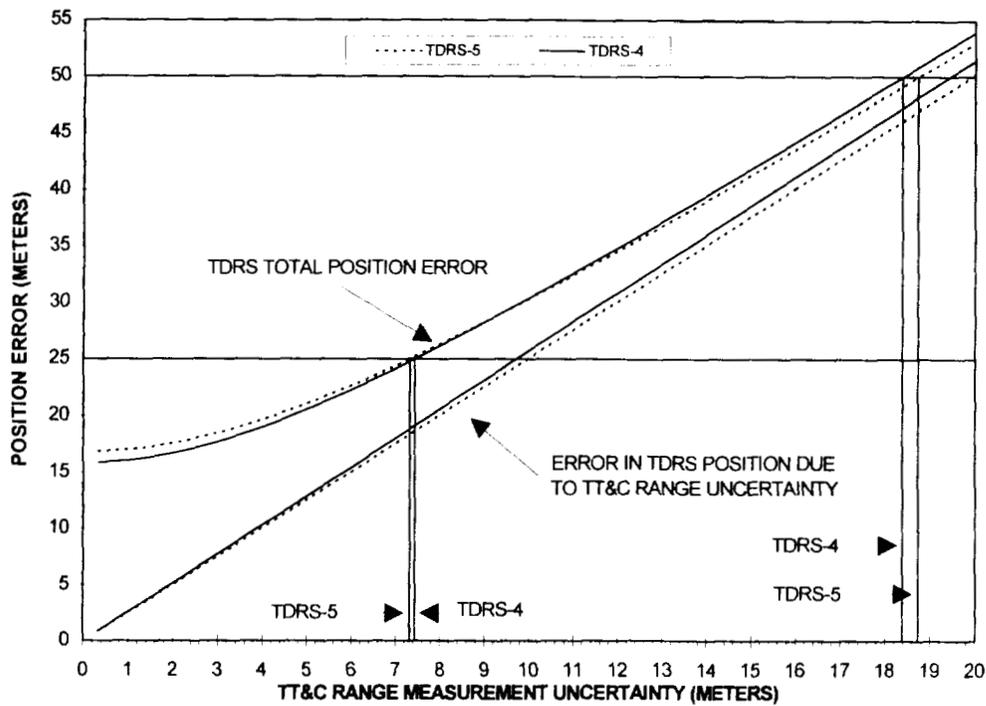

Figure 4. TDRS Orbit Determination Error as a Function of the TT&C Two-Way Range Uncertainty

Since there are no TDRS POEs for this time period, the quality of the TDRS trajectories produced using the GN method is assessed by comparing the trajectories with those produced from standard TDRS/TOPEX ACB solutions. The TDRS-4 GN trajectory differs from the TOPEX ACB trajectory by 69.486 meters RMS. For TDRS-5, the RMS value is 82.049 meters. These differences are comparable to the analysis error estimates of about 80 meters in Table 6. An additional indication of the TDRS accuracy can be obtained by using the TDRS trajectories as input for a TOPEX-only solution. The resulting TOPEX trajectory can be compared with the Cycle 21 TOPEX POE. Table 7 gives this result on the last line and also includes a sampling of TOPEX accuracies obtained through ACB methods over several time periods.

Table 7. Comparison of TOPEX POEs with TOPEX Ephemerides Determined From Various Simultaneous TDRS Ephemerides

Source of TDRS Orbit Files	TOPEX Solution Compared With POE RMS (Radial RMS) in Meters
TOPEX ACB solution: 7 days, Cycle 5	2.20 (0.28)
TOPEX ACB solution: 5 days, Cycle 6	1.60 (0.46)
ERBS ACB solution: 6 days, Cycle 5	3.60 (0.31)
TOPEX ACB solution: 5 days, Cycle 21	3.06 (0.30)
ERBS ACB solution: 5 days, Cycle 21	1.82 (0.52)
ERBS simultaneous solution GN tracking (no BRTS): 5 days, Cycle 21	16.06 (0.75)

These ERBS results suggest that using the modified ACB technique with GN tracking measurements in place of BRTS does not produce as accurate solutions as those that include the BRTS tracking measurements, which could result from several

factors. First, the relatively sparse amount of GN tracking of the user may not be sufficient to eliminate the effects of GN data noise and provide an adequate link to the ground to determine the TDRS orbits. More dense GN tracking of the TDRSS-user spacecraft may eliminate the effects of noise and improve the TDRS orbits. Second, the modified ACB technique, developed to accommodate the replacement of the BRTS tracking with the GN tracking, may not be optimal. Further refinements to this modified ACB technique may also improve TDRS orbit determination accuracy. It is interesting to note that the BRTS-included results in Table 7 indicate that three of the five solutions meet the stringent 39-centimeter (3σ) precision orbit determination radial accuracy requirement, indicating the relative merits of the ACB technique.

5.3 Other Strategies

Other authors have performed analyses for TDRS orbit determination using Global Positioning System (GPS) technology (Reference 5) and TDRSS-user satellite laser ranging (SLR) tracking measurements (Reference 3). The attainable TDRS orbit determination accuracy using SLR tracking measurements is approximately 3 meters (1σ), while the GPS method produces TDRS orbits estimated accurate to 50 meters (1σ). The major strengths and weaknesses for practical application of these strategies are discussed in Reference 4.

6.0 Conclusions and Recommendations

A number of orbit determination strategies have been analyzed and the achievable accuracy levels assessed. The primary goal of identifying technical approaches and procedures that meet the future TDRS orbit determination accuracy requirement of 75 meters (3σ) with and without the use of BRTS was achievable. In addition, several schemes for recovering accurate TDRS orbits following a TDRS maneuver were examined.

For performing high-accuracy TDRS orbit determination solutions with the use of BRTS tracking measurements, simultaneous solutions of the TDRS along with a well-chosen TDRSS-user are recommended. A detailed procedure for the analytical calibration of biases is outlined that significantly reduces the systematic errors arising from the biases in the range measurements. With simultaneous solutions of TDRS-4 and TDRS-5 with TOPEX, TDRS orbit determination solutions are obtained that are accurate to better than 15 meters. Simultaneous solutions with a TDRSS-user at a lower altitude, which experiences higher geopotential and atmospheric perturbation errors, will result in somewhat larger errors for TDRS solutions. Technical procedures are identified that can be good candidates for use in operations after further refinements.

High-accuracy TDRS postmaneuver solutions have been determined within 2 hours after a TDRS stationkeeping maneuver by exploiting the tracking measurements and orbits of a TDRSS-user and another TDRS, the orbits of which were not perturbed by the orbit-adjust maneuver. Accuracies of better than 25 meters are demonstrated. However, for robust and reliable procedures for postmaneuver recovery, it is recommended that the TDRS thrust vector be estimated so that premaneuver tracking information for the perturbed TDRS can be gainfully utilized.

A number of TDRS orbit determination strategies have been examined that exclude BRTS tracking measurements. The most attractive of these strategies is one that involves performing simultaneous solutions of the TDRSs with a TDRSS-user using the TDRSS tracking measurements for the user and the TT&C range measurements for the TDRS as the tie to the ground. Covariance analysis indicates that an accuracy of better than 25 meters (1σ) can be achieved provided that the TT&C range measurement uncertainty can be brought below about 7 meters. Once the actual measurements indicate that the uncertainties are below 7 meters, an orbit determination study is recommended to validate the covariance analysis results.

References

1. E. Doll, et al., "Improved Solution Accuracy for TDRSS-Based TOPEX/Poseidon Orbit Determination,", NASA Conference Publication 3265, *Proceedings of the Flight Mechanics/Estimation Theory Symposium*, National Aeronautics and Space Administration, Goddard Space Flight Center, Greenbelt, Maryland, May 17-19, 1994

2. D. H. Oza, et al., "Evaluation of Orbit Determination Using Dual-TDRS Tracking," AIAA-90-2925-CP, in : AIAA/AAS Astrodynamics Conference Proceedings, *A Collection of Technical Papers Part I*, published by AIAA, USA, 1990, p. 410

3. J. A. Marshall, et al., "An Assessment of TDRSS For Precision Orbit Determination," Paper No. AAS 95-104, presented at the AAS/AIAA Spaceflight Mechanics Conference, Albuquerque, New Mexico, February 13-16, 1995

4. C. Cox and D. H. Oza, *TDRS Orbit Determination: Operations Concepts for Using GPS Tracking and Alternative Technical Approaches*, 553-FDD-94/036/R0UD0, December 1994

5. M. Lichten, et al., "A Demonstration of TDRS Orbit Determination Using Differential Tracking Observables From GPS Ground Receivers," Paper No. AAS 93-160, *Advances in the Astronautical Sciences*

Operational Improvements of Long-Term Predicted Ephemerides of the Tracking and Data Relay Satellites (TDRSs)*

J. L. Kostoff and D. T. Ward
Computer Sciences Corporation
Lanham-Seabrook, Maryland, USA 20706

O. O. Cuevas and R. M. Beckman
National Aeronautics and Space Administration
Goddard Space Flight Center
Greenbelt, Maryland, USA 20771

Abstract

Tracking and Data Relay Satellite (TDRS) orbit determination and prediction are supported by the Flight Dynamics Facility (FDF) of the Goddard Space Flight Center (GSFC) Flight Dynamics Division (FDD). TDRS System (TDRSS)-user satellites require predicted TDRS ephemerides that are up to 10 weeks in length. Previously, long-term ephemerides generated by the FDF included predictions from the White Sands Complex (WSC), which plans and executes TDRS maneuvers. TDRSs typically have monthly stationkeeping maneuvers, and predicted postmaneuver state vectors are received from WSC up to a month in advance. This paper presents the results of an analysis performed in the FDF to investigate more accurate and economical long-term ephemerides for the TDRSs.

As a result of this analysis, two new methods for generating long-term TDRS ephemeris predictions have been implemented by the FDF. The Center-of-Box (COB) method models a TDRS as fixed at the center of its stationkeeping box. Using this method, long-term ephemeris updates are made semiannually instead of weekly. The impulse method is used to model more maneuvers. The impulse method yields better short-term accuracy than the COB method, especially for larger stationkeeping boxes. The accuracy of the impulse method depends primarily on the accuracy of maneuver date forecasting.

Introduction

The Flight Dynamics Facility (FDF) of the Goddard Space Flight Center (GSFC) Flight Dynamics Division (FDD) provides many Tracking Data Relay Satellite (TDRS) and TDRS System (TDRSS)-user ephemeris products, both short-term and long-term, every month to numerous users. Short-term products generally have spans of less than 2 weeks, while products greater than 2 weeks in length are considered long-term products. The recipients of these products include several spacecraft Payload Operations Control Centers (POCCs), the Space Network (SN), the Ground Network (GN), and the science community.

The support provided by the FDF includes the TDRS planning and scheduling products for many TDRSS-user spacecraft. Prior to the launch of the Hubble Space Telescope (HST) in 1990, there were no strict accuracy requirements for long-term TDRS products. The merged ephemeris method used at the time involved merging predicted ephemerides generated from FDF definitive solutions with those generated from the White Sands Complex (WSC) predicted postmaneuver vectors. WSC provides these predicted postmaneuver vectors about 30 days in advance, which was adequate for the long-term ephemerides generated at that time. With the launch of HST, however, the FDF was levied with its first tight long-term accuracy requirement (see Reference 1).

In response to these new requirements, the FDF performed an analysis to find an accurate, more cost-effective method to generate these long-term TDRS products. Two methods were identified: the Center-of-Box (COB) method and the impulse-modeled method. This paper gives an overview of the TDRS System, describes the two new methods for generating long-term TDRS ephemerides, and presents their applications to current and future missions.

The TDRS System (TDRSS)

TDRSS currently consists of a constellation of five TDRSs, a central command center in White Sands, New Mexico, called the White Sands Complex (WSC), and several auxiliary transponders. Five TDRSs in geostationary orbits have been deployed since 1983. Each TDRS actively tracks lower Earth-orbiting satellites and provides a primary link for their telemetry and command. The locations of the five TDRSs are distributed from 41 degrees west longitude to 275 degrees west longitude. TDRS-4 (TDRS-East) is currently in the eastern-most position at 41 degrees west longitude, TDRS-5 (TDRS-West) is at 174 degrees west longitude, TDRS-6 (TDRS-Stored) is at 46 degrees west longitude, TDRS-3 (TDRS-Spare) is at 171 degrees west longitude, and TDRS-1 is at 275 degrees west longitude. TDRS-3 and TDRS-5 mutually support and complement each other in the TDRS-West position, and TDRS-6 and TDRS-4 mutually support and complement each other in the TDRS-East position. These four TDRSs are all within direct view from WSC. TDRS-1 was moved to its 275-degrees-west location to provide additional real-time communications for the Compton Gamma Ray Observatory (GRO) spacecraft, which suffered a failure of its onboard tape recorders. This relocation allows 100-percent coverage for GRO in conjunction with TDRS-East and TDRS-West. A new ground terminal for the GRO Remote Terminal System (GRTS) was built for TDRS-1 at Canberra, Australia.

Around 1989, the National Aeronautics and Space Administration (NASA) entered upon a contract to provide C-band communication services for commercial satellites. The contract requires two TDRSs be maintained within ± 0.1-degree limits in both latitude and longitude to assure that their signals do not interfere with other commercial satellites. Currently, TDRS-West and TDRS-East are maintained within these 0.1-degree stationkeeping boxes. TDRS-1, TDRS-3, and TDRS-6 are maintained within ± 0.5-degree stationkeeping boxes in longitude only. The 0.1-degree stationkeeping box corresponds to a ± 70-kilometer box, with the half-diagonal of the box equal to 100 kilometers (see Figure 1). The 0.5-degree stationkeeping box corresponds to a ± 370-kilometer longitudinal 'box" with no latitude constraint. The geopotential induces a longitudinal (east-west) drift that is dependent on the longitude of the TDRS relative to the geoidal stable points. Inclination changes are caused by the gravitational forces of the Moon and the Sun (see Reference 2).
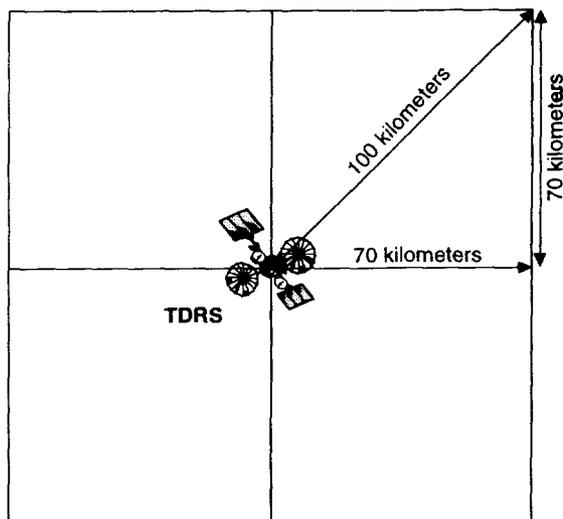

Figure 1. TDRS 0.1-Degree Stationkeeping Box

Each TDRS undergoes periodic stationkeeping maneuvers to maintain it in its individual stationkeeping box. The maneuver planning is the responsibility of WSC personnel, who rely on the FDF for daily and postmaneuver orbit determination support. North-south (N/S) stationkeeping maneuvers are required to maintain the orbit within the latitudinal constraint, and east-west (E/W) stationkeeping maneuvers are required to meet the longitudinal constraint. The 0.1-degree boxes require frequent maneuvers, approximately every 15 to 40 days, while the 0.5-degree boxes require less frequent maneuvers, approximately every 70–90 days. Table 1 summarizes these characteristics for each TDRS.

Table 1. Current Operational TDRSs (as of March, 1995)

TDRS	Location	Name	Inclination (degrees)	Stationkeeping Box Size (± degree) Longitude	Latitude	Days Between Maneuvers
1	275° west	Zone of exclusion	8.2	0.5	n/a	90
3	171° west	Spare	1.5	0.5	n/a	70
4	41° west	East	< 0.1	0.1	0.1	15
5	174.3° west	West	< 0.1	0.1	0.1	15
6	46° west	Stored	1.5	0.5	n/a	70

COB Method

The COB method refers to the satellite being modeled as fixed at the center of its stationkeeping box. This method is ideal for spacecraft that are maintained within a strict orbital constraint of a 0.1-degree stationkeeping box, such as TDRS-4 and TDRS-5. Such spacecraft may have their position approximated at the center of their stationkeeping box, thereby alleviating the need to model maneuvers. The error associated with this method is strictly the box size.

COB-modeled ephemerides are proposed for long-term predictions of TDRS positions but in general were not intended to replace short-term ephemeris products needed for acquisition. Although the idea behind COB allows for the use of the same vector to estimate the TDRS position over time, most FDF customers require an ephemeris representation of a specific format. Due to ephemeris requirements, these ephemerides are currently generated by propagating the COB vector using a point-mass Earth model. Theoretically, COB ephemerides would never need updating. Within the FDF, these ephemerides are updated semiannually to limit file lengths.

Standard COB modeling includes no perturbation forces and maintains the same longitude over several months for geostationary orbits. The main perturbation forces neglected in the COB method are the nonspherical geopotential terms, the solar-lunar gravitational potentials, and solar radiation.

Two variations of the standard COB method are the *offset* COB method and the *inclined* COB method. The offset COB method is effectively the same as the COB method, except that an offset is applied to the position used to generate the COB ephemeris. The stationkeeping box stays the same, the position that is used is just offset from the official center of the box. This method could be used if a spacecraft were being maintained in an area offset from the official center of its nominal stationkeeping box. Although this scenario may not be known ahead of time, historical data would show if the comparisons of long-term ephemerides with definitive solutions were biased east or west of the nominal COB. In such cases, a long-term offset of COB would be recommended to reduce observed errors between the definitive solutions and the COB ephemerides.

Temporary offsets may also be applied. If a TDRS maneuver were to exceed its box after a maneuver, a temporary offset could be applied. As the TDRS drifted back towards its center, this offset could then be removed. In practice, however, this offset can be applied until the next update of the ephemeris. For example, HST currently has a requirement to update the COB ephemeris when the definitive comparison exceeds 130 kilometers. In November 1994, the definitive comparison indicated that the TDRS had exceeded its stationkeeping box by a small amount. In this case, a temporary offset of 0.01 degree east of its nominal center was applied.

The inclined COB method is an alternative COB method for spacecraft that are not restricted in inclination. For example, the inclination of TDRS-1 is currently 8.2 degrees and will increase over time to a maximum inclination of 14 degrees, after which it will slowly decrease again (Reference 3). This inclination growth is caused by solar and lunar gravitation. Use of the COB method in these situations requires the application of forces in addition to those due to a point-mass Earth. Modeling the solar and lunar gravity for inclination variation and the J_2 (zonal) geopotential term for orbital precession increases the propagation accuracy.

Figure 2 gives an example of the accuracy of an inclined COB ephemeris for a TDRS maintained in a 0.2-degree stationkeeping box. Although the boxes mentioned within this paper are restricted to an 0.1-degree and 0.5-degree box, the

example illustrates that the errors associated with the COB method are equal to the box size. In the case of an 0.2-degree box, the errors should not exceed 200 kilometers (km).
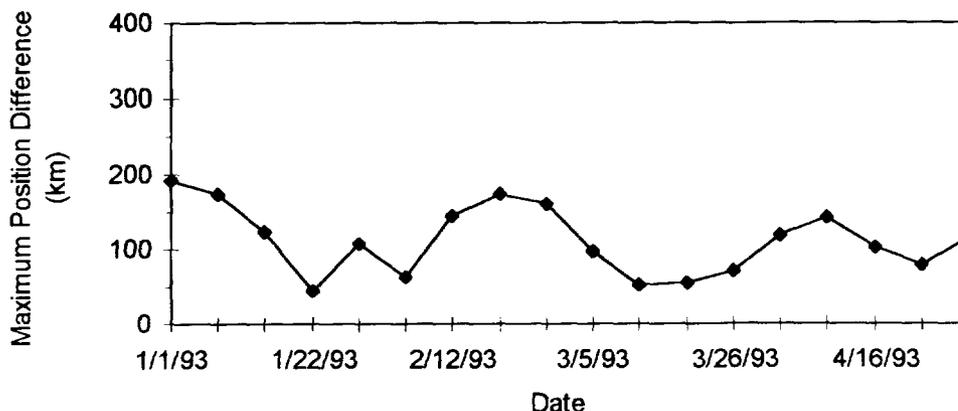

**Figure 2. TDRS-1 Inclined COB for a 0.2-Degree Box
(January 1, 1993, to April 30, 1993)**

Currently within the FDF, only the standard COB method has been implemented (for TDRS-East and TDRS-West). This has reduced the delivery schedule of TDRS-East and TDRS-West long-term product deliveries from a total of eight per week to eight every 6 months. The other three operational TDRSs have tighter accuracy requirements than COB modeling allows for their larger stationkeeping box size. For these TDRSs, the impulse method is used.

Impulse Method

Unlike the COB methods, the impulse method involves actually modeling TDRS maneuvers in the computation of ephemerides. For simplicity, these maneuvers are modeled impulsively rather than as finite burns. Using the standard geopotential model, the operational state vector is propagated with a ΔV applied on the maneuver dates predicted by the FDF after the last maneuver date announced by WSC. The instantaneous ΔV magnitudes are computed from the needed change in the drift rate, and the longitude drift table assures that the TDRS remains within its box. This method should results in the TDRS drifting back and forth parabolically from one edge of its box to the other, without leaving the box (Reference 4).

The impulse method is best suited for TDRSs that have infrequent maneuvers, such as those with a 0.5-degree stationkeeping box. Since N/S maneuvers are large and significantly disrupt E/W maneuver forecasts, an error of a few days in the maneuver forecast (which is hard to avoid with N/S maneuvers) would induce a 100-kilometer error for a 0.1-degree stationkeeping box. Therefore, impulse modeling is recommended only for E/W maneuvers in these large stationkeeping boxes. All TDRSs maintained within 0.5-degree boxes are not subject to inclination restraints and, therefore, are not subject to N/S maneuvers.

The impulse method is currently used for long-term modeling of ephemerides for TDRS-1, TDRS-3, and TDRS-6. These ephemerides are 14 weeks in length and are updated once per month in the FDF. On average, the errors associated with these ephemerides over a 7-week span are under 100 kilometers. The largest errors have occurred when changes to maneuver dates have occurred. For example, the FDF predicted maneuver date for a TDRS-1 maneuver in December of 1994 was within 1 day of the first announced maneuver date. The announced date was then changed by 6 days, resulting in errors over 200 kilometers. Figure 3 illustrates this example. The graph depicts the definitive comparisons of the TDRS-1 impulse-modeled ephemeris over a 14-week span. The 'inaccurate" December maneuver was first modeled in the TDRS-1 long-term ephemeris generated in September and was subsequently modeled in the updates performed in October and November. The three spikes in Figure 3 represent the error associated with the original maneuver date as seen in the September, October, and November updates. The solid black line represents the TDRS-1 accuracy requirements of 40-kilometers between ephemeris updates (every 4 or 5 weeks) and 100-kilometers for the following 6 weeks.
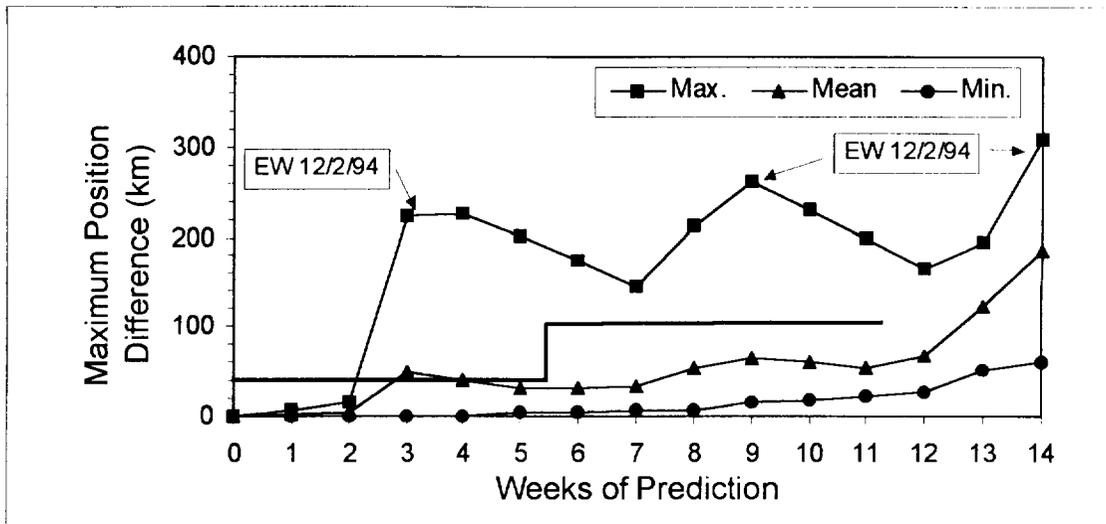
**Figure 3. TDRS-1 Long-Term Accuracy Using Impulse Method
(August 11, 1994, to February 23, 1995)**

It should be noted that these results are based on only 6 months of operational data. Although the effects of mismodeled maneuvers is noticeable, the number of maneuver date changes since August, 1994 may not accurately represent the true frequency of maneuver date changes. The new Second TDRS Ground Terminal (STGT) was undergoing testing with the TDRSs throughout the summer of 1994 and into the fall. In addition, the transition of TDRS control from the original White Sands Ground Terminal (WSGT) to STGT was performed in December. These situations required adjustments to planned maneuver dates to minimize interference with the transition activities on the ground. It is expected that the mean error after 3 weeks of prediction will decrease as more data become available.

COB Application to Current and Future Missions

Although the primary use of the COB method is for generating long-term predictions of TDRS positions, it can also be used for the short-term prediction by onboard computers (OBCs).

TDRSS-user satellites need to know both their own position and the position of any TDRS that tracks them or with which they communicate, so they can pass information through them. Certain user satellites require files to be uplinked to provide this information. This information can be provided in numerous ways. Some older satellites, such as the Upper Atmosphere Research Satellite (UARS), have limited computing power and, therefore, require a compact representation of the ephemeris that can be uplinked to the satellite efficiently and can be easily converted back into a usable form. This compact representation is based on a truncated Fourier series plus residuals. Other satellites with more data storage could have actual ephemerides uplinked to the spacecraft. For those with more computing capabilities, such as the soon-to-be-launched X-Ray Timing Explorer (XTE), a state vector could be uplinked to the spacecraft for propagation by the OBC. This method is the most efficient from an operations standpoint because only a vector is supplied, not an ephemeris or a Fourier representation. However, onboard propagation of the vector requires more extensive computing power. In the past, these methods typically were based on short-term ephemerides, requiring frequent updates.

An alternative to these methods is the use of the COB modeling for the TDRS representation for those missions that don't require short-term accuracies of under 130 kilometers for TDRS-East and TDRS-West. Depending on the OBC configuration, either COB ephemerides or COB state vectors could be delivered to a spacecraft project. For those OBC's propagating an ephemeris, vectors would be uplinked to the spacecraft and propagated by the OBC. Both methods would reduce the number of products to be delivered to the project and the need for postmaneuver updates. Ephemerides would be updated semi-annually and the COB state vectors would require updates only if a TDRS were repositioned.

As mentioned above, implementation of the use of COB in this manner is dependent on the spacecraft's required TDRS position accuracy. For example, the Tropical Rainfall Measurement Mission (TRMM) spacecraft, currently scheduled for launch in 1997, has tentatively agreed to a 0.5-degree requirement for absolute position accuracy for all TDRSs. The TRMM

project will received standard COB ephemerides for TDRS-East and TDRS-West and inclined COB ephemerides for the other TDRSs. Vectors will be uplinked to the spacecraft and propagated for several hours by the OBC using a point-mass Earth model. The X-ray Timing Explorer (XTE) spacecraft, scheduled for launch later this summer, has not settled on a TDRS requirement. However, its OBC can have specific modeling for each TDRS. Therefore, COB ephemerides could be used for the 0.1-degree box TDRSs and the impulse method used for the 0.5-degree box TDRSs. The XTE project has been advised of the advantages with COB modeling, but their initial proposals were at the 47-kilometer level position accuracy at 14 days, which is too small for the COB method to satisfy.

The HST provides a good illustration of the benefits of COB modeling. Unlike other spacecraft that use short-term ephemerides for their OBC uplinks and long-term ephemerides for planning, HST uses the long-term TDRS ephemerides for both functions. Shortly after HST was launched in April 1990, the 7-week TDRS ephemerides required for TDRS-East, TDRS-West, and TDRS-Spare were increased to 10 weeks in length. The TDRS position accuracy requirements at that time were 5 kilometers at 10 days, 100 kilometers at 3 weeks, and 310 kilometers at 10 weeks. Although the COB method would have satisfied the 3-week requirement, it would not have met the 10-day requirement.

In an effort to move to COB modeling, two alternatives were proposed to the HST project: (1) relaxing the 10-day, 3σ requirement from 5 kilometers to 200 kilometers or (2) delivering two ephemerides instead of one. In the second option, an operational short-term ephemeris would be delivered in addition to the COB ephemeris. The advantages would have been improved long-term accuracy and easy generation of products. However, the disadvantages would have been additional transmissions (twice as many per TDRS) and reduced convenience. There would also have been increased short-term errors soon after TDRS maneuvers.

Early discussions with the HST project indicated a preference for one ephemeris per TDRS. Further analysis by the HST project revealed that their total error would be smaller using a less accurate, smooth COB ephemeris compared with a more accurate merged ephemeris (see Reference 5). The discontinuities of merged-method ephemerides induced errors of up to 200 kilometers in the HST project's adaptation of the FDF ephemerides. In contrast, the project's adaptation of a COB-ephemeris induced new errors of only 0.02 kilometer. Therefore, a 130-kilometer TDRS accuracy requirement was agreed upon for COB generated ephemerides. For TDRS-Spare, the impulse method was recommended, and its requirements became 100 kilometers for the first 6 weeks and 400 kilometers for the last 8 weeks. The COB method reduced the maximum onboard errors for HST from 200 kilometers for TDRS maneuvers to 130 kilometers over all spans. In addition, because there is less overlap in COB deliveries, total storage space was reduced by a factor of eight for the project's TDRS ephemerides.

Conclusions and Recommendations

This paper has presented two alternative methods for generating TDRS long-term ephemerides: the COB method and the impulse method. The COB method maintains the TDRS position within the center of its stationkeeping box with an error that is strictly the box size. The impulse method provides a potentially more accurate model of the TDRS position by modeling TDRS maneuvers in computing the long-term ephemerides. However, just a 1-day error in maneuver forecasting can induce large errors in the ephemeris.

Based on this analysis, the question arises as to how to determine which method to use in a particular situation. The primary consideration in this determination is that the maximum error of the COB method is equal to the functional stationkeeping box size for the spacecraft. For a 0.1-degree box, the nominal maximum error is equal to 100 kilometers. However, due to occasional excursion beyond the 0.1-degree box, the maximum error currently guaranteed by the FDF is 130 kilometers. It is recommended that spacecraft with TDRS position accuracy requirements less than 130 kilometers use another method. The nominal maximum error for a 0.5-degree box is equal to 370 kilometers. In general, the COB method is recommended for 0.1-degree stationkeeping boxes, because these satellites are more tightly controlled. For nonequatorial satellites, the inclined COB method is recommended.

If more accuracy is required, the impulse modeling method has proven to be accurate because individual maneuvers are modeled. However, changes to the maneuver schedule or off-nominal maneuvers require updates to these ephemerides. In addition, 1-day errors in the modeling of large E/W maneuvers can induce errors of up to 70 kilometers. Since 0.1-degree stationkeeping boxes require N/S maneuvers, there is an even greater chance for large errors with this method. Therefore, the impulse modeling method is recommended for TDRSs with larger stationkeeping boxes that only perform E/W maneuvers.

In conclusion, the methods presented in this paper are intended to provide cost savings and accuracy improvements for both future and current users. Careful consideration of long-term TDRS accuracy requirements and alternative methods of attaining these accuracies can open up possibilities for cost and resource savings.

Acknowledgments

References

1. Computer Sciences Corporation, CSC/TM-82/6152, *Operations Support Computation Facility (OSCF) to Space Telescope (ST) Payload Operations Control Center (POCC) Interface Control Document, ST-ICD-32*, E. Zavaleta, April 1983, and December 1989 update.

2. B. N. Agrawal, *Design of Geosynchronous Spacecraft*, Prentice-Hall, Inc.: Englewood Cliffs, NJ, pp.,79-82, 1986.

3. Computer Sciences Corporation, Memorandum No. TDRS1-732-93010, *TDRS-1 Special Request*, memorandum from D. Mirabal (CSC), Orbit Determination Task, Code 553.2, to Goddard Space Flight Center Code 553.2, February 10, 1993.

4. European Space Agency, ESA-SP-1053, *Introduction to Geostationary Orbits*, E. M. Soop, November 1983

5. Computer Sciences Corporation, Memorandum No. 20:1293-002-GW, *Modifications to FDF-Provided TDRS Ephemeris Products,* memorandum from G. Welter (CSC), HST PASS Project, to HSTOMS SEB (and attached to memorandum from L. Felton, HST PASS Project Manager, to Goddard Space Flight Center Code 510.1), January 25, 1994.

FLIGHT MECHANICS/ESTIMATION THEORY SYMPOSIUM

MAY 16-18, 1995

SESSION 2

A PC-Based Magnetometer-Only Attitude and Rate Determination System for Gyroless Spacecraft[*]

M. Challa and G. Natanson
Computer Sciences Corporation (CSC)
Lanham-Seabrook, Maryland, USA 20706

J. Deutschmann and K. Galal
Goddard Space Flight Center (GSFC)
Greenbelt, Maryland, USA 20771

Abstract

This paper describes a prototype PC-based system that uses measurements from a three-axis magnetometer (TAM) to estimate the state (three-axis attitude and rates) of a spacecraft given no a priori information other than the mass properties. The system uses two algorithms that estimate the spacecraft's state—a deterministic magnetic-field only algorithm and a Kalman filter for gyroless spacecraft. The algorithms are combined by invoking the deterministic algorithm to generate the spacecraft state at epoch using a small batch of data and then using this deterministic epoch solution as the initial condition for the Kalman filter during the production run. System input comprises processed data that includes TAM and reference magnetic field data. Additional information, such as control system data and measurements from line-of-sight sensors, can be input to the system if available. Test results are presented using in-flight data from two three-axis stabilized spacecraft: Solar, Anomalous, and Magnetospheric Particle Explorer (SAMPEX) (gyroless, Sun-pointing) and Earth Radiation Budget Satellite (ERBS) (gyro-based, Earth-pointing). The results show that, using as little as 700 sec of data, the system is capable of accuracies of 1.5 deg in attitude and 0.01 deg/sec in rates; i.e., within SAMPEX mission requirements.

1 Introduction

The coarseness of the attitude information derived from the Earth's magnetic field, $\vec{B}$, limits the usefulness of magnetometers in attitude determination systems. However, magnetic field measurements offer two advantages: (1) measurements can be made at any time, regardless of the spacecraft's orientation, and (2) $\vec{B}$ usually changes direction rapidly enough to make computation of its time derivative possible. These changes made during the orbit are large enough to enable determination of all three Euler angles using only a three-axis magnetometer (TAM). The second feature suggests that the spacecraft's rates can be computed, in principle, by examining the time derivatives of $\vec{B}$. These advantages have prompted us to study contingency attitude algorithms which can use only TAM measurements.

It should be emphasized that the problem is nontrivial: we want to reliably estimate both attitude *and* rates of the spacecraft using *only* TAM measurements and *no* a priori information. A successful algorithm can then accommodate a Sun-sensor failure on a gyroless spacecraft such as the Solar, Anomalous, and Magnetospheric Particles Explorer (SAMPEX), as well as for a gyro-based spacecraft such as the Earth Radiation Budget Satellite (ERBS) when the gyros are not functional. In fact, our work is partly motivated by a control anomaly on ERBS (Kronenwetter et al., 1988) during a thruster-induced yaw maneuver that resulted in the spacecraft tumbling with rates of more than 2 deg/sec. As a result, both Sun and Earth sensor readings became unreliable and the gyro output was saturated. Similarly, control of the Relay Mirror Experiment (RME) satellite was lost after the failure of the Earth sensors (Natanson, 1992). In both the ERBS and RME cases, a TAM became the only functional attitude instrument. In addition to such contingencies, a TAM-only algorithm can also be of use during Sun/Earth acquisition wherein the attitude and rate estimates will enable a more efficient maneuver.

We present here a combined computational scheme invoking two different algorithms, deterministic attitude determination from magnetometer-only data (DADMOD) and the real-time sequential filter (RTSF), both of which have been successful in TAM-only situations. The DADMOD (Natanson et al., 1990 and 1991; Natanson, 1992) is an algorithm that relates the time derivatives of $\vec{B}$ in inertial and spacecraft body coordinates to determine the attitude and the body rates. The DADMOD has been successfully tested for ERBS under normal conditions, as well as for RME after the aforementioned horizon sensor

---

PRECEDING PAGE BLANK NOT FILMED

failure (Natanson, 1992). The RTSF (Challa, 1993; Challa et al., 1994) is a novel extended-Kalman filter, originally developed for SAMPEX, which estimates, in addition to the attitude, errors in rates propagated via Euler's equation. The RTSF can estimate rate errors as small as 0.0003 deg/sec (Natanson et al., 1993), and this feature makes it a very robust and accurate real-time algorithm. In particular, it has been shown (Challa, 1993; Challa et al., 1994) that the RTSF converges successfully in TAM-only situations using "inertial" initial conditions (IIC); i.e., the spacecraft is assumed at rest in the geocentric inertial coordinates (GCI) with its axes coinciding with the GCI axes.

Both DADMOD and RTSF, although successful, have their own drawbacks when used independently. The DADMOD provides at least two solutions and there is no a priori way (using residuals, etc.) to determine which is correct. The RTSF's IIC, on the other hand, do not guarantee convergence, and even then the convergence times are long (nearly 2000 sec). The solution we have adopted to overcome these difficulties involves using the DADMOD solutions at epoch to initialize the RTSF, the RTSF's residuals and rate errors being used to identify the correct solution. These deterministic initial conditions (DIC) for the RTSF are determined by the DADMOD, using a small (100 sec) batch of TAM measurements. The DICs then ensure as well as speed up convergence. Results using SAMPEX in-flight data on the combined scheme (Natanson et al., 1994) have demonstrated that accuracies of 1.5 deg in attitude and 0.01 deg/sec in the rates are possible even with an uncalibrated TAM. Remarkably, these accuracies are even within SAMPEX requirements under Sun-sensor-supported conditions. Encouraged by these preliminary results, we have developed a protoype PC-based system that automates this combined scheme; thus providing a tool for use in situations such as those mentioned earlier. The objective of this paper is to give an overview of the above system and to present additional results using SAMPEX and ERBS data.

The rest of the paper is organized as follows. Section 2 briefly describes the algorithms, Section 3 describes the system concepts and capabilities, Section 4 presents TAM-only results, and Section 5 provides conclusions and future directions.

2 Overview of Algorithms

2.1 Deterministic Attitude Determination From Magnetometer-Only Data

The attitude can be determined via the tri-axis attitude determination (TRIAD) algorithm (Wertz, 1985) if the components of two independent vectors can be obtained in the reference and body frames. The DADMOD approaches the problem by specifying these vectors to be $\vec{B}$ and its first time derivative, $\dot{\vec{B}}$. The components of these vectors are related via

$$A\vec{B}^R = \vec{B}^A$$

$$A\dot{\vec{B}}^R = \dot{\vec{B}}^A + \vec{\omega}^A \times \vec{B}^A$$

(1)

where A is the attitude matrix, $\vec{\omega}$ is the angular velocity vector, and superscripts R and A imply that the corresponding vectors are resolved in the reference and body frames, respectively. The crucial difficulty in implementing the TRIAD algorithm is that $\vec{\omega}$ is unknown.

As shown by Natanson et al. (1990), the problem can be cast in the form of transcendental equations as follows. Taking into account that the vector lengths must be the same in the different frames, the projection, $\vec{\omega}_\perp$, of $\vec{\omega}$ onto the plane perpendicular to $\vec{B}$, can be expressed as a function of an unknown angle, Φ, between the vectors $A[\vec{B}^R \times \dot{\vec{B}}^R]$ and $[\vec{B}^A \times \dot{\vec{B}}^A]$. The attitude matrix A then depends only on the angle Φ, and the problem involves determining two unknowns: the angle Φ and the component, ω_1, of $\vec{\omega}$ in the direction of $\vec{B}$. These unknowns can be related by combining the kinematic relationship between the second derivatives, $\ddot{\vec{B}}^A$ and $\ddot{\vec{B}}^R$, with the dynamics for the $\dot{\vec{\omega}}$ given by Euler's equation. This results in the following schematic equation (Natanson et al., 1990 and 1992):

$$\vec{\Lambda}_0(\Phi) + \vec{\Lambda}_1(\Phi)\omega_1 + \vec{\Lambda}_2\omega_1^2 = \vec{0}$$

(2)

where $\vec{\Lambda}_0$, $\vec{\Lambda}_1$, and $\vec{\Lambda}_2$ parametrically depend on the inertia tensor and control torques. Two coupled equations, quadratic in ω_1 and transcendental in Φ, are then obtained by projecting Equation (2) along two directions perpendicular to $\vec{B}$. By expressing ω_1 as a function of Φ from one of the quadratic equations and substituting into the other, one obtains an equation transcendental in Φ, which is then solved numerically.

2.2 Real-Time Sequential Filter

The RTSF's state vector X comprises the four components of the attitude quaternion, $\vec{q}$, and the three components of the rate correction, $\vec{b}$, to $\vec{\omega}^A$:

$$X = \begin{bmatrix} \vec{q}^T & \vec{b}^T \end{bmatrix}^T \tag{3}$$

The RTSF uses sensor data to estimate $\vec{q}$ as well as $\vec{b}$, with $\vec{b}$ being estimated kinematically in the same manner as gyro biases for a gyro-based spacecraft; i. e., by attributing differences between the measured and propagated attitudes to errors in $\vec{\omega}^A$. The $\vec{b}$ estimates are then used to correct $\vec{\omega}^A$, and these corrected rates are used as initial conditions to propagate Euler's equation to the next measurement time. The propagation of $\vec{b}$ is modelled via a first-order Markov model:

$$\frac{d\vec{b}}{dt} = -\tau^{-1}\vec{b} + \vec{\eta}_b \tag{4}$$

where $\vec{\eta}_b$ is a white noise term, and τ is a finite time constant. The novel feature of the RTSF is that, because b represents rate errors accumulated between measurements, a suitable value for τ is the time between measurements: 5 seconds for the SAMPEX data and 8 seconds for the ERBS data used here. (In contrast, the same model, when used for gyro bias estimation, requires τ of several hours.)

3 System Concepts and Description

The system presently has only algorithmic capabilites; thus graphics are not currently included. System input and output are performed through ASCII files or the screen. The executable file for the system occupies roughly 260 kilobytes of memory on an IBM PC-compatible workstation. Input to the system consists of a dataset of processed spacecraft data with minimal requirements of timetags, and measured and reference magnetic fields. Control torques from momentum wheels and magnetic torquers are used when available, with the RTSF's rate-error estimates, b, providing robustness against any missing control data when the rates are low. (See, for example, the ERBS nominal mode results in Section 4 where no control data were available.) The system can also use data from line-of-sight sensors (such as Sun-sensors) to utilize intermittently valid data from such sensors.

Broadly, the system performs the following steps during a run:

- Use a batch of between 20 and 50 data records (1 to 4 min) to generate DADMOD solutions for the epoch.

- Use the RTSF to process a short batch of data records (20 to 50) to identify the correct DADMOD solution based on acceptance criteria for TAM residuals and rate errors. If no DADMOD solution is acceptable, use IIC.

- Make a production run using the available data.

- At the end of the run, optionally generate predicted attitude and rates for a user-specified time span.

4 Results

4.1 SAMPEX Eclipse Data of 11/15/92

SAMPEX is the first of the Small Explorer satellites and has the following features:

- 550×675 km orbit with 82 deg inclination

- Sun pointing of the pitch axis subject to a velocity-avoidance constraint that requires a minimum angular separation between the yaw axis and the spacecraft's velocity

- Nominal pitch rate of one rotation per orbit (RPO)

- Attitude accuracy requirements of 2 deg on each axis

- Attitude-determination hardware: fine Sun sensor (FSS) for roll/yaw and TAM for pitch

- Attitude-control hardware: momentum wheel for pitch and magnetic torquer assembly (MTA) for roll/yaw

- Attitude-control hardware: momentum wheel for pitch and magnetic torquer assembly (MTA) for roll/yaw

The FSS and TAM measurements are used in a single-frame TRIAD algorithm on board the spacecraft for attitude determination (Frakes et al., 1992). These TRIAD attitude solutions, together with rates obtained by differencing them, are used here as truth models.

Two special situations should be noted: eclipses and Sun-magnetic field coalignments. During an eclipse, SAMPEX uses the last observed Sun vector along with the TAM measurements to generate TRIAD solutions. In addition, the MTA is turned off and attitude control is performed by the wheel only, under the assumption that the pitch axis remains directed along the Sun vector. It has been verified (Natanson et al., 1993) that, in the absence of maneuvers, the assumption of a constant Sun vector during an eclipse does not introduce serious attitude errors. The second situation, coalignment, is of particular interest because the pitch angle is not observable, which introduces large errors in the TRIAD solutions. Thus, onboard attitude determination and control are turned off during coalignment. These features of the SAMPEX control law are seen in the Figures 1 through 3, which span the duration of an eclipse on 11/15/92 and respectively present results using: (1) only the DADMOD; (2) only the RTSF (using IIC), and (3) the combined scheme (the RTSF using DIC).

Figure 1a presents the DADMOD solutions for the 3–2–3 Euler angles parametrizing the GCI-to-body frame attitude, with the TRIAD solutions serving as the truth model. The first and second Euler angles here identify the orientation of the wheel axis and should be essentially constant because there are no control torques, and environmental torques acting on the spacecraft are negligible. This situation is clearly seen in the top plot of Figure 1a where, although at least two DADMOD solutions exist for any given time, the correct solution agrees with the truth model and remains essentially constant. The third Euler angle of this 2–3–2 scheme identifies rotations about the wheel axis and nominally varies at ± 1 RPO. This situation is evident initially in the middle plot; during the period 1000–1800 sec, however, the velocity-avoidance constraint necessitated a wheel-induced maneuver away from Sun-pointing so that the third Euler angle remains constant during this period. Coalignment occurs briefly at about 450 sec into the eclipse and the large errors in the TRIAD solutions are clearly seen in the bottom plot of Figure 1a, which is an enlarged section of the middle plot. We see from Figure 1a that the DADMOD attitude estimates are accurate to within 5 deg.

Figure 1b presents the DADMOD solutions for the spacecraft rates along the body axes, with the truth here being the RTSF solutions. We see from Figure 1b that the DADMOD rate estimates are accurate to within 0.01 deg/sec.

Figure 2 presents RTSF results using IIC (i.e., with very large initial errors), the TRIAD results serving as truth models. In Figure 2a, roll and pitch represent the orientation of the body frame with respect to the nominal Sun frame, and the RTSF errors are defined as the deviations from the TRIAD solutions. We see that, although the initial attitude errors exceed 100 deg, these errors fall below 1.5 deg in about 2000 sec. This is corroborated by the TAM residuals (bottom plot), which are very large initially, but drop to below 5 mG around 2000 sec.

Figure 2b shows similar features with respect to the rates. The rates (top and middle plots) converge to within 0.01 deg/sec of the TRIAD solutions in about 1800 sec. The convergence of the RTSF rate estimates by 1800 sec agrees with the behavior of the rate-error estimates, which by then have fallen below 5 deg/hour (note the units). Another noteworthy feature in this figure is the oscillation in the RTSF's yaw rate. These oscillations occur at the spacecraft's nutational period of 120 sec and arise from integrating Euler's equation with large transverse rates during the initial stages of the run. However, the RTSF's rate-error estimates correctly damp the amplitude to negligible values by about 1800 sec.

Finally, Figure 3 presents results of the combined scheme (i.e., the RTSF using DIC). As can be see in Figure 3a, the results are vastly superior to those in Figure 2a (note the differences in scale), which is also indicated by the residuals. Note that, although the pitch errors appear to be substantial around coalignment, these errors are primarily due to the TRIAD estimates. The rate estimates also show a marked improvement, as also evidenced by the rate errors. Note the kink in the TRIAD pitch rate results during coalignment. This kink is entirely spurious and originates from differentiating the erroneous TRIAD attitude estimates (bottom plot of Figure 1a). Coalignment has no noticeable effect on the RTSF's estimates because the filter then relies on its propagated value of the unobservable pitch angle. See also Challa et al. (1994) for additional analysis of the RTSF's performance during a SAMPEX coalignment.

4.2 ERBS Nominal Mode Data of 1/15/89

The ERBS is a conventional scientific satellite and features (Nair et al., 1982) the following:

- 600 x 640 km orbit with inclination around 50 deg
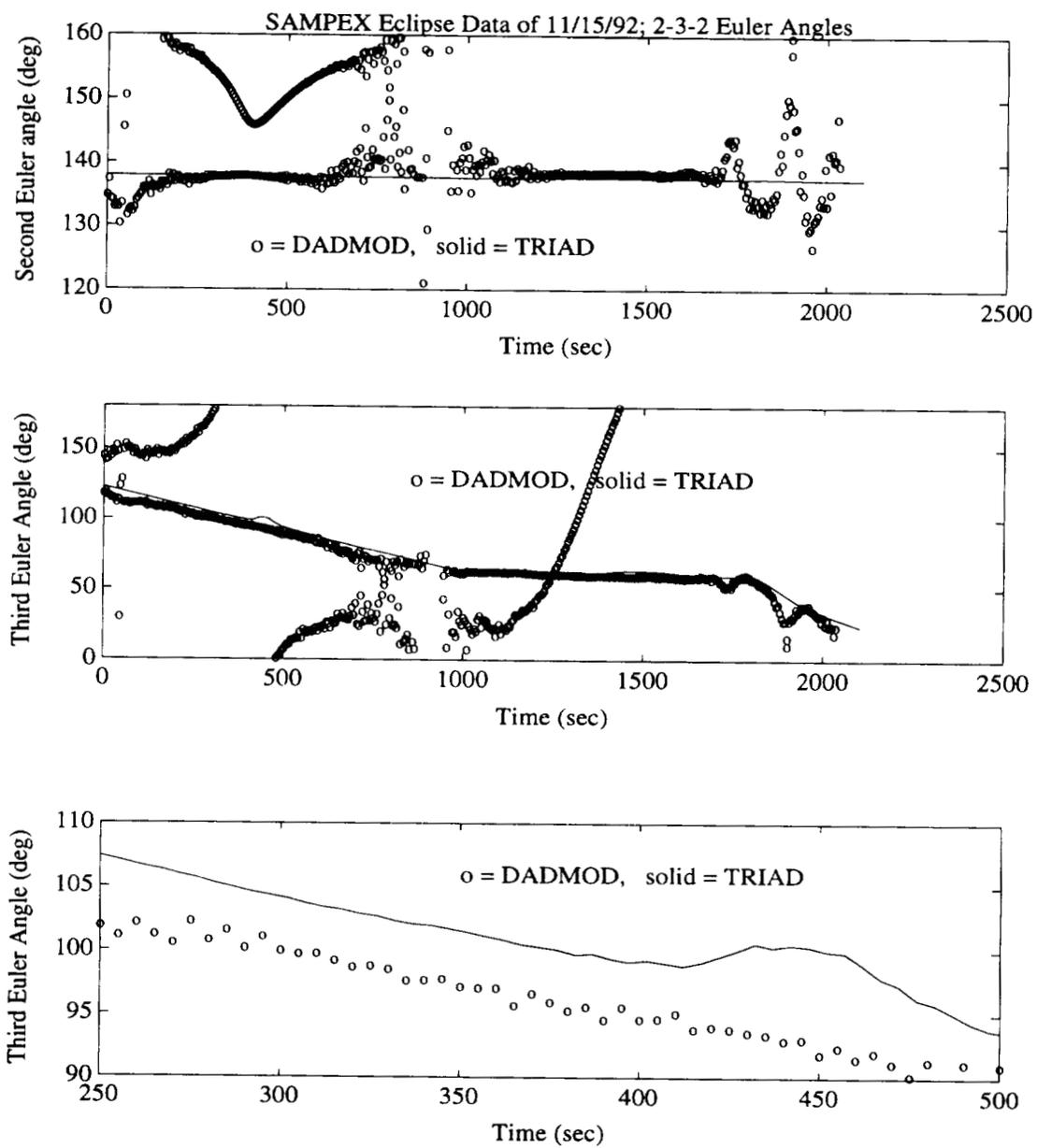
**Figure 1a. DADMOD Attitude Solutions Using SAMPEX Eclipse Data**
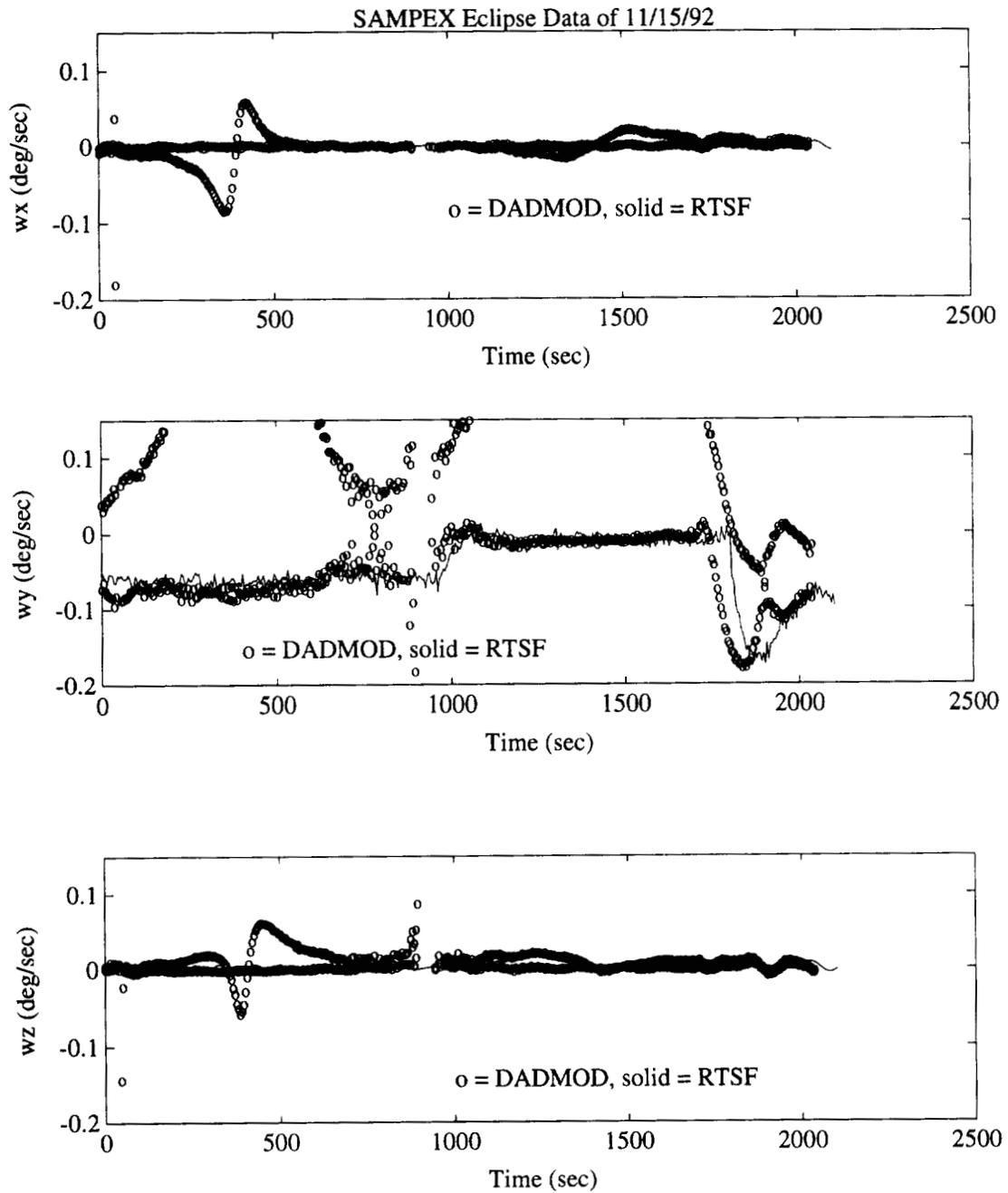
**Figure 1b. DADMOD Rate Solutions Using SAMPEX Eclipse Data**
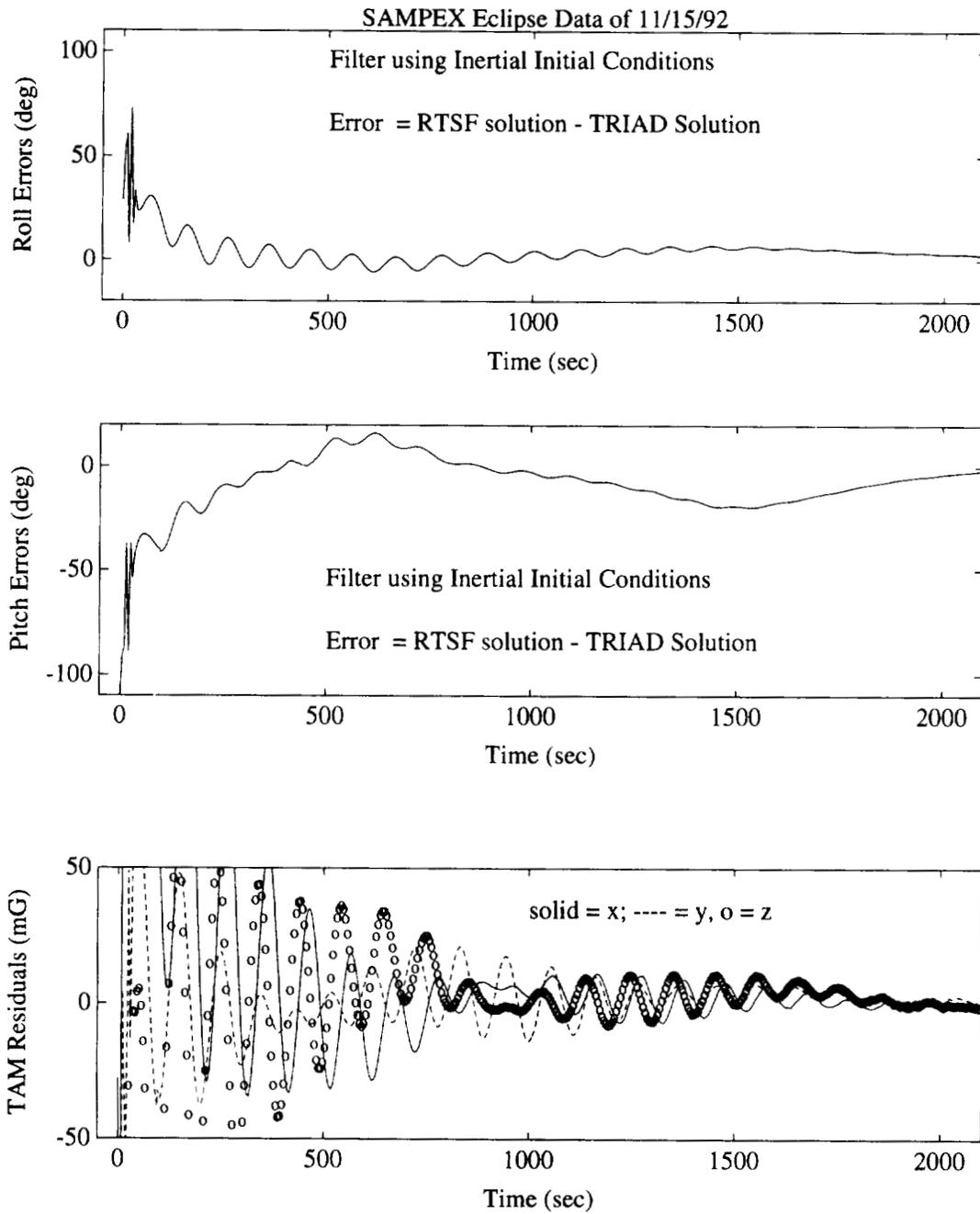
Figure 2a. RTSF Attitude Estimates and TAM Residuals Using SAMPEX Eclipse Data

89

C-2
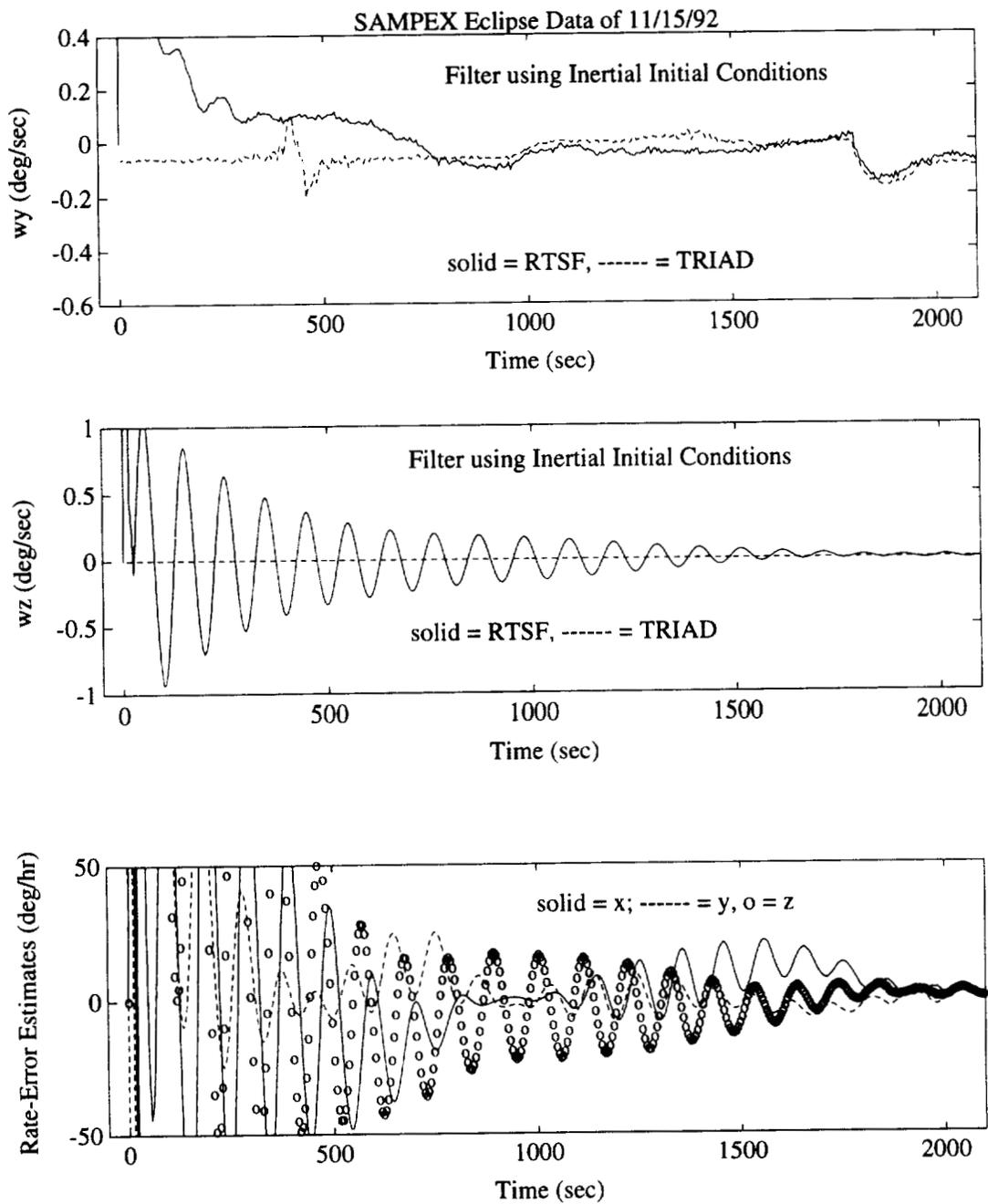
Figure 2b. RTSF Rate and Rate-Error Esimates Using SAMPEX Eclipse Data

SAMPEX Eclipse Data of 11/15/92

Filter using Deterministic Initial Conditions
Error = RTSF solution - TRIAD Solution

Filter using Deterministic Initial Conditions

Error = RTSF solution - TRIAD Solution

solid = x; ---- = y, o = z
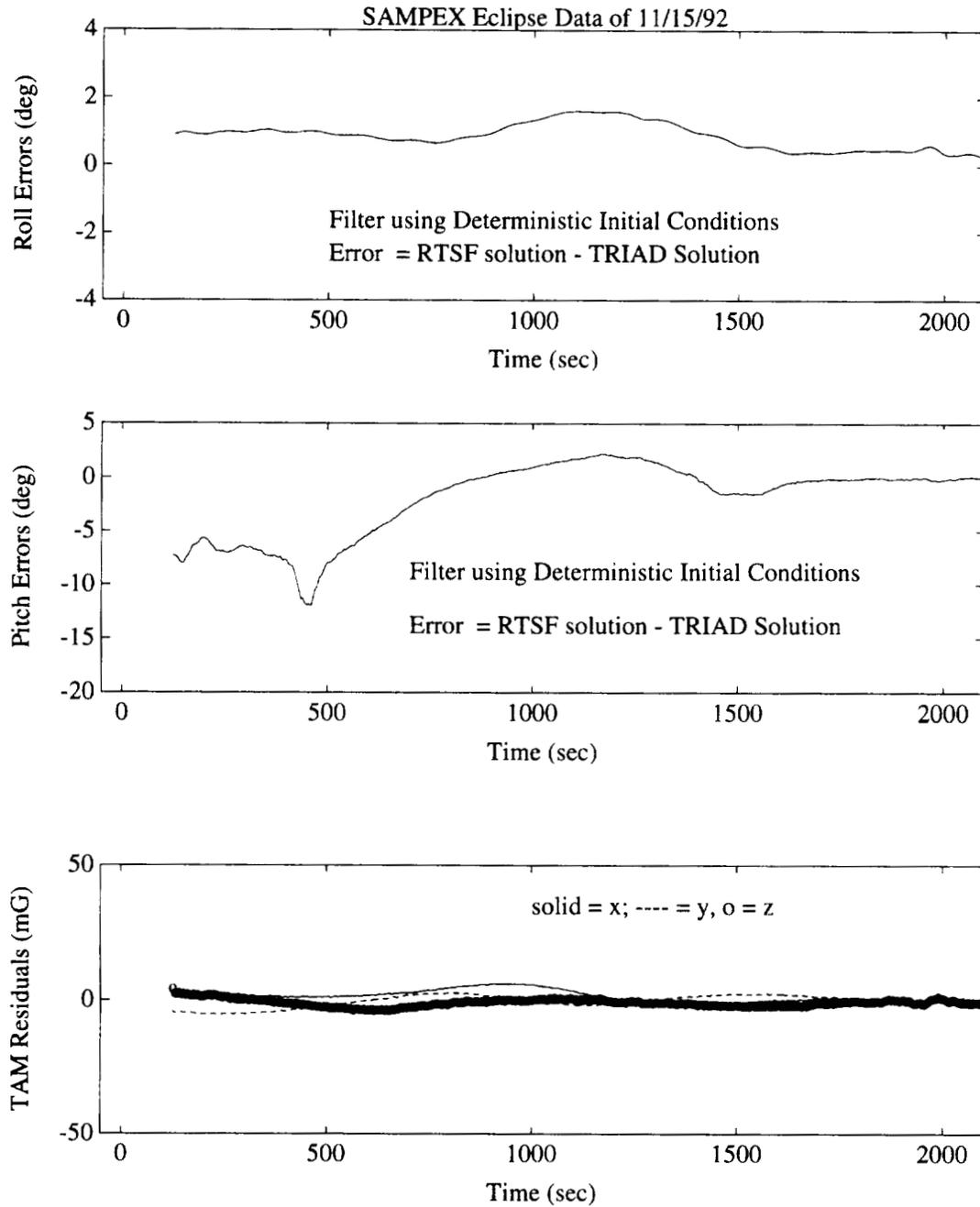
Figure 3a. Attitude Estimates and TAM Residuals From the Combined Scheme Using SAMPEX Eclipse Data
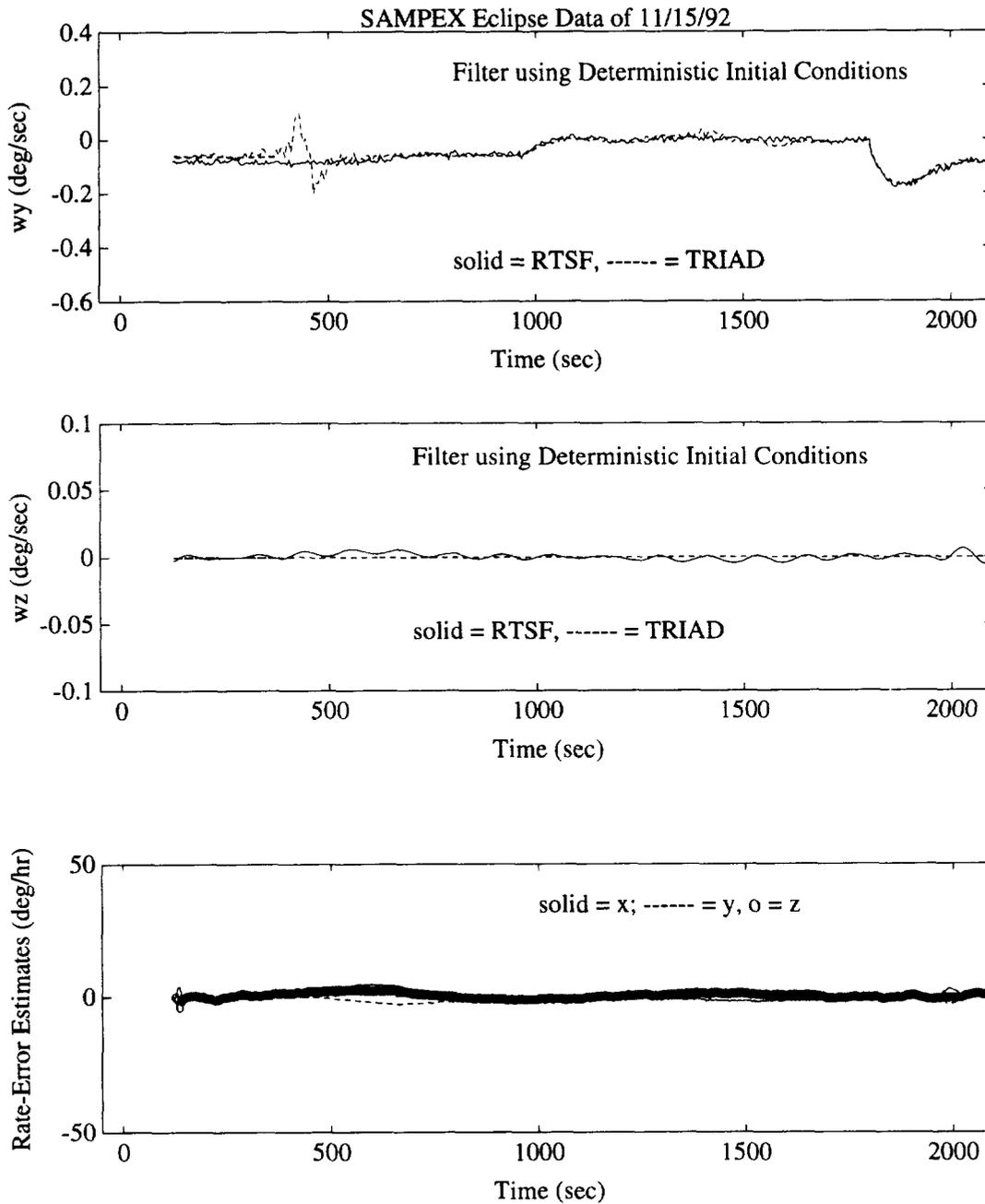
Figure 3b. Rate and Rate-Error Estimates From the Combined Scheme Using SAMPEX Eclipse Data

- Earth-pointing yaw axis

- Nominal pitch rate of 1 RPO

- Attitude accuracy requirements per axis of 0.25 deg; rate accuracy requirements per axis of 0.005 deg/sec

- Attitude-determination hardware: FSS, Earth sensor assembly (ESA), and TAM

- Attitude-control hardware: pitch momentum wheel, MTA, gyros, and thrusters

Although the spacecraft was functioning nominally during this data span, only TAM results were input to our system. In particular, no control data (wheel speed and magnetic torques) were made available; therefore, the system was run with the following limitations:

- The attitude truth model was generated by a batch estimator using data from the more accurate Sun sensor, Earth sensor, and gyro data. Gyro data serve as the truth model for the rates.

- No wheel data were input to the system. A constant, nominal wheel speed based on early prelaunch specifications was used. This is an incorrect assumption.

- No magnetic torquer data were input to the system and the magnetic control torques were set to zero. This is an incorrect assumption.

- Spacecraft inertia tensor and wheel parameters were based on early prelaunch specifications. The accuracies of these assumptions are unknown.

- Environmental torques were not computed.

- The RTSF's noise parameters were not tuned, other than setting the Markov time constant to the telemetry period of 8 sec.

The above limitations, together with the availability of accurate truth models, thus enable us to evaluate the robustness of the system as well as quantifying its performance.

The results using the combined scheme are presented in Figures 4a and 4b, and we see accuracies of 2 deg in attitude and 0.003 deg/sec in the rates. The quick convergence of the RTSF's estimates is also in agreement with the TAM residuals (Figure 4a) as well as the rate-error estimates (Figure 4b), which are very small throughout the run. The power of the combined algorithm is strikingly evident when we note that, despite of the above data deficiencies, the RTSF's rate estimates are better than those from the gyros!

5 Summary and Future Work

We find that the system provides an effective and easy-to-use tool for use in TAM-only situations, yielding 3-σ accuracies around 1.5 deg in attitude and 0.01 deg/sec in the rates. The system is able to provide accurate estimates under varied conditions. Thus, the results using SAMPEX data involved a gyroless spacecraft's complex motion during an eclipse, maneuvers, and coalignment. The results with ERBS data, on the other hand, involved nominal motion of a gyro-based spacecraft and were generated despite missing control data and inaccurate spacecraft mass properties. Remarkably, the SAMPEX results were within nominal mission requirements and the ERBS rate estimates were superior to the gyro measurements.

More studies are currently under way to further probe the effectiveness of the combined scheme and involve data from: (1) the ERBS tumble mentioned in Section 1, and (2) spinning spacecraft such as the Fast Auroral Snapshot Explorer (FAST).

Although the system currently runs on IBM PC-compatible workstations, the source code is fairly generic FORTRAN and can be modified easily for use on other platforms such as mainframe computers. Also, although the system requires a small initial batch of data to generate and test the DADMOD solutions, this initialization is very fast so the system can be adapted for real-time use. A requirement, however, is that processed telemetry and reference data must be supplied in a specific format. However, it is not difficult to generate this processed dataset by developing small computer programs that use the outputs from existing ground software.
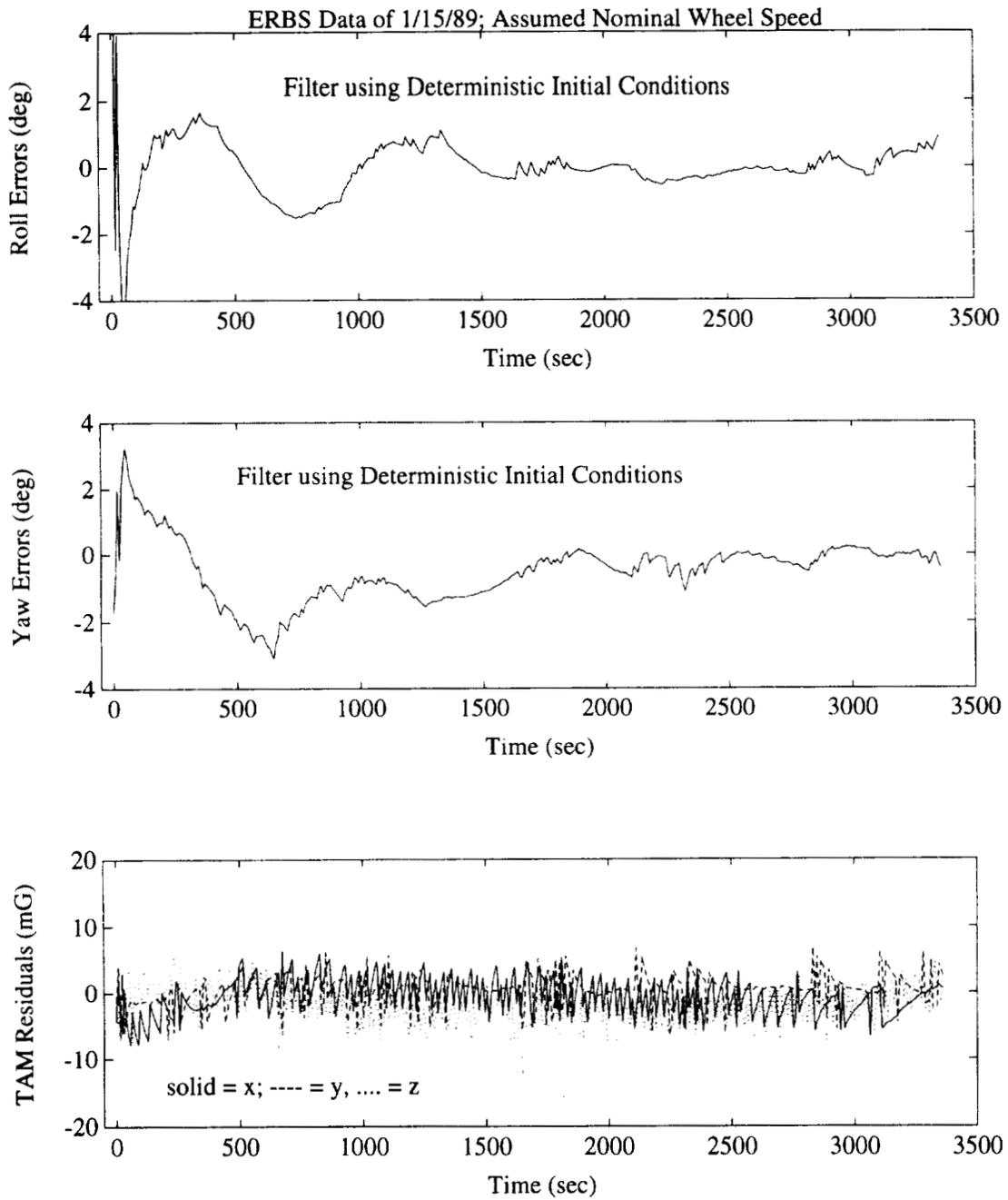
**Figure 4a. Attitude Estimates and TAM Residuals From the Combined Scheme Using Nominal ERBS Data**
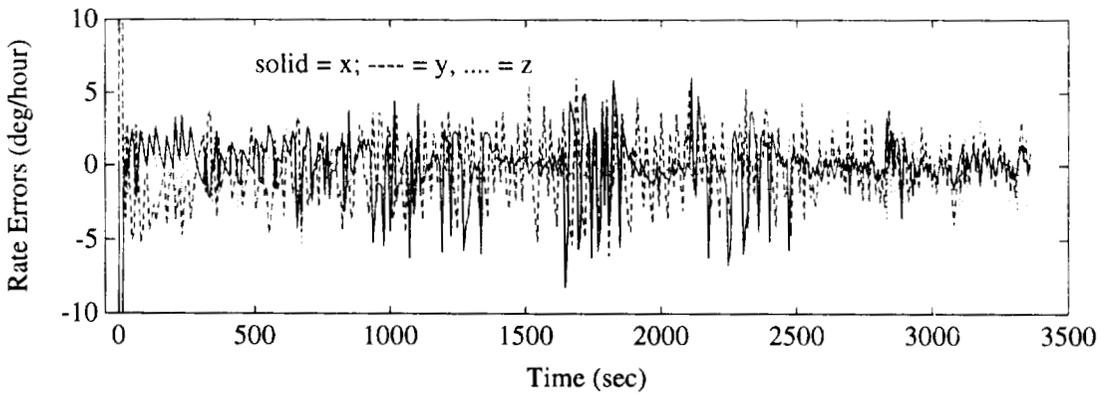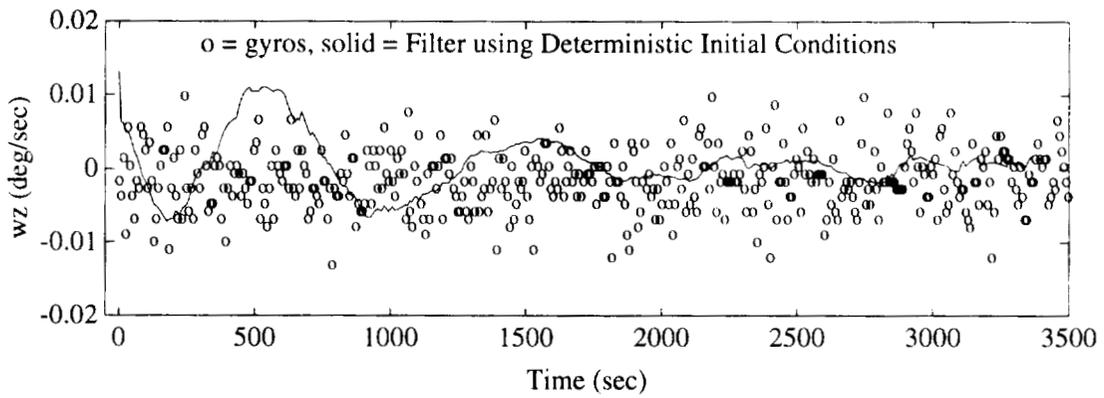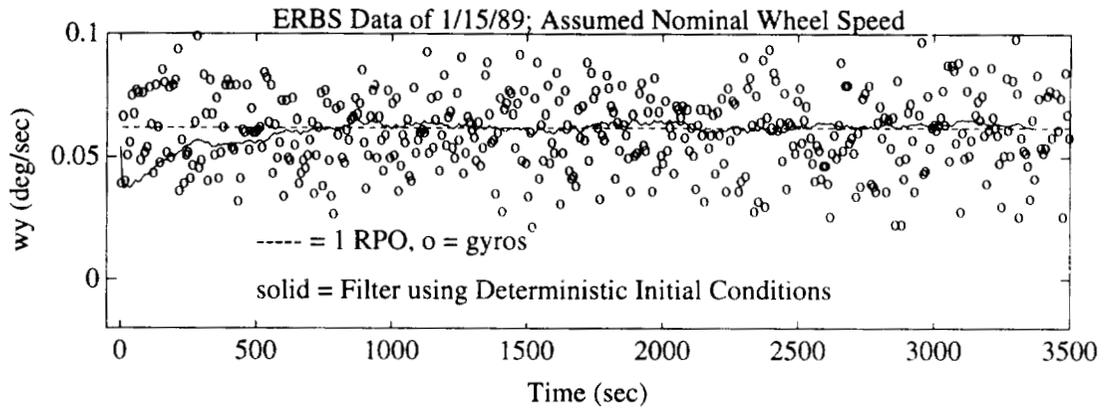
**Figure 4b. Rate and Rate-Error Estimates From the Combined
Scheme Using Nominal ERBS Data**

References

Challa, M. 1993. *Solar, Anomalous, and Magnetospheric Particle Explorer (SAMPEX) Real-Time Sequential Filter (RTSF): Evaluation Report*, NASA Goddard Space Flight Center, Flight Dynamics Division, 553-FDD-93/024R0UD0, prepared by Computer Sciences Corporation, April

Challa, M.; Natanson, G. A.; Baker, D. F.; and Deutschmann, J. 1994. *Advantages of Estimating Rate Corrections During Dynamic Propagation of Spacecraft Rates—Applications to Real-Time Attitude Determination of SAMPEX*, Flight Mechanics and Estimation Theory Symposium, NASA Goddard Space Flight Center, Greenbelt, MD, May

Frakes, J. P.; Henretty, D. A.; Flatley, T. W.; and Markley, F. L. 1992. *SAMPEX Science Pointing Modes with Velocity Avoidance*, Flight Mechanics and Estimation Theory Symposium, NASA/Goddard Space Flight Center, Greenbelt, MD, May

Kronenwetter, J.; Phenneger, M.; and Weaver, W. 1988. *Attitude Analysis of the Earth Radiation Budget Satellite (ERBS) Yaw Turn Anomaly*, Paper No. 18 for the Flight Mechanics/Estimation Theory Symposium, NASA/Goddard Space Flight Center, Greenbelt, MD, May

Nair, G.; Liu, K.; Fang, B.; Radomski, M.; Smith, S. 1982. *Earth Radiation Budget Satellite (ERBS) Attitude Ground Support System (AGSS) Functional Specifications and Requirements*, CSC/SD-82/6013, prepared for NASA/Goddard Space Flight Center by Computer Sciences Corporation, September

Natanson, G. A. 1992. *A Deterministic Method for Estimating Attitude From Magnetometer Data Only*, Paper No. IAF-92-0036, Proceedings of the World Space Congress, Washington, DC, September

Natanson, G. A.; Challa, M.; Kotaru, S.; Woodruff, C. 1993. *Attitude Dynamics Task: Attitude Determination Using Only Magnetometer Data for the Solar, Anomalous, and Magnetospheric Particle Explorer (SAMPEX)*, NASA Goddard Space Flight Center, Flight Dynamics Division, 553-FDD-93/076R0UD0, prepared by Computer Sciences Corporation, August

Natanson, G. A.; Keat, J.; McLaughlin, S. F. 1991. *Sensor and Advanced Attitude Studies: Deterministic Attitude Computation Using Only Magnetometer Data*, NASA Goddard Space Flight Center, Flight Dynamics Division, 554-FDD-91/010, prepared by Computer Sciences Corporation, March

Natanson, G. A.; McLaughlin, S. F.; Nicklas, R. C. 1990. *A Method of Determining Attitude From Magnetometer Data Only*, Flight Mechanics and Estimation Theory Symposium, NASA Goddard Space Flight Center, Greenbelt, MD, May

Natanson, G. A.; Challa, M. S.; Deutschmann, J.; Baker, D. F. 1994. *Magnetometer-Only Attitude and Rate Determination for a Gyroless Spacecraft*, Proceedings of the Third International Symposium on Space Mission Operations and Ground Data Systems, NASA Conference Publication 3281, Greenbelt, MD, pp. 791–798, November

Wertz J. S., ed. 1985. *Spacecraft Attitude Determination and Control*, D. Reidel Publishing Co., Dordrecht, Holland, 424–425.

Development of a Direct Match Technique for Star Identification on the SWAS Mission

Walter K. Daniel
IthacoTechnical Services
Lanham, Maryland, USA

Thomas E. Correll
Mark O. Anderson
Attitude Control and Stabilization Branch
Special Payloads Division
NASA Goddard Space Flight Center
Greenbelt, Maryland, USA

A direct match technique for star identification was developed for use with the star tracker on the SWAS spacecraft. In this technique, tracker searches are used in a two-step process for an implicit direct match star identification. A simulation of the star acquisition process was created and used in the preparation of guide star selection requirements. Flight software implementing this star acquisition technique has been developed and tested.

INTRODUCTION

The Submillimeter Wave Astronomy Satellite (SWAS) is a three-axis stabilized stellar-pointing spacecraft set for launch in July 1995. This mission is the third to be developed under the Small Explorer (SMEX) program. The scientific instrument is a submillimeter wave detector coupled with a spectrometer. The 3σ pointing requirements for this mission are 57 arcseconds about the X- and Y-axes and 28.5 arcminutes about the Z-axis.

SWAS ACS MODES

The SWAS Attitude Control System (ACS) must progress through other modes before star acquisition can begin. After separation from the Pegasus XL launch vehicle, analog electronics in the SWAS Attitude Control Electronics (ACE) Box will utilize a simple B-dot and precession controller to reduce body rates and point the solar panels at the Sun. After the flight computer has been activated and checked out, the ACS will be commanded to Digital Sun Pointing mode, a software version of the B-dot/precession controller.

The next mode is Inertial Sun Pointing (ISP) in which attitude determination is accomplished using a magnetometer, sun sensor, gyroscopes, and a Kalman filter. During ISP, the spacecraft

Z-axis is pointed at inertial targets near the North and South ecliptic poles. These targets ensure sufficient illumination of the solar panels in addition to satisfying instrument Earth limb avoidance requirements. When the spacecraft is North of the ecliptic plane, the North target is used; when South of the plane, the South target is used.

ISP pointing prepares the ACS for transition into Auto-Stellar Acquisition (ASA), a Stellar Pointing submode. During ASA, the spacecraft z-axis is pointed at the same North and South ecliptic pole targets, but attitude determination is accomplished with the star tracker, gyroscopes, and Kalman filter. ASA serves two purposes: to ease the transition from ISP to Stellar Pointing and to provide an attitude hold function when science targets have been missed.

There are three types of observations available during Stellar Pointing: Fixed, Nodding, and Mapping. Fixed observations require the ACS to maintain pointing of the instrument on a target. Nodding observations require that the ACS slew the spacecraft between on-source and off-source attitudes in order to allow for instrument calibration; the maneuvers can be up to 3.0° and the spacecraft must be settled to within 20 arcseconds in 15 seconds. Nodding and Mapping observations are similar except that maps comprise several points in a two-dimensional pattern. The ACS incorporates an efficient nonlinear slewing controller for timely maneuvering of the spacecraft between observational targets. A scientific timeline of the targets is uploaded to the spacecraft and the slew controller computes the approapriate slew to the next target on board.

SWAS STAR TRACKER

The star tracker on the SWAS spacecraft is a Ball Aerospace CT-601 CCD-based device. This tracker has a field of view of approximately 8.0° by 8.0° and can track up to five stars at once. Stars with instrument magnitudes between 1.0 and 6.0 can be located; the device will track any star brighter than the magnitude specified for a search. The basic CT-601 includes a Full Field search that continuously scans for stars in the field of view and a Directed search that locates stars in small 8.0 arcminute square windows. The SWAS tracker also includes a Reduced Field of View (RFOV) search that functions like the Full Field search but is of selectable size and location.

The star tracker reports positions of stars in terms of two angles α and β from the boresight of the device. The ACS flight software uses star unit vectors, so the tracker angles are converted to vectors and unitized. The equation that relates the angles to a vector is

$$S = - \tan(\beta) \, i + \tan(\alpha) \, j + k$$

where S is the star vector in the tracker frame, α and β are the tracker angles, and ijk are the unit vectors for the star tracker axes. Equations for computing tracker angles from a unit vector are

$$\alpha = \arctan(y/z)$$
$$\beta = - \arctan(x/z)$$

where x, y, and z are the components of the unit vector.

Testing of the star tracker and acquisition algorithms required equipment for stimulating the detector as well as simulating the tracker output. The CT-601 includes a small LED bonded in the optics that simulates a star; this device is under the control of the tracker microprocessor and is referred to as the Built-In Test Equipment (BITE) star. Ball also provided an external LED stimulator that fits over the tracker lightshade. Light from each of the five LEDs is focused by lenses to approximate point sources. Brightness of the five LEDs is controlled by an independent GSE computer. When dynamic simulator testing of the ACS is performed, a star tracker simulator is connected to the SWAS 1553 bus while the actual tracker is powered off. The star tracker simulator receives attitude quaternions from the dynamic simulator and star tracker commands from the flight computer, computes which stars are tracked, and sends the simulated star tracker data to the flight computer via the 1553 bus.

SWAS GUIDE STAR CATALOG

The CT-601 star tracker is a new device, so a new star catalog with the appropriate instrumental magnitudes was developed by the SWAS principal investigator's institution [1]. Personnel at the Smithsonian Astrophysical Observatory (SAO) converted the magnitudes in the Bright Star Catalog to CT-601 instrumental magnitudes to form the bulk of the SWAS star catalog. The magnitude conversion was developed by SAO based on test data from Ball. Stars from other catalogs were used to add dimmer visual stars that will appear bright enough to the CT-601 to be tracked. Those stars that were not suitable for use by the CT-601 (e.g., multiples) were flagged as unsuitable for use as guide stars. Locations for all stars were computed for 1996.5, approximately one year into the planned SWAS mission. As of early 1995, the SWAS star catalog contained approximately 4500 entries.

The star catalog is not stored on the SWAS spacecraft. The five stars for the two ASA targets are contained in EEPROM and loaded into memory whenever the flight computer performs a cold start. A unit vector in the J2000 frame and a CT-601 instrumental magnitude for each of the two to five guide stars for a scientific target are inserted into the Fixed, Nodding, or Mapping command for observing that target. If instrument magnitude errors are found during the mission, the errors can be corrected in the SWAS catalog so that future uses of those guide stars will be successful. Early in the mission, the star tracker will be powered on during ISP to gather observations of stars that will be used to validate magnitude conversion before star acquisition is attempted.

TWO-STEP STAR ACQUISITION

There are two types of star acquisitions: Auto-Stellar from ISP and Stellar or Auto-Stellar from a previous target. An accurate attitude solution is available for each type, so a direct match star identification technique [2] was used. The acquisition sequence is completed in two steps.

The first step in the star acquisition sequence is begun when the onboard attitude solution is within 100 arcseconds of the target attitude. The flight software formulates a RFOV search and

sends a command to the tracker via the 1553 bus. This search is designed to find a relatively bright, isolated star that is referred to as the "base" star. Ideally, the base star is located near the center of the FOV and is the brightest guide star for that target. When the tracker begins tracking one or more stars, the flight computer attempts to match the base star by magnitude. The flight software computes the α and β offsets between the predicted and observed positions of the matched base star, essentially the attitude errors about the x and y axes of the tracker. The z attitude error is almost unobservable near the center of the FOV, so it is assumed to be zero. This assumption is made using the nature of the attitude errors and the geometry of the spacecraft; note that this technique is equivalent to improving the attitude estimate by using just one observation.

The second step of the star acquisition sequence takes place after the base star is matched by magnitude. The α and β offsets are added to the predicted positions of the remaining "field" stars for the target. One Directed Search command for all field stars in the FOV is sent to the tracker with the improved position estimates based on the base star observation. The Directed Search windows are rather small (8.0 arcmin square) and only one star can be tracked in each. The finite size of these windows means that star can still be found if the z attitude error is nonzero (but still small). After one or more field stars are acquired and matched by magnitude, Kalman filter updating of the onboard attitude quaternion is begun.

Apart from magnitude matching, no explicit star identification is performed in this sequence. Star identification is implicit based upon the isolation of the base star and the small size of the Directed Search windows (see Figure 1). Magnitude matching is relatively loose because of the unknown nature of the CT-601 performance on orbit as well as the unproven SWAS guide star catalog. Early in the mission, search commands will be sent for stars 1.0 magnitude dimmer than expected and the magnitude matching range will be ± 0.75. With experience on orbit, the matching range may be reduced to make guide star selection easier.

GUIDE STAR SELECTION CRITERIA

For a star acquisition to be successful, the base star must be selected so that no other star within the magnitude matching range may appear in the RFOV window. Of course, the base star itself must be in the window. There are two valid approaches to choosing this window size: finding the largest window that the guide stars will support or setting the window larger than the expected attitude error at the beginning of the star acquisition. In addition to base star requirements, there are separation requirements for the field stars to ensure an accurate attitude solution.

Consider a RFOV window of size 2R by 2R (see Figure 2). If the window is centered on the predicted position of a base star, the attitude solution can be in error by as much as the angle R. To determine the maximum exclusion angle, consider the worst case misidentification (see Figure 3). If the base star is on the edge of the circle towards one corner, the farthest location in the search window from the base star is 2.414R away in the opposite corner. In the worst case, one star could be 0.75 magnitude brighter than predicted while another could be 0.75 dimmer, so the magnitude exclusion amount is 1.5 instrument magnitude. If a star within 1.5 magnitudes is an

8 degrees

Reduced FOV Search Window (2 deg x 2 deg)

Directed Search Window
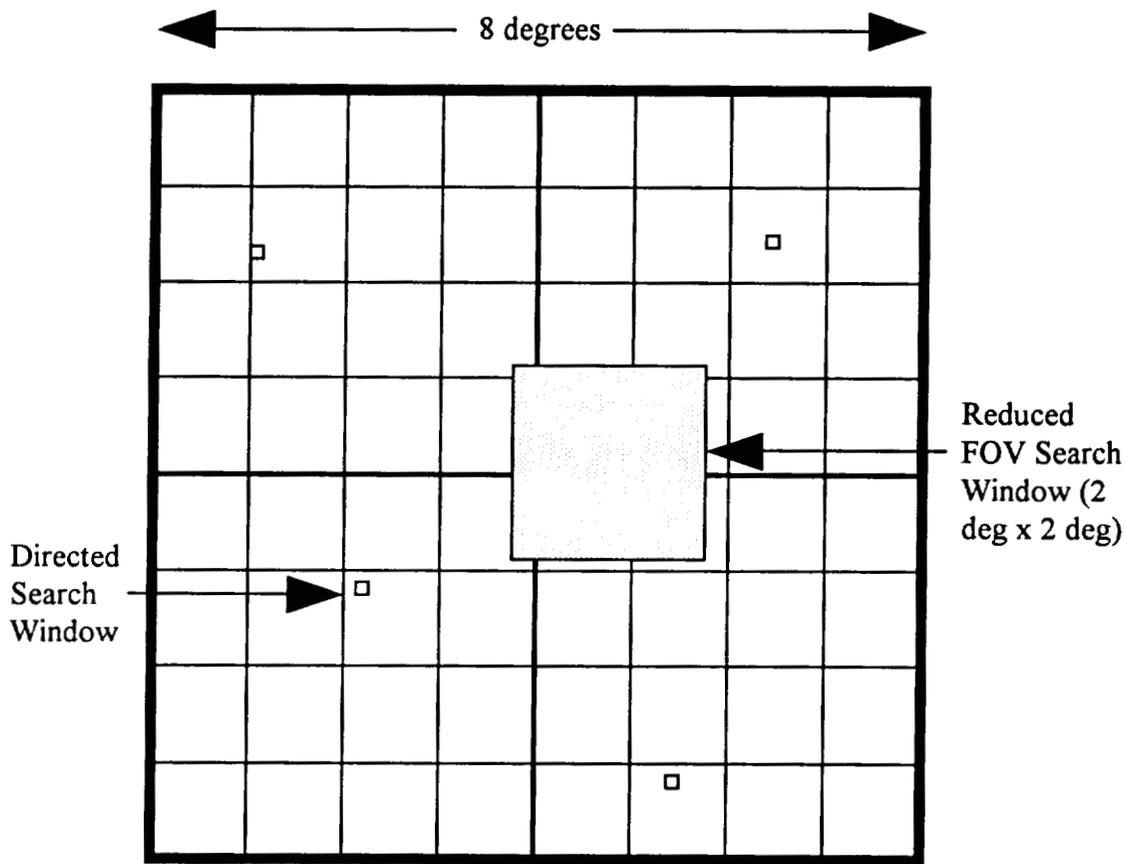
Window sizes are approximately to scale

Figure 1. SWAS Star Acquisition Search Windows

RFOV Window

2R

2R

R

predicted
position
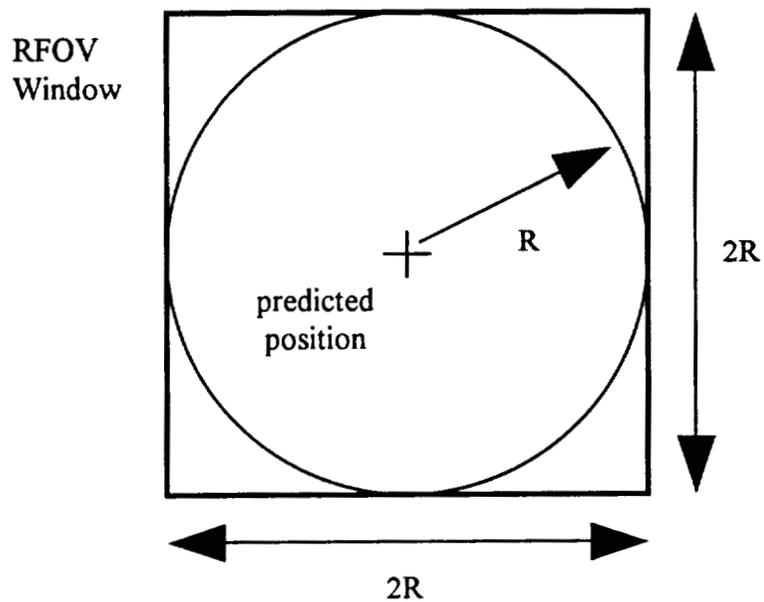
Figure 2. Reduced Field of View Window Size

R

1.414R

predicted
position

actual
position
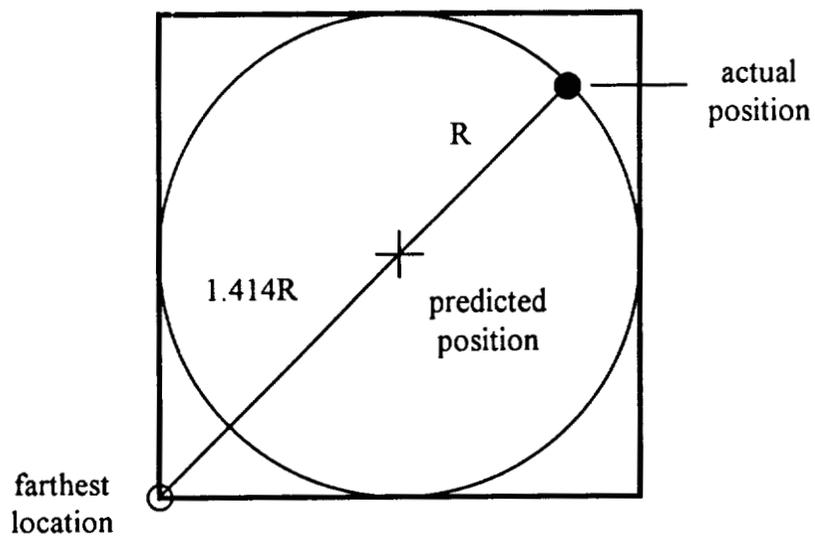
farthest
location

Figure 3. Basis for Exclusion Angle

angle E separated from the intended base star, the maximum allowable attitude error R is E/2.414 and the maximum RFOV window size is 2R (E/1.207).

The star Altais in the constellation Draco (see Figure 4) was chosen as the base star for the North ASA field. Altais has a predicted instrument magnitude of 2.86 is approximately 7.1° from the ecliptic pole [3]. Altais is the brightest star within 10° of the ecliptic pole. The nearest star of similar brightness is Epsilon Draconis with 3.69 instrument magnitude. The separation between the stars is 4.12°, so the maximum allowable error is 4.12°/2.414 or 1.7°. The largest allowable RFOV window is 3.4° square.

The South ASA field is based on Alpha Pictoris (see Figure 5), a relatively isolated star that is 6.9° from the ecliptic pole [3]. This star has a predicted instrument magnitude of 3.49 and is the brightest catalog star within 12° of the ecliptic pole. A nearby star with magnitude 4.67 is 4.82° from Alpha Pictoris, so the maximum allowable error is 4.82°/2.414 or 2.0°. The RFOV window for this target can be no larger than 4.0° by 4.0°.

When the spacecraft slews between science targets, the attitude is propagated using the gyroscopes only. The gyroscopes have been tested, so approximate performance parameters (drift rate, scale factor error, bias error) are known. These parameters were used in the high-fidelity SWAS Integrated Simulation to predict attitude determination error at the end of slews. Several runs were made for each slew angle to find the largest attitude error R for that slew. The results (Table 1) were tabulated for mission planning purposes [4]. As before, the RFOV window is 2R by 2R, but the star catalog must now be checked to verify that no other stars will appear in the window and be misidentified.

Table 1. Predicted Attitude Error as a Function of Slew Angle

Slew Angle (deg)	Attitude Error (deg)
5	0.023
10	0.030
20	0.050
30	0.072
40	0.093
60	0.140
90	0.210
120	0.280
150	0.340
180	0.410

Guide stars for each science target are chosen by the planning scientist for the mission. Personnel at SAO developed planning software for this task [5]. The planning software checks for other mission constraints such as solar panel illumination and instrument Earth avoidance, then searches the SWAS catalog for an appropriate base star. The slew angle from the previous target is used
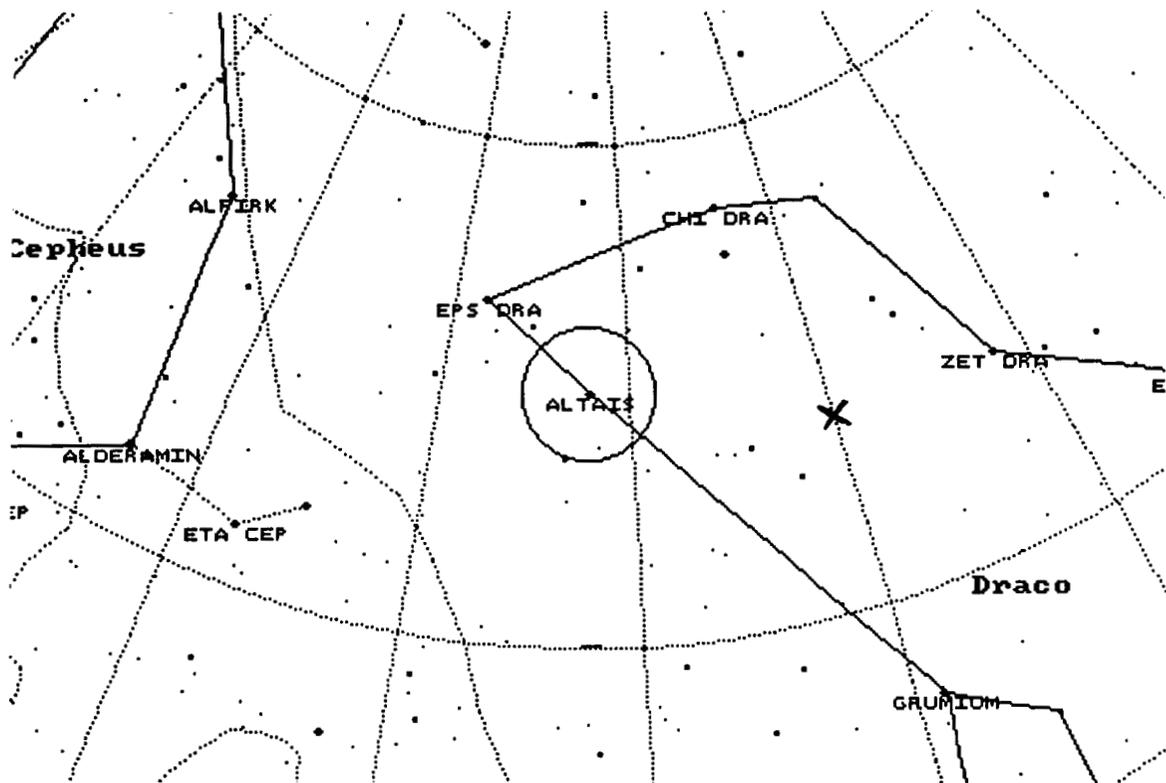
Figure 4. North Ecliptic Pole Region
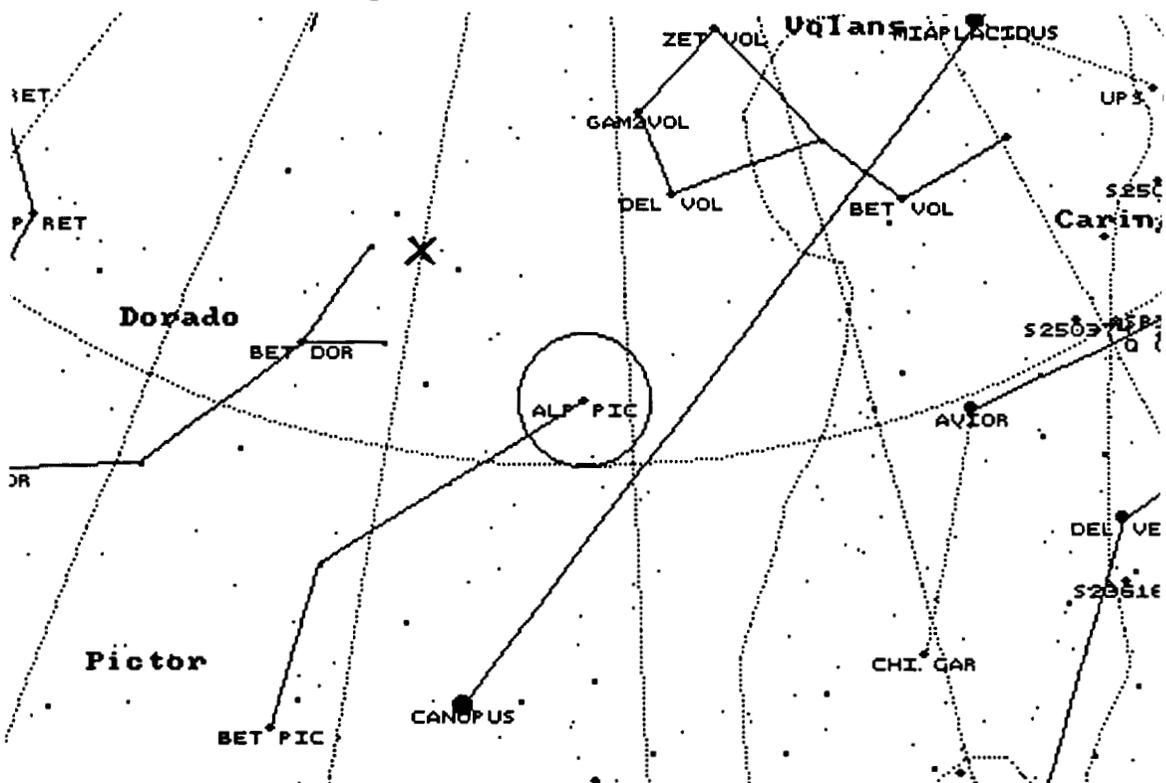
Figure 5. South Ecliptic Pole Region

to find the attitude error and RFOV window size for that target. Once a suitable base star has been found, the catalog is examined for suitable field stars. Most SWAS targets will be in the galactic plane, so five guide stars (one base plus four field stars) should be in the FOV. SWAS Integrated Simulation results indicated that if only two stars are in the FOV, those two stars must be separated by at least 3.0° for the attitude solution to be sufficiently accurate. The planning software checks field star separation so that this condition is met for two or more stars.

STAR ACQUISITION SIMULATION

A MATLAB simulation of the star acquisition process was developed to test the concept before the start of ACS flight software development. In this script, guide star unit vectors are rotated into the star tracker frame, tracker angles are computed, and RFOV and Directed searches are simulated. The script was used to test the process and evaluate numerous candidate star fields.

In the SWAS star acquisition process, guide star unit vectors in the inertial frame are rotated into the tracker frame using direction cosine matrices. In the MATLAB simulation, this rotation was accomplished with the matrix equation

$$S_t = A_{crr} * A_{bt} * A_{ib} * S_i$$

where S_i is the star unit vector in the inertial frame and S_t is the vector in the tracker frame. A_{ib} is the direction cosine matrix that transforms the vector from the inertial to the SWAS body frame; this matrix is extracted from the current attitude quaternion. The constant A_{bt} is the body-to-tracker transformation matrix made necessary by the mounting of the star tracker -83° about the z axis from the body frame. A_{crr} is an error matrix that allows deliberate introduction of small attitude errors about the X, Y, and Z axes for testing purposes.

Once the guide stars have been rotated into the tracker frame, the unit vectors are converted into tracker angles α and β for use in CT-601 search commands. The RFOV search for the base star is simulated by searching through the guide star list for that target. Once the base star is located, α and β offsets are computed and simulated Directed searches are performed. If no stars are found in the RFOV window, the star acquisition is aborted. If no stars are found in the Directed search windows, the star acquisition is aborted. If at least one field star is located, the acquisition is complete.

Numerous star fields and attitude error situations were examined with the completed star acquisition simulation. An important parameter is the amount of Z attitude error that will cause field stars to appear outside the Directed search windows. Runs with several different star fields showed that the Z error must be greater than 1.5° in order to cause difficulties; the expected Z error is typically 0.5°, so the assumption of zero Z attitude error inherent in the star acquisition process is valid for this mission.

Plots of the star tracker view are made by the MATLAB script. Figure 6 is a plot from a simulation of the North ASA field. The circles represent the predicted star locations while the target vector is the "+" symbol. The base star is shown by an asterisk while the field stars are shown by "x" symbols. Attitude errors of 0.25° about the X axis, 0.5° about the Y axis, and 0.25° about the Z axis were included in the simulation run portrayed by this plot. The use of the α and β offsets of the base to correct the locations of the Directed search windows for the field stars is rather clear in this plot. A plot from simulation run with the same errors for the South ASA field is shown in Figure 7.

FLIGHT SOFTWARE IMPLEMENTATION

After the star acquisition process was tested in simulation, the process was molded into an algorithm suited for coding in a real-time system [6]. The overall structure is that of a state machine in which different actions are performed in the different states. Up to five stars numbered 0 (primary base star), 1 (backup base star), 2, 3, and 4 are taken from the observation command. Failure checking was implemented in a separate module to catch star acquisition problems.

When the ACS software indicates that the spacecraft has neared the target and switched to the fine pointing controller, the first state "InitBaseStarAcq" is entered. In one 100 millisecond control cycle, the software formulates and sends the RFOV search for the base star. The next state is "AcsBaseStarSearch" in which the software examines the star tracker output in order to match the base star by magnitude. If the base star is not matched within a set time, the state switches the base index from 0 to 1 and restarts the star acquisition process. If the base star is matched by magnitude, the state computes the α and β offsets, predicts the positions of the field stars, and sends one Directed search command to the star tracker.

During "AcsStarFieldSearch," the software waits for the results of the Directed search command. Field stars are matched by magnitude and a separation index is calculated. This index is simply the sum of the squares of the separation angles between the field stars and the base star. When the index reaches a sufficiently high value, enough separated stars are available for an accurate attitude solution and the process continues. Early in the mission, the index must be greater than 16 square degrees, requiring a separation of 4° if there are just two guide stars for the target. After the index has exceeded the required value, updating of the Kalman filter attitude solution with star information can begin.

The "AcsStarFieldSearchUpdate" state serves two purposes. For most star acquisitions, the beginning of Kalman filter updates means that the spacecraft will slew to settle accurately on the target. Once the state detects settling, it checks for any missing guide stars and sends Directed search commands to reacquire them. This state also allows for multiple chances at recovering stars during Nodding and Mapping Observations. Once settling on the target takes place, the "AcsTrackField" state remains in force until a new Nodding/Mapping point is commanded or a new target comes in the scientific timeline. If the slew is to a new target, all tracker searches are discontinued and the star acquisition process starts again with the new guide stars.

N Altais field, 0.25/0.5/0.25 deg errors
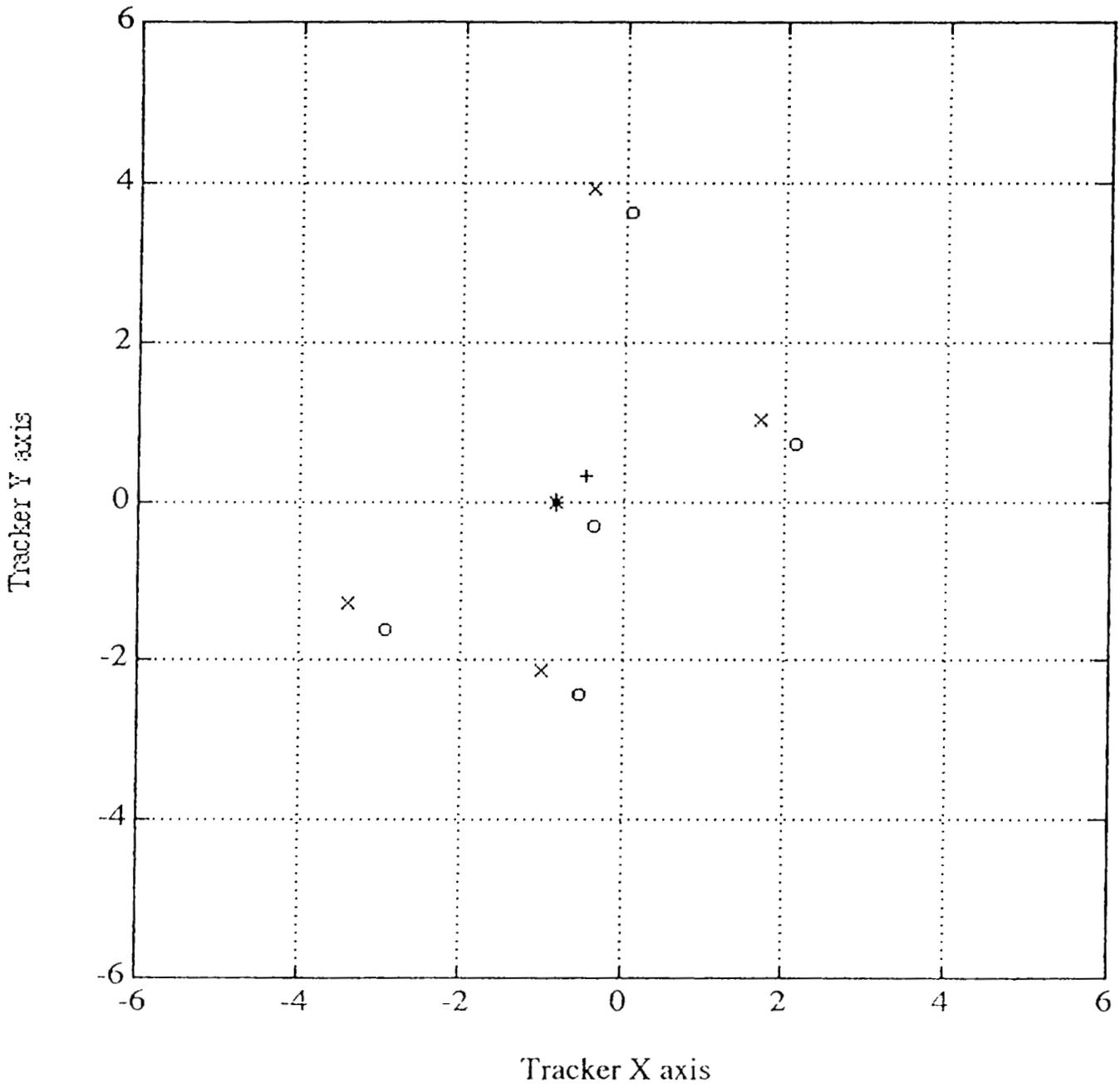
Figure 6. Simulation Plot of North Ecliptic Pole Star Field

S Alp Pic field, 0.25/0.5/0.25 deg errors
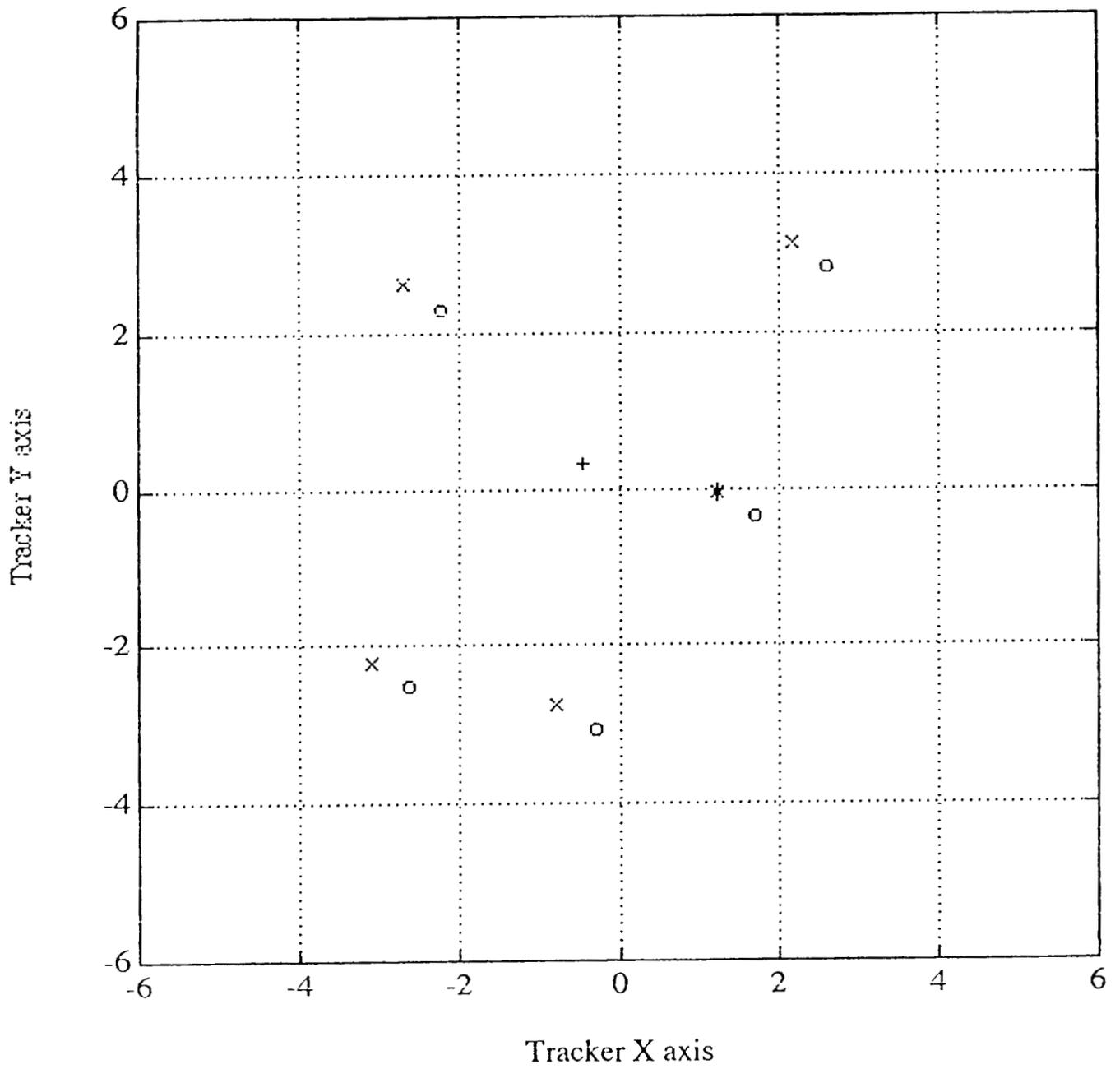
Figure 7. Simulation Plot of South Ecliptic Pole Star Field

Overall star acquisition failure is checked in an independent Failure Detection and Handling module. When the spacecraft first begins a star acquisition at a new target, the FDH module starts a star acquisition timer. If the acquisition has not been completed with a set period of time (300 seconds at the beginning of the mission), the module clears the tracker searches, sends a Full Field search command, waits for 45 seconds so that some stars can be found for later analysis on the ground, then aborts that target. If the spacecraft aborts from a science target, the ACS will command a slew to either the North or South ecliptic pole star field and begin an Auto-Stellar Acquisition. If the spacecraft aborts from ASA, the ACS drops to ISP and the remainder of the scientific timeline for that day is lost.

FLIGHT SOFTWARE TESTING

A significant amount of testing was done on the tracker, simulators, and flight software to verify the proper functioning of the star acquisition process.

The flight star tracker was shipped to Goddard about one year before final integration. Numerous tests were run on the tracker to characterize it for analysis, flight software, and star tracker simulator reasons. The internal BITE star, the GSE LEDs, and a collimated light source were used to stimulate the tracker and investigate the search limits. The flight tracker was also connected to the 1553 bus of the breadboard flight computer to test the interfaces between the tracker and the flight software. A test procedure was created to simulate a star acquisition with the flight tracker and GSE LEDs. The α and β angles for the simulated stars were measured, converted to unit vectors S_t, then rotated back into the simulated inertial frame (i.e., S_i) using the current attitude quaternion from the dynamic simulator setup. A target upload with these unit vectors and measure magnitudes was created and sent to the flight computer. Simulated acquisition were successful and typically faster than two seconds.

The flight tracker was also used to verify the accuracy of the star tracker simulator. Once the flight tracker was returned to Ball for integration in the SWAS instrument, star acquisition testing focused on the flight computer/dynamic simulator environment. Extensive testing of the routines including failure checking was conducted.

Once the instrument was delivered to Goddard and final integration completed, testing shifted to the flight environment. Hardware tests on the star tracker such as aliveness and phasing procedures were developed and performed. Flight software testing continued with the star tracker simulator used in conjunction with the dynamic simulator. While no major problems have been identified, some minor ones were found largely as a result of unexpected combinations of commands from the scientific timeline.

EARLY ORBIT OPERATIONS

The Flight Dynamics Facility will execute star tracker checkout procedures while the ACS is in ISP. FDF has a Real Time Attitude Determination System (RTADS) that allows for star pattern matching using the SKYMAP star catalog. The pattern matching technique used is by

van Bezooijen [7]. For example, the tracker telemetry can be processed to determine if the ISP attitude is accurate enough for an ASA to be successful.

CONCLUSIONS

The implict direct matching star identification technique used by the SWAS ACS with the Ball CT-601 star tracker has been proven effective in prelaunch tests. While the technique is not highly flexible, it has proven to be quite fast. The method of embedding the guide star information in target command uploads preserved a great deal of onboard storage for this modest Small Explorer mission. The SWAS guide star catalog can be updated based on flight experience to increase accuracy.

ACKNOWLEDGEMENTS

REFERENCES

1. Stauffer, J., "Creation of a Guide Star Catalog for the BASG CT-601 Star Tracker," Smithsonian Astrophysical Observatory, 1993.

2. Wertz, James R. (editor), "Spacecraft Attitude Determination and Control," D. Reidel Publishing Company, Dordrecht, Holland, 1978, pp. 259-262.

3. Haney, Mark A., "SkyGlobe 3.6," KlassM Software, Inc., Ann Arbot, Michigan, 1993.

4. Chen, J. Roger, "Proposed SWAS Star Field Selection Guidelines," K&D Research, Greenbelt, Maryland, September 1994.

5. Kleiner, S. C., "A Graphical Planning and Scheduling Toolkit for Astronomical Spacecraft," Smithsonian Astrophysical Observatory, 1994.

6. "SWAS ACS Flight Software Algorithm Document, Build 3, Revision L," NASA GSFC Special Payloads Division/Attitude Control and Stabilization Branch, Greenbelt, Maryland, January 1995.

7. Fink, D. and Shoup, D., "Application of Star Identification Using Pattern Matching to Space Ground Systems at GSFC," Flight Mechanics/Estimation Theory Symposium, Greenbelt, Maryland, May 1994 (NASA Conference Publication 3265), pp. 451-465.

ATTITUDE DETERMINATION USING AN ADAPTIVE
MULTIPLE MODEL FILTERING SCHEME

Quang M. Lam and Surendra N. Ray
Software Corporation of America
4601 Presidents Drive, Suite 350
Lanham, MD 20706

1.0 Background & Problem Identification

Attitude determination has been considered as a permanent topic of active research and perhaps remaining as a forever-lasting interest for spacecraft system designers. Its role is to provide a reference for controls such as pointing the directional antennas or solar panels, stabilizing the spacecraft or maneuvering the spacecraft to a new orbit. Least Square Estimation (LSE) technique was utilized to provide attitude determination for the Nimbus 6 and G. Despite its poor performance (estimation accuracy consideration), LSE was considered as an effective and practical approach to meet the urgent need and requirement back in the 70's. One reason for this poor performance associated with the LSE scheme is the lack of dynamic filtering or "compensation". In other words, the scheme is based totally on the measurements and no attempts were made to model the dynamic equations of motion of the spacecraft.

Another drawback of the LSE approach is the derivation of the variance matrix R (measurement noise covariance matrix). The LSE scheme employed by Nimbus 6 and G to compute the attitude determination literally "fix" the variance values of the roll and pitch components (per operating condition). For yaw and Digital Sun Aspect Sensor (DSAS) system components, even though they are "recursively" computed and updated on-line. They are derived from a "brute-force" approach rather than based on the "live" information or behaviors of the sensor reading (both DSAS and yaw attitude calculation from the Rate Measurement Package,RMP) to extract and update the measurement noise variances.

Other modern techniques applied to the attitude determination problem are the Kalman filtering or Extended Kalman filtering (EKF), H-infinity nonlinear estimation, or mixed H_2/H-infinity estimation. The Kalman filtering scheme is suitable for on-board attitude determination and for applications where constant tracking of a changing attitude is required. The technique is useful for on-board processing because it does not need to recycle through previously observed data and is frequently able to estimate the current state in real time. The Kalman filtering techniques (or H_2) is carried out with the assumption that the noise characteristics (process noise and measurement noise covariance matrices) are known (in the sense that the noise is either random with known statistical properties or has a fixed and known spectrum). In reality, the noise characteristics or statistics are unknown. Furthermore, there are additional error sources such as modeling error, truncation error (round-off), or linearization error which tend to degrade the performance of traditional Kalman filters. Truncation or round-off errors may be partially solved by using a Kalman filter variation, called a square-root filter, which substitutes the square root of the error covariance matrix for its full value in the filter gain equation. Another useful variation which is as numerically stable as the square root filter but which requires less computation is the UDU^T filter discussed by Bierman. To handle the noise variation uncertainties effects, adaptive filtering techniques have also been discussed and investigated to improve the performance accuracy of the Kalman filter.

2.0 Proposed Approach

We propose an adaptive filtering approach which employs a bank of Kalman filters to perform robust attitude estimation. The proposed approach, whose architecture is depicted in Figure 1, is essentially based on the latest proof on the interactive multiple model design framework to handle the unknown of the system noise characteristics or statistics. The concept fundamentally employs a bank of Kalman filter or submodel, instead of using fixed values for the system noise statistics for each submodel (per operating condition) as the traditional multiple model approach does, we use an on-line dynamic system noise identifier to "identify" the system noise level (statistics) and update the filter noise statistics using "live" information from the sensor model. The advanced noise identifier, whose architecture is depicted in Figure 2, is implemented using an advanced system identifier. To insure the robust performance for the proposed advanced system identifier, it is also further reinforced by a learning system which is implemented (in the outer loop) using neural networks to identify other unknown quantities such as spacecraft dynamics parameters, gyro biases, dynamic disturbances, or environment variations.
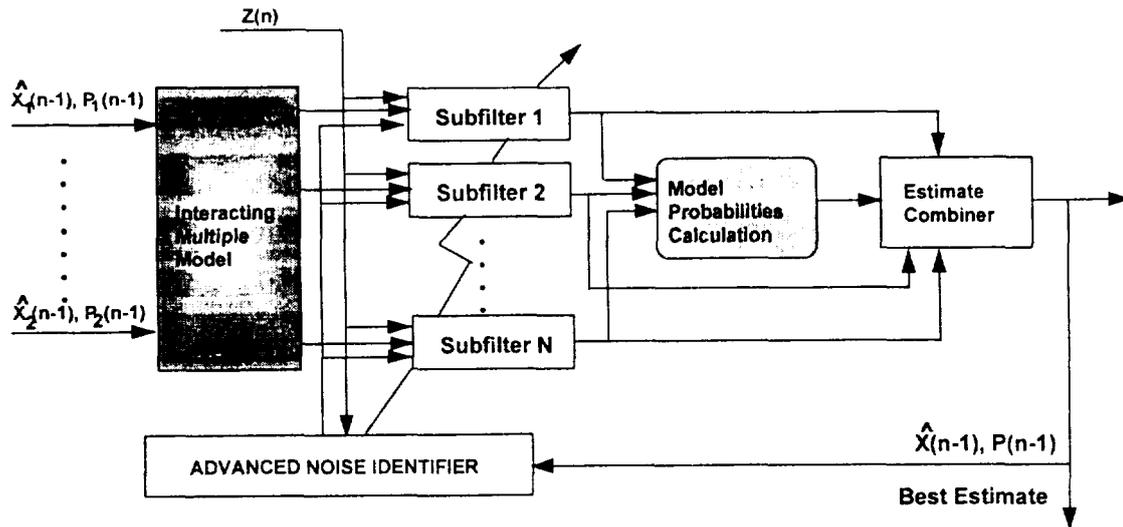
Figure 1: Attitude Determination Using Adaptive Multiple Model Filtering
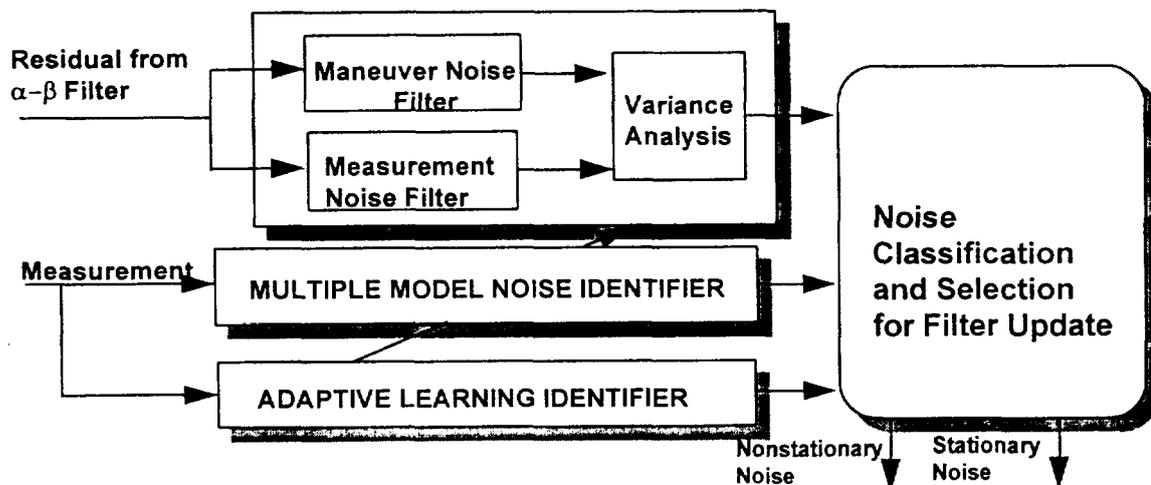
Figure 2: Architecture of Advanced Noise Identifier

The proposed noise identifier architecture will be implemented in such a way that it can handle all "noise spectrum" (e.g., stationary/nonstationary to white or color, etc.). The first two subsystems: a-b estimation scheme and interactive multiple model estimation scheme are strictly designed to handle noise identification while the third subsystem: Adaptive Learning Estimator is performing both noise and unknown parameter identification. The existence of the third subsystem is primarily intended for the performance improvement of the overall advanced system identifier.

References:

[1] F. L. Markley, N. Berman, U. Shaked, "Deterministic EKF-Like Estimator for Spacecraft Attitude Estimation," Proceedings of IEEE ACC, Baltimore, MD, June 1994

[7] J. T-H Lo, "Synthetic Approach to Optimal Filtering," Trans. on Neural Networks, Vol. 5, No. 5, Sep. 1994.

[8] Q. Lam et al, "Mass Property Identification: A Comparison Study Between Extended Kalman Filter and Neuro-Filter Approaches," Presented at the AIAA GN&C Conference, New Orleans, LA, August 1991.

[10] X. Li and Y. Bar-Shalom, "A Recursive Multiple Model Approach to Noise Identification," IEEE Trans. on Aerospace and Electronic Systems, Vol. 30, No. 3, July 1994

[13] J. R. Wertz, Spacecraft Attitude Determination and Control, Vol. 73, D. Reidel Publishing Co. 1978

[15] T. A. Chmielewski and P. R. Kalata, "Identification of Measurement and Maneuver Noise in a-b Target Tracking Systems," Proceedings of the IEEE ACC 1992.

OBSERVATIONAL MAGNETOMETER CALIBRATION WITH THE HUBBLE SPACE TELESCOPE'S NEW MAGNETOMETERS

Sidney M. Broude
AlliedSignal Technical Services Corporation

ABSTRACT

The two magnetometers recently replaced on the Hubble Space Telescope during the STS-61 Servicing Mission are now being used successfully for Coarse Attitude Determination during spacecraft vehicle safemode recovery operation. The magnetometer alignments relative to the spacecraft's vehicle's reference frame and the magnetic coupling of the sensors to the four magnetic torquer bars were determined. Coarse Attitude determination errors are now reduced to an average of 0.6 degrees.

Magnetometer Sensing System calibration and Coarse Attitude determination testing with the new calibration parameters is a geometrical problem. Telemetered earth magnetic field data was collected at twenty-six different vehicle attitudes. The spacecraft attitudes selected were distributed as widely apart as possible throughout the Geocentric Inertial Coordinate reference frame. It is also desirable to sample the Earth's magnetic field over as many different locations of the spacecraft's passage over the Earth as possible, within the limitation of the +/- 28.5 degree orbital inclination. A full range of magnetic moment outputs from the torquer bars needs to be sampled, +/- 3600 amp-meters squared, as well as data when the torquer bars have zero current. Graphic utilities were also developed to visually aid in optimizing the data collection process. Finally, a brief discussion of a method for collecting data for future calibrations is suggested.

1.0 INTRODUCTION

The Magnetic Sensing System (MSS) consists of the two magnetometers onboard the Hubble Space Telescope (HST). The changing Earth magnetic field vectors telemetered from the HST magnetometers during an HST orbit are used by the Payload Applications Support Software Operations (PASSOPS) Group to compute coarse attitudes. The attitude determination software uses the QUEST algorithm, which is described in Reference 1. In order to successfully calibrate the scale factor alignment matrices and biases of each magnetometer relative to the HST vehicle axes, it is necessary to account for the magnetic field from the four magnetic torquer bars onboard HST, which are used in vehicle momentum management. To perform accurate Coarse Attitude determinations the magnetometers need to be calibrated.

The intent of this paper is to focus on the MSS data collection aspects, the computation of the calibration parameters for the HST magnetometers and torquers, and the verification of the

MSS calibration results with computed coarse attitudes. Based on this experience a new method for acquiring data for the full MSS calibration is suggested.

2.0   CALIBRATION ALGORITHM

The MSS calibration algorithm is described below. The calibration will provide estimates of the misalignments for both magnetometers with respect to the HST vehicle axes, magnetometer biases, and the coupling matrix to the magnetic torquers. The software to perform the MSS calibration was developed by Computer Sciences Corporation as part of the HST PASS system. The inputs to the MSS calibration program include HST ephemeris data, a geomagnetic field model, MSS sensed magnetic field, fine attitude solutions, telemetered magnetic dipole moments from the four torquers bars, and database MSS calibration parameters. Nominally, the duration of the each record is set to be one minute to ensure that at least one telemetry update from each magnetometer and torquer rod is included in the prepared data record.

A standard Least Squares method is used to obtain the calibration parameters. The loss function is minimized with respect to the residual bias parameters. The residual bias parameters that are determined from minimizing the Loss Function are [S], [T], and b, which are defined below. The form of the matrix [T] is based on the far field approximation of a single dipole centered in the HST vehicle reference frame.

LOSS = SUM(i=1 to N) a(i)*|H(i) - b - [S]*B(i) - [T]*D(i)|**2
FUNCTION

where

N   = number of valid MSS observations

a(i) = normalized weight for the ith observation
     = 1/(|H(i)|**2 + a'**2)*Sum(j=1 to N)(|H(j)|**2 + a'**2)

H(i) = geomagnetic field measurement error
     = B(i) - [A]*B0(i)

[A] = Fine Attitude (Computed by FINATT PASS application)

B0(i) = geomagnetic field (gauss) in
         Geocentric Inertial Coordinates (GCI)

B(i) = magnetic field as measured by the MSS in the HST
         vehicle reference frame and converted for Magnetic
         Torquer Electronics (MTE) bias and offset bias (gauss)

a' =   user-specified weight

b =   offset bias (gauss)

[S]   =   misalignment bias matrix

[T]   =   bias in magnetic torquer coupling matrix (gauss per
            ampere-meter squared)
D(i)   =   3-by-1 magnetic moment vector in the HST vehicle
            reference frame (ampere-meters squared)

3.0 ORBITAL VERIFICATION CALIBRATION

Shortly after HST was launched in April 1990, magnetometer bias offsets were computed for each magnetometer. One orbit's worth of data, 96 minutes, is sufficient for the bias determination. The Coarse Attitude Determination Software includes the option for computing each magnetometer offset bias according to the attitude independent algorithm described in Ref. 2. The MSS calibration software (MSSCAL) also computes each magnetometer's offset bias together with each magnetometer's scale factor and alignment matrix. The magnetometer offset bias computation cannot be done separately from the magnetometer scale factor alignment matrice determination when MSSCAL is run. On option the MSSCAL software user may update each MTE coupling matrix.

In order to achieve an accurate alignment determination, magnetic field data needs to be gathered at HST pointing attitudes distributed as much as possible over the celestial sphere to achieve a good distribution of magnetic field components along each vehicle axis. Typically 25 spacecraft attitude pointings spread over the 4 pi steradians are used. Special attention is also needed to sample the full torquer range of +/- 3600 amp-meters**2. These special data requirements are met in time as HST maneuvers around the celestial sphere while conducting normal science operations. MSSCAL was not used successfully during orbital verification (OV) because of a lack of sufficiently well distributed data. During OV spacecraft pointings were generally confined to the vehicle safemode attitudes, - V1, or + V3 sunpoint, or to star clusters selected for calibration of the three Fine Guidance Sensors.It took a year before the first successful full magnetometer calibration was completed.

Table 1 lists examples of the accuracies for Coarse Attitude determinations with the two HST magnetometers after calibration of the offset biases with the attitude independent algorithm from Reference 2, but before the full calibration was performed. Approximately twenty minutes of MSS data is used for each Coarse Attitude determination. These intervals were specifically selected in order in include the higher range of magnetic moment outputs from the torquer bars experienced during HST vehicle momentum management, (+/- 3600 amp-meters**2).

Each Coarse Attitude error listed in Table 1 refers to the Root Sum Square (RSS) of the HST vehicle axis errors. A Fine Attitude, which is accurate to better than 7 arcseconds, was computed, using a combination of HST Fixed Head Star Trackers' (FHST) observations, and/or Fine Guidance Sensors, to be used as reference against which the Coarse Attitude accuracy was meas-

ured.   The RSS attitude error is derived from the   fourth
component of the quaternion which represents the angle between
the Coarse and Fine Attitude quaternions.   These attitude errors
were well above the required accuracy of 5 degrees (2 sigma),
especially during periods of high torquer bar output.

Figure 1 shows the magnetic moment output from the 4 HST
torquer rods over approximately one HST orbit at a pointing
attitude of Right Ascension (RA), 83.7 degrees, Declination
(DEC), 72.1 degrees, and Roll, 272 degrees.   Up to two HST or-
bits, approximately three hours of magnetic moments from each
torquer bar can be retained on the run time graphic display.   By
using this tool one is able to select an optimal time period with
the maximum range of magnetic moments for a given HST attitude
pointing when doing the full MSS calibration data preparation
with the PASSOPS FINATT software.
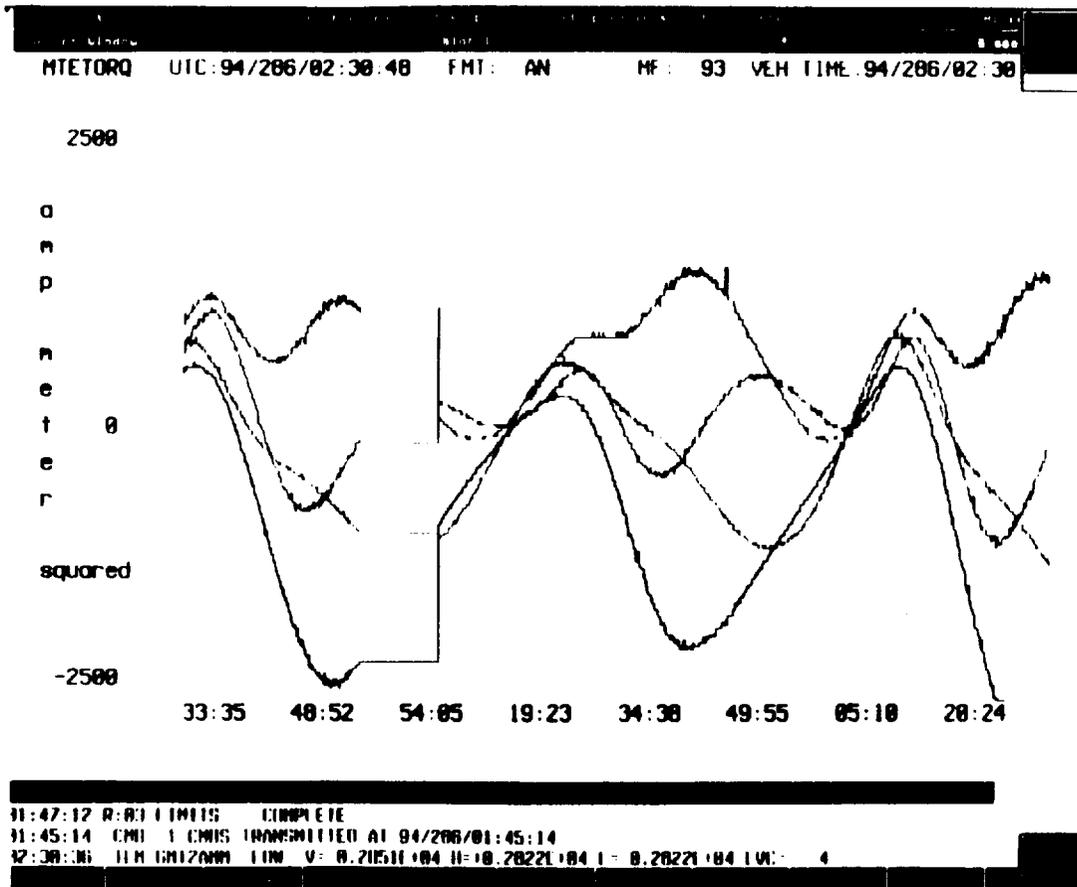
Figure 1: Magnetic Torques From the 4 HST Torquer Rods

Table 1: HST COARSE ATTITUDE ACCURACY USING TWO MAGNETOMETER SENSORS DURING PERIODS OF HIGH MAGNETIC TORQUER CURRENTS
(Calibrated Biases, Uncalibrated Scale/Alignment, and Torquer Coupling)

Time Period (Year.Day of Year/Universal Time)	Coarse Attitude Error (RSS) (Degrees)
1) 1991.009/03:51-04:09	4.0
2) 1991.010/03:54-04:12	5.0
3) 1991.011/04:02-04:15	7.4
4) 1991.016/05:24-05:42	9.9
5) 1991.021/03:06-03:31	8.9
6) 1991.025/00:55-01:12	18.0
7) 1991.136/00:01-00:18	16.3
8) 1991.197/13:45-14:03	26.3
9) 1991.206/05:16-05:33	7.3
10) 1991.208/04:01-04:24	8.2

4.0 POST ORBITAL VERIFICATION CALIBRATION

The first Full MSS calibration was completed by July 1991 - Reference 3. With the MSS parameters derived in July 1991 for initialization, the full calibration was redone and completed by April 1992 - Reference 4. Coarse Attitude determinations using the updated April 1992 MSS calibration had errors less than the five degree two sigma requirement. A slight improvement in Coarse Attitude determination was noted (Reference 5) in June 1992 when the MSS calibration with the April 1992 data set was redone with weight specified as the standard deviation of the residuals from the calibration Loss function.

5.0 FIRST SERVICING MISSION CALIBRATION

After the First HST Servicing Mission (FSM), the MSS calibration had to be redone because the HST magnetometers were replaced. The process was completed in three months without impacting HST science operations or other vehicle checkout activities by using serendipitous data collection. The December 1993 calibration data span lasted three weeks; and the verification data span was completed after one month. The verification data span lasted slightly longer than the calibration data span in order to avoid using any of the HST pointing attitudes used in the calibration.

Figure 2 shows the HST vehicle attitude pointings selected for acquiring MSS calibration data, and the pointings used to compute Coarse Attitudes to verify the new calibration parameters. The large data gap in Figure 2 coincides with the solar constraint zone during the December 1993 MSS calibration data collection.
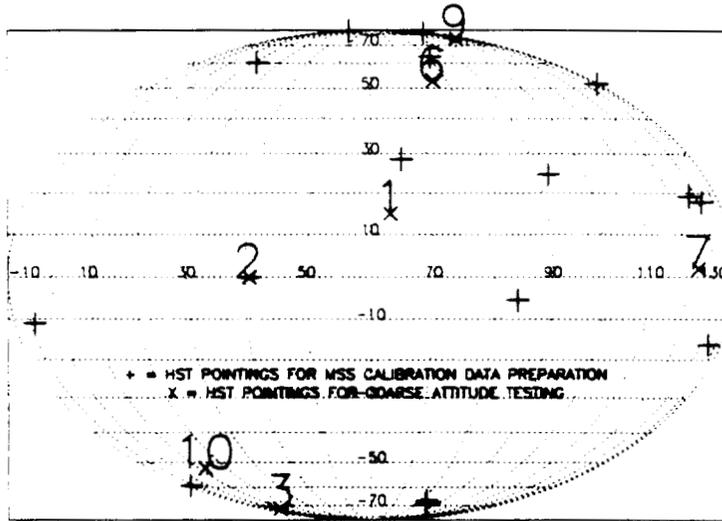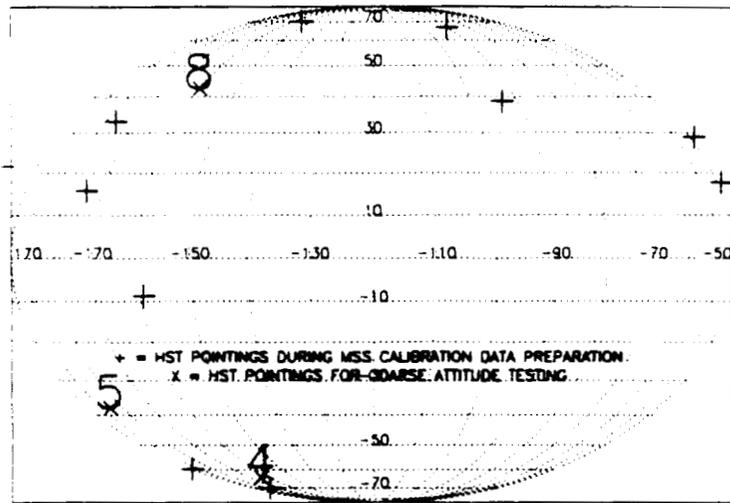
Figure 2: HST Pointings for MSS Calibration
(December 1993 MSS Calibration)

Typically at least 10 HST vehicle attitude pointings are selected to verify the new MSS calibration parameters record.

Table 2 lists the Fine Attitude pointings illustrated in Figure 2. The time noted is the midpoint of a five minute interval. The magnetic moment range occurs during the twenty minute time period that Coarse Attitude determination was performed to verify the calibration. Spacecraft passage through the South Atlantic Anomaly (SAA) is noted if it occurred during the twenty minute interval. The relevance of HST passage through the SAA will be examined latter in this section.

Table 3 lists the angular deviation between the Coarse and Fine Attitude quaternion for each of the test case attitudes numbered in Figure 2. Coarse Sun Sensor (CSS) observations were sometimes included as part of the study to test the effect on the

120

Coarse Attitude determination. The best result for Coarse Attitude determination test cases using the new MSS calibration record shows an average angular deviation of 0.6 degrees, with a standard deviation on 0.4 degrees. This result is highlighted at the bottom of Table 3. A Column Header Explanation for Table 3 is appended.

Figure 3 graphically represents the results in Table 3.

Table 2: HST Pointings Used to Test the December 1993 MSS Calibration of Scale, Alignment, Bias and Torquer Coupling

Test Attitude Number	Universal Time	Fine Attitude (RA,DEC,ROLL) (Degrees)			Magnetic Moment Range (Amp-meters**2)			SAA?
1) 94.002	08:27:30	63.2178	14.9311	110.0644	-116	to	1597	Yes
2) 94.010	02:52:32	40.7245	- 0.0749	105.6122	-2234	to	2064	Yes
3) 94.011	04:40:30	6.1297	-72.1848	81.3741	-2130	to	1538	Yes
4) 94.013	11:09:30	195.9780	-63.7722	252.4438	-831	to	1864	No
5) 94.016	16:42:30	174.7786	-37.8259	232.4462	-1221	to	3241	No
6) 94.028	05:44:30	76.1742	52.7765	71.9177	-1261	to	2411	No
7) 94.033	14:07:30	123.8483	1.9098	141.8252	-1854	to	1195	No
8) 94.036	12:55:30	200.3389	42.5863	293.4895	-2949	to	1366	No
9) 94.013	16:11:30	122.7403	74.9519	14.9680	-747	to	1036	No
10) 94.014	03:22:30	12.5868	-52.2190	93.6173	-2320	to	889	Yes

Table 3: RSS Coarse Attitude Residuals (Degrees) From Fine Attitudes At Test Attitudes (1-10) using the FSM MSS Calibration

Nominal (CSS)	Nominal	New MSS (CSS)	New MSS [(WT=.003)]	New MSS (CSS)	New MSS (Align) (+ Bias)	New MSS (Align+Bias) (Wt1=.003) (Wt2=.004)
1) 0.60	0.94	0.61	0.76	0.63	0.89	0.91
2) 1.11	0.26	0.93	0.38	1.00	0.30	0.41
3) 1.56	1.40	1.60	1.30	1.55	1.28	1.32
4) 0.44	0.41	0.15	0.12	0.09	0.20	0.08
5) 0.68	0.93	0.57	0.67	0.52	0.76	0.78
6) 0.90	0.54	0.92	0.43	0.93	0.29	0.41
7) 0.90	0.91	0.48	0.36	0.35	0.73	0.48
8) 0.50	0.66	0.38	0.13	0.48	0.53	0.49
9)	0.62		0.62		0.58	0.74
10)	1.32		1.18		1.07	1.00
Mean RSS Angular Deviation and Standard Deviation by Column						
Mean RSS 0.84	0.79	0.70	**0.60**	0.69	0.66	0.66
RMS 0.37	0.37	0.45	**0.40**	0.45	0.35	0.36

Table 3 Column Header Explanations

a) Nominal — The currently operational (pre FSM) MSS mag-
   (CSS)   netometer alignment, Bias, and Magnetic Torquer
                scaling/alignment matrice are used to compute
                the Coarse Attitude pointings of HST. HST
                Coarse Sun Sensor observations are included.

b) Nominal — Same as Nominal (CSS), but no CSS observations

c) New MSS — The December 1993 MSS calibration parameters are
   (CSS)   used to compute Coarse Attitudes.

d) New MSS — A user specified data weighting factor, a', from
      (CSS)   Section 2.1, was used when calibrating both MSS 1
   (WT= 0.003) and 2.

e) New MSS — Same as d), except no CSS observations are in-
   (WT= 0.003) include in Coarse Attitude determination

f) MSS   — A new MSS alignment and bias determination was
   (Align + Bias) computed with post FSM data. The magnetic tor-
                quer coupling is not recalibrated.

h) MSS   Same as MSS (Align + Bias), except MSS 1 and 2
   (Align + Bias) had different values for a' when the calibration
    (WT1 = 0.003) was performed for each sensor.
    (WT2 = 0.004)
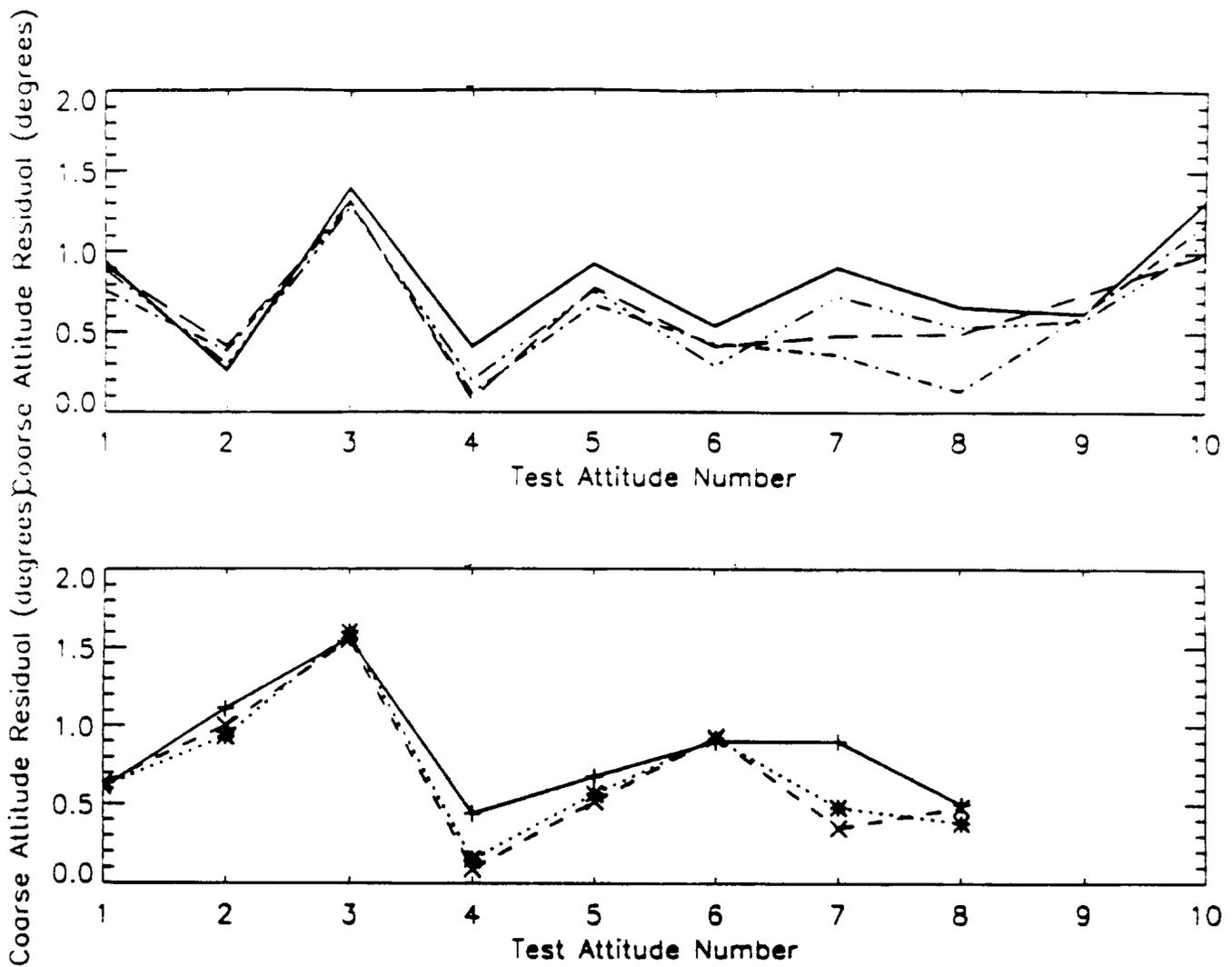
TYPE OF MSS CALIBRATION USED TO COMPUTE COARSE ATTITUDE	SYMBOL/LINESTYLE

PLOT I

b)	NOMINAL	Solid	–
f)	NEW MSS (WT= .003)	Dash dot	– .
g)	MSS (ALIGN + BIAS)	Dash dot dot	– . .
h)	MSS (ALIGN + BIAS) (WT1=.003, WT2=.004)	Long dashes	__ __ __

PLOT II

a)	NOMINAL (CSS)	+
c)	NEW MSS (CSS)	▾
e)	NEW MSS (CSS, WT= .003)	X

**Figure 3: Coarse Attitude Angular Deviation (RSS) vs. Attitude #
(December 1993 MSS Calibration)**

In Figure 3 HST pointing attitudes 1, 2, 3, and 10 occurred while HST was passing through the SAA region. Attitude pointings numbered 1, 3, and 10 showed Coarse Attitude angular deviations from the Fine Attitudes to be slightly greater than 0.6 degrees. The RSS deviation of the Coarse Attitudes versus the Fine Attitudes averaged 0.6 degrees over all of the HST pointings in the test sample of cases when the new MSS calibration parameters (December 1993) were used for input - Table 3 . In general the IGRF coefficients are supposed to be suitable for the magnetic field modeling in the SAA regions. Whether this becomes a problem or not in a future calibration attempt to slightly improve the accuracy of the MSS calibration parameters will have to be investigated further.

6.0 1990 INTERNATIONAL GEOMAGNETIC REFERENCE FIELD (IGRF) COEFFICIENTS AND UPDATES

In September of 1994 the MSS calibration software was updated to use a more current set of International Geomagnetic Reference Field (IGRF) coefficients - referenced to 1990. The previous IGRF coefficients available in the operational database were referenced to 1985. No information is currently available that quantifies what changes could be expected in the MSS calibration accuracies when changing over from the 1985 to the 1990 earth magnetic field model. All of the calibrations performed up to March 1994 used the 1985 IGRF coefficients. All of the accuracy requirements initially allocated for the HST Magnetic Sensing System sensors prior to HST launch were met following the HST First Servicing Mission MSS recalibration effort beginning in December 1993. A new MSS calibration may be undertaken in 1996 if 1995 IGRF coefficients become available then.

7.0 FUTURE ENHANCEMENTS

Redo MSS calibration with a 4 dipole model for the MTE based on the true locations of each torquer bar.

Redo the calibration as soon as the most current IGRF coefficients become available.

If the calibration is redone, it would be desirable to extend the data collection over one year to bridge gaps in HST pointings due to the sun's position on the celestial sphere.

Create a graphic utility to view the HST locations over the earth where the geomagnetic field is being sampled. Currently this done by hand calculation.

A method for acquiring MSS calibration data involves the use of the large scale maneuvers performed to calibrate the scale factor and alignment matrices of the HST Rate Gyro Assembly. FINATT is capable of computing attitudes during HST vehicle maneuvers. Beside the initial inaccuracies inherent in

spacecraft attitude determination due to the uncalibrated Fixed Head Star Tracker (FHST) alignments the star position uncertainty would be affected by a star position signal lag of 75 milliseconds - Ref. 6, Section 3.3.6.4. For a typical spacecraft maneuver rate of 6 degrees per minute the star position signal lag would introduce an offset inaccuracy of 27 arcseconds. Special arrangements and bright object avoidance planning would have to be made with the HST Pointing and Control Systems Engineers for permission to leave on the Fixed Head Star trackers running in MAP mode during the maneuver. A typical 6 degrees per minute vehicle maneuver should present no problems for a FHST's ability to lock a moving object and perform the usual dwell measurement for 20 seconds while the sensor is in map mode. A copious amount of data is currently available that shows the FHSTs locking onto moving targets, for example satellites, while operating in mapping mode and showing position displacements of 2-3 degrees over the 20 second tracking dwell time, - Figure 5. Magnetic moments from the torquers increase dramatically just prior to vehicle maneuver. Such a quick calibration capability for MSS scale, alignment, bias, and torquer coupling would have been especially helpful during the orbital verification deployment of HST and immediately thereafter. The large amount of time available prior to the launch of HST may have allowed for the development of a strategy to collect FHST data and avoid bright light occultation zones.
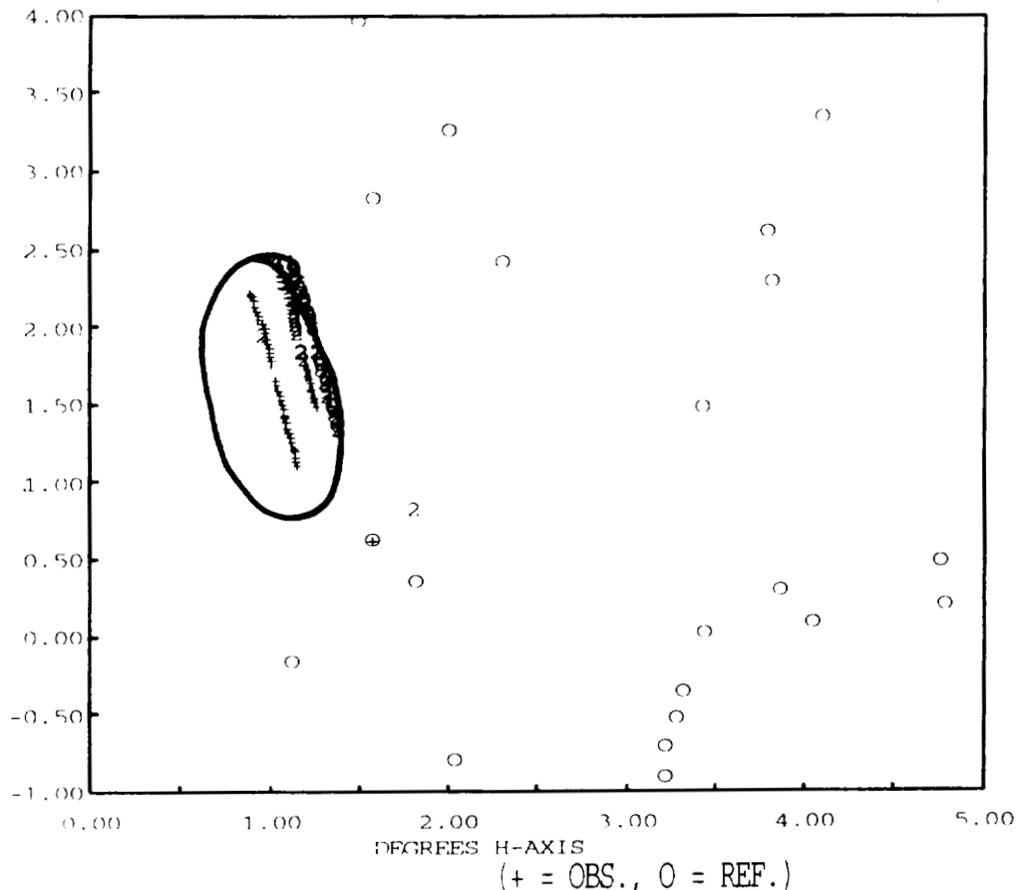

Figure 5: STS-61 observed in FHST-1 (1993.344 14:56:20 -14:57:30)

125

8.0 REFERENCES

1. Shuster, M.D. and Oh, S.D., "Three-Axis Attitude Determination from Vector Observations", Journal of Guidance and Control, Vol. 4, Jan.-Feb. 1981.

2. Davenport, P.B., Rumpl, W.M., and Welter, G.L., "In-Flight Determination of Spacecraft Magnetic Bias Independent of Attitude", GSFC Flight Mechanics/Estimation Theory Symposium, May 1988.

3. Testing a New HST Magnetometer and Torquer Alignment and MSS Bias Calibration, Memo to Jan Hodges, BFEC, Code 519.1, GSFC 7-30-91

4. Testing a New HST Magnetometer and Torquer Scale/Alignment and MSS Bias Calibration in 1992, Memo to Jan Hodges, BFEC, Code 519.1, GSFC, 4-27-92

5. Testing a New HST Magnetometer and Torquer Scale/Alignment and MSS Bias Calibration Computed with User Specified Weights, Memo to Jan Hodges, BFEC, Code 519.1, GSFC, 6-17-92

6. HST Design Characteristics Definitions Document, SMO 1030, Baseline Issue, 16 Jan 84, George C. Marshall Space Flight Center

9.0 ACKNOWLEDGEMENTS:

An Automated Method of Tuning an Attitude Estimator

by

Paul A.C. Mason[t] and D. Joseph Mook[tt]

Abstract

Attitude determination is a major element of the operation and maintenance of a spacecraft. There are several existing methods of determining the attitude of a spacecraft. One of the most commonly used methods utilizes the Kalman filter to estimate the attitude of the spacecraft.

Given an accurate model of a system and adequate observations, a Kalman filter can produce accurate estimates of the attitude. If the system model, filter parameters, or observations are inaccurate, the attitude estimates may be degraded. Therefore, it is advantageous to develop a method of automatically tuning the Kalman filter to produce the accurate estimates.

In this paper, a three-axis attitude determination Kalman filter, which uses only magnetometer measurements, is developed and tested using real data. The appropriate filter parameters are found via the Process Noise Covariance Estimator (PNCE). The PNCE provides an optimal criterion for determining the best filter parameters.

Introduction

The development of light-weight, low-cost spacecrafts that can accomplish complex tasks is essential to the success of many NASA missions (such as Mission to Planet Earth) as well as the success of many commercial missions. One way to ensure a light-weight, low-cost spacecraft is to place constraints on the amount of computer hardware. This constraint demands the use of computationally efficient algorithms that do not require a significant amount of CPU. Consequently, reducing the amount of required hardware improves the performance of the spacecraft and increases the probability of a success.

One of the many functions of a satellite is the gathering and processing of information. In most cases, this information is transmitted to a specified location. To successfully complete this objective, the orientation of the spacecraft must be known and controlled very precisely. In the past decade, there has been a significant amount of work in the area of attitude determination and attitude control [1-5]. During this period of time, attitude determination algorithms that utilize a combination of the measurements and a mathematical model to estimate the orientation of the spacecraft [6-7] were the most popular. One of the most commonly used and most robust estimators in attitude determination is the Kalman filter. The complexity of this estimator ranges from attitude-only estimator using a QUEST model to an extended Kalman filter with 36 states [8].

Attitude estimators like the Kalman filter are more robust than single-frame methods, such as TRIAD [2], QUEST [4], and FOAM [3]. For example, during periods of near coalignment (the pitch angle is nearly unobservable) or during an eclipse, a sequential estimator, such as the Kalman filter, can provide state estimates by propagating the states with the nominal model. Single-frame methods that rely on measurements can only produce anomalous estimates of the attitude. These estimates may endanger the success of the mission.

The most difficult filter parameter to determine in the Kalman filter is the process noise covariance, Q. In theory, the process noise is defined as a gaussian process. In real-world applications, the model error can be stochastic, deterministic, or a combination of both. Since the attitude determination problem is very nonlinear, there is a larger possibility for errors in the system model. These errors, along with any stochastic errors, are referred to as modeling errors. As the percentage of non-gaussian modeling errors increases, so does the difficulty in determining an appropriate process noise covariance. Therefore, it is beneficial to develop an algorithm that produces the filter parameters which yield accurate state estimates. In this paper, the PNCE, an algorithm that determines the appropriate filter parameters, is applied to attitude determination. This method provides an automated method of tuning the estimator to obtain reasonable state

---

[t] Graduate Research Assistant at the SUNY Buffalo. Currently an Assistant Professor in the Mechanical Engineering Dept. at the University of Florida.
[tt] Associated Professor at SUNY Buffalo

estimates without prior knowledge of the process noise covariance. The PNCE allows for the implementation of Kalman filter type algorithms in real-world applications where the true or the appropriate process noise covariance is not known.

If a spacecraft has rate sensing capability, then the attitude estimation is generally improved over non-rate sensing capable spacecraft. When this capability is not available, the attitude estimation can be improved by estimating the rates based on a model of the spacecraft rotational dynamics. The Solar Anomalous and Magnetospheric Particle Explorer (SAMPEX) [9] and Earth Radiation Budget Satellite (ERBS) [10] are two such spacecraft that do not have rate sensing capabilities. In the case of SAMPEX and ERBS, accurate attitude estimates are ensured by estimating the rates that are based on simple rotational dynamic models along with the attitude. These rotational models improve the overall estimation of the attitude. However, there is no general model for rotational dynamics.

In 1990, Chu and Harvey showed that models of the rotational dynamics could be identified [10-11] and that these models improved the overall estimation of the attitudes. However, obtaining these models can be time-consuming, and the models are only valid for the identified orbit. In 1993, Mook [12-13] described a numerical procedure of finding the appropriate dynamic model of the rates. This procedure can produce models that are valid over a duration longer than the orbit used in the identification. Consequently, this method can be used in prediction. This method is new and has not been applied to many spacecraft. Hence, there is still a need for a simple general model of the rotational dynamics.

To circumvent this problem of not having an accurate dynamic model, a commonly used gyro bias model, based on a Markov process, is used in place of complicated, difficult to obtain rotational dynamic models. This type of simple bias model has been successfully used in the Real-Time Sequential Filter (RTSF) [9]. RTSF uses the gyro bias model along with the basic theory of attitude determination to produce accurate attitude estimates. The accuracy of the estimates from RTSF are dependent on certain filter parameters. In many applications, the RTSF may require a manual tuning. The complexity of this task is a function of the known and unknown dynamics of a spacecraft.

The rest of this paper is divided into three parts Theory, Results, and Conclusion. The theory section reviews the formulation of the attitude estimator and the PNCE. The result section starts with a definition of the problem and the given filter parameters. Next, these parameters are used along with the PNCE to obtain accurate attitude estimates. The conclusion section summarizes the results and states a few observations.

Theory

With few exceptions, the dynamics of a spacecraft can be described in terms of classic mechanics. The dynamics of a spacecraft are a function of its orbit and attitude. In this work, only the dynamics associated with the attitude are addressed. The first step in this analysis is the definition of the attitude.

Attitude Determination: Definition

The attitude of a spacecraft is defined as its orientation. Attitude determination is the process of computing the orientation of the spacecraft relative to either an inertial reference or some object of interest, such as the earth. The attitude determination problem can be stated as: "Given measurements of angles or changes in angles with respect to the spacecraft and a reference, determine the orientation of the spacecraft."

Attitude measurements are produced by sensor such as Fine Sun Sensors (FSS), Three Axis Magnetometers (TAM) sensor, Horizon sensors, Star Trackers, etc. FSS and TAM measurements are used by algorithms like TRIAD [2], QUEST [4], FOAM [3], and the Kalman filter [5,14] to determine the orientation of the spacecraft. The accuracy of the attitude is a function of the sensors and the attitude determination algorithm. Attitude estimators use a combination of several attitude sensor measurements, which are usually associated with the three-axis attitude, to improve the reliability and accuracy of the algorithm.

Three-axis attitude is most conveniently thought of as a coordinate transformation from a reference axis in inertial space to an axis on the spacecraft. For a rigid body, or assumed rigid body spacecraft, the direction of cosine matrix or attitude matrix, A, represents the coordinate transformation that maps vectors from the reference frame to the body frame. This transformation can be described as

$$e_{body} = A e_{ref} \qquad (1)$$

128

where e_{body} and e_{ref} have components resolved along the body and reference axes, respectively. The attitude matrix consists of three orthogonal, right-handed triads $\hat{u}$, $\hat{v}$, $\hat{w}$ unit vectors fixed in the body, such that

$$\hat{u} \times \hat{v} = \hat{w} \qquad (2)$$

Hence, if one can specify the components of $\hat{u}$, $\hat{v}$, and $\hat{w}$ along the three axes of the coordinate frame, then the orientation can be determined completely.

The attitude matrix is a real orthogonal matrix that has many different orientation parameterizations. The type of parameterization used is dependent on the application. A commonly used parameterization is the Euler parameterization (Euler angles). On of the benefits of using this type of parameterization is that the Euler angles have some physical significance Another type of parameterizations is the quaternions parameterization, which is also known as the Euler symmetric parameterization.

Quaternion Parameterization

The term quaternion, which is sometimes referred to as Euler symmetric parameters, was first used by Hamilton [15] in 1843.

Many authors [16-20] have discussed the use of this four-parameter representation of the attitude. The advantage of using quaternions over Euler angles is that quaternions are not singular, unlike Euler angles. Because of its advantage, today, most attitude estimators utilize quaternion attitude representation instead of Euler angles. Quaternions are also easier to work with. However, the quaternions representation is not unique. This characteristic is discussed later in the text. The quaternions are defined by three primary parameters and an auxiliary parameter

$$\begin{bmatrix} q_1 & q_1 & q_1 \end{bmatrix} = \bar{e}\sin\left(\tfrac{\Phi}{2}\right)$$
$$q_4 = \cos\left(\tfrac{\Phi}{2}\right) \qquad (3)$$

where:
  $\bar{e}$ is a unit vector corresponding to the axis or rotation
  Φ is the angle of rotation
The quaternion parameterization is nonsingular because the quaternions are not independent. The quaternions are related by the following normalization constraint

$$q_1^2 + q_2^2 + q_3^2 + q_4^2 = 1 \qquad (4)$$

Quaternions can be defined in terms of the attitude matrix or the Euler angles. The reverse is also true, that the attitude matrix can be expressed in terms of the quaternions

$$A(q) = \begin{bmatrix} q_1^2 - q_2^2 - q_3^2 + q_4^2 & 2(q_1q_2 + q_3q_4) & 2(q_1q_3 - q_2q_4) \\ 2(q_1q_2 - q_3q_4) & -q_1^2 + q_2^2 - q_3^2 + q_4^2 & 2(q_2q_3 + q_1q_4) \\ 2(q_1q_3 + q_2q_4) & 2(q_2q_3 - q_1q_4) & -q_1^2 - q_2^2 + q_3^2 + q_4^2 \end{bmatrix} \qquad (5)$$

$$A(q) = \left(q_4^2 - \mathbf{q}^2\right)\mathbf{1} + 2\mathbf{q}\mathbf{q}^T - 2q_4 Q \qquad (6)$$

Being able to represent the attitude matrix as an algebraic function of the quaternions is another computational advantage of the quaternion representation. Now that the quaternions representation and the attitude matrix have been defined, the kinematics of the orientations and dynamic equations of motion can be addressed.

Kinematics and Dynamic equations of motion

Kinematics is the study of the orientation of the object rotating (with its body axis fixed on the body of the object) relative to some global frame of reference, which results in equations of motion of the orientation. These equations of motion are independent of the forces associated with the particular problem.

As defined in the literature, the kinematics relation for the orientation is

$$\dot{q} = \tfrac{1}{2}\Omega(w)q \qquad (7)$$

where the expression Ω of a variable α can be represented as

$$\Omega(\alpha) = \begin{bmatrix} -[\alpha \times] & \alpha \\ -\alpha^T & 0 \end{bmatrix}$$

$$[\alpha \times] = \begin{bmatrix} 0 & -\alpha_3 & \alpha_2 \\ \alpha_3 & 0 & -\alpha_1 \\ -\alpha_2 & \alpha_1 & 0 \end{bmatrix}$$

If α is defined as

$$\bar{\alpha} == \begin{bmatrix} \alpha_1 & \alpha_2 & \alpha_3 & 0 \end{bmatrix}^T$$

then $\Omega(\alpha)\theta = \theta \otimes \alpha$, where quaternion multiplication, $q_{v1} \otimes q_{v2}$, is defined as

$$q_{v1} \otimes q_{v2} = \begin{bmatrix} r_1 \\ p_1 \end{bmatrix} \otimes \begin{bmatrix} r_2 \\ p_2 \end{bmatrix} = \begin{bmatrix} r_1 \times r_2 + p_1 r_2 + p_2 r_1 \\ p_1 p_2 - r_1 \cdot r_2 \end{bmatrix} \qquad (8)$$

129

The attitude dynamic equations of motion, relating the time derivative of the angular momentum and the applied torque, is

$$\frac{dL}{dt} = N - w \times L = I\frac{dw}{dt} \qquad (9)$$

where N is the torque vector

$$N = \sum_{i=1}^{n} r_i \times F_i \qquad (10)$$

F is an external force. A spacecraft equipped with reaction or momentum wheels is not considered a rigid body. Therefore, the attitude dynamics equation must be modified

$$\frac{dL}{dt} = N - \left[I^{-1}(L - h) \right] xL = I\frac{dw}{dt} \qquad (11)$$

The body angular rates associated with this system are defined as

$$w = I^{-1}(L - h) \qquad (12)$$

The difference between the true quaternion and the estimated quaternion is

$$\hat{q} = q_{true} \otimes \delta q \qquad (13)$$

where $\hat{q}$ is the estimated quaternion and δq is the difference between the estimated and actual quaternion. Substituting this into the dynamic equation for the estimate (7) yields

$$\frac{d}{dt}\left(q_{true} \otimes \delta q \right) = \tfrac{1}{2}\Omega(\hat{w})\left(q_{true} \otimes \delta q \right)$$

$$\tfrac{1}{2} q_{true} \otimes w_{true} \otimes \delta q + q_{true} \otimes \frac{d\delta q}{dt} = \tfrac{1}{2} q_{true} \otimes \delta q \otimes \hat{w}$$

$$2\frac{d\delta q}{dt} = \delta q \otimes \hat{w} - w_{true} \otimes \delta q \qquad (14)$$

Note, δq is unique because it is defined as

$$\delta q = \begin{bmatrix} \alpha & 1 \end{bmatrix}^T \qquad (15)$$

Propagation equations

In this section, the estimation algorithm is formulated using the same filter formulation presented as Mook [12-13]. This formulation is mathematically rigorous and produces accurate estimates.

The propagation equations are based on the equations of motion. The seventh order state vector for this filter is

$$x(t) = \begin{bmatrix} \bar{q}(t) \\ L(t) \end{bmatrix} \qquad (16)$$

The dynamic equations are

$$\dot{q} = \tfrac{1}{2}\Omega(\hat{w})q \qquad (17)$$

$$\frac{dL}{dt} = N - \left[I^{-1}(L - h) \right] xL = I\frac{d\hat{w}}{dt} \qquad (18)$$

where the body angular are

$$\hat{w} = I^{-1}(L - h) \qquad (19)$$

N is defined by equation (10). The state space representation is

$$\frac{dX}{dt} = \begin{bmatrix} \tfrac{1}{2}\Omega(\hat{w}) & 0_{4\times3} \\ 0_{3\times4} & [\hat{w}\times] \end{bmatrix} \hat{X} + \begin{bmatrix} 0_{4\times1} \\ I_{3\times3} \end{bmatrix} N \qquad (20)$$

$$\frac{dX}{dt} \equiv f(w)X + BN \qquad (21)$$

For nonlinear systems, the error analysis is based on a linearization of the system. Defining $F \equiv \dfrac{\partial f}{\partial X}$, the error covariance can be written as

$$\frac{dP}{dt} = FP + PF^T + Q \qquad (22)$$

Update equations

The update equations for this filter formulation are the same as in the RTSF [21] formulation

$$y = \begin{bmatrix} \hat{V}_B \times \end{bmatrix} \alpha(-) + \Delta V_B \qquad (23)$$

The sensitivity matrix H can be defined as

$$H = \begin{bmatrix} [\hat{V}_B \times] & 0_{3\times3} \end{bmatrix} \qquad (24)$$

Consequently, y is linearly related to the state error

$$y = Hx(-) + \Delta V_B \qquad (25)$$

The update equations are

$$\begin{bmatrix} \alpha^{\bullet} \\ \delta L \end{bmatrix} = \Delta x = Ky \qquad (26)$$

$$\delta q = \begin{bmatrix} \alpha^{\bullet} \\ 1 \end{bmatrix} \qquad (27)$$

130

$$q^+ = q^- \otimes \delta q$$
$$L^+ = L^- + \delta L \tag{28}$$

$$P^+ = [I - KH]P^- \tag{29}$$

$$K = P^- H^T [H P^- H^T + R]^{-1} \tag{30}$$

Summary of algorithm

To summarize this algorithm, consider the following steps taken during the execution of the filter. It is assumed that all filter parameters are known ahead of time.

Given

- The initial attitude quaternion $\hat{q}_k(+)$
- The initial rate error $\hat{L}_k(+)$
- The initial error covariance $P_k(+)$

1. Propagate the states and error covariance using the updated or initial values of the state and the error. (17) and (18)
2. Compute the residual. (23)
3. Compute the update state, update covariance and Kalman gain. (26-30)
4. Go to 1

In the filter formulation above, the process noise is assumed to be a known gaussian process. For real-world application, the process noise is not known exactly. Therefore, the next logical step is to devise an algorithm that produces the appropriate covariance to produce accurate state estimates. The method used in this paper is referred to as the PNCE .

PNCE

The PNCE [21] is a parameter optimization technique that identifies filter parameters that produce near-optimal state estimates in the presence of model error. This algorithm can be thought of as an external optimality criterion for obtaining filter parameters, in particular the process noise covariance, Q. In the formulation presented here, the process noise covariance matrix is assumed diagonal. This diagonal form simplifies the optimization and is frequently used in research and applications. The accuracy of the PNCE algorithm is a function of the optimization process and the complexity of the functional form of process noise covariance.

Figure 1 contains a flow chart of the PNCE algorithm. The flow chart describes the steps taken by the PNCE to solve for the appropriate

covariance matrix. The major steps of the PNCE are given below:

1) Use Q_i in the Kalman-type filter to calculate the state estimates.
   a) For the initial step, Q_i is an initial covariance provided by the user.
2) The state estimates are used to evaluate the costs and constraints in the cost/constraint routine.
3) If the cost is not minimized or the constraints not satisfied, then the optimization routine calculates a new Q_i and return to step 1. If the costs are minimized and the constraints are satisfied, then the appropriate process noise covariance is found and PNCE stops.
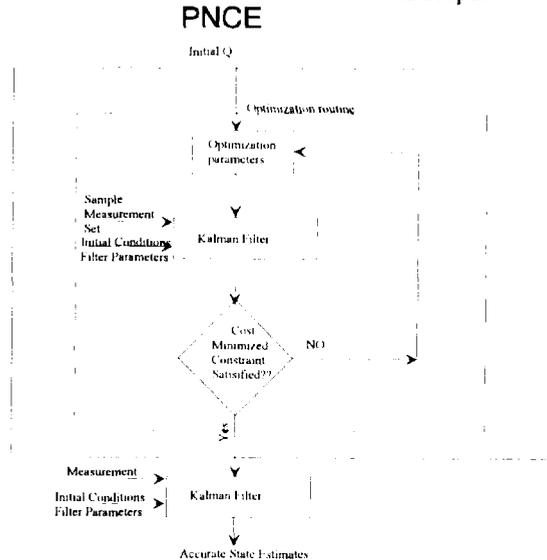

Figure 1 Flow chart of the PNCE algorithm

There are several advantages to this algorithm. First, it provides a consistent method of determining the appropriate process noise covariance. Another advantage is that the physical model error does not have to be a gaussian process to obtain accurate results. The physical model error is the model error associated with real-world applications. This error is not confined to gaussian process as defined in the original Kalman filter formulation. This allows the filter to be implemented in non-ideal environments, such as in real-world applications.

As shown in Figure 1, the PNCE is made up of several different components. The most important of these components is the cost/constraint routine.

Cost/Constraint Routine

131

In this section, the cost/constraint component of the PNCE is discussed. The cost/constraint routine is the second component of the PNCE algorithm. This component defines the accuracy of the estimate of the filter parameter estimation. This component is user and problem dependent.

Covariance Constraint

A major part of the cost/constraint routine is the Covariance Constraint. The covariance constraint was formulated by Mook and Junkins in 1985 [23]. This concept was developed as a part of another estimation algorithm, the Minimum Model Error algorithm. The covariance constraint states that the measurement-minus-estimate error covariance must match the measurement-minus-truth error covariance if the estimates mirror the truth. When this occurs the covariance constraint is satisfied. In the PNCE, the covariance constraint is a function of the process noise covariance, Q. The correct Q should produce estimates that fit the actual measurements with approximately the same error covariance as the actual measurement fit the truth. Therefor, the measurement noise distribution does not have to be completely gaussian to obtain accurate estimates. The covariance constraint can be expressed mathematically as:

$$E[(\tilde{y} - \hat{y})^T (\tilde{y} - \hat{y})] = R \qquad (31)$$

where:

R $(m \times m)$ is the measurement noise covariance

$\tilde{y}$ $(m \times 1)$ is the measurement vector

$\hat{y}(t)$ is the output estimate vector

The covariance constraint is the primary cost function used by the PNCE. However, other costs functions and constraints can be utilized to improve the results of the parameter identification. These additional functions and constraints, if used, are dependent on the application.

Simulation Results

In this section, the PNCE algorithm is used to develop an accurate attitude determination estimator based on real data. This data is obtained from telemetry files provided by NASA Goddard Space Flight Center, Flight Dynamics Branch. These telemetry files contained a nominal pass (nonevent) data set. A nonevent data set is used to ensure that the "truth" (from TRIAD) is available to evaluate the performance of the filter.

To maintain consistency, the same numerical values of the filter parameter used in the RTSF report [27] are used here. The inertia matrix, I, and the wheel inertial, I_{whl}, are

$$I = \begin{bmatrix} 15.516 & 0.0 & 0.0 \\ 0.0 & 21.621 & -0.194 \\ 0.0 & -0.194 & 15.234 \end{bmatrix} kg - m^2$$

$$I_{whl} = 0.0041488 \ kg - m^2$$

The total torque vector, N, and the angular momentum, h, are known inputs to the system. In this simulation study, the measurement noise covariance is obtained from the SAMPEX evaluation report [21].

For the Fine Sun Sensors (FSS) measurements, $\sigma^2_{FSS} = 6.346 \times 10^{-6}$. The error in the FSS measurement is primarily due to the digitization noise (0.5 deg). For the TAM measurements, the digitization noise is only about 0.3 mG and $\sigma^2_{TAM} = 3mG$. The time constant used in the gyro bias model is $\tau = 5.0\,sec$ (for playback). A distinctive feature of telemeter SAMPEX data is the large amount of white noise associated with the torques. The magnitude of the torques associated with this noise is 10^{-2}, which far exceeds the magnitude of the environmental torques of 10^{-6}.

The noise statistics, along with physical insight, are used to determine the growth rate of the error covariance. The growth rate is

$$(3*10^{-3})\Delta t \ \frac{rad^2}{sec^3}$$

This is an approximation of the process noise covariance, Q. Using this approximation, physical insight and tuning, the appropriate Q can be found, but this process can be time-consuming. In this experiment, an automated method of tuning the estimator, the PNCE, is used to determine the appropriate filter parameter.

Since the attitude estimator developed here only requires magnetometer data, some of the accuracy and reliability may be lost. This simulation is used to demonstrate that an accurate estimator can be developed automatically. To ensure robustness in the presence of additional modeling errors, the initial conditions are perturbed from their correct values.

For this study, the process noise covariance is assumed to be of the following form

$$Q = \begin{bmatrix} I_{3\times3}q_q & 0 \\ 0 & I_{3\times3}q_L \end{bmatrix}$$

where q_q and q_L are to be determined. Using the measurement noise, the PNCE determines the appropriate values for q_q and q_L.

$$q_q = 1.e-2 \qquad\qquad q_L = 9.64e-8$$

During non-event passes, good data from both FSS and TAM, TRIAD is considered to be near-perfect. Therefore, TRIAD is considered to be the Truth. A nonevent pass is part of an orbit or the whole orbit where an eclipse or other anomalies do not occur.

Figure 2-4 contain plots of the Roll, Pitch, and Yaw of the truth and of the estimator using the standard formulation. The state estimates are initially off but then converge to the truth quickly. This initial error is due to the initial condition error. Figure 5 contains a plot of the output estimates and the TAM measurement.

Formulation 1 Filter vs the Truth (TRIAD)
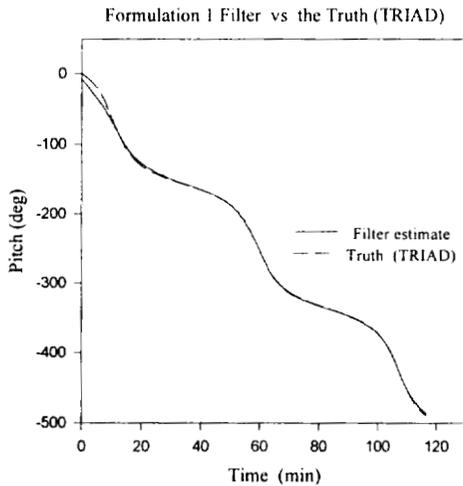
Figure 2 The estimated and true Pitch

Filter (First Formulation) vs the Truth (TRIAD)
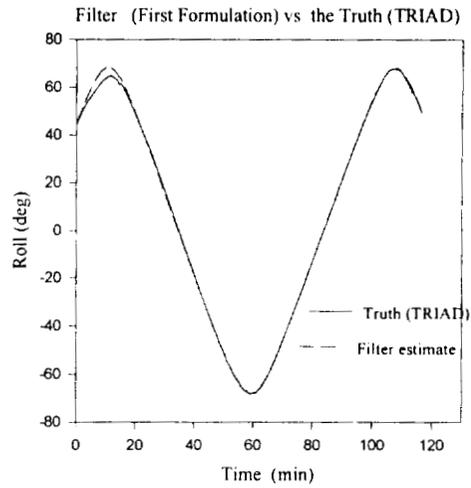
Figure 3 The estimated and true Roll

Filter (First Formulation) vs the Truth (TRIAD)
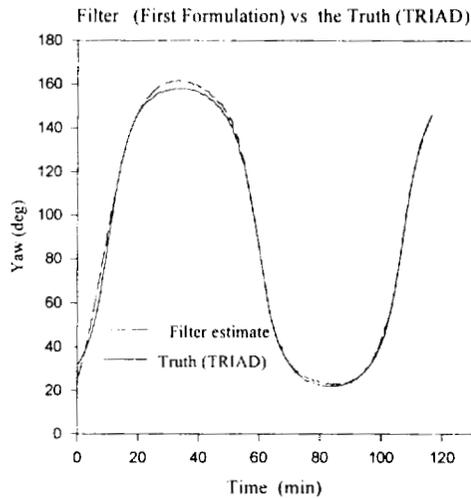
Figure 4. The estimated and true Yaw

133
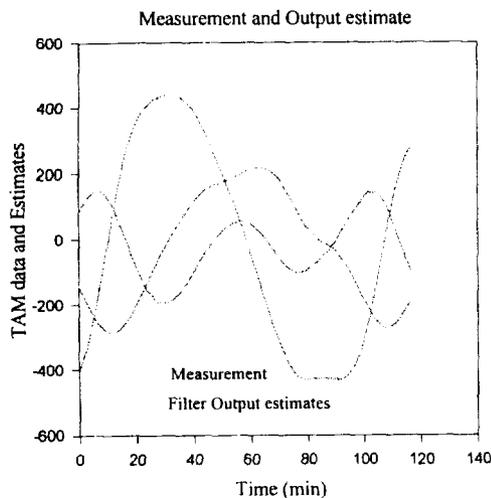
Figure 5 **The TAM measurements and the output estimates**

In the plots above, filter produce accurate estimates of the attitude and the output (the TAM measurements). Even though the initial conditions are perturbed, the filter is able to converge to the truth quickly. This illustrates the robustness of the PNCE and the present filter formulation.

Conclusion

The purpose of this paper is to demonstrate a new method for obtaining accurate state estimates for a three-axis magnetometer attitude estimator. This method, the PNCE, used statistical properties and a data set to determine the appropriate process noise covariance. The PNCE algorithm is utilized to develop an attitude filter. This filter formulations produced accurate attitude and output estimates.

From the results in this paper, it has been shown that the PNCE estimator is a robust algorithm that can account for deterministic linear model uncertainty and error in the initial conditions or the filter parameters.

References

[1]   Wahba, G., "A Least-Squares Estimate of Satellite Attitude," *SIAM Review*, Vol. 7, No. 3, July 1965, pp. 409.

[2]   Lerner, G. M., "Three-Axis Attitude Determination," *Spacecraft Attitude Determination and Control*, edited by J. R. Wertz, D. Reidel Publishing Co., Dordrecht, The Netherlands, 1978, pp. 420-428.

[3]   Markley F., L., "Attitude Determination from Vector Observations: A Fast Optimal Matrix Algorithm," *Journal of the Astronautical Sciences*, Vol. 41, No. 2, April-June,. 1993, pp. 261-280.

[4]   Shuster, M. D., Oh, S. D., "Three-Axis Attitude Determination from Vector Observation," *Journal of Guidance and Control*, Vol. 4, No. 1, 1981, pp. 70-77.

[5]   Shuster, M, "Kalman Filtering of Spacecraft Attitude and the Quest Model," *Journal of the Astronautical Sciences*, Vol. 38, No. 3, July-September. 1990, pp. 377-393.

[6]   Martel F., Pal, P. K., and Psiaki M. L., "Three-Axis Attitude Determination via Kalman Filtering of Magnetometer Data," *Proceedings of the 1988 Flight Mechanics Estimation Theory Symposium*, NASA Goddard, 1988.

[7]   Heyler, G. A., "Attitude Determination by Enhanced Kalman Filtering Using Euler Parameter Dynamics and Rotational Update Equations," *Proceedings of the AAS/AIAA Astrodynamics Specialist Conference*, No. A81-45832., Nevada, Aug. 1981.

[8]   Deutschmann, J., Rokni, M., and Bar-Itzhack, I., "Comparison and Testing of Extended Kalman Filters for Attitude Estimation of the Earth Radiation Budget Satellite," *Proceedings of the Flight Mechanics/Estimation Theory Symposium*, NASA Goddard Space Flight Center, 1990.

[9]   Challa, M. S., Natanson, G. A., Baker, D. E., and Deutschmann, J. K., "Advantages of Estimating Rate Corrections During Dynamic Propagation of Spacecraft Corrections During Dynamic Propagation of Spacecraft Rates-Applications to Real-Time Attitude Determination of SAMPEX," *Proceedings of the Flight Mechanics/Estimation Theory Symposium*, NASA Goddard, 1994, pp. 481-495.

[10]   Chu, D., Harvie, E., "Accuracy of the ERBS Definitive Attitude Determination System in the Presence of Propagation Noise," *Proceedings of the Flight Mechanics/Estimation Theory Symposium*, NASA Goddard, 1990, pp. 97-114.

[11]   Chu, D., Glickman, J., and Harvie, E., "Improvements in ERBS Attitude Determination Without Gyros," *Proceedings of the Flight*

Mechanics/Estimation Theory Symposium, NASA Goddard, 1992, pp. 185-200.

[12] Crassidis, J., Mook, D. J., De Peña, J., and Meyer, T., "Robust Attitude and Attitude Rate Estimation for Sampex," *Proceedings of the AAS/AIAA Astrodynamics Specialist Conference*, Cocoa Beach, Florida, February, 1994.

[13] De Peña, J., Crassidis, J., Mook, D. J., and Meyer, T., "MME-Based Attitude Dynamics Identification and Estimation for Sampex," *Proceedings of the Flight Mechanics/Estimation Theory Symposium Conference*, NASA Goddard, Greenbelt, Maryland, May, 1994.

[14] Shuster, M. D., "The quaternion in the Kalman filter," *Proceedings of the AAS/AIAA Astrodynamics Specialist Conference*, Victoria, B.C., Canada, Aug. 16-19, 1993.

[15] Hamilton, W. R., *Elements of Quaternions*, Longmans, Green Co., London 1866.

[16] Markley F., L., "Attitude Determination and Parameter Estimation Using Vector Observation: Theory," *Journal of the Astronautical Sciences*, Vol. 37, No. 1, January-March, 1989, pp. 41-58.

[17] Stuelpnagel, J., "On the Parameterization of the Three-Dimension Rotational Group," *SIAM Review*, Vol. 6, No. 1, Oct. 1964, pp. 422-430.

[18] Wilcox, J. C., "A New Algorithm for Strapped-Down Inertial Navigation," *IEEE Transactions on Aerospace and Electronic Systems*, Vol. AES-3, Sept. 1967, pp. 796-802.

[19] Markley F., L.," Parameterizations of the Attitude," edited by J.R. Wertz, D. Reidel, Dordrecht, the Netherlands, 1978.

[20] Wertz, J. R., *Spacecraft Attitude Determination and Control*, Kluwer, 1991.

[21] Challa, M. S., "Solar, Anomalous, Magnetospheric Particle Explorer (SAMPEX) Real-Time Sequence Filter (RTSF)," *Evaluation REPORT*, NASA Goddard, 1993.

[22] Mason, P. A. C., and Mook, D.J., "A Process Noise Covariance Estimator," *Proceedings of the AIAA Guidance, Navigation, and Control Conference*, Scottsdale, AZ, August, 1994.

[23] Mook, D. J., and Junkins, J. L., "Minimum Model Error Estimation for Poorly Modeled Dynamic Systems," *AIAA Journal of Guidance, Control and Dynamics*, Vol. II, No. 3, May-June 1988, pp. 256-261.

AN MME-BASED ATTITUDE ESTIMATOR
USING VECTOR OBSERVATIONS

John L. Crassidis
Goddard Space Flight Center, Code 712
Greenbelt, MD 20771

F. Landis Markley
Goddard Space Flight Center, Code 712
Greenbelt, MD 20771

Abstract

In this paper, an optimal batch estimator and filter based on the Minimum Model Error (MME) approach is developed for three-axis stabilized spacecraft. Three different MME algorithms are developed. The first algorithm estimates the attitude of a spacecraft using rate measurements. The second algorithm estimates the attitude without using rate measurements. The absence of rate data may be a result of intentional design or from unexpected failure of existing gyros. The third algorithm determines input-torque modeling error trajectories. All of the algorithms developed in this paper use attitude sensors (e.g., three-axis magnetometers, sun sensors, star trackers, etc). Results using these new algorithms indicate that an MME-based approach accurately estimates the attitude, rate, and input torque trajectories of an actual spacecraft.

Introduction

The attitude of a spacecraft can be determined by either deterministic methods or by utilizing algorithms which combine dynamic models with sensor data. Three-axis deterministic methods, such as TRIAD [1], QUEST [2], and FOAM [3], require at least two simultaneous vector measurements to determine the attitude (direction-cosine) matrix. An advantage of both the QUEST and FOAM algorithms is that the attitude of a spacecraft can be estimated using more than two measurements. This is accomplished by minimizing a quadratic loss function first posed by Wahba [4]. However, all deterministic methods fail when only one vector measurement is available, (e.g., magnetometer data only). Estimation algorithms utilize dynamic models, and subsequently can (in theory) estimate the attitude of a spacecraft using measurements of a single reference vector. Although all spacecraft in use today have at least two on-board attitude sensors, estimation techniques can be used to determine the attitude during anomalous periods, such as solar eclipse and/or sensor co-alignment.

The most commonly used technique for attitude estimation is the Kalman filter [5]. The Kalman filter utilizes state-space representations to both estimate plant dynamics and also filter noisy data. Errors in the dynamical model and measurement process are assumed to be modeled by a zero-mean Gaussian process with known covariance. The optimality criterion in the Kalman filter minimizes the trace error covariance between estimated responses and model responses. In theory, the Kalman filter does not require actual measurements to satisfy this optimality criterion; however, in actual practice measurements are often used to properly "tune" the filter estimates.

Smoothing algorithms further refine state estimates by utilizing both a "forward filter" and a "backward filter" (see e.g., Gelb [6]). An advantage of smoothing algorithms is that the error covariance is always less or equal to either the forward or backward filter alone. A disadvantage of smoothing algorithms is that they cannot be implemented in sequential (real-time) estimation.

In order for the Kalman filter to be truly optimal, both the measurement error process and model error process must be random Gaussian processes with known covariance. In most circumstances,

properties of the measurement error process are known a priori by utilizing statistical inferences applied to sensor measurements. However, model error statistics are not usually well known. In actual practice the determination of the model error covariance in the Kalman filter is usually obtained by an ad hoc and/or heuristic approach, which can result in suboptimal filter designs (e.g., determining random gyro drift rate). Also, in many instances, such as nonlinear model errors or non-stationary processes, the assumption of a stationary Gaussian process can lead to severely degraded state estimates.

For spacecraft attitude estimation, the Kalman filter is most applicable to spacecraft equipped with three-axis gyros as well as attitude sensors [7]. However, rate gyros are generally expensive and are often prone to degradation or failure. Therefore, in recent years rate gyros have been omitted (e.g., in Small Explorer (SMEX) spacecraft, such as Solar Anomalous Magnetospheric Particle Explorer (SAMPEX) spacecraft). To circumvent the problem of rate gyro omission or failure, analytical models of rate motion can be used. This approach has been successfully used in a Real-Time Sequential Filter (RTSF) algorithm which propagates state estimates and error covariances using dynamic models [8]. The estimation of dynamic rates by the RTSF is accomplished from angular momentum model propagation, and then correcting for these rates by using a "gyro bias" component in the filter design. A clear advantage of using dynamic models is shown for the case of sun-magnetic field near co-alignment. For this case, deterministic algorithms, such as TRIAD and QUEST, show anomalous behaviors with extreme deviations in determined attitudes. Since the RTSF propagates an analytical model of motion, attitude estimates are improved even when data from only one attitude sensor is available. However, the RTSF is essentially a Kalman filter in which the "gyro bias" model (and subsequently the angular momentum model correction) is assumed to be a Gaussian process with known covariance. Also, fairly accurate models of angular momentum are required in order to obtain accurate estimates. Subsequently, the design process for choosing the model error covariance becomes difficult.

In this paper, an optimal attitude estimation algorithm is developed which is capable of robust and accurate state estimation for spacecraft lacking accurate or any rate measurements and/or accurate dynamic models. This algorithm is based on the Minimum Model Error (MME) [9] batch-estimation approach. The advantages of the MME estimator over conventional Kalman strategies include: (i) no a priori statistics on the form of the model error are required, (ii) the actual model error is determined as part of the solution, and (iii) state estimates are free of jump discontinuities, which greatly smoothes out high measurement noise. The MME estimation approach has been successfully applied to numerous poorly-modeled dynamic systems which exhibit highly nonlinear behaviors (see, e.g. [10-11]). Previous MME studies used TRIAD-determined quaternions as measurements [12]. The formulations developed in this paper expand upon this method to include attitude sensors, such as three-axis magnetometers (TAM), fine sun sensors (FSS), star trackers, etc.

The organization of this paper proceeds as follows. First, a summary of the spacecraft attitude kinematics and sensor models is shown. Then, a brief review of the MME estimator for nonlinear systems is shown. Next, various MME-based algorithms are developed for the purpose of attitude estimation, which include: a simple linear algorithm which is used to smooth noisy rate measurements, an attitude estimator using rate measurement information, an attitude estimator without the utilization of any rate measurements, and an input torque estimator. Finally, these MME designs are used to estimate the attitude, rate, and input torque trajectories of the SAMPEX spacecraft in order to demonstrate the usefulness of these algorithms.

Attitude Kinematics and Dynamics

In this section, a brief review of the kinematic and dynamic equations of motion for a three-axis stabilized spacecraft is shown. The attitude is assumed to be represented by a quaternion, defined as

$$q \equiv \begin{bmatrix} q_{13} \\ q_4 \end{bmatrix} \tag{1}$$

with

$$\underline{q}_{13} \equiv \begin{bmatrix} q_1 \\ q_2 \\ q_3 \end{bmatrix} = \hat{\underline{n}} \sin(\theta/2) \tag{2a}$$

$$q_4 = \cos(\theta/2) \tag{2b}$$

where $\hat{\underline{n}}$ is a unit vector corresponding to the axis of rotation and θ is the angle of rotation. The quaternion kinematic equations of motion are derived by using the spacecraft's angular velocity ($\underline{\omega}$), given by

$$\dot{\underline{q}} = \frac{1}{2}\Omega(\underline{\omega})\underline{q} = \frac{1}{2}\Xi(\underline{q})\underline{\omega} \tag{3}$$

where $\Omega(\underline{\omega})$ and $\Xi(\underline{q})$ are defined as

$$\Omega(\underline{\omega}) \equiv \begin{bmatrix} -[\underline{\omega}\times] & \vdots & \underline{\omega} \\ \cdots\cdots & \vdots & \cdots\cdots \\ -\underline{\omega}^T & \vdots & 0 \end{bmatrix} \tag{4a}$$

$$\Xi(\underline{q}) \equiv \begin{bmatrix} q_4 I_{3\times3} + [\underline{q}_{13}\times] \\ \cdots\cdots\cdots\cdots\cdots \\ -\underline{q}_{13}^T \end{bmatrix} \tag{4b}$$

The 3×3 dimensional matrices $[\underline{\omega}\times]$ and $[\underline{q}_{13}\times]$ are referred to as cross product matrices since $\underline{a}\times\underline{b} = [\underline{a}\times]\underline{b}$, with

$$[\underline{a}\times] \equiv \begin{bmatrix} 0 & -a_3 & a_2 \\ a_3 & 0 & -a_1 \\ -a_2 & a_1 & 0 \end{bmatrix} \tag{5}$$

Since a three degree-of-freedom attitude system is represented by a four-dimensional vector, the quaternions cannot be independent. This condition leads to the following normalization constraint

$$\underline{q}^T\underline{q} = \underline{q}_{13}^T\underline{q}_{13} + q_4^2 = 1 \tag{6}$$

Also, the matrix $\Xi(\underline{q})$ obeys the following helpful relations

$$\Xi^T(\underline{q})\Xi(\underline{q}) = \underline{q}^T\underline{q}\, I_{3\times3} \tag{7a}$$

$$\Xi(\underline{q})\Xi^T(\underline{q}) = \underline{q}^T\underline{q}\, I_{4\times4} - \underline{q}\,\underline{q}^T \tag{7b}$$

$$\Xi^T(\underline{q})\underline{q} = \underline{0}_{3\times1} \tag{7c}$$

$$\Xi^T(\underline{q})\underline{\lambda} = -\Xi^T(\underline{\lambda})\underline{q} \text{ for any } \underline{\lambda}_{4\times1} \tag{7d}$$

The dynamic equations of motion, also known as Euler's equations, for a rotating spacecraft are given by ([13])

$$\dot{\underline{L}} = \underline{N} - \underline{\omega} \times \underline{L} = I_b \dot{\underline{\omega}} \qquad (8)$$

where $\underline{L}$ is the total angular momentum, $\underline{N}$ is the total external torque (which includes, e.g., control torques, aerodynamic drag torques, solar pressure torques, etc.), and I_b is the inertia matrix of the spacecraft. If reaction or momentum wheels are used on the spacecraft, the total angular momentum is given by

$$\underline{L} = I_b \underline{\omega} + \underline{h} \qquad (9)$$

where $\underline{h}$ is the total angular momentum due to the wheels. Thus, Equation (8) can be re-written as

$$\dot{\underline{L}} = \underline{N} - \left[I_b^{-1}(\underline{L} - \underline{h}) \right] \times \underline{L} \qquad (10)$$

The measurement model is assumed to be of the form given by

$$\underline{B}_B = A(\underline{q})\underline{B}_I \qquad (11)$$

where $\underline{B}_I$ is a 3×1 dimensional vector of some reference object (e.g., a vector to the sun or to a star, or the Earth's magnetic field vector) in a reference coordinate system, $\underline{B}_B$ is a 3×1 dimensional vector defining the components of the corresponding reference vector measured in the spacecraft body frame, and $A(\underline{q})$ is given by

$$A(\underline{q}) = \left(q_4^2 - \underline{q}_{13}^T \underline{q}_{13} \right) I_{3 \times 3} + 2 \underline{q}_{13} \underline{q}_{13}^T - 2 q_4 \left[\underline{q}_{13} \times \right] \qquad (12)$$

which is the 3×3 dimensional (orthogonal) attitude matrix.

Minimum Model Error Estimation

In this section, a brief review of the Minimum Model Error (MME) estimation algorithm is shown. The essential feature of this batch estimator is that actual model error trajectories are determined during the estimation process, unlike most filter/smoother algorithms which assume that the model error is a stochastic process with known properties. The MME algorithm determines the correction added to the assumed model which yields an accurate representation of the system's behavior. This is accomplished by solving an optimality condition using an output residual constraint. Therefore, accurate state estimates can be determined without the use of precise system representations in the assumed model.

The MME algorithm assumes that the state estimates are given by a preliminary model and a to-be-determined model error vector, given by

$$\dot{\hat{\underline{x}}}(t) = \underline{f}[\hat{\underline{x}}(t), \underline{u}(t), \underline{d}(t), t] \qquad (13a)$$

$$\hat{\underline{y}}(t) = \underline{g}[\hat{\underline{x}}(t), t] \qquad (13b)$$

where $\underline{f}$ is an $n \times 1$ model vector, $\hat{\underline{x}}(t)$ is an $n \times 1$ state estimate vector, $\underline{u}(t)$ is a $p \times 1$ vector of known inputs, and $\underline{d}(t)$ is an $n \times 1$ model error vector, $\underline{g}$ is a $q \times 1$ measurement (sensitivity) vector, and $\hat{\underline{y}}(t)$ is a $q \times 1$ estimated output vector. State-observable discrete measurements are assumed for Equation (13b) in the following form

$$\underline{\tilde{y}}(t_k) = \underline{g}_k\left[\underline{x}(t_k), t_k\right] + \underline{v}_k \tag{14}$$

where $\underline{\tilde{y}}(t_k)$ is a $q \times 1$ measurement vector at time t_k, and $\underline{v}_k$ is a $q \times 1$ measurement noise vector which is assumed to be a zero-mean, Gaussian distributed process with known covariance.

In the MME algorithm, the optimal state estimates are determined on the basis that the measurement-minus-estimate error covariance matrix must match the measurement-minus-truth error covariance matrix. This condition is referred to as the "covariance constraint," shown as

$$\left\{\underline{\tilde{y}}(t_k) - \underline{g}_k\left[\underline{\hat{x}}(t_k), t_k\right]\right\}\left\{\underline{\tilde{y}}(t_k) - \underline{g}_k\left[\underline{\hat{x}}(t_k), t_k\right]\right\}^T = R_k \tag{15}$$

where R_k is the element-by-element (known) measurement error covariance. However, problems may arise using Equation (15) which are attributed to "small sample" statistics [14]. Therefore, in the typical case where the measurement error process is stationary, the average covariance can be used, given by

$$\frac{1}{m}\sum_{k=1}^{m}\left\{\underline{\tilde{y}}(t_k) - \underline{g}_k\left[\underline{\hat{x}}(t_k), t_k\right]\right\}\left\{\underline{\tilde{y}}(t_k) - \underline{g}_k\left[\underline{\hat{x}}(t_k), t_k\right]\right\}^T \approx R \tag{16}$$

where m is the total number of measurements.

Next, the following cost function is minimized with respect to $\underline{d}(\tau)$

$$J = \frac{1}{2}\sum_{k=1}^{m}\left\{\underline{\tilde{y}}(t_k) - \underline{g}_k\left[\underline{\hat{x}}(t_k), t_k\right]\right\}^T R^{-1}\left\{\underline{\tilde{y}}(t_k) - \underline{g}_k\left[\underline{\hat{x}}(t_k), t_k\right]\right\} + \frac{1}{2}\int_{t_0}^{t_f}\underline{d}^T(\tau)\,W\,\underline{d}(\tau)\,d\tau \tag{17}$$

where W is an $n \times n$ positive-definite weighting matrix. The necessary conditions for the minimization of Equation (17) lead to the following two-point-boundary-value-problem (TPBVP) [9]

$$\underline{\dot{\hat{x}}}(t) = \underline{f}\left[\underline{\hat{x}}(t), \underline{u}(t), \underline{d}(t), t\right] \tag{18a}$$

$$\underline{d}(t) = -W^{-1}\left[\frac{\partial \underline{f}}{\partial \underline{d}}\right]^T \underline{\lambda}(t) \tag{18b}$$

$$\underline{\dot{\lambda}}(t) = -\left[\frac{\partial \underline{f}}{\partial \underline{\hat{x}}}\right]^T \underline{\lambda}(t) \tag{18c}$$

$$\underline{\lambda}(t_k^+) = \underline{\lambda}(t_k^-) + H^T(t_k)\left\{\underline{\tilde{y}}(t_k) - \underline{g}_k\left[\underline{\hat{x}}(t_k), t_k\right]\right\} \tag{18d}$$

$$H(t_k) \equiv \left.\frac{\partial \underline{g}}{\partial \underline{\hat{x}}}\right|_{\underline{\hat{x}}(t_k), t_k} \tag{18e}$$

where $\underline{\lambda}(t)$ is an $n \times 1$ co-state vector which is updated at each measurement point using Equation (18d). The boundary conditions are selected such that either $\underline{\lambda}(t_0^-) = \underline{0}$ or $\hat{\underline{x}}(t_0)$ is specified at the initial time and either $\underline{\lambda}(t_f^+) = \underline{0}$ or $\hat{\underline{x}}(t_f)$ is specified at the final time.

The solution of the TPBVP for a given weighting matrix yields a state estimate time trajectory which can be used to determine a measurement residual covariance matrix. The covariance constraint is satisfied when the proper balance between model error and measurement residual has been achieved. If the measurement residual covariance is higher than the known measurement error covariance (R), then W should be decreased to less penalize the model error. Conversely, if the residual covariance is lower than the known covariance, then W should be increased so that less unmodeled dynamics are added to the assumed system model. The optimal weighting matrix is therefore obtained when the covariance constraint in Equation (16) is satisfied.

Gyro Noise Smoother

Gyros tend to be noisy and have an inherent drift. Also, gyros are usually sampled at a higher frequency than attitude sensors. In order to first filter the noise, a simple MME-based smoothing algorithm can first be applied. This algorithm minimizes

$$J_g = \frac{1}{2} \sum_{k=1}^{m} \{ \tilde{\underline{\omega}}_g(t_k) - \hat{\underline{\omega}}_g(t_k) \}^T R_g^{-1} \{ \tilde{\underline{\omega}}_g(t_k) - \hat{\underline{\omega}}_g(t_k) \} + \frac{1}{2} \int_{t_0}^{t_f} \underline{d}_g^T(\tau) W_g \underline{d}_g(\tau) \, d\tau \tag{19}$$

subject to

$$\dot{\hat{\underline{\omega}}}_g(t) = \underline{d}_g(t), \qquad \hat{\underline{\omega}}_g(t_0) = \hat{\underline{\omega}}_{g0} \tag{20}$$

where $\hat{\underline{\omega}}_g(t)$ is the estimated gyro output, and $\underline{d}_g(t)$ is the model error correction. Minimizing Equation (19) leads to the following TPBVP

$$\dot{\hat{\underline{\omega}}}_g(t) = -W_g^{-1} \underline{\lambda}_g(t), \qquad \hat{\underline{\omega}}_g(t_0) = \hat{\underline{\omega}}_{g0} \tag{21a}$$

$$\dot{\underline{\lambda}}_g = \underline{0} \tag{21b}$$

$$\underline{\lambda}_g(t_k^+) = \underline{\lambda}_g(t_k^-) + R_g^{-1} \{ \tilde{\underline{\omega}}_g(t_k) - \hat{\underline{\omega}}_g(t_k) \}, \qquad \underline{\lambda}_g(t_f^-) = \underline{0} \tag{21c}$$

The solution of Equation (21) can be determined by using a steady-state Riccati transformation (see [15] for details). This transformation leads to the following

$$P_i = \sqrt{\frac{W_{g_i}}{R_{g_i} \Delta t}} \tag{22a}$$

$$\dot{\underline{h}}_i(t) = \left[\frac{P_i}{W_{g_i}} \right] \underline{h}_i(t) \tag{22b}$$

$$\underline{h}_i(t_k^-) = \underline{h}_i(t_k^+) - \frac{1}{R_{g_i}} \tilde{\underline{\omega}}_{g_i}(t_k), \qquad \underline{h}_i(t_f^+) = \underline{0} \tag{22c}$$

142

$$\hat{\underline{\omega}}_{g_i}(t) = \left[\frac{P_i}{W_{g_i}}\right]\hat{\underline{\omega}}_{g_i}(t) - \left[\frac{1}{W_{g_i}}\right]\underline{h}_i(t), \qquad \hat{\underline{\omega}}_{g_i}(t_0) = \hat{\underline{\omega}}_{g_{i_0}} \tag{22d}$$

where the subscript (i) represents each gyro measurement set, and Δt is the sampling interval. For a given weighting and measurement covariance, the first step is to determine the steady-state Riccati solution in using Equation (22a). Then, the inhomogeneous Riccati trajectory is solved backwards in time using Equation (22b), with discrete jumps at each measurement point given by Equation (22c). Finally, the smoothed gyro estimates are determined using Equation (22d). An advantage of this algorithm is not only the inherent smoothing properties, but also that the gyro estimates are totally continuous. Therefore, the generally discrete gyro measurements can be replaced with the continuous gyro estimates given by Equation (22d).

Attitude Estimation Using Rate Measurements

The MME attitude angular velocity estimation formulation using rate measurements minimizes the following cost function

$$J = \frac{1}{2}\sum_{k=1}^{m}\left\{\widetilde{\underline{B}}_B - A(\hat{\underline{q}})\underline{B}_I\right\}^T\bigg|_{t_k} R^{-1}\left\{\widetilde{\underline{B}}_B - A(\hat{\underline{q}})\underline{B}_I\right\}\bigg|_{t_k} + \frac{1}{2}\int_{t_0}^{t_f}\underline{d}^T(\tau)\,W\underline{d}(\tau)\,d\tau \tag{23}$$

subject to

$$\hat{\underline{q}}(t) = \frac{1}{2}\Omega\left[\widetilde{\underline{\omega}}_g(t) + \underline{d}(t)\right]\hat{\underline{q}}(t), \qquad \hat{\underline{q}}(t_0) = \hat{\underline{q}}_0 \tag{24}$$

where $\widetilde{\underline{\omega}}_g(t)$ is the rate measurement vector, $\hat{\underline{q}}(t)$ is the estimated quaternion, and $\widetilde{\underline{B}}_B$ and $\underline{B}_I$ are the spacecraft body measurement and corresponding inertial field vector, respectively. The model error ($\underline{d}$) is a correction to the rate measurements, which forces the model responses to satisfy the covariance constraint in Equation (16).

The TPBVP given by Equation (18) can be written as

$$\hat{\underline{q}}(t) = \frac{1}{2}\Omega\left[\widetilde{\underline{\omega}}_g(t) + \underline{d}(t)\right]\hat{\underline{q}}(t), \qquad \hat{\underline{q}}(t_0) = \hat{\underline{q}}_0 \tag{25a}$$

$$\underline{d}(t) + \frac{1}{2}W^{-1}\Xi^T(\hat{\underline{q}})\underline{\lambda}(t) = 0 \tag{25b}$$

$$\dot{\underline{\lambda}}(t) = \frac{1}{2}\Omega\left[\widetilde{\underline{\omega}}_g(t) + \underline{d}(t)\right]\underline{\lambda}(t) \tag{25c}$$

$$\underline{\lambda}(t_k^+) = \underline{\lambda}(t_k^-) + H^T\big|_{t_k} R^{-1}\left\{\widetilde{\underline{B}}_B - A(\hat{\underline{q}})\underline{B}_I\right\}\bigg|_{t_k}, \qquad \underline{\lambda}(t_f^+) = \underline{0} \tag{25d}$$

The sensitivity matrix H in Equation (25d) can be derived as

$$H = 2\Xi^T(l) \tag{26}$$

where

$$\underline{l} = \Psi(\hat{\underline{q}})\underline{B}_I \tag{27a}$$

$$\Psi(\hat{\underline{q}}) \equiv \begin{bmatrix} -\hat{q}_4 I_{3\times3} + [\hat{\underline{q}}_{13} \times] \\ \cdots\cdots\cdots\cdots \\ \hat{\underline{q}}_{13}^T \end{bmatrix} \tag{27b}$$

The extension to using multiple attitude sensors is accomplished by using a partitioned residual output and sensitivity matrix, given by

$$\begin{bmatrix} H_1^T & \cdots & H_q^T \end{bmatrix} \begin{bmatrix} \{\tilde{\underline{B}}_{B_1} - A(\hat{\underline{q}})\underline{B}_{I_1}\} \\ \vdots \\ \{\tilde{\underline{B}}_{B_q} - A(\hat{\underline{q}})\underline{B}_{I_q}\} \end{bmatrix} \tag{28}$$

The co-state update in Equation (25d) shows a nonlinear relationship with respect to the quaternion estimate. However, this nonlinearity can be reduced to be a *linear* function if the quaternions obey normalization and each attitude sensor is assumed isotropic. This can be shown by deriving the co-state update using

$$\frac{1}{2r}\frac{\partial}{\partial\hat{\underline{q}}}\left\{\left[\tilde{\underline{B}}_B - A(\hat{\underline{q}})\underline{B}_I\right]^T\left[\tilde{\underline{B}}_B - A(\hat{\underline{q}})\underline{B}_I\right]\right\} \tag{29}$$

where the measurement covariance is now assumed to be isotropic for each sensor (i.e., the measurement errors in each one of the axes are assumed equal). Therefore, $R = rI_{3\times3}$, which is a valid assumption for almost all attitude sensors. In order to determine the partial derivative in Equation (29), the following identities and definitions are used

$$E(\underline{B}_I) \equiv \begin{bmatrix} -[\underline{B}_I \times] & \vdots & -\underline{B}_I \\ \cdots\cdots & \vdots & \cdots\cdots \\ \underline{B}_I^T & \vdots & 0 \end{bmatrix} \tag{30a}$$

$$A(\hat{\underline{q}}) = -\Xi^T(\hat{\underline{q}})\Psi(\hat{\underline{q}}) \tag{30b}$$

$$\Psi(\hat{\underline{q}})\underline{B}_I = E(\underline{B}_I)\hat{\underline{q}} \tag{30c}$$

$$E(\underline{B}_I)E(\underline{B}_I) = -I_{4\times4}\underline{B}_I^T\underline{B}_I \tag{30d}$$

Equation (29) can now be re-written as

$$\frac{1}{2r}\frac{\partial}{\partial\hat{\underline{q}}}\left\{\tilde{\underline{B}}_B^T\tilde{\underline{B}}_B - 2\hat{\underline{q}}^T\Omega(\tilde{\underline{B}}_B)E(\underline{B}_I)\hat{\underline{q}} + I_{4\times4}(\underline{B}_I^T\underline{B}_I)(\hat{\underline{q}}^T\hat{\underline{q}})^2\right\} \tag{31}$$

The partial derivative in Equation (31) is given by

$$\frac{2}{r}\left\{\Omega(\tilde{\underline{B}}_B)E(\underline{B}_I)\hat{\underline{q}} + (\underline{B}_I^T\underline{B}_I)(\hat{\underline{q}}^T\hat{\underline{q}})\hat{\underline{q}}\right\} \tag{32}$$

Hence, if the quaternions obey normalization the following identity is true

$$\left\{\Omega(\tilde{\underline{B}}_B)\mathrm{E}(\underline{B}_I)\hat{\underline{q}} + (\underline{B}_I^T \underline{B}_I)\hat{\underline{q}}\right\} = \Xi(\underline{h})\left\{\tilde{\underline{B}}_B - A(\hat{\underline{q}})\underline{B}_I\right\} \tag{33}$$

Therefore, if the sensor measurements are isotropic, the co-state update in Equation (25d) is linear with respect to the quaternion estimate.

The TPBVP shown in Equations (25a)-(25d) can be solved by using gradient techniques. The basic gradient procedure is to first guess for the model error trajectory ($\underline{d}$). Then, integrate the quaternion states forward using Equation (25a) and co-states backward using Equation (25c) accounting for discrete jumps in Equation (25d). The next search direction is given by Equation (25b). This procedure is continued until convergence is achieved.

Attitude Estimation without Rate Measurements

In this section, the MME estimator is derived for spacecraft which lack any rate information. The formulation is based upon using Euler's equation for modeling the angular momentum. The MME problem for this case minimizes the following cost function

$$J = \frac{1}{2}\sum_{k=1}^{m}\left\{\tilde{\underline{B}}_B - A(\hat{\underline{q}})\underline{B}_I\right\}^T\bigg|_{t_k} R^{-1}\left\{\tilde{\underline{B}}_B - A(\hat{\underline{q}})\underline{B}_I\right\}\bigg|_{t_k} + \frac{1}{2}\int_{t_0}^{t_f}\underline{d}^T(\tau)\,W\underline{d}(\tau)\,d\tau \tag{34}$$

subject to

$$\begin{bmatrix}\dot{\hat{\underline{q}}}(t)\\\dot{\hat{\underline{L}}}(t)\end{bmatrix} = \begin{bmatrix}\frac{1}{2}\Omega(\hat{\underline{\omega}}) & 0_{4\times3}\\ 0_{3\times4} & -[\hat{\underline{\omega}}\times]\end{bmatrix}\begin{bmatrix}\hat{\underline{q}}(t)\\\hat{\underline{L}}(t)\end{bmatrix} + \begin{bmatrix}0_{4\times3}\\I_{3\times3}\end{bmatrix}\underline{N}(t) + \begin{bmatrix}0_{4\times3}\\I_{3\times3}\end{bmatrix}\underline{d}(t), \qquad \begin{bmatrix}\hat{\underline{q}}(t_0)\\\hat{\underline{L}}(t_0)\end{bmatrix} = \begin{bmatrix}\hat{\underline{q}}_0\\\hat{\underline{L}}_0\end{bmatrix} \tag{35}$$

where

$$\hat{\underline{\omega}}(t) = I_b^{-1}\left\{\hat{\underline{L}}(t) - \tilde{\underline{h}}(t)\right\} \tag{36}$$

where $\tilde{\underline{h}}$ is the measured angular momentum due to the wheels. Minimizing Equation (34) leads to the following TPBVP

$$\begin{bmatrix}\dot{\hat{\underline{q}}}(t)\\\dot{\hat{\underline{L}}}(t)\end{bmatrix} = \begin{bmatrix}\frac{1}{2}\Omega(\hat{\underline{\omega}}) & 0_{4\times3}\\ 0_{3\times4} & -[\hat{\underline{\omega}}\times]\end{bmatrix}\begin{bmatrix}\hat{\underline{q}}(t)\\\hat{\underline{L}}(t)\end{bmatrix} + \begin{bmatrix}0_{4\times3}\\I_{3\times3}\end{bmatrix}\underline{N}(t) + \begin{bmatrix}0_{4\times3}\\I_{3\times3}\end{bmatrix}\underline{d}(t), \qquad \begin{bmatrix}\hat{\underline{q}}(t_0)\\\hat{\underline{L}}(t_0)\end{bmatrix} = \begin{bmatrix}\hat{\underline{q}}_0\\\hat{\underline{L}}_0\end{bmatrix} \tag{37a}$$

$$\underline{d}(t) + W^{-1}\underline{\lambda}_L(t) = \underline{0} \tag{37b}$$

$$\begin{bmatrix}\dot{\underline{\lambda}}_q(t)\\\dot{\underline{\lambda}}_L(t)\end{bmatrix} = \begin{bmatrix}\frac{1}{2}\Omega(\hat{\underline{\omega}}) & \vdots & 0_{4\times3}\\ \cdots\cdots & \cdots\cdots & \cdots\cdots\\ \frac{1}{2}I_b^{-1}\Xi^T(\hat{\underline{q}}) & \vdots & -[\hat{\underline{\omega}}\times] + I_b^{-1}[\underline{L}\times]\end{bmatrix}\begin{bmatrix}\underline{\lambda}_q(t)\\\underline{\lambda}_L(t)\end{bmatrix}, \qquad \underline{\lambda}_L(t_f) = \underline{0} \tag{37c}$$

with discrete jumps in the co-states given by

$$\underline{\lambda}_q\left(t_k^+\right)=\underline{\lambda}_q\left(t_k^-\right)+H^T\Big|_{t_k}\;R^{-1}\left\{\underline{\widetilde{B}}_B-A(\hat{q})\underline{B}_I\right\}\Big|_{t_k}, \qquad \underline{\lambda}_q\left(t_f^+\right)=\underline{0} \tag{38}$$

The TPBVP given by Equations (37) and (38) can be solved by using a simple gradient-based search technique.

Input Torque Estimation

In this section, the MME estimator is used to estimate model error torques using angular rate trajectories. These angular rate trajectories are assumed to be known (e.g., from finite differenced attitude estimates, or from angular rate estimates from an MME design or other estimator). First, a measured angular momentum vector is determined by

$$\underline{\widetilde{L}}=I_b\underline{\omega}+\underline{\widetilde{h}} \tag{39}$$

In general, the angular momentum measurements in Equation (39) will be noisy due to the angular velocity measurements of the wheel speed. However, this noise is inherently smoothed by the MME estimator. The MME problem for determining the errors in the torque input of Euler's equation minimizes the following cost function

$$J=\frac{1}{2}\sum_{k=1}^{m}\left\{\underline{\widetilde{L}}-\hat{\underline{L}}\right\}^T\Big|_{t_k}\;R^{-1}\left\{\underline{\widetilde{L}}-\hat{\underline{L}}\right\}\Big|_{t_k}+\frac{1}{2}\int_{t_0}^{t_f}\underline{d}^T(\tau)\,W\underline{d}(\tau)\,d\tau \tag{40}$$

subject to

$$\dot{\hat{\underline{L}}}(t)=-\left[\underline{\omega}(t)\times\right]\hat{\underline{L}}(t)+\underline{N}(t)+\underline{d}(t), \qquad \hat{\underline{L}}(t_0)=\hat{\underline{L}}_0 \tag{41}$$

Minimizing Equation (40) leads to the following TPBVP

$$\dot{\hat{\underline{L}}}(t)=-\left[\underline{\omega}(t)\times\right]\hat{\underline{L}}(t)+\underline{N}(t)-W^{-1}\underline{\lambda}(t), \qquad \hat{\underline{L}}(t_0)=\hat{\underline{L}}_0 \tag{42a}$$

$$\dot{\underline{\lambda}}(t)=-\left[\underline{\omega}(t)\times\right]\underline{\lambda}(t) \tag{42b}$$

$$\underline{\lambda}\left(t_k^+\right)=\underline{\lambda}\left(t_k^-\right)+R^{-1}\left\{\underline{\widetilde{L}}-\hat{\underline{L}}\right\}, \qquad \underline{\lambda}\left(t_f^+\right)=\underline{0} \tag{42c}$$

The solution to the TPBVP in Equation (42) can be determined by using a Riccati transformation [15]. Applying this technique leads to the following equations

$$\dot{P}(t)=P(t)\left[\underline{\omega}(t)\times\right]+P(t)W^{-1}P(t)+\left[\underline{\omega}(t)\times\right]P(t) \tag{43a}$$

$$P\left(t_k^-\right)=P\left(t_k^+\right)+R^{-1}, \qquad P\left(t_f^+\right)=0 \tag{43b}$$

$$\dot{\underline{h}}(t)=\left\{P(t)W^{-1}-\left[\underline{\omega}(t)\times\right]\right\}\underline{h}(t)-P(t)\underline{N}(t) \tag{43c}$$

$$\underline{h}\left(t_k^-\right)=\underline{h}\left(t_k^+\right)+R^{-1}\underline{\widetilde{L}}\Big|_{t_k}, \qquad \underline{h}\left(t_f^+\right)=\underline{0} \tag{43d}$$

146

$$\dot{\underline{\hat{L}}}(t) = \left\{ -[\underline{\omega}(t) \times] - W^{-1} P(t) \right\} \underline{\hat{L}}(t) - W^{-1} \underline{h}(t) + \underline{N}(t), \qquad \underline{\hat{L}}(t_0) = \underline{\hat{L}}_0 \qquad (43e)$$

Therefore, the first step is to solve for the Riccati and inhomogeneous trajectories backwards in time using Equations (43a) and (43c), accounting for discrete jumps by Equations (43b) and (43d). Then, the angular momentum estimates are determined by integrating Equation (43e) forwards in time.

Attitude Estimation of an Actual Spacecraft

In this section, the MME estimation algorithms previously developed are used to estimate the attitude, rate, and input torque trajectories of the SAMPEX spacecraft using vector measurement observations. The SAMPEX general mission is to study energetic particles and various types of rays. The spacecraft is three-axis stabilized in a 550 by 675 km elliptical orbit with an 82° inclination. The attitude control hardware consists of a magnetic torquer assembly (MTA) and a reaction wheel assembly (RWA). The attitude determination hardware consists of five coarse Sun sensors (CSS) (primarily for Sun-acquisition), one fine Sun sensor (FSS), and a three-axis magnetometer (TAM). Also, no rate gyroscopic instruments are present on the spacecraft.

The onboard computer routine to determine attitude is based upon the TRIAD [1] deterministic method. The spacecraft is controlled by the MTA to maintain the fixed solar arrays perpendicular to the sun-line. The RWA is used to point the instrument boresight axis as required by the scientific mission. During eclipse no sun measurements are available from the FSS. Attitude control is maintained by using a constant sun-line vector as a "pseudo-measurement," so that both the MTA and RWA are still utilized. During vector co-alignment, the spacecraft is placed in a "coast" mode in which the MTA is not used (see [16] for more details). The required nominal attitude determination accuracy is ±2°. During anomalous conditions (eclipse and/or measurement vector co-alignment) the attitude cannot be determined by deterministic methods, such as TRIAD. The MME algorithms presented in this paper can determine the attitude using TAM measurements only, so that attitude accuracy may be checked for any deviations from nominal performance.

The inertial field trajectories are obtained by using a 8th order spherical harmonic model of the Earth's magnetic field with International Geomagnetic Reference Field (IGRF) coefficients. Magnetometer measurements by the TAM are known to be extremely accurate (within 0.3 mG). However, experience has shown that errors in the magnetic field model have a standard deviation of about 3 mG [17]. Therefore, 9 mG^2 is chosen for the diagonal elements of the measurement covariance matrix.

The first test case involves using both TAM and FSS measurements. A plot of the finite differenced angular rates using TRIAD determined attitudes is shown in Figure 1. These rates are extremely noisy, which is due to the large digitization noise associated with the FSS measurements. The TRIAD determined rates are next used in the first MME formulation (with rate information), along with the TAM and FSS measurements. A plot of the MME estimated rates is shown in Figure 2. Clearly, these rates are smoother than the TRIAD determined rates. Next, the MME input torque estimator is applied using these estimated rates. A plot of the MME determined input torques is shown in Figure 3. These torques correspond to a correction to the dynamic model, so that the model responses match the vector measurement observations.

The second case involves using TAM measurements only to estimate the attitude and angular rates. The MME attitude estimator without rate measurements is used for this case. A plot of the estimated angular rate trajectories is shown in Figure 4. These angular rate estimates clearly show a rotation about the spacecraft's y-axis, which is the desired motion. A plot of the error between the estimated MME attitudes and the attitudes determined by TRIAD is shown in Figure 5. A slight hangoff is seen in the pitch axis. This may be due to nonlinear effects in the magnetic field model (this hangoff is also seen in Kalman filter approaches for other spacecraft such as UARS). However, the MME algorithm is able to determine attitudes to within 0.3° using TAM data only. This can be useful in determining the attitude when deterministic methods fail.

Conclusions

In this paper, several MME algorithms were presented for use in attitude estimation using vector measurement observations. The first algorithm used angular rate measurements to determine attitude estimate trajectories. The second algorithm estimated the attitude trajectories without any rate measurement information. The third algorithm determined the required torque input trajectories so that the model responses match the vector observations. An advantage of all of these algorithms is that quaternion normalization was maintained, since linearization of the dynamic model was not needed. The MME-based algorithms were then applied to an actual spacecraft. Results indicated that an MME-based approach provides a robust algorithm which can be used to determine the attitude, rate, and modeling error torque trajectories of a spacecraft from vector measurements.

Acknowledgments

References

[1] Lerner, G.M., "Three-Axis Attitude Determination," *Spacecraft Attitude Determination and Control*, edited by J.R. Wertz, D. Reidel Publishing Co., Dordrecht, The Netherlands, 1978, pp. 420-428.

[2] Shuster, M.D., and Oh, S.D., "Attitude Determination from Vector Observations," *Journal of Guidance and Control*, Vol. 4, No. 1, Jan.-Feb. 1981, pp. 70-77.

[3] Markley, F.L., "Attitude Determination from Vector Observations: A Fast Optimal Matrix Algorithm," *The Journal of the Astronautical Sciences*, Vol. 41, No. 2, April-June 1993, pp. 261-280.

[4] Wahba, G., "A Least-Squares Estimate of Satellite Attitude," Problem 65-1, *SIAM Review*, Vol. 7, No. 3, July 1965, pg. 409.

[5] Kalman, R.E., "A New Approach to Linear Filtering and Prediction Problems," *Transactions of the ASME, Journal of Basic Engineering*, Vol. 82, March 1962, pp. 34-45.

[6] Gelb, A., *Applied Optimal Estimation*, MIT Press, Cambridge, Mass., 1974.

[7] Lefferts, E.J., Markley, F.L., and Shuster, M.D., "Kalman Filtering for Spacecraft Attitude Estimation," *Journal of Guidance, Control and Dynamics*, Vol. 5, No. 5, Sept.-Oct. 1982, pp. 417-429.

[8] Challa, M.S., Natanson, G.A., Baker, D.E., and Deutschmann, J.K., "Advantages of Estimating Rate Corrections During Dynamic Propagation of Spacecraft Rates-Applications to Real-Time Attitude Determination of SAMPEX," *Proceedings of the Flight Mechanics/Estimation Theory Symposium*, NASA-Goddard Space Flight Center, Greenbelt, MD, 1994, pp. 481-495.

[9] Mook, D.J., and Junkins, J.L., "Minimum Model Error Estimation for Poorly Modeled Dynamic Systems," *Journal of Guidance, Control and Dynamics*, Vol. 3, No. 4, Jan.-Feb. 1988, pp. 367-375.

[10] Stry, G.I., and Mook, D.J., "An Analog Experimental Study of Nonlinear Identification," *Nonlinear Dynamics*, Vol. 3, No. 1, pp. 1-11.

[11] McPartland, M.D., and Mook, D.J., "Nonlinear Model Identification of Electrically Stimulated Muscle," *Proceedings of the IFAC Symposium on Modeling and Control in Biomedical Engineering*, Galveston, TX, March 1994, pp. 23-24.

[12] DePena, J., Crassidis, J.L., McPartland, M.D., Meyer, T.J., and Mook, D.J., "MME-Based Attitude Dynamics Identification and Estimation for SAMPEX," *Proceedings of the Flight Mechanics/Estimation Theory Symposium*, NASA-Goddard Space Flight Center, Greenbelt, MD, 1994, pp. 497-512.

[13] Markley, F.L., "Equations of Motion," *Spacecraft Attitude Determination and Control*, edited by J.R. Wertz, D. Reidel Publishing Co., Dordrecht, The Netherlands, 1978, pp. 510-523.

[14] Freund, J.E., and Walpole, R.E., *Mathematical Statistics*, Prentice-Hall Inc., Englewood, NJ, 1987.

[15] Crassidis, J.L., Mason, P.A.C., and Mook, D.J., "Riccati Solution for the Minimum Model Error Algorithm," *Journal of Guidance, Control and Dynamics*, Vol. 16, No. 6, Nov.-Dec. 1993, pp. 1181-1183.

[16] Flatley, T.W., Forden, J.K., Henretty, D.A., Lightsey, E.G., and Markley, F.L., "On-board Attitude Determination and Control for SAMPEX," *Proceedings of the Flight Mechanics/Estimation Theory Symposium*, NASA-Goddard Space Flight Center, Greenbelt, MD, 1990, pp. 379-398.

[17] Challa, M.S., *Solar, Anomalous, and Magnetospheric Particle Explorer (SAMPEX) Real-Time Sequential Filter (RTSF)*, Evaluation Report, NASA-Goddard Space Flight Center, Greenbelt, MD, April 1993.
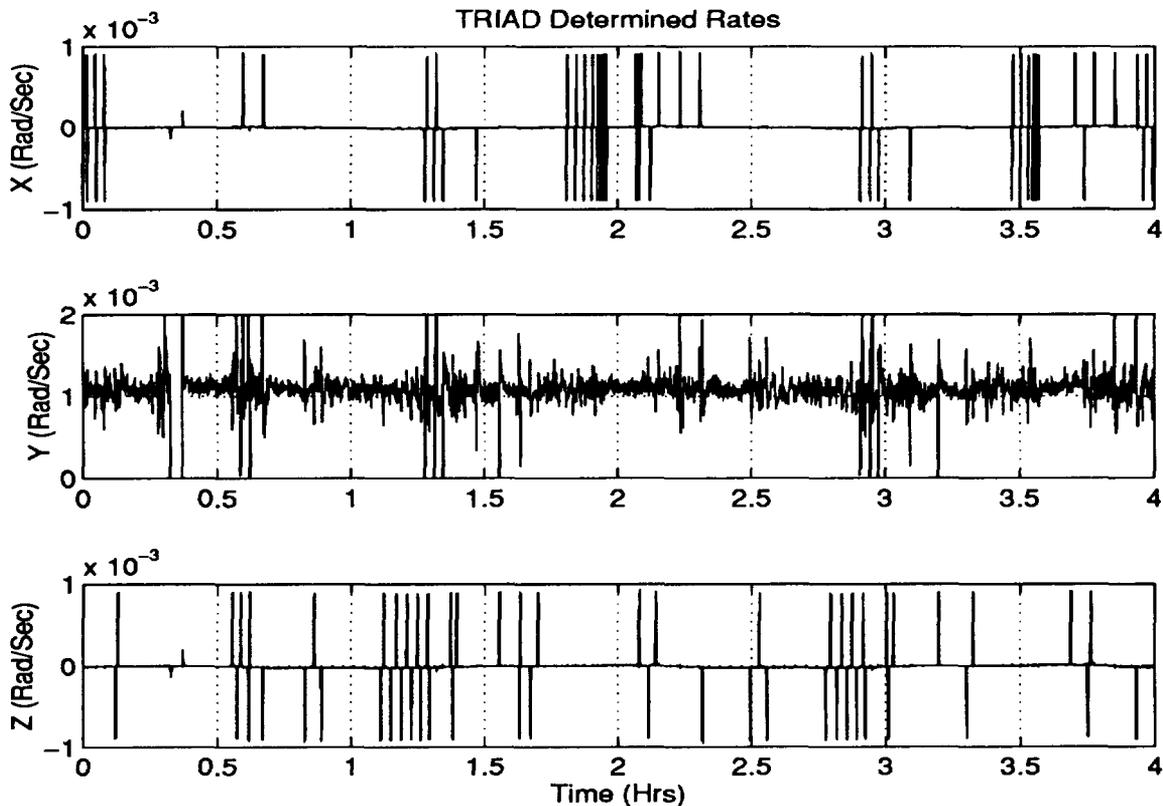
Figure 1 Plot of TRIAD Determined Attitude Rates
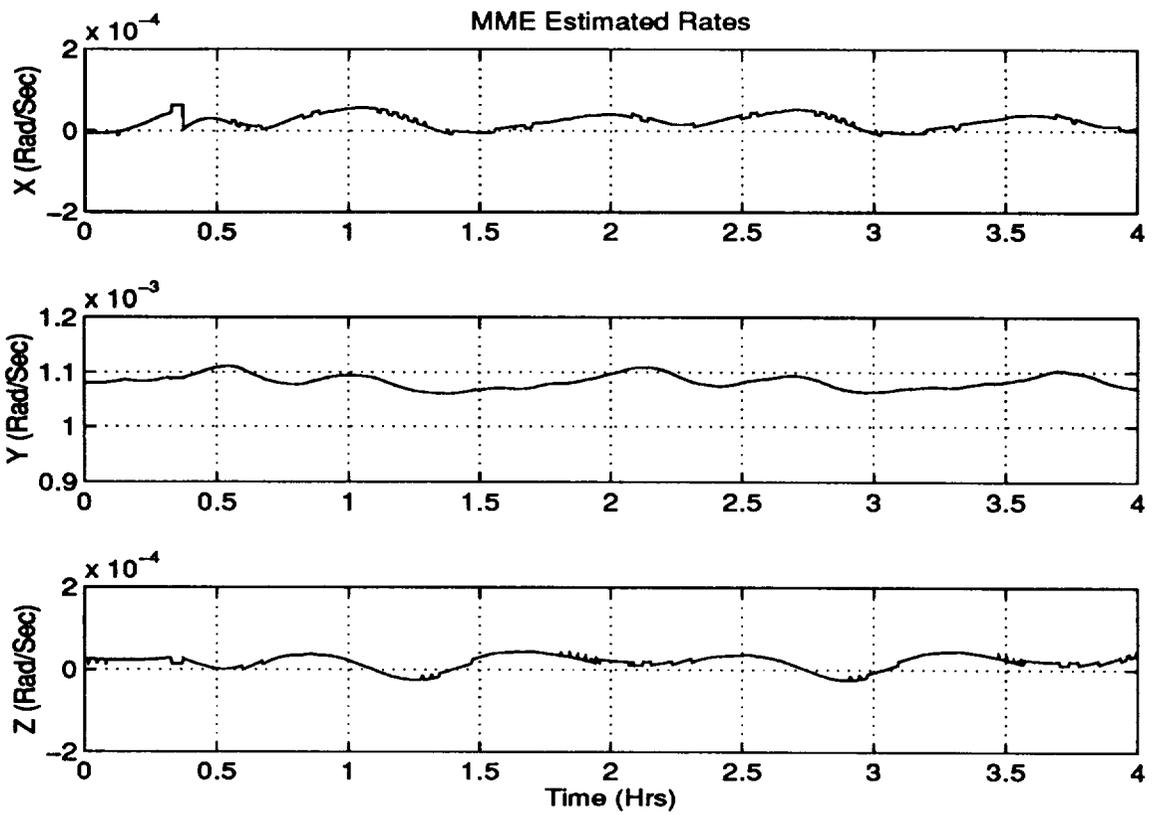
Figure 2 Plot of MME Estimated Rates
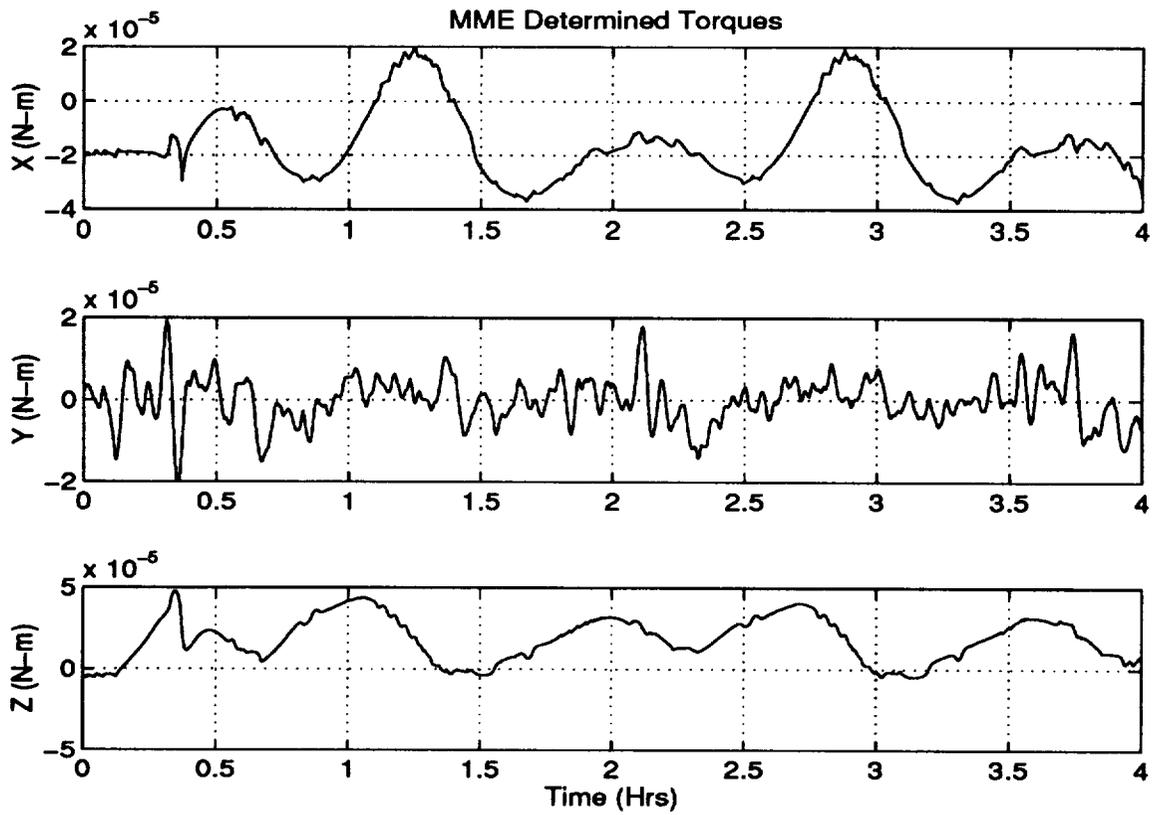
Figure 3 Plot of MME Determined Input Torques
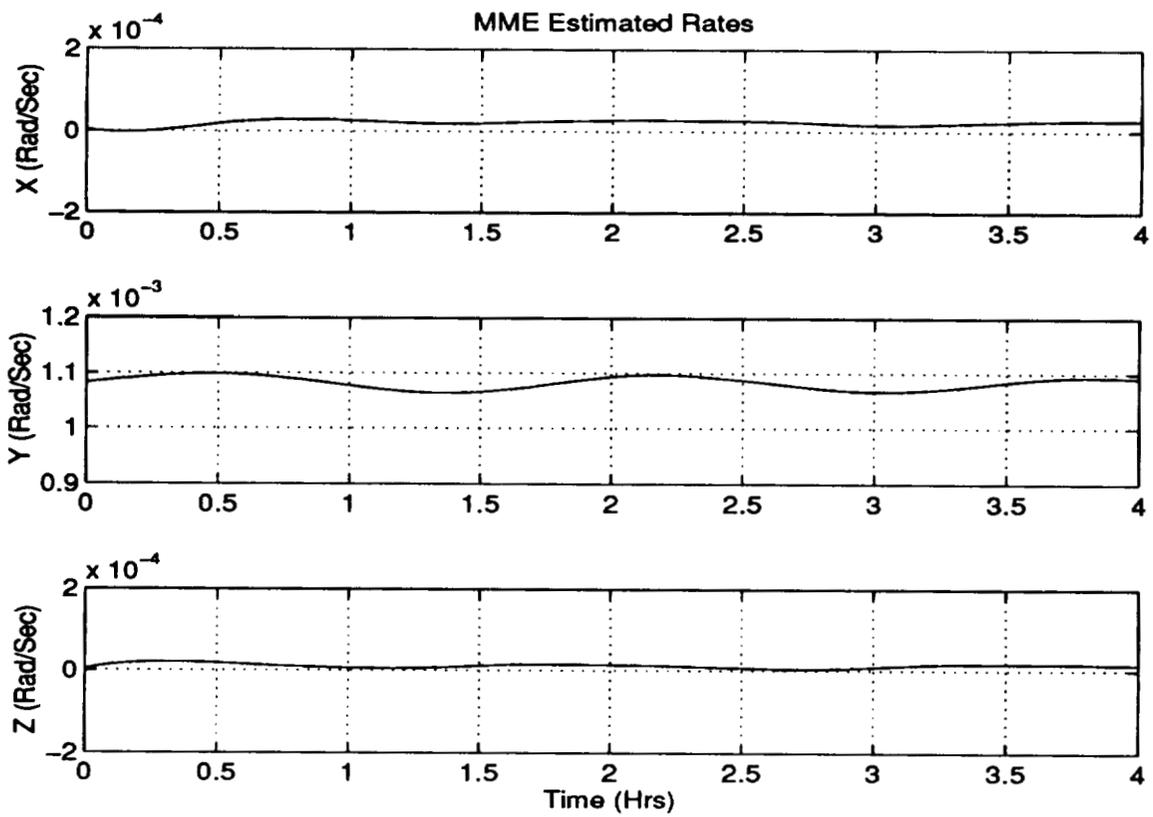
Figure 4 Plot of MME Estimated Rates Using TAM Data Only
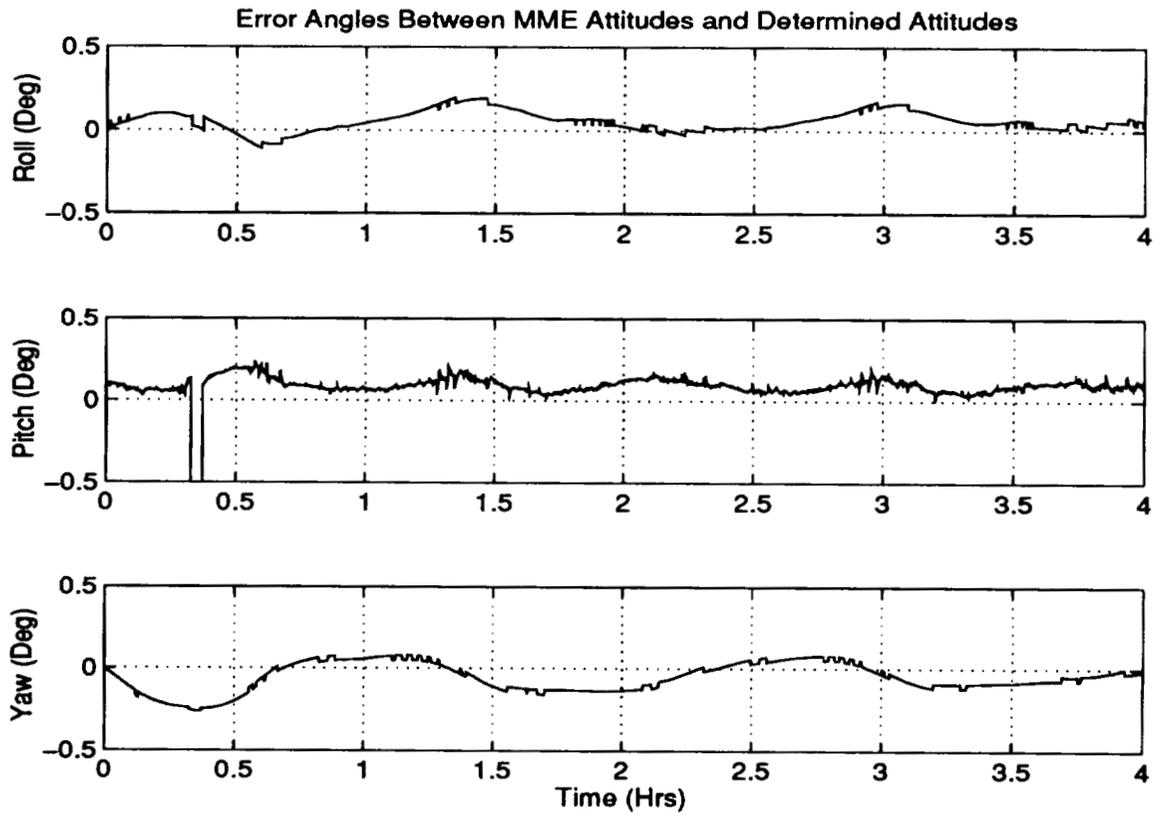
Figure 5 Plot of Attitude Errors Between TRIAD and MME

Post Kalman Progress

David Sonnabend*

Abstract

In a paper here last year, [2], an idea was put forward that much greater performance could be obtained from an observer, relative to a Kalman filter, if more general performance indices were adopted, and the full power spectra of all the noises were employed. Considerable progress since then is reported here. Included are an extension of the theory to regulators, direct calculation of the theory's fundamental quantities — the noise effect integrals — for several theoretical spectra, and direct derivations of the Riccati equations of LQG and Kalman theory yielding new insights.

1 Notation

Uppercase bold roman letters are 2 dimensional arrays; e.g., $\mathbf{F}$. Lowercase bold roman or greek letters are column vectors; e.g., $\mathbf{x}$. Lowercase greek subscripts are indices. Overdots signify time derivatives; e.g., $\dot{x} = dx/dt$. A T superscript denotes transpose. Overbars signify mean values; e.g., $\overline{w}$. Underbars denote random processes with the bias, if any, removed; e.g., $\underline{\mathbf{w}}(t) = \mathbf{w}(t) - \overline{\mathbf{w}}$. Hats indicate estimates; e.g., $\hat{x}$. Sines and cosines are denoted by s and c respectively.

$\mathbf{B} = n \times w$ process noise state distribution matrix
$c_t =$ state or estimation error settling time concern level
$\mathbf{C} = n \times n$ matrix of white noise Lyapunov constraints
$\mathbf{F} = n \times n$ plant matrix
$\mathbf{g}(\mathbf{u}) =$ general controls distribution function
$\mathbf{G} = n \times u$ controls distribution matrix
$h(t) =$ impulse response function
$\mathbf{H} = z \times n$ measurement partials matrix
$\mathcal{H} =$ variational Hamiltonian
$\mathbf{I} = n \times n$ identity matrix
$J =$ overall performance index
$J_t =$ settling time performance index
$\mathbf{K} = n \times z$ observer feedback gain matrix
$\mathbf{L} = u \times n$ regulator feedback gain matrix
$m =$ order of a Butterworth filter or noise source
$\underline{\mathbf{M}} = n \times n$ matrix used in the calculation of $\mathbf{P}_x$
$n =$ number of elements in the state vector $\mathbf{x}(t)$
$\mathbf{N} =$ solution of Lyapunov equation
$\mathbf{P}_x = n \times n$ covariance matrix of $\mathbf{x}(t)$
$\mathbf{P}_\epsilon = n \times n$ covariance matrix of $\epsilon(t)$
$\mathbf{Q}(\omega) = n \times n$ combined noise matrix
$\overline{R}_w(0) =$ average power of $\mathbf{w}(t)$
$\Re(x) =$ real part of x
$\mathbf{S}_v(\omega) = v \times v$ power spectral density of $\mathbf{v}(t)$
$\mathbf{S}_w(\omega) = w \times w$ power spectral density of $\mathbf{w}(t)$
$t =$ time, or more generally, independent variable in state equations
$t_s =$ settling time of regulator or observer
$\text{Tr}\,[\mathbf{P}] =$ trace of $\mathbf{P}$
$u =$ number of elements in the control vector $\mathbf{u}(t)$
$\mathbf{u}(t) = u$ element vector of controls

---

*President, Analytical Engineering Co., Boulder, CO, 303-530-9641

$\mathbf{U} = u \times u$ controls weighting matrix

v = number of elements in measurement noise vector $\mathbf{v}(t)$

$\mathbf{v}(t) = v$ element measurement noise vector

$\mathbf{V} = z \times v$ measurement noise distribution matrix

w = number of elements in the process noise vector $\mathbf{w}(t)$

$\mathbf{w}(t) = w$ element process noise vector

$\mathbf{W} = z \times w$ process noise cross distribution matrix

$\mathbf{x}(t) = n$ element state vector

$\mathbf{X} = n \times n$ state weighting matrix

$\mathbf{Y} = n \times w$ observer process noise effect matrix

z = number of elements in the measurement vector $\mathbf{z}(t)$

$\mathbf{z}(t) = z$ element measurement vector

$\mathbf{Z} = n \times n$ system matrix

$\mathbf{0}$ = zero vector or matrix

$\mathbf{\Gamma} = z \times z$ combined measurement noise matrix

δ_k^j = Kronecker delta ($=1$ if $j = k$; $=0$ otherwise)

$\boldsymbol{\delta}(t) = z$ element measurement residuals vector

$\boldsymbol{\epsilon}(t) = n$ element estimation error vector

$\mathbf{\Theta} = n \times n$ combined weighting matrix

λ = eigenvalue of $\mathbf{Z}$

$\mathbf{\Lambda} = n \times n$ matrix of Lagrange multipliers

$\mathbf{\Xi} = n \times n$ estimate error weighting matrix

$\mathbf{\Phi} = n \times n$ noise effect integral

ω = angular frequency

ω_c = break frequency of noise spectrum

ω_h = half power frequency of noise spectrum

2 Regulator and Observer Structure

Throughout this paper, I'll be dealing with systems specified by an n element state vector $\mathbf{x}(t)$, obeying a set of 1st order ordinary differential equations. I'll assume that, after some suitable linearization, these may be written:

$$\dot{\mathbf{x}}(t) = \mathbf{F}\mathbf{x}(t) + \mathbf{g}[\mathbf{u}(t)] + \mathbf{B}\mathbf{w}(t) \tag{1}$$

Here, $\mathbf{u}(t)$ is a u element control vector, and $\mathbf{w}(t)$ is a w element process noise vector. Each element $w_j(t)$ is regarded as stationary, and described by the power spectral density $S_{wj}(\omega)$, where ω is angular frequency. Also, $\mathbf{F}$ is the "plant" matrix, and $\mathbf{W}$ is the process noise distribution matrix, both regarded as independent of time. While some $w_j(t)$ might affect more than 1 state equation, $\mathbf{W}$ is constructed so that all the $w_j(t)$ are statistically independent. Finally, the possibly nonlinear $\mathbf{g}[\mathbf{u}(t)]$ expresses the effect of the controls on the state.

In a linear proportional regulator, where the intent is to hold $\mathbf{x}(t)$ close to zero, in spite of $\mathbf{w}(t)$, we take

$$\mathbf{g}[\mathbf{u}(t)] = \mathbf{G}\mathbf{u}(t) \tag{2}$$

for some fixed $n \times u$ matrix $\mathbf{G}$; and then let

$$\mathbf{u}(t) = -\mathbf{L}\mathbf{x}(t) \tag{3}$$

for some fixed $u \times n$ matrix $\mathbf{L}$. When these relations are substituted into (1) there follows:

$$\dot{\mathbf{x}}(t) = \mathbf{Z}\mathbf{x}(t) + \mathbf{B}\mathbf{w}(t) \tag{4}$$

where

$$\mathbf{Z} \equiv \mathbf{F} - \mathbf{G}\mathbf{L} \tag{5}$$

I shall refer to the $n \times n$ matrix $\mathbf{Z}$ as the regulator system matrix. It will reappear in another guise in observer theory below. The next section will deal with new methods for choosing the feedback gain

matrix **L**, and how to calculate the performance. As a 1st application, Linear Quadratic Gaussian theory (LQG) is derivable from this more general theory. A sketch of the proof is given in Section 5.

Turning now to observers, suppose a system is described by the state equations (1). We wish to determine the current value of $\mathbf{x}(t)$ by the use of these, supported by some set of measurements $\mathbf{z}(t)$. Suppose further, that after some suitable linearization, these measurements are described by the model

$$\mathbf{z}(t) = \mathbf{z}_B + \mathbf{Hx}(t) + \mathbf{Vv}(t) + \mathbf{Ww}(t) \tag{6}$$

a z element vector. The 1st term on the right is the assumed known bias in the measurements, partly due to undesired offsets in the instrument, and partly from the linearization. Next, the assumed fixed $z \times n$ matrix **H** comes from the linearization, and is known in estimation lingo as the "measurement partials".

The measurements are assumed to be contaminated by some set of v statistically stationary noises $\mathbf{v}(t)$. Like the process noise $\mathbf{w}(t)$, a fixed $z \times v$ distribution matrix **V** is introduced to insure that all the $v_k(t)$ are independent. As it sometimes happens that measurements are also contaminated by the process noise, I have included such a term, with an appropriate distribution matrix **W**. It was required in [2]; however, in most practical cases the term can be omitted; still, its presence leads to an interesting generalization.

An observer based on these plant and measurement models starts with an estimate $\hat{\mathbf{x}}(t)$ of $\mathbf{x}(t)$. This is generated by a computer simulation of the deterministic parts of the plant equations (1), corrected as follows by the measurements:

$$\dot{\hat{\mathbf{x}}}(t) = \mathbf{F\hat{x}}(t) + \mathbf{g}[\mathbf{u}(t)] + \mathbf{B\overline{w}} + \mathbf{K}\delta(t) \tag{7}$$

where what estimation types like to call the "residuals" are defined by:

$$\delta(t) = \mathbf{z}(t) - \mathbf{z}_B - \mathbf{H\hat{x}}(t) - \mathbf{V\overline{v}} - \mathbf{W\overline{w}} \tag{8}$$

that is, the difference between the actual measurements $\mathbf{z}(t)$ and their reconstruction in the computer. Here, the biases $\overline{\mathbf{w}}$ and $\overline{\mathbf{v}}$ in the noises are assumed known. The $n \times z$ feedback gain matrix **K** is named for Kalman; but in the more general theory in Section 4, it's not derived with the Kalman filter assumptions.

On introducing the error in the estimate:

$$\epsilon(t) \equiv \hat{\mathbf{x}}(t) - \mathbf{x}(t) \tag{9}$$

the residuals (8) may be rewritten as

$$\delta(t) = \mathbf{V}\underline{\mathbf{v}}(t) + \mathbf{W}\underline{\mathbf{w}}(t) - \mathbf{H}\epsilon(t) \tag{10}$$

When this is substituted into (7), and the plant equations (1) are subtracted, there results:

$$\dot{\epsilon}(t) = \mathbf{Z}\epsilon(t) + \mathbf{KV}\underline{\mathbf{v}}(t) + \mathbf{Y}\underline{\mathbf{w}}(t) \tag{11}$$

in which

$$\mathbf{Z} \equiv \mathbf{F} - \mathbf{KH} \quad ; \quad \mathbf{Y} \equiv \mathbf{KW} - \mathbf{B} \tag{12}$$

I will call the $n \times n$ matrix **Z** the observer system matrix, in order to stress the similarity of (11) to the regulator behavior (4). Indeed, one may regard this observer as a regulator, whose intent is to force the observation error $\epsilon(t)$ close to zero, in spite of all the noises. Observer performance when subject to arbitrary noise is discussed in Section 6; and the specialization to the now obsolete Kalman theory in Section 7.

A few observations. In either of these systems, it must be possible to choose the feedback gain (**L** or **K**) such that $\mathbf{Z} < \mathbf{0}$ (negative definite). If this isn't possible, then either (4) or (11) will diverge, and the system is said to be uncontrollable or unobservable. In what follows, I'll always assume that such a choice is possible.

155

The theory presented here got started about 5 years ago, when W. M. McEneaney, in unpublished notes, demonstrated that the terminal covariance of $\epsilon(t)$ in a Kalman filter could be calculated directly, if everything was stationary, without integrating any differential equations. The idea was extended to regulators, and to arbitrary noise power spectra, in [1]. Several other papers on the subject have been written, culminating in last year's paper here, [2]. A book [3], examining the subject in much greater depth, and containing all the proofs, is now nearing completion.

3 Regulator Performance

In the above regulator, with statistically stationary noise, initial transients will die out, and the statistics of $\mathbf{x}(t)$ will tend to asymptotic values. Of these, the mean and the covariance are the most important. I'll sketch the results to date of the new theory; but page limits prevent my giving the proofs, or much discussion. Following that, I'll discuss a more general performance index than is usually seen in regulator design.

Starting with the mean, if expectation is applied to (4), then after settling:

$$\overline{\mathbf{x}} = -\mathbf{Z}^{-1}\mathbf{B}\overline{\mathbf{w}} \tag{13}$$

where, since $\mathbf{Z} < \mathbf{0}$, it's non–singular. Thus, $\mathbf{x}(t)$ has a bias if and only if $\mathbf{w}(t)$ has one.

As for the covariance, since (4) is linear, it has a solution for $\mathbf{x}(t)$ in terms of an integral over $\mathbf{w}(t)$. From this, the outer product of $\mathbf{x}(t)$ with itself may be constructed as a double integral, and the expectation applied, leading by and by to an expression for the terminal covariance $\mathbf{P}_x$ of $\mathbf{x}(t)$, in terms of a double integral over the autocovariance of $\mathbf{w}(t)$. On applying a Fourier transformation, the expression is converted to the frequency domain, and after working through another page of dense algebra, this general result emerges:

$$\mathbf{P}_x = \int_0^\infty \left[\left(\mathbf{Z} + \omega^2\mathbf{Z}^{-1}\right)^{-1}\underline{\mathbf{N}}(\omega) + \underline{\mathbf{N}}(\omega)\left(\mathbf{Z}^T + \omega^2\mathbf{Z}^{-T}\right)^{-1} \right] d\omega \tag{14}$$

where $\underline{\mathbf{N}}(\omega)$ is the solution of the Lyapunov equation

$$\mathbf{Z}\underline{\mathbf{N}}(\omega) + \underline{\mathbf{N}}(\omega)\mathbf{Z}^T = \mathbf{B}\underline{\mathbf{S}}_w(\omega)\mathbf{B}^T \equiv \underline{\mathbf{Q}}(\omega) \tag{15}$$

Here, $\underline{\mathbf{S}}_w(\omega)$ is a diagonal matrix, whose non–zero element $\underline{S}_{wjj}(\omega)$ is the one sided power spectral density of $\underline{w}_j(t)$. Also, the normalization of the Fourier transform is such that the average power in $\underline{w}_j(t)$ is

$$R_{wj}(0) = \int_0^\infty \underline{S}_{wjj}(\omega)d\omega \tag{16}$$

Thus, for a given gain $\mathbf{L}$, $\mathbf{Z}$ is calculated from (5). Then $\underline{\mathbf{N}}(\omega)$ is determined by by solving (15) for each of a dense set of ω values; after which $\mathbf{P}_x$ is obtained by the numerical integration of (14). Tedious, but at least all the $\underline{S}_{wjj}(\omega)$ vanish above some finite ω, for any practical spectra.

This was the status of the theory in the earlier papers. Since then, a dramatic improvement in this procedure has been found. By construction from (14) it is easy to show that $\mathbf{P}_x$ obeys its own Lyapunov equation:

$$\mathbf{Z}\mathbf{P}_x + \mathbf{P}_x\mathbf{Z}^T = \underline{\mathbf{M}} + \underline{\mathbf{M}}^T \tag{17}$$

where

$$\underline{\mathbf{M}} = \sum_{j=1}^w \mathbf{\Phi}_j\mathbf{B}_j\mathbf{B}_j^T \tag{18}$$

Here, $\mathbf{B}_j$ is the jth column of $\mathbf{B}$, and

$$\mathbf{\Phi}_j \equiv \int_0^\infty \left(\mathbf{Z} + \omega^2\mathbf{Z}^{-1}\right)^{-1}\underline{S}_{wjj}(\omega)d\omega \tag{19}$$

I have called these quantities the noise effect integrals. The current progress in determining these for several theoretical spectra is given in Sections 4 and 8. Note that, while numerical integration may still be needed to find some $\mathbf{\Phi}_j$, there is now only one Lyapunov equation to solve to get $\mathbf{P}_x$.

In modern control theory, as applied to regulators, it's common to measure performance by a linear–quadratic index as follows:

$$J = \mathrm{Tr}\,[(\mathbf{X} + \mathbf{L}^T\mathbf{U}\mathbf{L})(\mathbf{P}_x + \bar{\mathbf{x}}\,\bar{\mathbf{x}}^T)] \tag{20}$$

Here, $\mathbf{X}$ is a weighting matrix, intended to express dislike for each of the elements $x_j(t)$. In a practical weighting scheme we require both $\mathbf{X} > 0$, and that it be symmetric. In "Bryson weighting", $\mathbf{X}$ is diagonal, and each X_{jj} is the inverse square of the level of $x_j(t)$ that would cause a given amount of pain. Similarly, $\mathbf{U}$ is a weighting matrix, intended to express dislike for the use of controls. If it's obtained by Bryson weighting, the diagonal element U_{kk} is the inverse square of the level of $u_k(t)$ that would cause the same amount of pain. Note that J is dimensionless, if it's constructed in this way. Overall, if you believe that this J truly expresses your desires in the design of your regulator, then it only remains to find that value of the gain $\mathbf{L}$ that yields minimum J. I'll not get into the derivation of (20), as it's given in most books on the subject.

While most theoretical work tends to rely on some variation of (20), there are other issues the designer must face. Perhaps most important is settling time; i.e., the time for the regulator to recover from arbitrary initial conditions, or unmodeled disturbances. In the system (4), settling consists of the behavior of n modes, each of which settles exponentially according to the eigenvalues of $\mathbf{Z}$. More precisely, if some eigenvalue is $\lambda = \sigma + i\rho$, then the settling time of the corresponding mode is $-1/\sigma$ (all $\sigma < 0$); and the overall settling time t_s is the largest of these.

In the improved theory, concern for settling time is dealt with by adding some function of t_s to J. I have used t_s/c_t, where c_t is the time that yields the same level of pain used in the state and control weightings. However, a case could be made for using the square of this instead, or perhaps the sum of such terms for each eigenvalue. In any case, the added term doesn't depend on the noise, only the choice of $\mathbf{L}$.

4   White, Colored, & Butterworth Noise

In this section I'll begin the analysis of the noise effect integrals $\boldsymbol{\Phi}$, treating those cases where $S(\omega)$ doesn't vanish above some finite ω. The simplest of these is "white" noise, for which $S(\omega) = S$. Note that, by this definition, white noise can't have a bias, as this would imply an infinite spike at $\omega = 0$. Some readers may have heard me fulminate against this stuff before; here I'll confine my antipathy to pointing out that any such process would have to contain infinite power, for which our universe lacks the resources. Still, the assumption that all noises are white has led to the enormous practical simplifications of LQG and Kalman theory, to where white noise has acquired a sort of mystical reality. It's my hope that papers such as this will convince readers that the promise of better performance outweighs mathematical and numerical simplicity.

Enough fulmination. An involved argument based on an eigensystem decomposition of $\mathbf{Z}$ leads to a set of scalar arctangent integrals. Reconstruction then yields

$$\boldsymbol{\Phi} = -(\pi/2)S\mathbf{I} \tag{21}$$

where $\mathbf{I}$ is the $n \times n$ identity matrix. Observe that this result appears to be independent of $\mathbf{Z}$, a property not possessed by any other $S(\omega)$ I've looked at. This is the root cause of the simplifications of LQG and Kalman theory. Not quite independent — the analysis depends critically on $\mathbf{Z} < 0$. For the reader interested in verifying this result, caution: of the half dozen or so references on my shelf listing arctangent expansions, none were completely correct.

Next, colored noise. Some in the field regard any non–white noise as colored; but most accept the definition of a colored noise $u(t)$ as obeying

$$\dot{u}(t) = \omega_c[w(t) - u(t)] \tag{22}$$

where $w(t)$ is white, and ω_c is the "break" frequency. The power spectrum of such a process may be shown to be

$$S(\omega) = \frac{2R(0)\omega_c}{\pi(\omega^2 + \omega_c^2)} \tag{23}$$

157

where $R(0)$ is the average power. Physically, $u(t)$ is the result of passing white noise through a 1st order linear filter, whose break frequency is ω_c. I've never seen such a spectrum, and I doubt that you have; its utility comes from a well known technique, in which (22) is appended to the plant equations, when the white noise source is included in either the process or measurement noises, as needed. As the new ideas don't require this artifice, I'll not discuss it further. Properties of colored noise are that $S(\omega_c) = S(0)/2$, and that half of the total power is in the "tail", i.e., in the region $\omega_c \leq \omega \leq \infty$.

If (23) is substituted into (19), a sort of partial fractions expansion causes the white noise integral above to surface, leading to

$$\boldsymbol{\Phi} = R(0)\left(\mathbf{Z} - \omega_c \mathbf{I}\right)^{-1} \tag{24}$$

So long as $\mathbf{Z} < \mathbf{0}$, the matrix on the right is non-singular, and this formula is a big improvement over infinite numerical integration.

Since real noises generally roll off much faster than colored noise, I have introduced a generalization I've called "Butterworth" noise. It is the result of passing white noise through an m pole low pass Butterworth filter. The power spectrum of such a process may be shown to be:

$$S_m(\omega) = \frac{2m}{\pi\omega_c}\mathrm{s}\left(\frac{\pi}{2m}\right)R(0)\left[1 + \left(\frac{\omega}{\omega_c}\right)^{2m}\right]^{-1} \tag{25}$$

Since (25) reduces to (23) for $m = 1$, colored noise might be referred to as 1 pole Butterworth noise. The property $S(\omega_c) = S(0)/2$ continues to hold for all m; but the fraction of the total power in the tail drops rapidly with increasing m; e.g., 0.21945 for $m = 2$, and .098931 for $m = 4$. As a practical matter, instruments troubled by broad band noise frequently have Butterworth circuits added prior to digitization, to avoid "aliasing". The resulting spectrum tends to look rather like (25), with ω_c chosen well below the sampling frequency. If this sounds like your situation, then $m = 4$ is what you are most likely to encounter, as it has a straightforward implementation by a circuit comprising 2 operational amplifiers.

If (25) is substituted into (19), the same technique used for colored noise works, yielding an analytic solution good for all m:

$$\boldsymbol{\Phi}_m = \omega_c^{2m}\mathrm{s}\left(\frac{\pi}{2m}\right)R(0)\left[\omega_c^{2m}\mathbf{I} + (-1)^m\mathbf{Z}^{2m}\right]^{-1}$$
$$\left\{\sum_{j=1}^{m}(-1)^j\omega_c^{-2j}\mathbf{Z}^{2j-1}\csc\left[\frac{\pi(2m - 2j + 1)}{2m}\right] - \frac{m}{\omega_c}\mathbf{I}\right\} \tag{26}$$

It's not hard to show that this reduces to the colored noise effect integral (24) for $m = 1$. As for more poles, I'll tabulate the next few:

$$\boldsymbol{\Phi}_2 = R(0)\left(\mathbf{Z}^3 - \omega_c^2\mathbf{Z} - \sqrt{2}\omega_c^3\mathbf{I}\right)\left(\mathbf{Z}^4 + \omega_c^4\mathbf{I}\right)^{-1} \tag{27}$$

$$\boldsymbol{\Phi}_3 = \frac{1}{2}R(0)\left(2\mathbf{Z}^5 - \omega_c^2\mathbf{Z}^3 + 2\omega_c^4\mathbf{Z} + 3\omega_c^5\mathbf{I}\right)\left(\mathbf{Z}^6 - \omega_c^6\mathbf{I}\right)^{-1}$$
$$= R(0)\left(\mathbf{Z}^2 - 2\omega_c\mathbf{Z} + \frac{3}{2}\omega_c^2\mathbf{I}\right)\left(\mathbf{Z} - \omega_c\mathbf{I}\right)^{-1}\left(\mathbf{Z}^2 - \omega_c\mathbf{Z} + \omega_c^2\mathbf{I}\right)^{-1} \tag{28}$$

$$\boldsymbol{\Phi}_4 = R(0)\left[\mathbf{Z}^7 - k_1\omega_c^2\mathbf{Z}^5 + k_1\omega_c^4\mathbf{Z}^3 - \omega_c^6\mathbf{Z} - k_2\omega_c^7\mathbf{I}\right]\left(\mathbf{Z}^8 + \omega_c^8\mathbf{I}\right)^{-1} \tag{29}$$

where

$$k_1 = \sqrt{2} - 1 = 0.4142135624 \quad ; \quad k_2 = 2\sqrt{2 - \sqrt{2}} = 1.5307337295$$

Additional results for $m \leq 8$ will appear in [3].

5 LQG Theory

While I have railed against white noise above, it is the foundation of the popular Linear–Quadratic–Gaussian method of designing some kinds of control systems. For a regulator, the assumptions are that all the noise is white and has a Gaussian probability density, and that we wish to choose the feedback gain **L** to minimize the performance index (20). I'll show how the main results of LQG theory for regulators may be derived from the new theory. As will be seen, no use is made of the Gaussian assumption, showing that it's irrelevant in this context.

To begin, if the noise is all white, then $\mathbf{Q}(\omega)$ is independent of ω in (15); so this must also be true of $\underline{\mathbf{N}}(\omega)$. Thus, (14) is reduced to a pair of terms involving the white noise effect integral (21), from which $\mathbf{P}_x = -\pi\underline{\mathbf{N}}$; and on substituting this back into (15) we have:

$$\mathbf{C} \equiv \mathbf{Z}\mathbf{P}_x + \mathbf{P}_x\mathbf{Z}^T + \pi\underline{\mathbf{Q}} = 0 \tag{30}$$

This set of constraints must be enforced while minimizing J. To do this I'll introduce the variational Hamiltonian

$$\mathcal{H}(\mathbf{P}_x, \mathbf{L}, \mathbf{\Lambda}) = \mathrm{Tr}\left[\mathbf{\Theta}\mathbf{P}_x + \mathbf{\Lambda}\mathbf{C}\right] \tag{31}$$

where $\mathbf{\Lambda}$ is a symmetrical matrix of Lagrange multipliers, and the last term is really the sum over the direct product of $\mathbf{\Lambda}$ and $\mathbf{C}$. Also

$$\mathbf{\Theta} \equiv \mathbf{X} + \mathbf{L}^T\mathbf{U}\mathbf{L} \tag{32}$$

and, from (13), the $\bar{\mathbf{x}}$ term has disappeared, because white noise by definition has no bias.

When formulated in this way, the necessary conditions for a minimum are that $\mathcal{H}(\mathbf{P}_x, \mathbf{L}, \mathbf{\Lambda})$ be stationary, relative to variations in $\mathbf{P}_x$ and $\mathbf{L}$. It's not hard to show that the 1st set of conditions leads to another Lyapunov relation

$$\mathbf{\Theta} + \mathbf{\Lambda}\mathbf{Z} + \mathbf{Z}^T\mathbf{\Lambda} = 0 \tag{33}$$

from which it may be shown that $\mathbf{\Lambda} > 0$, and is thus non–singular. The other necessary condition leads to

$$\mathbf{L} = \mathbf{U}^{-1}\mathbf{G}^T\mathbf{\Lambda} \tag{34}$$

and we see why it was important to make **U** non–singular. It only remains to expand $\mathbf{\Theta}$ and $\mathbf{Z}$ in (33), and eliminate **L** with (34). After cancelling terms, we are left with

$$\mathbf{\Lambda}\mathbf{G}\mathbf{U}^{-1}\mathbf{G}^T\mathbf{\Lambda} = \mathbf{\Lambda}\mathbf{F} + \mathbf{F}^T\mathbf{\Lambda} + \mathbf{X} \tag{35}$$

This is the central result in LQG theory for regulators. After solving this matrix Riccati equation for $\mathbf{\Lambda}$, (34) yields the optimal **L**; and $\mathbf{P}_x$ may be obtained by solving the Lyapunov equation (30). If desired, J may then be found from (20). In other treatments I've seen of this problem, $\mathbf{\Lambda}$ is introduced by quite different routes. Its interpretation as a matrix of Lagrange multipliers is, I think, new.

6 Observer Performance

In contrast to the regulator, the inclusion of the known biases in the observer (7) and (8), and the measurement model (6), mean that the estimate error $\epsilon(t)$ is free of bias, as may be seen from (11). The procedure for determining the covariance $\mathbf{P}_\epsilon$ of $\epsilon(t)$ follows the same plan as that of $\mathbf{P}_x$ in the regulator, leading to the same result (14), with $\mathbf{P}_\epsilon$ replacing $\mathbf{P}_x$. Again, $\underline{\mathbf{N}}(\omega)$ obeys a Lyapunov equation:

$$\mathbf{Z}\underline{\mathbf{N}}(\omega) + \underline{\mathbf{N}}(\omega)\mathbf{Z}^T = \mathbf{K}\mathbf{V}\underline{\mathbf{S}}_v(\omega)\mathbf{V}^T\mathbf{K}^T + \mathbf{Y}\underline{\mathbf{S}}_w(\omega)\mathbf{Y}^T \equiv \underline{\mathbf{Q}}(\omega) \tag{36}$$

There is an important difference from regulator theory — this time $\mathbf{Q}(\omega)$ depends on the feedback gain **K** — but the direct evaluation of $\mathbf{P}_\epsilon$ is pretty much the same. The improved procedure (17) also works here, with $\mathbf{P}_\epsilon$ replacing $\mathbf{P}_x$; but this time

$$\underline{\mathbf{M}} = \sum_{j=1}^{v} \mathbf{\Phi}_j[\mathbf{K}\mathbf{V}]_j[\mathbf{K}\mathbf{V}]_j^T + \sum_{k=1}^{w} \mathbf{\Phi}_k\mathbf{Y}_k\mathbf{Y}_k^T \tag{37}$$

159

and as before, $[\mathbf{KV}]_j$ is the jth column of $\mathbf{KV}$, and $\mathbf{Y}_k$ is the kth column of $\mathbf{Y}$. Also, $\mathbf{\Phi}_j$ is again the noise effect integral (19); while $\mathbf{\Phi}_k$ is similar, but depending on the measurement noise spectrum $S_{vkk}(\omega)$.

If observers measured performance in the same way as regulators, then from (20), and the discussion following it, we would measure observer performance by:

$$J = \text{Tr}\,[\mathbf{\Xi}\mathbf{P}_\epsilon] + J_t \tag{38}$$

where $\mathbf{\Xi}$ is a symmetric weighting matrix, expressing our concern for the errors $\epsilon(t)$; and J_t penalizes observer settling time, and is constructed from the eigenvalues of the observer system matrix $\mathbf{Z}$. A straightforward way to get $\mathbf{\Xi}$ is Bryson weighting, as discussed in Section 3. In contrast with (20), the bias term is missing because $\epsilon(t)$ is unbiased; and the control weighting term is missing, because $\mathbf{P}_\epsilon$ doesn't depend on $\mathbf{u}(t)$, and control usage isn't a concern of the observer designer. This is the performance index employed in the new theory; but it's not seen today, largely because Kalman theory (see next section) is based on a different, and quite inferior idea.

7 Kalman Theory

Like LQG theory, Kalman theory for observers can be deduced directly from the more general results in the last section. A "Kalman filter" is an observer with the structure given in Section 2, but burdened with 2 rather unfortunate assumptions. One is that all the process and measurement noises are white and Gaussian, which I have already excoriated in Section 4. The other is that observer performance be measured by the residuals (8), rather than the estimation errors $\epsilon(t)$. Penalizing residuals has some statistical justification, but fails to consider what designers want to achieve.

In present practice, almost every observer has been constructed from some extension of Kalman theory. Today's practical filters have been built from a set of improvements introduced by very competent people, many of whom I have known and respect. However, nearly all of them are essentially applied mathematicians, more concerned with rigor than physical reality and the needs of the designer. Rigor is fine; but it ain't everything.

I'll begin with the performance index. This is tricky, because, in Kalman theory, the residuals are weighted by the inverse covariance of the measurement errors, which for white noise is zero. This is usually side stepped by some flummery involving a Dirac delta function, eventually leading to a performance index of the form (38), but without the J_t term. However, by starting from (10), we can prove without flummery that the Kalman assumption leads to

$$J = \text{Tr}\,[\mathbf{H}^T\mathbf{\Gamma}^{-1}\mathbf{H}\mathbf{P}_\epsilon] \equiv \text{Tr}\,[\mathbf{\Theta}\mathbf{P}_\epsilon] \tag{39}$$

where

$$\mathbf{\Gamma} \equiv \pi\big(\mathbf{V}\mathbf{S}_v\mathbf{V}^T + \mathbf{W}\mathbf{S}_w\mathbf{W}^T\big) \tag{40}$$

Unlike LQG theory, this $\mathbf{\Theta}$ doesn't depend on the gains. The 1st term in $\mathbf{\Gamma}$ corresponds to what's usually seen in Kalman theory, but the latter comes from including the process noise in the measurement model, a modest generalization. It should be clear that $\mathbf{\Gamma}$ will be non–singular, provided some noise contaminates every measurement.

The next step follows LQG theory. If all the noises are white, then $\mathbf{P}_\epsilon = -\pi\underline{\mathbf{N}}$, and the Lyapunov relation becomes

$$\mathbf{C} \equiv \mathbf{Z}\mathbf{P}_\epsilon + \mathbf{P}_\epsilon\mathbf{Z}^T + \pi\underline{\mathbf{Q}} = 0 \tag{41}$$

We again need to minimize J, relative to $\mathbf{K}$, and subject to the constraints (41). As in Section 5, we may use a variational Hamiltonian:

$$\mathcal{H}(\mathbf{P}_\epsilon,\,\mathbf{K},\,\mathbf{\Lambda}) = \text{Tr}\,[\mathbf{\Theta}\mathbf{P}_\epsilon + \mathbf{\Lambda}\mathbf{C}] \tag{42}$$

and the necessary conditions for a minimum are that it's stationary with respect to variations in $\mathbf{P}_\epsilon$ and $\mathbf{K}$.

For the 1st set of conditions, the dependence of $\mathcal{H}(\mathbf{P}_\epsilon,\,\mathbf{K},\,\mathbf{\Lambda})$ on $\mathbf{P}_\epsilon$ is the same as the earlier $\mathcal{H}(\mathbf{P}_x,\,\mathbf{L},\,\mathbf{\Lambda})$ on $\mathbf{P}_x$; so we are again led to (33). This time, the relation only serves to establish that $\mathbf{\Lambda} > 0$, and is therefore non–singular.

In working out the 2nd set of necessary conditions, observe that, unlike LQG theory, Θ doesn't depend on $\mathbf{L}$, but $\underline{\mathbf{Q}}$ does. On expanding $\mathbf{Z}$ and $\mathbf{Y}$ with (12), it can be rewritten as

$$\pi\underline{\mathbf{Q}} = \mathbf{K}\Gamma\mathbf{K}^T - \mathbf{K}\Psi^T - \Psi\mathbf{K}^T + \mathbf{A} \tag{43}$$

where

$$\mathbf{A} \equiv \pi\mathbf{B}\mathbf{S}_w\mathbf{B}^T \quad ; \quad \Psi \equiv \pi\mathbf{B}\mathbf{S}_w\mathbf{W}^T \tag{44}$$

Differentiation of the Hamiltonian with respect to $\mathbf{K}$ is now possible, eventually leading to

$$\mathbf{K} = \left(\mathbf{P}_\epsilon\mathbf{H}^T + \Psi\right)\Gamma^{-1} \tag{45}$$

I'll note that the non–singularity of Λ and Γ are both needed in proving (45). Actually, we have already seen that Γ can be singular only if some measurement is uncontaminated. If there is no noise, then $\Psi = 0$, and from (11), $\epsilon(t) \to 0$; so that $\mathbf{P}_\epsilon = 0$, when any $\mathbf{K}$ could be chosen, so long as $\mathbf{Z} < 0$. You can work out intermediate cases yourself.

When (45) is substituted back into (41), an algebraic Riccati equation in $\mathbf{P}_\epsilon$ emerges:

$$\mathbf{P}_\epsilon\Theta\mathbf{P}_\epsilon + (\Psi\Gamma^{-1}\mathbf{H} - \mathbf{F})\mathbf{P}_\epsilon + \mathbf{P}_\epsilon(\mathbf{H}^T\Gamma^{-1}\Psi^T - \mathbf{F}^T) + \Psi\Gamma^{-1}\Psi^T - \mathbf{A} = 0 \tag{46}$$

As the only unknown here is $\mathbf{P}_\epsilon$, it may be solved for numerically, when (45) immediately yields the optimal (choke) $\mathbf{K}$. This looks pretty complicated; but if process noise wasn't included in the measurement model, then $\Psi = 0$, and (46) and (45) reduce to well known Kalman results.

As a final note, I'll point out that no use was made of the usual assumption that the noises are Gaussian; so that assumption is unnecessary. That it was required in Kalman theory may be traced to the need to equate minimum error covariance to the notion of achieving the maximum likelihood that you've got it right, a statistical finesse not essential to the theory.

8   Bounded Polynomial Noises

It's often true that measurement noise can be studied in the laboratory, and accurate power spectra determined. Unexpected bumps in the spectrum may then be used to uncover problems that can be alleviated by design improvements. By contrast, process noises are hard to measure; and even if known, have little application in current design practice. Since the new theory demands this information, what do we do if we can't get it? Well, as a general rule, the better our information, the better our ultimate performance should be. If our information on some spectrum is poor, any existing measurements should be combined with physical reasoning to estimate the average power and shape of the spectrum.

If the estimated spectrum shape is analytically simple, it may be possible to evaluate the noise effect integral (19), for a given $\mathbf{Z}$, without direct numerical integration. This has already been done for several spectra in Section 4. Here, the general class of shapes characterized by bounded polynomials is examined; and a few are completely worked out, along with a general procedure for extending the list.

The general problem is solvable provided we can evaluate the class of integrals defined by:

$$\mathbf{F}(\mathbf{Z}, k, t) = \int_0^t (\mathbf{Z} + \omega^2\mathbf{Z}^{-1})^{-1}\omega^k d\omega \tag{47}$$

It can be shown that these integrals are all given by:

$$\mathbf{F}(\mathbf{Z}, k, t) = (-1)^{k/2}\mathbf{Z}^k\left[\tan^{-1}(t\mathbf{Z}^{-1}) + \sum_{j=1}^{k/2}\frac{(-1)^j}{2j-1}t^{2j-1}\mathbf{Z}^{1-2j}\right] \qquad \text{(k even)} \tag{48}$$

$$\mathbf{F}(\mathbf{Z}, k, t) = (-1)^{(k-1)/2}\mathbf{Z}^k\left[\frac{1}{2}\ln(\mathbf{I} + t^2\mathbf{Z}^{-2}) + \sum_{j=1}^{(k-1)/2}\frac{(-1)^j}{2j}t^{2j}\mathbf{Z}^{-2j}\right] \qquad \text{(k odd)} \tag{49}$$

For these formulas to be helpful, it's necessary to have a clear understanding of what's meant by the arctangent and the logarithm of a matrix. With considerable care about the regions of convergence, these matrix functions may be defined by power series generalized from known scalar series; although I must again caution the reader that all the standard references I've seen get at least the arctangent wrong. Anyway, it may be shown that, with these functions so defined, they may be evaluated by these relations:

$$\tan^{-1}(\mathbf{A}) = \int_0^1 (\mathbf{A}^{-1} + x^2 \mathbf{A})^{-1} dx \tag{50}$$

$$\ln(\mathbf{I} + \mathbf{A}) = \int_0^1 (\mathbf{A}^{-1} + y\mathbf{I})^{-1} dy \tag{51}$$

In both cases, since the integration interval is fixed, evaluation by the Gaussian technique will yield any required accuracy, without much calculation. Both these formulas run into numerical trouble for large $\mathbf{A}$; methods for modifying them to remove the difficulties will be given in [3].

For the simplest application of this machinery, consider the flat bounded spectrum; i.e., white noise that has somehow been cut off sharply. For this, $S(\omega) = R(0)/\omega_c$ for $0 \le \omega \le \omega_c$, and zero otherwise. On applying the above relations we find

$$\mathbf{\Phi} = \frac{R(0)}{\omega_c} \int_0^{\omega_c} (\mathbf{Z} + \omega^2 \mathbf{Z}^{-1})^{-1} d\omega = \frac{R(0)}{\omega_c} \mathbf{F}(\mathbf{Z}, 0, \omega_c) = \frac{R(0)}{\omega_c} \tan^{-1}(\omega_c \mathbf{Z}^{-1}) \tag{52}$$

While there is no practical way to generate a process with this spectrum, it may be considered as the limit of Butterworth noise, with the same $R(0)$ and ω_c, as $m \to \infty$. I'm not sure how to prove this; but I've tested it numerically at $m = 8$, with good agreement.

The next order of complexity is the linear spectrum. It has a peak value at $\omega = 0$, drops linearly to zero, and terminates. More precisely,

$$S(\omega) = \frac{R(0)}{\omega_c} \left(1 - \frac{\omega}{2\omega_c}\right) \qquad (0 \le \omega \le 2\omega_c) \tag{53}$$

and zero otherwise. On applying the above theory, the corresponding noise effect integral becomes

$$\mathbf{\Phi} = \frac{R(0)}{\omega_c} \left[\tan^{-1}(2\omega_c \mathbf{Z}^{-1}) - \frac{1}{4\omega_c} \mathbf{Z} \ln(\mathbf{I} + 4\omega_c^2 \mathbf{Z}^{-2})\right] \tag{54}$$

Onward. The cubic power spectrum is initially flat, then falls off according to a cubic polynomial, flattening again and terminating when it reaches zero. The spectrum may be shown to be:

$$S(\omega) = \frac{R(0)}{\omega_c} \left[1 - 3\left(\frac{\omega}{2\omega_c}\right)^2 + 2\left(\frac{\omega}{2\omega_c}\right)^3\right] = \frac{R(0)}{\omega_c} \left(1 - \frac{\omega}{2\omega_c}\right)^2 \left(1 + \frac{\omega}{\omega_c}\right) \tag{55}$$

for $0 \le \omega \le 2\omega_c$ and zero otherwise. This looks superficially like colored noise; but only 3/16 of the power is in the tail, compared to half for colored noise; and the frequency within which half of the total power is found is $0.53277\,\omega_c$, compared to ω_c for colored noise. This time the noise effect integral turns out to be

$$\mathbf{\Phi} = \frac{R(0)}{\omega_c} \left[\left(\mathbf{I} + \frac{3}{4\omega_c^2} \mathbf{Z}^2\right) \tan^{-1}\left(2\omega_c \mathbf{Z}^{-1}\right) - \frac{1}{8\omega_c^3} \mathbf{Z}^3 \ln\left(\mathbf{I} + 4\omega_c^2 \mathbf{Z}^{-2}\right) - \frac{1}{\omega_c} \mathbf{Z}\right] \tag{56}$$

This spectrum was employed in [2] to describe satellite drag variations, for which very little flight data exists. However, most of the numerical work was based on a more or less equivalent colored noise spectrum, as the noise effect integral theory had not yet been implemented.

All these spectra (not including white noise) might be called 2 parameter spectra, as they are completely prescribed by $R(0)$ and ω_c. There are other possibilities for 2 parameter spectra, and a considerable range of choices for 3 parameters, none of which have been looked at. Moreover, I believe that most spectra we're likely to encounter could be reasonably approximated by some combination of bounded polynomials. Further afield, there are several theoretical spectra, such as that for thermal noise, for which we might be able to calculate $\mathbf{\Phi}$ analytically.

9 Low & High Frequency Noises

For theoretical purposes, it's interesting to see what happens if a particular noise spectrum $S(\omega)$ is concentrated in a band well below the system dynamics; i.e., ω_c is much closer to the imaginary axis than any of the eigenvalues of Z. To do this, we can let $\omega_c \to 0$ in each of the above noise effect integrals, while holding $R(0)$ fixed. Except for white noise, where the idea is meaningless, the results for all spectra are

$$\lim_{\omega_c \to 0} \Phi = R(0)Z^{-1} \tag{57}$$

We may conclude that the shape of the spectrum doesn't much matter, if the bulk of the power is well below the system dynamics. This also serves as a valuable check on the formulas for each Φ.

In the converse situation, where ω_c is well above the system dynamics, i.e., where ω_c is much further from the imaginary axis than any eigenvalue of Z, we get a rather different result. This time, since we expect only the low frequency power to have much effect, we hold $S(0)$ constant, while letting $\omega_c \to \infty$, rather than fixing $R(0)$. This time, for every spectrum above,

$$\lim_{\omega_c \to \infty} \Phi = -\frac{\pi}{2}S(0)I \tag{58}$$

As Z doesn't appear in the result, we now find that everything looks like white noise, and the dynamics make little difference, if they are slow compared to ω_c. And we have another valuable check on the Φ formulas.

10 What's Next?

The new approach to optimal estimation and control, advanced in this paper, is barely a beginning. If the history of the development of LQG and Kalman theory is any guide, it will be several years before the theory will be developed to the point where it sees regular use in design, and begins to enter the engineering curriculum. After the next few months, my crystal ball gets pretty murky; but here is my vision, for what it's worth.

To begin, I plan to be able to fill orders for [3] before the end of this year. At around 200 pages, it will greatly amplify on the present paper, including material on noise statistics, power spectra, and matrix manipulation that's difficult (occasionally impossible) to find elsewhere. Also planned for that book are an extension of the present theory to cover the practical situation where an observer is used as the source of information for a regulator; so that both sets of optimal feedback gains need to be found. Further additions should include a beginning in understanding the transient behavior of the state and estimation error covariances; and several examples of the application of the theory, showing the improvements that may be expected relative to LQG or Kalman theory.

Further afield, I see the next major extension is in the area of sampled and quantized measurements, and discrete updates both in controls and observation. The present theory might be regarded as the oversampling limit of a fully digital implementation, with unlimited computational resources. This causes 3 new issues to surface. 1st, better performance costs money — terms could be added to our performance index penalizing increased digital precision, and more rapid sampling and updates. 2nd, even in the absence of noise, an exact model of the measurements is no longer possible. That is, all the available information (the complete set of past measurements and current and prior state estimates) is insufficient for an exact reconstruction of the current measurement. This is true whether "sample" means a true point measurement, or an average over the sampling interval. 3rd, settling times may be affected by these digital details. These issues have all been examined in the context of current practice, but will need to be revisited within the new performance philosophy.

Another matter of great practical importance will be to deal with non–stationary systems; i.e., those in which the plant and measurement parameters, and the noise properties, may vary with time. In present practice, such problems are treated by something amounting to a continuous integration of a matrix Riccati equation, causing the covariances and feedback gains to evolve in time. Unfortunately, at this writing, I have no clear view of how these methods might be generalized to encompass arbitrary noise power spectra. Indeed, even the notion of a quasi–stationary spectrum will need a careful definition.

There are several other obvious shortcomings. All the noise and measurement biases are here assumed known and invariant. The techniques of bias estimation and integral control are well known; and it should be possible to bring them into the new theory, without much difficulty. Another issue is robustness; i.e., how to deal with errors in the knowledge of the system parameters. I expect that this will require *lots* of work.

Another issue swept under the rug at the beginning of the paper was linearization — where did all those fixed matrices come from? While this has long given us pain, and matters are far from settled in current practice, I doubt that the new theory will be any worse in this respect. And then there are your insights. Overall, I welcome anyone who wants to contribute to this newborn field. Talk to me.

References

[1] D Sonnabend, "Terminal Covariance", JPL EM 314-48, 6–11–90.

[2] D Sonnabend, "Measuring Attitude with a Gradiometer", Proc. FM/ETS, P. 315, Goddard SFC, 5–94.

[3] D Sonnabend, "Regulators, Observers, & Power Spectra", in preparation.

FLIGHT MECHANICS/ESTIMATION THEORY SYMPOSIUM

MAY 16-18, 1995

SESSION 3

Development of a Robust Star Identification Technique for Use in Attitude Determination of the ACE Spacecraft

Mark Woodard
Goddard Space Flight Center (GSFC)
Greenbelt, Maryland, USA

Dave Rohrbaugh
Computer Sciences Corporation (CSC)
Lanham-Seabrook, Maryland, USA

ABSTRACT

The Advanced Composition Explorer (ACE) spacecraft is designed to fly in a spin-stabilized attitude. The spacecraft will carry 2 attitude sensors - a digital fine Sun sensor and a charge coupled device (CCD) star tracker - to allow ground-based determination of the spacecraft attitude and spin rate. Part of the processing that must be performed on the CCD star tracker data is the star identification. Star data received from the spacecraft must be matched with star information in the SKYMAP catalog to determine exactly which stars the sensor is tracking. This information, along with the Sun vector measured by the Sun sensor, is used to determine the spacecraft attitude.

Several existing star identification (star ID) systems were examined to determine whether they could be modified for use on the ACE mission. Star ID systems which exist for three-axis stabilized spacecraft tend to be complex in nature and many require fairly good knowledge of the spacecraft attitude, making their use for ACE excessive. Star ID systems used for spinners carrying traditional slit star sensors would have to be modified to model the CCD star tracker. The ACE star ID algorithm must also be robust, in that it will be able to correctly identify stars even though the attitude is not known to a high degree of accuracy, and must be very efficient to allow real-time star identification.

The paper presents the star ID algorithm that was developed for ACE. Results from prototype testing are also presented to demonstrate the efficiency, accuracy, and robustness of the algorithm.

I. INTRODUCTION

The Advanced Composition Explorer (ACE) spacecraft will be launched in August 1997. The spacecraft will be placed into a spin-stabilized attitude. The spacecraft will carry a pair of Adcole two-axis digital Sun sensors and a Ball Aerospace CT-631 series charged-coupled device (CCD) star tracker. Telemetry data from these sensors will be downlinked to allow spacecraft attitude determination at the NASA Goddard Space Flight Center (GSFC). Both spin rate and spin axis attitude will be open-loop controlled by ground commanded hydrazine thruster firings.

Following launch, GSFC personnel will design and execute a series of trajectory maneuvers to transfer ACE from a low earth orbit to a Lissajous orbit about the Sun-earth L1 libration point. The following constraints are levied on the spacecraft attitude by the mission design:

1) The spin axis (the spacecraft +Z axis) must be maintained within 20° of the spacecraft-Sun line for power, thermal, and science instrument safety reasons

2) The spacecraft high-gain antenna boresight, which is along the spacecraft -Z axis, must be maintained with 3° of nadir to allow sufficient link margin for radio frequency (RF) communications with the Deep Space Network (DSN) ground stations

3) The spacecraft spin rate must be maintained to 5.0 ± 0.1 RPM.

II. ALGORITHM DESCRIPTION

General Description of Algorithm

In general, stars are identified by processing data obtained while the star tracker is tracking stars, such as intensities and positional information, and comparing these data with similar data in a star catalog. The star catalog, which is usually a subset of the SKYMAP Master Catalog created for specific missions, is searched until a "match" of the data is found, indicating a successful star identification. For ACE, a mission-specific star catalog will also be created. The creation of this catalog is discussed in more detail later in this section. The star ID algorithm will search the catalog using the following criteria: star magnitude, and the angle between the star vector and the Sun vector. The Sun vector will be propagated in the spacecraft body coordinate frame to the time of each star angle measurement. Propagating the Sun vector in body coordinates has one major advantage over transferring the Sun vector to GCI coordinates; knowledge of the attitude is not required to do the former since the Sun's location with respect to the stars is relatively the same in either the body frame or the GCI frame. This allows the star ID algorithm to be much more robust. The major concern of taking this approach is the propagation of the Sun vector, which is discussed later.

Sensor Overview

A brief overview of the attitude sensors onboard ACE is appropriate at this stage to help explain the functionality of the star ID algorithm. Sensor data will be telemetered to the ground every major frame cycle (16 seconds) for 2-3 hours daily during the spacecraft's only pass.

Each of the two sets of Sun sensors has a ±64° field of view (FOV). One Sun sensor boresight is parallel with the spacecraft spin axis while the other is canted down 120°. This allows for the pair of Sun sensors to have complete hemispherical coverage. This is important to note, not because they are needed to get a fix on the spacecraft attitude, but because generating a Sun pulse is necessary for propagating the Sun vector with respect to time. The Sun sensor can operate in two modes: normal mode and high rate mode. In normal mode, the sensor mimics a slit Sun sensor, generating a time-tagged Sun pulse once per spin period (every 12 seconds). In high rate mode, the sensor is operated as a three-axis sensor, yielding time-tagged angles along the x and y axes. The Sun sensor takes 11 measurements per second in high rate mode.

The CT-631 CCD star tracker has a 20° x 20° FOV and is capable of tracking up to 5 stars simultaneously. The CCD star tracker can also operate in both normal and high rate mode and will retain information on the brightest stars observed. In normal rate mode, one set of star tracker data is transmitted every fourth major telemetry frame. This set consists of up to 4 star observations. These observations are all obtained in the same spin revolution and each pertains to a different star. In high rate mode, every major frame consists of one set of star tracker data. This set of data consists of up to 10 unique observations from the same spin period. The star tracker is mounted on the side of the spacecraft, its boresight 90° from the primary Sun sensor boresight. All star observations will contain a vertical angle measurement, taken as each star crosses the center of the FOV of the sensor (i.e. when the horizontal angle is zero). The tracker will be capable of determining a predicted spacecraft spin rate as it tracks stars through its FOV. The star tracker uses a 'picket fence" algorithm to search for star observations. This algorithm partitions the band which is swept out by the star tracker FOV into hundreds of 'pickets", each of which is .4° wide and 20° high. During each full spacecraft revolution, the star tracker views every 8th picket and searches for stars within those pickets. The 'picket fence" search is advanced one picket during subsequent revolutions. This pattern continues for 8 complete revolutions (nominally 96 seconds), at which time the entire FOV band has been searched. Once a star is observed it continues to be tracked until it leaves the FOV.

Creation of Star Catalog

A star catalog must be created in order to test the star ID prototype. There are no scientific constraints on ACE which require it to target any particular star or set of stars. This will allow the creation of a star catalog which is more conducive to the star identification process. The main goal was to generate a star catalog which contained few enough stars to promote quick identification and enough stars that at least 4-6 would be observed every spacecraft revolution. Limiting the magnitude of stars in the mission specific catalog to 3.5 reduces the number of calculations performed in the star ID algorithm and still contains enough stars to assure that there will be several to identify each spin period. The SKYMAP Master Catalog contains approximately 300 stars of magnitude 3.5 or brighter. Uniform distribution suggests a star population of about one every 12-square degree section of the celestial sphere. This star density will yield approximately 50 stars in any band swept out by the star tracker FOV during a revolution. Using the 'picket fence" algorithm previously discussed means that about 6 stars will be observable during each revolution. These

predictions corroborate the findings of Ball Aerospace (reference 1) regarding the number of stars available for observation during each revolution of ACE.

An additional element driving the creation of the star catalog is the fact that CCD star trackers are most sensitive at red passbands when measuring star magnitudes. The SKYMAP Master Catalog does not contain red passband data for many stars. The star catalog analysis section at Computer Sciences Corporation (CSC) has developed the Instrumental Red Magnitude Prediction System (reference 2). This system is capable of predicting red passband magnitude data for SKYMAP stars that do not have observed values. The accuracy of the predicted values is within .25 magnitude for fairly bright stars but decreases to as much as 2.5 magnitudes for dim stars, which is another advantage of using stars that are 3.5 magnitude or brighter. The stars being used for the mission specific catalog will be run through the Instrumental Red Magnitude Prediction System before being placed in the catalog; however, this was not done for the testing of the star ID prototype since the sensor models used to generate test data did not emulate sensitivity in the red passband.

Sensor Models

Modeling both Sun sensor and star tracker data was necessary to verify that the star ID algorithm was properly identifying stars. Simplified models were developed to help conserve time. Running the sensor models enabled more accurate predictions of how the identification process would work, in addition to providing test data for the algorithm itself. The Sun sensor model generates time dependent x and y angles. The star tracker model generates a list of all stars in the FOV band for a user specified attitude. This list is then trimmed down to include only the 5 or 6 brightest stars. A pseudo measurement file is constructed from the resulting Sun sensor and star tracker observations. The sensor models are capable of simulating nutation. Nutation will be discussed in later sections.

Algorithm Steps

Obtain Sun Vector

The Sun vector in the sensor frame is determined using the standard conversion from α and β (which are the angle measurements between the Sun vector and the projections of the Sunline onto the X-Z and Y-Z planes, respectively) as follows:

$$\hat{S}_{SS} = \frac{1}{(1 + \tan^2 \alpha + \tan^2 \beta)^{1/2}} \begin{bmatrix} \tan\alpha \\ \tan\beta \\ 1 \end{bmatrix}$$

which is translated into body coordinates as follows:

$$\hat{S}_B = M_{BSS}\hat{S}_{SS}$$

where M_{BSS} is the alignment matrix which describes the transformation from the Sun sensor coordinate frame to the body coordinate frame.

The Sun vector can be calculated this way regardless of which mode the Sun sensor is in. If the sensor is in low-rate mode (operating as a slit sensor), α will be 0 and β will be the angle measured at the time $\alpha = 0$ occurs. The same measurements can be derived for the sensor when it is operating in high-rate mode as well. Normally, this mode yields values for both α and β at each measurement time.

Process Star Tracker Data

Convert the time-tagged star measurements to the body frame as follows:

$$\hat{U}_B = M_{BST}\hat{U}_{ST}$$
where

$$\hat{U}_{ST} = \frac{1}{(1 + \tan^2 \theta)^{1/2}} \begin{bmatrix} 0 \\ \tan\theta \\ 1 \end{bmatrix}$$

and θ is the vertical angle measured when the horizontal position is 0. M_{BST} is the alignment matrix which describes the transformation from the star tracker coordinate frame to the body coordinate frame.

This vector will be calculated for each observed star.

Propagate Sun Vector

The most important part of the star ID algorithm is the propagation of the measured Sun vector in the body frame. Since the algorithm compares the angle between the Sun vector and the star vector, it is imperative that the distances between the Sun vector and the star vector be the same in

both the GCI reference frame and the body frame. The only way to assure this is to propagate the measured Sun vector to the time the star measurement occurred. ACE is spinning at 5 rpm. This translates to a phase angle shift of 30° per second. At this rate, even small miscalculations will cause the calculation of the vector to be off by several degrees. Aside from the spin rate factor, there are additional sources of error which can affect the accuracy of the propagation. The Sun vector can be propagated as such:

$$\hat{S}'_B = \begin{bmatrix} \cos\phi & \sin\phi & 0 \\ -\sin\phi & \cos\phi & 0 \\ 0 & 0 & 1 \end{bmatrix} \hat{S}_B$$

where

$\phi = \omega \, \Delta t$
ω = spin rate
Δt = time between Sun measurement and star observation

The value of ϕ is directly dependent on these two variables. Decreasing Δt is one way to improve the calculation of ϕ. This can be accomplished by placing the sensors in high rate mode. In high rate mode, Sun sensor data is measured 11 times per second. At this high rate, if no propagation were done the error would still be only 1.36°. In low rate mode, more care must be taken to reduce the amount of error resulting from large values of Δt. High rate mode cannot be maintained for extended periods of time because or battery restrictions.

The calculation of ω may be the trickiest part. For testing purposes, it was assumed that the spin axis and the spacecraft +z axis are parallel. In reality, this will not be the case. Changes in the spacecraft center of mass and torque's applied to the spacecraft resulting from maneuver thrusts will alter the location of the spin axis. This will cause the +z axis to "wobble" about the angular momentum vector. This "wobble" is commonly referred to as nutation. Nutation will affect the calculation of the spacecraft spin rate (reference 3), which in turn, will affect the propagation of the Sun vector. The nutation angle will be determined as part of the ground processing of attitude data and can be fed back into calculations for adjusting the spin vector. It is yet to be determined how accurately the attitude ground support system will evaluate the nutation angle. Until that time, it is difficult to predict how much of an effect this will have on the actual propagation of the Sun vector. It may be desirable to place the spacecraft into high rate mode at the beginning of each pass until the ground system can come up to speed and assist in the calculation of such parameters as the spin rate. The star tracker will also downlink predicted

values for the spin rate which can be utilized to help determine the actual spin rate.

It is assumed, for the purpose of testing the star ID algorithm, that nutation will be .25°, the spin rate is known to within the required .1 rpm, and the alignment on the Sun sensor is known to within .5°. Taking these sources into consideration, a 2° error in the propagated vector is more than sufficient to model the worst case scenario.

Calculate Observed Sun Vector/Star Vector Angle

The observed angle between the propagated Sun vector and the processed star vector is calculated using the standard dot product method:

$$\zeta_O = \cos^{-1}(\hat{U}_B \bullet \hat{S}'_B)$$

Calculate Reference Sun Vector/Star Vector Angle

For each star in the star catalog, the angle between the Sun vector and the star position vector must be calculated. This is most easily accomplished in the GCI reference frame since positional information in the star catalog is stored as GCI x, y, and z coordinates. The Sun vector in the GCI reference frame can be obtained from the Solar Lunar Planetary (SLP) ephemeris file. The SLP file will be available to the star ID software since it is used in other parts of the ACE attitude ground support system. The reference Sun vector/star vector angle is calculated for each star in the catalog as follows:

$$\zeta_R = \cos^{-1}(\hat{U}_{GCI} \bullet \hat{S}_{GCI})$$

where

$$\hat{U}_{GCI} = \begin{bmatrix} X_{GCI} \\ Y_{GCI} \\ Z_{GCI} \end{bmatrix}$$

is the position of the star in GCI coordinates obtained from the star catalog and $\hat{S}_{GCI}$ is obtained directly from the SLP file. These calculations should be processed in advance to save time during the real-time processing. The angles can be stored in a file and read in when needed for comparison. Since the catalog will contain only 300 stars the calculations of the angle between each star and the Sun vector will be done almost instantaneously. Calculation of

the reference angle is independent of time. While it is true that the Sun moves in the GCI reference frame, the movement is minuscule during the time period in question. This implies that the Sun does not move relative to the stars in either the body frame or the GCI frame. This allows comparison of the two angles without any knowledge of the spacecraft attitude.

Match Star Information

For each star measured, loop through the star catalog using the matching criteria: the magnitude difference between the measured and reference star, and difference between the measured and reference Sun/star angle (ζ_o and ζ_R). Compare both criteria for every star in the catalog. If the absolute value of the differences between the measured and reference values is less than a predetermined tolerance then that particular observed star has been identified. This process is repeated for each observed star:

Do for each observed star ...

If $|Mag_{observed\ star} - Mag_{catalog\ star}| < \varepsilon_M$ and

If $|\zeta_o - \zeta_R| < \varepsilon_A$ then

Star identification completed, return time-tagged position of measured star and repeat process for next observed star

Else continue

<Process completed>

The tolerances are specified by the user. For testing the prototype the tolerances were set as follows:

$\varepsilon_M = .3125$

The accuracy of the Instrumental Red Magnitude Prediction System is .25 and the magnitude resolution of the ACE star tracker is .0625, so .3125 was chosen as a worst case value. Although CCD trackers are relatively new, several missions prior to ACE will fly the CCD star tracker, including SOHO and XTE. This experience should lead to a more refined calibration of the Instrumental Red Magnitude Prediction System which should reduce the .25 error somewhat.

$\varepsilon_A = 2.0$ degrees

This value is derived from possible errors resulting in the propagation of the Sun vector, which was previously discussed.

III. PROTOTYPING AND ANALYSIS

Verification of Results

Development of the star ID prototype has been completed and will become part of the ACE attitude ground support system once it has been fully tested. Testing continues at the writing of this paper. Final results of the testing phase will be reported at the FMET symposium in May, although preliminary results are discussed in the next section.

IV. SUMMARY AND CONCLUSIONS

Tests were run on the pseudo sensor measurement file and the results are very promising. The sensor models were run for several different spacecraft attitudes and Sun angles. The number of observed stars in the measurement file was between 26 and 40 stars for every case. This indicates that between 3 and 5 stars will be available during each revolution. The star observations are currently being checked against all other stars in the star catalog. Preliminary results show that most test cases yield a single star identification which is the desired result. For some cases there are at most 2 stars being identified, resulting in an ambiguous identification. This situation is undesirable if it occurs too often, although in this case, there is only one ambiguous identification occurring some of the time. One solution to this is to simply flag those star identifications as ambiguous and use the remaining star data. Therefore, at least 2 or more vectors will be available every revolution in addition to the Sun vector for attitude determination.

VII. REFERENCES

1. Ball Aerospace and Communications Group, P93-801-80, Proposal for CT-631 Star Tracker for the ACE Spacecraft, (Volume 1), Ball Electro-Optics and Cryogenics Division, June 1993

2. Computer Sciences Corporation, CSC/TR-93/6124, SKYMAP Requirements, Functional, and Mathematical Specifications: Instrumental Red Magnitude Prediction Subsystem, (Volume 2), A. Miller and M. Slater, October 1993

3. NASA Goddard Space Flight Center, Optimal Attitude Maneuver Execution for the ACE Mission, (paper submitted for the Flight Mechanics/Estimation Symposium), M. Woodard and D. Baker, May 1995

4. J. R. Wertz, ed., Spacecraft Attitude Determination and Control, Dordrecht, Holland: D. Reidel, 1978

5. Computer Sciences Corporation, "Proposed Algorithm for Performing Star Identification for ACE", (memorandum), D. Rohrbaugh, September 1994

Optimal Attitude Maneuver Execution for the Advanced Composition Explorer (ACE) Mission

Mark A. Woodard [*] , David F. Baker [†]

ABSTRACT

The Advanced Composition Explorer (ACE) spacecraft will require frequent attitude reorientations in order to maintain the spacecraft high gain antenna (HGA) within 3 degrees of earth-pointing. These attitude maneuvers will be accomplished by employing a series of ground-commanded thruster pulses, computed by ground operations personnel, to achieve the desired change in the spacecraft angular momentum vector. With each maneuver, attitude nutation will be excited. Large nutation angles are undesirable from a science standpoint. It is important that the thruster firings be phased properly in order to minimize the nutation angle at the end of the maneuver so that science collection time is maximized.

The analysis presented derives a simple approximation for the nutation contribution resulting from a series of short thruster burns. Analytic equations are derived which give the induced nutation angle as a function of the number of small thruster burns used to execute the attitude maneuver and the phasing of the burns. The results show that by properly subdividing the attitude burns, the induced nutation can be kept low. The analytic equations are also verified through attitude dynamics simulation and simulation results are presented. Finally, techniques for quantifying the post-maneuver nutation are discussed.

I. INTRODUCTION

The Advanced Composition Explorer (ACE) spacecraft will be launched in August 1997. The spacecraft will be placed into a spin-stabilized attitude. The spacecraft will carry a pair of Adcole two-axis digital Sun sensors and a Ball Aerospace CT-631 series charged-coupled device (CCD) star tracker. Telemetry data from these sensors will be downlinked to allow spacecraft attitude determination at the NASA Goddard Space Flight Center (GSFC). Both spin rate and spin axis attitude will be open-loop controlled by ground commanded hydrazine thruster firings.

Following launch, GSFC personnel will design and execute a series of trajectory maneuvers to transfer ACE from a low earth orbit to a Lissajous orbit about the Sun-earth L1 libration point. The following constraints are levied on the spacecraft attitude by the mission design:

1) The spin axis (the spacecraft +Z axis) must be maintained within 20° of the spacecraft-Sun line for power, thermal, and science instrument safety reasons

2) The spacecraft high-gain antenna boresight, which is along the spacecraft -Z axis, must be maintained with 3° of nadir to allow sufficient link margin for radio frequency (RF) communications with the Deep Space Network (DSN) ground stations

3) The spacecraft spin rate must be maintained to 5.0 ± 0.1 RPM.

---

[*] Aerospace Engineer, Flight Dynamics Division, NASA/Goddard Space Flight Center, Greenbelt, Maryland 20771.
[†] Aerospace Engineer, Flight Dynamics Division, NASA/Goddard Space Flight Center, Greenbelt, Maryland 20771. Mr. Baker is currently a doctoral candidate at Princeton University.

The ACE attitude and orbit control system (AOCS) consists of a set of 10 1-lb$_f$ hydrazine thrusters placed around the spacecraft structure. The thrusters are mounted in pairs; 4 of the thrusters are oriented to provide axial forces and 6 provide radial forces. The thrusters can be commanded to fire either individually or in groups. The ACE thruster layout is shown in Figure 1. Groups I and II are the upper deck (+Z) thrusters; groups III and IV are the lower deck (-Z) thrusters. Axial thrusters are denoted as 'A', while radial thrusters are denoted as 'R'.
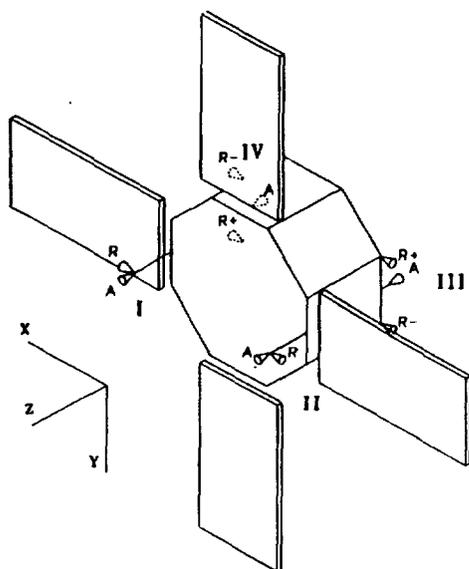
Figure 1. ACE Thruster Locations

Once the Lissajous orbit has been achieved, orbit stationkeeping maneuvers will be performed about once every eight weeks. More frequently, attitude maneuvers will need to be performed to maintain the HGA within 3° of nadir. Since the L1 point moves relative to inertial space at the sidereal rate (0.9829° per *solar* Earth day), attitude reorientations will need to be performed at least every 6.1 days to maintain the HGA within the ±3 degree deadband.

When spacecraft maneuvers are performed, a certain amount of nutation will be induced. ACE carries a passive onboard nutation damper to dissipate the excess spacecraft rotational kinetic energy introduced during a maneuver

and thereby decrease nutation over time as an exponentially decaying function. The 1/e time constant for the ACE nutation damper is 9.5 hours, so nutation will be damped very slowly.

Nutation is undesirable for ACE since it can cause errors in science data collection. The ACE Command and Data Handling (C&DH) subsystem uses the Sun sensor to measure the period of the last spin. It then divides the spin period into 16384 ticks, with an equal time allotted per tick, and places science instrument data into resulting sectors. In the presence of nutation, the observed spin period, P, will vary as

$$\Delta P \cong \frac{2\Theta}{\Omega_s \cdot \tan\beta} \qquad (1)$$

where

Θ = nutation angle
Ω_s = z-axis angular velocity (spin rate)
β = angle between the Z-axis and the spacecraft-Sun line

Any variation in the spin period greater than approximately 7 msec will cause science data to be placed into the wrong sector and will necessitate reprocessing of science data on the ground. To avoid reprocessing of data, the attitude should be controlled to minimize ΔP. This can be accomplished in one of three ways. The first two ways would be to increase spin rate or Sun angle (Ω_s or β); however, these parameters are constrained by the mission constraints listed above. The more effective way is to minimize the nutation angle, Θ, during each maneuver. By keeping the induced nutation angle small throughout the duration of the maneuver, the impact to science data collection will be minimized. The analysis below investigates how this may be accomplished during the ACE attitude maneuvers and identifies methods to use in planning and executing the maneuvers.

II. ANALYSIS

The goal of this analysis is to explore strategies for performing spacecraft attitude maneuvers

174

while keeping the induced spin-axis nutation angle, Θ, small. First, the total thruster on time to achieve a 6 degree maneuver is computed. For properly centered burn arcs of finite length, the angular momentum change in the desired maneuver direction is given as:

$$\delta H = \frac{2F \cdot R_m \cdot \sin \alpha}{\Omega_s} \qquad (2)$$

where

F = thruster force, 4.448 N
R_m = thruster moment arm
α = burn arc half-angle
Ω_s = nominal spin rate, $\pi/6$ radian/sec

For each thruster, the moment arm normal to the spin axis was computed from information provided by the spacecraft manufacturer. The results are given in Table 1. Note that the moment arm varies significantly, based on thruster location; the moment arm for an upper deck axial thruster is nearly twice that of a lower deck radial thruster.

Table 1. ACE Thruster Moment Arms

Thruster Location	Thruster Orientation	Thruster Moment Arm
Upper Deck	Axial	0.78 m
	Radial	0.60 m
Lower Deck	Axial	0.69 m
	Radial	0.40 m

An attitude maneuver could be performed by firing 1 lower deck radial thrusters several times until the desired attitude reorientation is achieved. Assuming no initial nutation, the spin axis and the angular momentum vector, **H**, are coincident prior to the maneuver. When the thruster is fired, the change in angular momentum, δH, is directed perpendicular to the spin axis, and thus **H**. The angular change in the spin axis direction, Γ, is given as:

$$\Gamma \cong \frac{\delta H}{H} = \frac{\delta H}{I_3 \cdot \Omega_s},$$

or,

$$\Gamma = \frac{2 \cdot F \cdot R_m \cdot \sin \alpha}{I_3 \cdot \Omega_s^2} \qquad (3)$$

where

I_3 = the principal moment of inertia

(The calculated values of I_3 are 373.44 kg-m^2 at beginning-of-life (BOL) and 334.19 kg-m^2 at end-of-life (EOL). An average value of 353.82 kg-m^2 will be used in this analysis.)

For 1 thruster burning for 1 second, $\alpha = 15°$, and

$$\Gamma = \frac{2\ (4.448\ N)\ (0.40\ m)\ (\sin\ 15°)}{(353.82\ kg\text{-}m^2)\ (\pi/6\ rad/sec)^2} = 0.0095\ rad$$

The total thruster on time required to achieve the desired 6° attitude maneuver is given by

$$t = \frac{(6\ deg)\ (\pi/180)}{0.0095\ rad} = 11.02\ seconds$$

However, if the 1 second pulses were broken down into shorter pulses, the maneuver could be executed more efficiently. The following analysis also shows that shorter pulses will induce less nutation.

A simple approximation for the nutation contribution resulting from a series of short burns is derived by making the following assumptions:

- the spacecraft is a rigid body
- the spacecraft is axially symmetric ($I_1 = I_2 = I_T$)
- the nutation angle, Θ, remains small, so $\cos\Theta \approx 1$
- small burns are treated impulsively (the width of the burn arc is neglected)
- spacecraft torques are small; torque-free motion is assumed
- there is no initial nutation prior to the maneuver.

175

The basic attitude dynamics of a nutating body states that the spacecraft principal Z axis, **Z**, revolves around the angular momentum vector, **H**, at the inertial nutation rate, $\Omega_1 = I_3/I_T \cdot \Omega_s$. Then, **Z** revolves $2\pi \cdot I_3/I_T$ radians about **H** during the course of one spin period. The angle ϕ can be defined as the angular rotation of the spacecraft between thruster burns and is represented as:

$\phi = \pi^* I_3/I_T$ for 1 small burn per ½ revolution,
$\phi = 2\pi^* I_3/I_T$ for 1 small burn per 1 revolution,
$\phi = 3\pi^* I_3/I_T$ for 1 small burn per 1½ revolution,
etc.

The ACE attitude maneuvers will be modeled as a number of small burns that are performed after each successive spacecraft rotation by the angle ϕ. By assuming small nutation angles, the offset between **Z** and **H** for each small burn may be added vectorially to get the approximate position of **Z** relative to **H** at the end of the maneuver. The components of **Z** in the plane perpendicular to **H** may be expressed conveniently as the real and imaginary parts of a complex sum as follows:

$$\delta\Theta = \frac{\Gamma}{n} \cdot \left[1 + e^{j\phi} + e^{j2\phi} + \dots + e^{j(n-2)\phi} + e^{j(n-1)\phi} \right] \quad (4)$$

where

$\delta\Theta$ = final position of **Z** relative to **H**
Γ = total attitude motion required in the attitude maneuver
n = number of small burns used to perform the maneuver

By multiplying each term in equation 4 by the quantity $e^{i\phi}$, we get

$$e^{j\phi} \cdot \delta\Theta = \frac{\Gamma}{n} \cdot \left[e^{j\phi} + e^{j2\phi} + \dots + e^{j(n-1)\phi} + e^{j(n)\phi} \right] \quad (5)$$

Equations 4 and 5 can then be differenced to yield

$$\delta\Theta = \frac{\Gamma}{n} \cdot \frac{\left(1 - e^{jn\phi}\right)}{\left(1 - e^{j\phi}\right)} \quad (6)$$

The nutation angle induced by the maneuver is just the magnitude of this vector in the complex plane. This magnitude can be derived from equation 6 by using the equality

$$e^{in\phi} = \cos(n\phi) + i \cdot \sin(n\phi) \quad (7)$$

Thus,

$$|\delta\Theta| = \frac{\Gamma}{n} \cdot \frac{\left|\left[1 - \cos(n\phi)\right] - i\left[\sin(n\phi)\right]\right|}{\left|(1 - \cos\phi) - i(\sin\phi)\right|}$$

This equation reduces to

$$|\delta\Theta| = \frac{\Gamma}{n} \cdot \sqrt{\frac{1 - \cos(n\phi)}{1 - \cos\phi}} \quad (8)$$

Equation 8 thus gives an approximation for the nutation angle, $\delta\Theta$, induced by an attitude maneuver of size Γ that is subdivided into a number of small burns, n. It is immediately apparent from this equation that the induced nutation angle can be reduced by sufficiently increasing the value of n, i.e., by dividing the maneuver into as many small burns as possible. For ACE, the smallest allowable burn time is dictated by the thruster command resolution and is equal to 32 msec. It is also clear from equation 8 that the induced nutation angle is directly proportional to the size of the maneuver, Γ. Thus, nutation could be reduced by performing attitude maneuvers more frequently than every 6 days and by maintaining a tighter deadband on the HGA-nadir angle than the allowable 3 degrees.

Based on this knowledge, we can estimate how much nutation would be induced for a maneuver using a ±1 degree deadband and the maximum number of small burns (minimum pulsewidth.) This gives a burn arc half-angle of

$$\alpha = \frac{1}{2} \cdot (0.032 \sec) \cdot (30°/\sec) = 0.48°$$

From equation 3, we compute that each small burn moves the spin axis 0.0176°; thus it will

take approximately 114 small burns of a lower deck radial thruster to achieve the 2° maneuver.

The function given in equation 8 are shown in Figures 2 and 3 for the two lowest values of ϕ, which represent thrusting once per 1/2 revolution and once per revolution, respectively. (*Higher values of ϕ were also analyzed. However, the results were essentially the same as those for the two lowest values of ϕ. Since the time required to execute a maneuver increases with ϕ, the results from using higher values of ϕ are not presented.*) Figures 2 and 3 show that the functions exhibit a sinusoidal behavior under an envelope proportional to 1/n. The envelope represents the maximum expected induced nutation angle for an attitude maneuver subdivided into an integral number of small burns. The envelope is minimized for the case of 1 small burn executed per revolution (Figure 3.)

An analytic expression can be derived for the envelope by using Taylor Series expansion of the cosine terms and assuming that the ratio I_3/I_T is close to 1.50. (*This number gives values of ϕ that are integral multiples of $\pi/2$ and simplifies the cosine terms in equation 8.*) This assumption is valid for the deployed ACE spacecraft configuration from BOL to EOL. The Taylor Series expansion reduces to:

$$\delta\Theta_{max} = \frac{\Gamma}{n} \cdot \sqrt{2\left[1 + (2\phi_1 - 3\pi)\right]} \qquad (9)$$

for $\phi_1 = \pi^* \, I_3/I_T$ (1 small burn per 1/2 revolution, as seen in Figure 2),

or,

$$\delta\Theta_{max} = \frac{\Gamma}{n} \cdot \sqrt{1 - \frac{(\phi_2 - 3\pi)^2}{12}} \qquad (10)$$

for $\phi_2 = 2\pi^* \, I_3/I_T$ (1 small burn per 1 revolution, as seen in Figure 3)

The size of the envelope at the far right end of the horizontal axis in each figure represents how much nutation should be expected at the end of a maneuver when using a single lower deck radial thruster. The induced nutation angle is approximately 0.0237 ° when using ϕ_1 and 0.0177 ° when using ϕ_2. This suggests that the final nutation angle for ϕ_2 will be only 75% of that for ϕ_1. Thus, even though using ϕ_2 will take twice as long as using ϕ_1 to execute the maneuver (22.6 minutes vs. 11.6 minutes), more than 2-¾ hours [*ln(0.0237)·9.5 hours)*] of nutation damping time can be avoided. When using the axial thrusters, the maneuver will be complete after about 58 small burns. The induced nutation will be nearly twice as high (approximately 0.0461 ° for ϕ_1 and 0.0345 ° for ϕ_2) as with the radial thrusters. This increase is caused because the larger moment arm imparts larger, less impulsive, torques on the spacecraft with each thruster burn. Therefore, it is desirable to use the radial thrusters instead of the axial thrusters to perform attitude maneuvers.

Note that the 1/n envelope represents a conservative estimate of what the induced nutation will be after n thruster firings. In theory, the induced nutation should actually be less, as dictated by equation 8. The true nutation angle should actually fall along the sinusoidal curve as shown in Figure 3. In practice, though, it will be difficult to predict the true shape of the sinusoid, since that would require an accurate prediction of the phase angle, ϕ, and consequently the ratio I_3/I_T. Predictions of the inertia properties, based on onboard fuel estimates, will be maintained for ACE, but may be in error by several percentage points.
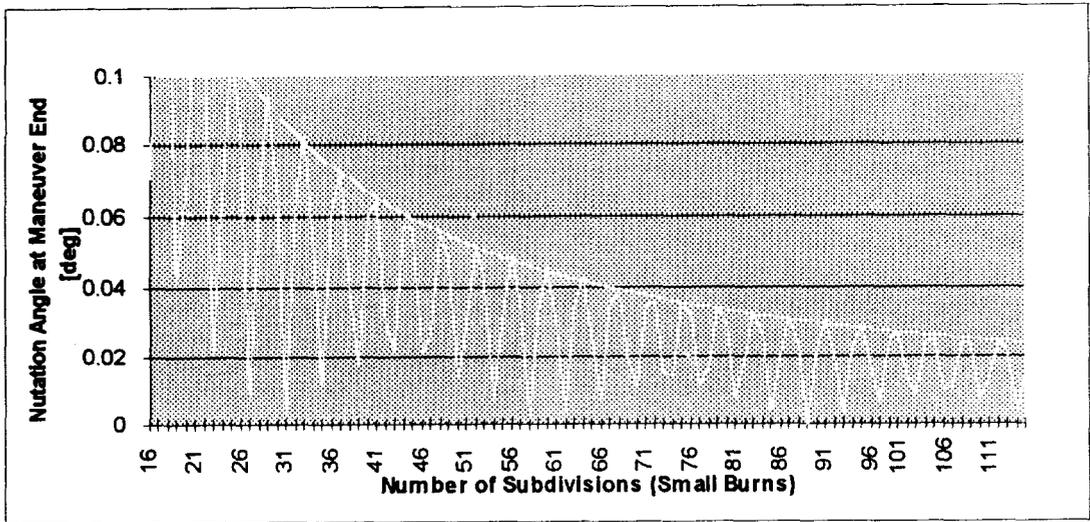
Figure 2. ACE Nutation: 1 Burn per 1/2 Revolution
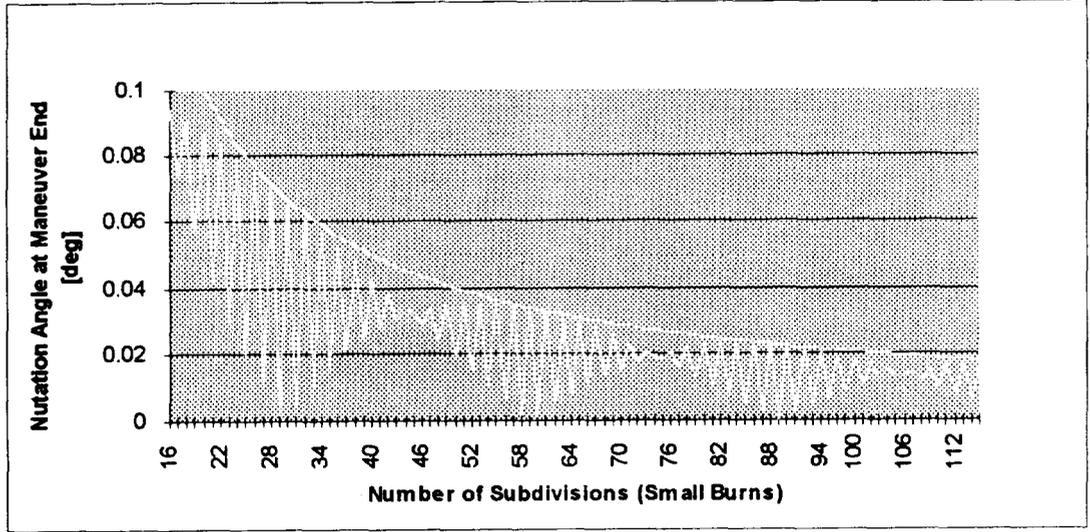
Figure 3. ACE Nutation: 1 Burn per 1 Revolution

III. VERIFICATION VIA SIMULATION

A dynamics simulator developed from PC-MATLAB was used to verify the accuracy of the analytic equation for the induced nutation angle given in Equation 8. The dynamics simulator models the ACE thruster burns and integrates the equations of motion to predict the effect on the spacecraft attitude.

The dynamics simulator was run and compared with the results shown in Figure 3. The following scenario was used in the simulation:

- a 2° attitude maneuver was modeled,
- firing of the lower deck thruster, IIIR, was simulated,
- thruster pulsing was once per spacecraft revolution,
- the minimum on-time of .032 sec was used,
- the simulation was run for 1400 sec (approximately 116 thruster firings.)

178

The simulation results are shown in Figure 5. The Figure shows the actual nutation angle as it changes during the course of the 2° attitude maneuver. The nutation angle changes after each thruster burn, and varies from about 0.001° to 0.032°. At the end of the attitude maneuver (after 1368 seconds), the residual nutation is approximately 0.024°. This agrees within about 25% to the value of 0.0177° derived in the previous section.

Nutation Amplitude
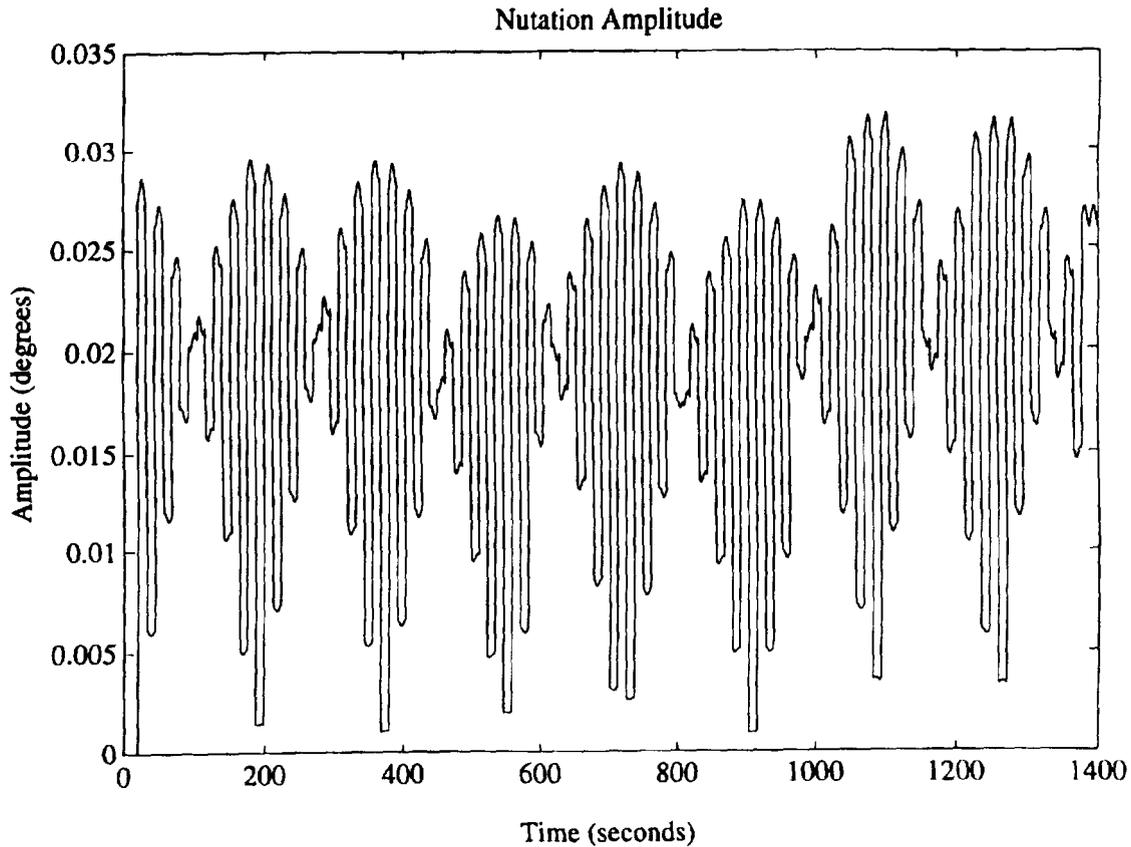
Figure 4. Dynamics Simulation of ACE Nutation During an Attitude Maneuver

IV. NUTATION MONITORING

Following each attitude maneuver, ground operations personnel will need to quantify the amount of nutation induced. From the preceding analysis, we can expect nutation to be somewhat less than 0.025°. The nutation angle can be computed from the telemetered sensor data provided that the sensor accuracy is less than the actual nutation angle. The ACE Sun sensor is the Adcole model 27990. It is accurate only to ~0.25°, so it will not be useful for observing small nutation angles. The star

tracker is the Ball Aerospace (BASG) model CT-631. It is accurate to ~0.025° (~1.5 arc-min) and therefore may provide observability of post-maneuver nutation angles.

The CT-631 sensor has a 20° x 20° field of view (FOV) and is typically used on three-axis stabilized spacecraft. Some modifications to the onboard star searching and tracking algorithms allow its use on a spinning spacecraft, such as ACE. For ACE, the star tracker is mounted with its boresight 90° form the spacecraft Z-axis. As the spacecraft spins, the star tracker views a swath of the sky that is 20° x 360°. Due

to star tracker processing limitations, this swath cannot be viewed as a continuum, but must be divided into 900 "pickets". Each picket is a region of the sky which is 0.4° x 20°. The FOV swath is viewed as a "picket fence", which has all 900 pickets placed in adjunction. Figure 5 shows the pickets which the ACE star tracker searches during one spacecraft revolution. During each full spacecraft revolution, the star tracker views every 8th picket and searches for stars within those pickets. During subsequent spacecraft revolutions, the "picket fence" is advanced by one picket, and every 8th picket is again observed. After 8 complete revolutions (nominally every 96 seconds), the entire 20 degree field of view band has been searched.
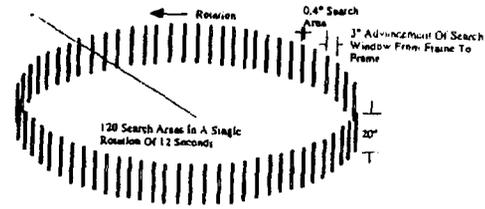
Figure 5. ACE Star Tracker Sky Search

For a nutating spacecraft, a fixed celestial object (such as a star) varies in declination sinusoidally relative to a spacecraft-mounted sensor (such as a star tracker) with an amplitude equal to twice the nutation angle. This effect is illustrated in Figure 6. The high-frequency sinusoidal curve represents the actual declination angle relative to the sensor and the 8 squares represent the observed declination angle, sampled every 96 seconds. The spacecraft nutation angle can then be observed by collecting enough simultaneous observations of the object such that the object passes through the full range of declination angles.
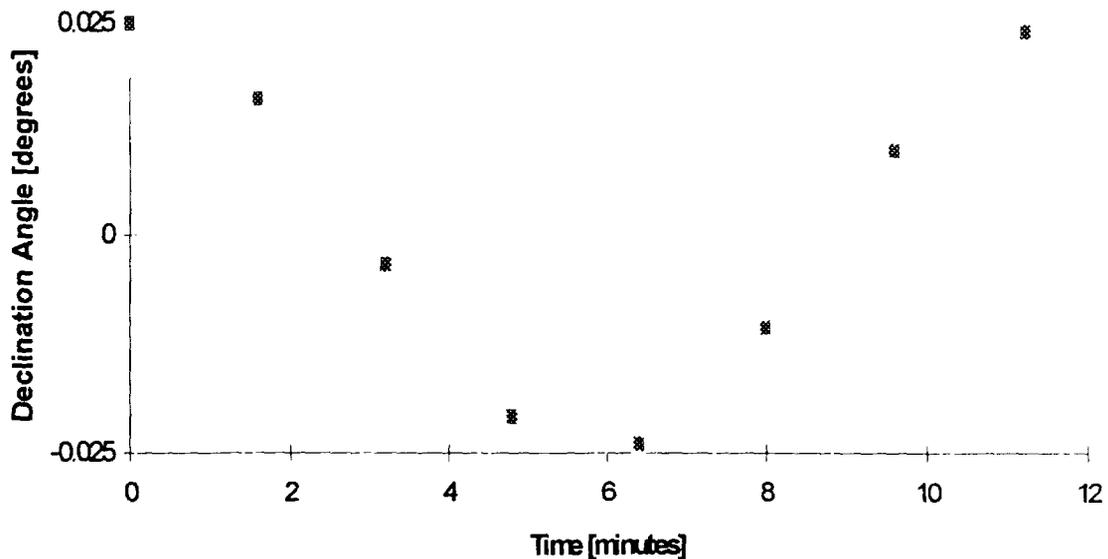
Figure 6. Effect of Nutation on Star Tracker Observations

The object also precesses at the inertial nutation rate, Ω_I, defined as

$$\Omega_I = \left(\frac{I_3}{I_T}\right) \cdot \Omega_s \qquad (11)$$

where

I_3 = the major moment of inertia ,
I_T = the transverse moment of inertia, defined as $(I_1 \cdot I_2)^{1/2}$, and
Ω_s = the spacecraft spin rate.

For ACE, the ratio I_3/I_T is always fairly close to a value 1.5. This means that between subsequent observations of a given star (after 8 spacecraft revolutions), the star has precessed along its sinusoidal path (relative to the sensor) by approximately 1.5 · 8 · 360 degrees, or approximately 12 complete revolutions. Since a sine curve repeats itself after each complete 360 degree cycle, subsequent observations of a given star by the ACE star tracker will show little change in declination. Thus many star observations will need to be collected in order to determine the nutation angle. The number of observations required is a function of actual spin rate and the inertia ratio. Figure 6 illustrates this effect for ACE, using typical values of 5 RPM for the spin rate and 1.483 for the inertia ratio. After about 8 samples, or 11.2 minutes, the observed declination angle has gone through the full range of declination angles.

In the general case, the amount of time required to observe the full range of declination angles depends on the actual inertial nutation rate, which is a function of both the actual spin rate and inertia ratio, as implied in equation 11. A parametric study will be performed to see how that function behaves for ACE. In general, it is desirable to minimize the amount of time needed to observe the nutation effect.

For ACE, the spin rate is required to be maintained at 5.0 ± 0.1 RPM. The inertia ratio, I_3/I_T, will be approximately 1.494 at beginning-of-life and, as propellant is expelled, will

decrease to a value approximately 1.471 at end-of-life. Thus, the following relations can be used:

$$\Omega_s = \Omega_0 + \varepsilon_\Omega \qquad (12)$$

where

Ω_s = actual spacecraft spin rate,
Ω_0 = nominal spin rate, $\pi/6$ rad/sec,
ε_Ω = allowable spin rate variation, $|\varepsilon_\Omega| \leq \pi/300$ rad/sec,

and

$$\frac{I_3}{I_T} = 1.5 - \varepsilon_I \qquad (13)$$

where

ε_I = variation in inertia ratio, a small positive number.

These two equations can be substituted into the original equation to give the inertial nutation rate as

$$\Omega_I = \left(1.5 - \varepsilon_I\right) \cdot \left(\Omega_0 + \varepsilon_\Omega\right) \qquad (14)$$

which when expanded gives

$$\Omega_I \cong 1.5 \cdot \Omega_0 + 1.5 \cdot \varepsilon_\Omega - \Omega_0 \cdot \varepsilon_I \qquad (15)$$

After 8 complete revolutions, the phase shift, $\Delta\phi$, of the star will be

$$\Delta\phi = (8 \cdot 2\pi) \cdot \frac{\Omega_I}{\Omega_0}$$

or

$$\Delta\phi = 24\pi + 24\pi \cdot \frac{\varepsilon_\Omega}{\Omega_0} - 16\pi \cdot \varepsilon_I \qquad (16)$$

The term 24π can be ignored, since it is a multiple of 2π, and will not effect the phase shift computation. The absolute value of the remaining terms can be used to express the

magnitude of the phase shift, whether left or right. The equation then becomes

$$\Delta\phi = \left| 24\pi \cdot \frac{\varepsilon_\Omega}{\Omega_0} - 16\pi \cdot \varepsilon_I \right| \qquad (17)$$

This angle, $\Delta\phi$, again represents a small phase shift along the sinusoid, achieved after 8 successive revolutions. The nutation angle can only be characterized after many such small phase shifts take the observation through a complete phase cycle of 2π. The time, t, in minutes, required to complete this cycle is then

$$t = 8 \cdot \left(\frac{2\pi}{\Omega_0} \right) \cdot \left(\frac{2\pi}{\Delta\phi} \right) \cdot \left(\frac{1\,\text{min}}{60\,\text{sec}} \right) \qquad (18)$$

which reduces to

$$t = \left| \frac{45 \cdot \varepsilon_\Omega}{\pi} - 5 \cdot \varepsilon_I \right|^{-1} \text{minutes} \qquad (19)$$

By using spin rates in units of RPM, the equation simplifies to

$$t = \left| 1.5 \cdot (\Omega_s - \Omega_0) + 5 \cdot \left(\frac{I_3}{I_T} \right) - 7.5 \right|^{-1} \qquad (20)$$

Equation 20 is plotted in Figure 7 using the full range of values for Ω_s and I_3/I_T.
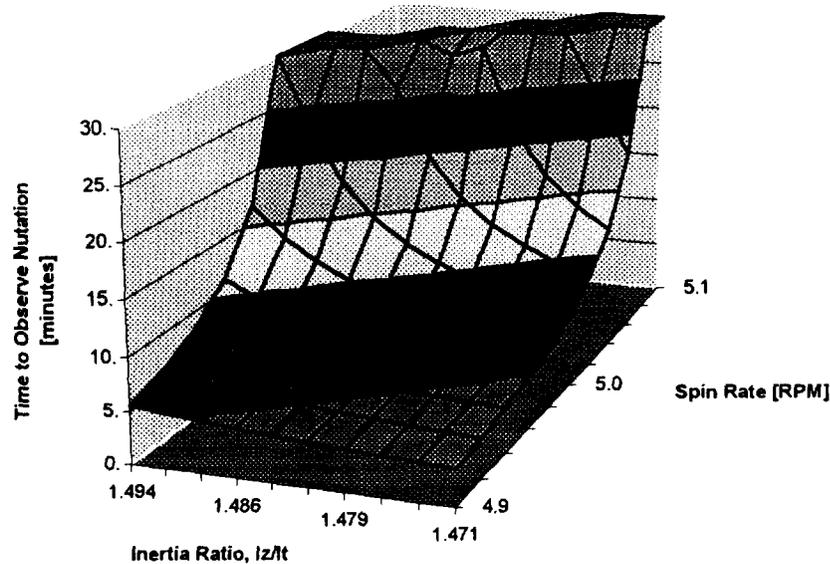
Figure 7. Nutation Observation Times

Figure 7 shows graphically the time, in minutes, required to observe the ACE nutation angle for a given spin rate and inertia ratio. The graph is truncated on the vertical axis at 30 minutes; approximately 20% of the combinations of spin rate and inertia ratio are above this plateau and will require more than 30 minutes of star data to characterize the nutation angle. This indicates that for randomly chosen values of spin rate and inertia ratios, we can observe the nutation angle

C-3

within 30 minutes 80% of the time. This percentage can be increased to nearly 100% by maintaining a spin rate of less than 5 RPM. Nutation observation time also decreases as the inertia ratio decreases; this will be the trend as the life of the mission goes on, and hydrazine fuel is periodically used to perform maneuvers.

V. SUMMARY AND CONCLUSIONS

Strategies have been developed for planning and executing ACE attitude maneuvers that will allow spacecraft nutation to be controlled. Nutation monitoring techniques have also been identified. In summary,

- by properly subdividing the attitude maneuvers, the induced nutation can be kept low
- there is an advantage to using one thruster pair pulse per revolution instead of two
- performing the maneuvers with the radial instead of the axial thrusters will reduce the induced nutation by a factor of nearly 1/2
- maintaining a spin rate of less than 5 RPM will assist in quickly assessing the post-maneuver nutation angle. As a secondary advantage, a lower spin rate will provide the spacecraft with less gyroscopic stiffness and allow attitude maneuvers to be performed more efficiently.

VI. ACKNOWLEDGMENTS

VII. REFERENCES

1) J. R. Wertz et al., **Spacecraft Attitude Determination and Control**, ISBN 90-277-0959-9, D. Reidel Publishing Company.

2) Peter C. Hughes, **Spacecraft Attitude Dynamics**, ISBN 0-471-81842-9, John Wiley & Sons.

3) "Advanced Composition Explorer (ACE) Critical Design Review (CDR)", presentation materials, November 1-3, 1994.

4) D. F. Baker, "ACE Attitude Maneuver Durations", interoffice memorandum, March 18, 1993.

5) D. Junker, "Maneuver Nutation Impact on Science Data Collection", interoffice memorandum, November 7, 1994.

6) M. McCullough, ACE Thruster Locations", interoffice memorandum, December 20, 1994.

7) J. W. Hunt, "Spin-period Variation vs. Nutation", interoffice memorandum, December 22, 1994.

Experience from the In-Flight Calibration of the Extreme Ultraviolet Explorer (EUVE) and Upper Atmosphere Research Satellite (UARS) Fixed Head Star Trackers (FHSTs)

Michael Lee
Goddard Space Flight Center (GSFC)
Greenbelt, Maryland, USA

Abstract

Since the original post-launch calibration of the FHSTs on EUVE and UARS, the Flight Dynamics task has continued to analyze the FHST performance. The algorithm used for inflight alignment of spacecraft sensors is described and the equations for the errors in the relative alignment for the simple 2 star tracker case are shown. Simulated data and real data are used to compute the covariance of the relative alignment errors. Several methods for correcting the alignment are compared and results analyzed. The specific problems seen on orbit with UARS and EUVE are then discussed. UARS has experienced anomalous tracker performance on an FHST resulting in continuous variation in apparent tracker alignment. On EUVE, the FHST residuals from the attitude determination algorithm showed a dependence on the direction of roll during survey mode. This dependence is traced back to time tagging errors and the original post launch alignment is found to be in error due to the impact of the time tagging errors on the alignment algorithm. The methods used by the FDF to correct for these problems is described.

I. Introduction

The Flight Dynamics Facility (FDF) has implemented the algorithm described by Shuster, et. al. (Reference 1) in the Multimission Three-Axis Stabilized Spacecraft (MTASS) Flight Dynamics Support System (FDSS). This system has been used to determine alignments among the FHSTs and the Fine Sun Sensors (FSSs) for the EUVE and UARS missions. Although the software is capable of computing alignments for the Earth Sensor Assemblies on UARS, the nature of the Earth Sensors (residuals varying by an order of .1 deg over the period of an orbit) makes the algorithm inappropriate for use for these sensors. The algorithm has performed well for these missions, but is being replaced by a method devised by William Davis of CSC for the next generation of sensors; specifically, Charge Coupled Device (CCD) Star Trackers which provide multiple star observations simultaneously (Reference 2). In the time

since UARS was launched (September 12, 1991), the FDF has become experienced in the application of the alignment algorithm and has an increased understanding of some of the implications and pitfalls associated with the algorithm and with alignment calculation in the general sense.

II. Overview of Alignment Algorithm

Once a spacecraft has been launched, only relative sensor alignments can be observed. Any attempt to compute absolute alignments must include a priori information from pre launch data. The algorithm, from a high level point of view, is comprised of the following steps:

(1) Measurements from the sensors are grouped together based on the times the measurements were made. Ideally, simultaneous measurements are desired for this approach. As an attempt to minimize the impacts of propagation errors, only observations relatively close in time are propagated to a common time using the gyro data. The actual criteria for grouping is an user input, usually observations closer in time than 2 seconds are grouped. The maximum propagation errors for FDF processing is less than .1 arcsec based on observed gyro performance.

(2) The derived measurements then used for the alignment process are the differences in the dot products of the reference and the observed vectors. This derived measurement is independent of the attitude.

(3) A maximum likelihood estimate of the alignments is computed which minimized the appropriate weighted sum of the squares of the differences between observed and reference scalar products of the star directions.

III. Mission Descriptions (Sensor Complements)

For both UARS and EUVE, the primary sensor complement consists of 2 FHSTs (arbitrarily designated as FHST 1 and FHST 2), 1 FSS and the gyros (the NASA Standard Inertial Reference Unit, DRIRU-II). Normal onboard and ground processing uses the FHSTs and the gyros for attitude determination. For the current FSS transfer function, a substantial sampling of observations across the FSS field of view (FOV) is required in order to accurately align the FSS. During normal mission operations, this data is not routinely available. However, the alignment of the FHSTs can be determined relative to each other without recourse to FSS data, and this is the normal operational procedure. The problem is now well defined; given a sensor complement of two FHSTs and the gyros, what is the best approach to maintaining the alignment of the FHSTs.

IV. Statistics of 2 FHST Alignment

Reference 1 gives the complete mathematical derivation of the alignment algorithm for multiple sensors. However, the simpler 2 FHST case of concern for the two missions (EUVE and UARS) is worth examining in its own right. Following the derivation of Reference 1, let the unit vector to the observed star in the sensor frame be denoted by $\hat{U}_{i,k}$, where i = 1 or 2 for FHST 1 or FHST 2 and k is a time index. The observed vector is related to the true vector by

$$\hat{U}_{i,k} = \hat{U}_{i,k}^{true} + \Delta\hat{U}_{i,k} \tag{1}$$

with $\Delta\hat{U}_{i,k}$ assumed Gaussian, zero-mean and white with covariance $R_{\hat{U}_{i,k}}$.

The measurements from the two FHSTs are assumed to be statistically independent. Let $\hat{W}_{i,k}$ denote the measured direction in the spacecraft body frame. Then the alignment matrix for FHST i, S_i, is the orthogonal matrix defined by

$$\hat{W}_{i,k} = S_i\hat{U}_{i,k} \tag{2}$$

and, therefore,

$$\hat{W}_{i,k} = S_i(\hat{U}_{i,k}^{true} + \Delta\hat{U}_{i,k}) \equiv \hat{W}_{i,k}^{true} + \Delta\hat{W}_{i,k} \tag{3}$$

At this point define the misalignment matrix by $S_i = M_i S_i^0$ with S_i^0 the a priori alignment matrix. To first order in the misalignment vectors Θ_i,

$$M_i = I + \begin{bmatrix} 0 & \theta_3 & -\theta_2 \\ -\theta_3 & 0 & \theta_1 \\ \theta_2 & -\theta_1 & 0 \end{bmatrix} \equiv I + [[\Theta_i]] \tag{4}$$

with I the identity matrix. As in Reference 1, do not confuse the subscripts on θ denoting components of the vector Θ_i with the subscripts on Θ_i which label the FHSTs. Define the "uncalibrated" body-referenced observation vector as

$$\hat{W}_{i,k}^0 \equiv S_i^0\hat{U}_{i,k} \tag{5}$$

and write

$$\hat{W}_{i,k}^0 = M_i^T\hat{W}_{i,k} \approx (I - [[\Theta]])\hat{W}_{i,k}^{true} + \Delta\hat{W}_{i,k}^0 \tag{6}$$

with M_i^T denoting the transpose of M_i . To achieve attitude independence, we now consider the dot products of the observation vectors for the two FHSTs and ...te that (neglecting the random

errors in the reference vectors) the dot products of the true observation vectors can be replaced by the dot products of the reference vectors to write the equation from Reference 1,

$$\hat{W}_{1,k}^0 \bullet \hat{W}_{2,k}^0 \cong \hat{V}_{1,k} \bullet \hat{V}_{2,k} + (\hat{W}_{1,k}^0 \times \hat{W}_{2,k}^0) \bullet (\Theta_1 - \Theta_2) + \hat{W}_{1,k}^{true} \bullet \Delta\hat{W}_{2,k}^0 + \hat{W}_{2,k}^{true} \bullet \Delta\hat{W}_{1,k}^0 \qquad (7)$$

Define the measurement

$$z_k = \hat{W}_{1,k}^0 \bullet \hat{W}_{2,k}^0 - \hat{V}_{1,k} \bullet \hat{V}_{2,k} = (\hat{W}_{1,k}^0 \times \hat{W}_{2,k}^0) \bullet (\Theta_1 - \Theta_2) + \Delta z_k \cong H_k(\Theta_1 - \Theta_2) + \Delta z_k \qquad (8)$$

with

$$\Delta z_k \cong \hat{W}_{1,k}^{true} \bullet \Delta\hat{W}_{2,k}^0 + \hat{W}_{2,k}^{true} \bullet \Delta\hat{W}_{1,k}^0 \qquad (8a)$$

and

$$H_k = (\hat{W}_{1,k}^0 \times \hat{W}_{2,k}^0)^T . \qquad (8b)$$

Replace $\hat{W}_{i,k}^{true}$ by $\hat{W}_{i,k}^0$ (to lowest order in the covariance) so that the statistics of Δz_k are given by

$$E\langle \Delta z_k \rangle = 0$$

$$E\langle \Delta z_k^2 \rangle = P_{z_k} = (\hat{W}_{1,k}^0)^T R_{\hat{W}_{2,k}^0} \hat{W}_{1,k}^0 + (\hat{W}_{2,k}^0)^T R_{\hat{W}_{1,k}^0} \hat{W}_{2,k}^0 \qquad (9)$$

With our assumptions, the $\Delta\hat{W}_{i,k}^0$ will be Gaussian, zero-mean and white. Further assume the errors to be uniformly distributed so that (for unit measurement vectors) the covariance of the measurement vector errors in the body frame can be written in the form:

$$R_{W_{i,k}}^0 = \sigma_i^2(I - \hat{W}_{i,k}^0 \hat{W}_{i,k}^{0\,T}) \qquad (10)$$

for σ denoting the standard deviation of the measurement error. The application of maximum likelihood estimation techniques to compute $\Psi = (\Theta_1 - \Theta_2)$ leads to the negative-log-likelihood function

$$J_\Psi(\Psi) = \frac{1}{2}\sum_k \left[(z_k - H_k\Psi)^T P_{z_k}^{-1}(z_k - H_k\Psi)\right] + \log(\det P_{z_k}) + \log(2\pi) \qquad (11)$$

Minimizing $J_\Psi(\Psi)$ over Ψ gives

$$P_{\Psi\Psi}^{-1}\Psi^* = \sum_k H_k^T P_{z_k}^{-1} z_k \qquad (12)$$

and

$$P_{\Psi\Psi}^{-1} = \sum_k H_k^T P_{z_k}^{-1} H_k \qquad (13)$$

Results from this last equation for the covariance of the relative alignment computation will be shown and discussed in later sections. Note that the variable Ψ is the difference in the misalignment vectors Θ_i showing explicitly that only the relative alignment of FHST 1 to FHST 2 can be computed based on in-flight data.

To determine the actual alignments for the individual sensors requires that a priori information on the alignments be provided.

The algorithm as implemented in the FDF takes the a priori misalignment matrices M_i and the covariance associated with them as input.

V. Covariance of Relative Alignment for EUVE for Simulated Data

An idealized case was simulated, using the EUVE spacecraft star tracker configuration, in which the observation vectors are evenly distributed over the FOVs of each tracker. The relative positions of the UARS star trackers are nearly identical, so that the results can be applied to either spacecraft. The computed covariance of the relative alignment error (in the EUVE body frame) is

$$P_{\psi\psi} = \begin{bmatrix} 62.058103 & 0.012787 & 0.008896 \\ 0.012787 & 100.752449 & -35.601872 \\ 0.008896 & -35.601872 & 12.780823 \end{bmatrix}$$

(14)

where, for convenience, the covariance matrix is given in the units of arcsec (squared). The importance, or lack thereof, of the scaling of the covariance matrices will be discussed later. The covariance matrix in this form does not tell us much, so consider the eigenvectors and eigenvalues. The eigenvalues, λ_i , arranged as a vector and ordered from smallest to largest, are listed below:

$$\vec{\lambda} = \begin{pmatrix} .178 \\ 62.058 \\ 113.355 \end{pmatrix} arc\sec^2$$

(15)

Instead of listing the eigenvectors, denote the three (unitized) eigenvectors as $\vec{\varepsilon}_i$, corresponding to the λ_i . Then $\vec{\varepsilon}_1$ turns out to be along the cross product of the boresight of FHST 1 with the boresight of FHST2. $\vec{\varepsilon}_3$ is along the average of the two bore sights, and the second eigenvector is given by $\vec{\varepsilon}_3 \times \vec{\varepsilon}_1$. The covariance matrix can be written as

$$P_{\psi\psi} = \lambda_1 \varepsilon_1 \varepsilon_1^T + \lambda_2 \varepsilon_2 \varepsilon_2^T + \lambda_3 \varepsilon_3 \varepsilon_3^T$$
$$= \lambda_1 \varepsilon_1 \varepsilon_1^T + \tfrac{1}{2}(\sqrt{\lambda_2}\varepsilon_2 + \sqrt{\lambda_3}\varepsilon_3)(\sqrt{\lambda_2}\varepsilon_2 + \sqrt{\lambda_3}\varepsilon_3)^T + \tfrac{1}{2}(\sqrt{\lambda_2}\varepsilon_2 - \sqrt{\lambda_3}\varepsilon_3)(\sqrt{\lambda_2}\varepsilon_2 - \sqrt{\lambda_3}\varepsilon_3)^T$$

(16)

The computed eigenvalues λ_2 and λ_3 can be seen to be related by

189

$$\sqrt{\frac{\lambda_2}{\lambda_3}} = \tan(\alpha/2) \tag{17}$$

for α denoting the angle between the FHST bore sights (72.996 deg for EUVE). With this result, it can be seen that

$$P_{\Psi\Psi} = \lambda_1 \varepsilon_1 \varepsilon_1^T + \frac{1}{2}(\lambda_2 + \lambda_3)\left\{\hat{B}_1 \hat{B}_1^T + \hat{B}_2 \hat{B}_2^T\right\} \tag{18}$$

for $\hat{B}_i$ the unit vector along the boresight of FHST i. This is an important result: for the case of ideally distributed observations (evenly over the FOVs of both trackers), the error in the computed relative alignment angle has a large component along each FHST boresight and a much smaller component in the direction of the cross product of the bore sights. Dividing the uncertainty equally between the two trackers, the relative alignment uncertainty (1-sigma) for FHST i is given by $\sqrt{\frac{\lambda_1}{2}}$ about the cross product of the bore sights and by

$$\sqrt{\frac{1}{2}(\lambda_2 + \lambda_3)} \tag{19}$$

about the boresight $\hat{B}_i$. The reference frame defined by the eigenaxes for the simulated ideal case, will be denoted as the "average boresight frame."

VI. Results: Covariances of Relative Alignment for UARS and EUVE

Since launch, FHST 1 for UARS has exhibited anomalous behavior. The scale factor relating the FHST output to a measurement position has been decreasing monotonically with respect to time and the alignment has undergone an apparent rotation about the nominal boresight of the tracker. This anomaly has been reported on several missions previously (References 2 and 3), and is not the intended subject of this paper. The scale factor is adjusted routinely so that the net FHST measurement noise is equivalent to that of the unaffected FHSTs.

For UARS, the FDF attitude operations task routinely computes the relative alignment of the star trackers in order to monitor the behavior of the anomalous tracker. Since these alignments are not intended for uplink to the UARS spacecraft, only 2 hours of data are used. Assuming the 1-sigma FHST error for UARS to be 12 arcsec (based on typical residuals seen in the attitude determination process), this leads to fairly large variations in the covariances. The estimate of the error based on equation

(19) in the determination of the FHST rotation about its boresight is typically of the order of 50 arcsec based on 2 hours of data.

Data was collected from a recent (January 19 through 21, 1995) set of slews for EUVE, resulting in a total of 2779 observation pairs. The eigenvalues ε_i of the alignment covariance matrix were calculated using equations 8b, 10 and 13, and assuming FHST noise of 23.5 arcsec based on results from routine attitude determination. The angle from ε_1 to the cross product of the EUVE bore sights was 0.36 deg while $\vec{\varepsilon}_3$ was at an angle of 0.23 degrees from the average of the bore sights. The eigenvalues of the covariance matrix (using the 23.5-arcsec FHST error number) were as follows:

$$\vec{\lambda} = \begin{pmatrix} 0.4 \\ 263. \\ 423. \end{pmatrix} \text{arcsec}^2$$

giving an estimate of 19 arcsec as the 1-sigma error in the determination of the FHST rotation about its boresight. The near alignment of the eigenaxes with the average boresight frame indicates that the FHST field of views were covered uniformly enough to approach the idealized case simulated in Section IV.

VI. Discussion of Covariance Results

As shown, inflight data can only determine the relative alignment between the two trackers. This leaves 3 degrees of freedom in the determination of the two alignment matrices for the two trackers. A common approach, one used on EUVE, is to arbitrarily choose one sensor (FHST 2 for EUVE) as the reference and apply the results from the inflight data to adjusting the alignment of the other sensor only. This approach is reasonable for the first post launch alignment using inflight data. However, if this approach is followed for following alignments, the inaccuracy in the alignment of the reference sensor about its boresight (on the order of an arc minute for UARS and EUVE based on recent alignment data) will result in a large shift of the non-reference sensor. Experience has shown that an one arc minute rotation of FHST 2 about its boresight will result in about a 1 arcsec change in the computed attitude. Holding FHST 2 fixed and forcing FHST 1 to adjust for the same apparent rotation will result in about a 20 to 30 arcsec change in the attitude. The exact attitude changes seen will depend on the location of the observed stars in the FHST FOVs

Any method for choosing the 3 extra degrees of freedom can be used initially; but, once this choice has been made, it is clear that care must be taken for later alignment updates. The inflight alignment process can determine the separation angles between sensors with good accuracy (down to the 1 arcsec level given sufficient data) but the determination of the sensor orientation about its boresight should be considered a much "noisier" value. As shown by the simulation for the ideal data case, the relative alignment error can be considered to be concentrated about the sensor bore sights. The usual desire when updating sensor alignments inflight is to reduce the impact of the new alignments on the attitude determination process. For UARS and EUVE, the science instruments' pointing is known relative to the spacecraft attitude, and a significant disturbance in the spacecraft attitude would require a realigning of the science instrument. For UARS, the original post launch alignment was computed after the science instruments had already been aligned to the onboard computer's determined attitude. This is not a wise procedure, but the FDF responded by forcing the computed FHST alignments to leave the average boresight frame invariant. This constraint minimized the attitude disturbance resultant from the alignment process.

When the next inflight alignment update is made, a suggestion based on operational experience and the results in Section V is to give relative weights to the existing alignments for each sensor *i* as described below.

As stated previously, the covariance of the current (prior to the alignment process) is input to the algorithm. These covariances are input in the body frame of the spacecraft. This allows the unobservable degrees of freedom to be determined based on the a priori information. The suggested way to prescribe these covariances is as follows. Weigh the variance of the error about the cross product of the two FHSTs by a product of $\dfrac{\lambda_1}{\lambda_2 + \lambda_3}$ relative to that about the boresight $\hat{B}_i$. For the EUVE and UARS missions, which share similar sensor geometries, the idealized values can be used, giving a relative weighing factor of 0.00086. The covariance of the previous alignment for FHST i, P_i, is then given by

$$P_i = c\left[\frac{\lambda_1}{2}\left\{\left(\hat{B}_1 \times \hat{B}_2\right)\left(\hat{B}_1 \times \hat{B}_2\right)^T\right\} + \frac{1}{2}\left(\lambda_2 + \lambda_3\right)\hat{B}_i\hat{B}_i^T\right]$$

where the c term is provided to scale the covariance in order to reduce the effect of the previously computed alignment

on the current processing. In operations, the usual approach is to allow the alignment to be determined mainly by the data input to the algorithm. The previous alignment is based on old data and the uncertainty is not well known (FHSTs alignment might not be updated in the onboard processing for months at a time) or the task is interested in trending the alignment results based solely on the current data. This will result in computed alignments which adjust the separation angle between the two trackers equally relative to the spacecraft body frame, and which allow each sensor to adjust its rotation about its boresight freely (for Scale terms large with respect to the assumed FHST noise). The impact on attitude determination due to this approach will be small unless the computed alignments result in large boresight rotations.

On UARS, the FHST 1 anomaly has resulted in a rotation of 1050 arcsecs since launch (as of November 1994). In this example, the impact on the ground attitude determination is still fairly small - a typical case shows a 7 arcsec change in the attitude determined based on the corrected alignment. The corrected alignment results in a large reduction in the FHST residuals (by a factor of approximately 5). Since UARS is constantly rotating at a 1 revolution per orbit rate (RPO), the boresight rotation effects tend to cancel due to averaging over the FOV.

An inertially fixed spacecraft would suffer a range of attitude errors resulting from a FHST misaligned about its boresight depending on the location of the observed stars in the tracker FOV. If the tracked star is exactly along the FHST boresight, the error in the observation would be zero, but this error would increase with the radial distance from the boresight to the edge of the FOV. The actual attitude disturbance seen would depend on the relative placement of the FHSTs, but would be limited in the worst case to be no greater than the error due to the boresight rotation in an observation at the farthest allowable point from the center of the FOV. The UARS and EUVE missions limit the observations used in the attitude determination process (onboard) to be within 4 degrees of the FHST boresight. The 1050 arcsec rotation of UARS results in a 73 arcsec error in the observation vector at 4 degrees from the boresight.

VI. EUVE FHST Data Timing Problems

For the EUVE mission, the FDF routinely performs attitude determination and updates various data bases so that the long term performance of the sensors can be monitored. For FHST trending, EUVE is put into the Survey mode, where the spacecraft rotates at 3 revolutions per orbit (3-RPO or approximately .19

deg/sec) about the x-axis (denoted as the roll axis) in the body frame. This allows multiple stars to sweep through the FHST FOVs and so is valuable for attaining information on the FHST performance. The rotation in the Survey mode can be either positive or negative about the x-axis, and it was noted that the averaged FHST residuals in the z-axis in the body frame showed a dependence on the roll direction. The y-axis is nearly parallel to the average boresight direction and the y-residuals show little impact due to the rotation about the x-axis. Figure 1, which displays the average of the FHST 1 residuals for EUVE for days when EUVE was in Survey mode (Flight day is the number of days since launch), clearly shows this dependence.

EUVE: FHST1 Z Residuals for Survey Mode
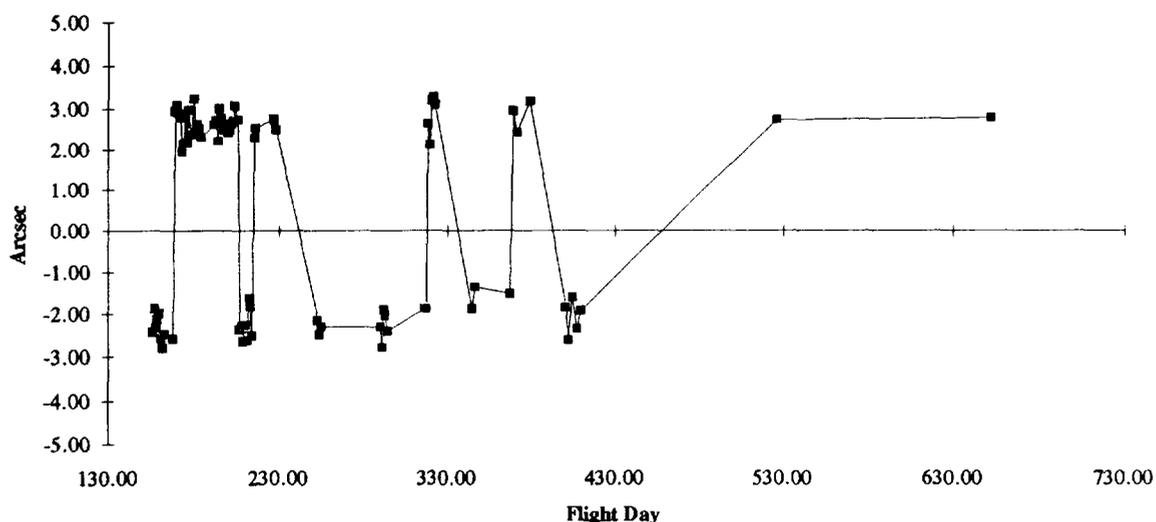
Figure 1

The negative average residuals occurred on days where the rotation rate was positive about the x-axis, while the positive residuals coincided with negative roll rates. For comparison, the plot for the x-axis residual (which are unaffected by rotations about the x-axis) shows no such behavior (Figure 2).

EUVE: FHST 1 Roll Residuals for Survey Mode
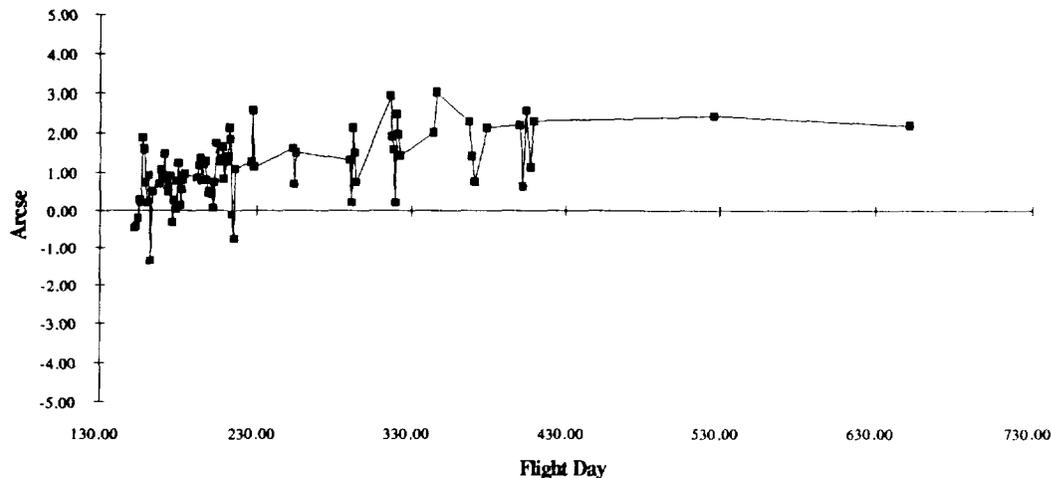
Figure 2

Although the magnitudes of the FHST residuals were still acceptable, it is clear that there is a systematic error in the FHST observations. FHST alignments were computed using positive roll data and compared to alignments which used just negative roll data. The alignments based on negative roll data only, when expressed in the spacecraft body frame, showed a relative alignment change of 79 arcsecs about the x-axis.

The dependence of FHST performance on roll direction implies a potential timing problem in the data. Residuals from some sample attitude determination processes (using a 2 hour time span) were collected and used to create a histogram to display the number of residuals with a given error (using a bucket size of approximately .5 arcsec). For the z-axis residuals, the errors are displayed as a time (in seconds) which would give the computed error based on the 3-RPO rotation rate. The reason for this will be discussed later. Figure 3 shows the histogram for the z-residuals for FHST 1 while Figure 4 contains the same plot for FHST 2. Data from a 2 hour time span on June 11, 1992 was used for these plots.

EUVE: Histogram of FHST1 Z Residuals
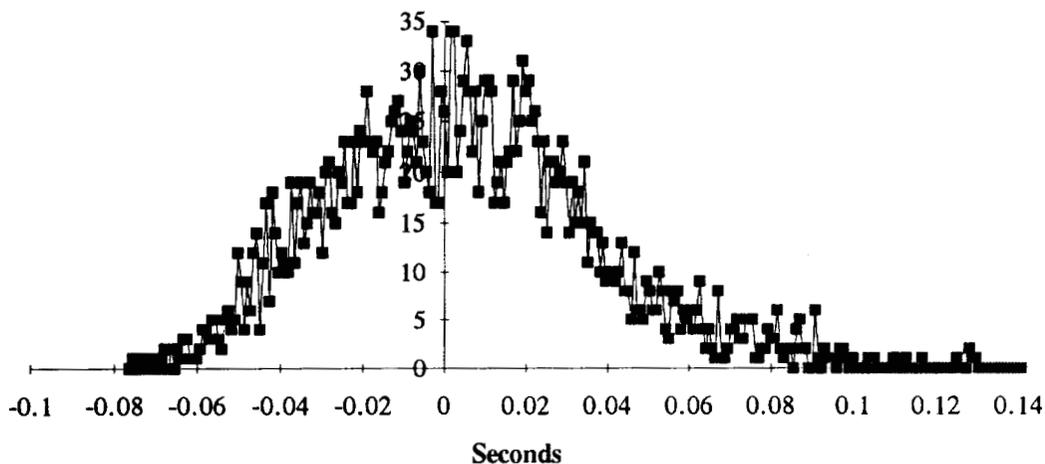
Figure 3

EUVE: Histogram of FHST2 Z Residuals
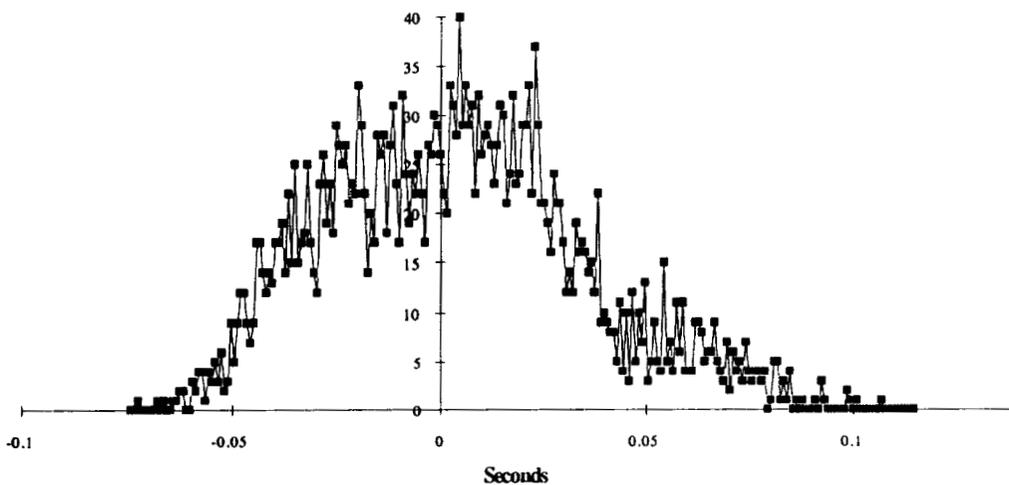
Figure 4

As before, the x-axis histogram of residuals for one of the FHSTs, FHST 1, is shown in Figure 5 for comparison. In this figure the residuals are in arcsecs.
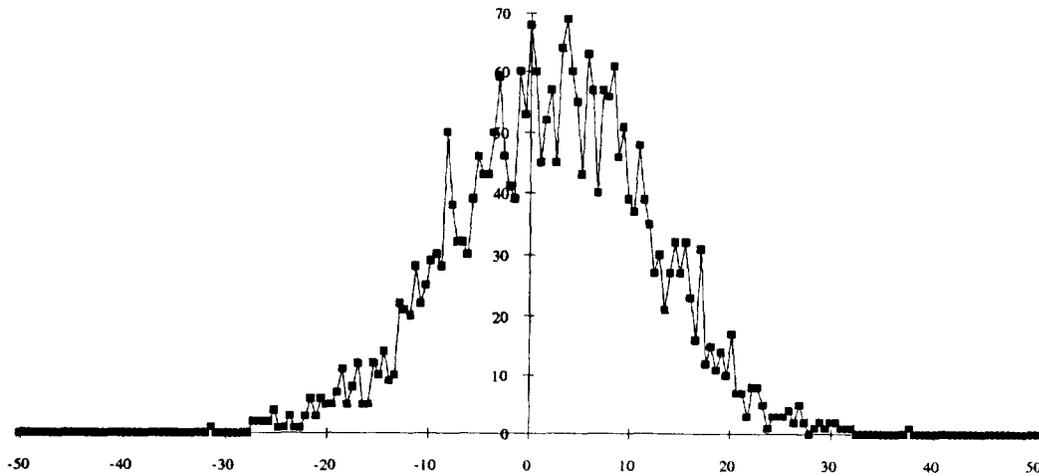
Figure 5

Note that the x-axis histogram in Figure 5 is symmetrical about zero while the z-axis residual histograms are not. The z-axis residuals can be affected by time tagging errors while the x-axis residuals are invariant. What can be seen is that the z-axis residuals extend out twice as far in the positive direction. The sample cycle of the FHST should now be described.

When a star is being tracked by the FHST, vertical and horizontal measurements (in the FHST frame) are alternated every 0.05 seconds. A complete star observation is made every 0.1 seconds. On the ground, we apply time offsets to apply a time tag which, it was hoped, would be within -0.05 to +0.05 of the actual measurement time. The results shown in Figures 3 and 4 can be explained if the vertical observation is occasionally an additional 0.05 seconds old, as the vertical FHST observation translates roughly into the Z-axis of the spacecraft body. These larger residuals occur with no discernible pattern in the observations.

VI. EUVE FHST Data Timing Problem: Discussion and Correction

The data used to align the FHSTs for EUVE post launch consisted entirely of positive roll data only. For calibration of star trackers, it is desirable to operate the spacecraft in a maneuvering mode so that many different stars will pass through all areas of the FOVs. Unfortunately, it can be seen that this makes the observations sensitive to time tagging problems. Based on the EUVE experience, calibration slews should include rotations in both the positive and negative directions about the

197

slew axes. This will allow the ground processing to check for consistency in the solutions and therefore to observe any time tagging errors. This was not done for the initial EUVE post launch alignments, which leaves the problem of making the correction.

Various approaches to calculating the correct alignment have been implemented. First is to take alignment solutions based on negative roll data and average the relative alignment correction with solutions based solely on positive roll data. Second is to perform new maneuvers that have equal time spans with positive and negative rolling. Third, the large residual observations which appear to contain the additional 0.5 second delay can be edited from the alignment process. Unfortunately, the third approach proved unfruitful. Although the dependence of the alignment results on the roll direction could be reduced, the nature of the time tag error is that observations within the .1 error span can still be in error although the observation residuals do not appear as outliers. The second approach is feasible if the number of observations during the positive roll time period is exactly equal to the number of observations during the negative roll time period. This is an unwieldy constraint, leaving the first option as the one actually taken for the operational solution to the problem. The net correction of 40 arcsec in the alignment was made following the guidelines suggested in this paper, so that the maximum attitude disturbance is less than 3 arcsec for EUVE in inertial mode.

Acknowledgments

References

1. Shuster, M. D., and Pitone, D. S., "Batch Estimation of Sensor Alignments. I. Relative Alignment Estimation," *Journal of the Astronautical Sciences,* Vol. 39, No. 4, October-December 1991b

2. Goddard Space Flight Center, Flight Dynamics Division, 554-FDD-91/070R0UD2, Multimission Three-Axis Stabilized Spacecraft (MTASS) Flight Dynamics Support System (FDSS) Functional

Specifications, J. Klein (CSC), et al., prepared by Computer
Sciences Corporation, November 1993

SAMPEX Special Pointing Mode

F. Landis Markley, Thomas W. Flatley
Guidance and Control Branch, Code 712
NASA Goddard Space Flight Center,
Greenbelt, MD 20771

Theodore Leoutsakos
SMEX Flight Operations
AlliedSignal Technical Services Corporation
Seabrook, MD 20771

Abstract

A new pointing mode has been developed for the Solar, Anomalous, and Magnetospheric Particle Explorer (SAMPEX) spacecraft. This pointing mode orients the instrument boresights perpendicular to the field lines of the Earth magnetic field in regions of low field strength and parallel to the field lines in regions of high field strength, to allow better characterization of heavy ions trapped by the field. The new mode uses magnetometer signals and is algorithmically simpler than the previous control mode, but it requires increased momentum wheel activity. It was conceived, designed, tested, coded, uplinked to the spacecraft, and activated in less than seven months.

Introduction

The Solar, Anomalous, and Magnetospheric Particle Explorer (SAMPEX), the first of the Small Explorer series of spacecraft, was launched July 3, 1992 into an 82 degree inclination orbit with an apogee of $\approx$670 km and a perigee of $\approx$520 km [1]. The scientific purpose of SAMPEX is to study solar energetic particles, anomalous cosmic rays, magnetospheric relativistic precipitating electrons, and galactic cosmic rays. The spacecraft carries four instruments to carry out this mission: the Low Energy Ion Composition Analyzer (LEICA), the Heavy Ion Large Telescope (HILT), the MAss Spectrometer Telescope (MAST), and the Proton Electron Telescope (PET).

Figure 1 shows the spacecraft mechanical configuration. The solar arrays are fixed with their outward normals along the spacecraft +y axis; power constraints require this axis to be sun-pointing at all times. The instrument fields-of-view all point along the spacecraft +z axis. The original instrument pointing requirement was to point the z-axis as closely to the local zenith as possible in the polar regions, consistent with the sun-pointing requirement [2–4]. The original SAMPEX attitude control mode was the Orbit Rate Rotation (ORR) mode with the y-axis always sun-pointed and the z-axis rotating around the sun line at one revolution per orbit, synchronized such that the z-axis points as close to zenith as possible when the spacecraft reaches the northernmost and southernmost points in its orbit [3–4]. A later requirement, known as "velocity avoidance" was to avoid pointing the instrument boresights in the direction of spacecraft motion, to avoid damage by orbiting debris to delicate thin multilayer entrance windows in the HILT instrument. An algorithm to accomplish this was incorporated into the ORR mode [3].
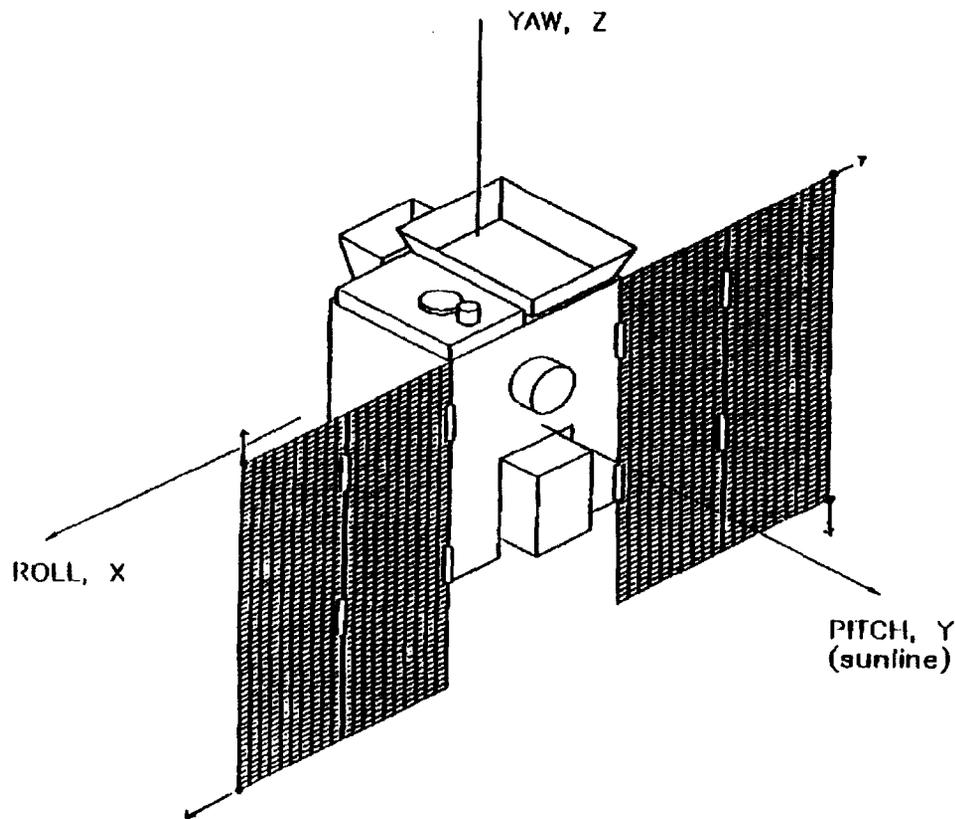
Figure 1. SAMPEX Configuration

Data taken during the first two years of the mission confirmed the existence of a third radiation belt surrounding the Earth, in addition to the two Van Allen belts containing trapped electrons and protons, respectively [5–7]. The new belt, whose existence had been predicted 15 years earlier, contains trapped heavy ions, principally O, N, and Ne. Figure 2 shows MAST Data on oxygen ions, including galactic cosmic rays (circles), anomalous cosmic rays (triangles) and trapped anomalous cosmic rays (crosses) [7]. Analysis of the MAST data showed that the trapped particles are observed primarily when the instrument is viewing near 90 degrees to the local magnetic field line. With the ORR pointing mode, this viewing angle varies with a three-month period. In order to increase data collection on the trapped heavy ions, it was desirable to change the pointing algorithm to orient the instrument boresights perpendicular to the magnetic field line during every passage through the regions containing these particles. Figure 2 served as the "requirements document" from Dan Baker, a project scientist, and Glenn Mason, the SAMPEX Principal Investigator, to investigate such a modification.

The region of most interest is in the South Atlantic, and analysis of the magnetic field contours shown in Figure 3 revealed that this region can be characterized as a region of low magnetic field strengths [8]. In order to satisfy these revised science requirements, the SAMPEX pointing mode was modified using the strength of the magnetic field as a delimiter to point the spacecraft perpendicular to the magnetic field vector whenever the field is determined to be less than some

Figure 2. Requirements Specification for SAMPEX Special Pointing Mode

specified value (e.g. 0.30 gauss). This pointing is accomplished by using magnetometer data to determine the field direction in the spacecraft reference frame. Since the magnetometer data was judged to provide a good pointing reference, the pointing specification was changed in the high-field regions to as close to the magnetic field vector as possible, consistent with the constraint that the y-axis be pointed at the sun. At northern latitudes, the desired orientation is anti-parallel to the field, and in the south the orientation is parallel to the field. In both cases, then, the spacecraft points away from the earth in the polar regions.

This paper contains a brief review of the SAMPEX attitude control system and a detailed discussion of the modifications for the new pointing mode. This is followed by a discussion of the testing and implementation of the new mode and initial on-orbit performance results.
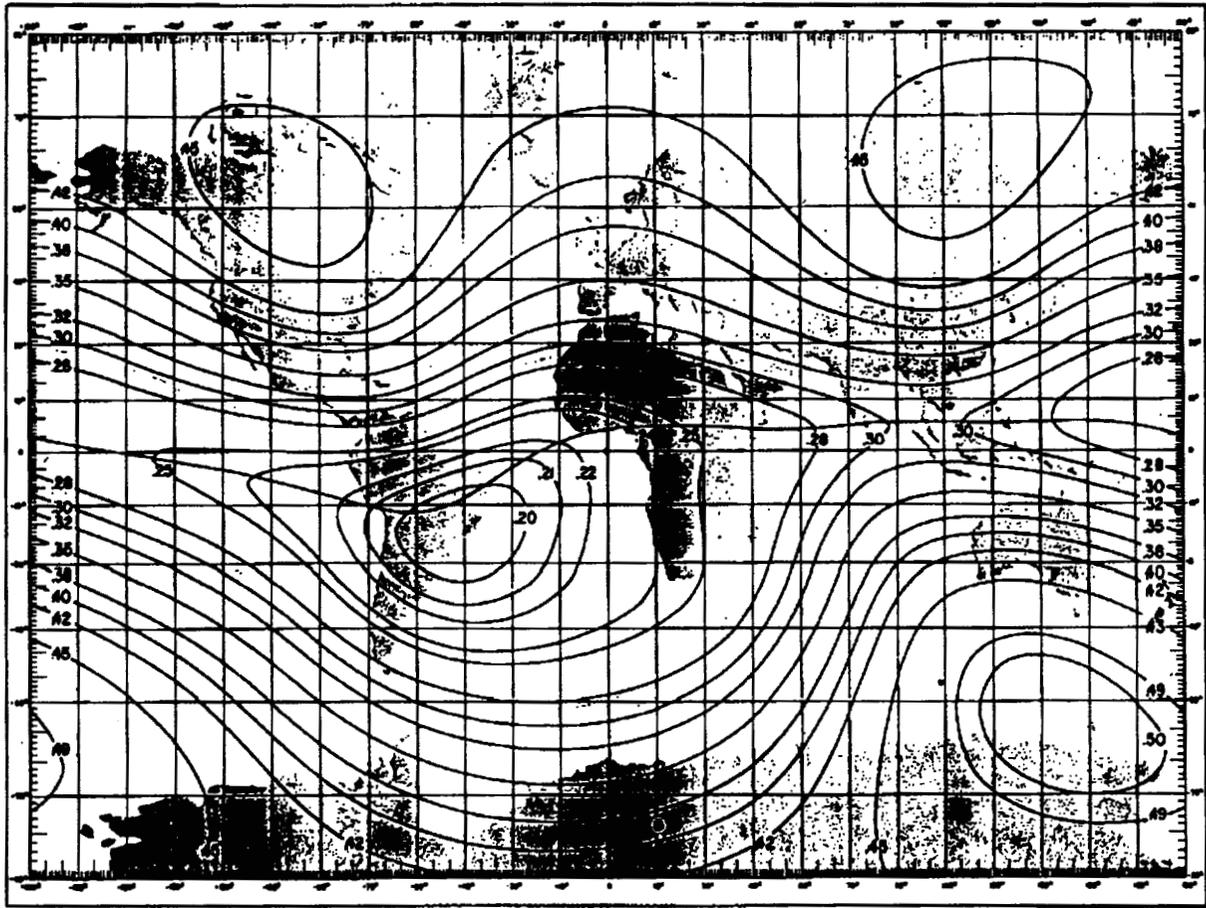
Figure 3. Lines of Constant Magnetic Field Strength (in Gauss) at 600 km Altitude

SAMPEX Control Modes

The original SAMPEX attitude control system is described in References [2–4], so only a brief overview will be provided here. The attitude actuators in SAMPEX are an orthogonal triad of magnetic torquers and a single reaction wheel with its angular momentum along the y (pitch) axis. The reaction wheel angular momentum serves to keep the pitch axis sun-pointing even when the sun is behind the Earth, so that full power is available when SAMPEX emerges from eclipse.

The spacecraft attitude is estimated by means of the TRIAD algorithm, or "algebraic method" [9–11]. This requires knowledge of two vectors in both the spacecraft body frame and an inertial reference frame. When SAMPEX is in sunlight, these are the ambient magnetic field vector (**b** in the body frame and **B** in the inertial frame) and the unit vector to the sun (**s** in the body frame and **S** in the inertial frame). The magnetic field vector and sun unit vector in the spacecraft body frame are computed from three-axis magnetometer (TAM) and digital sun sensor (DSS) measurements, respectively. The inertial magnetic field vector is computed from an onboard spacecraft ephemeris and International Geomagnetic Reference Field model [12], and the inertial sun vector is computed

from an onboard solar ephemeris. When SAMPEX is in eclipse, the spacecraft pitch axis vector

$$\mathbf{j} \equiv [0\ 1\ 0]^T \tag{1}$$

is substituted for the DSS-measured sun vector $\mathbf{s}$, which is unavailable; and these are used along with $\mathbf{b}$, $\mathbf{S}$, and $\mathbf{B}$ for attitude determination. This assumes that the angular momentum stiffness of the wheel keeps the pitch axis direction from drifting significantly during eclipse.

The spacecraft angular velocity is computed by differentiating the TRIAD-computed attitude matrix A;

$$\begin{bmatrix} 0 & \omega_3 & -\omega_2 \\ -\omega_3 & 0 & \omega_1 \\ \omega_2 & -\omega_1 & 0 \end{bmatrix} = \tfrac{1}{2}\left[\dot{A}A^T - \left(\dot{A}A^T\right)^T \right]. \tag{2}$$

Then the total spacecraft angular momentum is given by

$$\mathbf{H} = I\omega + \mathbf{H}_w, \tag{3}$$

where I is the spacecraft moment-of-inertia tensor and $\mathbf{H}_w$ is the reaction wheel angular momentum. The computed values of ω are very noisy because of the 0.5 degree resolution of the DSS, so the system angular momentum $\mathbf{H}$ is filtered with a first-order lag (or "constant gain Kalman filter") with a time constant of 50 seconds [4].

The magnetic torquers are used to control the magnitude and direction of the system angular momentum when SAMPEX is in sunlight. The desired angular momentum magnitude, denoted by H_0, is 0.6 Nms. The desired direction is along the pitch axis (to damp spacecraft nutation), and along the sunline (to keep the solar arrays sun-pointing). Thus an undesired component of spacecraft angular momentum $\Delta\mathbf{H}$ can be computed as

$$\Delta\mathbf{H} = \left(\mathbf{H} - H_0\mathbf{j}\right) + \left(\mathbf{H} - H_0\mathbf{s}\right) = 2\mathbf{H} - H_0\left(\mathbf{j} + \mathbf{s}\right). \tag{4}$$

The magnetic torquers are commanded to have dipole moment

$$\mathbf{m} = k_{mag}\Delta\mathbf{H} \times \mathbf{b}, \tag{5}$$

where k_{mag} is a constant gain. The magnetic control is turned off during eclipse, since motion of the angular momentum vector is undesirable when DSS data are unavailable.

Reaction wheel torque commands are used to control spacecraft pitch motion, the rotation about the pitch axis. These commands are based on the calculation of a "target vector" in body coordinates, with the reaction wheel being torqued to bring the z-axis into alignment with the target. The orbit rate rotation (ORR) computation of the target vector resulted in slowly varying reaction wheel speed and spacecraft pitch rate [3, 4]. Since the "Special Pointing" mode replaces ORR, this computation will not be discussed here. The actual computation of the pitch error and of the reaction wheel commands are in References [2-4] and will not be repeated, either.

Attitude determination is adversely affected if the magnetic field vector and the sun vector are close to parallel. On SAMPEX, in sunlight, attitude calculations and pitch control are both inhibited if these vectors are within 5 degrees of each other. In the dark, these functions are inhibited in the larger exclusion region where the angle is less than 40 degrees, since unavoidable angular momentum drift also adversely affects attitude determination accuracy in eclipse. This disabling of pitch control during periods of coalignment of the magnetic field and sun vectors is referred to as "coast mode." The pitch control was disabled in ORR by "freezing" the reaction wheel speed at the value it had at entry to coast mode, which resulted in a constant pitch rate through the coast. Magnetic control continues to be exercised in coast mode in sunlit portions of the orbit.

Special Pointing Mode

The new Special Pointing mode modifies the calculation of the target vector to meet the revised pointing requirements outlined above. Different calculations are used in the high-field-strength and low-field-strength regions. The ephemeris-based inertial field $\mathbf{B}$ is used to distinguish these regions, since use of the TAM-based field $\mathbf{b}$ could result in toggling between the two regimes due to measurement noise.

In the low-field region, $|\mathbf{B}| \leq 0.3$ Gauss, the target vector $\mathbf{u}$ is to be perpendicular to both the sun vector $\mathbf{s}$ and the magnetic field vector $\mathbf{b}$. This requirement is obviously satisfied by choosing the target vector in the direction of the cross product $\mathbf{s} \times \mathbf{b}$. The negative of this vector clearly satisfies the same requirement. One and only one of these two vectors is more than 90 degrees from the velocity vector, and we choose this one to satisfy the velocity avoidance requirement. Since the magnetic control keeps the sun vector within a few degrees of the pitch axis vector $\mathbf{j}$, the cross product $\mathbf{s} \times \mathbf{b}$ can be well approximated by $\mathbf{j} \times \mathbf{b}$, so the target vector is computed as

$$\mathbf{u} = \frac{\pm 1}{\sqrt{b_1^2 + b_3^2}} \begin{bmatrix} b_3 \\ 0 \\ -b_1 \end{bmatrix}, \tag{6}$$

where we choose the upper sign if $\mathbf{V} \bullet (\mathbf{S} \times \mathbf{B}) \leq 0$ and the lower sign if $\mathbf{V} \bullet (\mathbf{S} \times \mathbf{B}) > 0$, with $\mathbf{V}$ being the spacecraft velocity vector in inertial coordinates, which is computed from the onboard ephemeris. Note that ephemeris-computed vectors in the inertial frame are used to make binary decisions, in order to prevent toggling between grossly different pointing vectors; but that the TAM-sensed magnetic field vector in the body frame is used to compute the actual pointing vector.

The angle between the target vector and the body z-axis is computed as a pitch error angle, which is used to generate a wheel command. This angle is generally small, but it is on the order of 90 degrees during transitions between parallel pointing and perpendicular pointing. In these cases, the wheel is commanded in the direction that requires the smallest pitch rotation to null the pitch error. Due to changing geometry however, some time during a passage through a low field region, a 180 degree pitch maneuver is generally required to satisfy the avoidance requirement. The Special Pointing algorithm assures that any 180 degree turns will be executed in a direction away from the velocity vector. Thus a computed pitch error angle magnitude greater than 2.5 radians is taken to signify a large reorientation maneuver. The sign of the x-axis component of the spacecraft velocity

vector **v** in the body frame is then used to determine the direction of this maneuver, such that the instrument boresights are rotated away from the velocity vector rather than toward it.

In the high-field region, $|\mathbf{B}| > 0.3$ Gauss, the target vector **u** is to be perpendicular to pitch axis and as close as possible to parallel or antiparallel to the magnetic field vector **b**. Thus the target vector is given by

$$\mathbf{u} = \frac{\pm 1}{\sqrt{b_1^2 + b_3^2}} \begin{bmatrix} b_1 \\ 0 \\ b_3 \end{bmatrix}, \tag{7}$$

where the positive sign is used when SAMPEX is in the southern hemisphere and the negative sign in the northern hemisphere, as determined from the onboard ephemeris. In the high-field region the existing onboard velocity avoidance algorithm [3] is still used.

During "coast mode," the reaction wheel speed angular momentum is commanded to the fixed value of 0.6 Nms, rather than to its instantaneous value at entry to coast mode as in the ORR mode. Since the total system angular momentum is maintained at 0.6 Nms by magnetic torquer commands, this has the effect of halting spacecraft attitude motion in coast mode. This change was necessitated by the observation that coast mode could be entered during one of the rapid 90 degree or 180 degree repointings of the spacecraft, and holding the spacecraft pitch rate constant at a high value could result in several pitch rotations during coast mode. This undesirable behavior was actually seen in some simulations, but is avoided by the final pointing law.

Simulations

Figures 4 and 5 show the results of simulations of the new Special Pointing mode. These simulations were performed using a modified version of the FORTRAN program used to simulate the earlier SAMPEX pointing algorithms. The performance of the SAMPEX pointing modes depends on the relative orientation of the sun vector and the orbit plane, which is specified by the local time of the ascending node of the orbit. This local time is 6 am for the simulation of Figure 4 and noon for Figure 5. Figure 6 shows a simulation of the ORR pointing mode for the same noon orbit as is illustrated in Figure 5. All these figures show only the first five hours of 25-hour simulations. The 25-hour length of the simulations was chosen to sample the full range of magnetic field geometries as the Earth completes a little more than one full rotation. In each case, the remaining 20 hours of the simulation were qualitatively similar to the five hours shown. Simulations of a 9 am orbit gave results intermediate between those shown in Figures 4 and 5.

The upper plot in the first (a) half of each figure shows the magnetic field strength. Shading is used to highlight the low-field regions, i.e. the regions with $|\mathbf{B}| \leq 0.3$ Gauss, where pointing perpendicular to the field line is desired. The Special Pointing mode attempts to point parallel or antiparallel to the field lines in the unshaded regions. The coast mode flag is also shown on this plot; there are no coast mode intervals in the 6 am orbit and several in the noon orbit. The 9 am orbit, which is not shown, had only two eclipse coast mode intervals in the five hour period.

The curve below the magnetic field strength plots shows the angle between the instrument boresights and the local zenith. After an initial transient, this is always less than 90 degrees for the
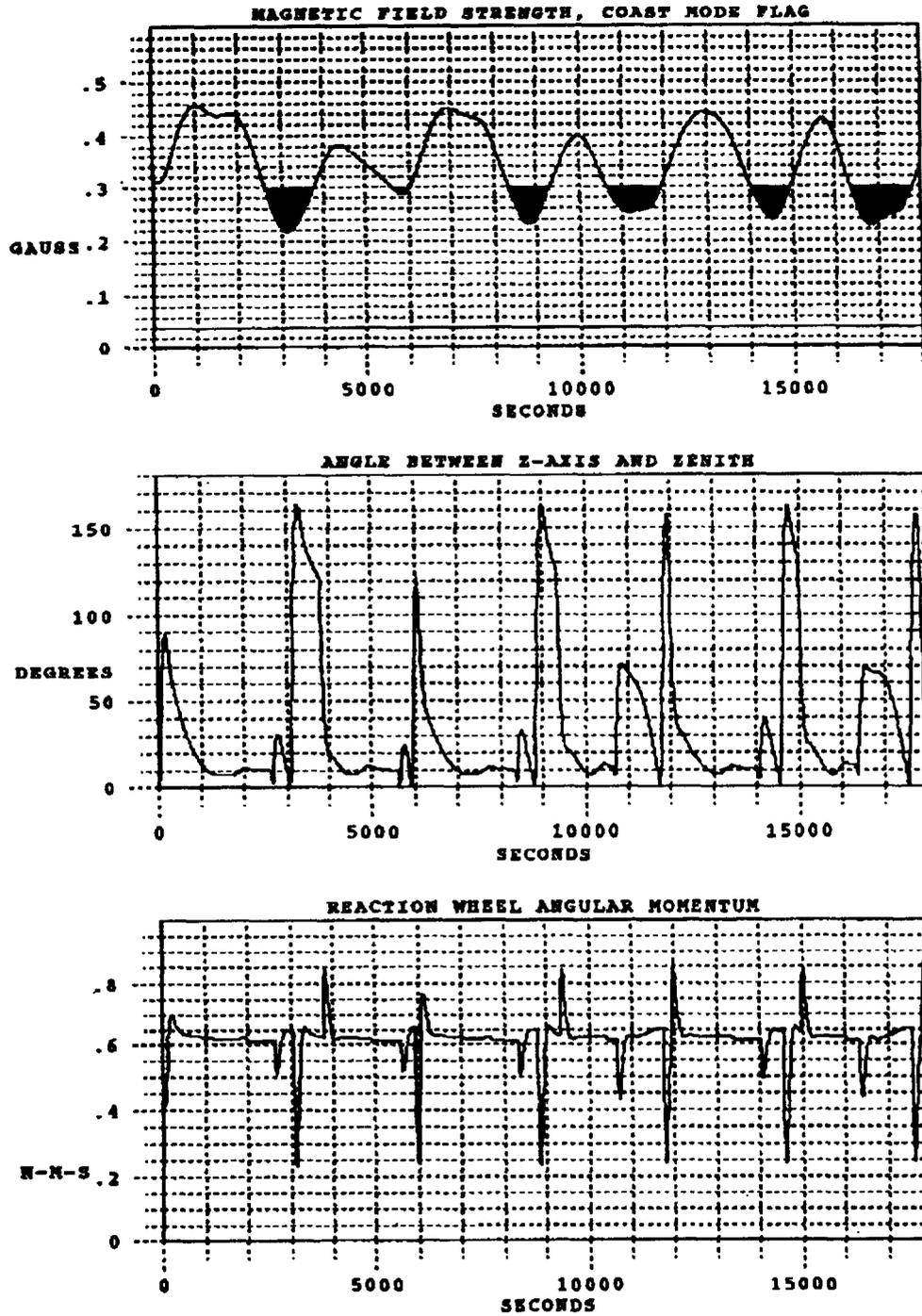
Figure 4a. Simulation of SAMPEX Special Pointing Mode for a 6 am Orbit
Magnetic field strength, coast mode flag, zenith angle, reaction wheel angular momentum

208
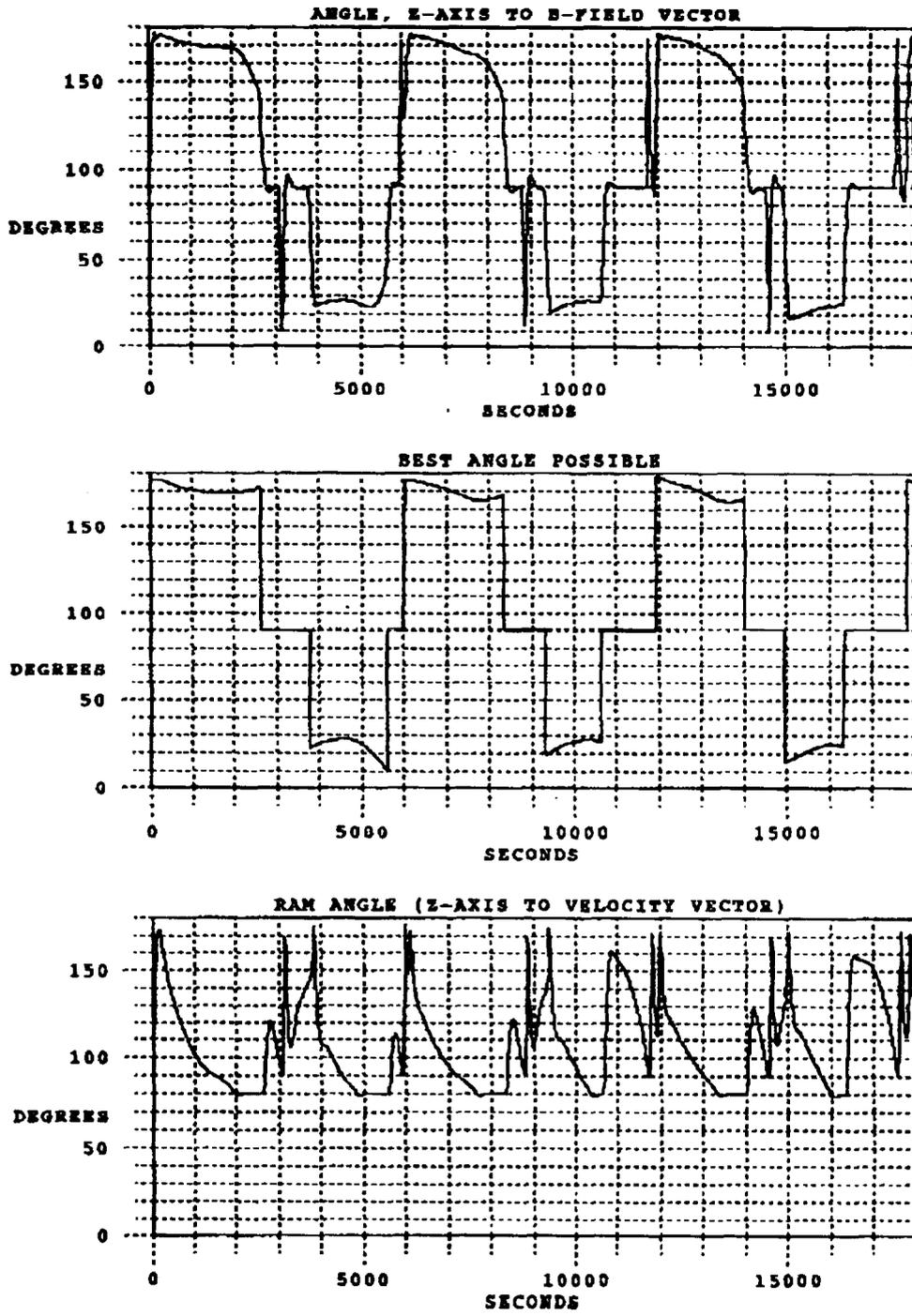
Figure 4b. Simulation of SAMPEX Special Pointing Mode for a 6 am Orbit
Instrument boresight to magnetic field angle, ram angle
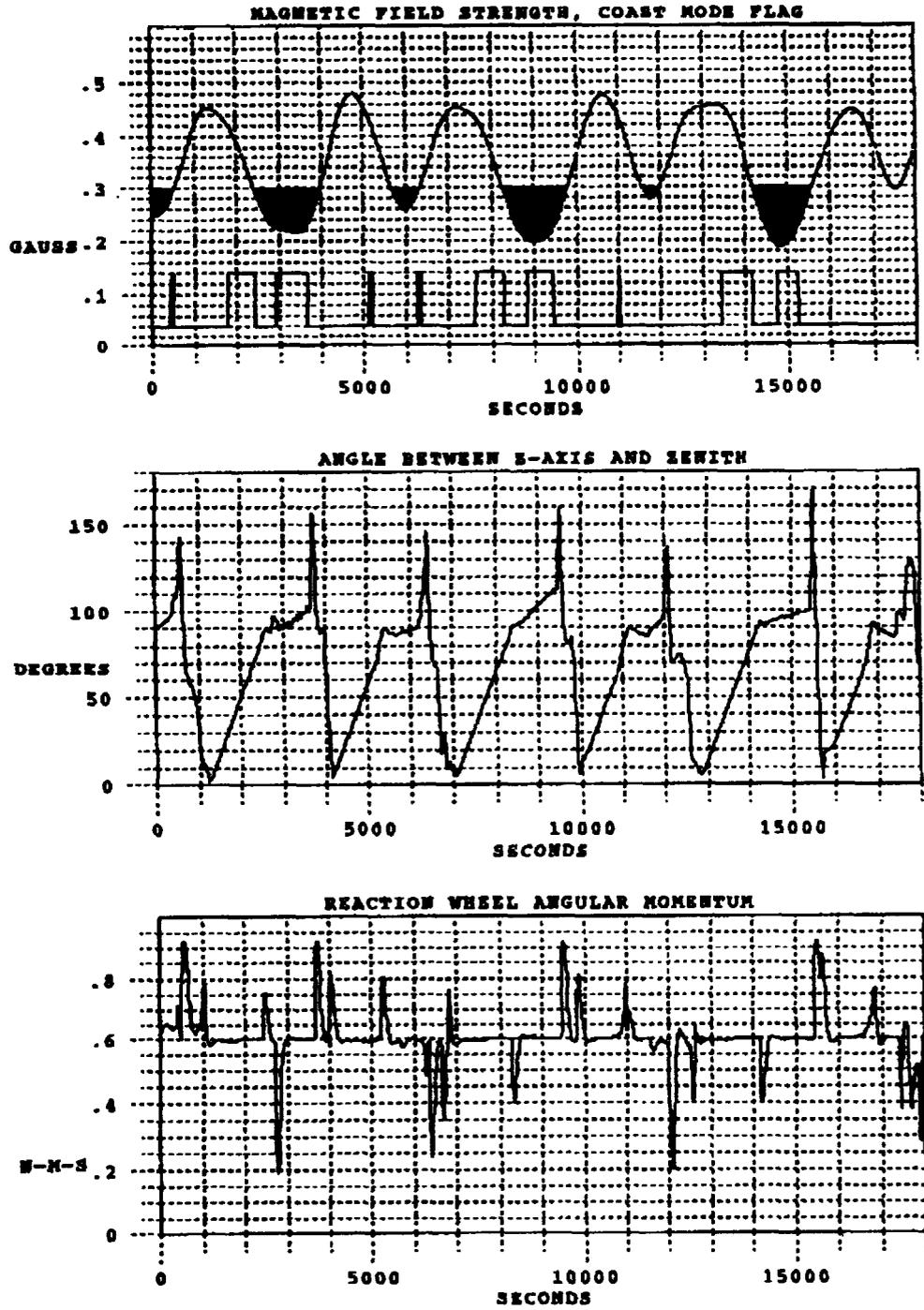
Figure 5a. Simulation of SAMPEX Special Pointing Mode for a Noon Orbit
Magnetic field strength, coast mode flag, zenith angle, reaction wheel angular momentum

210
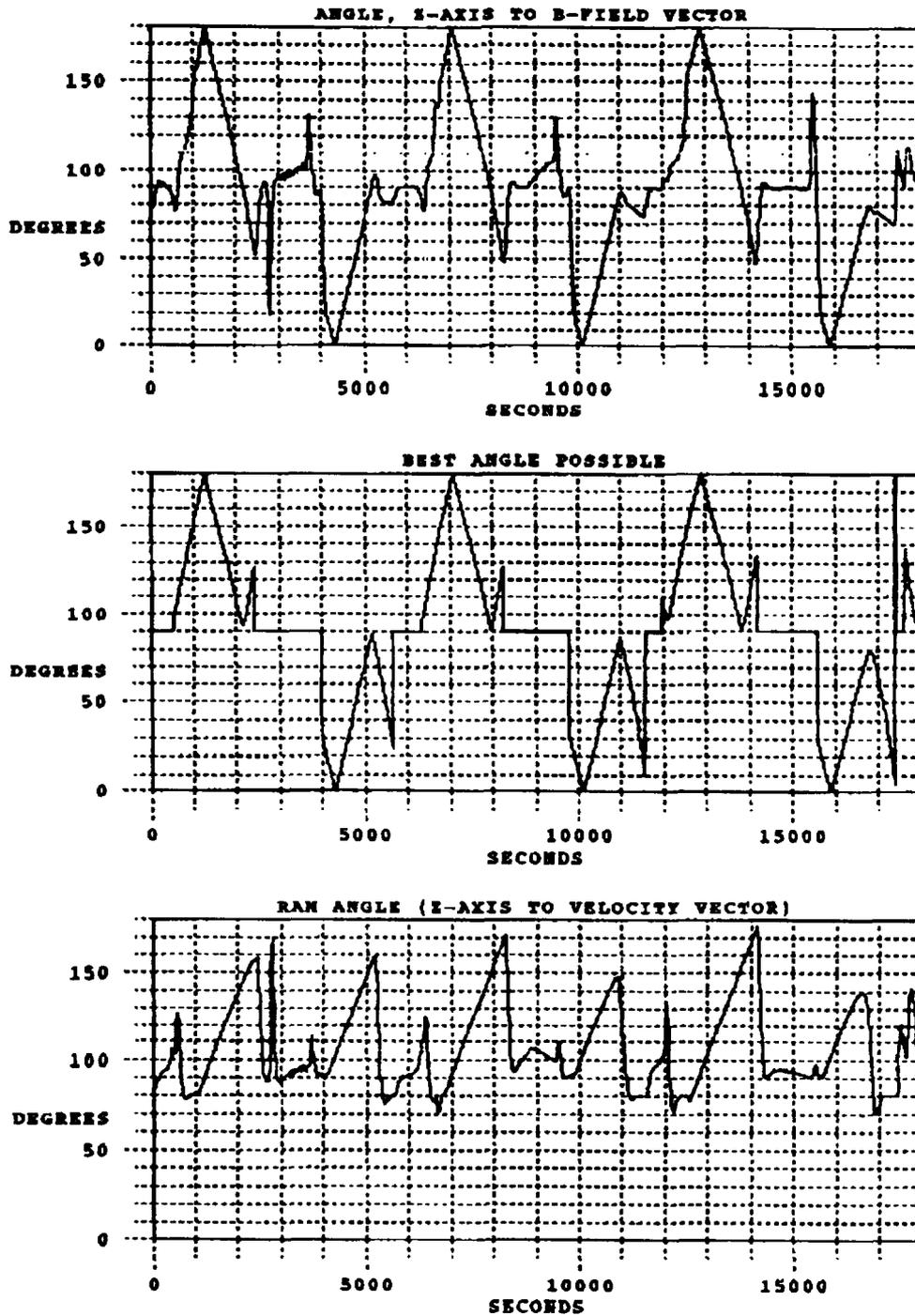
Figure 5b. Simulation of SAMPEX Special Pointing Mode for a Noon Orbit
Instrument boresight to magnetic field angle, ram angle
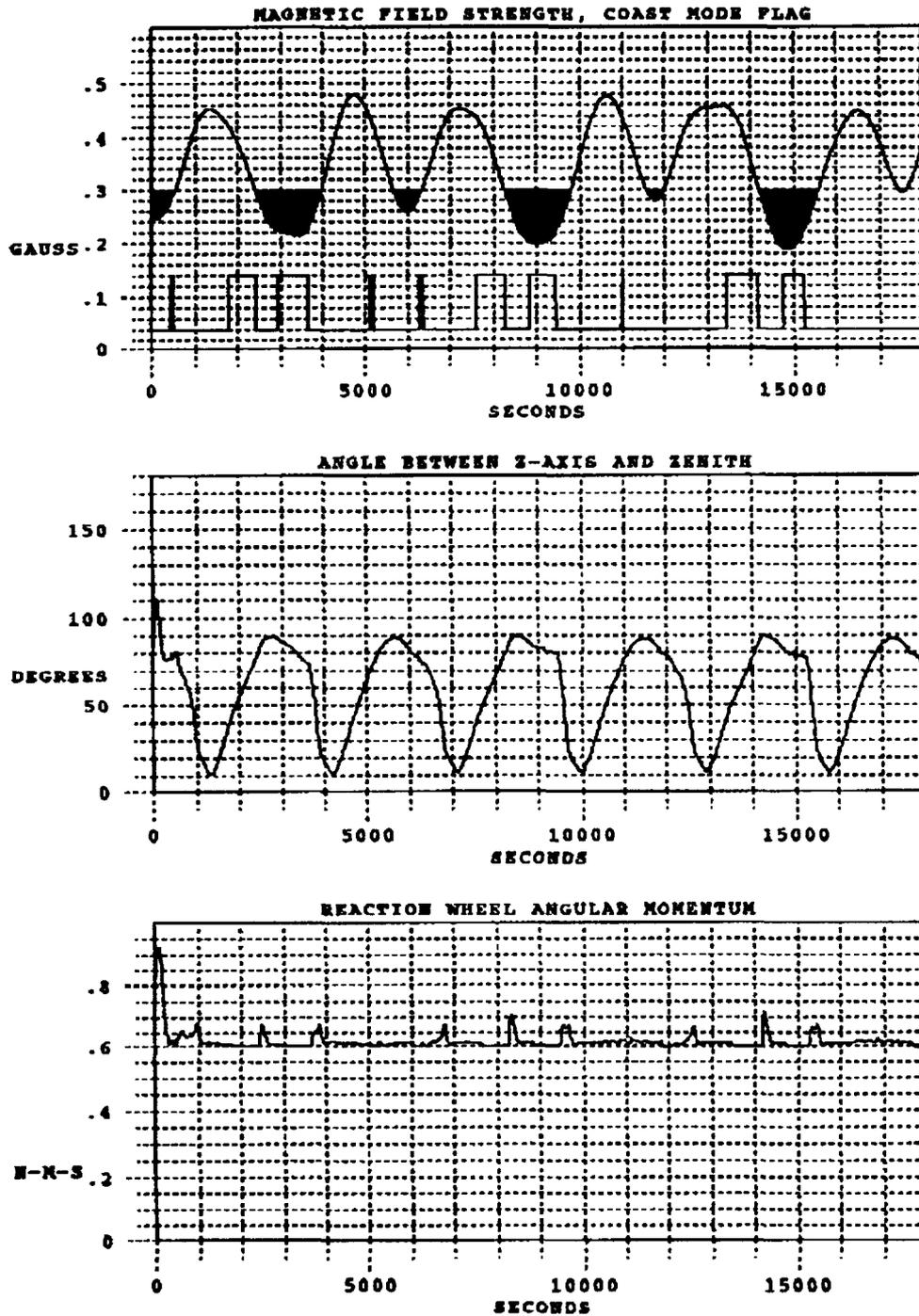
Figure 6a. Simulation of SAMPEX Orbit Rate Rotation Mode for a Noon Orbit
Magnetic field strength, coast mode flag, zenith angle, reaction wheel angular momentum
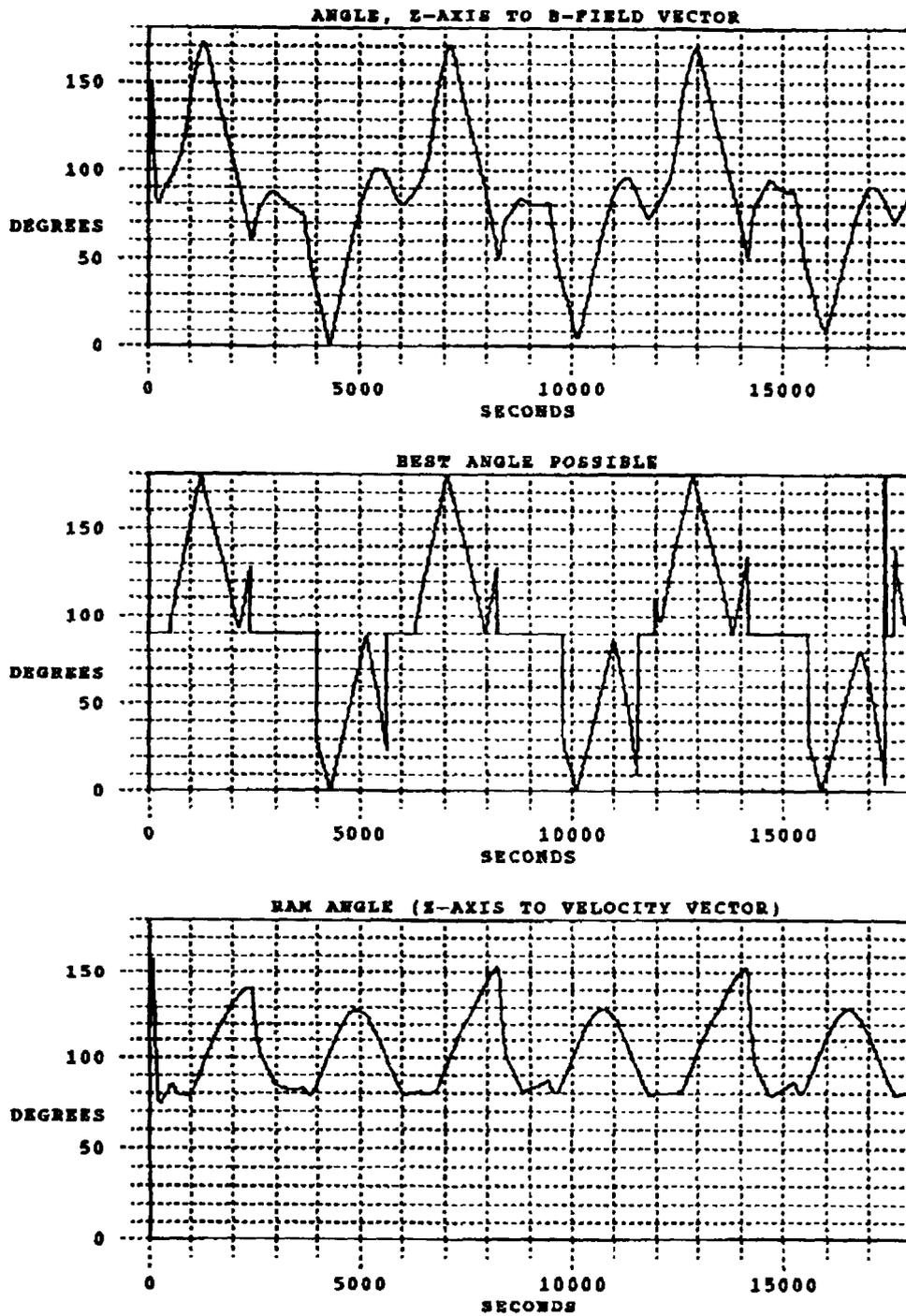
Figure 6b. Simulation of SAMPEX Orbit Rate Rotation Mode for a Noon Orbit
Instrument boresight to magnetic field angle, ram angle

213

ORR simulation shown in Figure 6. This means that the instruments are always pointing generally away from the Earth in the ORR mode. This angle often exceeds 90 degrees when the Special Pointing mode commands pointing perpendicular to the magnetic field lines. This is required for velocity avoidance in this case, and does not cause any problems for the data collection. The plots at the bottom of the (a) part of each of the figures show the reaction wheel angular momentum. These indicate the increased reaction wheel activity required by the Special Pointing mode.

The upper plot in second (b) half of each pair of plots shows the simulated angle between the instrument boresights and the magnetic field lines. This should be compared with the plot immediately below, which shows the ideal pointing angle. This is the best angle possible, consistent with the requirement that the SAMPEX y-axis be sun-pointing, but ignoring velocity-avoidance constraints. It can be seen that the Special Pointing mode comes quite close to ideal pointing in most cases. The spikes in the upper curve in Figure 4 at about 3200 sec, 7800 sec, and 14,600 sec are due to the 180 degree velocity avoidance maneuvers in the perpendicular-pointing region that were discussed above. Some of these spikes, slightly shifted in time, appear in Figure 5 as well. The bottom plot of the (b) half of each figure shows the ram angle, the angle between the instrument boresights and the spacecraft velocity. The velocity avoidance algorithm was set to restrict this angle to be greater than 80 degrees. This constraint is satisfied in the most part, but there are minor violations in coast mode.

Implementation

Actual implementation of the modified pointing law required changes to the computer code in the Recorder/Packetizer/Processor (RPP) onboard the spacecraft. A formal Configuration Control Request (SAMPEX CCR# RPP-015) was submitted to the SAMPEX Flight Software Configuration Control Board (CCB). The algorithms were transmitted from the Guidance and Control Branch, Code 712, to the Flight Software Systems Branch, Code 512, for conversion into flight code. Flight Software Systems personnel developed a patch to the existing onboard software and tested it in the Code 512 Software Development and Validation Facility (SDVF), which includes a flight-like RPP. Extensive simulations were performed to match the results of the Code 712 simulations. After thorough review of the code and simulation results by both the CCB and the scientists, the modified software was approved by the CCB, uplinked to the spacecraft, and activated on May 26, 1994, less than seven months after initial request by project scientists to develop the new pointing mode.

Discussion

The development of the new "Special Pointing" mode for SAMPEX shows the advantage of having a flexible, reprogrammable attitude control system on a spacecraft. The rapid development of space-qualified microprocessor-based control systems makes it possible to provide such systems even on the small, light, and inexpensive Small Explorer spacecraft. The payoff is that the control algorithms can be modified to address revised science requirements responding to new opportunities revealed by data collected in the early part of a mission. The rapid development of the new SAMPEX pointing algorithms in less than seven months from initial expressions of interest by project scientists to operational flight code also serves as an example of outstanding teamwork and cooperation between scientists, engineers, programmers, and flight operations personnel.

The new algorithm is algorithmically much simpler than the orbit rate rotation control, but it results in frequent pitch reorientations to meet the new requirements. These use more spacecraft power, and also put more stress on the reaction wheel. Neither power nor reaction wheel life is a concern, however, since the SAMPEX power system has more than adequate margins to meet the increased demands, and the reaction wheel was designed and qualified for flight environments much more demanding than SAMPEX. Initial experience with the new pointing mode has been trouble-free, and the prospects for new science are exciting.

References

[1] D. N. Baker, G. M. Mason, O. Figueroa, G. Colon, J. G. Watzin, and R. M. Aleman, "An Overview of the Solar, Anomalous, and Magnetospheric Particle Explorer (SAMPEX) Mission," *IEEE Transactions on Geoscience and Remote Sensing*, Vol. 31, No. 3, pp. 531–541, May 1993

[2] Thomas W. Flatley, Josephine K. Forden, Debra A. Henretty, E. Glenn Lightsey, and F. Landis Markley, "On-board Attitude Determination and Control Algorithms for SAMPEX," NASA/GSFC Flight Mechanics/Estimation Theory Symposium, Greenbelt, MD, May 22–24, 1990

[3] Joseph P. Frakes, Thomas W. Flatley, Josephine K. San, Debra A. Henretty, F. Landis Markley, and E. Glenn Lightsey, "SAMPEX Science Pointing with Velocity Avoidance," AAS/AIAA Spaceflight Mechanics Meeting, Colorado Springs, CO, February 24–26, 1992

[4] Jon D. McCullough, Thomas W. Flatley, Debra A. Henretty, F. Landis Markley, and Josephine K. San, "Testing of the On-board Attitude Determination and Control Algorithms for SAMPEX," NASA/GSFC Flight Mechanics/Estimation Theory Symposium, Greenbelt, MD, May 5–7, 1992

[5] Douglas Birch, "Earth Has Third Zone of Radiation, "*Baltimore Sun*, Vol. 313, No. 9, p. 16A, May 26, 1993

[6] Vincent Kiernan, "Small Explorer Satellite Finds Radiation Belt," *Space News*, March 31–June 6, 1993

[7] J. R. Cummings, A. C. Cummings, R. A. Mewaldt, R. S. Selesnick, E. C. Stone, and T. T. von Rosenvinge, "New Evidence for Geomagnetically Trapped Anomalous Cosmic Rays," *Geophysical Research Letters*, Vol. 20, No. 18, pp. 2003–2006, September 15, 1993

[8] E. G. Stassinopoulos, "World Maps of Constant B, L, and Flux Contours," NASA SP-3054, Goddard Space Flight Center, 1970

[9] H. D. Black, "A Passive System for Determining the Attitude of a Satellite," *AIAA Journal*, Vol.2, No. 7, pp. 1350–1351, July, 1964

[10] G. M. Lerner, "Three-Axis Attitude Determination," in *Spacecraft Attitude Determiunation and Control*, J. R. Wertz (editor), D. Reidel, Dordrecht, Holland, 1978

[11] M. D. Shuster and S. D. Oh, "Three-Axis Attitude Determination from Vector Observations," *Journal of Guidance and Control*, Vol. 4, No. 1, pp.70–77, January–February, 1981

[12] R. A. Langel, "International Geomagnetic Reference Field: The Sixth Generation," *Journal of Geomagnetism and Geoelectricity*, Vol. 44, pp. 679–707, 1992

USE OF NONLINEAR IDENTIFICATION IN ROBUST ATTITUDE AND ATTITUDE RATE ESTIMATION FOR SAMPEX

D. Joseph Mook[*]   Juan De Peña[†]   Kelly Trost[+]   Jung Wen[+]   Michael McPartland[‡]

Department of Mechanical and Aerospace Engineering

State University of New York at Buffalo, Buffalo, NY 14260

ABSTRACT

A method is described for obtaining optimal attitude estimation/identification algorithms for spacecraft lacking attitude rate measurement devices (rate gyros), and then demonstrated using actual flight data from the Solar, Anomalous, and Magnetospheric Particle Explorer (SAMPEX) spacecraft. SAMPEX does not have on-board rate sensing, and relies on sun sensors and a three-axis magnetometer for attitude determination. The absence of rate data normally reduces both the total amount of data available and the sampling density (in time) by a substantial fraction. In addition, attitude data is occasionally unavailable (for example, during sun occultation). As a result, the sensitivity of the estimates to model uncertainty and to measurement noise increases. In order to maintain accuracy in the attitude estimates, there is an increased need for accurate models of the rotational dynamics. The Minimum Model Error(MME)/Least Square Correlation(LSC) algorithm accurately identifies an improved model for SAMPEX to be used during periods of complete data loss or extreme noise. The model correction is determined by estimating only one orbit(the identification pass) just prior to the assumed data loss(the prediction pass). The MME estimator correctly predicted the states during the identification phase, but more importantly determines the necessary model correction trajectory, $d(t)$. The LSC algorithm is then used to find this trajectory's functional form, $\underline{H}(\hat{\underline{x}}(t))$. The results show significant improvement of the new corrected model's attitude estimates as compared to the original uncorrected model's estimates. The possible functional form of the correction term is limited at this point in the study to functions strictly of the estimated states. The results, however, strongly suggest that functions based on the relative position of the satellite may also be possible candidates for future consideration.

A Simple Method for Verifying the Deployment of the TOMS-EP Solar Arrays

N95- 27782

James R. Koppersmith and Eleanor Ketchum
NATIONAL AERONAUTICS AND SPACE ADMINISTRATION
GODDARD SPACE FLIGHT CENTER
Greenbelt, Maryland, USA 20771

Abstract

The Total Ozone Mapping Spectrometer-Earth Probe (TOMS-EP) mission relies upon a successful deployment of the spacecraft's solar arrays. Several methods of verification are being employed to ascertain the solar array deployment status, with each requiring differing amounts of data. This paper describes a robust attitude-independent verification method that utilizes telemetry from the coarse Sun sensors (CSSs) and the three-axis magnetometers (TAMs) to determine the solar array deployment status—and it can do so with only a few, not necessarily contiguous, points of data.

The method developed assumes that the solar arrays are deployed. Telemetry data from the CSS and TAM are converted to the Sun and magnetic field vectors in spacecraft body coordinates, and the angle between them is calculated. Deployment is indicated if this angle is within a certain error tolerance of the angle between the reference Sun and magnetic field vectors. Although several other methods can indicate a non-deployed state, with this method there is a 70-percent confidence level in confirming deployment as well as a nearly 100-percent certainty in confirming a non-deployed state. In addition, the spacecraft attitude (which is not known during the first orbit after launch) is not needed for this algorithm because the angle between the Sun and magnetic field vectors is independent of the spacecraft attitude. This technique can be applied to any spacecraft with a TAM and with CSSs mounted on the solar array(s).

Introduction

The TOMS-EP will be launched into a 340.5 x 964.9 km polar orbit with an inclination of 99.3 degrees. The final mission orbit will be at 955 km after a series of orbit-raising maneuvers.
Upon being inserted into its initial preliminary orbit, the TOMS-EP spacecraft (Fig. 1) is to unfold its solar arrays and begin generating power from the incoming solar radiation. Since the spacecraft does not have an indicator in telemetry for solar array deployment, ground solutions to verify the status have been developed by the TOMS-EP Flight Support Team (FST). These solutions were originally divided into three verification paths: a power path (looking at battery voltage and current), a gyro path (looking at the change in spacecraft rotation due to solar array deployment), and a coarse Sun sensor path (using CSS to calculate Sun vector to determine array status). Of particular interest to the authors was the coarse Sun sensor path.

Any method of verifying deployment with the CSSs requires knowledge of the array and CSSs' geometry. The axis of the solar arrays are aligned along the spacecraft pitch (Y) axis. They are rotated, however, into a paddle wheel configuration with the offset being 45 degrees. This was done to maximize energy gathering over the entire orbit. The CSSs are physically attached to the arrays in a manner such that their boresights are 45 degrees off the plane of the arrays. The result is that the boresights are perpendicular to the roll (X) axis and 45 degrees away from the pitch (Y) and yaw (Z) axes (Figure 2). If the arrays are fully deployed, the Sun can be detected in two adjacent CSS; in one CSS, if the Sun is directly aligned with the boresight; or no CSS if the Sun is perfectly aligned with positive or negative roll axis. Consequently, this means that the Sun cannot be detected by CSS2 and CSS4 at the same time, nor CSS1 and CSS3. The sensors, in effect, are domes reporting the

angle of the Sun up from the base of the dome. With this angle, a circle of solutions are identified which is a circle parallel with the base of the

Figure 1 - TOMS-EP Spacecraft
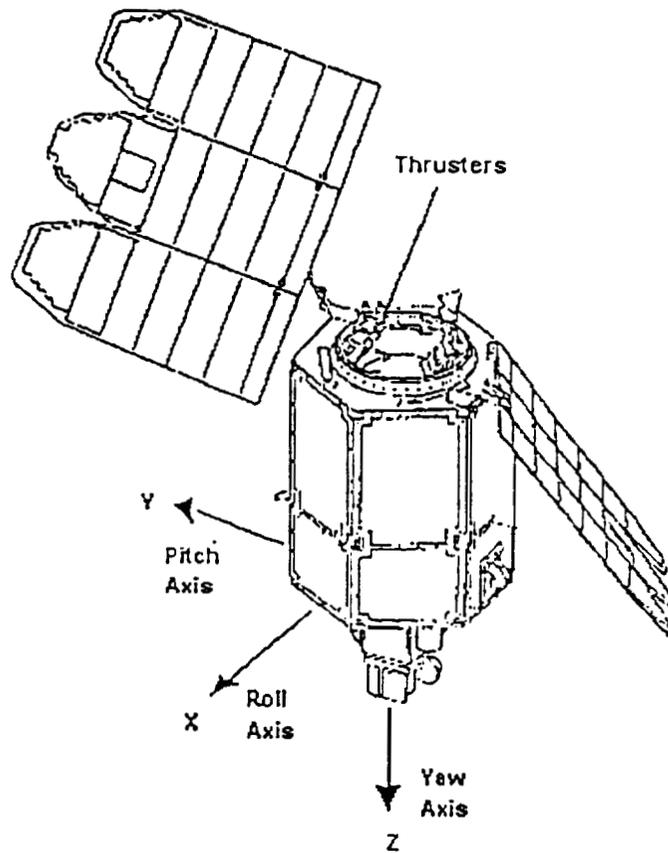
Figure 2 - CSS Numbering and Alignment
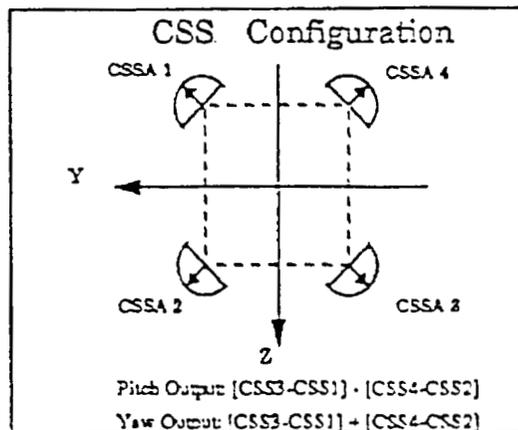
dome. By using the reported angles from two coarse Sun sensors, the circles of solutions will intersect in two places, thereby creating an ambiguity. This ambiguity will be discussed as it relates to determining the deploy and non-deploy status of the solar arrays.

The coarse Sun sensor path initially developed for the mission has several levels of verification that can be employed. The initial check just uses the aforementioned knowledge of the CSS and solar array geometry to determine if the panels are stowed. The second level of verification utilizes a Sun vector solution which relies on two CSSs having Sun presence. Within a certain accuracy, it can determine the solar array status for the fully stowed and four partially deployed cases. The fully deployed case must rely upon TAM or power data to obtain a deterministic solution. This method, however, needs approximately 7 to 8 minutes of CSS data to converge on a solution with a 95% success rate for the stowed and partial configurations. This necessity of a significant span of data at the very first pass was the impetus for the authors to search for a verification method that needed fewer data points.

This solution capitalizes on the attitude independent relationship between the Sun vector and the magnetic field vector. The Sun vector can be computed by using CSS measurements while the magnetic field vector is obtained from the TAM. Both measurements are resolved in the body coordinate system so the angle between the vectors can be computed using their dot products. This angle can then be compared to the angle between the corresponding reference Sun and magnetic field vectors. Though the reference vectors are in Geocentric Inertial Coordinates (GCI), the angle between them is independent of the specific coordinate system. The reference angle and observed angle can then be compared. Within a specified error tolerance, it can be ascertained whether the solar arrays are deployed or not.

Operational Scenario

Shortly after TOMS-EP's separation from the Pegasus, and the spacecraft processor (SP) wake-up, the stored commands for solar array panels deployment are activated. As noted earlier, there is no indicator available in the to directly verify panel deployment. Additionally, since the spacecraft is in shadow, there is no Sun position data available from the coarse Sun sensors (CSS) which are located on the outer corners of the solar panels. Since the verification method utilizes the Sun data from the CSSs, it is not until the spacecraft exits the shadow and telemetry data from the CSSs becomes available that the procedure can be performed. The first ground contact opportunity for the spacecraft becomes available approximately twenty minutes after insertion. This pass over the McMurdo ground station lasts for nearly 12 minutes. Depending on the day of the year when the launch takes place, the spacecraft could still be in the shadow for at least a portion of the contact period at McMurdo. The verification will be performed again at the Indian Ocean-Seychelles (IOS) pass which occurs approximately forty six minutes after orbit insertion. If the data from this method and the other paths do not indicate proper deployment with a high degree of confidence, the onboard computer (OBC) can be commanded to the redundant side to reattempt the solar array deployment process.

Solar Array Deployment Verification Algorithm

As mentioned previously, the solar array deployment verification algorithm uses the fact that the angle between two vectors is independent of the reference coordinate system. It does require,

however, that the sensors measurements be resolved in the same coordinate system. The procedure for this algorithm is very simple but that is essential to its inherent robustness and versatility.

The algorithm begins by computing the reference angles (in GCI coordinates) between the Sun vectors and the Earth's magnetic field vectors for the time span in question. For this application, it would be the span of the McMurdo pass. These Sun vectors are obtained by using the Solar, Lunar, Planetary (SLP) ephemeris tables. The magnetic field vectors are computed with an 8th order estimate of the Earth's magnetic field using a spacecraft ephermeris as input. A simple dot product calculation determines the GCI reference angle as a function of time.

$$\theta_{ref} = \text{acos}(\hat{S}_J \cdot \hat{B}_J)$$

where:

$\hat{S}_J$ = reference Sun vector

$\hat{B}_J$ = reference magnetic field vector

In a similar manner, telemetered observations of the solar array mounted CSS and the body mounted TAM are used to calculate the observed angle between the Sun vector and Earth's magnetic field (in spacecraft body coordinates). It should be noted that the computation of the observed Sun vector in spacecraft body coordinates has a built in assumption that the solar arrays have deployed properly.

$$\theta_{obs} = \text{acos}(\hat{S}_B \cdot \hat{B}_B)$$

where:

$$\hat{S}_B = \begin{bmatrix} \sqrt{1 - \frac{1}{255^2}(I_1^2 + I_2^2 + I_3^2 + I_4^2)} \\ \frac{1}{255\sqrt{2}}(I_1 + I_2 - I_3 - I_4) \\ \frac{1}{255\sqrt{2}}(-I_1 + I_2 + I_3 - I_4) \end{bmatrix}$$

and

I_i = CSS cell currents for i = 1 to 4 (0 < I < 255)

$\hat{B}_B$ = unitized measured magnetic field vector (computed from TAM data)

Differences between the observed and reference angles which are greater than an expected tolerance indicate that the solar arrays have not deployed properly. The tolerance is a function of sensor accuracy, spacecraft position errors, timing errors etc...

$$\theta_{obs} - \theta_{ref} < \varepsilon$$

222

The following section addresses the above errors as well as the interpretation of the algorithm results.

Interpretation of Solar Array Deployment Algorithm Output

In performing the angular separation comparison between the reference and observed vectors, error in the observation must be considered. Therefore, the angular separations should not be expected to be exactly the same, but should differ within some error tolerance. The total error is relatively large, which significantly affects the interpretation of the results. There are several error sources that are considered for this solar array deploy check method: the measurement uncertainty for the CSS and the TAM, the error associated with the magnetic field model, time variations between TAM and CSS readings, as well as in the orbit arc, and finally the error associated with the true spacecraft orbit.

The dominant error source is the measurement uncertainty for the CSS, which is 10 degrees. This value is conservative as it results mostly from a "Sunrise" effect. This "Sunrise" effect, or time just after end of shadow, has been shown to create an error as large as 5 degrees for currently flying spacecraft with a similar orbit and CSS. However, only 2 seconds later , this effect shrinks to a value on the order of 0.1 degrees.

The measurement uncertainty for the TAM, which includes all biases and misalignments, is assumed to be 2 degrees. The uncertainty in the reference magnetic field is 1 degree.

The error associated with time corresponds to the fact that there could be a 4 or 5 second error in the Flight Dynamics Facility's (FDF) time correction as well as a 13 second time error in the CSS current data (the observed Sun vector/TAM vector/clock time may be separated by up to 13 seconds). Furthermore, at McMurdo, 1 degree of orbit arc error corresponds to roughly 2° of magnetic field error; at IOS, which is far from the poles, there is about 1.5 degree of magnetic field error for every 1 degree of orbit arc error. The spacecraft moves roughly 1 degree of orbit arc in 18 seconds and 0.5 degrees in 9 seconds. Resultingly, the error at McMurdo could be 2 degrees while at IOS it could be 1.5 degrees.

Finally, there is an error associated with uncertainty in the spacecraft ephemeris. The ephemeris generated for TOMS-EP is based on the insertion vector supplied by the launch site; hence the accuracy of the predicted orbit depends on the accuracy of the insertion vector. Off nominal injections, of course, would yield much larger errors. If there is no data available from the launch vehicle, FDF will know ahead of time, and will consequently know that this check is not at all accurate. Analysis indicates that TOMS-EP may see a maximum of 1 degree along track error in the predicted ephemeris. Using the computation mentioned in the above paragraph, this would mean an additional error of 2 degrees in the magnetic field model at McMurdo and 1.5 degrees at IOS.

The error budget associated with the solar array deploy verification is shown in Table 1 with total error being 17 degrees. The interpretation of the absolute difference between the observed and reference angles as it applies to the solar array deploy status is explored in the ensuing sections.

If one or more of the sampled observations minus the expected, for both sets of sets of angles (noting the ambiguity in the CSSs), lies outside the 17 degree error budget, the solar arrays cannot be fully deployed (Figure 3). It is important to note which CSSs are reporting that they see the Sun. By nature of their fully deployed configuration, two, one, or none CSSs can see the Sun at any given time. If more than two see the Sun then the arrays are not fully deployed. If two, and only two, see the Sun throughout the pass, and the error is outside the 17 degree budget, then a non-deploy can only be reported for the solar panel, or portions of both panels that houses those CSSs. The complete picture can be determined if all 4 CSSs see the Sun (in sets of two) during the pass. If samples fall outside the error budget for each pair of CSSs, neither of the arrays deployed completely.

Table 1 - Error Budget

Source	Error (degrees)
CSS Measurement Uncertainty	10
TAM Measurement Uncertainty	2
Magnetic Field Model Error	1
Ground Telemetry Time Error	2
Spacecraft Ephemeris Error	2
Total Error	17

Figure 3 - Reference - Observed for Non-Deploy Case
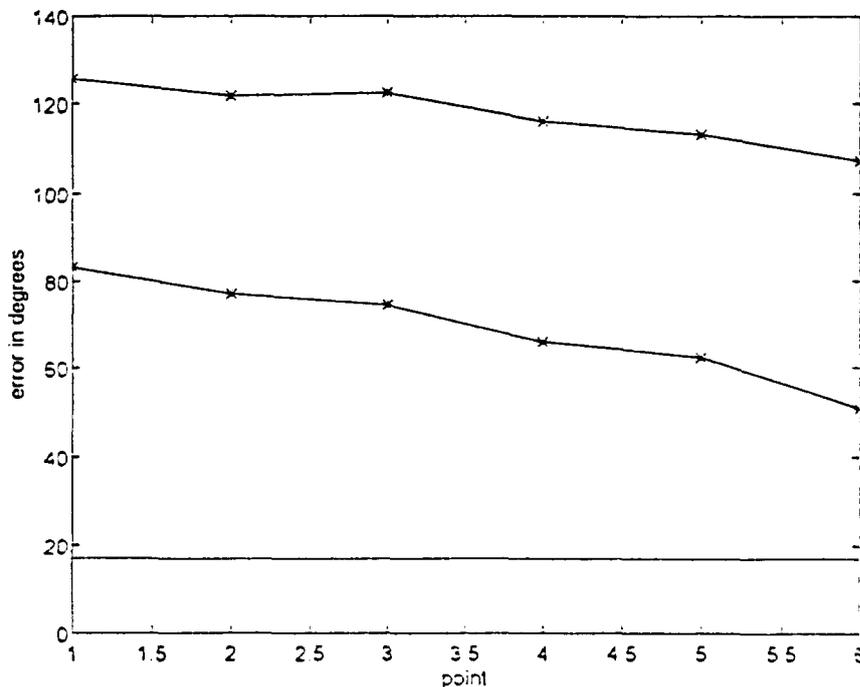
Although the converse of the above section is not necessarily true, some conclusions can be drawn with some level of confidence. If all observations lie within the error budget, for one or both sets of angles (again, noting the ambiguity in CSSs), there is a good chance that the solar array(s) are deployed, again dependent on which CSSs are reporting Sun presence. Analysis has been performed to investigate when a likely non-deployed situation (includes one or more detonator failures) can look like a deploy, i.e. if the angle under consideration could still match the predicted within 17 degrees[2]. Even if it's the improper choice for ambiguity resolution, as there is no way to tell during this check, it would still falsely appear as a deploy. The investigation showed that a deploy can be correctly reported 70% of the time. These odds improve when several points can be taken throughout the pass and compared, and all lie within the 17 degree budget. Also, this study showed that if the spacecraft incurs a rate of rotation, which TOMS-EP is likely to have at injection, the likelihood of a non-deployed state reporting an error less than 17 degrees through the pass is more remote still.

Figure 4 - Reference - Observed for Deploy Case

225
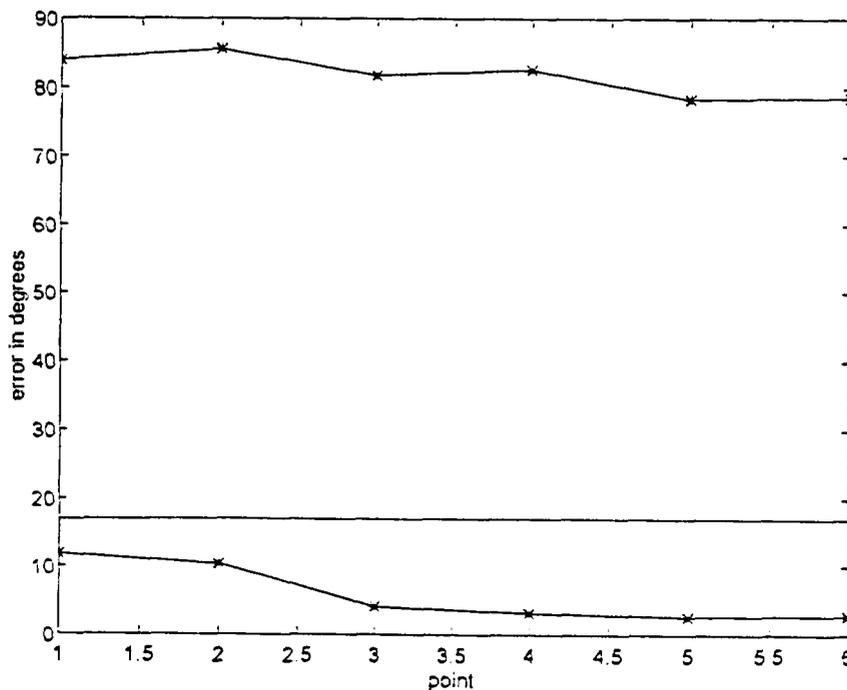
Analysis and Simulation Results

The work performed by N. Tull [2] ran through a sphere of possible Sun and magnetic field vectors. These were input into the solar array deployment algorithm to not only determine the percentage of deploy and non-deploy confirmations, but also to gain confidence in the algorithm itself. In addition to this analysis to confirm the algorithm's performance, the deployment algorithm has been used in TOMS-EP simulations with success. Several minutes after the McMurdo pass was completed, the Flight Dynamics facility was able to determine, to a high degree of confidence, if the arrays were deployed. Through the simulations, the procedures for implementing the algorithm were tested and refined.

Summary

The solar array deployment algorithm was developed as a quick method for use with TOMS-EP. It is robust and will allow a quick determination of the solar array status. To recap. if one or more observed angles between the magnetic field and Sun line differ from the expected separation angle by more than the 17 degree error budget, one or both of the solar arrays are not fully deployed. This depends, though, on which CSS are giving data. If all of the observed angles differ from the expected by less than the error budget, a deployed state is known with 70 % likelihood for one or both solar arrays. These odds go up markedly with increased data points and when the spacecraft has a rotation rate, which is expected for the initial TOMS-EP orbit insertion.

References

1. T. Mendenhall, TRW Memorandum, "CSSA Function," March 21, 1994

2. N. Tull, Internal NASA Memorandum, "Predicting the Deployment of TOMS Solar Arrays Based on Solar and Magnetic Field Data," August, 1994

Earth Horizon Modeling and Application to Static Earth Sensors on TRMM Spacecraft[*]

J. Keat and M. Challa
Computer Sciences Corporation (CSC)
Lanham-Seabrook, Maryland, USA

D. Tracewell and K. Galal
Goddard Space Flight Center (GSFC)
Greenbelt, Maryland, USA

Abstract

Data from Earth sensor assemblies (ESAs) often are used in the attitude determination (AD) for both spinning and Earth-pointing spacecraft. The ESAs on previous such spacecraft for which the ground-based AD operation was performed by the Flight Dynamics Division (FDD) used the Earth scanning method. AD on such spacecraft requires a model of the shape of the Earth disk as seen from the spacecraft. AD accuracy requirements often are too severe to permit Earth oblateness to be ignored when modeling disk shape. Section 2 of this paper rexamines and extends the methods for Earth disk shape modeling employed in AD work at FDD for the past decade. A new formulation, based on a more convenient Earth flatness parameter, is introduced, and the geometric concepts are examined in detail. It is shown that the Earth disk can be approximated as an ellipse in AD computations.

Algorithms for introducing Earth oblateness into the AD process for spacecraft carrying scanning ESAs have been developed at FDD and implemented into the support systems. The Tropical Rainfall Measurement Mission (TRMM) will be the first spacecraft with AD operation performed at FDD that uses a different type of ESA—namely, a static one—containing four fixed detectors D_i (i = 1 to 4). Section 3 of this paper considers the effect of Earth oblateness on AD accuracy for TRMM. This effect ideally will not induce AD errors on TRMM when data from all four D_i are present. When data from only two or three D_i are available, however, a spherical Earth approximation can introduce errors of 0.05 degrees to 0.30 degrees on TRMM. These oblateness-induced errors are eliminated by a new algorithm that uses the results of Section 2 to model the Earth disk as an ellipse.

1. Introduction

Data from Earth sensor assemblies (ESAs) often are used in attitude determination (AD) for both spinning and Earth-pointing spacecraft. Past spacecraft with AD operations performed at the Flight Dynamics Division (FDD) used Earth scanning ESAs. The Tropical Rainfall Measurement Mission (TRMM) will be the first such spacecraft to use a different type of ESA—namely, a static Earth sensor assembly (SESA), built by Barnes Engineering Company, that comprises four detectors D_i (i = 1 to 4) to sense the Earth horizon at four equally spaced points.

AD algorithms that use ESA data require a model of the shape of the Earth disk as seen from the spacecraft. Frequently, AD accuracy requirements are too severe to permit the simple approximation that the Earth is a sphere, yielding a perfectly circular disk. In such cases, a more exact disk shape model, which includes the effect of Earth oblateness, is needed. The methodology prescribed by Liu[1] has provided the basis for Earth oblateness and disk shape modeling at FDD since the late 1970s.

Techniques for including Earth oblateness in AD and for correcting attitudes in which it has not been included, on either spinning or Earth-pointing spacecraft using scanning ESAs, have been used at FDD for many years[2,3,4]. No analogous techniques were available previously at FDD for spacecraft that carry the Barnes SESA. As discussed later, such spacecraft do not require a correction for Earth oblateness in AD if the spacecraft, like TRMM, is nominally oriented along the geodetic nadir or horizon bisector nadir (rather than along the geocentric nadir) and if data from all four D_i are available. However, conditions in which data from only two or three of the four D_i are present are not infrequent. While attitude (roll and pitch angles) can be computed with data from only two or three adjacent D_i, the simple AD algorithms previously used in these cases permit Earth oblateness-induced AD errors.

This paper is divided into two subsequent sections. In Section 2, Liu's Earth disk shape analysis is re-examined and extended, and some of the concepts are explored in more detail. The structure of Section 2 largely follows that of Reference 1, and some of the material presented in Section 2 has appeared earlier in References 5 and 6. In Section 3, a new AD algorithm is prescribed for TRMM when data from only three or two D_i are present.

2. Earth Horizon Modeling

2.1 The Earth Spheroid (ES)

Previous AD work at FDD involving nonspherical Earth modeling approximated the Earth as an oblate spheroid prescribed as follows:

$$x^2 + y^2 + z^2[1 - f]^{-2} = a^2 \tag{1}$$

where a is the equatorial radius, and f is the flattening. The figure specified by Eq. (1) is called the Earth spheroid (ES) here. It was noted recently by Challa[5], however, that using a different flattening parameter α related to f as follows

$$\alpha = -1 + (1 - f)^{-2} \tag{2}$$

is convenient because it facilitates the use of vector methods. Assuming $f = 1/298.257$, Eq. (2) yields $\alpha = 1/148.379$; thus the Earth's α is approximately $2f$.

Eq. (2) enables Eq. (1) to be written as

$$\vec{r} \bullet \vec{r} + \alpha[\vec{r} \bullet \hat{z}]^2 = a^2 \tag{3}$$

where $\hat{z}$ is a unit vector from the geocenter, O, along the North pole axis, and $\vec{r}$ is the geocentric radius vector to an arbitrary point on the ES.

We view Eq. (3) as a constraint on $\vec{r}$, which we call the *ES constraint*. Our immediate goal is to define, on the ES, the Earth horizon contour as seen from a spacecraft, S. This requires specifying one more constraint on $\vec{r}$, and this topic is addressed in the following sections (2.2 and 2.3).

2.2 The Horizon Spheroid (HS)

Define the following scalar field

$$f(\vec{r}) = \vec{r} \bullet \vec{r} + \alpha[\vec{r} \bullet \hat{z}]^2 \tag{4}$$

and let $\vec{g}(\vec{r})$ be its gradient

$$\vec{g}(\vec{r}) = 2 \left[\vec{r} + \alpha (\vec{r} \bullet \hat{z}) \hat{z} \right] \tag{5}$$

We view Eq. (4) as specifying an infinite family of oblate spheroids, each with constant equatorial radius sqrt $(f(\vec{r}))$ and all elements of the family having flattening α and center at O. Let $E(\vec{r})$ denote the spheroid at the tip of $\vec{r}$ and let $T(\vec{r})$ be the tangent plane to $E(\vec{r})$ at $\vec{r}$. Then $\vec{g}(\vec{r})$ is orthogonal to $T(\vec{r})$.

Let $\vec{s}$ be a vector from O to a spacecraft, S. Let $\vec{h}(\vec{r})$ be a vector from S to $\vec{r}$. Obviously,

$$\vec{h}(\vec{r}) = \vec{r} - \vec{s} \tag{6}$$

Our second constraint on $\vec{r}$ is that S, and hence $\vec{h}(\vec{r})$, lie in $T(\vec{r})$. Then,

$$\vec{h}(\vec{r}) \bullet \vec{g}(\vec{r}) = 0 \tag{7}$$

Eq. (7) is the first form of the second constraint on $\vec{r}$. Satisfaction of this constraint implies that the tip of $\vec{r}$ is a horizon point of $E(\vec{r})$. A more explicit form of Eq. (7) can be obtained by introducing Eqs. (5) and (6) into it to produce

$$\vec{r} \bullet [\vec{r} - \vec{s}] + \alpha [\vec{r} \bullet \hat{z}][\hat{z} \bullet (\vec{r} - \vec{s})] = 0 \tag{8}$$

To transform Eq. (8) into a form that clearly shows the shape of the figure defined by the second constraint, add $(\vec{s}/2) \bullet (\vec{s}/2)$ to both sides and factor. For simplicity, then introduce $\vec{v} = \vec{r} - \vec{s}/2$. The result is

$$\vec{v} \bullet \vec{v} + \alpha [\vec{v} \bullet \hat{z}]^2 = \frac{\vec{s}}{2} \bullet \frac{\vec{s}}{2} + \alpha \left[\hat{z} \bullet \frac{\vec{s}}{2}\right]^2 \tag{9}$$

Eq. (9) shows that the second constraint requires the tip of $\vec{r}$ to lie on an oblate spheroid, called the horizon spheroid (HS) here. Similarly, we call the second constraint the horizon spheroid constraint. The HS is centered at $\vec{s}/2$ and, like the ES, has flattening α. The equatorial plane of the HS is parallel to that of the ES, and its equatorial radius is the square root of the term on the right side of Eq. (9). Points O and S both lie on the HS.

2.3 The Horizon Plane (HP)

Eqs. (3) and (8) constitute a pair of constraints on $\vec{r}$ which, when solved for $\vec{r}$, define a closed curve, called here the *horizon contour* (HC), which is the ES horizon seen from S and specified on the ES. Geometrically, the HC is the intersection of two oblate spheroids; namely, the ES and HS, as illustrated in Fig. 1.
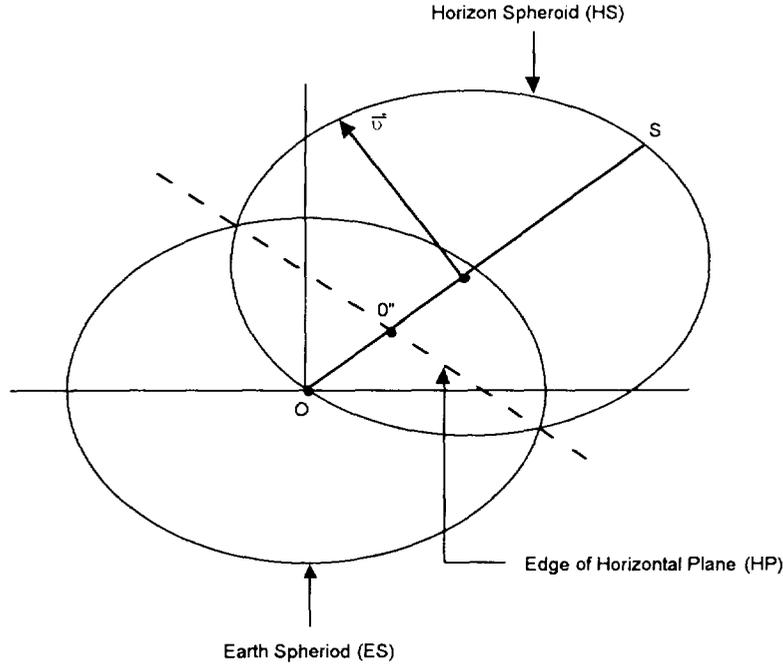
Figure 1. *Earth Spheroid, Horizon Spheroid, and Horizon Plane*

The geometry and the solution for $\vec{r}$, however, can be simplified by replacing the HS constraint by a new constraint formed from the ES and HS ones. To develop this new constraint, first note that Eqs. (4) and (5) show that $\vec{r} \bullet \vec{g}(\vec{r}) = 2f(\vec{r})$ and Eqs. (6) and (7) indicate $\vec{r} \bullet \vec{g}(\vec{r}) = \vec{s} \bullet \vec{g}(\vec{r})$. Hence

$$\vec{s} \bullet \vec{g}(\vec{r}) = 2f(\vec{r}) \tag{10}$$

Eq. (10) is merely another form of the HS constraint. Eqs. (3) and (4) show that the ES constraint can be written as merely

$$f(\vec{r}) = a^2 \tag{11}$$

The initial equation for the new constraint is produced by inserting Eq. (11) into Eq. (10) to obtain trivially

$$\vec{s} \bullet \vec{g}(\vec{r}) = 2a^2 \tag{12}$$

For a more useful form of the new constraint, first introduce Eq. (5) into Eq. (12) and manipulate to obtain

$$\vec{m} \bullet \vec{r} = a^2 \tag{13}$$

where

$$\vec{m} = s\left[\hat{s} + \alpha \hat{z} \cos \lambda'\right] \tag{14}$$

In Eq. (14) we have factored $\vec{s}$ into $\vec{s} = s\hat{s}$ and introduced λ' as the co-latitude angle between $\hat{s}$ and $\hat{z}$. Using $\vec{m} = m\hat{m}$, Eq. (14) indicates that

$$m = s\left[1 + 2\alpha \left(1 + 0.5\alpha\right) \cos^2 \lambda'\right]^{1/2} \tag{15}$$

Define the following vector $\vec{n}$ along $\hat{m}$:

$$\vec{n} = n\hat{m} \tag{16}$$

where

$$n = a^2 / m \tag{17}$$

Eq. (13) then can be written as

$$\vec{r} \bullet \hat{m} = n \tag{18}$$

Eq. (18) is the second form of the new constraint. Analysis of Eq. (18) shows it constrains the tip of $\vec{r}$ to lie on a plane whose normal is along $\hat{m}$ and whose distance from O is n. This plane and the new constraint are called the *horizon plane* (HP) and HP constraint here. An alternate derivation of Eq. (18) is presented in Ref. 5.

Some later-needed properties of the HP will be delineated before proceeding. Fig. 2 shows the geometry. With the exception of $\hat{E}$, all vectors on this figure lie in a plane normal to the HP. O' is the tip of the perpendicular from O to the HP, and O'' is the intersection of $\vec{s}$ with the HP. The position vectors of O' and O'' with respect to O are given by $\vec{n}$ and $s_1\hat{s}$, respectively. The distance between O'' and S is given by s_2; thus, $s_1 + s_2 = s$. The term b is the distance between O' and O''. The unit vectors $\hat{E}$ and $\hat{N}$ are directed along local East and local North, respectively, at O' and define the HP. The triad ($\hat{E}, \hat{N}, \hat{m}$) defines a reference frame centered at O'. The vector $\hat{m}$ makes angles σ and ε_m with $\hat{z}$ and $\hat{s}$, respectively. Note that ε_m is a small angle, since the ES is very nearly spherical; the size of ε_m has been exaggerated on Fig. 2 for clarity.
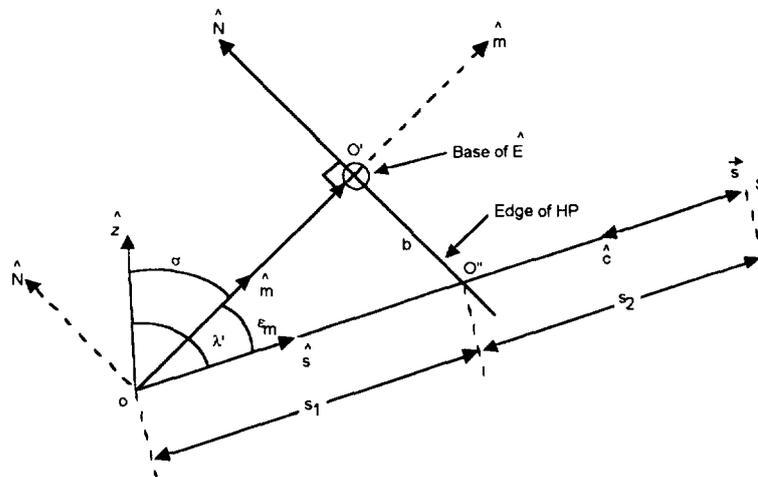
Figure 2. Horizon Plane Geometry and Variables

The following important relations can be derived using the material presented above:

$$\cos\sigma = \hat{m} \bullet \hat{z} = [s/m][1+\alpha]\cos\lambda' \tag{19}$$

$$\sin\sigma = [s/m]\sin\lambda' \tag{20}$$

$$\cos\varepsilon_m = \hat{s} \bullet \hat{m} = [s/m]\left[1 + \alpha\cos^2\lambda'\right] \tag{21}$$

$$\sin\varepsilon_m = [s/m]\,\alpha\sin\lambda'\cos\lambda' \tag{22}$$

$$\hat{E} = \hat{z} \times \hat{s}/\sin\lambda' \tag{23}$$

$$\hat{N} = \hat{m} \times \hat{E} = [s/(m\sin\lambda')]\left[\hat{z}\left(1 + \alpha\cos^2\lambda'\right) - \hat{s}(1+\alpha)\cos\lambda'\right] \tag{24}$$

$$b = [\alpha a^2/m]\cos\lambda'\sin\lambda'\left[1+\alpha\cos^2\lambda'\right]^{-1} \tag{25}$$

$$s_1 = [a^2/s]\left[1 + \alpha\cos^2\lambda'\right]^{1} \tag{26}$$

$$s_2 = s\left[1 + \alpha\cos^2\lambda' - (a/s)^2\right]\left[1+\alpha\cos^2\lambda'\right]^{-1} \tag{27}$$

Note that Eqs. (21) and (15) yield

$$\cos\varepsilon_m \approx 1 - \frac{\alpha^2 \sin^2\lambda'\cos^2\lambda'}{2} \tag{28}$$

Thus, the angle between $\hat{s}$ and $\hat{m}$ is given by

$$\varepsilon_m \approx \alpha\sin\lambda'\cos\lambda' \tag{29}$$

except for the cases $\lambda' = 0$ and $\lambda' = \pi/2$. Thus, the geocenter-to-spacecraft vector $\vec{s}$ generally differs from the normal to the HP by an angle of the order of the flattening factor α.

It will be shown in Section 2.4 that the locus of the horizon points in the HP is an ellipse, and it will then be shown that the spacecraft views this ellipse slightly obliquely.

2.4 The Horizon Ellipse (HE)

The HC now is specified by Eqs. (3) and (18) as the intersection of a spheroid and a plane; namely, the ES and the HP, as illustrated in Fig 1. To solve these equations, express $\vec{r}$ as

$$\vec{r} = \vec{n} + \vec{w} \tag{30}$$

with $\vec{w} \bullet \vec{n} = 0$. Thus, $\vec{w}$ lies in the HP, with its base at O'. Eq. (30) thus requires $\vec{r}$ to satisfy the HP constraint. To further restrict $\vec{r}$ to satisfy the ES constraint, insert Eq. (30) into Eq. (3). After manipulation, we obtain

$$\vec{w} \bullet \vec{w} + \alpha\left[\vec{w} \bullet \hat{z}\right]^2 + 2\alpha[\vec{n} \bullet \hat{z}][\vec{w} \bullet \hat{z}] = a^2 - \vec{n} \bullet \vec{n} - \alpha[\vec{n} \bullet \hat{z}]^2 \tag{31}$$

Eq. (31), in conjunction with Eq. (30), specifies the HC.

Eq. (31) can be transformed into a simpler form by specifying the position vector of the horizon point relative to O'' rather than relative to O'. Letting $\vec{q}$ be this new position vector and noting that $\overrightarrow{O''O'} = b\hat{N}$ as is evident from Fig. 2, we thus have

$$\vec{w} = \vec{q} - \hat{N}b \tag{32}$$

with $\vec{q}$, like $\vec{w}$, restricted to the HP.

When Eq. (32) is inserted into Eq. (31), it can be shown, with much work, that a pair of terms cancel out, yielding the following simpler result:

$$\vec{q} \bullet \vec{q} + \alpha_E \left[\hat{N} \bullet \vec{q} \right]^2 = a^2{}_E \tag{33}$$

where

$$\alpha_E = \alpha \left[\hat{N} \bullet \hat{z} \right]^2 = \alpha [s/m]^2 \sin^2 \lambda' \tag{34}$$

$$a^2{}_E = a^2 - \vec{n} \bullet \vec{n} - \alpha [\vec{n} \bullet \hat{z}]^2 \left[1 + \alpha \left(\hat{N} \bullet \hat{z} \right)^2 \right]^{-1}$$

$$= a^2 \left[1 + \alpha \cos^2 \lambda' - (a/s)^2 \right] \left[1 + \alpha \cos^2 \lambda' \right]^{-1} \tag{35}$$

Eq. (33) shows that the shape of the HC in the HP is an ellipse, called the *horizon ellipse* (HE) here. The center of the HE is at O'', its flattening is α_E and its semi-major axis is a_E along $\hat{E}$. The HC's elliptical shape and the important fact that its center is on $\vec{s}$ were noted in Ref. 5.

2.5 The Earth Disk (ED)

We use the term *Earth disk* (ED) here to denote the figure of the Earth as seen from S. The next task is to specify the ED's shape from the preceding material on the HP and HE. Fig. 3 shows the geometry.
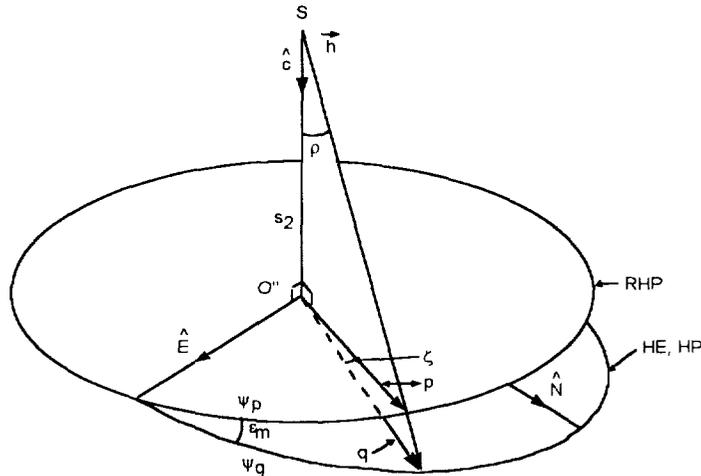
Figure 3. Earth Angular Radius ρ Geometry

The previous section (2.4) showed that the HP is not quite orthogonal to $\vec{s}$. So we will define a new plane, called here the *rotated horizon plane* (RHP), which is orthogonal to $\vec{s}$. The RHP is formed by rotating the HP about $\hat{E}$ through angle ε_m. Let $\vec{q} = q\hat{q}$ be a vector on the HE at an azimuth angle ψ_q from $\hat{E}$. Let $\vec{p} = p\hat{p}$ be the vector in the RHP corresponding to $\vec{q}$. Let ψ_p be the azimuth angle of $\vec{p}$ from $\hat{E}$. $\vec{p}$ is formed by projecting $\vec{q}$ along the vector $\vec{h}$ onto the RHP, where $\vec{h}$ is the horizon vector from S to the tip of $\vec{q}$. Obviously, the locus $\vec{p}(\psi_p)$ in the RHP is not an ellipse centered at O''. Designate the small angle between $\vec{p}$ and $\vec{q}$ as ζ. The following important equations can be derived:

$$p = q \cos\zeta \left[1 + (q/s_2)\sin\zeta \right]^{-1} \tag{36}$$

$$\sin\zeta = \sin\psi_q \sin\varepsilon_m \tag{37}$$

$$\cos\zeta = c_1 \cos\varepsilon_m \tag{38}$$

$$\sin\psi_q = c_1 \sin\psi_p \tag{39}$$

$$\cos\psi_q = c_1 \cos\varepsilon_m \cos\psi_p \tag{40}$$

$$c_1 = \left[1 - \sin^2\varepsilon_m \cos^2\psi_p\right]^{-0.5} \tag{41}$$

$$q = a_E\left[1 + \alpha_E \sin^2\psi_q\right]^{-0.5} \tag{42}$$

Let ρ be the angle at S between $\bar{h}$ and the unit geocentric nadir vector $\hat{c} = -\hat{s}$. The shape of the ED will be specified by the locus of $\rho(\psi_p)$ around it. It turns out that the simplest result is obtained using the arcctn function:

$$\rho = \mathrm{arcctn}(s_2/p) \tag{43}$$

Insert Eq. (36) into Eq. (43), and use Eqs. (37) through (42) and earlier equations as necessary. After much work, the following important result ensues:

$$\rho = \mathrm{arcctn}\left\{\left[1 + \alpha\cos^2\lambda'\right]^{-1}\left[\alpha\sin\lambda'\cos\lambda'\sin\psi_p + \mathrm{ctn}\rho_c\left[1 + \alpha\left(k_1 + k_2\sin^2\psi_p\right)\right]^{0.5}\right]\right\} \tag{44a}$$

where

$$k_1 = \cos^2\lambda'\left[1 + \sec^2\rho_c\left(1 + \alpha\cos^2\lambda'\right)\right] \tag{44b}$$

$$k_2 = \sin^2\lambda'\left[1 + \alpha\cos^2\lambda'\sec^2\rho_c\right] \tag{44c}$$

$$\rho_c = \arcsin(a/s) \tag{45}$$

ρ_c above is merely the usual angular radius, from S, of a fictitious spherical Earth with radius a and center at O.

Eqs.(44a) through (44c) were derived earlier in Ref. 6 using a different approach. Ref. 6 shows, by analytical and numerical means, that Eqs. (44a) through (44c) are equivalent to Eq. (4-24) of Ref. 1.

2.6 The Earth Disk Ellipse Approximation

The Earth's α is small enough to permit Eqs. (44a) through (44c) to be linearized in it with acceptable accuracy. The result is

$$\mathrm{ctn}\rho = \mathrm{ctn}\rho_c\left[1 + 0.5\alpha\left\{\cos^2\lambda'\sec^2\rho_c\sin^2\rho_c + 2\sin\lambda'\cos\lambda'\tan\rho_c\sin\psi_p + \sin^2\lambda'\sin^2\psi_p\right\}\right] \tag{46}$$

Eqs. (44) and (46) specify disk angular radius ρ relative to the geocentric nadir z_c. We wish to generalize Eq. (46) to specify disk radius relative to lines close to z_c. Fig. 4 shows the geometry on the unit celestial sphere (UCS). Point P here lies on the extension of z_c onto the UCS. The reference origin is to be moved from P south through small angle ε to a new point P_ε by transforming Eq. (46) from variables ρ, ψ_p to new ones $\rho_\varepsilon, \psi_\varepsilon$. For now, ε is assumed to be arbitrary, but small enough to permit small angle approximations and ruthless linearizations. Fig. 4 then yields

$$\mathrm{ctn}\rho = \mathrm{ctn}\rho_\varepsilon\left[1 + \varepsilon\sec\rho_\varepsilon\csc\rho_\varepsilon\sin\psi_\varepsilon\right] \tag{47}$$

$$\sin^2\psi_p = \sin^2\psi_\varepsilon\left[1 - 2\varepsilon\,\mathrm{ctn}\rho_\varepsilon\cos^2\psi_\varepsilon\csc\psi_\varepsilon\right] \tag{48}$$

$$\sin\psi_p = \sin\psi_\varepsilon\left[1 - \varepsilon\,\mathrm{ctn}\rho_\varepsilon\cos^2\psi_\varepsilon\csc\psi_\varepsilon\right] \tag{49}$$

Insert Eqs. (48) and (49) into Eq. (46) and equate to Eq. (47). This produces an equation in the desired terms ε, ρ_ε, ψ_ε. However, it is not evident how to solve it for ρ_ε in closed form.
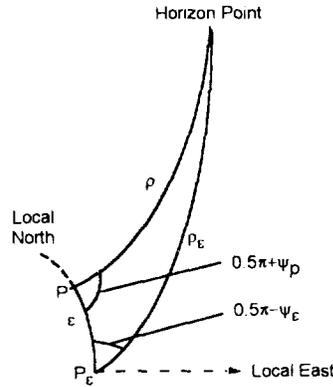
Figure 4. Origin Translation on Unit Celestial Sphere (UCS)

The difficulty will be handled by now restricting the work to a single, highly important case. Specifically, ε now will be limited to the value that causes the two terms involving itself and sin ψ_ε, respectively to cancel. The subscript HB, for *horizon bisector*, will be used to denote this ε and terms pertaining to it. The resulting equation for ε_{HB} is

$$\varepsilon_{HB} = \alpha \cos \lambda' \sin \lambda' \sin^2 \rho_c \tag{50}$$

It should be realized that ε_{HB} is the angle between z_c and a line, z_{HB}, called here the *horizon bisector nadir*. An alternate name, the *apparent nadir*, has been used by Flatley[7] who performed the original work on the concept. The resulting equation for $\text{ctn}\,\rho_{HB}$ when Eq. (50) is used is

$$\text{ctn}\,\rho_{HB} = \text{ctn}\,\rho_c \left[1 + 0.5\alpha \left\{ \cos^2 \lambda' \sec^2 \rho_c \sin^2 \rho_c + \sin^2 \lambda' \sin^2 \psi_{HB} \right\} \right] \tag{51}$$

Solving Eq. (51) for ρ_{HB} and linearizing in α produces

$$\rho_{HB} = a_E \left[1 - 0.5\alpha_E \sin^2 \psi_{HB} \right] \tag{52a}$$

where

$$a_E = \rho_c - 0.5\alpha \cos^2 \lambda' \sin^3 \rho_c \sec \rho_c \tag{52b}$$

$$\alpha_E = 0.5(\alpha/\rho_c) \sin \rho_c \cos \rho_c \sin^2 \lambda' \tag{52c}$$

Eqs. (52a) through (52c) show that the ED can be approximated by an ellipse, centered at ρ_{HB} with flattening α_E and semi-major axis a_E along local East. This result was derived earlier in Ref. 6 by different means. A MATLAB study, described in Ref. 6, indicated that for the Earth α, the ellipse approximation is accurate to about 1e-5 degrees. It should be realized, however, that the ellipse exists only on an abstract mathematical plane, not on a physical one. Geometrically, the figure of the Earth seen from S can, of course, best be considered to exist on the UCS, not on a plane.

3. Application to TRMM Attitude Determination

3.1 Introduction

Fig. 5 shows the nominal TRMM SESA FOV geometry on a circular ED. The basic outputs of the SESA are the four positive penetration angles X_i between the Earth IR horizon and the detector D_i bases. Spacecraft attitude is specified by a 2×1 vector $\underline{\beta}$ of the angular deviation of the SESA and spacecraft body axis $z_S = z_B$ from the HB nadir line z_{HB}. There are two main steps in the AD process. First, the X_i are transformed into an SESA frame, S, attitude vector $\underline{\beta}_S = [\phi_S \theta_S]^T$ using the

algorithms discussed below. Second, $\underline{\beta}_S$ is transformed into a spacecraft body, B, frame vector $\underline{\beta}_B = \left[\phi_B \theta_B\right]^T$ by a rotation $\underline{\beta}_B = R\underline{\beta}_S$. Our current interest is only in the first of these two operations. The ϕ and θ are roll and pitch angles; determination of yaw is done separately and requires a separate sensor.
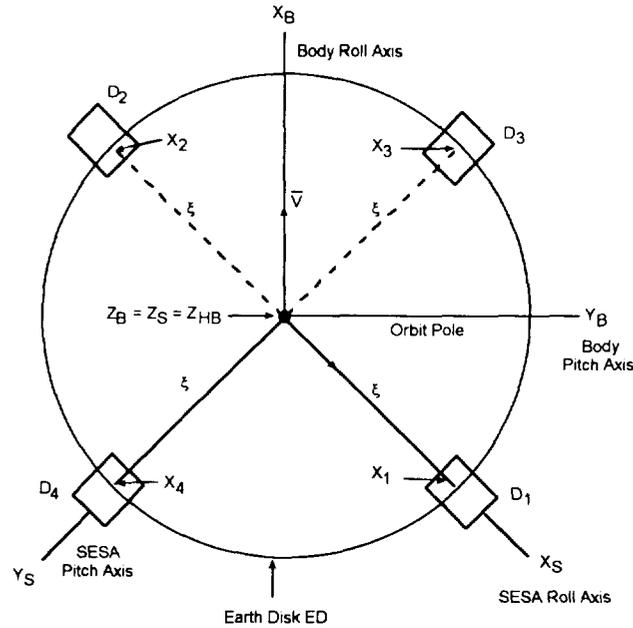
Figure 5. Nominal SESA FOV Geometry on Earth Disk (ED)

3.2 The Standard SESA AD Algorithms

The standard algorithms for computing $\underline{\beta}_S$ from the X_i imply a spherical model of the Earth. When all four X_i are available, we use

$$\phi_S = 0.5\left[X_4 - X_3\right] \tag{53}$$

$$\theta_S = 0.5\left[X_2 - X_1\right] \tag{54}$$

If only three X_i are available, either Eq. (53) or Eq. (54) will be unusable, requiring a new algorithm for the affected angle. For example, if X_3 is missing, then ϕ_S is computed via

$$\phi_S = X_4 - 0.5\left[X_1 + X_2\right] \tag{55}$$

and if X_1 is missing, θ_S is computed via

$$\theta_S = X_2 - 0.5\left[X_3 + X_4\right] \tag{56}$$

Analogous algorithms are used when X_2 or X_4 is missing. The function of the r al terms in Eqs. (55) and (56) is to compensate for deviation of altitude from that which yields all $X_i = 0$ in the nominal spherical Earth attitude condition.

When the X_i from two adjacent D_i, say D_1 and D_3, are missing, we use

$$\phi_S = X_4 - X_{AVG} \tag{57}$$

$$\theta_S = X_2 - X_{AVG} \tag{58}$$

with

237

$$X_{AVG} = X_R - \alpha_R \left[h - h_R \right] \tag{59}$$

where h is actual altitude, h_R is a reference altitude, X_R is the nominal spherical Earth X_i at h_R, and α_R is a scale factor.

3.3 Proposed AD Algorithms to Compensate for Earth Oblateness

Section 2.6 demonstrated that to first order in α, the ED is an ellipse with center P_{HB} on z_{HB}. Therefore, due to symmetry, Earth oblateness will not introduce an error into the attitude computed by Eqs. (53) and (54). Numerical studies using the software package MATLAB showed that, in fact, this result does not depend on the first order approximation in α. Thus, Earth oblateness does not induce an AD error when all four X_i are available and used.

Our MATLAB studies, however, also showed that Earth oblateness induces a significant AD error on TRMM when only three or two X_i are available and Eqs. (55) through (59) are used. This error varies from 0 to 0.05 degrees in the $3 - X_i$ case and from 0.05 to 0.30 in the $2 - X_i$ one. To eliminate the AD errors in the $3 - X_i$ and $2 - X_i$ cases, we have proposed that Eqs. (55) through (59) be replaced by a new algorithm based on the elliptical ED model from Section 2.6. The main steps of this algorithm are as follows.

(1) Compute the azimuth angles ψ_{D_i} of the D_i relative to local East via

$$\psi_{D_i} = \psi - \psi_v - \psi_{D_i B} \tag{60}$$

where ψ is the spacecraft yaw angle, $\psi_{D_i B}$ is the constant azimuth angle of each D_i relative to x_B, and ψ_v is the spacecraft velocity angle relative to local East. ψ_v can be computed using

$$\psi_v = \pi/2 - \arctan \left(\cos i / \cos \left(\omega + f \right) \right) \tag{61}$$

where i, ω, and f are orbit inclination, argument of perigee, and true anomaly, respectively.

(2)   Use the ψ_{D_i} to compute the ED radii ρ_{D_i} at the D_i using Eq. (52). Then compute the nominal penetration angles X_{iNOM} via $X_{iNOM} = \psi_{D_i} - \xi$; where ξ is the detector mounting angle on Fig. 5.

(3) Compute the ϕ_S and/or θ_S that cannot be computed by Eq. (53) and/or Eq. (54) via

$$\phi_S = X_i - X_{iNOM} \tag{62}$$

$$\theta_S = X_j - X_{iNOM} \tag{63}$$

where X_i and X_j are the proper available penetration angles. Theory indicates this algorithm should almost perfectly eliminate Earth oblateness-induced AD errors in the $2 - X_i$ and $3 - X_i$ cases.

Acknowledgments

References

1. Liu, K., "Earth Oblateness Modeling," in *Spacecraft Attitude Determination and Control*, J. Wertz, editor, D. Reidel, Dordrecht, Holland, 1978

2. Nair, G., et al., *Earth Radiation Budget Satellite (ERBS) Ground Support System (AGSS) Functional Specification and Requirements*, Computer Sciences Corporation,CSC/SD-82/6013, September 1982

3. Goddard Space Flight Center, Flight Dynamics Division, 553-FDD-93/032R1UD0, *Multimission Three-Axis Stabilized Spacecraft (MTASS) Flight Dynamics Support System (FDSS) Mathematical Background*, prepared by Computer Sciences Corporation, June 1994

4. Ottenstein, N., et al., *Multimission Spin-Axis Support System (MSASS) Functional Specification Revision 1*, Computer Sciences Corporation, 554-FDD-90/085R1UDO, prepared for Goddard Space Flight Center under Contract NAS 5-31500

5. Goddard Space Flight Center, Flight Dynamics Division 553-FDD-94/030R0UD0, *Attitude Determination Using Static Earth Sensors*, M. Challa, prepared by Computer Sciences Corporation, August 1994

6. Keat, J.E., "Shape of the Earth as Seen from Space," unpublished memo to Liu and Challa, September 1, 1994

7. Flatley, T.W., "TRMM Yaw," memo from 712.3/TRMM ACS lead analyst, D. McGlew, to Distribution, November 16, 1992

FLIGHT MECHANICS/ESTIMATION THEORY SYMPOSIUM

MAY 16-18, 1995

SESSION 4

A Modified Proportional Navigation Scheme for Rendezvous and Docking with Tumbling Targets: The Planar Case

Norman Fitz-Coy[†] and Ming-Cheng Liu [*]
AeMES Department
University of Florida

A two-phase proportional navigation scheme is developed for the case of two rigid bodies engaged in a rendezvous/docking maneuver. The target vehicle is nonmaneuvering, but does have constant nonzero angular and linear velocities. Under these conditions, it is shown that previously obtained solutions are not applicable. Analytical solutions are obtained leading to relationships between the transverse and LOS navigation constants. It is shown that the transverse navigation constant for the second phase of the maneuver must be 2. Also, initial conditions necessary for rendezvous are presented.

Introduction

The concepts of proportional navigation have been widely developed for the terminal phase of intercept problems [1-4]. To a lesser extent, some form of proportional navigation has found application in rendezvous problems [5-8]. Regardless of the application (i.e., intercept or rendezvous), these studies have all used point mass bodies for both the target and chase vehicles. For intercept type problems, this is not an issue since one is only interested in two points occupying the same location in space at the same time. However, for rendezvous and docking type problems, this is a significant issue. For example, it is possible for two points other that the berthing mechanism points to come in contact with each leading to conditions which may not be favorable for the overall mission.

In a recent paper [8], true proportional navigation was modified to include a commanded acceleration proportional to the centripetal acceleration (i.e., along the LOS). It was shown that this modification resulted in a simultaneous zeroing of the range-to-go and range-to-go rate, a condition necessary for rendezvous. The short comings of this analysis is that this is applicable only to rendezvous maneuvers between point masses. If this procedure is applied to rigid bodies (i.e., bodies with finite dimensions), then contact between the bodies may occur prior to rendezvous as is depicted in Fig. 1. In this paper, further modifications of the guidance scheme of Ref. 8 are presented and discussed. These modifications specifically address (i) the issue of contact prior to docking and (ii) targets which are both translating and rotating. Both these issues arise due to the consideration of rigid bodies as opposed to point masses.
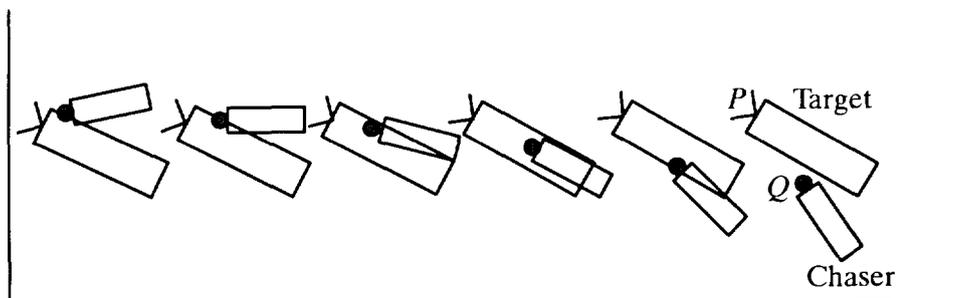
Fig. 1   Interference Associated with finite dimension bodies

†   Assistant Professor; Member: AIAA, AAS
*   Graduate Research Assistant

Kinematic Equations

Consider the planar rendezvous scenario as depicted in Fig. 2. The target vehicle translates with constant velocity $\vec{V}_T$ and rotates with constant angular velocity $\vec{\omega}_T$. The target vehicle has a berthing mechanism at point P which is located with respect to the vehicle's center of mass (c.m.) by $\vec{r}_P$. The chase vehicle has its berthing mechanism at point Q which is located with respect to the vehicle's c.m. by $\vec{r}_Q$. For convenience, the docking and the grapple mechanisms are both assumed to be aligned with their respective position vectors.

Let $\mathcal{F}_C$, $\mathcal{F}_G$, $\mathcal{F}_N$, and $\mathcal{F}_T$ be respectively, coordinate frames attached to the chase vehicle, the LOS vector, the inertial space, and the target vehicle. For motion in the xy-plane, denote the attitude and angular velocity of $\mathcal{F}_T$ relative to $\mathcal{F}_N$ by ϕ and $\vec{\omega}_T = \dot{\phi}\hat{k}$, respectively. Similarly, denote the attitude and angular velocity of $\mathcal{F}_C$ relative to $\mathcal{F}_G$ by β and $\vec{\omega}_C = \dot{\beta}\hat{k}$. Finally, define the LOS frame $\mathcal{F}_G$ in such a manner that the LOS vector is $\vec{r} = -r\,\hat{j}_G$ and denote the attitude and angular velocity of this frame relative to $\mathcal{F}_T$ by θ and $\vec{\omega}_G = \dot{\theta}\hat{k}$, respectively.

The inertial acceleration of the c.m. C_C of the chase vehicle is

$$\ddot{\vec{R}}_C = \vec{\Omega}_T \times (\vec{\Omega}_T \times \vec{r}_P) + \overset{\circ\circ}{\vec{r}} + \overset{\circ}{\vec{\Omega}}_G \times \vec{r} + \vec{\Omega}_G \times (\vec{\Omega}_G \times \vec{r}) + 2\vec{\Omega}_G \times \overset{\circ}{\vec{r}}$$

$$- \overset{\circ}{\vec{\Omega}}_C \times \vec{r}_Q - \vec{\Omega}_C \times (\vec{\Omega}_C \times \vec{r}_Q) \tag{1}$$

where $(\overset{\circ}{\ })$ denotes the time derivative of the components of a vector and $\vec{\Omega}_T \triangleq \vec{\omega}_T$, $\vec{\Omega}_G \triangleq \vec{\omega}_T + \vec{\omega}_G$, and $\vec{\Omega}_C \triangleq \vec{\omega}_T + \vec{\omega}_G + \vec{\omega}_C$ are the absolute angular velocities of $\mathcal{F}_T$, $\mathcal{F}_G$, and $\mathcal{F}_C$, respectively. Coordinatizing Eq. (1) in $\mathcal{F}_G$ (i.e., the LOS frame) results in

$$\ddot{\vec{R}}_c = a_{LOS\perp}\,\vec{i}_G + a_{LOS}\,\vec{j}_G \tag{2}$$

where

$$a_{LOS\perp} = \varrho\ddot{\delta} + 2\dot{\varrho}\dot{\delta} + \ddot{\beta}[r_{Qx}\sin\beta + r_{Qy}\cos\beta] - \dot{\phi}^2[r_{Px}\cos\theta + r_{Py}\sin\theta]$$

$$+ (\dot{\delta}^2 + \dot{\beta}^2)[r_{Qx}\cos\beta - r_{Qy}\sin\beta] \tag{3}$$

and

$$a_{LOS} = -\ddot{\varrho} + \varrho\dot{\delta}^2 + \dot{\phi}^2[r_{Px}\sin\theta - r_{Py}\cos\theta] - \ddot{\delta}[r_{Qx}\cos\beta - r_{Qy}\sin\beta]$$
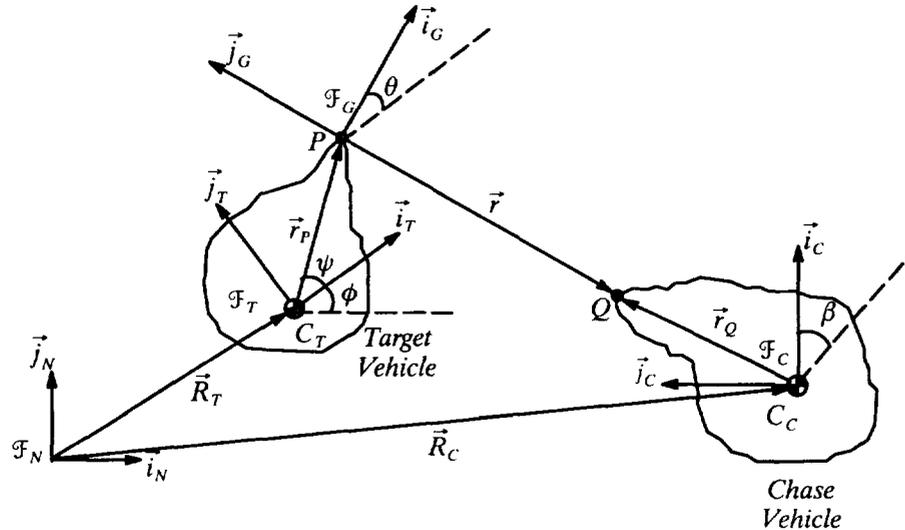
$$+ 2\dot{\delta}\dot{\beta}[r_{Qx}\sin\beta + r_{Qy}\cos\beta] \tag{4}$$

Fig. 2   Rendezvous Geometry

For convenience, the following definitions were utilized:

$$\delta \triangleq \dot{\theta} + \dot{\phi} \tag{5}$$

and

$$\varrho \triangleq r + r_{Q_x}\sin\beta + r_{Q_y}\cos\beta \tag{6}$$

where δ represents the absolute angular velocity of $\mathcal{F}_C$ and ϱ represents the projection of the vector from point P to C_c onto the LOS direction; we will refer to this quantity as the "pseudo-range-to-go" to distinguish it from the true range-to-go r.

Navigation Scheme

The proposed navigation acceleration are defined as

$$a_{LOS_{\perp_C}} \triangleq \lambda_{LOS_\perp}\dot{\varrho}\delta - \dot{\phi}^2[r_{P_x}\cos\theta + r_{P_y}\sin\theta] + \ddot{\beta}[r_{Q_x}\sin\beta + r_{Q_y}\cos\beta]$$
$$+ (\dot{\delta}^2 + \dot{\beta}^2)[r_{Q_x}\cos\beta - r_{Q_y}\sin\beta] \tag{7}$$

$$a_{LOS_C} \triangleq -\lambda_{LOS}\varrho\dot{\delta}^2 + \dot{\phi}^2[r_{P_x}\sin\theta - r_{P_y}\cos\theta] - \ddot{\delta}[r_{Q_x}\cos\beta - r_{Q_y}\sin\beta]$$
$$+ 2\dot{\delta}\dot{\beta}[r_{Q_x}\sin\beta + r_{Q_y}\cos\beta] \tag{8}$$

where $\lambda_{LOS_\perp}$ and λ_{LOS} are respectively the transverse and LOS navigation constants. The first terms of Eqs. (7) and (8) are the "classical" proportional terms proposed by Yaun and Hsu [8]. The remaining terms of Eqs. (7) and (8) are required to compensate for the angular velocity of the target and the angular velocity and angular acceleration of the chase vehicle

Equating the kinematic accelerations with the proposed navigation accelerations, the equations of relative motion can be developed as

$$\varrho\dot{\delta} + 2\dot{\varrho}\delta = \lambda_{LOS_\perp}\varrho\delta \tag{9}$$

$$\ddot{\varrho} - \varrho\dot{\delta}^2 = \lambda_{LOS}\varrho\dot{\delta}^2 \tag{10}$$

which are similar to those developed in Ref. 8. It was shown that these equations have solutions

$$\delta = \delta_0\left(\frac{\varrho}{\varrho_0}\right)^{a-1} \tag{11}$$

$$\dot{\varrho}^2 = \frac{\lambda_{LOS} + 1}{a}\varrho_0^2\delta_0^2\left[\left(\frac{\varrho}{\varrho_0}\right)^{2a} - 1\right] + \dot{\varrho}_0^2 \tag{12}$$

where $a \equiv \lambda_{LOS_\perp} - 1$. By specifying ϱ and $\dot{\varrho}$ at some point in the trajectory (e.g., at rendezvous), Eq. (12) becomes a constraint relationship between $\lambda_{LOS_\perp}$ and λ_{LOS}. In Ref. 8, Yaun and Hsu used the conditions that the range-to-go and range-to-go rate are zero at rendezvous to develop a specific relationship between $\lambda_{LOS_\perp}$ and λ_{LOS}. In terms of the "pseudo" quantities, these conditions can be restated as: $\varrho \rightarrow \varrho_f$ (since $r \rightarrow 0$ implies $\varrho = r_{Q_x}\sin\beta_f + r_{Q_y}\cos\beta_f$) and $\dot{\varrho} \rightarrow 0$ (assuming $\dot{\beta} = 0$). These conditions are no longer valid since we are concerned with rigid bodies rather than point masses. In fact, if one uses these conditions, the scenario depicted in Fig. 1 is generated. To avoid any contact prior to docking, we divide the maneuver into two guidance phases. In phase 1, the chase vehicle aligns itself with the target vehicle and acquires the angular velocity of the target vehicle. In phase 2, the chase vehicle maintains the angular velocity of the target and simultaneously reduces the range-to-go and range-to-go rate to zero. In both phases of flight, the following conditions are required for the chase vehicle:

- The berthing mechanism is aligned with the LOS (i.e., $\beta_{f_1} \approx 0$).

- The angular velocity of the vehicle relative to the LOS is small (i.e., $\dot{\beta}_{f_1} \approx 0$).

These conditions are can be enforced with an attitude controller onboard the vehicle.

The desired terminal conditions at the end of each maneuver phase are as follows.
Phase 1

245

- The LOS vector is parallel to $\vec{r}_p$ (i.e., $\theta_{f_1} \cong 2m\pi + \frac{\pi}{2} + \psi$ where m is the number of revolutions of the chase vehicle with respect to the target frame and ψ is the angle between the vector $\vec{r}_p$ and the $\vec{i}_T$ axis).

- The LOS relative rotation rate is zero (i.e., $\dot{\theta}_{f_1} = 0$).

- The two vehicles must be separated by some distance ϱ_{f_1} which must be greater than or equal to the sum of the largest dimension of each vehicle in order to avoid contact (i.e., $\varrho_{f_1} = r_1 + r_{Q_x}\sin\beta_{f_1} + r_{Q_y}\cos\beta_{f_1} > 0$; see Fig 3)

- The chase vehicle has some residual closing velocity as ϱ_{f_1} (i.e., $\dot{\varrho}_{f_1} = \dot{r}_1 + \dot{\beta}_{f_1}(r_{Q_x}\cos\beta_{f_1} - r_{Q_y}\sin\beta_{f_1}) < 0$)

Phase 2

- The LOS rotation rate is maintained at zero throughout this phase thereby ensuring proper alignment of the vehicles (i.e., $\dot{\theta}_{f_1} = 0$ and $\theta_{f_1} \cong 2m\pi + \frac{\pi}{2} + \psi$).

- The grappling mechanism of the chase vehicle approaches the docking port of the target vehicle (i.e., $\varrho_{f_2} = r_{Q_x}\sin\beta_{f_2} + r_{Q_y}\cos\beta_{f_2}$).

- The range-to-go rate approaches zero as $\varrho \to \varrho_{f_2}$ (i.e., $\dot{\varrho}_{f_2} = \dot{\beta}_{f_2}(r_{Q_x}\cos\beta_{f_2} - r_{Q_y}\sin\beta_{f_2})$

These requirements place constraints on the initial conditions of the chase vehicle at the beginning of the rendezvous maneuver. The initial conditions constraints are addressed below.

$$\varrho_{f_1} = l_{max_T} + l_{max_C}$$

Target Vehicle C_T

Chase Vehicle C_C
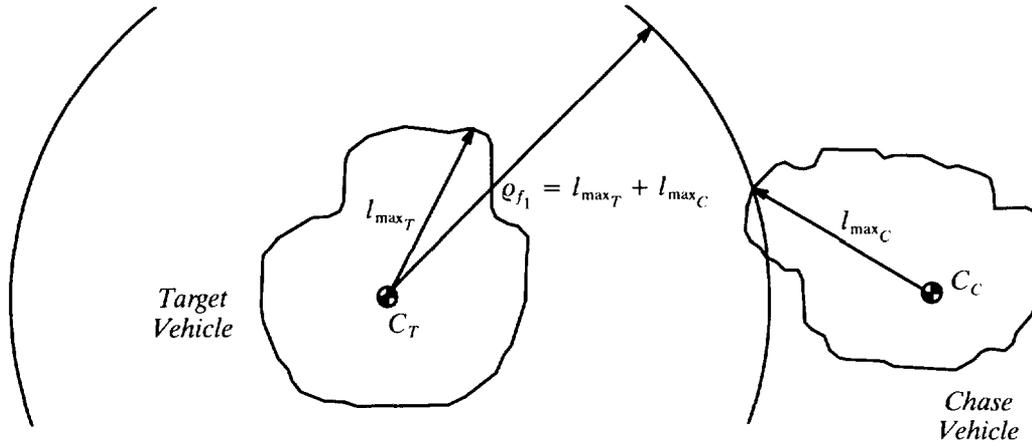
Fig. 3   Radius for noninterference

Since the initial and terminal conditions are different for each phase, the relationship between the guidance constants will also be different for each phase. We now develop these relationship, first for phase 1 and then phase 2.

Relationship between $\lambda_{LOS\perp}$ and λ_{LOS}

By substituting the appropriate initial and terminal conditions for phase 1 into Eq. (12), the following relationship between $\lambda_{LOS\perp}$ and λ_{LOS} is

$$\lambda_{LOS_1} = \frac{\dot{\varrho}_{f_1}^2 - \dot{\varrho}_{01}^2}{\varrho_{01}^2\delta_{01}^2} \frac{\alpha_1}{(\frac{\varrho_{f_1}}{\varrho_{01}})^{2\alpha_1} - 1} - 1 \tag{13}$$

where $\alpha_1 = \lambda_{LOS\perp_1} - 1$. This constraint relationship between $\lambda_{LOS\perp_1}$ and λ_{LOS_1} assures a specific closing velocity $\dot{\varrho}_{f_1}$ at the end of the first stage. As is expected, the relationship developed in Ref. 8 is obtained when $\varrho_{f_1} = \dot{\varrho}_{f_1} \equiv 0$.

Similarly, substitution of the appropriate initial and terminal conditions for phase 2 results in the following relationship between the guidance constants where $\alpha_2 = \lambda_{LOS\perp_2} - 1$. Note that the initial conditions of phase 2 are the terminal conditions of phase 1.

$$\lambda_{LOS_2} = -\frac{\dot{\varrho}_{fi}^2}{\varrho_{fi}^2 \delta_{fi}^2} \frac{a_2}{(\frac{\varrho_{f2}}{\varrho_{fi}})^{2a_2} - 1} - 1 \tag{14}$$

Phase 1 Solution

We now develop an expression for the absolute attitude of LOS frame, δ, as function of ϱ. First, we rewrite Eq. (11) as

$$d\delta = \delta_0 \left(\frac{\varrho}{\varrho_0}\right)^{a-1} dt = \delta_0 \left(\frac{\varrho}{\varrho_0}\right)^{a-1} \frac{d\varrho}{\dot{\varrho}} \tag{15}$$

where $\dot{\varrho}$ is obtained from Eq. (12). For the first phase of flight, Eq. (12) can be written as

$$\dot{\varrho} = -\frac{1}{k^{1/2}}(c_2 - c_1 \varrho^{2a})^{1/2} = -\frac{1}{(-k)^{1/2}}(c_1 \varrho^{2a} - c_2)^{1/2} \tag{16}$$

where the negative sign is chosen to ensure $\dot{\varrho} < 0$ and

$$k \triangleq \varrho_{fi}^{2a_1} - \varrho_{01}^{2a_1} \tag{17}$$

$$c_1 \triangleq \dot{\varrho}_{01}^2 - \dot{\varrho}_{fi}^2 > 0 \tag{18}$$

$$c_2 \triangleq \dot{\varrho}_{01}^2 \varrho_{fi}^{2a_1} - \dot{\varrho}_{fi}^2 \varrho_{01}^{2a_1} \tag{19}$$

From the definition of k, we observe that $a_1 < 0$ or $a_1 > \frac{1}{2}$ which implies that $\lambda_{LOS\perp_1} < 1$ or $\lambda_{LOS\perp_1} > 3/2$. The case of $a_1 < 0$, both k and c_2 are positive. However, for the case of $a_1 > \frac{1}{2}$, k is negative and c_2 is sign indefinite. Since the solution of Eq. (15) is dependent on the sign of c_2, for the remainder of this paper, we consider the case of $a_1 < 0$.

Substituting Eq. (16) into Eq. (15) and integrating from the initial conditions to the terminal conditions of stage 1 yields

$$\delta_{fi} - \delta_{01} = \frac{\delta_{01}}{a_1 \varrho_{01}^{(a_1-1)}} \left[\frac{k}{c_1}\right]^{1/2} \left\{ \sin^{-1}\left[\frac{\dot{\varrho}_{fi}^2 k}{c_2}\right]^{1/2} - \sin^{-1}\left[\frac{\dot{\varrho}_{01}^2 k}{c_2}\right]^{1/2} \right\} \tag{20}$$

Now, an expression for the time-of-flight can be obtained from

$$T = \int_{t_{0i}}^{t_{fi}} dt = \int_{\varrho_{0i}}^{\varrho_{fi}} \frac{d\varrho}{\dot{\varrho}} \tag{21}$$

Substitution of $\dot{\varrho}$ from Eq. (16) results in

$$T_1 = -k^{1/2} \int_{\varrho_{01}}^{\varrho_{fi}} \frac{d\varrho}{(c_2 - c_1 \varrho^{2a_1})^{1/2}} \tag{22}$$

In general, for arbitrary values of $a_1 < 0$, Eq. (22) has no known anti-derivative and therefore must be evaluated numerically. (Solutions are available for integer values of a_1)

We now use Eq. (20) together with Eq. (22) to calculate the initial condition of ϱ_{01} that will provide the desirable LOS attitude at the end of stage one.

Phase 1 Initial Conditions

First, the requirement that $\dot{\theta}_{fi} = 0$ at the end of the first phase places a constraint on the initial relative attitude rate of the guidance frame. Combining Eqs. (5) and Eq. (11) with the condition $\dot{\theta}_{fi} = 0$ we observe

$$\dot{\theta}_{01} = \phi\left[\left(\frac{\varrho_{01}}{\varrho_{fi}}\right)^{a_1-1} - 1\right] \tag{23}$$

247

where ϱ_{f1} replaces ϱ. Thus, the initial LOS rate is defined by the initial and final pseudo-range-to-go and the transverse navigation constant of phase 1.

Second, the requirement that $\theta_{f1} = 2m\pi + \frac{\pi}{2} + \psi$ places a constraint on the initial value of the pseudo-range-to-go rate. To evaluate this constraint, we integrating Eq. (5) with $\dot{\phi} = \omega_T$ over the entire time-of-flight T_1 to get

$$\delta_{f1} - \delta_{01} = \theta_{f1} - \theta_{01} + \dot{\phi}T_1 \tag{24}$$

Substituting the right hand side of Eq. (20) for $\delta_{f1} - \delta_{01}$, the right hand side of Eq. (22) for T_1, and the requirement $\theta_{f1} = 2m\pi + \frac{\pi}{2} + \psi$, Eq. (24) becomes

$$\frac{4m + 1}{2k^{1/2}}\pi + \frac{\psi - \theta_{01}}{k^{1/2}} = \frac{\delta_{01}}{a_1 \varrho_{01}^{(a_1 - 1)} c_1^{1/2}} \left\{ \sin^{-1}\left[\frac{\varrho_{f1}^2 k}{c_2}\right]^{1/2} - \sin^{-1}\left[\frac{\varrho_{01}^2 k}{c_2}\right]^{1/2} \right\} + \int_{\varrho_{01}}^{\varrho_{f1}} \frac{\dot{\phi}d\varrho}{(c_2 - c_1\varrho^{2a_1})^{1/2}} \tag{25}$$

An analytical solution for $\dot{\varrho}_{01}$ cannot be obtained since $c_1 = c_1(\dot{\varrho}_{01})$ and $c_2 = c_2(\dot{\varrho}_{01})$ (see Eqs. (18) and (19)) and the integral in Eq. (25) does not have an explicit anti-derivative. However, a solution for $\dot{\varrho}_{01}$ can be obtained from Eq. (25) using an iterative scheme. In this paper, Newton's method was used. For the cases analyzed, we assumed $m = 0$, implying the chase vehicle makes no complete revolution in phase 1.

Stage 2 Solution

The primary function of the guidance algorithm in this phase of the maneuver is to reduce both the range-to-go and the range-to-go rate to zero while maintaining the alignment of the berthing mechanisms. That is, throughout the entire second stage, we require $\dot{\theta}=0$. This is equivalent to (see Eq. (5))

$$\dot{\delta}_2 = \dot{\delta}_{0_2} = \dot{\phi} \tag{26}$$

Substituting this relationship into Eq. (11), the general solution for $\dot{\delta}$, yields

$$\dot{\phi} = \dot{\phi} \left(\frac{\varrho}{\varrho_{02}}\right)^{(a_2 - 1)} \tag{27}$$

Since ϱ varies throughout the process, the above equality holds if and only if $a_2 = 1$ which implies $\lambda_{LOS_{\perp_2}} = 2$. With $a_2 = 1$ and λ_{LOS_2} as defined in Eq. (14), $\dot{\varrho}$ can be determined from Eq. (12) as

$$\dot{\varrho} = \dot{\varrho}_{02} \left[\frac{\varrho_{f2}^2 - \varrho^2}{\varrho_{f2}^2 - \varrho_{02}^2}\right]^{1/2} \tag{28}$$

which is zero when $\varrho = \varrho_{f2}$.

This completes the analysis. We now apply the results of the analysis to a typical rendezvous and docking scenario.

Numerical Simulation

The simulated results were obtained by numerically integrating the relative motion equations written in terms of the range-to-go r instead of the pseudo-range-to-go ϱ. In doing so, we are able to include the dynamics associated with the chase vehicle (i.e., the effects of its attitude controller). The state vector used was $[r \; \delta \; \beta \; \dot{r} \; \dot{\delta} \; \dot{\beta}]$. A fixed step size ($\Delta t = 0.001$), fourth-order Runge-Kutta integration algorithm was used to numerically integrate the differential equations.

Conditions for a typical scenario are shown in Table 1. For this scenario, the initial rendezvous conditions determined from Eqs. (23) and (25) are $\dot{\theta}_{01} = -0.4918$ and $\dot{\varrho}_{01} = -237.54$, respectively. An initial misalignment of $\beta = 0.05$ and an initial alignment rate of $\dot{\beta} = 0.04$ were used for the chase vehicle.

248

Table 1. System Configuration

r_{01}	1000	ψ	0
V_T	300	θ_{01}	$3.77(1.2\pi)$
$\dot{\phi}$	0.5	α_{01}	$4.712(1.5\pi)$
r_{Px}	10	$\lambda_{LOS\perp_1}$	0.95
r_{Py}	0	r_{fl}	15
r_{Qx}	0	$\dot{r}_{fl}$	-10
r_{Qy}	5	$\lambda_{LOS\perp_2}$	2

Figures 4- 8 show the simulation results for the scenario depicted in Table 1. Parts (c) and (d) of Figs. 4 and are enlargements of the terminal phase of flight depicted in parts (a) and (b). Figure 4 shows the flight data for the first stage. Notice that the range-to-go rate $\dot{r}$ goes to the designated value of -10 as range-to-go r goes to the specified value of 15. Also the relative LOS attitude θ goes to the desirable value of $90°$ (1.57 rad.) as the relative LOS attitude rate $\dot{\theta}$ goes to approximately zero.
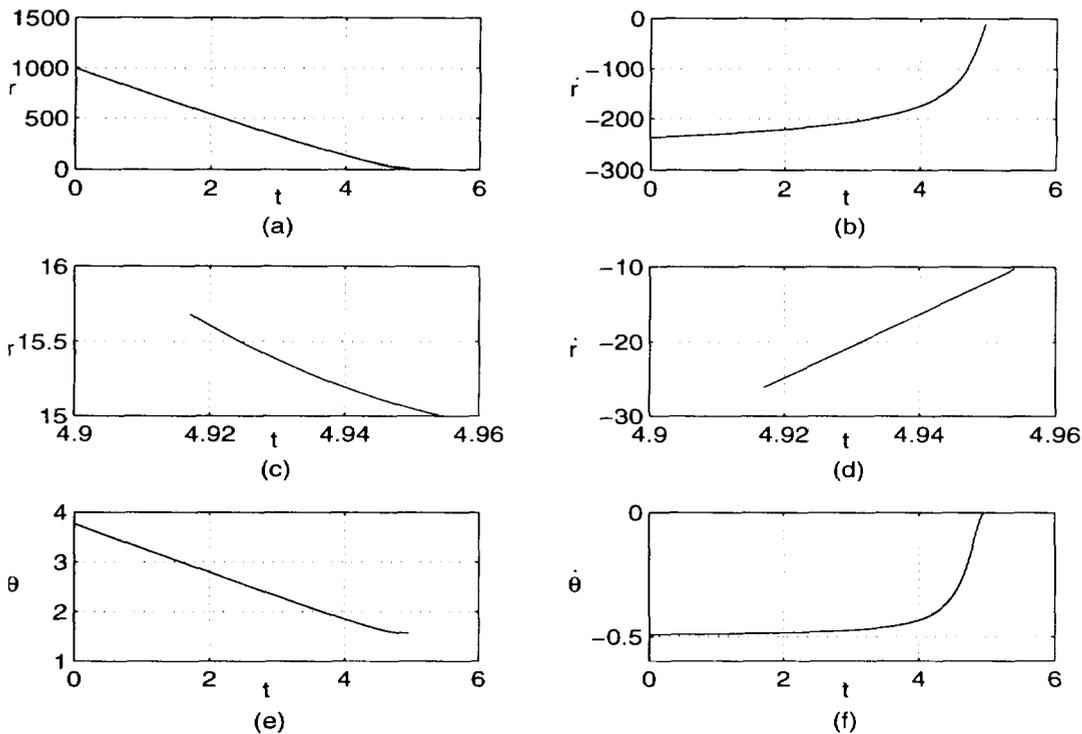
Fig. 4   Phase 1 flight data

Figure 5 shows the flight data for the second stage. Notice that the range-to-go rate $\dot{r}$ and the range-to-go r simultaneously approach zero. Also the relative LOS attitude θ is maintained within the proximity of the desirable value of $90°$ (1.57 rad.). The slight variations are due to the relative LOS attitude rate $\dot{\theta}$ being close to zero but not exactly zero throughout the second stage. This is not a consequence of the numerics, but rather a consequence of the fact that an actual attitude controller was modelled for the chase vehicle.
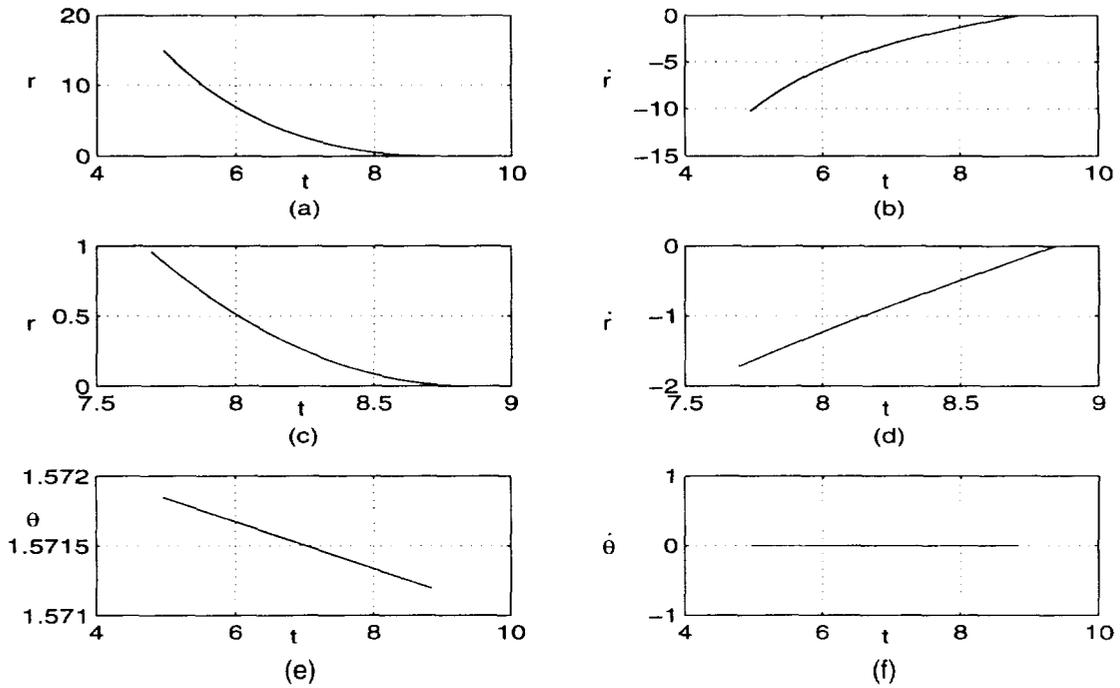
Fig. 5 Phase 2 flight data

Figure 6 shows the accelerations commanded throughout the maneuver. The curves on the left half of the plot are the acceleration commands for phase 1 and the curves on the right half of the plot are for phase 2. Notice that since $\vec{r} = -r \, \hat{\vec{j}}_{G}$, then the a_{LOS} accelerations shown represent accelerations in the positive r-direction.
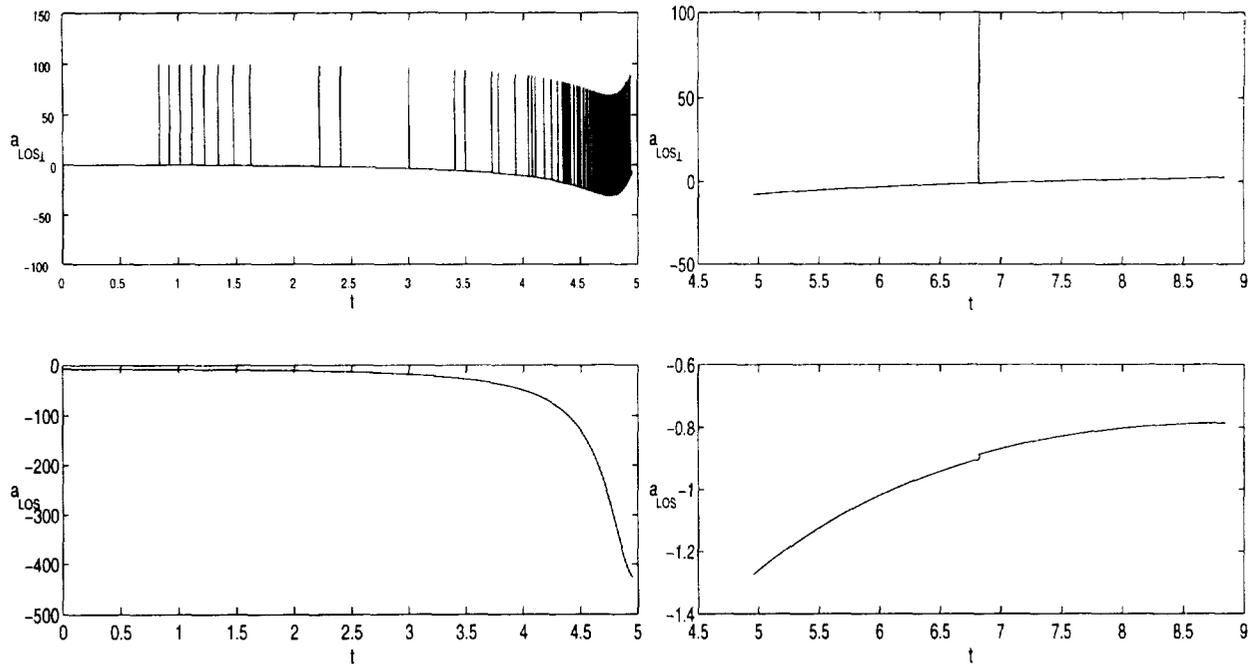
Fig. 6 Profiles of commanded accelerations

Figures 7 and 8 show the terminal portions of phases 1 and 2, respectively. Figure 7 shows the chase vehicle approaching the target from above and acquiring properly alignment with the target at the end of the first stage.
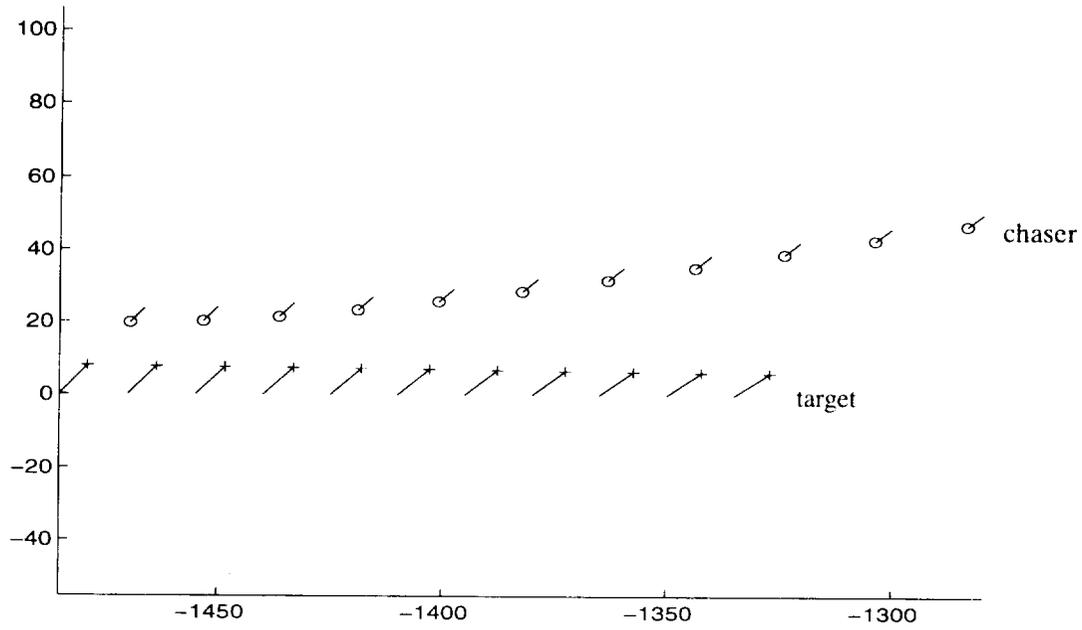
Fig. 7   Alignment of chase and target vehicles at the end of phase 1

Figure 8 shows that, during the second stage, the chase vehicle is able to maintain it's attitude with respect to the target while it nulls the distance between the grappling arm and the docking port. It also shows that, at the end of the second stage, the chase vehicle docks with the target with the proper relative attitude as specified.
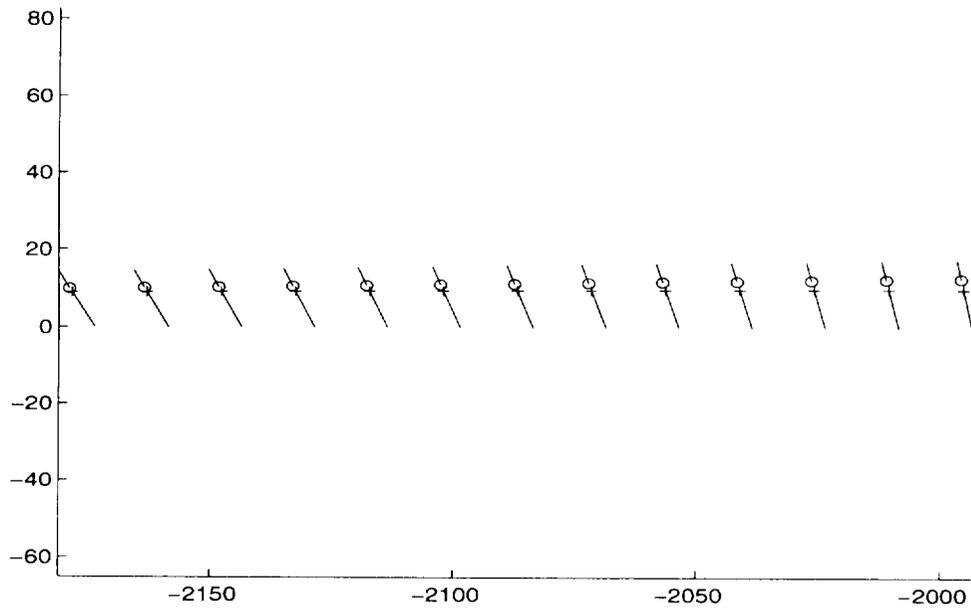
Fig. 8   Docking at the end of phase 2

Conclusion

Solutions to the equations of motion of two rigid bodies engaged in a planar rendezvous and docking maneuver are obtained. Some solutions are analytic whereas others are pseudo-analytic. It was shown that rendezvous and dock of rigid bodies require a two phases maneuver. In the first phase, the LOS rotation rate is driven to zero while aligning the berthing mechanisms of the two vehicles, and in the second phase, the LOS rate is maintained at zero while the range-to-go and range-to-go rates are simultaneously driven to zero. The second phase of the maneuver requires a transverse navigation constant of 2. An illustrative example is presented.

Future work involves the integration of appropriate sensor and actuator models and a proof-of-concept demonstration.

Acknowledgement

References

1. Murtaugh S. A., and Criel, H. E., "Fundamentals of Proportional Navigation," *IEEE Spectrum*, Vol. 3, No. 6, pp.75-85, 1966.

2. Locke, A. S., Guidance, Princeton, N. J. : Van Nostrand, 1955.

3. Guelman, M., "The Closed-form Solution of True Proportional Navigation," *IEEE Transactions on Aerospace and Electronics Systems*, AES-12, pp 472-482, July 1976.

4. Cochran, J. E., Jr., No, T. S., and Thaxton, D. G., "Analytical Solutions to a Guidance Problem," *Journal of Guidance, Control & Dynamics*, Vol. 14, No. 1, Jan.-Feb. 1991, pp. 117-122.

5. Jensen, D.L., "Kinematics of Rendezvous Maneuvers," *Journal of Guidance, Control & Dynamics*, Vol. 7, No. 3, May-June 1984, pp. 307-314.

6. Guelman, M., "Guidance for Asteroid Rendezvous," *Journal of Guidance, Control & Dynamics*, Vol. 14, No. 5, Sept.-Oct. 1991, pp. 1076-1083.

7. Niemi, N. J., "Investigation of a Terminal Guidance System for a Satellite Rendezvous," *AIAA Journal*, Vol. 1, No. 2, Feb. 1963, pp. 405-411.

8. Yuan, P-J, and Hsu, S-C, "Rendezvous Guidance with Proportional Navigation," *Journal of Guidance, Control & Dynamics*, Vol. 17, No. 2:Engineering Notes, 1993.

Telemetry Down-link Doppler as an Attitude Sensor for Spin Stabilized Spacecraft.*

S. D. Hendry
AlliedSignal Technical Services Corporation
Columbia, Maryland, USA

Abstract. The communications antenna on a spin stabilized spacecraft is seldom located on the spin axis, hence, the antenna is in motion relative to the center of mass of the spacecraft. The Doppler shift observed at the ground or space relay communications receivers will include oscillations whose frequency and amplitude are functions of the motion of the antenna and the attitude of the spacecraft relative to the line of sight (LOS). This functional dependence creates the possibility of estimating attitude parameters from Doppler measurements. This paper presents mathematical models of Doppler oscillations from spinning spacecraft, including the effects of nutation. Algorithms for estimating spin rate, attitude and nutation angle are described. Results of analysis of Doppler tracking of GOES-8 and WIND are also discussed.

Introduction. Doppler tracking measurements are usually treated as equivalent to measurements of the range-rate of the spacecraft center of mass. However, Doppler measurements actually measure the range rate of the antenna, which during attitude maneuvers or spin stabilization has its own motion relative to the center of mass. A simple model for a spinning spacecraft is to assume that the angular momentum and angular velocity vectors are collinear. Then, unless the antenna location is on the spin axis, the antenna will have uniform circular motion relative to the spacecraft center of mass, so that the range rate will vary sinusoidally. The frequency of this motion is the spin rate; the amplitude of the motion is a function of the angle between the LOS direction and the spin axis. Hence, Doppler data can be used to estimate the orientation of the spin axis. There are two major phenomena that may invalidate this simple model. One is nutation, where the angular velocity vector is rotating about the (inertially fixed) angular momentum vector. The other is multipath, where the propagation path from the spacecraft antenna to the tracker includes reflections from other parts of the spacecraft, parts which have different Doppler shifts than does the antenna. In addition, a spacecraft may have more than a single antenna. Multipath will not be discussed in this paper.

Apparent amplitude of Doppler oscillations. The amplitude of the oscillations in Doppler tracking caused by satellite rotation is a function of the antenna location, the rotation rate, and the aspect angles relative to the uplink and downlink trackers. For the purpose of deriving this functional dependence, effects of nutation will be ignored, hence, the spin axis is assumed to be coincident with the angular momentum vector, which is fixed in inertial coordinates. The inertial coordinate system will have the spin axis as the z-axis, and the x- and y-axes orthogonal. The following parameters will be used,

$\hat{s}$ - -unit vector along spin axis

$\hat{u}$ - -unit vector along LOS from uplink tracker to spacecraft in inertial coordinates

$\quad \hat{u} = i u_1 + j u_2 + k u_3$

$\hat{d}$ - -unit vector along LOS from downlink tracker to spacecraft in inertial coordinates

$\quad \hat{d} = i d_1 + j d_2 + k d_3$

r_A - -distance from spin axis to antenna

$\hat{s}$ - -unit vector along spin axis

$\bar{r}(t)$ - -position vector of antenna relative to spacecraft center of mass in inertial coordinates

$\quad \bar{r}(t) = i r_1(t) + j r_2(t) + k r_3$

$\bar{v}(t)$ - -velocity vector of antenna relative to spacecraft center of mass in inertial coordinates

ω_s - -spin rate in $\dfrac{radians}{sec}$

The position and velocity of the antenna as functions of time can be written,

$$\bar{r}(t) = \mathbf{i}\, r_A \cos(\omega_s t) + \mathbf{j}\, r_A \sin(\omega_s t) + \mathbf{k} r_3$$

$$\bar{v}(t) = \frac{d}{dt}\bar{r}(t) = r_A \omega_s \left(-\mathbf{i} \sin(\omega_s t) + \mathbf{j}\cos(\omega_s t) \right)$$

The projections of the LOS vectors on the antenna velocity are,

$$\hat{u} \bullet \bar{v}(t) = \left(\hat{u} - (\hat{u} \bullet \hat{s})\hat{s} \right) \bullet \bar{v}(t) = r_A \omega_s \left(-u_1 \sin \omega_s t + u_2 \cos \omega_s t \right)$$

$$\hat{d} \bullet \bar{v}(t) = \left(\hat{d} - (\hat{d} \bullet \hat{s})\hat{s} \right) \bullet \bar{v}(t) = r_A \omega_s \left(-d_1 \sin \omega_s t + d_2 \cos \omega_s t \right)$$

Where c is the speed of light in the same units as range rate and f_T is the transmit frequency in Hz , define

$$\Delta_f = \frac{K f_T}{c}$$

K is the turnaround ratio of the spacecraft transponder: K = 240/221 for NASA S-band trackers. The range rate oscillation and associated frequency deviation observed at the downlink tracker are,

$$\dot{R}_\Delta(t) = r_A \omega_s \left(-(u_1 + d_1)\sin \omega_s + (u_2 + d_2)\cos \omega_s t \right)$$

$$f_\Delta(t) = \dot{R}_\Delta(t)\Delta_f$$

The expression for frequency deviation can be converted to amplitude-phase form,

$$f_\Delta(t) = A \cos(\omega_s t + \phi)$$

The amplitude of the frequency oscillation is,

$$A = r_A \omega_s \Delta_f \sqrt{(u_1 + d_1)^2 + (u_2 + d_2)^2}$$

$$= r_A \omega_s \Delta_f \left\| \hat{u} + \hat{d} - \left((\hat{u} + \hat{d}) \bullet \hat{s} \right)\hat{s} \right\|$$

$$= r_A \omega_s \Delta_f \sqrt{\|\hat{u}\|^2 + \|\hat{d}\|^2 + 2(\hat{u} \bullet \hat{d}) - \left((\hat{u} + \hat{d}) \bullet \hat{s} \right)^2}$$

$$= r_A \omega_s \Delta_f \sqrt{2 + 2(\hat{u} \bullet \hat{d}) - \left((\hat{u} + \hat{d}) \bullet \hat{s} \right)^2}$$

For 2-way tracking, where the transmit and receive trackers are the same, the amplitude reduces to

$$A = 2 r_A \omega_s \Delta_f \sqrt{1 - (\hat{u} \bullet \hat{s})^2}$$

The 1-way amplitude would be half the 2-way. Note that there is a 180 deg ambiguity; if the spin vector is replaced by it's negative, i.e., the direction of spin is reversed or the spacecraft is flipped over, the apparent Doppler oscillation amplitude will be the same.

Estimating attitude. Given that the spin rate is known, all the parameters in the above equations are known except the spin axis unit vector. The absolute value of the projection of the spin axis unit vector onto a known vector can be solved for as follows:

254

$$(2 \text{-} \text{way}) \quad |\hat{u} \cdot \hat{s}| = \sqrt{1 - \frac{A^2}{4r_A^2 \omega_s^2 \Delta_f^2}}$$

$$(1 \text{-} \text{way}) \quad |\hat{u} \cdot \hat{s}| = \sqrt{1 - \frac{A^2}{r_A^2 \omega_s^2 \Delta_f^2}}$$

$$(3 \text{-} \text{way}) \quad |(\hat{u} + \hat{d}) \cdot \hat{s}| = \sqrt{2 + 2(\hat{u} \cdot \hat{d}) - \frac{A^2}{r_A^2 \omega_s^2 \Delta_f^2}}$$

The last equation can be rewritten in terms of unit vectors by normalizing,

$$(3 \text{-} \text{way}) \quad \left| \frac{(\hat{u} + \hat{d})}{\|\hat{u} + \hat{d}\|} \cdot \hat{s} \right| = \sqrt{1 - \frac{A^2}{r_A^2 \omega_s^2 \Delta_f^2 \left(2 + 2(\hat{u} \cdot \hat{d})\right)}}$$

From this point on, it will be assumed that the Doppler tracking observations have been reduced to a set of projections and unit vectors,

$$a_k = |\hat{x}_k \cdot \hat{s}|; \quad 0 \le a_k \le 1$$

Each projection is equivalent to an angle,

$$\xi_k = \cos^{-1}(a_k); \quad 0 \le \xi_k \le \frac{\pi}{2}$$

When many observations (projections and unit vectors) are available, a least squares solution can be computed. Depending on geometry, several solutions are possible, so initiating the least squares algorithm properly is important. If the attitude is the only unknown, the right ascension (α) and declination (δ) of the spin axis can be solved for directly by a non-linear least squares routine,

$$\text{Minimize } e = \sum_{k=1}^{K} \left(a_k - \left| \begin{bmatrix} \cos\delta\cos\alpha \\ \cos\delta\sin\alpha \\ \sin\delta \end{bmatrix} \cdot \hat{x}_k \right| \right)^2$$

If another parameter such as antenna radius from spin axis is uncert.. may also be solved for. The MATLAB™ Optimization Toolbox installed on FDF LANs contains built functions for minimizi. .

Analysis of GOES-8 Doppler Tracking. GOES-8 was launched 13 April 1994. Doppler tracking was received at FDF from DS46 (Canberra) 3-way with the Indian Ocean Station (IOS or SEYS) teleme .y system as the transmit site. For data taken from approximately 0700Z to 0740Z, the spacecraft was spin stabilized. Figure 1 shows the Doppler oscillations from valid data obtained during this time. Shown by a dotted line is the estimate of amplitude derived from these oscillations. The measured rotation rate is 0.0182 Hz, while the distance of the antenna from the spin axis is assumed to be 3.3 meters. Figure 2 depicts contours of the surface generated by varying right ascension from 25 to 75 deg and declination from -50 to 0 deg and plotting the reciprocal of the resultant RMS error between the measured projection and the vector dot product. Further analysis showed that the fit could be improved if r_A was varied as well. The MATLAB routine LEASTSQ in the Optimization Toolbox was used to solve for right ascension, declination and antenna radius from the spin axis. The routine was run twice, initialized with each of the angle pairs found above and with r_A initialized at 3.3 meters. The solutions were,

RMS error	0.042	0.044
Right ascension (deg)	62.2	59.7
Declination (deg)	-24.7	-16.7
Antenna radius from spin axis (m)	2.79	2.76
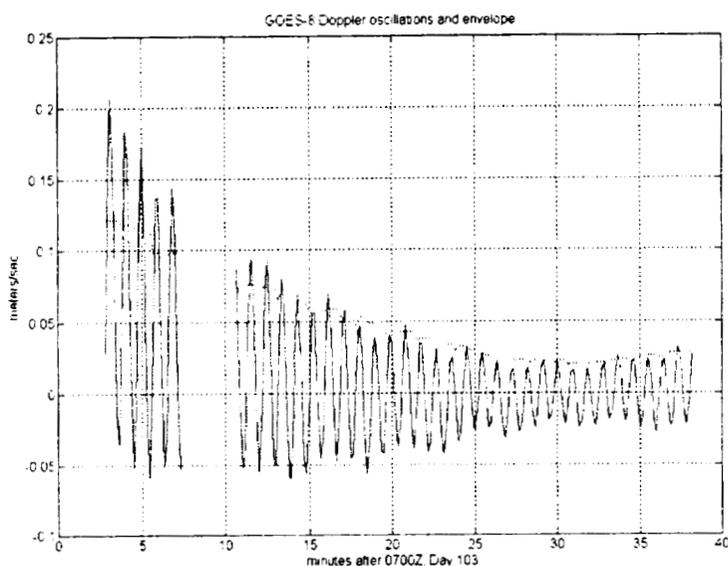
Figure 1. GOES-8 Doppler Tracking.

Since the observations were not exactly co-planar, the solution with the smaller RMS error would be the more likely candidate for the true attitude. The planned attitude after separation was $\alpha = 61.7$ deg and $\delta = -25.0$ deg, according to reference 1. Figure 3 shows the fit obtained by comparing the projection of the solved for spin attitude on the unit vectors with the projections measured from tracking data.
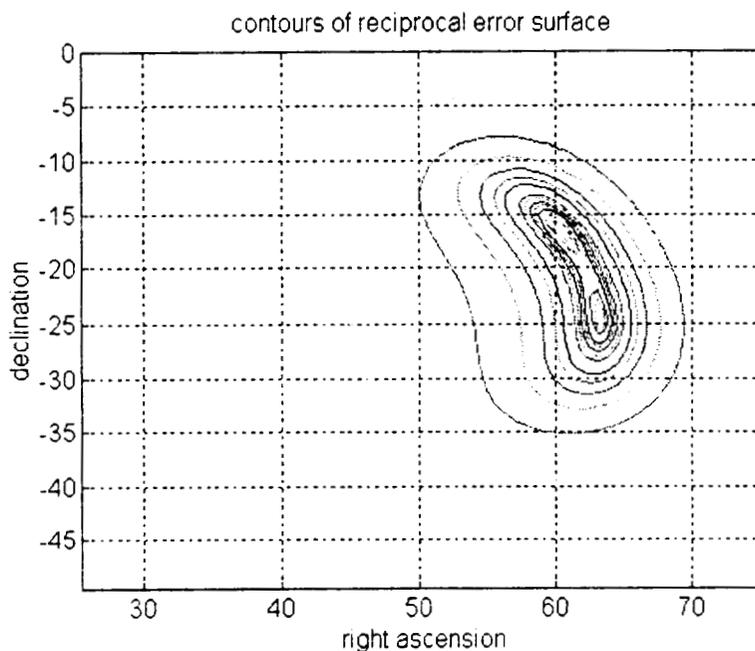
Figure 2. Error Surface.
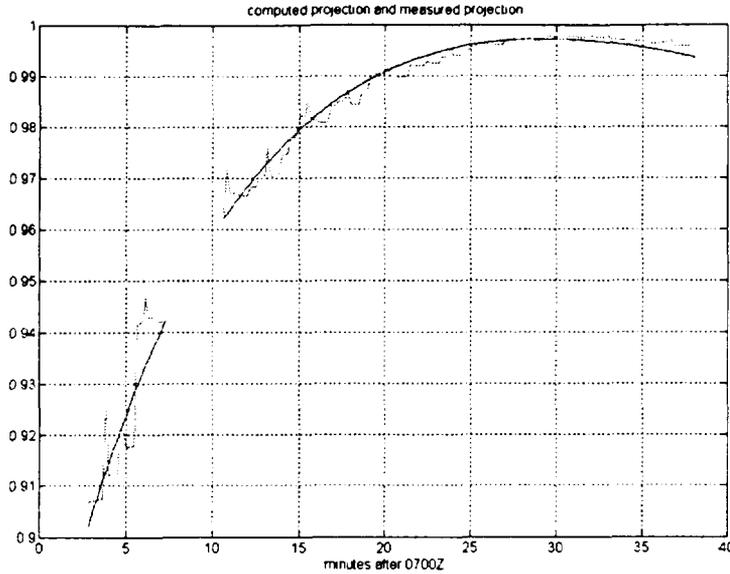
Figure 3. Measured versus computed projections.

Spinning spacecraft attitude dynamics (nutation). Analysis of the dynamics of a rigid spinning spacecraft in order to predict the effects of such motion on Doppler tracking data uses the following parameters:

1. The spacecraft major moments of inertia, in Kg-m^2. The nominal axis of rotation is assumed to be the z-axis, so the values are represented as a vector [Ix Iy Iz], where the labels x, y and z are assigned so that the entries are in monotonic (lowest to highest or highest to lowest) order. The choice of the axis with the intermediate moment of inertia as the spin axis is unstable and will not be considered.

2. The location of the spacecraft antenna in meters, as a vector [x_A y_A z_A] in body coordinates. The assignment of x_A, y_A and z_A should be consistent with the moments of inertia.

3. The angle β of the LOS vector with the angular momentum vector.

4. The angular momentum magnitude L.

5. The initial nutation angle θ_0, which is assumed to be small.

Reference 2 is the source of the basic attitude dynamics relationships in the following. The convenient inertial reference frame has the angular momentum vector along the z-axis, with the x and y orthogonal. The time reference is chosen so that at t=0, the angular velocity vector is in the body x-z plane, so the angular velocity vector in body coordinates is,

$$\vec{\omega}_{b0} = i_b \omega_{10} + j_b 0 + k_b \omega_{30} = i_b \frac{L \sin\theta_0}{Ix} + k_b \frac{L \cos\theta_0}{Iz}$$

$$\omega_{10} \approx \frac{L\theta_0}{Ix}, \quad \omega_{30} \approx \frac{L}{Iz}$$

257

The kinetic energy E is,

$$E = \frac{Ix\omega_{10}^2 + Iz\omega_{30}^2}{2} = \frac{1}{2}\left(\frac{L^2 \sin^2 \theta_0}{Ix} + \frac{L^2 \cos^2 \theta_0}{Iz} \right)$$

The "parameter" m is given by,

$$m = \frac{(Ix - Iy)(L^2 - 2IzE)}{(Iz - Iy)(L^2 - 2IxE)} = \frac{(Ix - Iy)L^2\left(1 - Iz\left(\frac{\sin^2 \theta_0}{Ix} + \frac{\cos^2 \theta_0}{Iz}\right)\right)}{(Iz - Iy)L^2\left(1 - Ix\left(\frac{\sin^2 \theta_0}{Ix} + \frac{\cos^2 \theta_0}{Iz}\right)\right)}$$

$$= \frac{(Ix - Iy)\left(\frac{(Ix - Iz)\sin^2 \theta_0}{Ix}\right)}{(Iz - Iy)\left(\frac{(Iz - Ix)\cos^2 \theta_0}{Iz}\right)} \approx \frac{Iz(Iy - Ix)}{Ix(Iz - Iy)}\theta_0^2$$

Define the "normalized" parameter,

$$m_0 = \frac{Iz(Iy - Ix)}{Ix(Iz - Iy)} \approx m / \theta_0^2.$$

The body nutation rate is,

$$\omega_p = \pm\sqrt{\frac{(Iz - Iy)(L^2 - 2IxE)}{IxIyIz}} = \pm\sqrt{\frac{(Iz - Iy)L^2\left((Iz - Ix)\cos^2 \theta_0\right)}{IxIyIz^2}}$$

$$\approx \pm\frac{L}{Iz}\sqrt{\frac{(Iz - Iy)(Iz - Ix)}{IxIy}} \approx \pm\omega_{30}\sqrt{\frac{(Iz - Iy)(Iz - Ix)}{IxIy}}$$

where the "+" is used if Ix > Iy > Iz and "-" if Ix < Iy < Iz.

Finally, the amplitude of the y body component of angular velocity is,

$$\omega_{20} = \sqrt{\frac{L^2 - 2IzE}{Iy(Iy - Iz)}} = L\sqrt{\frac{(Ix - Iz)\sin^2 \theta_0}{IxIy(Iy - Iz)}} \approx L\theta_0\sqrt{\frac{(Ix - Iz)}{IxIy(Iy - Iz)}}$$

$$= \frac{L\theta_0}{Iy}\sqrt{\frac{IxIy - IyIz}{Ix(Iy - Iz)}} = \frac{L\theta_0}{Iy}\sqrt{\frac{IxIy - IyIz - IxIz + IxIz}{Ix(Iy - Iz)}} = \frac{L\theta_0}{Iy}\sqrt{1 + \frac{Iz(Ix - Iy)}{Ix(Iy - Iz)}}$$

$$= \frac{L}{Iy}\sqrt{\theta_0^2 + m} = \frac{L}{Iy}\theta_0\sqrt{1 + m_0}$$

The angular velocity vector as a function of t (sec) is given by,

$$\omega_1 = \omega_{10}cn(\omega_p t | m)$$

$$\omega_2 = -\omega_{20}sn(\omega_p t | m)$$

$$\omega_3 = \omega_{30}dn(\omega_p t | m)$$

258

where sn, cn and dn are the Jacobian elliptic functions. When m << 1, approximations for the Jacobian elliptic functions are,

$$sn(x|m) \approx \sin(x)$$

$$cn(x|m) \approx \cos(x)$$

$$dn(x|m) = 1 - \frac{m}{2}\sin^2(x) = 1 - \frac{m}{4} + \frac{m}{4}\cos(2x)$$

So the angular velocity vector in body coordinates can be written,

$$\omega_1 = \omega_{10}cn(\omega_p t|m) \approx \omega_{10}\cos(\omega_p t)$$

$$\omega_2 = -\omega_{20}sn(\omega_p t|m) \approx -\omega_{20}\sin(\omega_p t)$$

$$\omega_3 = \omega_{30}dn(\omega_p t|m) \approx \omega_{30}\left[1 - \frac{m}{4} + \frac{m}{4}\cos(2\omega_p t)\right]$$

The instantaneous velocity of the antenna in body coordinates is found by crossing the angular velocity vector with the antenna position vector. The antenna velocity is then rotated to inertial coordinates and projected on the LOS vector to give the range-rate of the antenna as a function of spinning.

The Euler rotation angles for angles θ and ψ can be found by solving,

$$\begin{bmatrix} L_{b1} \\ L_{b2} \\ L_{b3} \end{bmatrix} = A_{313}(\phi,\theta,\psi)\begin{bmatrix} 0 \\ 0 \\ L \end{bmatrix} = L\begin{bmatrix} \sin\theta\sin\psi \\ \sin\theta\cos\psi \\ \cos\theta \end{bmatrix}$$

$$\Rightarrow \begin{bmatrix} \omega_1 \\ \omega_2 \\ \omega_3 \end{bmatrix} = \begin{bmatrix} \dfrac{L\sin\theta\sin\psi}{Ix} \\ \dfrac{L\sin\theta\cos\psi}{Iy} \\ \dfrac{L\cos\theta}{Iz} \end{bmatrix}$$

So the minimum and maximum values of nutation angle are,

$$\theta_{min} = \theta_0$$

$$\theta_{max} = \sqrt{\theta_0^2 + m} \approx \theta_0\sqrt{1 + m_0}$$

This implies,

$$\frac{\theta_{max}^2}{\theta_0^2} \approx \frac{\theta_0^2 + m}{\theta_0^2} = 1 + \frac{m}{\theta_0^2} = \frac{Iy(Iz - Ix)}{Ix(Iz - Iy)}$$

which agrees with equation 16-114 in reference 2.

The angular velocity vector in body coordinates can now be written as,

259

$$\omega_1 \approx \frac{L}{Ix}\theta_0 cn(\omega_p t | m)$$

$$\omega_2 \approx \frac{-L}{Iy}\theta_{max} sn(\omega_p t | m)$$

$$\omega_3 \approx \frac{L}{Iz}$$

Sine and cosine of the Eulerian angle ψ can be found as functions of time by solving,

$$\tan\psi = \frac{Ix\omega_1}{Iy\omega_2} \Rightarrow \sin\psi = \frac{Ix\omega_1}{\sqrt{Ix^2\omega_1^2 + Iy^2\omega_2^2}}; \cos\psi = \frac{Iy\omega_2}{\sqrt{Ix^2\omega_1^2 + Iy^2\omega_2^2}}$$

$$\sqrt{Ix^2\omega_1^2 + Iy^2\omega_2^2} = L\theta_0\sqrt{cn(\omega_p t|m)^2 + (1+m_0)sn(\omega_p t|m)^2}$$

$$= L\theta_0\sqrt{1 + m_0 sn(\omega_p t|m)^2} = L\theta$$

$$\sin\psi = \frac{Ix\omega_1}{\sqrt{Ix^2\omega_1^2 + Iy^2\omega_2^2}} \approx \frac{Ix\left(\dfrac{L\theta_0}{Ix}\right)cn(\omega_p t|m)}{L\theta} = \frac{\theta_0}{\theta}cn(\omega_p t|m)$$

$$\cos\psi = \frac{Iy\omega_2}{\sqrt{Ix^2\omega_1^2 + Iy^2\omega_2^2}} \approx \frac{Iy\left(\dfrac{-L\theta_{max}}{Iy}\right)sn(\omega_p t|m)}{L\theta} = \frac{-\theta_{max}}{\theta}sn(\omega_p t|m)$$

A differential equation relating ϕ to θ and ψ is,

$$\dot\phi = (\omega_1\sin\psi + \omega_2\cos\psi)/\sin\theta = L\left(\frac{\sin^2\psi}{Ix} + \frac{\cos^2\psi}{Iy}\right) = \frac{L}{Ix} + \frac{L(Ix-Iy)\cos^2\psi}{IxIy}$$

$$\approx L\left(\frac{1}{Ix} + \frac{\theta_0^2(Ix-Iz)(Ix-Iy)sn(\omega_p t|m)^2}{\theta^2 Ix^2(Iy-Iz)}\right)$$

$$\approx L\left(\frac{1}{Ix} + \frac{\theta_0^2(Ix-Iz)(Ix-Iy)sn(\omega_p t|m)^2}{(\theta_0^2 + m\,sn(\omega_p t|m)^2)Ix^2(Iy-Iz)}\right)$$

To get the frequency of oscillation of terms involving $\cos\phi$ and $\sin\phi$, the average is needed.

$$<\dot\phi> \approx L\left(\frac{1}{Ix} + \left(\frac{\theta_0^2(Ix-Iz)(Ix-Iy)}{Ix^2(Iy-Iz)}\right)\frac{1}{2K}\int_{-K}^{K}\frac{sn(\omega_p t|m)^2\,dt}{(\theta_0^2 + m\,sn(\omega_p t|m)^2)}\right)$$

where K is the half period of the Jacobian elliptic functions (ref. 3, section 16). The integral may be approximated by substituting sin for sn since m is small,

$$\frac{1}{2K}\int_{-K}^{K}\frac{sn(\omega_p t|m)^2\,dt}{\left(\theta_0^2+m\,sn(\omega_p t|m)^2\right)} \approx \frac{\omega_p}{\pi}\int_{\frac{-\pi}{2\omega_p}}^{\frac{\pi}{2\omega_p}}\frac{\sin^2(\omega_p t)dt}{\left(\theta_0^2+m-m\cos^2(\omega_p t)\right)}$$

$$=\frac{1}{\pi}\int_{\frac{-\pi}{2}}^{\frac{\pi}{2}}\frac{\sin^2(x)dx}{\left(\theta_0^2+m-m\cos^2(x)\right)}=\frac{1}{m}\left(1-\sqrt{\frac{\theta_0^2}{\theta_0^2+m}}\right)$$

(integration formula 262 in ref. 4)

Substituting for the integral,

$$<\dot\phi>\approx L\left(\frac{1}{Ix}+\left(\frac{\theta_0^2(Ix-Iz)(Ix-Iy)}{Ix^2(Iy-Iz)}\right)\frac{1}{m}\left(1-\sqrt{\frac{\theta_0^2}{\theta_0^2+m}}\right)\right)$$

$$=L\left(\frac{1}{Ix}+\left(\frac{(Ix-Iz)(Ix-Iy)}{Ix^2(Iy-Iz)}\right)\frac{\theta_0^2}{m}\left(1-\sqrt{\frac{1}{1+m/\theta_0^2}}\right)\right)$$

$$=L\left(\frac{1}{Ix}+\left(\frac{(Ix-Iz)(Ix-Iy)}{Ix^2(Iy-Iz)}\right)\frac{Ix(Iz-Iy)}{Iz(Iy-Ix)}\left(1-\sqrt{\frac{Ix(Iz-Iy)}{Iy(Iz-Ix)}}\right)\right)$$

$$=L\left(\frac{1}{Ix}+\left(\frac{(Ix-Iz)}{IxIz}\right)\left(1-\sqrt{\frac{Ix(Iz-Iy)}{Iy(Iz-Ix)}}\right)\right)$$

$$=\frac{L}{Iz}+\left\{\begin{array}{l}+\dfrac{L}{Iz}\sqrt{\dfrac{(Iz-Ix)(Iz-Iy)}{IxIy}}\;;Iz>Ix\\[3mm]-\dfrac{L}{Iz}\sqrt{\dfrac{(Iz-Ix)(Iz-Iy)}{IxIy}}\;;Ix>Iz\end{array}\right\}\approx\omega_{30}-\omega_p$$

Thus, the signals $\cos\phi$ and $\sin\phi$ oscillate at an average frequency approximately equal to the difference of the spin rate and the nutation frequency.

Estimation. With the preceding derivation, it is now possible to write the component of measured range-rate caused by antenna motion as a function of known parameters, signals with known frequencies and amplitudes and parameters to be estimated. The parameters are:

parameter	Name	known or to be estimated
L	angular momentum magnitude	either
θ	nutation angle	to be estimated
β	LOS angle	either
Ix, Iy, Iz	moments of inertia	known
m_0	normalized parameter of elliptic function	known
x_A, y_A, z_A	body coordinates of antenna	known

261

$$\bar{v}(t) = \frac{d}{dt}\left\{ A_{313}^{-1}(\phi,\theta,\psi) \begin{bmatrix} x_A \\ y_A \\ z_A \end{bmatrix} \right\}$$

$$\approx \frac{d}{dt}\begin{bmatrix} (\cos\psi\cos\phi - \sin\psi\sin\phi)x_A + (-\sin\psi\cos\phi - \cos\psi\sin\phi)y_A + \theta z_A \cos\phi \\ x \\ \theta\sin\psi x_A + \theta\cos\psi y_A + z_A \end{bmatrix}$$

$$= \frac{d}{dt}\begin{bmatrix} \cos(\phi+\psi)x_A + -\sin(\phi+\psi)y_A + \theta\cos\phi z_A \\ x \\ \theta\sin\psi x_A + \theta\cos\psi y_A + z_A \end{bmatrix}$$

The second component will not be used and so is not calculated, since the LOS vector in inertial coordinates is assumed to be,

$$\mathbf{LOS} = \begin{bmatrix} \sin\beta \\ 0 \\ \cos\beta \end{bmatrix}$$

The measured range-rate will be the dot product of the LOS vector and the inertial velocity, hence the incremental range-rate due to antenna motion that will be measured by the tracker is the sum of two components. The two components will be evaluated separately.

If the LOS direction were parallel to the angular momentum vector, the range-rate due to antenna motion is, where Φ is an unknown phase angle,

$$\dot{R}_V \approx \frac{d}{dt}\left(\theta\sin\psi x_A + \theta\cos\psi y_A + z_A \right)$$

$$\approx \frac{d}{dt}\left(x_A \theta_0 cn(\omega_p t|m) - y_A \theta_{max} sn(\omega_p t|m) + z_A \right)$$

$$= \left(-x_A \theta_0 sn(\omega_p t|m) - y_A \theta_{max} cn(\omega_p t|m) \right)\omega_p dn(\omega_p t|m)$$

This will be called the "vertical component" of the antenna motion. It can be rewritten as,

$$\dot{R}_V \approx \left(-x_A \theta_0 sn(\omega_p t|m) - y_A \sqrt{1+m_0}\,\theta_0 cn(\omega_p t|m) \right)\omega_p dn(\omega_p t|m)$$

$$\approx \theta_0 \omega_p \sqrt{x_A^2 + (1+m_0)y_A^2}\,\cos(\omega_p t + \Phi)$$

So the vertical component is a signal oscillating at the nutation rate and with amplitude proportional to the minimum nutation angle.

The horizontal component is a bit more complicated.

262

$$\dot{R}_H = \frac{d}{dt}\left[(\cos\psi\cos\phi - \sin\psi\sin\phi)x_A + (-\sin\psi\cos\phi - \cos\psi\sin\phi)y_A + z_A\theta\cos\phi\right]$$

$$= \frac{d}{dt}\left[x_A\left(\frac{-\theta_{max}}{\theta}sn(\omega_p t|m)\cos\phi - \frac{\theta_0}{\theta}cn(\omega_p t|m)\sin\phi\right) + y_A\left(\frac{\theta_{max}}{\theta}sn(\omega_p t|m)\sin\phi - \frac{\theta_0}{\theta}cn(\omega_p t|m)\cos\phi\right) + z_A\theta\cos\phi\right]$$

$$= \frac{d}{dt}\left[\frac{\theta_0}{\theta}\left(x_A\left(-\sqrt{1+m_0}sn(\omega_p t|m)\cos\phi - cn(\omega_p t|m)\sin\phi\right) + y_A\left(\sqrt{1+m_0}sn(\omega_p t|m)\sin\phi - cn(\omega_p t|m)\cos\phi\right)\right) + z_A\theta\cos\phi\right]$$

The ratio θ_0 / θ has essentially no dependence on θ, so the nutation component of antenna motion is, where Φ' and Φ'' are unknown phase angles,

$$\dot{R}_{HN} = \frac{d}{dt}\left(z_A\theta\cos\phi\right)$$

$$= z_A\left(\dot{\theta}\cos\phi - \theta\dot{\phi}\sin\phi\right) \approx z_A\left(\dot{\theta}\cos\phi - \theta(\omega_{30} - \omega_p)\sin\phi\right)$$

$$\approx -z_A\theta_0\sqrt{1+\frac{m_0}{2}}(\omega_{30} - \omega_p)\sin((\omega_{30} - \omega_p)t + \Phi') +$$

$$\frac{z_A\theta_0 m_0}{2\sqrt{4+2m_0}}\left[(\omega_{30} + \omega_p)\sin((\omega_{30} + \omega_p)t + \Phi') - (\omega_{30} - 3\omega_p)\sin((\omega_{30} - 3\omega_p)t + \Phi')\right]$$

So the horizontal nutation component is a signal oscillating at a frequency equal to the difference of the spin rate and the nutation rate, together with sidebands at intervals of $\pm 2\omega_p$, all with amplitudes proportional to the minimum nutation angle.

WIND Nutation Estimation. During initial phases of FDF support of the WIND mission, Doppler tracking data was used to monitor the spin rate and nutation angle of the spacecraft. The purpose was to provide a back-up to on-board attitude sensor telemetry, with the emphasis on measurement of nutation angle immediately prior to the Lanyard Boom deployment. The WIND spacecraft was launched on 1 November 1994. WIND is spin stabilized with a nominal spin rate of 20 RPM. WIND is equipped with a nutation damper with a nominal time constant of 1400 seconds. The spacecraft is cylindrical, with the z-(spin) axis being the axis of the cylinder. The Medium Gain Antenna (MGA) is extended from the negative z face of the cylinder. Figure 4 shows the WIND spacecraft configuration. The WIND attitude is maintained with the spin axis parallel to the south ecliptic pole, effectively perpendicular to the LOS.
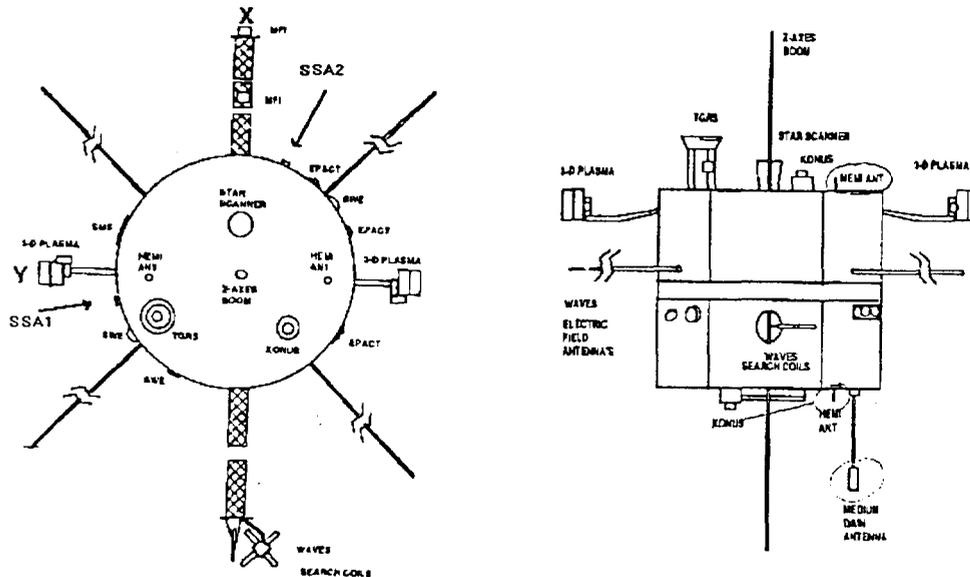
Figure 4. WIND Configuration.

The nutation estimation results for the first (of three) thruster flush burns will be presented. During the maneuver, the WIND moments of inertia were 741, 678 and 912 Kg-m^2. The MGA body coordinates are (0.14,-1.15,-2.68) meters. For WIND's attitude, according to the analysis above, the Doppler signal will contain a component at a frequency approximately equal to 1.3 times the spin rate, with an amplitude proportional to the minimum nutation angle (the nutation angle oscillates between minimum and maximum values since WIND is not axially symmetric). For the assumed WIND configuration, the minimum nutation angle in degrees can be estimated by finding the amplitude of this component in meters/sec, and dividing it by (0.007SR), where SR is the spin rate in RPM.
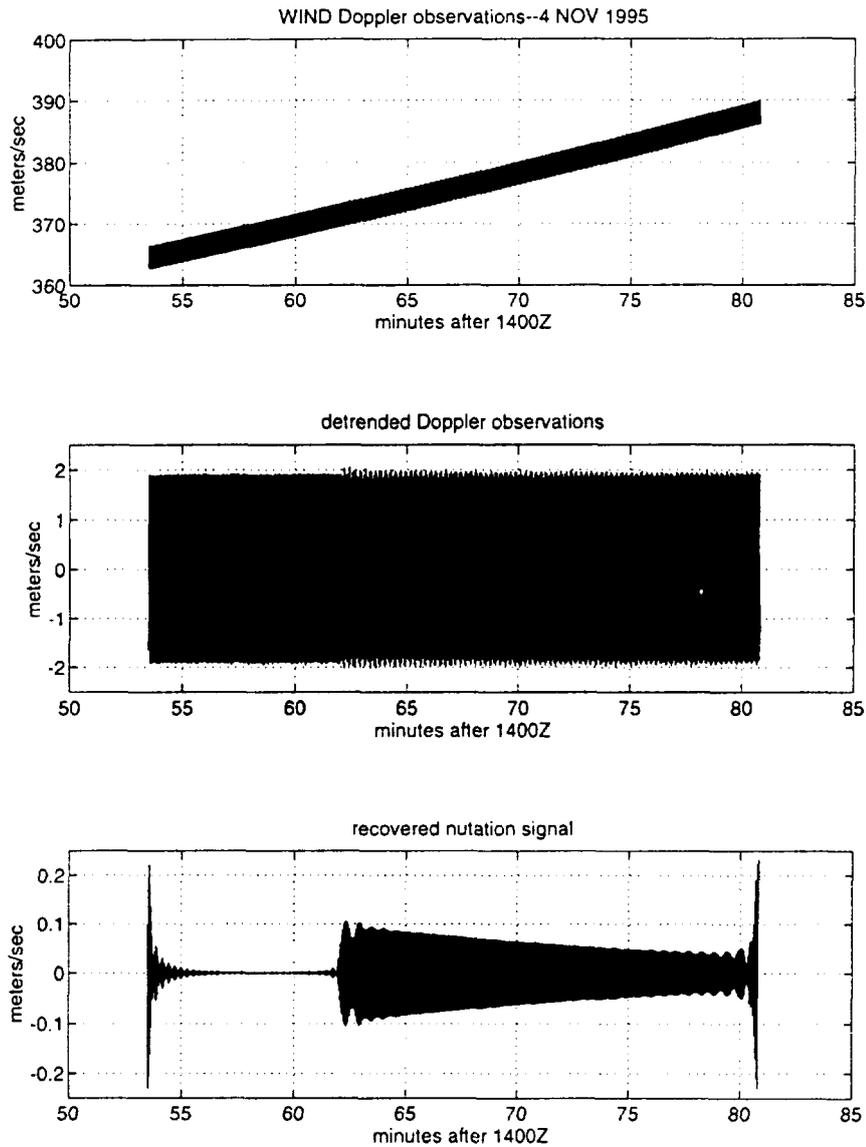
Figure 5. WIND Doppler Signal Processing

The topmost plot in figure 5 shows WIND range-rate for the period of the thruster flush maneuver. The middle plot shows the detrended data, used as the input to a Discrete Fourier Transform (DFT) algorithm. The lowest plot is the recovered nutation signal obtained by performing the inverse DFT on only those frequency components near the expected location of the nutation signal. Since some frequency components of the desired signal are lost, and some of other signals are included, there are large oscillations at the beginning and end of the recovered signal; these are known as the Gibb's Phenomenon (ref. 5, pp. 73-75). The nutation signal was "envelope detected" and scaled by $1/(.007SR)$ to obtain the minimum nutation angle (θ_0) as a function of time. The comparison is with Sun Sensor Assembly #2 on WIND (listed as SSA2 in figure 4.). SSA2 is 30 degrees away from the X-axis, so the largest nutation angle it sees is between θ_0 and θ_{MAX}. The Doppler nutation signal was further scaled by ,

$$\sqrt{1 + \frac{m_0}{2} - \frac{m_0}{2} \cos\left[2\left(\frac{30\pi}{180}\right)\right]}; m_0 \approx 0.49$$

to put the SSA2 and Doppler signals on the same reference. Figure 6 shows the comparison of the detrended SSA2 angles and the scaled Doppler nutation signal amplitude.
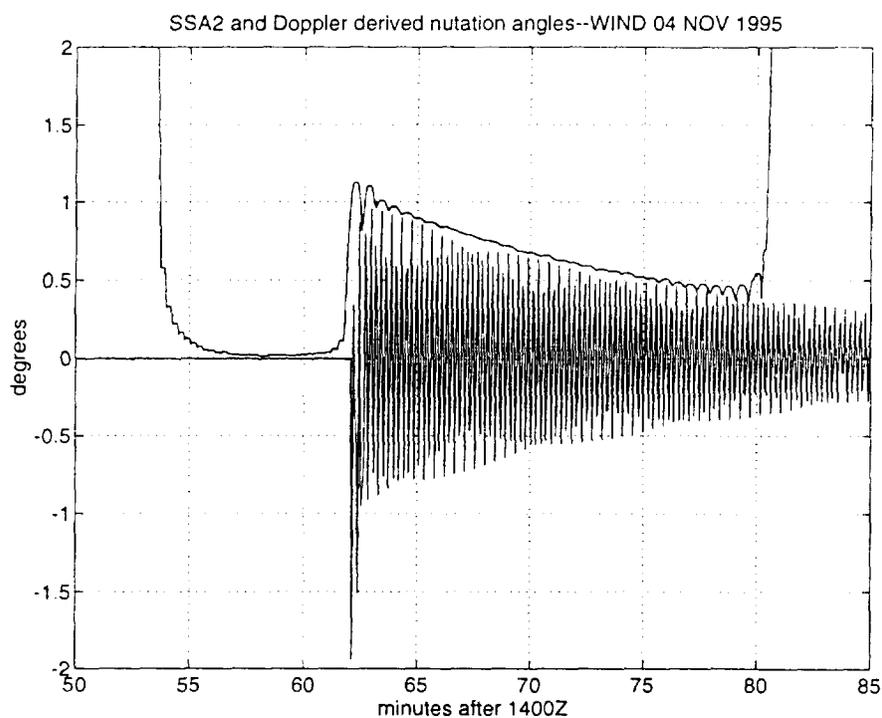
Figure 6. Comparison of Sun Sensor 2 and Doppler Nutation.

Conclusions. For spinning spacecraft, processing of Doppler tracking data for attitude parameters can be a useful adjunct to on-board attitude sensors. For "smaller, cheaper" missions it could possibly replace on-board sensors. In order to be useful for real time attitude estimation, further algorithm development should be done; for example, a digital phase-locked loop (DPLL) implementation for tracking spin rate and demodulating the nutation signal.

265

References.

1. Computer *Sciences* Corporation (CSC) Memo 54814-18 reporting GOES-I attitude determination, dated 15 June 1994.

2. Wertz, J. R. (ed.), Spacecraft Attitude Determination and Control, Kluwer, Dordrecht, The Netherlands, 1978.

3. Abramowitz, M. and I. A. Stegun (eds.), Handbook of Mathematical Functions, Dover, New York, 1965.

4. Selby, S. M. (ed.), Handbook of Tables for Mathematics, 3rd ed., Chemical Rubber Company, Cleveland, 1967.

5. Hamming, R. W., Digital Filters, Prentice-Hall, Englewood Cliffs, 1977.

Multi-Spacecraft Coherent Doppler and Ranging
for Interplanetary Navigation

Vincent M. Pollmeier
Jet Propulsion Laboratory
California Institute of Technology

Abstract

Future plans for planetary exploration currently include using multiple spacecraft to simultaneously explore one planet. This never before encountered situation, places new demands on tracking systems used to support navigation. One possible solution to the problem of heavy ground resource conflicts is the use of multi-spacecraft coherent radio metric data, also known as, bent-pipe data. Analysis of the information content of these data types show that the information content of multi-spacecraft Doppler is dependent only on the frequency of the final downlink leg and is independent of the frequencies used on other legs. Numerical analysis shows that coherent bent-pipe data can provide significantly better capability to estimate the location of a lander on the surface of Mars, than can direct lander to Earth radio metric data. However, this is complicated by difficulties in separating the effect of a lander position error from that of an orbiter position error for single passes of data.

Introduction

As plans are being made to send multiple spacecraft simultaneously to the same planet, it has become apparent that this places a considerable burden on the ability of Earth based tracking resources to provide the levels and types of support traditionally provided. In the past NASA's Deep Space Network (DSN) has been able to meet the needs of spacecraft whose visibility periods overlapped by using extra resources or by negotiated compromises in scheduling. This was in part achievable because overlapping visibility periods were generally a transient phenomena, which orbital motion would correct. However, with the development of the *Mars Surveyor* program, it is planned that the DSN will have to support multiple spacecraft in orbit around or landed on the surface of Mars. During certain phases of this program, it is envisioned that four or more spacecraft (some combination of landers and orbiters) may simultaneously be in operation This will require the development of new techniques and operational methods, including in the of navigation.

Traditionally operational deep space navigation has been performed by using coherent 2 way Doppler and ranging between an Earth station and the spacecraft. In this mode of operation an uplink signal is sent from the Earth to a spacecraft, where the frequency of the received signal is used by the spacecraft to control the frequency of the signal transmitted back to Earth. Additionally, a ranging signal (or signals) can be modulated on the uplink, demodulated by the spacecraft receiver and remodulated onto the downlink, allowing for the measure of the round-trip light time to the spacecraft. These tracking data types were provided in passes which typically lasted from four to eight hours. The total amount of coverage varied from three passes/per week to continuous coverage. It can be seen that it would be difficult to provide this level of support to two or more spacecraft which have a 100% visibility overlap without committing large amounts of DSN ground resources for years at a time.

Alternative tracking methods do exist, such as receiving a noncoherent downlink with a multichannel receiver. This however, places a great reliance on the stability of the spacecraft oscillator. Analysis (Ref. 1) indicates that reasonable accuracies can be met with such a noncoherent system, but that these accuracies are not equal to a coherent system. A second option is to track one spacecraft in the traditional manner, and to have that spacecraft receive, process, and telemeter to the Earth noncoherent signals sent by other spacecraft which are nearby. Such a system has significant advantages in that the radio system for the secondary spacecraft can be much smaller in that it is not necessary to provide a link to the Earth. However this system is highly dependent on the stability of oscillators on both spacecraft and on the accuracy of the Doppler extraction and telemetering system on the relay. Analysis performed to support the never exercised MBR relay, between Russian Mars landers and the *Mars Observer* spacecraft (Ref. 2.) indicates that by far the limiting error source for that system was the stability of the lander oscillator. However a system midway between the current coherent tracking process and the telemetered system could be developed. This system would utilize a coherent

radio link between the Earth station and both spacecraft. This "bent-pipe" data would not have any dependence on spacecraft oscillators, would not require a Doppler extraction/telemetry system, and would not require the support of simultaneous uplinks from the Earth.

Bent-Pipe Tracking

A bent-pipe tracking scheme is illustrated in Figure 1. In this case a radio signal of frequency, f_{tE}, is broadcast from an Earth station. This signal is received by the first spacecraft (SC₁), with the shifted frequency, f_{r1a}, and then is coherently rebroadcast with frequency, f_{t1a}, to the second spacecraft (SC₂), where the received frequency is f_{r2}. SC₂ then coherently rebroadcasts the data with frequency, f_{t2}, to SC₁, where it is received with the frequency, f_{r1b}, and coherently broadcast with the frequency, f_{t1b}. Finally the signal is received at the Earth station with a measured receipt frequency of f_{rE}. The length and rate of change of the length of the four radio links are designated respectively, $\rho_1, \dot{\rho}_1, \rho_2, \dot{\rho}_2, \rho_3, \dot{\rho}_3,$ and $\rho_4, \dot{\rho}_4$.
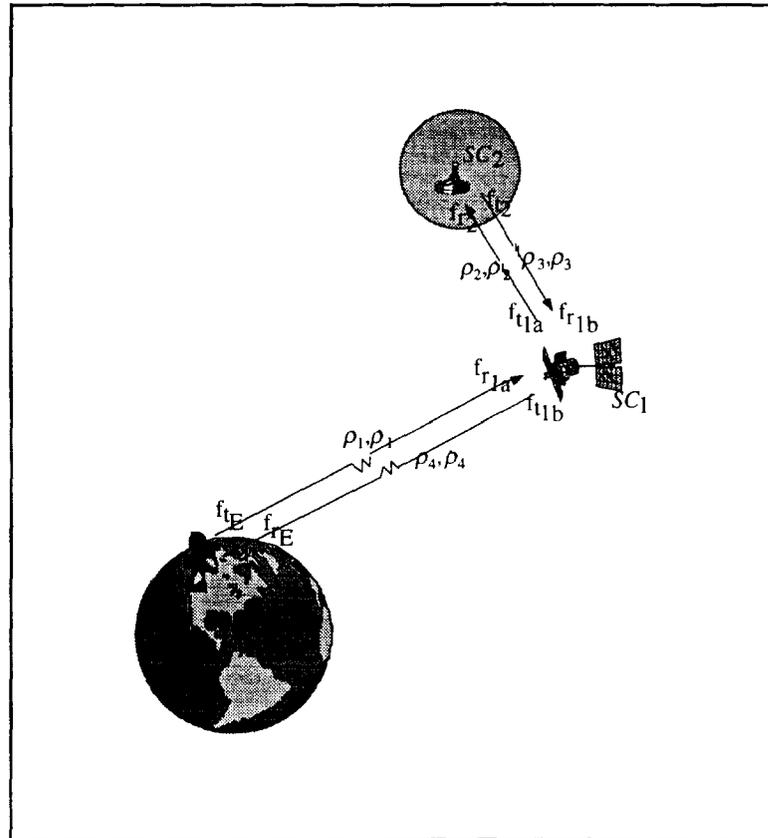
Figure 1: Two spacecraft bent pipe tracking

Observables

By convention, the Doppler radio metric observable, O, is defined as:

$$O = f_{tE} \, r_1 \, r_2 \, r_3 - f_{rE}$$

<Eq. 1>

where:

268

$r_1 \equiv$ the frequency turn around ratio between leg 1 & leg 2 $\left(\dfrac{f_{t1a}}{f_{r1a}}\right)$

$r_2 \equiv$ the frequency turn around ratio between leg 2 & leg 3 $\left(\dfrac{f_{t2}}{f_{r2}}\right)$

$r_3 \equiv$ the frequency turn around ratio between leg 3 & leg 4 $\left(\dfrac{f_{t1b}}{f_{r1b}}\right)$

However, working backward from the received signal, f_{rE}:

$$f_{rE} = \left(\frac{1 - \dfrac{\dot{\rho}_4}{c}}{\sqrt{1 - \left(\dfrac{\dot{\rho}_4}{c}\right)^2}}\right) f_{t1b} + \varepsilon_4$$

<Eq. 2>

where:

$\dot{\rho}_4 \equiv$ the rate of change of the length of the final radio link
$\varepsilon_4 \equiv$ noise and other effects (including transmission
media) on the final downlink leg
$c \equiv$ the speed of light

In the interest of streamlining the notation, a function is introduced to replace the first factor on the right hand side of Eq.. 2, the Doppler shift multiplier.

$$d(x) = \left(\frac{1 - \dfrac{x}{c}}{\sqrt{1 - \left(\dfrac{x}{c}\right)^2}}\right)$$

<Eq. 3>

thereby reducing Eq.. 2 to:

$$f_{rE} = d(\dot{\rho}_4)\, f_{t1b} + \varepsilon_4$$

<Eq. 4>

Given the definition of the turn around ratio, it is possible to redefine f_{t1b}:

$$f_{t1b} = r_3\, f_{r1b}$$

<Eq. 5>

However,

$$f_{r1b} = d(\dot{\rho}_3)\, f_{t2} + \varepsilon_3$$

<Eq. 6>

where:

$\dot{\rho}_3 \equiv$ the rate of change of the length of the second
intermediate leg
$\varepsilon_3 \equiv$ noise and other effects (including transmission
media) on the second intermediate leg

recursively substituting Eq.. 6 into Eq.. 5 and that result into Eq.. 4:

$$f_{rE} = d(\dot{\rho}_4) r_3 \left(d(\dot{\rho}_3) f_{t2} + \varepsilon_3 \right) + \varepsilon_4$$

<Eq. 7>

which expands to

$$f_{rE} = d(\dot{\rho}_4)\, d(\dot{\rho}_3)\, r_3\, f_{t2} + d(\dot{\rho}_4)\, r_3\, \varepsilon_3 + \varepsilon_4$$

<div align="right"><Eq. 7a></div>

repeating the steps of Eq.. 5 and Eq.. 6 on the transmission leg from SC_1 to SC_2:

$$f_{t2} = r_2\, f_{r2}$$

<div align="right"><Eq. 8></div>

$$f_{r2} = d(\dot{\rho}_2)\, f_{t1a} + \varepsilon_2$$

<div align="right"><Eq. 9></div>

recursively substituting as before

$$f_{rE} = d(\dot{\rho}_4)\, d(\dot{\rho}_3)\, d(\dot{\rho}_2)\, r_3\, r_2\, f_{t1a} + d(\dot{\rho}_4)\, d(\dot{\rho}_3)\, r_3\, r_2\, \varepsilon_2 + d(\dot{\rho}_4)\, r_3\, \varepsilon_3 + \varepsilon_4$$

<div align="right"><Eq. 10></div>

continuing to the Earth to SC_1 leg:

$$f_{t1a} = r_1\, f_{r1a}$$

<div align="right"><Eq. 11></div>

$$f_{r1a} = d(\dot{\rho}_1)\, f_{tE} + \varepsilon_1$$

<div align="right"><Eq. 12></div>

and as before

$$f_{rE} = d(\dot{\rho}_4)\, d(\dot{\rho}_3)\, d(\dot{\rho}_2)\, d(\dot{\rho}_1)\, r_3\, r_2\, r_1\, f_{tE} + d(\dot{\rho}_4)\, d(\dot{\rho}_3)\, d(\dot{\rho}_2)\, r_3\, r_2\, r_1\, \varepsilon_1$$
$$+ d(\dot{\rho}_4)\, d(\dot{\rho}_3)\, r_3\, r_2\, \varepsilon_2 + d(\dot{\rho}_4)\, r_3\, \varepsilon_3 + \varepsilon_4$$

<div align="right"><Eq. 13></div>

Assuming for the purposes of this data content analysis that the final four terms in Eq.. 13 are very small in comparison to the first term and can be dropped, Eq.. 13 simplifies to

$$f_{rE} \approx d(\dot{\rho}_4)\, d(\dot{\rho}_3)\, d(\dot{\rho}_2)\, d(\dot{\rho}_1)\, r_3\, r_2\, r_1\, f_{tE}$$

<div align="right"><Eq. 14></div>

substituting back in the function introduced in Eq.. 3:

$$f_{rE} \approx \left(\frac{1 - \dfrac{\dot{\rho}_4}{c}}{\sqrt{1 - \left(\dfrac{\dot{\rho}_4}{c}\right)^2}} \right) \left(\frac{1 - \dfrac{\dot{\rho}_3}{c}}{\sqrt{1 - \left(\dfrac{\dot{\rho}_3}{c}\right)^2}} \right) \left(\frac{1 - \dfrac{\dot{\rho}_2}{c}}{\sqrt{1 - \left(\dfrac{\dot{\rho}_2}{c}\right)^2}} \right) \left(\frac{1 - \dfrac{\dot{\rho}_1}{c}}{\sqrt{1 - \left(\dfrac{\dot{\rho}_1}{c}\right)^2}} \right) r_3\, r_2\, r_1\, f_{tE}$$

<div align="right"><Eq. 15></div>

this then becomes

$$f_{rE} \approx \frac{\left(1 - \dfrac{\dot{\rho}_4}{c} - \dfrac{\dot{\rho}_3}{c} + \dfrac{\dot{\rho}_3\dot{\rho}_4}{c^2}\right)\left(1 - \dfrac{\dot{\rho}_2}{c} - \dfrac{\dot{\rho}_1}{c} + \dfrac{\dot{\rho}_1\dot{\rho}_2}{c^2}\right)}{\sqrt{\left(1 - \left(\dfrac{\dot{\rho}_4}{c}\right)^2 - \left(\dfrac{\dot{\rho}_3}{c}\right)^2 + \left(\dfrac{\dot{\rho}_3\dot{\rho}_4}{c^2}\right)^2\right)\left(1 - \left(\dfrac{\dot{\rho}_4}{c}\right)^2 - \left(\dfrac{\dot{\rho}_3}{c}\right)^2 + \left(\dfrac{\dot{\rho}_3\dot{\rho}_4}{c^2}\right)^2\right)}}\, r_1\, r_2\, r_3\, f_{tE}$$

<div align="right"><Eq. 15a></div>

since all of the $\dot{\rho}$ terms are much smaller than c, the numerator of Eq.. 15a can be approximated as 1 (this has the effect of ignoring the relativistic correction to the Doppler shift) and the numerator expanded.

$$f_{rE} \approx \begin{pmatrix} 1 - \dfrac{\dot{\rho}_2}{c} - \dfrac{\dot{\rho}_1}{c} + \dfrac{\dot{\rho}_2 \dot{\rho}_1}{c^2} - \dfrac{\dot{\rho}_4}{c} + \dfrac{\dot{\rho}_4 \dot{\rho}_2}{c^2} + \dfrac{\dot{\rho}_4 \dot{\rho}_1}{c^2} - \dfrac{\dot{\rho}_4 \dot{\rho}_2 \dot{\rho}_1}{c^3} \\ - \dfrac{\dot{\rho}_3}{c} + \dfrac{\dot{\rho}_3 \dot{\rho}_2}{c^2} + \dfrac{\dot{\rho}_3 \dot{\rho}_1}{c^2} - \dfrac{\dot{\rho}_3 \dot{\rho}_2 \dot{\rho}_1}{c^3} + \dfrac{\dot{\rho}_4 \dot{\rho}_3}{c^2} - \dfrac{\dot{\rho}_2 \dot{\rho}_3 \dot{\rho}_4}{c^3} \\ - \dfrac{\dot{\rho}_1 \dot{\rho}_3 \dot{\rho}_4}{c^3} + \dfrac{\dot{\rho}_1 \dot{\rho}_2 \dot{\rho}_3 \dot{\rho}_4}{c^4} \end{pmatrix} r_1\, r_2\, r_3\, f_{tE}$$

<Eq. 16>

Ignoring all second order effects, Eq.. 16 can be further approximated and simplified to

$$f_{rE} \approx \left(1 - \frac{\dot{\rho}_1}{c} - \frac{\dot{\rho}_2}{c} - \frac{\dot{\rho}_3}{c} - \frac{\dot{\rho}_4}{c} \right) r_1\, r_2\, r_3\, f_{tE}$$

<Eq. 17>

substituting Eq.. 17 into Eq.. 1:

$$O \approx f_{tE}\, r_1\, r_2\, r_3 - \left(1 - \frac{\dot{\rho}_1}{c} - \frac{\dot{\rho}_2}{c} - \frac{\dot{\rho}_3}{c} - \frac{\dot{\rho}_4}{c} \right) r_1\, r_2\, r_3\, f_{tE}$$

<Eq. 18>

and finally

$$O \approx \left(\frac{\dot{\rho}_1}{c} + \frac{\dot{\rho}_2}{c} + \frac{\dot{\rho}_3}{c} + \frac{\dot{\rho}_4}{c} \right) r_1\, r_2\, r_3\, f_{tE}$$

<Eq. 19>

A bent-pipe range observable, R, is defined as:

$$R = \frac{\rho_1}{c} + \frac{\rho_2}{c} + \frac{\rho_3}{c} + \frac{\rho_4}{c} - n(A)$$

<Eq. 20>

where:

$$\rho_1 \cdots \rho_4 \equiv \text{the path length of each radio link}$$
$$n \equiv \text{unknown integer multiplier}$$
$$A \equiv \text{range modulus (a function of ground hardware configuration)}$$

Given the definitions of the range and Doppler observables from Eq.'s 20 and 18, the sensitivity of the observable to any parameter z can be readily calculated.

$$\frac{\partial O}{\partial z} \approx \left(\frac{\partial(\dot{\rho}_1)}{\partial z} + \frac{\partial(\dot{\rho}_2)}{\partial z} + \frac{\partial(\dot{\rho}_3)}{\partial z} + \frac{\partial(\dot{\rho}_4)}{\partial z} \right) \frac{r_1\, r_2\, r_3}{c} f_{tE}$$

<Eq. 21>

$$\frac{\partial R}{\partial z} \approx \frac{\left(\dfrac{\partial(\rho_1)}{\partial z} + \dfrac{\partial(\rho_2)}{\partial z} + \dfrac{\partial(\rho_3)}{\partial z} + \dfrac{\partial(\rho_4)}{\partial z} \right)}{c}$$

<Eq. 22>

A conclusion that can be readily drawn from Eq.'s 21 and 22 that is not intuitive is that the information content in a coherent radio metric data point is (to first order) only dependent on the frequency on the final downlink leg. For example, for a radio link where the first leg is X band, the second is S-band, the third is S-band, and the final leg is X-band, typical values for the three turn around ratios and transmit frequency are $r_1 = \frac{221}{749} = 0.2951$, $r_2 = \frac{240}{221} = 1.086$, $r_3 = \frac{880}{240} = 3.666$, and $f_{tE} = 7.2$ GHz (Ref. 3), while for an S-band/UHF/UHF/X-band link the corresponding values would be $r_1 = \frac{25}{132} = 0.1894$, $r_2 = \frac{749}{737} = 1.016$, $r_3 = \frac{13840}{669} = 20.69$, and $f_{tE} = 2.1$ GHz. In both of these examples, the term, $r_1\, r_2\, r_3\, f_{tE}$, is equal to 8.4 GHz. This result is more than simply an interesting detail. Since to first order (and ignoring transmission media effects), the data content does not depend on the frequency of the inter-spacecraft links, the choice

of frequencies and transponders for the this link can be made without regard to navigation issues. This can be a significant cost savings issue. Additionally from an operational perspective, it is not possible (without extra information) for the operator of the ground tracking system to know what frequency is being used on the spacecraft/spacecraft link. However all that is required is that the product of the three turn around ratios be known.
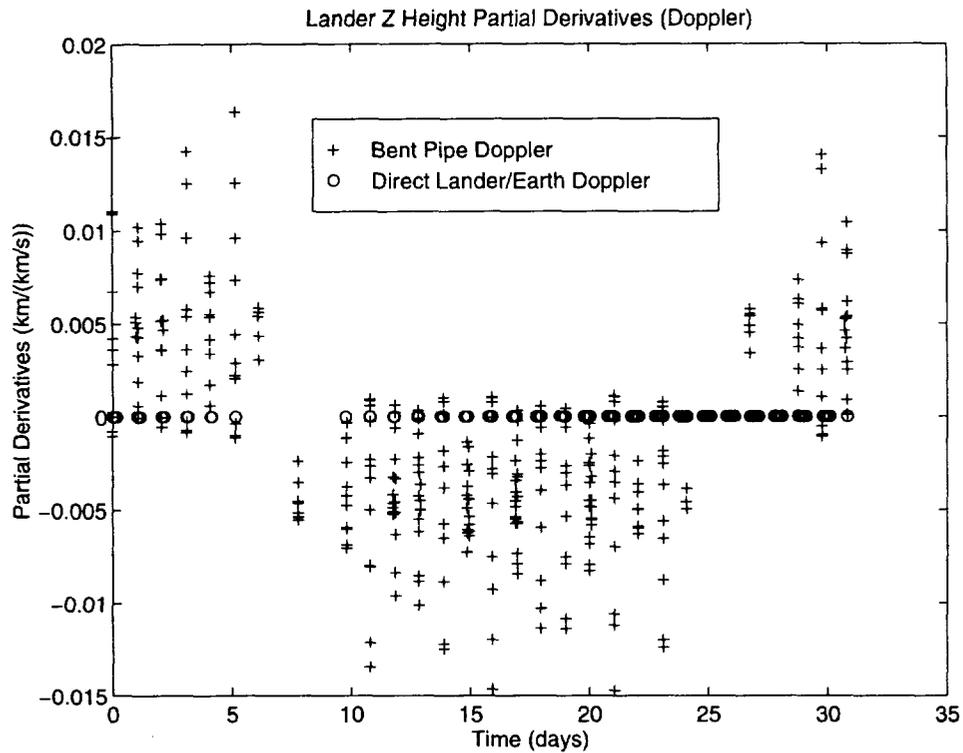
Figure 2: Comparison of bent pipe Doppler and traditional Doppler lander Z-height sensitivity

Numerical Analysis

Equations 19 and 22 give the partial derivatives of a Doppler and range observation with respect to an arbitrary parameter z. From these it is possible to calculate the approximate sensitivity of a number of observations to parameters of interest. For the purpose of this initial study, the case of an orbiter about Mars and a lander on the surface is examined. The orbiter in question, is in a near polar orbit with a semi-major axis of 3775 km. This is the approximate orbit planned for *Mars Observer* and currently planned for *Mars Global Surveyor* (Ref. 4). A lander is located at approximately 30° North latitude. One quantity of strong interest is the ability to determine the location of the lander on the surface. It has been known for some time that Earth based tracking of landers on Mars has difficulty in determining the Z - height component of the position vector in a cylindrical coordinate frame. Figures 2 and 3 clearly show that bent-pipe Doppler and range data exhibit a sensitivity to this parameter that is more than an order of magnitude larger than that for direct lander/Earth tracking. It should be noted that given the low polar orbiter chosen for this case, the sensitivity to this parameter in the bent pipe data is much greater than it would be for a high equatorial orbiter.

The bent pipe Doppler data also exhibit much larger sensitivity to lander spin axis knowledge and longitude knowledge than the traditional Earth based lander Doppler. Figure 4 clearly indicates that the partials for spin axis and longitude are approximately 10 to 20 times larger than the corresponding partials for the conventional Doppler.

Unfortunately, this enhanced sensitivity does little good, if it is not possible to separate the lander position from other parameters. Detailed covariance analysis of a similar problem (Ref. 2), indicates that tracking arcs on the order of a week to a month are required to completely separate the knowledge of the orbiter position and the lander position. Single passes are extremely poor in the ability to separate the two spacecraft. The reason for this is clearly indicated in Figure

272

5. The partial derivatives of lander position and orbiter epoch state are given over a single pass (the first pass in the data arc). The similarity in structure between the two sets of partials, especially the orbiter Cartesian x, and the lander z-height location, make it very nearly impossible to separate the position estimates for the two spacecraft given a short data arc.
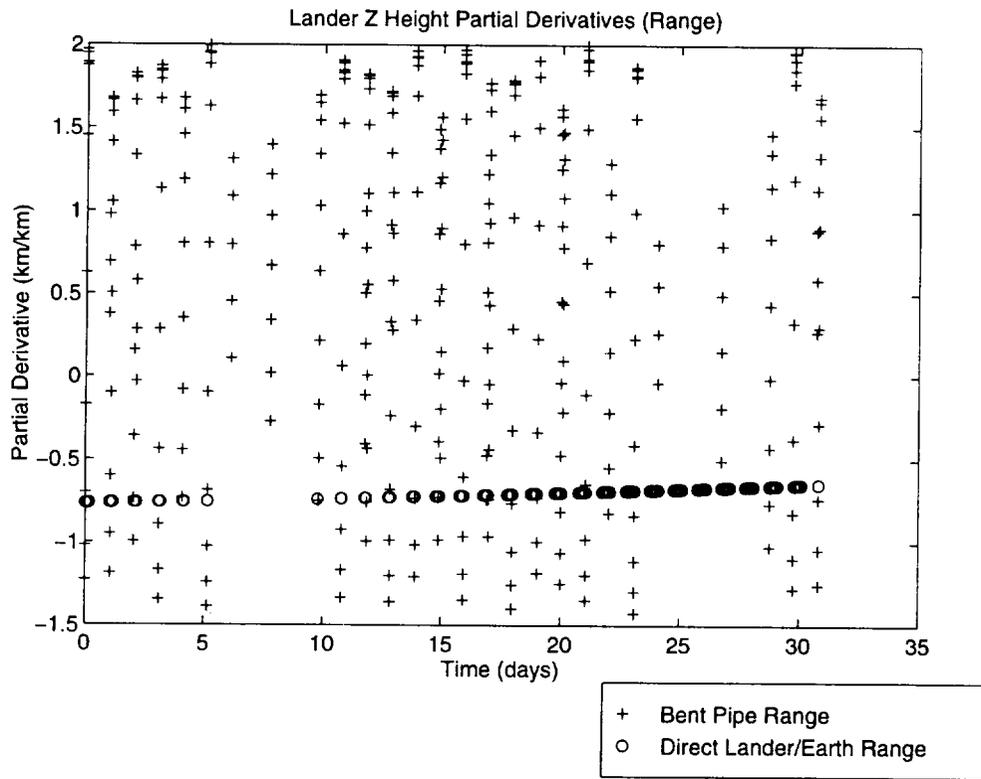
Figure 3: Comparison of bent pipe range and traditional range lander Z-height sensitivity
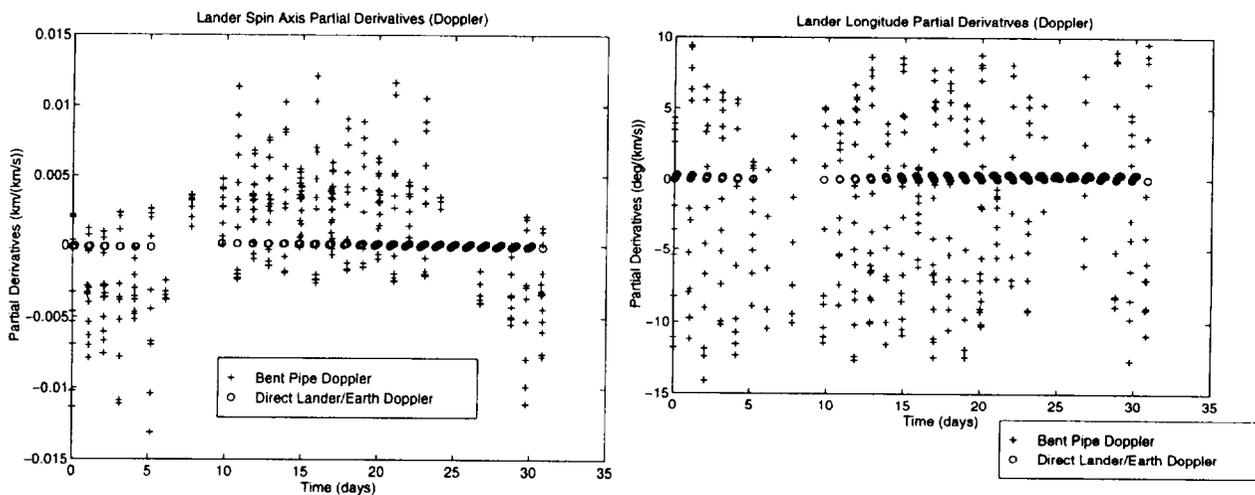
Figure 4: Comparison of bent pipe & traditional Doppler sensitivities to lander location spin axis & longitude
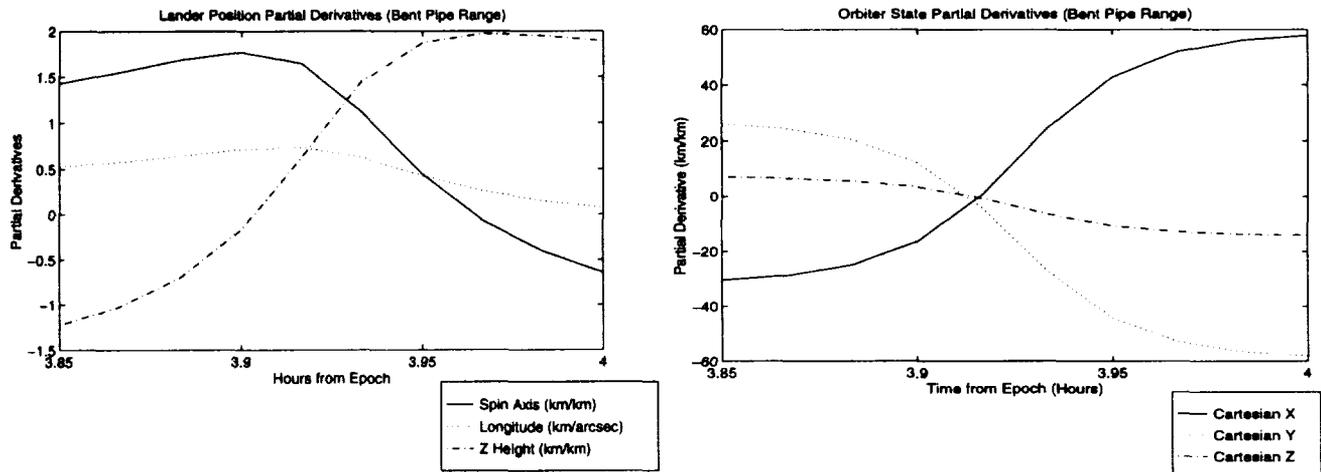
Figure 5: Comparison Orbiter state and lander location partials for a single pass of bent pipe Doppler

Operational Considerations

It is apparent that there is a high probability that coherent bent pipe Doppler and ranging data will provide sufficient information to allow the navigation of an orbiter and a lander at Mars. However, a brief examination of the operational feasibility of such a system from a ground and spacecraft hardware position is in order. Given current analog phase-lock-loop (PLL) receivers used by interplanetary spacecraft, the procedure for acquiring a coherent bent pipe link would be to, first, sweep the uplink to the first spacecraft, slow enough and wide enough to ensure lock. Then repeat the sweep to attempt to acquire lock of the second spacecraft. This second sweep will have to be slow enough that the first spacecraft does not drop lock. Then a sweep of the signal to reacquire the downlink signal at the first spacecraft may be needed. Finally the signal is received on the ground and a coherent link is established. This process would place considerable overhead on the tracking bandwidth of the spacecraft receivers, the width of the total tracking loop, and the amount of time required to acquire a signal. Given that for the geometry identified in this short study, the longest pass of bent pipe Doppler data acquired is 12 minutes long, it seems improbable that a link could be set up in this time. However if the orbiter were in a somewhat higher orbit, and directly controlled receivers used, it should be possible to set up a link. However the need for a controlled receiver could possibly offset the cost savings accrued due to the lack of a required direct to Earth link.

Once a coherent link is set up, if the frequency shifts too much or too quickly radio lock may be lost. Given that the radio signal to be received by the spacecraft will have the Doppler shifts of multiple legs it is of some concern that the total shift would be too great to maintain lock. Figure 6 shows the range rates for the lander and the orbiter for both bent pipe and traditional tracking methods. It can be seen that the motion of Mars relative to the Earth station is the dominant error source and the summation of the two signals would result in less than 40% increase in maximum Doppler shift over that from conventional Doppler. Thus it is unlikely that this alone could preclude the acquisition of bent pipe Doppler data.

Conclusion

Coherent bent pipe Doppler and ranging data can provide useful information for the navigation of multiple spacecraft at a given target which is independent of the frequency used on the inter-spacecraft link. However, the operational complexities involved in acquiring a link would most likely require the use of a controlled receiver, rather than the analog PLL receivers currently used for the majority of deep space missions and would preclude the acquisition of data during extremely short visibility periods. Consequently, this data type would not be useable for the support of a lander and a low mapping orbiter of the *Mars Observer* or *Mars Global Surveyor* type. However, for some types of missions

such a system could significantly decrease the resource conflicts inherent in supporting multiple spacecraft at a single source.

More study is needed of the detailed requirements on the spacecraft telecommunications system of acquiring a coherent bent pipe link. Additionally, the ability to separate the position knowledge of a lander and an orbiter or of two orbiters needs to be more fully investigated than was possible in the scope of the study. Finally, other data types such as two-way coherent telemetered Doppler between an orbiter and a lander should be investigated. This data has similar information content, and fewer separability problems, but may have additional theoretical and implementation obstacles.

Range Rate for Mars Orbiter and Lander
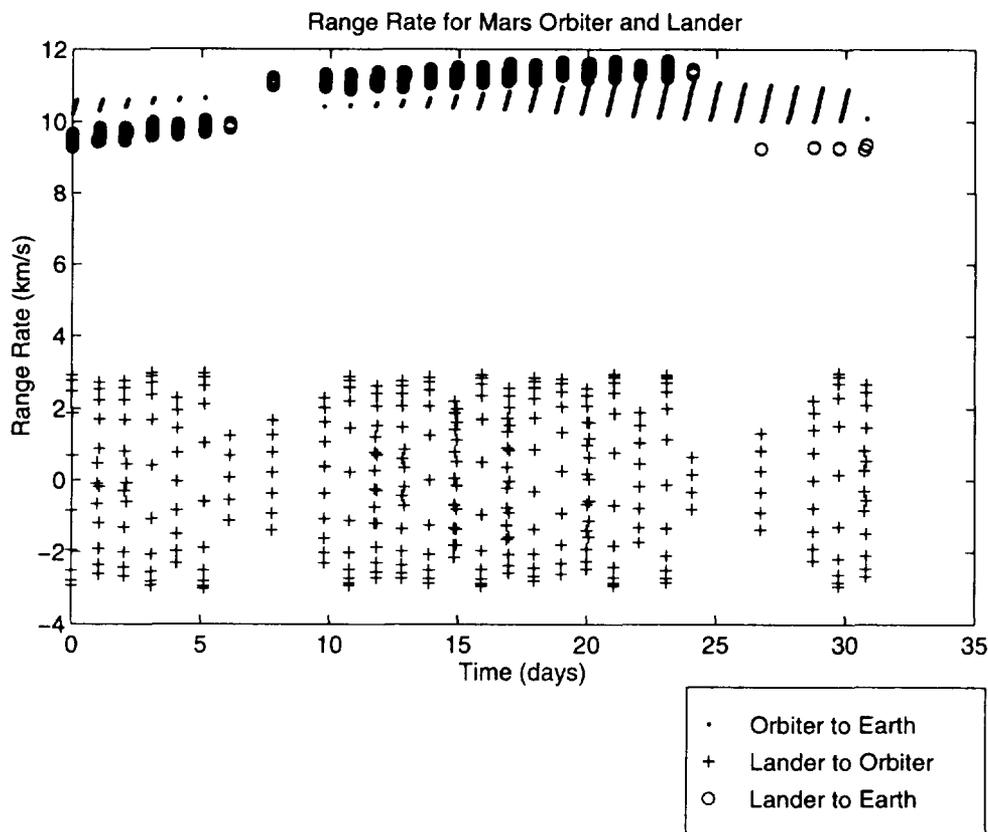
Figure 6: Comparison of range rates for various combinations of lander and orbiter observations

Acknowledgments

References

1) Bhaskaran, S., "Application of Non-Coherent Data Types for Deep Space Navigation," TDA Progress Report, 42-121, January - March 1995.

2) Eckstein, M. C., Gill, E., and Pollmeier, V. M., "Analysis of the Orbit Determination Accuracy of the Mars-94 Orbiter," International Symposium on Space Flight Dynamics, St. Petersburg - Moscow, Russia, 22 May 1994.

3) "Navigation Plan, Mars Observer Project," Jet Propulsion Laboratory, internal document, JPL D-3820, Rev. C, 15 June 1990

4) "ODP/DPTRAJ Reference Manual, Vol. 1," Jet Propulsion Laboratory, internal document, JPL D-263, Rev. D, 15 October 1991.

ULYSSES ORBIT DETERMINATION
AT HIGH DECLINATIONS

Timothy P. McElrath and George D. Lewis
Jet Propulsion Laboratory (JPL), California Institute of Technology
Pasadena, California, USA

Abstract

The trajectory of the Ulysses spacecraft caused its geocentric declination to exceed 60° South for over two months during the Fall of 1994, permitting continuous tracking from a single site. During this time, spacecraft operations constraints allowed only Doppler tracking data to be collected, and imposed a high radial acceleration uncertainty on the orbit determination process. The unusual aspects of this situation have motivated a re-examination of the Hamilton-Melbourne results, which have been used before to estimate the information content of Doppler tracking for trajectories closer to the ecliptic. The addition of an acceleration term to this equation is found to significantly increase the declination uncertainty for symmetric passes. In addition, a simple means is described to transform the symmetric results when the tracking pass is non-symmetric. The analytical results are then compared against numerical studies of this tracking geometry and found to be in good agreement for the angular uncertainties. The results of this analysis are applicable to the Near Earth Asteroid Rendezvous (NEAR) mission and to any other missions with high declination trajectories, as well as to missions using short tracking passes and/or one-way Doppler data.

Introduction

The Ulysses mission is a cooperative project of NASA and the European Space Agency (ESA) to send a spacecraft equipped to measure charged and neutral particles, magnetic fields, electro-magnetic waves, and ultraviolet and X-ray emissions over the polar regions of the Sun. Following a Jupiter gravity assist, the Ulysses spacecraft reached South heliographic latitudes in excess of 70 degrees for 132 days starting in June, 1994. Following this time the spacecraft was continuously in view from the Canberra complex of the NASA/JPL Deep Space Network (DSN) from early October to mid-December, and outside of these dates the spacecraft was still in nearly continuous view for some time.

While Ulysses has typically been tracked for ten hours per day, with two-way Doppler and range observations being made simultaneously with telemetry reception, the Sun-spacecraft-Earth geometry during the South solar pass caused the predicted return of solar-induced nutation to the spin-stabilized spacecraft to occur. The method used to control nutation utilized active, unbalanced attitude thruster firings, commanded by the spacecraft in response to conscan measurements of the uplink radio signal. As a result, the Ulysses spacecraft required a continuous, undisturbed uplink during nutation control operations, which extended from August, 1994 through January, 1995. Although the DSN complexes did not have a continuous view throughout this time, an uplink signal and telemetry acquisition for spacecraft monitoring were provided through the use of the ESA tracking station at Kourou, French Guiana. The same situation arises again during the North solar pass, with nutation operations running from late March to October, 1995.

While the nutation control approach used by Ulysses permitted two-way coherent Doppler data to be collected continuously during DSN passes, the ranging tones generated by DSN stations cause enough modulation of the uplink to result in spurious attitude control pulses. Consequently, no ranging data was collected during nutation operations. In addition, the unbalanced nature of the thruster firings meant that up to two cm/sec of delta-V was imparted to the spacecraft per day in the direction toward the Earth. These events were clearly visible in the Doppler data, which has a sensitivity of 0.1 mm/sec under ideal conditions. While the average effect of these events was modelled, based on the average angular rate of the Earth as seen from

C-4

the spacecraft, the thruster firings did not occur in an evenly spaced manner. In addition, even if every individual thruster firing could be detected in the tracking or telemetry data (which was not the case), the number of thruster events in a typical three-month data arc was two orders of magnitude more than could be estimated as discrete events using the JPL orbit determination software. Consequently, thruster firing events of more than 1 mm/sec (representing three to four pulses) were dealt with discretely, and the rest of the activity was approximated using the continuous model, and estimated as a series of independent accelerations lasting three hours, with an *a priori* uncertainty of 10^{-10} km/sec^2.

The trajectory reconstruction requirement for Ulysses is 1000 km (1σ), which would be difficult to meet in the ecliptic under these conditions. However, the high declination of the trajectory would be expected to provide a highly accurate estimate of the geocentric angular position of the spacecraft. The basis for this expectation is the work done by Hamilton and Melbourne in Reference 1. Based on these results, a one-day pass at typical declination and range values for Ulysses would have an expected plane-of-sky uncertainty of about 47 km (or about 140 nanoradians (nrad)), as will be shown in detail later. While this is a highly accurate result, the effect of adding acceleration uncertainty would be expected to increase the plane-of-sky uncertainty. The exact amount of the increase is not immediately obvious, and so the motivation of much of the following analysis is to derive the effect of acceleration uncertainty on the information content of a pass of Doppler data. It should be mentioned that although the Doppler tracking does not directly measure the Earth-spacecraft range, which must also be known to meet the reconstruction requirement, the relative motion of the Earth and the spacecraft over a typical hundred-day data arc is generally sufficient to determine the geocentric range to within an order of magnitude or better of the plane-of-sky position uncertainty.

Analysis

The full derivation of the data equation for a Doppler observation of a distant spacecraft is given in Reference 1, and also revisited with minor corrections by Muellershoen in Reference 2, so only the final result before linearization about the nominal right ascension will be given here. It should be noted, however, that none of the approximations made to reach this result required that the spacecraft declination be small, so this result is as valid for Ulysses as for any spacecraft in the ecliptic, with the only restriction being that the geocentric range be large compared to the radius of the Earth. The topocentric velocity of a distant spacecraft, $\dot{\rho}$, is given by

$$\dot{\rho} \simeq \dot{r} + \omega r_s \cos\delta \sin(\theta - \theta_0) \tag{1}$$

where

$\dot{\rho}$ = Doppler observable

$\dot{r}$ = spacecraft's geocentric range-rate

ω = Earth's rotation rate

r_s = distance from tracking station to Earth's spin axis

δ = spacecraft's declination

θ = tracking station's right ascension

θ_0 = spacecraft's right ascension

It can almost be proven by inspection that this is the right form, in consideration of the characteristic lengths and the periodicity of the motions involved. Equation (1) can be linearized about an *a priori* relative right ascension, which can then be expressed as a function of time, by re-defining $(\theta - \theta_0)$ as $\omega(t - t_0)$, such that the spacecraft is at the station longitude when $t = 0$. Since ωt_0 is small, we have

$$\dot{\rho} \simeq \dot{r} + \omega r_s \cos\delta \sin\omega t - \omega t_0 \omega r_s \cos\delta \cos\omega t$$
$$\simeq a + b\sin\omega t + c\cos\omega t \tag{2}$$

where

$$a = \dot{r}$$
$$b = \omega r_s \cos \delta$$
$$c = -\omega t_0 \omega r_s \cos \delta$$

As an aside, it should be noted that representing Doppler data in this form is not unique to navigation at JPL. For instance, radio science processing of Doppler data has been done using equation (2) and the first-order expansion of equation (2) in time, as described in Reference 3. The resulting "six-parameter fit" is fairly efficient in removing all of the dynamics present in a pass of Doppler data for gravity wave detection purposes.

Equation (2) can be extended to handle the effect of a constant radial acceleration by adding a term qt, where q is the acceleration magnitude in the geocentric direction.

$$\dot{\rho} \simeq a + b \sin \omega t + c \cos \omega t + qt \tag{3}$$

The epoch at which the acceleration term does not contribute to the velocity is in the middle of the data arc. Any other placement of the epoch causes a correlation between the radial velocity and the radial acceleration, which adds undesirable complexity to the problem.

Before proceeding to take partials of $\dot{\rho}$ with respect to the four parameters, it is worth noting that b and c may be replaced by new parameters b' and c' such that $\omega t' = \omega t + \phi$ is the new argument of the sine and cosine in equation (3). The angle ϕ then becomes the right ascension of the spacecraft relative to the tracking station when $t' = 0$. This allows tracking passes that are not symmetric about culmination to be represented by a simple rotation of the estimate covariance, which is much simpler algebraically than carrying a non-symmetric start and stop time for a tracking pass throughout the derivation. If q is redefined with an epoch in the middle of the non-symmetric pass, and a is redefined as $\dot{r}$ in the center of the non-symmetric pass, then no further changes of variables are necessary. Consequently, the covariance for a symmetric pass will be obtained before any further considerations of asymmetry.

The partial derivatives matrix H of $\dot{\rho}$ with respect to a, b, c, and q for a series of measurements at times t_i is

$$H = \begin{pmatrix} 1 & \sin \omega t_1 & \cos \omega t_1 & t_1 \\ 1 & \sin \omega t_2 & \cos \omega t_2 & t_2 \\ \vdots & \vdots & \vdots & \vdots \end{pmatrix} \tag{4}$$

Using standard weighted least-squares formulation, the covariance P is

$$P = (H^T H)^{-1} \sigma_{\dot{\rho}}^2 \tag{5}$$

where $\sigma_{\dot{\rho}}^2$ is the variance of Doppler observations. The information array $\Lambda(= H^T H)$ is

$$\Lambda = \begin{pmatrix} N & \sum_j \sin \omega t_j & \sum_j \cos \omega t_j & \sum_j t_j \\ \sum_j \sin \omega t_j & \sum_j \sin^2 \omega t_j & \sum_j \sin \omega t_j \cos \omega t_j & \sum_j t_j \sin \omega t_j \\ \sum_j \cos \omega t_j & \sum_j \sin \omega t_j \cos \omega t_j & \sum_j \cos^2 \omega t_j & \sum_j t_j \cos \omega t_j \\ \sum_j t_j & \sum_j t_j \sin \omega t_j & \sum_j t_j \cos \omega t_j & \sum_j t_j^2 \end{pmatrix} \tag{6}$$

If the summation limits are symmetric with respect to the time origin (which is the time the spacecraft is at culmination) then all the odd functions will vanish. It is useful to introduce the following definitions:

279

ψ = half-pass length in radians

S = sampling interval (60 sec)

N = number of points less 1

$$= \frac{2\psi}{S\omega}$$

It should be noted that in JPL navigation software the assumed accuracy of Doppler data is always referenced to a 60-seconds sample interval, making 60 seconds a convenient choice for S. The integral approximations of the summations in equation (6) can be expressed as

$$\sum_j f(\omega t_j) = \sum_{\omega t_j = -\psi}^{\omega t_j = \psi} f(\omega t_j)$$

$$= \frac{N}{2\psi} \int_{-\psi}^{\psi} f(\varphi) d\varphi$$

$$= \frac{1}{S\omega} \int_{-\psi}^{\psi} f(\varphi) d\varphi \tag{7}$$

Performing the integrals of the information array and replacing N with $2\psi/(S\omega)$, the following result is obtained:

$$\Lambda = \frac{1}{S\omega} \begin{pmatrix} 2\psi & 0 & 2\sin\psi & 0 \\ 0 & \psi - \frac{1}{2}\sin 2\psi & 0 & (2/\omega)(\sin\psi + \psi\cos\psi) \\ 2\sin\psi & 0 & \psi + \frac{1}{2}\sin 2\psi & 0 \\ 0 & (2/\omega)(\sin\psi + \psi\cos\psi) & 0 & (2\psi^3)/(3\omega^2) \end{pmatrix} \tag{8}$$

Note that $1/\omega$ shows up in the last column and row of Λ each time there is a factor of t_j that does not include ω.

Before inverting the information array, it is worth noting that the acceleration uncertainty often has some *a priori* information associated with it. If $\sigma_{q_a p}$ is the *a priori* uncertainty in the acceleration, then the last term of Λ is

$$\Lambda(4,4) = (2\psi^3)/(3S\omega^3) + Q^2 \tag{9}$$

with

$$Q^2 = \frac{\sigma_\rho^2}{\sigma_{q_a p}^2}$$

where σ_ρ appears due to the way the covariance will be defined. Typical values for $\sigma_{q_a p}$ are 10^{-12} km/sec^2, although for Ulysses the value is 2 orders of magnitude larger, as mentioned above. Assuming a typical (if conservative) measurement uncertainty of 1 mm/sec over a 60-second count time, the ratio Q^2 varies from 10^8 to 10^{12} for values of $\sigma_{q_a p}$ between 10^{-10} and 10^{-12} km/sec^2, which brackets the values of the first term of $\Lambda(4,4)$. Consequently one may expect two sets of solutions depending of the value of $\sigma_{q_a p}$, with the solution for small $\sigma_{q_a p}$ being equivalent to the original Hamilton-Melbourne result with no acceleration term at all. For the some choices of Q, the result will depend equally on the both sets of solutions, but for most values one set will prevail.

The task of inverting Λ to get the covariance is made much easier by observing that Λ is really just two two-by-two matrices, as can be seen by reordering the parameters such that the state vector is $(a\ c\ b\ q)$. The inverse can then be obtained by inverting the two small matrices separately, giving the result

$$\sigma_a^2 = S\omega\sigma_\rho^2 \left[\frac{\psi + \frac{1}{2}\sin 2\psi}{2\psi^2 + \psi\sin 2\psi - 4\sin^2 \psi} \right] \tag{10}$$

$$\sigma_{ac} = S\omega\sigma_\rho^2 \left[\frac{-2\sin \psi}{2\psi^2 + \psi\sin 2\psi - 4\sin^2 \psi} \right] \tag{11}$$

$$\sigma_c^2 = S\omega\sigma_\rho^2 \left[\frac{2\psi}{2\psi^2 + \psi\sin 2\psi - 4\sin^2 \psi} \right] \tag{12}$$

$$\sigma_b^2 = S\omega\sigma_\rho^2 \left[\frac{\frac{2}{3}\psi^3 + Q^2 S\omega^3}{Q^2 S\omega^3(\psi - \frac{1}{2}\sin 2\psi) - 2\left(2\psi^2 - \frac{\psi^4}{3} + 2(1 - \psi^2)\sin^2 \psi + \left(\frac{\psi^3}{6} - 2\psi\right)\sin 2\psi\right)} \right] \tag{13}$$

$$\sigma_{bq} = S\omega^2\sigma_\rho^2 \left[\frac{-2(\sin \psi - \psi\cos \psi)}{Q^2 S\omega^3(\psi - \frac{1}{2}\sin 2\psi) - 2\left(2\psi^2 - \frac{\psi^4}{3} + 2(1 - \psi^2)\sin^2 \psi + \left(\frac{\psi^3}{6} - 2\psi\right)\sin 2\psi\right)} \right] \tag{14}$$

$$\sigma_q^2 = S\omega^3\sigma_\rho^2 \left[\frac{\psi - \frac{1}{2}\sin 2\psi}{Q^2 S\omega^3(\psi - \frac{1}{2}\sin 2\psi) - 2\left(2\psi^2 - \frac{\psi^4}{3} + 2(1 - \psi^2)\sin^2 \psi + \left(\frac{\psi^3}{6} - 2\psi\right)\sin 2\psi\right)} \right] \tag{15}$$

Equations 10-12 are identical (after some minor algebra) to comparable equations in Refs. 1 and 2. The complete independence of the uncertainty of a and c from the effects of adding an acceleration term is striking, although in retrospect it can be explained due to the orthogonality of the even functions 1 and $\cos \omega t$ with the odd functions $\sin \omega t$ and t. Equations 13-15 show the two families of solutions depending on the value of Q. The value of $S\omega^3$ is 2.33×10^{-11} sec^{-2}, which requires Q^2 to be on the order of 10^{12} sec^2 (corresponding to $\sigma_{q_{ap}} = 10^{-12}$ km/sec^2) to dominate these equations. When Q^2 is sufficiently large, σ_b^2 approaches the form found in Refs 1 and 2, which is always smaller than σ_c^2. Thus the effect of adding significant acceleration uncertainty to a symmetric pass is to change the identity of the best-determined angular parameter from b to c. This effect can be clearly seen in Figure 1, which plots the estimate uncertainty for each parameter (including b with and without an acceleration uncertainty) as a function of the pass half-width ψ.
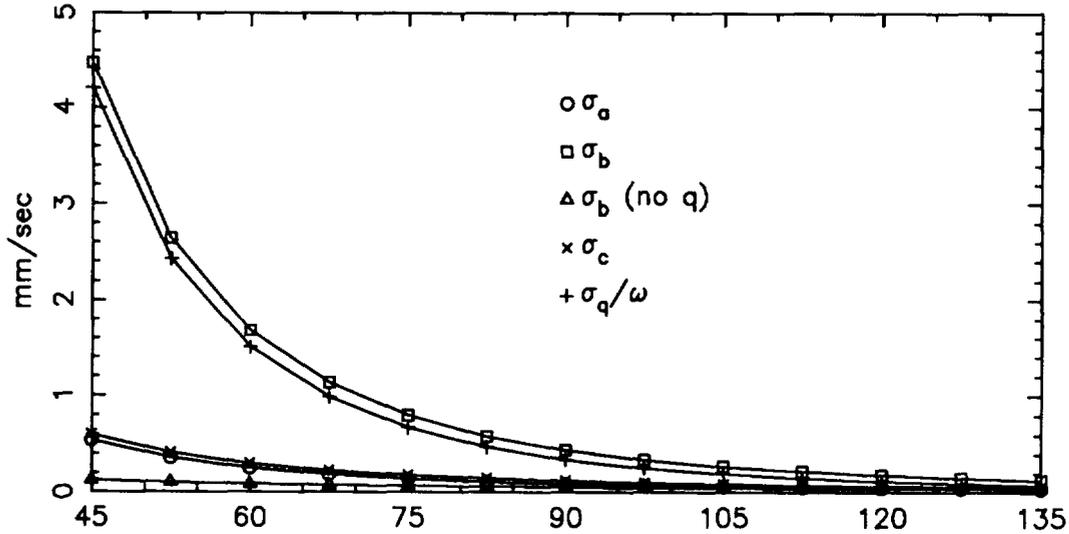
Figure 1: Parameter sigmas vs. pass half-width ψ (in degrees)

The two non-zero correlation coefficients are suggested by the close proximity of a to c and b to q/ω in Figure 1. The equations for the correlation coefficients are

$$\rho_{ac} = \frac{-2^{\frac{1}{2}} \sin \psi}{\psi(1 + \frac{1}{2\psi} \sin 2\psi)^{\frac{1}{2}}} \tag{16}$$

$$\rho_{bq} = \frac{-6^{\frac{1}{2}}(\sin \psi - \psi \cos \psi)}{\psi^2(1 - \frac{1}{2\psi} \sin 2\psi)^{\frac{1}{2}}} \tag{17}$$

assuming $Q^2 S \omega^3$ is small relative to other terms. As noted in Ref. 1, $-1.0 \leq \rho_{ac} \leq -0.9$ for pass lengths of 12 hours or less. However, tracking for 24 hours completely removes this correlation. On the other hand, $-1.0 \leq \rho_{bq} \leq -0.9$ for pass lengths of up to 20 hours, and $\rho_{bq} = -0.78$ for a 24-hour pass. This seems reasonable in consideration of the expansions of $(1 - \cos t)$ and $(t - \sin t)$ about zero, whose first non-zero terms are $t^2/2$ and $t^3/6$ respectively. If the geocentric angular velocity and acceleration of the a spacecraft was small enough that a 36 hour pass could be analyzed with these equations, ρ_{bq} would be -0.11, but this is unlikely ever to be the case in practice. The values of ρ_{bq} and ρ_{ac} are plotted in Figure 2.
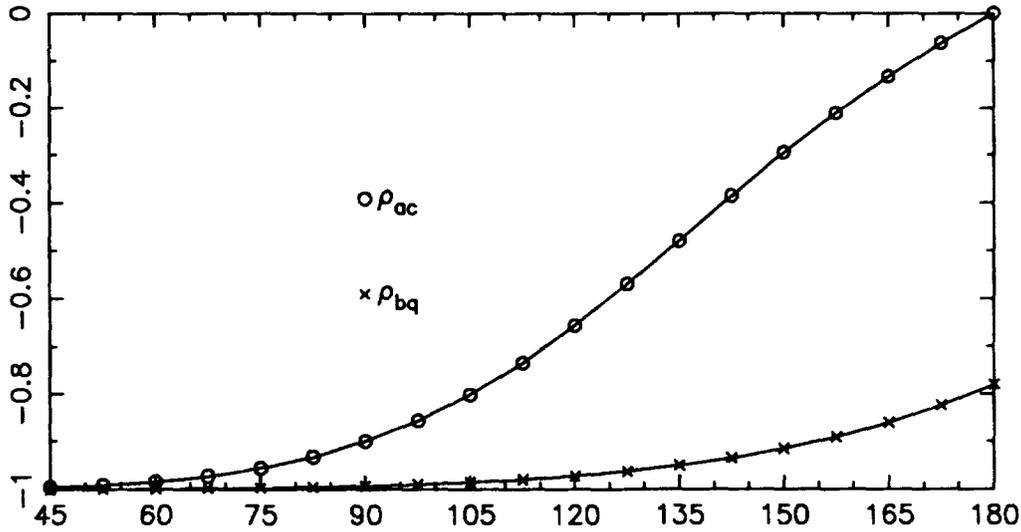
Figure 2: Correlation coefficients vs. pass half-width ψ (in degrees)

At this point it is useful to give the relationship between a, b, and c and $\dot{r}$, α, and δ. At the time of Ref. 1, station location errors were a significant concern, but in the modern era, Very Long Baseline Interferometry (VLBI) measurements have reduced these errors to 10 cm or less 1σ, which largely remove their effect from estimates of the geocentric angular position of a spacecraft. Otherwise, the station longitude errors increase the right ascension uncertainty, and r_s errors increase both right ascension and declination uncertainty. It can be easily shown that

$$\sigma_{\dot{r}}^2 = \sigma_a^2 \tag{18}$$

$$\sigma_\delta^2 \simeq \frac{\sigma_b^2}{(r_s \omega)^2 \sin^2 \delta} \tag{19}$$

$$\sigma_\alpha^2 \simeq \frac{\sigma_c^2}{(r_s \omega)^2 \cos^2 \delta} \tag{20}$$

$$\sigma_{\dot{r}}^2 = \sigma_q^2 \tag{21}$$

by making use of the fact that ωt_0 is small (for Equation (20)). The usual navigation concern has been with declinations at or near zero, which causes a singularity in σ_δ for this approximation, although higher-order

terms and data arcs extending into regions of higher declination usually mitigate this effect in practice. A similar singularity would seem to exist at $\delta = 90°$ for α, but this can be resolved by noting that the geocentric angular direction perpendicular to δ can be expressed $\alpha_n = \alpha \cos \delta$, so

$$\sigma_{\alpha_n}^2 = \cos^2 \delta \sigma_\alpha^2$$

$$\simeq \frac{\sigma_c^2}{(r_s \omega)^2} \tag{22}$$

again making use of the fact that ωt_0 is small. There is still a problem at exactly $\delta = 90°$ because both b and c go to zero and cannot be separated. However, this situation is much less severe and more easily avoided than the problem that arises at zero declination.

The uncertainty predictions of these analytical results can now be evaluated using the Ulysses trajectory to produce high- and low-declination examples, which will later be checked against purely numerical results. On November 12, 1994, the declination of Ulysses was $-75°$, and the distance from the Earth was 330 million km. Neglecting the effects of acceleration uncertainty for the moment, and assuming a 24-hour pass (typical passes at the same station were over 6 days long), the following values are obtained:

$$\sigma_{\dot{r}} = 0.0264 \text{ mm/sec}$$
$$\sigma_b = 0.0373 \text{ mm/sec}$$
$$\sigma_\delta \simeq 102 \text{ nrad}$$
$$\sigma_c = 0.0373 \text{ mm/sec}$$
$$\sigma_\alpha \simeq 380 \text{ nrad}$$
$$\sigma_{\alpha_n} \simeq 98 \text{ nrad}$$

The results above use 5205 km as a typical value of r_s for DSN stations. In terms of absolute position, the uncertainty is 32.4 km and 33.6 km in the direction of right ascension and declination, respectively, for an overall plane-of-sky position uncertainty of 46.7 km. If acceleration uncertainty with no *a priori* is included, the declination uncertainty increases to 163 nrad, or 53.6 km, for a total plane-of-sky position uncertainty of 62.6 km. Thus for very long passes at high declinations the effect of adding acceleration uncertainty is not severe.

In contrast, a 12 hour pass without acceleration uncertainty for a spacecraft with a declination of 10° would produce angular uncertainties of 324 nrad and 800 nrad for right ascension and declination, respectively. The large increase in the declination uncertainty is mostly due to the $(1/\sin \delta)$ term, as otherwise the declination uncertainty would be less than the right ascension uncertainty, due to the fact that $\sigma_c > \sigma_b$ when no acceleration is estimated. If acceleration uncertainty is included, the declination uncertainty increases to 6660 nrad, due to the large increase in σ_b. The addition of acceleration uncertainty therefore almost destroys any information about declination for spacecraft at fairly low declinations.

As mentioned earlier, the case of tracking passes that are not symmetric about the time of the spacecraft culmination may be handled by a rotation of the symmetric results. If ϕ is the offset of the center of the pass from the culmination point, then

$$\begin{pmatrix} c' \\ b' \end{pmatrix} = \begin{pmatrix} \cos \phi & -\sin \phi \\ \sin \phi & \cos \phi \end{pmatrix} \begin{pmatrix} c \\ b \end{pmatrix} \tag{23}$$

where b' and c' are the parameters b and c rotated by ϕ. The rotation matrix in equation (23) can be extended to be a full mapping matrix M, where

$$M = \begin{pmatrix} 1 & 0 & 0 & 0 \\ 0 & \cos\phi & -\sin\phi & 0 \\ 0 & \sin\phi & \cos\phi & 0 \\ 0 & 0 & 0 & 1 \end{pmatrix}$$ (24)

Then the covariance P' of $(a\ c'\ b'\ q)$ is given by

$$
\begin{aligned}
P' &= MPM^T \\
&= \begin{pmatrix}
\sigma_a^2 & \cos\phi\,\sigma_{ac} & \sin\phi\,\sigma_{ac} & 0 \\
\cos\phi\,\sigma_{ac} & \cos^2\phi\,\sigma_c^2 + \sin^2\phi\,\sigma_b^2 & \sin\phi\cos\phi(\sigma_c^2 - \sigma_b^2) & -\sin\phi\,\sigma_{bq} \\
\sin\phi\,\sigma_{ac} & \sin\phi\cos\phi(\sigma_c^2 - \sigma_b^2) & \cos^2\phi\,\sigma_b^2 + \sin^2\phi\,\sigma_c^2 & \cos\phi\,\sigma_{bq} \\
0 & -\sin\phi\,\sigma_{bq} & \cos\phi\,\sigma_{bq} & \sigma_q^2
\end{pmatrix}
\end{aligned}
$$ (25)

Equation (25) could be used to tailor the symmetry of the pass to obtain a better measurement of one angular direction at the expense of the other. However, the usefulness of these equations in the past would have been limited, because typical tracking passes for spacecraft in the ecliptic were over eight hours long anyway, and introducing asymmetry in the pass would have meant shortening the total tracking time, which is guaranteed to produce poorer results. In addition, the difficulty in measuring low values of declination means that a symmetric pass is generally the most desirable geometry in such cases.

This limitation does not apply to spacecraft at high declinations or to tracking schedules that have short pass lengths for programmatic reasons. In addition to Ulysses, an example of the first case would be NEAR after the Earth flyby, when the spacecraft is continuously in view for three months (longer than was the case for Ulysses) from the DSN complex at Canberra. Following the first 30 days after the flyby, NEAR requires only three 8-hour passes/week for telemetry purposes, as described in Reference 4. While NEAR navigation requires even fewer passes, Doppler data is expected from all telemetry passes, and so the 3 passes per week could be distributed to provide the same amount of information about both angular components. This can be accomplished by orienting the midpoints of the passes 6 hours (90°) apart. However, information about one component of the geocentric direction is often more important to navigation performance than information about the other component, which could lead to all the tracking being concentrated at one geometry. In the case of short pass lengths, such as the sparse four-hour passes typically proposed for Discovery missions during their cruise phases, the uncertainty in right ascension exceeds the uncertainty in declination for declinations over 8°. This might warrant specifying non-symmetric passes if right ascension information is important to the mission navigation.

While Ulysses is fairly unique in having a large acceleration uncertainty, such scenarios are possible on other spacecraft in contingency modes (which is actually the case for Ulysses as well). When the acceleration uncertainty exceeds about 10^{-11} km/sec^2, the declination uncertainty is maximized for a symmetric pass, so fixed-length tracking passes could be oriented in a non-symmetrical way to mitigate this effect. However, for spacecraft in the ecliptic, it is limited how much can be accomplished by this strategy, due to the half-day viewperiods and the additional uncertainty of media effects at low elevations, which degrade non-symmetric passes more than symmetric ones.

Another application of these equations is the use of one-way Doppler as a measurement, which is dependent on the stability of the spacecraft oscillator. (Two-way Doppler is also dependent on the stability of the reference oscillator at the tracking station, but the required stability is much more easily achieved on the ground than on a spacecraft). A parameter estimating a frequency rate on a spacecraft oscillator has the same form as an acceleration parameter, so $\dot{f}$ could be substituted for q throughout these equations. As a frequency bias f_b is also typically present, $\sigma_a^2 = \sigma_r^2 + \sigma_{f_b}^2$, which limits the knowledge of geocentric range-rate to the a priori uncertainty of the frequency bias or a frequency bias estimate obtained over a several-month data arc.

Unfortunately, it must be noted that the estimation technique used for Ulysses operations, which involved eight independent accelerations per day, has not been successfully dealt with analytically. However, work

284

will continue in this area, because it should not require an inordinate amount of effort to develop this theory, especially with the existence of the results already presented here.

Numerical Results

The numerical results presented here were obtained using the JPL Orbit Determination Program, which includes both single-batch and batch-sequential least-squares modes. Both simulated and real tracking data with time spans ranging from 12 hours to two months were used to obtain the estimate covariances and orbit solutions discussed here.

In order to test the accuracy and relevance of the analytical results presented so far, the examples given above were simulated using the reconstructed Ulysses trajectory. On November 12, 1994, which at $-75°$ is close to the maximum declination encountered in the southern pass, a total of 144 Doppler points with a 600 second sample time were simulated over 24 hours centered on spacecraft culmination. Only the geocentric angular position and range-rate were estimated to keep the filter from trying to estimate parameters that are only very poorly determined from one day of tracking, and no acceleration term was initially included. The resulting plane-of-sky uncertainty in the declination and right ascension directions was 54.0 km and 32.8 km, respectively. The right ascension uncertainty is almost exactly the same as the theoretical result presented earlier, while the declination result is 60 per cent higher. When a single radial acceleration is included with an *a priori* uncertainty of 10^{-10} km/sec^2 the results are 54.7 km and 33.2 km, which is very close to the predicted values, and the acceleration uncertainty was reduced to 1.1×10^{-12} km/sec^2, which is actually 35 per cent smaller than the predicted value. In each case, the radial velocity uncertainty was 5 mm/sec, which is about 200 times larger than the prediction. In both of these cases the numerically-computed correlation between the radial velocity and the right ascension is almost one, while the analytical correlation is zero. While this explains the larger radial velocity at one level, it is not clear why the correlation does not behave as predicted. Fortunately, the angular uncertainties are of primary interest, and the radial velocity uncertainty is still much better determined than any other velocity component.

The low declination case was examined using a 12 hour pass centered around culmination of the reconstructed Ulysses trajectory on December 10, 1992. In the absence of acceleration uncertainty, the plane-of-sky uncertainty in the declination and right ascension directions was 947 nrad and 363 nrad, respectively, which is about 15 per cent higher than predicted above. However, when acceleration was estimated, the plane-of-sky uncertainties were 6640 nrad and 446 nrad, respectively, and the acceleration uncertainty was 2.45×10^{-11} km/sec^2. The declination uncertainty is almost exactly as predicted, but the right ascension and acceleration uncertainty are about 40 per cent higher. The radial velocity uncertainty varies from 16 mm/sec without acceleration uncertainty, which is about 200 times larger than predicted, to 108 mm/sec with acceleration uncertainty. In contrast to the results above, the numerically-computed correlation between declination and radial velocity is almost -1 for both these cases, and the correlation between radial velocity and right ascension is about -0.6. The declination and acceleration are highly correlated, as expected, so the radial velocity uncertainty increases with the declination uncertainty when acceleration is added to the filter. However, the reason for the high correlation between declination and radial velocity is not explained, nor is the difference between the radial velocity correlations for these two examples. It may be that the direction and magnitude of the angular rate of the spacecraft, and/or the radial acceleration of the spacecraft, play a greater role than expected. Fortunately, the angular uncertainties behave as expected for both of these cases, so the analytic results can still be used as an approximation of the angular information content of a pass of Doppler data.

The actual strategy used by Ulysses was evaluated using the high declination case ($\delta = -75°$) by adding eight accelerations, each active over a three hour period and with an *a priori* uncertainty of 10^{-10} km/sec^2, which resulted in plane-of-sky uncertainties of 531 km and 535 km for the declination and right ascension directions, and a radial velocity uncertainty of 83 mm/sec. This roughly corresponds to the result of combining eight 4-hour passes, so it appears that while there is some continuity of angular information between acceleration intervals, the acceleration uncertainty at this level is enough to almost separate the estimates.

The result of extending one day data arcs to sixty to a hundred days is highly dependent on the trajectory of the spacecraft being tracked. The Ulysses trajectory is inclined almost 80° to the ecliptic, and the spacecraft velocity during the Southern pass is high due to its proximity to perihelion, which occurred in March, 1995. All of this contributes to a significant geometry change over any time span of two months or more during

the Southern pass, which helps to determine all of the components of the spacecraft state by mapping the observable quantities at one time into non-observable quantities at different epoch.

These long-arc effects are demonstrated on a time span extending one month on either side of November 12, 1994. During this time the spacecraft declination varied between $-63°$ and $-75°$, and the spacecraft was continuously in view from the Canberra complex of the DSN. A total of 7790 usable Doppler points at 10 minute intervals were obtained during this time. There were seven attitude thruster events big enough to warrant separate treatment as impulsive delta-Vs as well. The estimated parameters included spacecraft state, solar pressure coefficient, one component of each impulsive maneuver, and a radial acceleration for each three-hour interval. The effects of the following consider parameters were also included: station locations, Earth ephemeris, and media calibrations. The filter parameters and Ulysses operational orbit determination techniques are described in much more detail in Reference 5, and will not be repeated here.

Solutions were obtained in this manner for a nominal *a priori* acceleration uncertainty of 10^{-10} km/sec^2, which was used operationally, and an alternate smaller *a priori* uncertainty of 10^{-11} km/sec^2. In both cases the smoothed covariance was mapped to the plane-of-the sky in the midpoint of the data arc. The nominal case produced an uncertainty of 74 km and 71 km in the declination and right ascension directions, and a range and range-rate uncertainty of only 42 km and 11 mm/sec. Since the geocentric range at this time is close to the heliocentric range, the primary effect determining the geocentric range is the heliocentric period of the spacecraft. Every parameter that can be compared with the similar one-day case above shows eight-fold improvement, which attests to the strength of the Earth-Sun-spacecraft geometry in determining the orbit based on such relatively poor one-day results.

While the nominal case had no consider parameters that made an appreciable difference in the results, the alternate case was strongly affected by the day-time component of the ionosphere. Before any non-estimated parameters were considered, the plane-of-sky uncertainties were 9 km in each component, while the range and range-rate uncertainties were 38 km and 1.4 mm/sec, respectively. After consider effects are applied, the plane-of-sky uncertainties were 19 km each, the range was unchanged, and the range-rate uncertainty was 2.5 mm/sec. These results show that the large *a priori* radial acceleration uncertainty increases the plane-of-sky uncertainty within the data arc, even though the radial uncertainty, based on the measurements over the entire data arc, is unchanged. It should also be noted that the Doppler data do not fit well at all for the alternate case, whereas the nominal case easily produces post-fit residual rms values of 0.13 mm/sec, well below the 1 mm/sec data weight. The nominal case also demonstrates that operational Ulysses solutions had difficulty meeting the 1000 km reconstruction requirement when data arcs of two to three months were used.

Conclusions

The Ulysses orbit determination experience provided the impetus to re-examine the information content of a single pass of Doppler data. Extending previous derivations to 24-hour passes and high declinations was found to be possible without difficulty, and a radial acceleration term was added. The acceleration term was found to significantly degrade declination estimates for symmetric passes. A simple means was developed to rotate the results of a symmetric pass to any other tracking geometry. While the agreement of the analytical results with numerical results leaves something to be desired in radial velocity, the analytical results are a useful predictor of angular and acceleration accuracy. The long-arc results show that the relative motion of the Earth and the spacecraft in their orbits around the Sun produces a much better result than could be obtained from a short-arc estimate.

Acknowledgements

References:

1. Hamilton, T. W., and Melbourne, W., G. "Information Content of a Single Pass of Doppler Data from a Distant Spacecraft," *JPL Space Programs Summary 37-39*, Vol. 3, May 31, 1966.

2. Muellerschoen, R. J. "Information Content of a Single Non-Symmetric Pass of Doppler Data from a Distant Spacecraft," JPL Interoffice Memorandum 314.5-1029, July 1, 1986.

3. Bertotti, B., Ambrosini, R., Asmar, S. W., Brenkle, J. P., Comoretto, G.,Giampieri, G., Iess, L., Messeri, A., Vecchio, R., Wahlquist, H. D. "Ulysses' Gravitational Wave Experiment Report on the First Opposition," pg. 32, Istituto di Fisica dello Spazio Interplanetario, Frascati, Italy, December 1991.

4. "NEAR Detailed Mission Requirements," pg. 2-3, Johns Hopkins University/ Applied Physics Laboratory Document, November 1994.

5. McElrath, T. P, Tucker, B., Criddle, K. E., Menon, P. R., Higa, E. S. "Ulysses Navigation at Jupiter Encounter," AIAA/AAS Astrodynamics Conference, AIAA 92-4524, 10-12 August 1992.

Application of Non-coherent Doppler Data Types for Deep Space Navigation

Shyam Bhaskaran
Jet Propulsion Laboratory
California Institute of Technology
Pasadena, California

Abstract

Recent improvements in computational capability and Deep Space Network technology have renewed interest in examining the possibility of using one-way Doppler data alone to navigate interplanetary spacecraft. The one-way data can be formulated as the standard differenced-count Doppler or as phase measurements, and the data can be received at a single station or differenced if obtained simultaneously at two stations. A covariance analysis is performed which analyzes the accuracy obtainable by combinations of one-way Doppler data and compared with similar results using standard two-way Doppler and range. The sample interplanetary trajectory used was that of the Mars Pathfinder mission to Mars. It is shown that differenced one-way data is capable of determining the angular position of the spacecraft to fairly high accuracy, but has relatively poor sensitivity to the range. When combined with single station data, the position dispersions are roughly an order of magitude larger in range and comparable in angular position as compared to dispersions obtained with standard data two-way types. It was also found that the phase formulation is less sensitive to data weight variations and data coverage than the differenced-count Doppler formulation.

I Introduction

With increasing emphasis on controlling the costs of deep space missions, several options are being examined which decrease the costs of the spacecraft itself. One such option is to fly spacecraft in a non-coherent mode, that is, the spacecraft does not carry a transponder capable of coherently returning a carrier signal. Historically, one-way Doppler data have not been used as the sole data type due to the instability of spaceborne oscillators, the use of S-band frequencies, and the corresponding error sources which could not be adequately modelled. However, with the advent of high-speed workstations and more sophisticated modelling ability, the possibility of using one-way Doppler is being re-examined. This paper assesses the navigation performance of various one-way Doppler data types for use in interplanetary missions. As a representative interplanetary mission, the Mars Pathfinder spacecraft model and trajectory were used to perform the analysis. Comparisons are given between results employing Doppler data formulated as standard differenced-count Doppler (which yields a frequency measurement) as well as accumulated carrier phase (which yields a distance measurement, usually given in terms of cycles). Combinations of one-way data obtained simultaneously at two different stations and then differenced (to produce an angular type measurement) and single station one-way data are shown to produce results which may satisfy future mission requirements.

II Spacecraft Trajectory

In order to perform the analysis, a representative interplanetary trajectory was needed. The one used in this study is the Mars Pathfinder cruise from Earth to Mars. The spacecraft is injected into its trans-Mars trajectory on January 3, 1997, and reaches Mars on July 4, 1997. A schematic of this trajectory is shown in Figure 1. In between, there are four Trajectory Correction Maneuvers (TCMs) (on February 2, March 3, May 5, and June 24), with mean magnitudes of 22.1, 1.4, 0.2, and 0.1 m/s, respectively. The first two are to remove an injection targeting bias which the initial interplanetary trajectory contains in order to satisfy planetary quarantine
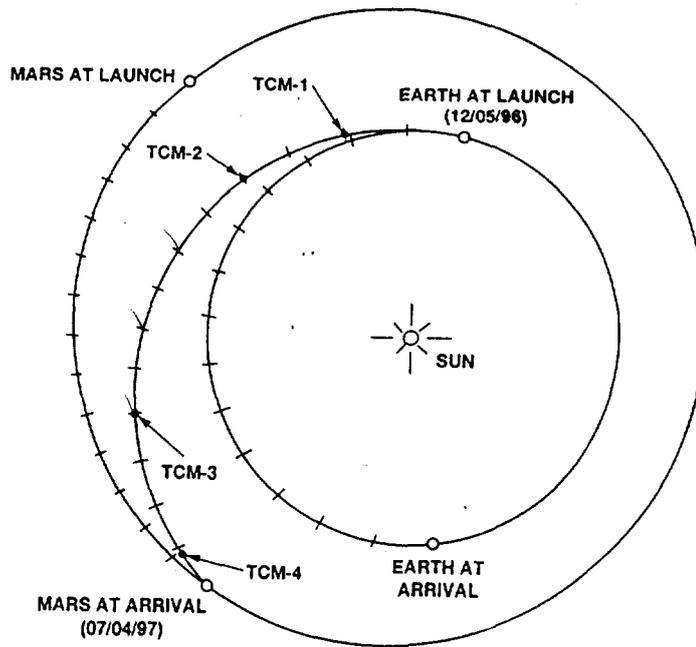
Figure 1: Mars Pathfinder Trajectory
(provided by P. H. Kallemeyn, Mars Pathfinder Navigation)

requirements. The final two are used to precisely target the spacecraft for its final approach and entry into the Martian atmosphere. Since Pathfinder goes directly from its interplanetary trajectory to atmospheric entry, the aim point of the targeting maneuvers is chosen such that the entry flight path angle is between $14.5°$ and $16.5°$ [1]. This corresponds to an entry corridor in the B-plane (a plane perpendicular to the incoming asymptote of the trajectory and passing through the center of mass of Mars) of about 50 km wide in the cross-track direction. The downtrack and normal direction constraints are chosen to ensure that the spacecraft reaches the landing site with a 99% probability of being within a 200 km downtrack by 100 km crosstrack ellipse[1].

III Doppler Measurement Model

When operating in one-way mode, the Deep Space Network (DSN) measures the Doppler frequency of the carrier signal received from a spacecraft by comparing it with a reference frequency generated by a local oscillator. The two signals are differenced, and a counter measures the accumulated phase of the resultant signal over set periods of time, called the count time. The total phase change over the count time, divided by the count time, produces a measure of the Doppler shift of the incoming signal, with which the range rate of the spacecraft can be inferred. This is referred to as differenced-count Doppler, the standard measurement used for all deep space missions thus far. If instead, the original phase data themselves are used, a measure of the change in the range of the spacecraft over the length of the pass is obtained, with the initial range at the start of the pass being an unknown. Although in principle this a fairly powerful data type, it has not been used in the past due to operational problems associated with cycle slips, whereby the receiver momentarily loses lock with the incoming signal. Advances in technology over the years, however, have made cycle slips less frequent, and thus there is renewed interest in examining the possibility of using the phase measurement directly as a data type.

The four data types investigated in this study were one-way Doppler, one-way differenced Doppler, one-way phase, and one-way differenced phase. In order to obtain a qualitative understanding of what information is

available with these data, some simple equations will be presented. Neglecting error sources and relativistic effects for the moment, one-way Doppler data is approximately proportional to the topocentric range-rate of a spacecraft:

$$f \approx f_T(\dot{\rho}/c) \tag{1}$$

where

f = the observed Doppler shift of the carrier signal
f_T = the carrier frequency transmitted by the spacecraft
$\dot{\rho}$ = the station-spacecraft range rate, and
c = the speed of light.

Hamilton and Melbourne [2] derived a simple approximation for the topocentric range rate seen at a tracking station in terms of the cylindrical coordinates of the station and the geocentric range rate, right ascension, and declination of the spacecraft:

$$\dot{\rho} \approx \dot{r} + \omega r_s cos\delta sin(\omega t + \alpha_s + \lambda_s - \alpha) \tag{2}$$

where

$\dot{r}$ = the geocentric range rate of the spacecraft
α, δ = the geocentric right ascension and declination of the spacecraft
ω = the rotation rate of the earth
α_s = the right ascension of the sun
r_s, λ_s = the spin radius and longitude of the station.

Thus, the signal seen at the station represents the sum of the geocentric velocity of the spacecraft and short term sinusoidal variations due to the rotation of the Earth. The amplitude of the sinusoidal variation is proportional to the cosine of the declination of the spacecraft, and its phase includes information about the right ascension. Now, if the signals received simultaneously at two stations are differenced, the geocentric range rate drops out of the equation and only the periodic variations are left. This implies that differenced Doppler data are incapable of directly measuring the range of the spacecraft, but can better resolve its angular position than the undifferenced data. In addition, the differenced data are nearly insensitive to short term variations in the velocity, such as those due to short thruster firings.

If eqn.(1) is now integrated over the interval from t_0 to t, the following expression for the Doppler phase is obtained:

$$\phi_t - \phi_{t_0} \approx f_T(\rho_t - \rho_{t_0})/c \tag{3}$$

where

ρ = the topocentric range of the spacecraft at times t and t_0, and
ϕ = the measured phase of the carrier signal at times t and t_0.

Thus, the phase of the received carrier signal at a given time measures the change in range from the previous time. At the beginning of the pass, there will be an unknown bias representing the initial range to the spacecraft. An analytical approximation for the difference of two range measurements received simultaneously at two stations can be written in terms of the baseline vector between them as [3]:

$$\Delta\rho \approx r_B cos\delta cos(\alpha_B - \alpha) + z_B sin\delta \tag{4}$$

where

r_B = baseline component normal to the Earth's spin axis
z_B = baseline component parallel to Earth's spin axis
α_B = the baseline right ascension
α = the spacecraft right ascension
δ = the spacecraft declination.

Once again, it can be seen that differencing the data removes direct information about the radial distance to the spacecraft and the result is given in terms of its angular position.

All data used in this analysis were assumed to be obtained at X-band frequencies (7.2-8.4 GHz). The differenced data types were taken when the spacecraft was visible simultaneously from two DSN stations above an elevation cutoff of 15 degrees. This resulted in overlaps of roughly four hours in length occurring over the Goldstone-Madrid and Goldstone Canberra baselines throughout the data arc. No data over the Canberra-Madrid baseline could be obtained.

Data scheduling was set as follows. Single station one-way data were taken during every other pass at all three DSN sites, starting at the beginning of the Mars Pathfinder trajectory (January 3, 1997) and ending at the data cutoff on June 19, 1997. This results in roughly 14,000 points (at 10 minute intervals). Two-station differenced data was scheduled at every overlap until the data cutoff date, resulting in approximately 6000 points. The assumed noise levels used were 0.1 and 1.0 cycles for phase data, and 0.05 and 0.5 mm/s for the Doppler data.

IV   Orbit Determination Error Analysis

Orbit determination is composed of several steps: generation of a reference trajectory, compution of observational partial derivatives with respect to the reference trajectory, and correction of the trajectory and error model parameters using an estimation algorithm, or filter. The associated error covariance of the estimated parameters is also obtained as part of this procedure. The error covariance analysis was performed using a modified version of JPL's standard orbit determination program software called MIRAGE [4]. MIRAGE is capable of modelling time varying stochastic parameters which have different "batch" lengths, that is, time steps over which the parameters are piecewise continuous.

In order to obtain a realistic estimate of the covariance, the dynamic forces affecting the spacecraft and the error sources affecting the data must be modelled properly. A detailed analysis of these model parameters has already been performed for the Mars Pathfinder mission [5]; the results will be summarized here. In the filter model, all known dynamic parameters and significant Doppler error sources are modelled and explicitly estimated. The dynamic parameters included the spacecraft state (position and velocity), coefficients for solar radiation pressure, random non-gravitational accelerations, and spacecraft maneuvers. The solar radiation pressure and random accelerations each have three components: a radial one along the earthline and two cross line-of-sight ones which are mutually orthogonal to the radial direction. These are modelled as stochastic Gaussian colored noise parameters, that is, an estimate is made for the parameters within each batch, and their values from one batch to another are statistically correlated with a characteristic decorrelation time input by the user. The solar radiation pressure coefficients vary slowly over the course of the mission as the reflectivity of the spacecraft changes so the decorrelation time of these parameters was set to 60 days. The uncertainties are roughly 5% of the nominal values of the coefficients. Stochastic accelerations are needed to model small thruster firings, such as those used for attitude updates. The size and frequency of these firings results in accelerations with decorrelation times of 5 to 6 days and an rms magnitude of about $2\mathrm{x}10^{-12}$ km/s^2 in the radial direction and $1\mathrm{x}10^{-12}$ km/s^2 in the crosstrack directions. Spacecraft maneuvers are deterministic in nature and, in general, can be modelled as impulsive velocity changes placed at the midpoint of the maneuver time. Experience on previous missions has shown that the maneuver magnitude can be controlled to around 1% accuracy, so the a-priori uncertainty in the maneuver parameters was set to 1% of the expected size of the ΔV for each midcourse maneuver. No constraints were placed on the direction. Table 1 summarizes all of the statistical values used in the filter.

Error sources which affect the data include media calibration errors (wet and dry troposphere, day and night ionosphere), solar plasma effects, Earth platform calibration errors (station location in cylindrical coordinates, pole location in cartesian x and y coordinates), and Earth rotation (UTC). The delays in the signal caused by its path through the troposphere and ionosphere are modelled, but errors still remain. Currently, the troposphere model is good to 5 cm and the ionosphere to 3 cm [6]. The errors vary at a relatively high frequency, and so the decorrelation time is set to a few hours. The station location set and its associated uncertainties are the DE234 coordinates developed for use by the Mars Observer (MO) mission [7]. The station location uncertainties were modified to approximately account for precession and nutation modelling errors as well. These values are assumed fixed for the duration of the Pathfinder trajectory. The polar motion and UTC variations can be predicted by the DSN to a level of around 10 to 15 cm, and they vary on the order 1 to 2 days. The a-priori uncertainties of

292

Table 1: A-priori 1σ Uncertainties of Filter Parameters

Parameter	A-priori Uncertainty	Correlation Time
Position (x, y, z)	100.0 km	-
Velocity $(\dot{x}, \dot{y}, \dot{z})$	1.0 m/s	-
Solar Radiation Pressure Coefficient (radial)	0.07	60 days
Solar Radiation Pressure Coefficient (cross line-of-sight)	0.02	60 days
Stochastic Acceleration (radial)	2.4×10^{-12} mm/s^2	5 days
Stochastic Acceleration (cross line-of-sight)	0.8×10^{-12} mm/s^2	5 days
Maneuvers	1% of nominal value	-
Station Locations (spin radius, z-height, longitude)	0.1 m	-
Troposphere (wet)	5 cm	2 hours
Dry Troposphere (dry)	5 cm	2 hours
Ionosphere (day)	3 cm	4 hours
Ionosphere (night)	1 cm	1 hour
Pole X and Y	0.1 m	2 days
Earth Rotation (UTC)	0.15 m	1 day

these error model parameters, along with their characteristic decorrelation time if they are stochastic variables, are also shown in Table 1. One point to note is that the Mars ephemeris uncertainties were not included in the filter. This was done so that the computed dispersions reflect only the strengths and weaknesses of the data in determining the spacecraft trajectory.

When one-way Doppler data are used, several additional error sources must also be taken into account. For single station data, the largest error source is the frequency drift of the spacecraft oscillator. Ultra Stable Oscillators of the class used by the Galileo and Mars Observer spacecraft are expected to be stable to around 1 part in 10^{12} over time spans of around a day. Over longer time spans, however, the frequency will wander and must be modelled. The method used to model this error source is to treat the bias as a random walk parameter. Qualitatively, the random walk model allows the parameter to move away from its value at the previous batch time step by an amount constrained by its given a-priori uncertainty. It differs from a Gaussian white or colored noise stochastic parameter in that the parameter does not simply oscillate around its mean value, but is allowed to wander from one time step to the next. This model was also intended to approximately account for solar plasma fluctuations, which induce frequency variations on the order of 1 part in 10^{14} over one day. For this study, a fairly modest stability of 1 part in 10^9 over the course of a day was assumed to be the nominal. The value for the oscillator bias is updated every hour, and its a-priori sigma corresponds to the change in frequency over an hour expected for the given stability.

The one-way Doppler phase formulation requires six additional parameters in the estimate list. Phase data is measured by counting the integer number of zero crossings of the signal; a resolver then determines the fractional portion of the phase at a given time. Initially, however, there will be an ambiguity in the number of cycles it took for the signal to reach the ground, and the phase when the receiver locks onto the signal. To account for this, a phase bias at all three DSN stations is included in the filter. The a-priori uncertainty of the bias is set to 1000 cycles (essentially infinity), and the parameter is reset at the beginning of each pass. Also, during data acquisition, the station clocks have small drifts relative to a time standard which cause the phase count to drift as well. The drift is calibrated at the stations using data from the Global Positioning System, but residual errors remain. The magnitude with which the drift manifests itself in the phase count is about 6×10^{-4} cycles/sec, so a phase drift parameter with this value for the a-priori uncertainty is also included in the filter. Once again, the parameter is reset at the beginning of each pass.

The primary advantage of using differenced data is that the spacecraft oscillator drift is effectively cancelled out when the single station Doppler data are differenced, thus removing a major error source. However, an additional error source will appear: the asynchronicity of the clocks at the two receiving stations. Currently, the clocks are calibrated to about the 5 nsec level (based on examination of Frequency and Timing Standard reports distributed weekly by the DSN) between each pair of stations. Thus, a parameter which represents this timing mismatch is added to the filter estimate list. In addition, the differenced phase data still requires parameters

Table 2: A-priori 1σ Uncertainties of One-way Measurement Error Parameters

Parameter	A-priori Uncertainty	Correlation Time
Frequency Bias	0.366 Hz	Random walk, value reset every hour
Phase Bias	1000 cycles	White noise, value reset at each pass
Phase Drift	6.0×10^{-4} cycles/s	White noise, value reset at each pass
Clock Offset	5 nsec	White noise, value reset at each pass

Table 3: 1σ Dispersion Ellipses in Radial-Transverse-Normal Coordinates

	Data Type(s) Used	Data Weight	$\sigma(\text{RxTxN})$ (km)
1	2-way Doppler + 2-way Range	0.05 mm/s 2.0 m	3.9 x 6.4 x 7.2
2	Differenced 1-way Phase	0.1 cycles	360.9 x 20.3 x 11.6
3	Differenced 1-way Phase	1.0 cycles	476.8 x 23.9 x 12.1
4	Differenced 1-way Doppler	0.05 mm/s	428.5 x 23.7 x 11.3
5	Differenced 1-way Doppler	0.5 mm/s	1307.0 x 63.3 x 19.3
6	Differenced 1-way Phase + 1-way Phase	0.1 cycles 0.1 cycles	66.4 x 10.8 x 11.5
7	Differenced 1-way Phase + 1-way Phase	1.0 cycles 1.0 cycles	68.7 x 12.1 x 12.1
8	Differenced 1-way Doppler + 1-way Doppler	0.05 mm/s 0.05 mm/s	76.9 x 12.7 x 11.1
9	Differenced 1-way Doppler + 1-way Doppler	0.5 mm/s 0.5 mm/s	254.1 x 33.7 x 18.7
10	Differenced 1-way Phase + 2-way Doppler	0.1 cycles 0.05 mm/s	6.7 x 8.3 x 11.1
11	Differenced 1-way Doppler + 2-way Doppler	0.05 mm/s 0.05 mm/s	6.8 x 8.4 x 10.8
12	2-way Doppler	0.05 mm/s	14.4 x 14.4 x 23.7

to model the phase bias and drift which, in this case, are errors in the differenced phase measurement due to relative clock drifts between the two station pairs. The magnitudes of the uncertainties are kept the same as before. All one-way measurement error parameters and uncertainties are summarized in Table 2.

V Results

Although normally the results of a covariance analysis of an interplanetary trajectory are given in terms of encounter coordinates, the so-called B-plane system, it is more instructive in this case to present the uncertainties in radial-transverse-normal (RTN) coordinates. In RTN coordinates, the radial direction is along the Earth-spacecraft vector, the transverse direction is in the plane defined by the radius and the velocity vector, and the normal direction is perpendicular to both, forming an orthogonal triad. When viewed in this frame, it is easier to see in which direction the various data types have their greatest strength.

Table 3 shows the results of the covariance analysis in RTN coordinates for all combinations of data tried thus far. The first element in the table is a "nominal" result using a standard tracking schedule for Pathfinder which includes standard two-way Doppler and range. It can be seen that the radial uncertainty is best determined, with the cross line-of-sight directions being marginally worse with a maximum uncertainty of 7.2 km. These results when mapped to the Mars B-plane are sufficient to meet the requirements of Pathfinder.

The second and third entries in the table were obtained using only one-way phase data, weighted at 0.1 and 1.0 cycles, respectively. The result clearly shows the ability of the differential data type to determine the angular position of the spacecraft as seen from the Earth. Using a data weight of 0.1 cyles, the normal direction is determined to 11.6 km, which compares fairly well with the 7.2 km result using Doppler and range. The

uncertainty in the transverse direction does not compare quite as well, about a factor of three times worse than the nominal, but is still at a reasonable magnitude. The radial direction however, is very poorly determined, with the uncertainty using differenced phase data being about two orders of magnitude worse than the standard case. Changing the data weight from 0.1 to 1.0 cycles has little effect in the transverse and normal directions, but degrades the radial sigma by around 30%.

For comparison, the uncertainties using differenced one-way data formulated as Doppler frequency measurements were also examined (entries 4 and 5 in Table 3). The results are fairly similar to those of differenced phase data in the transverse and normal directions when the tighter data weight was used on the differenced Doppler. With the data weighted at 0.5 mm/s, however, the numbers are degraded considerably, especially in the radial direction.

Due to its inability to effectively discern the range to the spacecraft, it is highly unlikely that one-way differenced data alone would be sufficient to satisfy the navigation requirements of any realistic missions. It is desirable therefore to augment the differenced data with another data type, the obvious choice being single station one-way data. Entries 6 and 7 in Table 3 show the results of combining one-way phase with differenced phase at the two data weights. The effect is quite dramatic in the radial direction, with the uncertainty brought down from 360.9 and 476.8 km to 66.4 and 68.7 km. This is still over an order of magnitude larger than the nominal case, but it is now at a level which could satisfy mission requirements. In the transverse direction, the uncertainties were brought down to very near the values of the nominal. The additional data had almost no effect in the normal direction. It is interesting to note that with the additional data, the data weight made very little difference in the final results.

The same effect is seen when one-way Doppler data is added to differenced one-way Doppler at the tight data weight (entry 8 of Table 3). The uncertainty values in the transverse and normal directions are are now fairly close to those obtained with the phase data, and the radial sigma is only worse by around 15%. The case with the lower data weight (entry 9 of Table 3), however, does not show similar behavior. The radial sigma has been brought down by an order of magnitude, but its value is still too large to be of use in many missions.

Entries 10 and 11 in Table 3 show the results of using differenced phase and Doppler augmented by standard two-way Doppler data at a rate of one pass per week. This result is included to show what to expect if a spacecraft has a transponder onboard but with no ranging capability. These values indicate that navigation performance is only slightly degraded if two-way range is replaced by the differenced one-way data types. Comparison with the final entry in the table (2-way Doppler only) shows that the differenced data type improves the solution by a factor of two in all three components.

The results so far using one-way data assume a spacecraft oscillator stability of one in 10^9 over the course of a day. The question can then be raised as to how a better or worse oscillator would affect the orbit determination accuracies. The effect would be negligible if only the differenced data types were used, but it will make a difference when single station data is added. Figures 2 and 3 present the results when the oscillator stability varies from one part in 10^7 to one in 10^{14} over one day for the differenced phase plus phase, and differenced Doppler plus Doppler cases, respectively. In both cases, the tighter data weight was assumed. As can be seen from these plots, there is a sharp knee in the curve which takes place at around the 10^{10} value in the radial directions for both phase and Doppler. The transverse and normal sigmas change very little as a function of oscillator stability. At a stability level of 10^{12}, the phase formulation case is now quite comparable in all three components to the standard two-way Doppler and range results, and the Doppler formulation is only slightly worse. Further improvements in stability do not seem to make much difference. This implies that a spacecraft carrying a USO of the class used by Galileo or Mars Observer can conceivably approach the navigation accuracies achieved with two-way data types.

Another useful figure of merit is the amount of single station one-way data employed. The nominal results are based on a dense tracking schedule of using every other available pass. Figures 4 and 5 present the results if the amount of single station data is reduced to one pass per day, one pass per week, and one pass per month (the differenced data are assumed to remain at the nominal schedule, and the tight data weight was used). Once again, it can be seen that the transverse and normal sigmas are affected very little. The radial sigmas, however, show small changes when the data is thinned to once per day, and then a marked degradation when thinned further. The effect is more pronounced in the case of the differenced phase Doppler formulation, with the radial sigma dropping from its nominal value of around 80 km to a worst case of nearly 200 km. The phase formulation does not suffer as much, as the decrease is only from 65 to 120 km.
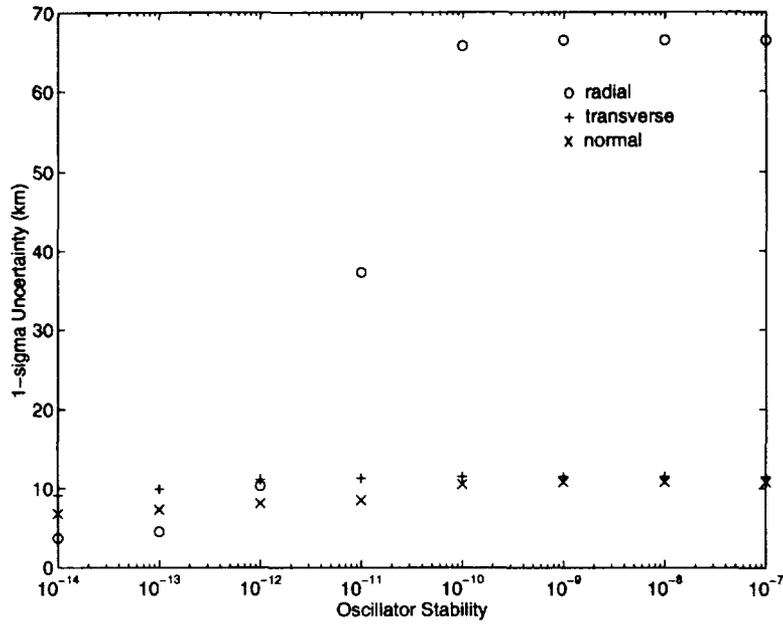
Figure 2: Sensitivity of Position Uncertainty to Oscillator
Stability for Differenced Phase + Phase Data
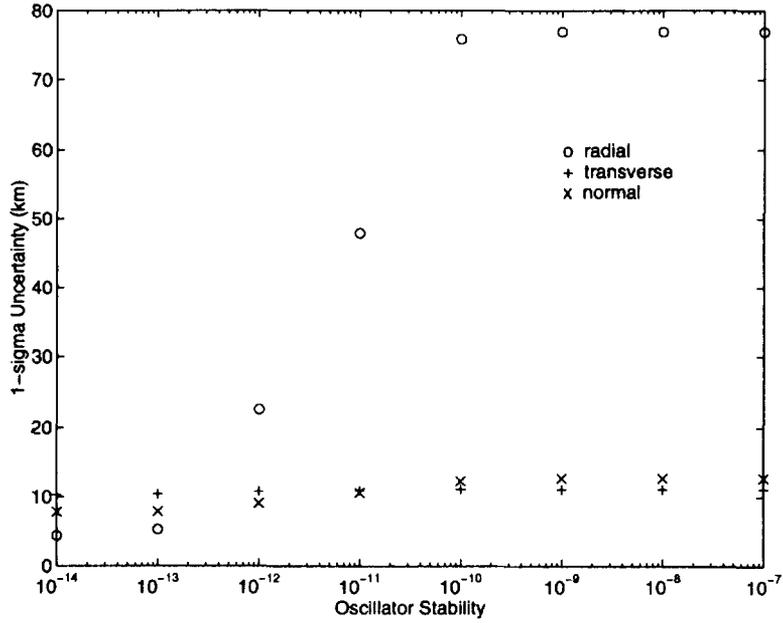
Figure 3: Sensitivity of Position Uncertainty to Oscillator
Stability for Differenced Doppler + Doppler Data
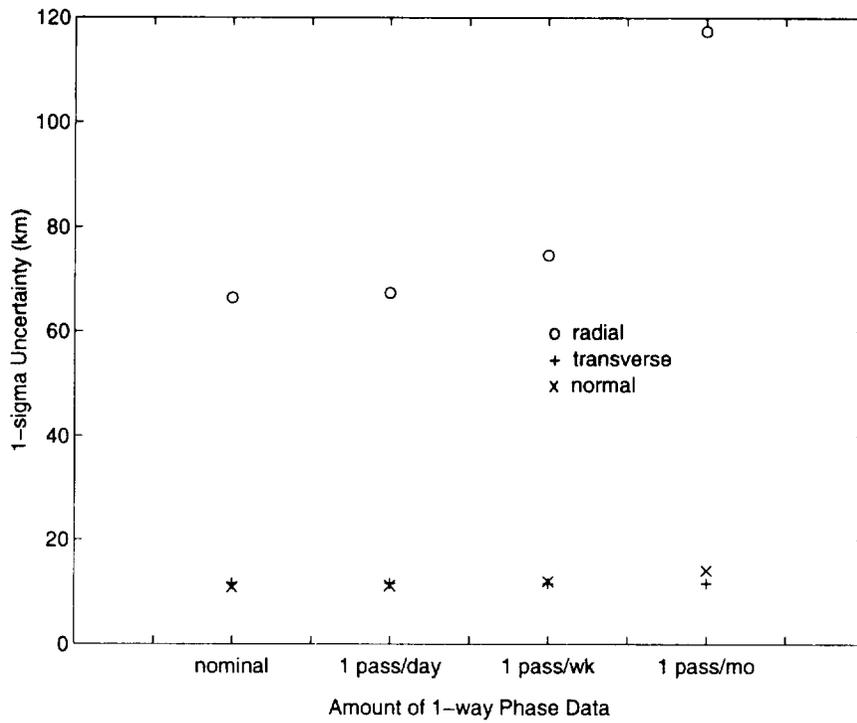
Figure 4: Sensitivity of Position Uncertainty to Amount of Single Station Data Coverage for Differenced Phase + Phase Data
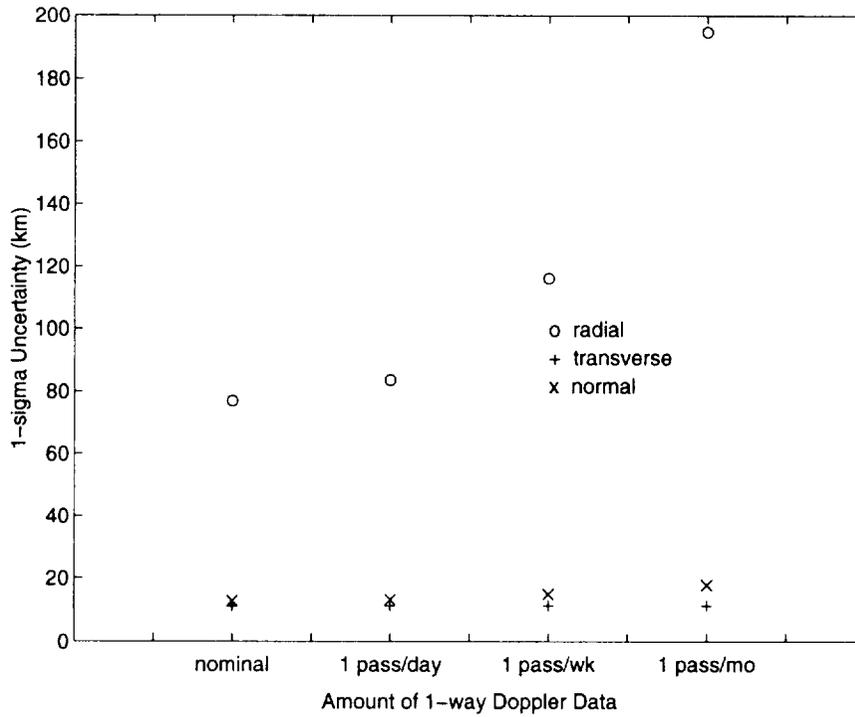

Figure 5: Sensitivity of Position Uncertainty to Amount of Single Station Data Coverage for Differenced Doppler + Doppler Data

VI Conclusions

The results of this study suggest that a combination of single station and two-station differenced one-way data types may be a realistic option for some interplanetary missions. This may be somewhat surprising because it has long been assumed that a very stable frequency is needed to render one-way data usable. However, it has been shown here that with a modest oscillator, reasonable results can be obtained by combining data which have different strengths and with the proper mathematical formulation of the data and filter. In particular, the estimation of the spacecraft's angular position in the sky can be nearly as good as with standard data types, although the spacecraft's radial position is relatively poorly determined. If a very good oscillator (stability of one part in 10^{12} over a day, or better) is available, then the accuracy in all three components may approach those obtained with standard navigation data types. One point to note, though, is that the oscillator stabilities were measured over a day. For a noncoherent system to be confidently used would require pre-flight testing of the oscillator over these time periods; something which has not been generally done in the past. Also, the results indicate that the phase formulation of Doppler data is superior in some respects to the differenced phase Doppler formulation in terms of navigation accuracies. At the tight data weights and with good data coverage, the values are comparable, but the phase data shows less sensitivity to decreasing data weights or coverage.

In practice, the choice of using non-coherent data types for navigation depends on the particular mission scenario and its requirements. In the case of the Mars Pathfinder mission, the geometry of the trajectory is such that the radial uncertainty maps almost completely into the time-of-flight direction (parallel to the incoming asymptote of the trajectory) in the Mars B-plane. Since the critical requirement is to maintain the proper entry angle (determined by the components perpendicular to the incoming asymptote), the degradation in performance is not severe. For example, if the entire Earth-Mars transfer were navigated using only differenced and single station one-way phase, the probability of successful entry is still approximately 70% (the probability is over 99% using two-way Doppler data). This value is obviously too low for Pathfinder to use non-coherent data as its baseline, but it is acceptable as a backup if the transponder fails. If the spacecraft were to go into orbit, however, the navigation accuracies using non-coherent data might be adequate, depending on other factors such as propellant constraints, orbit maintenance requirements, etc. For missions whose geometry results in the radial sigma being of primary importance though, the switch to a non-coherent navigation system may not be advisable. Ultimately, the trade-off between cost and performance must be evaluated on a mission-by-mission basis, and no one answer is applicable to all cases.

Acknowledgements

References

1. P. H. Kallemeyn, Mars Pathfinder Navigation Plan, JPL Internal Document, JPL-D 11349, July, 1994.

2. T. W. Hamilton and W. G. Melbourne, "Information Content of a Single Pass of Doppler Data From a Distant Spacecraft", *JPL Space Programs Summary 37-39*, vol. III, March-April 1966, pp.18-23, May 31, 1966.

3. S. W. Thurman, "Deep-Space Navigation with Differenced Data Types Part I: Differenced Range Information Content", *TDA Progress Report 42-103*, Jet Propulsion Laboratory, Pasadena, California, pp. 47-60, November 15, 1990.

4. J. R. Guinn, and P. J. Wolff, "TOPEX/Poseidon Operational Orbit Determination Results Using Global Positioning Satellites", Paper AAS 93-573, presented at the AAS/AIAA Astrodynamics Specialist Conference, Victoria, B.C., August 16-19, 1993.

5. S. W. Thurman, "Orbit Determination Filter and Modeling Assumptions for MESUR Pathfinder Guidance and Navigation Analysis", JPL Internal Document JPL-IOM 314.3-1075, October 15, 1993.

6. Deep Space Network System Functional Requirements and Design: Tracking System (1988 through 1993), DSN Document 821-19, Rev. C, (JPL D-1662, Rev. C), April 15, 1993, p. 3-4.

7. W. M. Folkner, "DE234 Station Locations and Covariance for Mars Observer", JPL Internal Document JPL IOM 335.1-93-013, May 26, 1992.

The Transition of GTDS
to
the Unix Workstation Environment

by
D. Carter, R. Metzinger, R. Proulx, and P. Cefola
The Charles Stark Draper Laboratory
Cambridge, Massachusetts

Future Flight Dynamics systems should take advantage of the possibilities provided by current and future generations of low-cost, high performance workstation computing environments with Graphical User Interface. The port of the existing mainframe Flight Dynamics systems to the workstation environment offers an economic approach for combining the tremendous engineering heritage that has been encapsulated in these systems with the advantages of the new computing environments.

This paper will describe the successful transition of the Draper Laboratory R&D version of GTDS from the IBM Mainframe to the Unix workstation environment. The approach will be a mix of historical timeline notes, descriptions of the technical problems overcome, and descriptions of associated SQA issues.

The detailed list of topics to be addressed includes:

1. Mainframe version enhancements at CSDL

  Elimination of Assembly language routines
  Elimination of dependence on H-Fortran Library routines
  Removal of Overlay

2. Porting to the VAX VMS environment

  Compile issues
  Run-time issues

3. Porting to Unix environment

  the Sun SPARC
  the SGI

4. Porting the Databases

  Potential Models
  Atmosphere Models
  SLP files
  Misc.

5. Database Maintenance: Porting TRAMP

6. Running GTDS under Unix:

  JCL replacement
  File system issues
  Printing system issues

7. Validation and SQA

Test Suite
Results
Numerical Accuracy (Floating Point formats)
Speed
Configuration Control/Traceability
Commonality Issues

8. Adding a User Friendly Menu Driven User Interface to drive GTDS

User Interface
Data Dictionary
GTDS_Executive: creating the "card" deck file

Title: Flight Dynamics Software in a Distributed Network Environment

Authors: J Jeletic (NASA/GSFC), D. Weidow (NASA/GSFC), D. Boland (CSC)

As with all NASA facilities, the announcement of reduced budgets, reduced staffing, and the desire to implement smaller/quicker/cheaper missions has required the Agency's organizations to become more efficient in what they do. The Flight Dynamics Division (FDD) is no exception. Although the flexibility and high quality products and services provided in the past have been the major reason for the FDD's success, today's business climate has changed. The FDD now finds itself in direct competition with other government agencies and private industry to provide efficient flight dynamics services and products to the user community. The FDD, in response to this new business climate, is making significant strides to maintain the quality and flexibility of the services and products available while significantly reducing the cost and cycle time associated with this support.

This effort is characterized by the following objectives:

1. Continue to provide quality flight dynamics services and products.

2. Reduce software development costs, software maintenance costs, and software development cycle time through common approaches, common software, and strict adherence to standards across flight dynamics applications.

3. Reduce operations costs through automation and streamlined work flow.

4. Expand customer base to offer flight dynamics services and products to government, industry, and university customers world wide.

5. Maximize the use of distributed systems concepts and open systems technologies to provide configurable and flexible system solutions to our customers.

To accomplish these objectives, the FDD has initiated the development of the Flight Dynamics Distributed System (FDDS). The underlying philosophy of FDDS is to build an integrated system that breaks down the traditional barriers of attitude, mission planning, and navigation support software to provide a uniform approach to flight dynamics applications. Through the application of open systems concepts and state-of-the-art technologies, including object-oriented specification concepts, object-oriented software, and common user interface, communications, data management, and executive services, the FDD will reengineer most of it's six million lines of code. The FDDS will allow flight

dynamics applications to be quickly and efficiently configured into systems, large and small, and customized to satisfy the needs of the customer being supported. These systems will reside within a transportable workstation based environment, allowing flight dynamics services and products to be provided through the Flight Dynamics Facility (FDF) or from within the control center environment by physically locating the systems and their operation at the customer site.

FLIGHT MECHANICS/ESTIMATION THEORY SYMPOSIUM

MAY 16-18, 1995

SESSION 5

DETERMINING GPS AVERAGE PERFORMANCE METRICS

G. V. Moore
Lockheed Martin Corporation
Management & Data Systems

ABSTRACT:

Analytic and semi-analytic methods are used to show that users of the GPS constellation can expect performance variations based on their location. Specifically, performance is shown to be a function of both altitude and latitude. These results stem from the fact that the GPS constellation is itself non-uniform. For example, GPS satellites are over four times as likely to be directly over Tierra del Fuego than over Hawaii or Singapore. Inevitable performance variations due to user location occur for ground, sea, air and space GPS users. These performance variations can be studied in an average relative sense.

A semi-analytic tool which symmetrically allocates GPS satellite latitude belt dwell times among longitude points is used to compute average performance metrics. These metrics include: average number of GPS vehicles visible, relative average accuracies in the radial, intrack and crosstrack (or radial, north/south, east/west) directions, and relative average PDOP or GDOP. The tool can be quickly changed to incorporate various user antenna obscuration models and various GPS constellation designs. Among other applications, tool results can be used in studies to: predict locations and geometries of best/worst case performance, design GPS constellations, determine optimal user antenna location and understand performance trends among various users.

A DEMONSTRATION OF UNIFIED TDRS/GPS TRACKING AND ORBIT DETERMINATION

B. Haines, S. Lichten, J. Srinivasan and L. Young

Jet Propulsion Laboratory, California Institute of Technology

Pasadena, California 91109

ABSTRACT

We describe results from an experiment in which TDRS and GPS satellites were tracked simultaneously from a small (3 station) ground network in the western United States. We refer to this technique as "GPS-like tracking" (GLT) since the user satellite—in this case TDRS—is essentially treated as a participant in the GPS constellation. In the experiment, the TDRS K_u-band space-to-ground link (SGL) was tracked together with GPS L-band signals in enhanced geodetic-quality GPS receivers (TurboRogue). The enhanced receivers simultaneously measured and recorded both the TDRS SGL and the GPS carrier phases with sub-mm precision, enabling subsequent precise TDRS orbit determination with differential GPS techniques. A small number of calibrated ranging points from routine operations at the TDRS ground station (White Sands, NM) were used to supplement the GLT measurements in order to improve determination of the TDRS longitude. Various tests performed on TDRS ephemerides derived from data collected during this demonstration—including comparisons with the operational precise orbit generated by NASA Goddard Space Flight Center—provide evidence that the TDRS orbits have been determined to better than 25 m with the GLT technique.

Improvements to enable 10 m accuracy are also discussed. Drawing on these results, as well as experiences with automated Topex/Poseidon and GPS orbit determination at the Jet Propulsion Laboratory (JPL), we discuss prospects for using GLT to operationally collect and process TDRS data for orbit determination, including delivery of solutions within a few hours after maneuvers — all in a very low cost, highly automated system with ground sites close to White Sands. Its high potential for inexpensive, automated high-performance tracking should render the GLT technique attractive to designers of NASA, military and commercial systems used for orbit determination of satellites at geosynchronous as well as other altitudes.

1. INTRODUCTION

The Global Positioning System (GPS) is rapidly emerging as the tracking system of choice for a variety of Earth orbiting spacecraft missions. A conventional approach to GPS-based orbit determination involves a GPS flight receiver on board the user spacecraft. For satellites flying in low-Earth orbit (LEO) well underneath the shell formed by the GPS constellation, a wide range of configurations can be considered. The simplest consists of a minimal GPS flight instrument requiring only a fraction of a watt of power and a few hundred grams mass [*Lichten et al.*, 1995]. Better performance can be achieved with a more conventional flight receiver. For the highest accuracy, data from ground GPS trackers can be combined with the flight data. Using this approach, it has recently been demonstrated that orbits for the Topex/Poseidon oceanographic satellite could be determined to better than 3 cm (RMS) in the radial direction using GPS [*Bertiger et al.*, 1994]. This result can be attributed in large part to the continuous tracking and multi-directional observing geometry afforded by GPS in the 1,340 km altitude orbit occupied by Topex/Poseidon.

An alternative to carrying a GPS flight receiver employs instead a simple beacon on the user spacecraft. The beacon signal is tracked along with signals from the GPS spacecraft in an enhanced GPS ground receiver. This approach, which we call GPS-like tracking (GLT), exploits GPS to precisely determine station coordinates, and media delays and to provide clock synchronization at the ground stations. In contrast to conventional GPS-based orbit determination, a geometric solution for the user orbit is generally not achievable and models of the forces perturbing the spacecraft motion must then be used together with the observations. A limitation for low-Earth orbiters is that the fraction of time during which the beacon illuminates ground sites is typically small. Nonetheless, this alternative remains attractive for certain applications because it can exploit a pre-existing beacon signal (e.g., for telemetry) and requires no additional spacecraft hardware for dedicated orbit determination.

309

The GLT method is particularly attractive for spacecraft in high altitude orbits (Figure 1): while the practical observability of GPS signals degrades rapidly as a function of altitude above the GPS constellation, the number of ground stations that can be kept in permanent view of a beacon signal increase [e.g., *Wu*, 1985] . At geostationary orbit, a ground network can be designed that is permanently in view of the beacon signal, providing uninterrupted tracking.
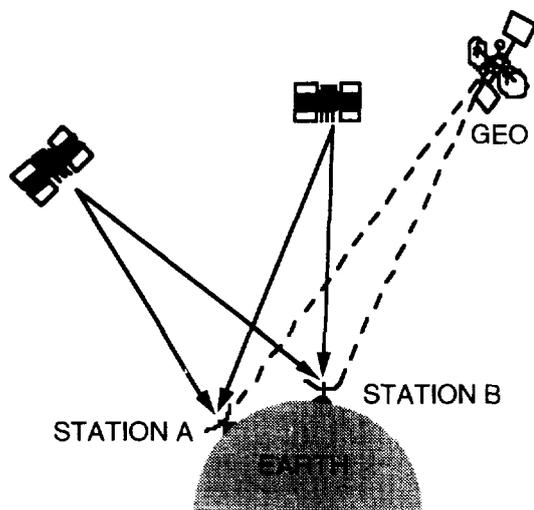
Fig 1. Differential GPS-like tracking (GLT) applied to geosynchronous orbiter. Four simultaneous observations of GPS carrier phase and pseudorange enable removal of transmitter and receiver clock offsets. After tracking for 12–24 hours, the GPS orbits can be determined to a few tens of centimeters. In GLT, the carrier phase of the high-Earth orbiter is also included and its orbit similarly estimated. This relationship is discussed further by *Lichten et al.* [1993].

1.1 TDRS ORBIT DETERMINATION

An attractive candidate for applying the GLT technique is NASA's Tracking and Data Relay Satellite (TDRS) System. The TDRS space segment currently consists of 5 geosynchronous orbiters and is used by NASA to support positioning and data relay activities for a wide variety of Earth orbiting spacecraft. Accurate real-time position knowledge of the TDRSS spacecraft is required to support certain users: though the most stringent current requirement is 200 m (1 σ) for the Space Transportation System (STS), the planned Earth Observing System (EOS) platform calls for 25 m (1 σ) accuracy of the TDRS ephemerides [*Cox and Oza*, 1994].

The current TDRS orbit determination system is based on the relay of coherent signals through unmanned transponders at globally distributed remote tracking sites. These remote beacons are collectively referred to as the

Bilateration Ranging Transponder System (BRTS). Evaluation of the TDRS ephemerides suggests that orbit accuracy is maintained to better than 50 m using the operational BRTS method [*Cox and Oza*, 1994]. This level of accuracy does not meet the future EOS requirement; moreover, the scheduling of BRTS observations consumes TDRS antenna time that could otherwise be used for servicing user spacecraft. In recognition of this, a number of studies aimed at identifying alternative methods for TDRS orbit determination have been undertaken [see also *Marshall et al.*, 1995; *Oza et al.*, these proceedings].

1.2 GPS-LIKE TRACKING OF TDRS

Under the direction of NASA, JPL has investigated a number of potential new strategies for determining the TDRS orbits [*Nandi et al.*, 1992; *Haines et al.*, 1992]. Judged the most promising among them was a hybrid approach which combined elements of GLT with a specialized form of interferometric tracking over very short baselines (Connected Element Interferometry or CEI; see *Edwards et al.*, 1991).

The short baseline scenario is necessitated by the nature of the existing TDRS space-to-ground link (SGL). The TDRS SGLs illuminate only a limited area of the southwestern U.S. surrounding the TDRS Earth station in White Sands, New Mexico (Figure 2). This precludes the use of globally dispersed stations for tracking the SGL. However, if a GLT network fitting within the SGL footprints could be designed to deliver the desired accuracy, significant benefits could be gained: 1) The SGL is always on when the TDRS is servicing users. Thus the signal can be passively monitored and no TDRS services need be scheduled for orbit determination. 2) The SGL is broadcast at K$_u$-band (13.731 GHz). At this frequency, the delay caused by the presence of charged particles along the signal path (i.e., ionosphere delay) rarely exceeds a few cm in equivalent range. This contrasts with the BRTS tracking, which is based on the lower frequency S-band transmissions which are significantly delayed by the ionosphere. (Several meters of delay is typical.) 3) A small ground network in the vicinity of the White Sands complex (WSC) has many operational advantages: all the sites can be readily accessed for maintenance, and communications links to the Earth station can be made reliable and short.

Following the direction of NASA, JPL designed an experiment to demonstrate the feasibility of this technique. The foundation of the experiment is simultaneous tracking of GPS and TDRS signals over short baselines to determine the TDRS orbit [*Lichten et al.*, 1993]. Coincident observation of GPS and TDRS

signals in the same ground receiver enables calibrations of clock errors [Dunn et al., 1991, 1993] and tropospheric delays [Lichten, 1990], supplanting the fiber optic links and expensive calibration devices that are needed in a connected element network. An added benefit is the ability of GPS to provide very precisely (sub cm) the positions of the tracking stations relative to one another, and the network orientation in the terrestrial reference frame [Blewitt et al., 1992].

We note that the GLT method described herein uses a measurement type known in the GPS community as "differential carrier phase". It is instructive to think of the phase measurement as a range observation that is biased by an amount corresponding to an unknown integer number of cycles along the transmission path. Each modified TurboRogue station tracks the phase of the TDRS SGL with great precision (enabled by GPS). Contained in the station-differenced phase data is very precise information on the velocity of the TDRS spacecraft in the plane-of-sky. Using the information in a standard dynamical orbit determination strategy determines very precisely five of the six osculating (classical) elements that describe the geosynchronous TDRS orbit. In order to determine the last component— the longitude of the satellite orbit or its down track position in inertial space—some knowledge of the range to the spacecraft is needed. To provide this information, we used data from routine ranging done at WSC.

Additional information on the heritage of the technique, and initial results are given by Haines et al. [1994]. Herein we summarize the experiment configuration and initial findings and report on some extended results intended to address the operational potential of the method.

2. JANUARY 1994 DEMONSTRATION

The TDRS/GPS tracking demonstration took place from January 16–22, 1994. GPS and TDRS satellites were tracked simultaneously from three sites: El Paso, TX, Socorro, NM, and Pasadena, CA (Figure 2). This configuration permitted us to test the performance of side-lobe tracking, as JPL is in a fortuitous location that placed it in the first side lobe of the SGLs from both TDRS-5 (175° W) and TDRS-3 (62° W). The other two stations, operated from motel rooms in El Paso and Socorro, were within the main beam of the SGL of both TDRS-3 and 5.

The cornerstone of each tracking station was an enhanced TurboRogue GPS receiver. The TurboRogue, developed at JPL [Meehan et al., 1992] and currently globally distributed in a 50+ receiver network used for precise GPS orbit determination and a variety of geodetic

and tectonic studies [Zumberge et al., 1994], was augmented for this experiment with a small, K_u-band horn antenna (opening dimensions 17 X 14 cm) and a K_u- to L-band downconverter. In addition, the TurboRogue software was modified to measure and record the phase of the TDRS SGL with the same sub-mm precision and receiver time-stamp as GPS carrier phase measurements. This system architecture produces data products that significantly simplify subsequent orbit determination processing.
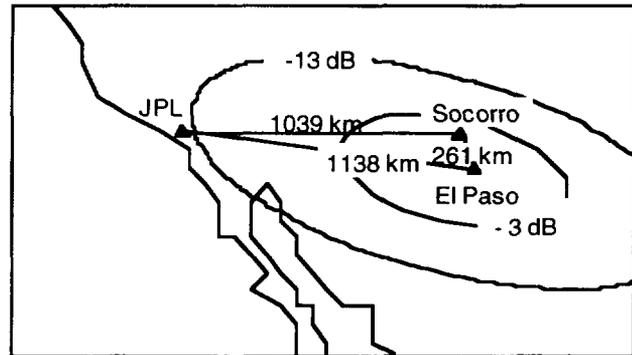
Fig 2. Configuration of TDRS/GPS tracking network. The footprint of the TDRS-3 space-to-ground link (SGL) during the January 1994 experiment is shown.
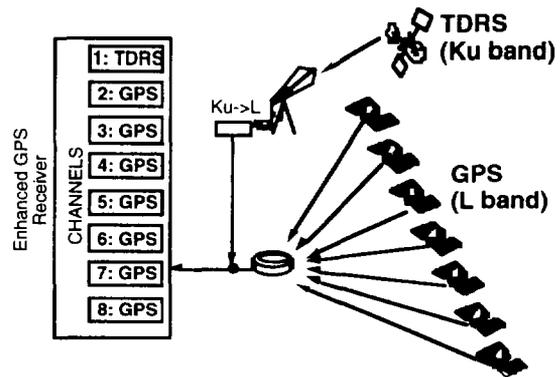
Fig 3. Schematic for the GPS ground receiver enhanced to simultaneously track TDRS along with GPS satellites. For the TDRS SGL, which is at 13.731 GHz, a small separate antenna with down converter was added.

2.1 DATA

Data collection commenced on January 16 with tracking of TDRS-3. Also known as TDRS-Central, this spacecraft was seen at an elevation of approximately 30° when viewed from White Sands. TDRS-3 was tracked for nearly 5 days before the stations were reconfigured to track TDRS-5 (January 21). This spacecraft presently occupies the western slot and is seen at an elevation of only 10° from White Sands. Although the TDRS-5 track spanned only 18 hours, this session was useful for

understanding the effects of tracking at lower elevations. A time line showing the data coverage for the experiment is given in Figure 4. Depending on the station, 85–95% tracking coverage was achieved over the course of the experiment. The largest data outage occurred on Jan. 18 when the TDRS-3 SGL was switched off for approximately 7 hours to support an antenna maintenance activity at WSC. All three sites did experience a significant number of phase interruptions over the duration of the experiment: the longest period of time during which all three stations tracked without a single loss of lock was about 20 hr. We believe that the number of phase breaks can be greatly reduced in future demonstrations with changes to the receiver configuration.
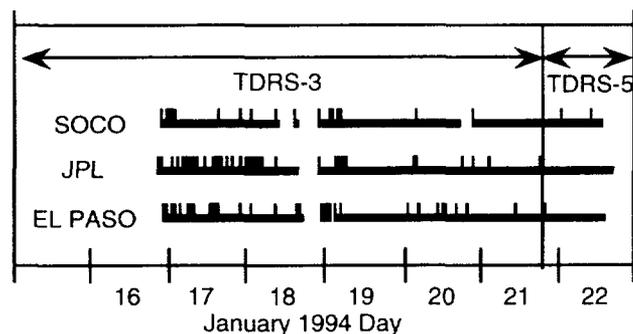
Fig 4. Time line showing data coverage at each of the three GPS stations over the course of the TDRS tracking experiment. Solid horizontal bars indicate the receiver was tracking. Vertical bars indicate that a loss of lock occurred.

Figure 5 depicts a sample of the raw TDRS-3 data from each of the three sites. The top panel gives the raw phase measurement converted to a biased 3-way range (White Sands to TDRS-3 to GPS terminal) and the bottom panel gives the signal-to-noise ratio. The range data show the expected diurnal signature from the geosynchronous TDRS orbits. For TDRS-3, the peak to peak variation of the 3-way range was ~200 km, while for TDRS-5 (not shown) the variation was only ~30 km. This disparity is attributable primarily to the different orbits occupied by the spacecraft: TDRS-3 was inclined by 0.7° relative to the equator, while the TDRS-5 inclination was only 0.07°. The TDRS-3 orbit was also slightly more eccentric. Also worthy of note in Figure 5 is the lower characteristic SNR for the JPL station. This reflects the decrease in signal strength associated with observing the SGL in the side lobe of the antenna pattern.

As explained previously, ranging information to TDRS is needed to fix the longitude of the spacecraft. To satisfy this requirement, we used range observations from routine Tracking Telemetry and Control (TT&C) activities at White Sands. These observations are based on tracking of

the K_u-band SGL with 18-m antennae located at the central ground terminal. The range data are not intended for precise orbit determination (a service which is presently provided by the BRTS system). As such, the observations can contain large systematic biases that, without calibration, preclude achievement of high accuracy in determining the longitude of the TDRS orbits.
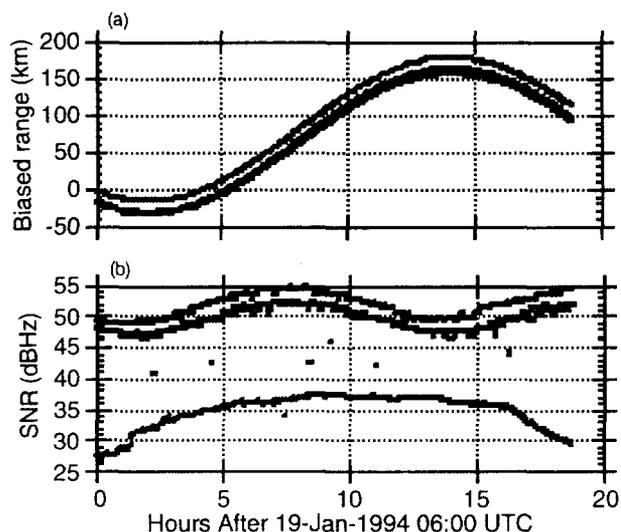
Fig 5. Biased range (Panel A) and signal-to-noise ratio (Panel B) from TDRS-3 carrier phase tracked at JPL, El Paso, and Socorro on January 19, 1994. The station with the low SNR is at JPL, which tracked TDRS-3 from within the first sidelobe.

In order to estimate the range biases, we calibrated the TT&C range data against the precise TDRS orbits generated at GSFC using the BRTS system. Shown in Fig. 6 are the residuals of the TT&C range with respect to the BRTS orbits for TDRS-3 over the course of the experiment. Biases as large as 50 m (one-way) can be seen. (Note the bias estimates also reflect uncertainty in station coordinates, errors in the BRTS orbits, and potential inconsistencies in the processing of the data.)
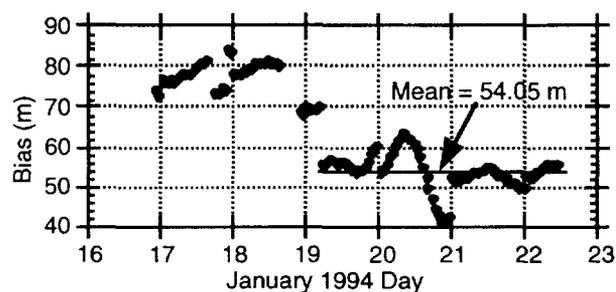
Fig 6. Residuals of White Sands TDRS-3 range data with respect to BRTS-derived orbit from Goddard Space Flight Center. A 1-way bias of 54.1 m was used in this study to calibrate the TDRS-3 range data for periods after 06:00 UTC on January 19, 1994.

For TDRS-5, which was observed from an elevation of 10° from WSC, the partial derivative of the range bias with respect to the spacecraft longitudinal position is about 1/8. This implies that a 10 m one-way (20 m two-way) range bias could translate into an 80-m error in the longitude component of the TDRS, underscoring the proper calibration of the ranging system.

2.2 SOLUTION STRATEGY

The unified TDRS/GPS orbit solutions were computed using the GIPSY/OASIS II software [Webb and Zumberge, 1993]. Table 1 outlines the solution strategy. With the exception of a few elements that are not consistent with a real-time solution, the strategy for processing the 3-station TDRS data mirrors that presently used at JPL in the routine, highly automated processing of GPS data from the much larger (80+ station) global Intl. GPS Service for Geodynamics (IGS) network [Zumberge et al., 1994]. In particular, zenith wet troposphere delays were estimated as stochastic random-walk parameters, and clock offsets were estimated as stochastic white noise processes at each measurement batch.

We note that satellite states for the TDRS and all GPS spacecraft were estimated, with a priori for the latter coming from the broadcast ephemerides. Inasmuch as the GPS data are collected at only three ground stations, and they are quite close, the GPS orbit errors are undoubtedly nonuniform over the globe. In this study, GPS provides clock synchronization and media calibration for our network in the southwestern U.S. In this context, regional improvement of the GPS orbits is adequate. Additional details on the solution strategy are provided by Haines et al. [1994].

The TDRS phase data were modeled as three-way measurements (i.e., 2 legs and 3 participants). Although it is instructive to think of TDRS as the originator of the signal (in the manner of GPS), this is not strictly correct. The signal originates at White Sands, and is transmitted to TDRS which serves as a "bent-pipe" transponder, redirecting the signal to the ground. It follows that we do not solve for the TDRS clock offset in our orbit determination procedure, but rather the offset of the master frequency generator on the ground at WSC. This modeling ensures that the Doppler signature from the uplink is handled properly, i.e. it is not incorrectly absorbed in the TDRS clock solution. The range data from WSC were modeled as simple 2-way measurements.

Station coordinates for the TDRS/GPS terminals in El Paso, Socorro and Pasadena were fixed at precise values determined a priori using the GPS data collected at the

sites. Details on this procedure are discussed by Haines et al. [1994]. Their results suggest that the station coordinates have been determined at the cm level relative to the geocenter. For the 18-m WSC antennae that collect the range data, we used coordinates provided by NASA in the WGS-84 system. We did not have a GPS receiver at WSC and therefore were unable to estimate improved coordinates. Any error in this station coordinate will manifest itself as a range bias, which we estimated via external calibration (as described in the previous section).

TABLE 1. ESTIMATION STRATEGY FOR GPS/TDRS ANALYSIS

Data Noise (150 s observations)	
GPS carrier phase	1 cm
TDRS carrier phase	1 cm
GPS pseudorange	1 m
TDRS two-way range (1/hr)	5 m

A-priori for estimated parameters	
TDRS position (X, Y, Z)	100 km
TDRS velocity (X, Y, Z)	1 m/s
TDRS solar radiation pressure coeff.	100 %
TDRS carrier phase biases	1 s
WSC range bias (1 way)	1 m
GPS position (X, Y, Z)	100 km
GPS velocity (X, Y, Z)	1 m/s
GPS carrier phase biases	1 s
GPS spacecraft clock offset	1 s white
GPS gnd. station clock offset[1]	1 s white
White Sands station clock offset 1 s white	
GPS gnd. station zenith wet trop.	40 cm +5 cm/√day random walk
1 El Paso clock fixed	

Models and constants	
TDRS solar rad. pressure model	Bus
TDRS area	40 m^2
TDRS mass	1807 kg
GPS solar rad. pressure model	T10/T20
Polar motion (X, Y)	IERS-B
Earth rotation (UT1 – UTC)	IERS-B
GPS Station locations	ITRF'91
White Sands station location	WGS-84
Luni-solar perturbations	DE-200
Earth gravity field	JGM-3 (12X12)

2.3 ORBIT DETERMINATION RESULTS

We consider first 4 separate orbit arcs: three for TDRS-3 and one for TDRS-5. The arc lengths vary from 18 to 21 hours and span the period from January 19 06:00 UTC to January 22 13:00 UTC. For TDRS-3, the calibration

correction of 54.1 m was applied *a priori* to all the range data. For TDRS-5, which was tracked from a separate antenna at WSC, range data were not available at this writing. For range observations to TDRS-5, we simulated measurements from WSC using the BRTS orbit from GSFC.

2.3.1 Postfit Residuals

Table 2 gives the statistics of fit for the four precise TDRS orbit solutions. The root-mean-square (RMS) post-fit observation residuals for the TDRS and GPS phase measurements were 2.6–5.8 mm and 2.8–3.0 mm respectively. That the TDRS phase data can be fit nearly as well as the GPS phase is encouraging, and suggests that the TDRS data quality is excellent (Figure 7). The GPS pseudorange, which is important for determining the clocks offsets, was fit to 0.3 m (RMS). In the cases where the TDRS 2-way range were included, these observations were fit to between 1 and 3 m (RMS). While these numbers are instructive for estimating bounds on the measurement noise, they reveal little about the orbit accuracy. For this, we examine the formal errors and overlap statistics of the TDRS orbit solution, and compute differences with respect to the BRTS-derived orbit from GSFC.

TABLE 2. ROOT-MEAN-SQUARE POSTFIT TRACKING DATA RESIDUALS FOR TDRS.

S/C	Arc Epoch (UTC)	TDRS Phase (mm)	TDRS Range (m)	GPS Phase (mm)	GPS Range (m)
TDRS-3	19-JAN 06:00	2.6	2.8	2.8	0.3
	19-JAN 21:00	5.8	1.9	3.0	0.3
	20-JAN 21:45	3.2	1.0	2.9	0.3
TDRS-5	21-JAN 19:48	2.0	NA	2.7	0.3
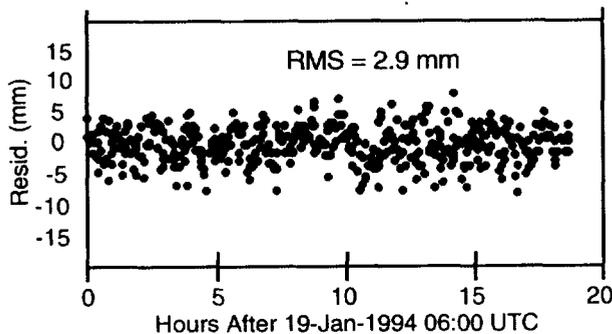
Fig 7. Postfit residuals for carrier phase from TDRS-3 as tracked by TurboRogue GPS receiver in Socorro, NM.

2.3.2 Internal Assessments of Orbit Error

Formal "noise-only" errors for the 4 orbit solutions were mapped over the respective arcs, and the results are summarized in Figure 8. Errors are decomposed into the height, cross- and down-track components of the orbit position. The largest errors are in the down-track component, for which the RMS values are typically 15 m. We note that the down-track errors are due in large part to the range bias, which is being estimated with an *a priori* standard deviation of 1 m (*one-way*). There is essentially no information for the estimation of the bias; it serves only to inflate the formal errors so that they are more realistic.
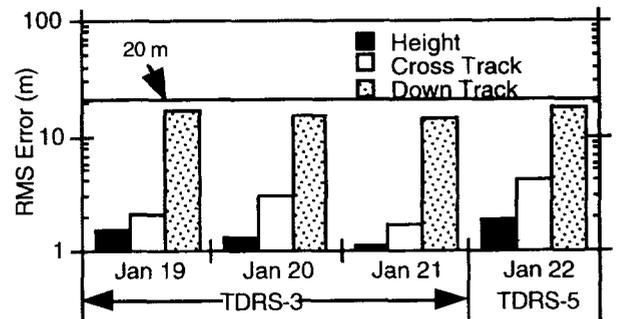
Fig 8. Bar graph showing RMS formal errors of TDRS orbit solutions computed as part of this study. The first three solutions correspond to TDRS-3 and the last to TDRS-5. The arcs vary between 18 and 20 hours in length.

Two of the TDRS-3 orbit solutions overlap by ~4 hr (Figure 9). The RMS differences of the two solutions during the overlap is 2, 11, and 12 m in height, cross track and down track respectively. These differences suggest that the orbit precision is better than 25 m (RMS).
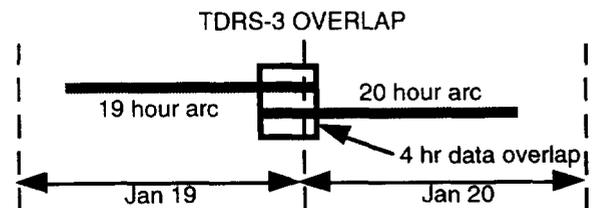
Fig 9. Schematic of orbit overlap for TDRS-3 orbit comparison. The RMS differences in height, cross track and down track during the overlap are 2, 12 and 11 m respectively.

2.3.3 External Assessments of Orbit Error

While the formal errors and overlap statistics from the solutions are instructive for characterizing the general behavior of the orbit errors, it is important to note that

314

they may represent underestimates of the actual orbit error, and thus should be interpreted with caution. Systematic error sources, such as those due to unmodeled solar radiation pressure effects, non-random variations in the tracking observations, and errors in Earth rotation and orientation parameters can augment considerably the actual orbit error. A better measure of the orbit accuracy is thus gained from external comparisons. To this end, we compared our TDRS orbit solutions against the precise BRTS-derived orbits. These orbits are thought to be accurate to 50 m or better in total position (1-σ). The comparisons were performed in the inertial (J2000) reference frame.

Figure 10 shows the difference of our solution for TDRS-3 and the BRTS orbit for the first orbit solution (epoch of 19-JAN-1994 06:00 UTC). The RMS differences in height, cross and down track are 2, 22, and 14 m respectively. This level of agreement is considered quite encouraging, and was somewhat unexpected given published estimates of the errors in the BRTS orbits. It should be remembered, however, that the down track component of our orbit (i.e. longitude) is constrained to match the BRTS orbits in the bias term via the range calibration.
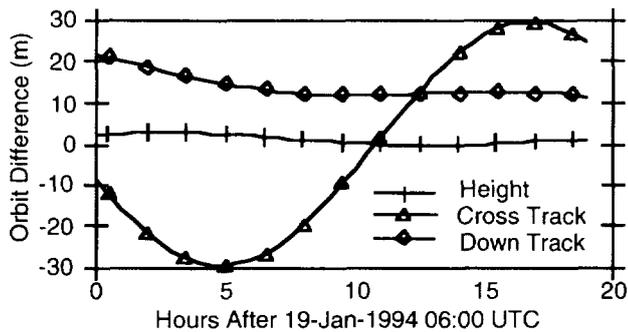
Fig 10. Time series of TDRS-3 inertial orbit differences (this study vs. BRTS orbit from Goddard Space Flight Center) for January 19, 1994. The RMS differences in height, cross track, and down track are 1.6 m, 22.4 m and 14.2 m respectively.

Figure 11 summarizes the differences with respect to the BRTS orbits for all four solutions. The RMS differences range from 1 to 9 m in height, 13 to 30 m in cross track, and 14 to 30 m in down-track, and the maximum difference over the entire ~3 day span is 52 m. Especially encouraging are the results for TDRS-5, which was tracked at a very low elevation (10°). Moreover, the signature that TDRS-5 traced in the plane of sky was very compact compared to the one for TDRS-3. Despite these important differences, the TDRS-5 orbit accuracy appears only slightly degraded.
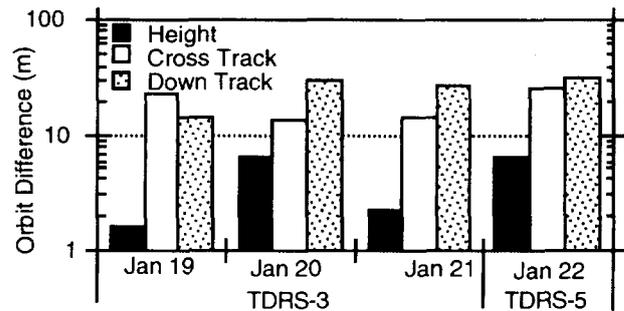
Fig 11. Bar graph summarizing RMS TDRS orbit differences (this study vs. BRTS). he first three solutions correspond to TDRS-3 and the last to TDRS-5. The arc lengths vary between 18 and 20 hours in length. The largest excursion over the entire set of comparisons is 52 m.

2.3.4 Covariance Analysis

Building on the results of the evaluation of the tracking data from the January 1994 experiment, we performed a covariance analysis to further assess the orbit accuracy. In this study, the sensitivities of the TDRS orbit to certain unestimated parameters were also computed and used to augment the formal "noise-only" error contribution. These unestimated or "consider" parameters are included in covariance analyses to yield more realistic error estimates. The consider parameters and their associated errors (1σ) are given in Table 3.

TABLE 3. CONSIDER PARAMETERS AND UNCERTAINTIES FOR COVARIANCE ANALYSIS.

Consider Parameters	
TDRS solar radiation pressure coeff.	2 %
WSC one-way range bias	1 m
WSC zenith wet troposphere (range)	10 cm
Ionosphere delay (K_u-band)	100 % Bent
Gravity model error	50 % JGM-3 – WGS-84
Tracking station baselines	1 cm East 1 cm North 2 cm Vertical
X, Y Pole Motion	10 cm
UT1–UTC	3 msec

With the exception of the solar radiation pressure coefficient and WSC range bias, all other parameters were treated in accordance with the estimation strategy shown in Table 1. In keeping with a conservative approach, the solar radiation pressure coefficient and WSC range bias were not estimated, rather they were treated as consider parameters. In order to account for the possibility of anomalies in tracking the SGL (as experienced in the actual experiment; compare Figure 4), the phase biases

were occasionally reset according to the assumption that at least one of the three stations (El Paso, Socorro, or JPL) would lose lock every 8 hours on average. Also noteworthy is the absence of consider parameters for the location of the WSC range station. Any error in this position would be reflected in the range bias computed from the BRTS orbit. (In practice, the range station could be surveyed in with the remote TurboRogue stations at the cm level using a GPS survey. Any residual error would be negligible in comparison with the uncalibrated portion of the range bias.)
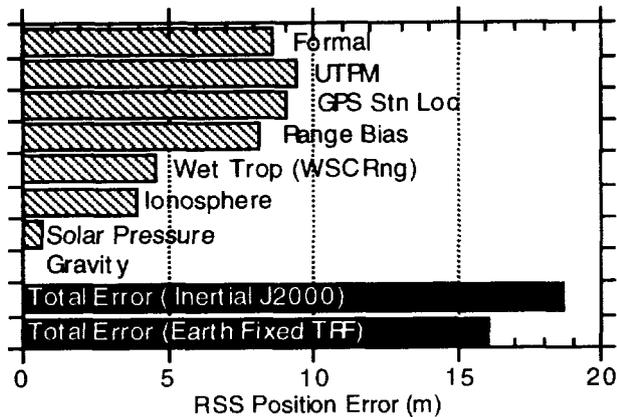

Fig 12. Relative contributions of various error sources for TDRS-5 orbit determination based on covariance analysis. These results apply to TDRS-5 data collected during the January, 1994 experiment (18 hour arc). Note that errors in the Earth rotation and orientation parameters (UTPM) lead to significant errors in orbit positions referred to the inertial (J2000) frame but not to the terrestrial reference frame (TRF).

Shown in Figure 12 are the errors for the TDRS-5 orbit solution (epoch 21-JAN-1994 19:48 UTC) separated by source. The TDRS-5 case was selected because this spacecraft occupies the western orbit slot, and the results are of greater operational consequence than the corresponding results for TDRS-3. Evidenced in the Figure are the dominant contributions of the formal "noise- only" errors and the station location errors for the GPS/TDRS tracking terminals. These error sources are particularly important in shorter arcs, i.e. spanning less than a full diurnal revolution of the spacecraft, as the solution will have enhanced sensitivity to errors associated with the measurement models. Errors in the parameters describing the Earth orientation and rotation (UT1–UTC and X, Y Polar Motion or "UTPM") are also large contributors, but have very little effect on orbit positions referred to the Earth-fixed terrestrial reference frame (TRF). The next largest error source is the range bias. As the range bias has been calibrated using the BRTS orbit, it was assigned an a priori standard deviation of 1 m (1 way). A more realistic estimate of the range bias from the WSC would augment the orbit error

significantly. (This will be discussed further in Section 3.1.2.) The total RSS 3-d orbit error is < 20 m for this ~18-hr solution. This result corroborates the findings of the internal and external orbit tests described earlier, and suggests that the TDRS orbit accuracies achieved for the experiment are better than 25 m (1 σ).

2.3.5 Special Arc Length Studies

A critical requirement for TDRS orbit determination is the prompt recovery of the trajectory estimates after a station-keeping maneuver. In recognition of this, we have examined the effects of reducing the arc length on the error in the recovered orbit. Our nominal orbit solution for this comparison is a 34-hr arc for TDRS-3. Gradually shorter tracking data arcs were used in computing orbit solutions for comparison with this nominal ephemeris. Depicted in Figure 13 are the differences with respect to the nominal 34-hr solution; these results suggest that 75 m orbit precision is being approached with only 4 hours of tracking. (The current requirement for STS is 200 m (1 σ) within 4 hours after a maneuver [Cox and Oza, 1994].) Differences of the 12-hr arc with respect to the nominal are less than 20 m in all components.
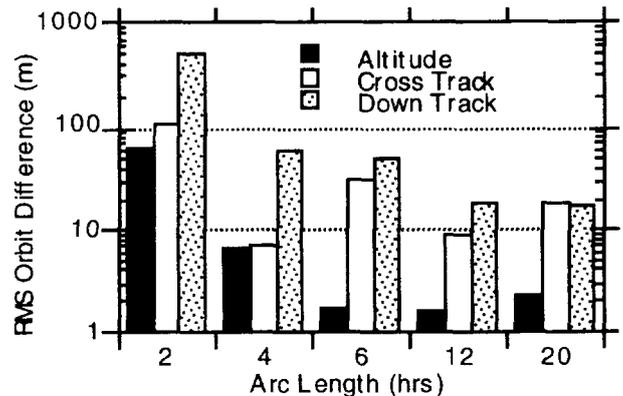
Fig 13. Effect of solution arc length on precision of recovered TDRS-3 orbit. The orbit differences shown are taken with respect to a nominal 34-hr solution.

The results in Figure 13 are instructive, but show only internal consistency of a single set of test solutions for TDRS-3. Clearly, additional work is warranted on the issue of rapid trajectory recovery. This is discussed at greater length in Section 3.2.

3. FUTURE DEMONSTRATIONS

For the TDRS study, there are a number of outstanding issues that should be addressed in examining the

316

operational viability of the GLT approach. We plan to perform another demonstration of the system in which all stations are deployed in the immediate vicinity of White Sands within the main beam of the SGLs. A smaller network (~100 km baselines) will be used and the duration of the demonstration will be extended so that some maneuvers can be tracked. A new ground station is in place at White Sands (Second TDRS Ground Terminal or STGT), and a close examination of the new TT&C range data is also warranted. In anticipation of this demonstration, some covariance analyses have been performed to assist in the design of the experiment.

3.1 COVARIANCE ANALYSES

For the covariance study, the towns of Las Cruces, Truth or Consequences and Tularosa, New Mexico were selected for the tracking sites. These towns all lie within the main beam and baselines among them form a triangle with ~100 km legs surrounding the TDRS White Sands station. With the exception of the tracking stations, the assumptions for the covariance study are identical to those comprising the estimation strategies outlined in Tables 1 and 3. TDRS-5 was chosen for the subject of this covariance study owing to the greater operational interest.

3.1.1. Nominal TDRS Orbit Determination

For nominal orbit determination, we assumed that the same arc length (42 hours) currently applied in the processing of the BRTS data would be used. With this nominal approach, the covariance analyses suggest that the 25 m orbit accuracy requirement for TDRS can be readily met with a properly designed system (Figure 14). The largest contributor to the TDRS-5 orbit error is mismodeling of the UTPM parameters. As noted earlier, the UTPM errors have negligible impact on the accuracy of the orbit in the Earth-fixed TRF.

3.1.2 WSC Range Bias

The next largest error source from the covariance result (Figure 14) is the bias of the range measurements from WSC. Recall that an *a priori* value of 1 m (one-way, equivalent to 2 m two-way) was assigned to this parameter in the covariance analysis. One meter is optimistic, being considerably smaller than the design specification of the ranging system at the STGT [*Cox and Oza*, 1994]. This prompted us to perform an analysis to determine the maximum range bias that could be tolerated before the future TDRS orbit determination requirement of 25 m is exceeded. *Nandi et al.* [1992] performed a similar evaluation for a connected element network near WSC, but the assumptions were somewhat different. Most notable among the differences, the noise figure of the

differenced phase observables in their study was due mostly to unmodeled tropospheric fluctuations. Since we are using GPS to estimate the zenith troposphere [*Lichten*, 1990], the errors should be significantly smaller.
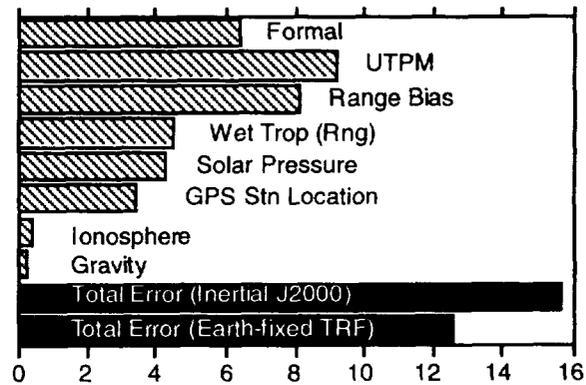
Fig 14. Relative contributions of various errors sources on future TDRS-5 orbit determination (3-d) based on covariance analysis. This exercise assumes baselines of ~100 km for the GPS/TDRS stations, and a 42 hr arc. The total 3-d orbit error is 12–16 m, depending on the reference frame.
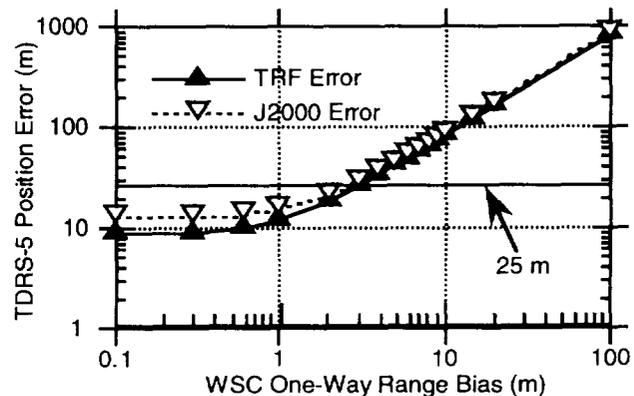
Fig 15. Expected Position Error for TDRS-5 (RSS) as a function of the WSC one-way range bias for 100 km network from covariance analysis. The one-way bias must be known to better than 3 m in order to support 25 m orbit determination for TDRS. (Equivalently, the two-way bias must be known to 6 m or better.) The orbit error is given in both the inertial (J2000) and terrestrial reference frames (TRF).

Figure 15 gives the expected 3-d orbit accuracy (RSS) for TDRS-5 as a function of the one-way range bias. The plot indicates that the one-way range bias must be kept under 3 m in order to maintain the orbit error below 25 m (1 σ). (The fundamental observation is a two-way range from WSC to TDRS and back to WSC. Strictly speaking, therefore, the only requirement is that the total observation bias accumulated over both the uplink and downlink must be kept below 6 m. The distribution of the bias errors on the uplink and downlink is not important, as long as the total bias is less than 6 m.) Keeping in mind

317

that orbit errors attributable to the "consider" parameters in our covariance analyses scale in a linear fashion, it can be seen (compare Figure 14) that the range bias emerges as the leading contributor to the orbit error once its one-way value exceeds ~1 m. This behavior is further illustrated in Figure 15, which shows the total 3-d orbit error increasing in an approximate linear fashion once the bias exceeds 3 m. For these regimes, the expected RSS position error can be approximated using the partial derivative of the range bias with respect to the satellite longitude. As noted earlier, for observing TDRS-5 at 10° elevation from WSC, the value of this partial is about 1/8. Hence a 1-way bias of 10 m will result in an orbit with a 3-d accuracy of about 80 m. The error will be manifest almost entirely as a simple bias in the longitude of the satellite position. In order to meet the EOS requirement for TDRS-5 (TDRS-West) orbit determination, the one-way range bias should thus be kept below 3 m. This result applies in an approximate sense to operational TDRS satellites in the eastern slot as well (e.g., TDRS-4), since the elevation as seen from WSC is nearly the same.

The STGT ranging system is undergoing testing at WSC, and the ranging data from there should be improved. If the new system cannot routinely deliver the required accuracy in nominal operations, a calibrated measurement might be obtained by tapping into the uplink and downlink at White Sands with additional enhanced TurboRogue receivers. The TT&C ranging tones would be tracked directly in the TurboRogues, which would be placed in the system as close to the respective STGT antennae as possible in order to mitigate cable and other hardware delays.

Another alternative for obtaining range data from WSC is to use the observations from the BRTS beacon. The BRTS range observations are derived from a TDRS service. The transmissions are made at S band, so the ionosphere delay is of some concern. Fortunately, this can be calibrated quite effectively with a colocated GPS receiver. Even with the unmodeled ionospheric delays, the BRTS range is considered more accurate than the TT&C range. We note that in this scenario, only the BRTS beacon at WSC would be used. None of the remote BRTS sites would be required. Though this option will be investigated, we will focus first on using the TT&C data.

3.1.3 Limiting Orbit Accuracy

Figure 15 also suggests that, with unbiased range measurements (< 1 m), the 3-d orbit accuracy (1 σ) for TDRS-5 can be brought below 10 m using the GLT technique. Though this remains to be demonstrated with actual data, it nonetheless underscores the remarkable precision of the differenced phase observables. That these

measurements taken over very short baselines (~100 km) have the potential to support 10 m orbit accuracy for a geosynchronous spacecraft is a testimony to the powerful ability of the GPS data to enable ultra-precise time transfer and reliable calibrations of atmospheric delays.

3.2 TRAJECTORY RECOVERY

An additional important requirement for TDRS orbit determination is the trajectory can be recovered rapidly after a station-keeping maneuver. Results from the January 1994 demonstration (Figure 13) provide evidence that the current STS requirement of 200 m TDRS orbit accuracy within 4 hours of a maneuver can be met. Additional data should be collected under a variety of conditions to make a more compelling case; this will be one of the primary goals of our next demonstration.

For improved accuracies in post-maneuver trajectory recovery, additional options can be explored. Since the short-baseline differenced phase data is not strong enough to recover the trajectory at the 25-50 m level from a cold start in a few hours, we would attempt to include the maneuvers(s) in the orbit solution arc [e.g., *Nandi et al.*, 1992]. In the simplest approach, a velocity impulse could be estimated at the burn time. (Even if the time of the burn could not be supplied *a priori*, or it could be detected by interrogating the continuous phase observations in a preprocessor. In recent analysis of similar GLT data from the Inmarsat geosynchronous spacecraft [*Kelecy et al.*, 1994], we readily detected a station-keeping maneuver in prefit tracking data residuals.) Estimating a velocity impulse at the burn time has been applied effectively for recovering the GPS orbits after a maneuver [*Lichten and Bertiger*, 1989]. Since the station-keeping maneuvers of a geosynchronous satellite are generally long in duration, more advanced approaches might prove necessary (e.g., estimating of stochastic accelerations in the presence of higher-resolution ground tracking.)

4. DISCUSSION

The results from the January 1994 TDRS/GPS tracking demonstration suggest that the short-baseline GLT method can be used to deliver TDRS orbits with accuracies better than 25 m in total position. Achievement of this level of accuracy is contingent on the availability of a small number of calibrated range observations from WSC with one-way biases known to about 3 m or better. Covariance studies provide evidence that, with a properly designed system, 10 m TDRS orbit accuracies can be approached using this method. In an actual operational scenario, it would be necessary to obtain these results in real time. In this context, we note that entire orbit determination procedures were run on HP work stations,

and that the sequence of programs required to generate an ephemeris file consume a cumulative CPU time of only a few minutes. These program sequences can be automated, as has been done for computing Topex/Poseidon orbits [*Wu et al.*, 1993]. In a recent demonstration of the Topex/Poseidon automated system, orbit estimates were delivered within 24 hours of the receipt of the flight data. For this exercise, a combination of orbit fits and predictions permitted achievement of 3D accuracies better than 1 m (better than 15 cm radially) in real time.

Although the tracking station equipment was operated and monitored by JPL scientists and engineers during the January 1994 demonstration, it is straightforward to adapt the current setup for unattended, continuous operation. The enhanced GPS receiver and antennae can be combined with a modem and phone line to permit automatic monitoring and data offloading by remote computer. Expected tracking station maintenance and repair is minimized due to the high level of autonomy and low system component count. This feature has in fact already been demonstrated with the performance of the continuously operating global network of Rogue and TurboRogue GPS receivers. The maturity of GPS technology, flexibility of the TurboRogue architecture, and simplicity of the demonstrated tracking station all contribute to low expected system costs.

If some of the issues addressed in Section 3 can be addressed in the next demonstration, then the short-baseline GLT method offers some distinct advantages for future TDRS tracking. Among them are: 1) low-cost of the small antennae and enhanced GPS receivers in comparison with larger systems typically used for geosynchronous tracking; 2) accuracy rivaling connected element networks for the calibration of media, Earth platform and timing errors from the simultaneous observation of TDRS and GPS; 3) operational convenience and maintainability afforded by a small, simple tracking stations in the vicinity of White Sands (as opposed to the present global network); and 4) processing system that lends itself to a high-level of automation, even on a desktop work station.

Similar benefits could be shared by other future missions adopting the GLT technique. In the case of the NASA Deep Space Network, which supports high-Earth orbiters in addition to deep space probes, valuable large antenna time could be freed up for more dedicated interplanetary tracking sessions. The high potential for inexpensive tracking should also be attractive to designers of NASA, military and commercial systems used for orbit determination of geosynchronous satellites.

REFERENCES

Bertiger, W. I., *et al.*, GPS Precise tracking of Topex/Poseidon: Results and implications, *J. Geophys. Res.*, Vol. 99(C12), pp. 24,449–24,464, 1994.

Blewitt, G., M. Hellin, F. Webb, U. Lindqwister, and R. Malla, Global coordinates with centimeter accuracy in the International Terrestrial Reference Frame Using GPS, *Geophys. Res. Lett.*, Vol. 19, 853-856, May 4, 1992.

Cox, C., and D. Oza, Tracking and Data Relay Satellite (TDRS) Orbit Determination: Operations Concepts for Using Global Positioning System (GPS) Tracking and Alternative Technical Approaches, CSC Report 553-FDD94/036/R0UD0, December, 1994.

Dunn, C. E., S. Lichten, D. Jefferson and J. Border, Sub-nanosecond clock synchronization and precision deep space tracking, Proceedings of the 23rd Annual Precise Time and Time Interval Meeting, NASA CP 3159, 1991.

Dunn, C. E., D. C. Jefferson, S. M. Lichten, J. B. Thomas, Y. Vigue, and L. E. Young, Time and position accuracy using codeless GPS, Proceedings of the 25th Annual Precise Time and Time Interval Meeting, NASA CP 3267, 169–179, 1993.

Edwards, C., D. Rogstad, D. Fort, L. White, and B. Iijima, A demonstration of real-time connected element interferometry for spacecraft navigation, *Adv. in Astronaut. Sci.*, 76, 1179–1192, 1991.

Haines, B. J., S. M. Lichten, R. P. Malla and S. C. Wu, A review of GPS-based tracking techniques for TDRS orbit determination, paper presented at NASA Goddard Flight Mechanics Estimation Theory Symposium, NASA CP 3186, 117–127, May, 1992.

319

Haines, B., S. Lichten, R. Muellerschoen, D. Spitzmesser, J. Srinivasan, S. Stephens, D. Sweeney and L. Young, A novel use of GPS for determining the orbit of a geosynchronous satellite: The TDRS/GPS tracking demonstration, proceedings of the 7th Intl. Tech. Mtg. of the Inst. of Navigation (GPS '94), pp 191–202, Salt Lake City, September, 1994.

Kelecy, T. M., A. Brown, W. Bertiger, S. Wu and S. Lichten, Orbit and ranging analysis of the Inmarsat AOR-West geostationary satellite, proceedings of the 50th Annual Mtg. of the Institute of Navigation, Colorado Springs, June, 1994.

Lichten, S. M., and W. I Bertiger, Demonstration of Sub-Meter GPS Orbit Determination and 1.5 Parts in 10^8 Three-Dimensional Baseline Accuracy, *Bulletin Geodesique*, Vol. 63, pp. 167-189, 1989.

Lichten, S. M., Precise estimate of troposphere path delays with GPS techniques, Jet Propulsion Laboratory Telecommunications and Data Acquisition Progress Report (JPL Internal Document), Vol. 42–100, 1–12, February 15, 1990.

Lichten, S. M., C. D. Edwards, L. E. Young, S. Nandi, C. Dunn, and B. Haines, A demonstration of TDRS orbit determination using differential tracking observables from GPS ground receivers, AAS Paper 93-160, AAS/AIAA Space Flight Mechanics Conference, Pasadena, Calif., February, 1993.

Lichten S., R. Muellerschoen, J. Srinivasan, U. Lindqwister, T. Munson, S.–C. Wu, B. Haines, J. Guinn, and L. Young, An automated low-Earth orbit determination system with high accuracy real-time capability, proceedings of the Natl. Tech. Mtg. of the Institute of Navigation, Anaheim, January, 1995.

Marshall, J. A., F. Lerch, S. Luthcke, R. Williamson and J. Chan, As assessment of TDRSS for precision orbit determination, AAS Paper 95–104, AAS/AIAA Space Flight Mechanics Conference, Albuquerque, February, 1995.

Meehan, T. K., Srinivasan, J. M. D. Spitzmesser, C, Dunn, J. Ten, J. B. Thomas, T. Munson, and C. Duncan, The TurboRogue GPS receiver, Proceedings of the 6th IGS Conference on Satellite Positioning, Columbus, OH, 1992.

Nandi, S., C. Edwards, and S. C. Wu, TDRSS orbit determination using short-baseline differenced carrier phase, paper presented at NASA Goddard Flight Mechanics Estimation Theory Symposium, NASA CP 3186, 103-115, May, 1992.

Oza, D., *et al.*, Accurate orbit determination strategies for the TDRS, these proceedings.

Webb, F. H., and J. Zumberge, An Introduction to GIPSY/OASIS II, Course notes, Boulder, CO, July, 1993.

Wu, S. C., Differential GPS approaches to orbit determination of high-altitude satellites, AAS paper 85-430, presented at Astrodynamics Specialists Conference, Vail, Colo., August, 1985.

Wu, S. C., R. J. Muellerschoen, W. I. Bertiger, T. P. Yunck, Y. E. Bar-Sever, and T. N. Munson, Automated precision orbit determination for Topex/Poseidon with GPS, AAS Paper 93–756, Astrodynamics Specialists Conference, Victoria, B. C., Canada, August, 1993.

Zumberge, J, R. Neilan, G. Beutler, and W. Gurtner, The International GPS Service for Geodynamics—Benefits to users, proceedings of the 7th Intl. Tech. Mtg. of the Inst. of Navigation (GPS '94), pp 1663–1666, Salt Lake City, September, 1994.

GPS as an Orbit Determination Subsystem[*]

Richard Fennessey, Pat Roberts, Robin Knight, and Bart Van Volkinburg
Lockheed Technical Operations Company. Inc. (LTOC)

Abstract

This paper evaluates the use of Global Positioning System (GPS) receivers as a primary source of tracking data for low-Earth orbit satellites. GPS data is an alternative to using range, azimuth, elevation, and range-rate (RAER) data from the Air Force Satellite Control Network antennas, the Space Ground Link System (SGLS). This evaluation is applicable to missions such as Skipper, a joint US and Russian atmosphere research mission, that will rely on a GPS receiver as a primary tracking data source.

The Detachment 2, Space and Missile Systems Center's Test Support Complex (TSC) conducted the evaluation based on receiver data from the Space Test Experiment Platform Mission 0 (STEP-0) and Advanced Photovoltaic and Electronics Experiments (APEX) satellites. The TSC performed orbit reconstruction and prediction on the STEP-0 and APEX vehicles using GPS receiver navigation solution data, SGLS RAER data, and SGLS angles-only (azimuth and elevation) data. For the STEP-0 case, the navigation solution based orbits proved to be more accurate than SGLS RAER based orbits. For the APEX case, navigation solution based orbits proved to be less accurate than SGLS RAER based orbits for orbit prediction, and results for orbit reconstruction were inconclusive due to the lack of a precise truth orbit. After evaluating several different GPS data processing methods, the TSC concluded that using GPS navigation solution data is a viable alternative to using SGLS RAER data.

I. Introduction and Background

Detachment 2, Space and Missile Systems Center performs test, evaluation, and operations in support of U.S. Air Force research satellite programs. Orbit and telemetry operations are conducted through the global Air Force Satellite Control Network (AFSCN) and the Test Support Complex (TSC) located at Onizuka Air Station in Sunnyvale, California. The TSC currently performs orbit determination using range, azimuth, elevation, and range-rate data from a Space Ground Link System (SGLS) ground antenna network.

Orbit states for AFSCN vehicles must be determined and propagated with sufficient accuracy (approximately 1 minute in-track) to support antenna scheduling 2-3 weeks in advance. The AFSCN currently operates approximately 100 on-orbit vehicles. In addition to this, activities such as ground site testing, launch rehearsals, and maintenance/downtime compete for time with the AFSCN's 16 ground antennas. Large propagation error can lead to replanning and scheduling of the satellite contacts. These scheduled contacts can be lost due to conflicts with other network users. A minute is a large in-track error for a low-Earth satellite orbit prediction but it happens with dynamic atmosphere conditions and especially if a scheduled on-orbit maneuver is canceled or changed.

GPS receivers have been placed on several space vehicles, primarily as a data source for precise orbit determination in a non-realtime mode. Detachment 2 has processed GPS data for its vehicles, the Space Test Experiment Platform Mission 0 (STEP-0), the Radar Calibration (RADCAL) satellite, and the Advanced Photovoltaic and Electronics Experiments (APEX) satellite. The STEP-0 spacecraft uses a Rockwell Advanced Satellite Technology (AST) V six channel GPS receiver. RADCAL and APEX use a Trimble Advanced Navigation Sensor (TANS) Quadrex, coarse acquisition (C/A), GPS receiver. Future programs, such as Skipper, a joint US and Russian

---

atmosphere research mission, will use a GPS receiver as the primary source of orbit tracking data. The TSC vehicles with GPS receivers are summarized in Table 1.

Table 1. Detachment 2 Spacecraft with GPS Receivers

Spacecraft	Launch	Orbit Inclination/Size	Mission
RADCAL	Jun 93	89.5 deg / 800 x 800 km	Radar Calibration U.S. Government space ranges
STEP-0	Mar 94	105 deg / 550 x 560 km	Autonomous navigation, laser and radio frequency measurement
STEP-2	May 94	82 deg / 600 x 800 km	Support Signal Identification Experiment
APEX	Aug 94	70 deg / 380 x 2500 km	Advanced battery and solar cell experiments
Skipper	Sep 95	98 deg / Initially 800 x 800 km, then 135 x 800 km	Atmosphere measurement, US/Russian joint mission

Though many TSC vehicles have GPS receivers, Skipper is the first TSC mission for which GPS will be the primary tracking data source. A SGLS ranging transponder is not being placed on the vehicle because of cost. Orbit prediction accuracies for Skipper must be sufficient to perform perigee raise maneuvers after low perigee operations near an altitude of 135 km. The end-of-mission activities include taking atmospheric measurements as the vehicle re-enters within site of the Kwajelien Atoll or the Kaena Point radar in Hawaii. Orbit determination and prediction will be challenging due to the limitation of only four ground contacts per day and a high drag environment due to a low perigee altitude. Using angles-only tracking data for orbit fits, even for eight contacts per day, can yield mediocre results (kilometers of error). Obtaining a reliable drag (B-factor) solution is the biggest problem since an error in this parameter will yield large errors in the propagation.

There are currently three options available for obtaining orbit position required for Skipper mission planning, scheduling, and experiment evaluation: GPS, SGLS angles only, and Air Force Space Command Space Surveillance Center (SSC) orbital elements. The current plan is to use navigation solutions from the Trimble TANS receiver to produce orbits. The backup plan is to use azimuth and elevation from SGLS and/or use SSC element sets.

The only orbit state information available to the TSC, other than SGLS based ephemeris, is from external agencies. Without the tracking data, the TSC obtains orbital elements from the SSC. For vehicles that have had an on-orbit anomaly such as a power or transmitter failure, commanding contacts are attempted until options are exhausted. It is crucial that the AFSCN antennas be pointed within the 0.25 degree half beamwidth (approximately 4 km at 1000 km range) for these recovery attempts. In this case, the pointing information is solely dependent on the SSC elements or on the propagation of aging TSC orbit elements.

Using STEP-0 and APEX GPS data processing, the TSC evaluated the use of an on-board GPS receiver as an orbit determination subsystem. GPS orbit determinations were compared to the SGLS based orbit determination system. The RADCAL satellite is not used in this study since it does not have a SGLS transponder. In addition, the TSC operates the STEP-2 which has a GPS receiver. The TSC does not have access to this data since payload telemetry is collected at another location.

II. Tracking Data and Orbit Determination Systems

The TSC performed orbit determinations for the STEP-0 and APEX spacecraft using SGLS, GPS navigation solutions, and SGLS angles-only data. Table 2 contains the data types and quantity used for orbit determination. The data types and amount are similar for both the STEP-0 and APEX vehicles. Twenty-four hour data spans were used for all the test cases. Data gaps of up to 2 hours exist in some STEP-0 GPS data spans. The SGLS and angles-only tracking data are not continuous. There are gaps of several hours between some ground contact times. Contact time for the STEP-0 vehicle is approximately 8 - 12 minutes. APEX is in a higher orbit, 380 x 2500 km, and its contact times vary from 10 - 20 minutes.

322

Table 2. Data Fitting for STEP-0 and APEX Orbit Reconstruction

Orbit Determination Data Source	Data Density STEP-0	Data Density APEX	Span (Days)	Data Fitting Methodology
GPS Nav Solutions	1/minute	1/minute	1	Batch Fit
SGLS R,RR,Az,El	100 points per contact (approx 8 contacts/day)	60 points per contact (approx 5 contacts/day)	1	Batch fit
Az, El (angles-only)	100 points per contact (approx 8 contacts/day)	60 points per contact (approx 5 contacts/day)	1 2*	Batch fit
Raw GPS	1/sec	1/sec	1	Differential GPS

* APEX used two days of angles-only data

Since most people outside the AFSCN are not familiar with the SGLS data. Table 3 describes the uncertainties in the four SGLS measurements. In some cases the uncertainties are due limitations in the modeling capabilities of of AFSCN observation processing and orbit determination software. The totals for uncertainty are worst case since the uncertainties are just summed.

Table 3. AFSCN SGLS Worst Case Measurement Uncertainties

| Uncertainty Type | Measurement Type | | | |
	Azimuth	Elevation	Range	Range Rate
Data Noise	0.02 deg	0.02 deg	5 meters	1 cm/sec
Bias	0.02 deg	0.02 deg	15 meters	1 cm/sec
Refraction*	0	0.02 deg	100 meters (15)**	3 cm/sec
Station Location	0	0	5 meters	0
Time Bias***	0	0	7 meters	4 cm/sec
Total	0.04 deg	0.06 deg	134 meters (47)	9 cm/sec

* The current AFSCN software models Troposheric refraction with a monthly average model and does not model Ionospheric refraction. This is not a measurement limitation but a software one.
** The large Range uncertainty is due to the unmodeled Ionospheric refraction around maximum solar activity at low elevations. This number is significantly less (15 meters) if the data used is limited to elevations above 10 degrees and throughout the "cooler" portion of the solar cycle.
*** The time bias for all stations is 1 millisecond.

The GPS receiver characteristics/configuration for STEP-0 and APEX are summarized in Table 4. APEX uses the TANS receiver which uses six channels to track and process coarse acquisition (C/A) code[1]. This receiver is not space hardened. The AST V receiver was designed to collect and process both the C/A code and precise (P) code. Since STEP-0 was launched after the full operations capability declaration of the GPS constellation, it does not receive P code, except from one of the older Block 1 GPS satellites. Hence, the STEP-0 receiver is effectively C/A-code-only with the current status of the GPS constellation.

Table 4. GPS Receiver Configurations used in Study

Receiver	Antennas	Channels	Code Processing	Pseudo-range	Carrier Phase
AST V (STEP-0)	1	6	C/A and P	Yes	Yes*
TANS (APEX)[1]	3	6	C/A only	Yes	Yes

* 1 sec destructive count - long periods (minutes) of carrier could not be reconstructed

Three different astrodynamic software systems were used to process the orbit tracking data from both vehicles. These are summarized in Table 5. The Command and Control Segment (CCS) used the WGS-84 41 x 41 geopotential, Jacchia 60 static atmosphere, and solar and lunar perturbations in a least squares batch fit for SGLS and angles-only orbit determination.

Table 5. Orbit Determination Software Systems

Orbit Software	Description
CCS	Orbit and telemetry processing system from the U.S. Air Force that performs orbit determination using SGLS track data.
MIRAGE	GPS differential processing system from the Jet Propulsion Lab used for processing TOPEX and modified to handle STEP-0 receiver data format.
TRACE	Astrodynamic analysis package from the Aerospace Corporation that can perform orbit determination on Earth-fixed Cartesian ephemeris such as GPS navigation solutions.

Since CCS does not perform differential correction on Earth fixed Cartesian vectors, the Trajectory Analysis and Orbit Determination Program (TRACE) system was used to fit the GPS navigation solutions. It uses similar force modeling and least squares technique as does CCS for performing the orbit determinations and propagation. Editing was performed to remove nonvalid or noisy navigation solutions.

The differential GPS solution for STEP-0 used the Jet Propulsion Lab's Multiple Interferometric Ranging Analysis and GPS Ensemble (MIRAGE) software. This system uses data from the NASA world-wide GPS receiver network so that it can effectively remove selective availability (SA) effects. MIRAGE uses the most sophisticated force modeling of the three systems. The force modeling includes a 50 x 50 truncated Joint Gravity Model (JGM) geopotential, Drag Temperature Model (DTM) atmosphere, solid earth and ocean tides, solar radiation, and empirical accelerations[2].

All orbits were reconstructed using 24 hour data spans except for APEX angles-only orbits, which used 2 days of data. For the STEP-0 orbit reconstruction cases, the differential GPS trajectory is used as a truth baseline to judge accuracy performance. APEX used a SGLS based orbit as a comparison baseline since a differential GPS based orbit was not available.

For the orbit propagation comparisons, the reconstructed orbits are propagated for one week and compared to a truth baseline. Fourteen days of SGLS based reconstructed orbits are used for the orbit prediction truth for both STEP-0 and APEX. Figure 1 shows an overview of the orbit determination and comparison process. Angle-only orbits are included in both the reconstruction and prediction test cases since the TSC wants to evaluate a backup orbit capability for the Skipper program.
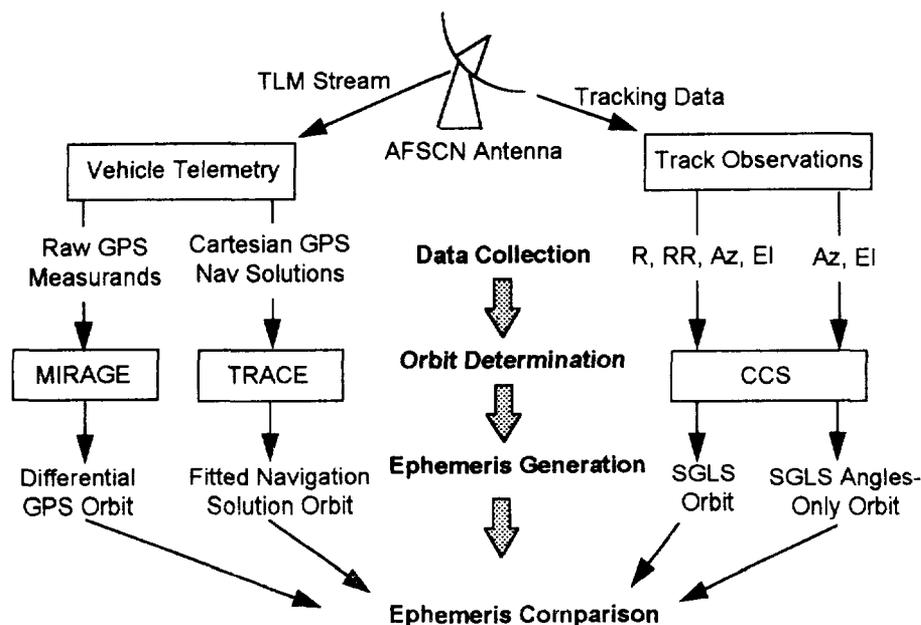
Figure 1. Orbit Determination and Ephemeris Comparison Process

III. Orbit Reconstruction

Differential GPS processing was performed for the STEP-0 vehicle. This yields position accuracy better than 10 m (3 sigma) [2]. Figure 2 shows STEP-0 orbit reconstruction accuracy compared to the differential GPS based ephemeris. Both the navigation solution fits and SGLS show consistency within a 30 m RMS. Orbit determination results using the once-per-minute navigation solution fair better with an average RMS difference for the six days of 15.7 m. Over the same comparison spans, SGLS showed an average root mean square (RMS) difference of 22.6 m. These position difference RMSs are based on a 24 hour span of three dimensional ephemeris differences at five minute increments. The differential GPS based ephemeris is used as the baseline since it is considered to have the best absolute accuracy.
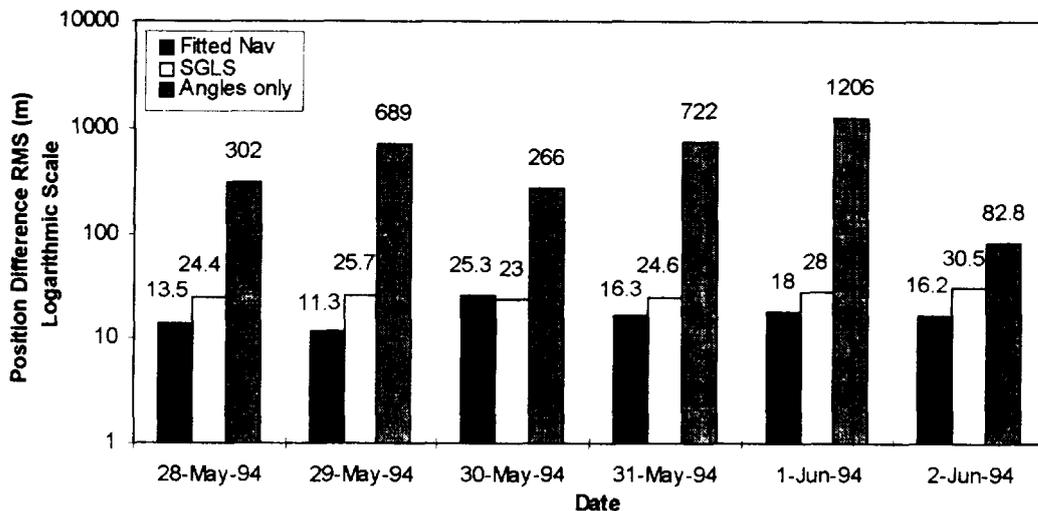
Figure 2. SGLS, Fitted Navigation Solutions, and SGLS Angles-only Orbits Compared to Differential GPS Based Orbit (STEP-0)

Orbit determination residuals for a STEP-0 navigation solution fit are shown in Figure 3. This case is representative of all the STEP-0 navigation solution fits. It has an RMS of the 3-D position residuals of 56.6 m and a standard deviation of 27.0 m. The prominent errors here appear to be induced by SA. Many of these orbit determination runs had data gaps of a couple hours. This was due to lost telemetry or that the receiver was not tracking and provided non-valid navigation solutions.
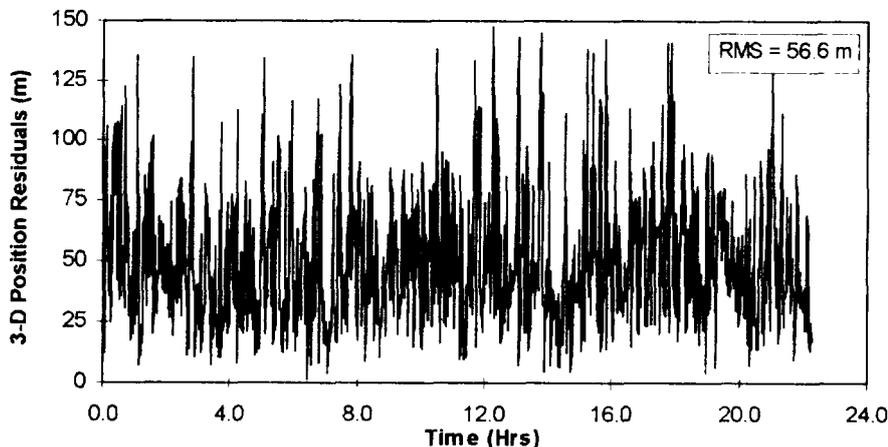
Figure 3. Residuals for STEP-0 Navigation Solution Fit, 31 May 1994

Since APEX does not have highly accurate ephemeris available, such as differential GPS solutions, GPS orbit determination results are compared to a SGLS baseline. Figure 4 shows fitted navigation solutions and angles only orbits compared to a SGLS baseline. Note that these angle-only orbits use two days of data. Results were so bad with one day fits that an additional day of data was used. The additional day is prior to the date of the test case as shown in Figure 4.
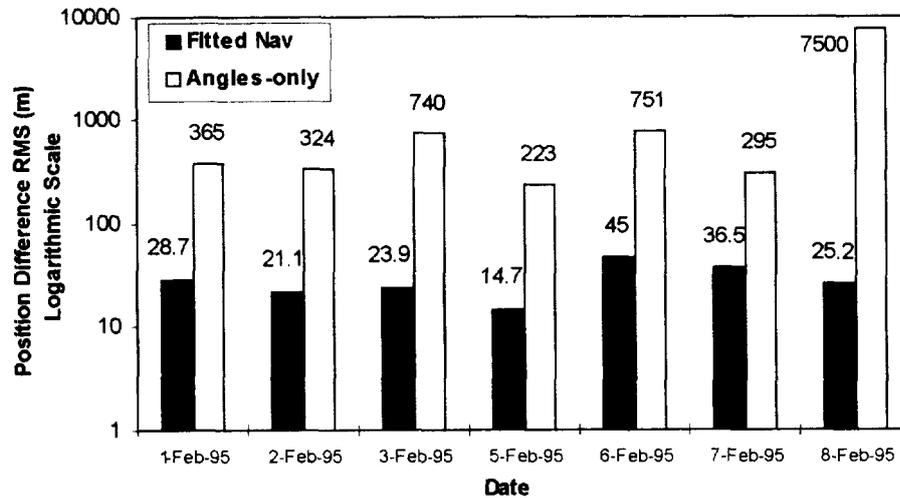
Figure 4. Fitted Navigation Solutions and SGLS Angles-only Orbits Compared to SGLS Based Orbit (APEX)

Orbit determination residuals for an APEX navigation solution fit are shown in Figure 5. It has a 3-D position residual RMS of 72.5 m and a standard deviation of 33.5 m. The RMS is 12 m higher than that for the STEP-0 navigation solution residuals. Since these orbit comparisons are at different time periods, it is possible that the GPS constellation SA implementation level could be different. It also might be attributed to both the receiver performance and vehicle orbit differences. APEX's perigee is 380 km and ionospheric signal delay could have contributed to the error at lower altitude regions.
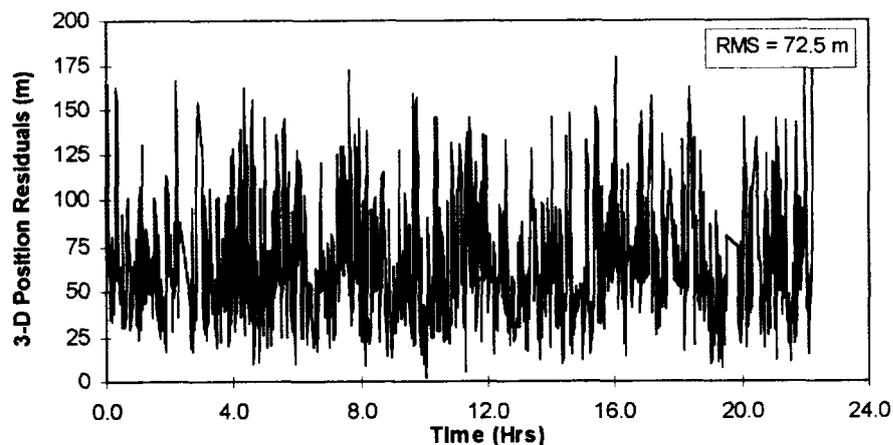
Figure 5. Residuals for APEX Navigation Solution Fit, 1 Feb 1995

IV. Orbit Propagation

The propagation results use the same orbit determination cases as used in the reconstruction comparisons as described in Table 2. The differential GPS orbits are not used in the propagation performance cases and an additional day of STEP-0 orbit determinations was added for June 3. Each test case uses and orbit based on one

day of orbit determination data (two days for APEX angles-only) and propagates it for one week. Seven days of tracking data were used for both the STEP-0 and APEX test cases. These were propagated and compared to 14 days of reconstructed SGLS 24 hour truth orbits.

Figure 6 shows the average error growth for one week of propagation for STEP-0. Note that these prediction errors are the average of all seven cases. For example, the day four value of 46 km in Figure 6 is the average prediction error for each of the seven angles-only orbits at the four day point. For all seven of the SGLS predictions, the standard deviation was nearly 50% of the average prediction error. For example, the second day SGLS average prediction error of 1.05 km had a standard deviation of .51 km. This is 48% of the average prediction error. The average standard deviations for all seven days of navigation solution, SGLS, and angles-only predictions were 77%, 50%, and 63% of the prediction error values, respectively.
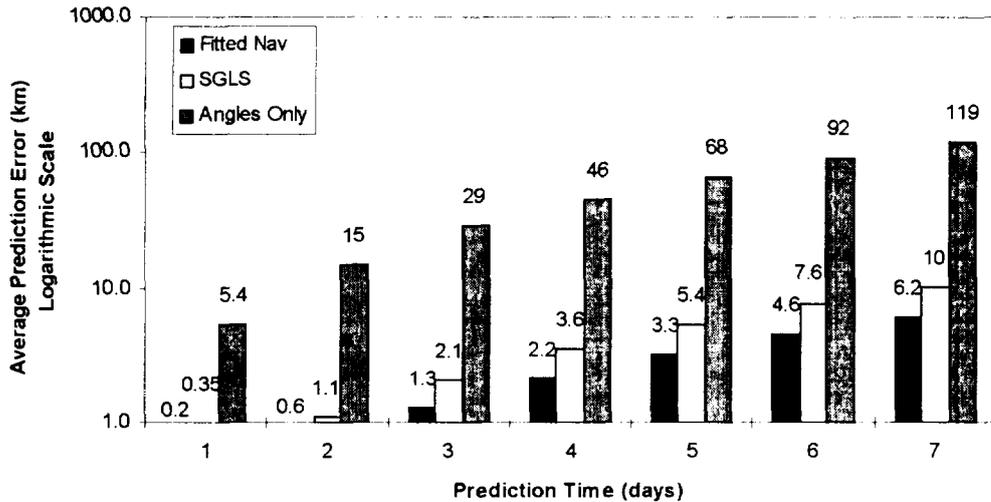

Figure 6. Propagation Error for Fitted Navigation Solutions, SGLS, and Angles-only Orbits
Compared to SGLS Truth Baseline (STEP-0)

Even for the best atmosphere models, density uncertainty is generally the greatest error source in low earth orbit propagation. High amounts of solar activity increase atmospheric density at a given orbital altitude. If the solar activity during the orbit propagation period is not approximately the same as during the orbit determination period, this leads to significant in-track prediction errors. Figure 7 shows the F10.7 and Ap indices during the time of the STEP-0 test case propagations. Orbits determined in the time from about 30 May to 1 June will be predicting with a drag that is to high. Hence, the vehicle will be predicted to arrive earlier than actual arrival over ground sites. Prediction accuracies for orbits generated from 29 - 31 May had significantly higher prediction errors than the other orbits.
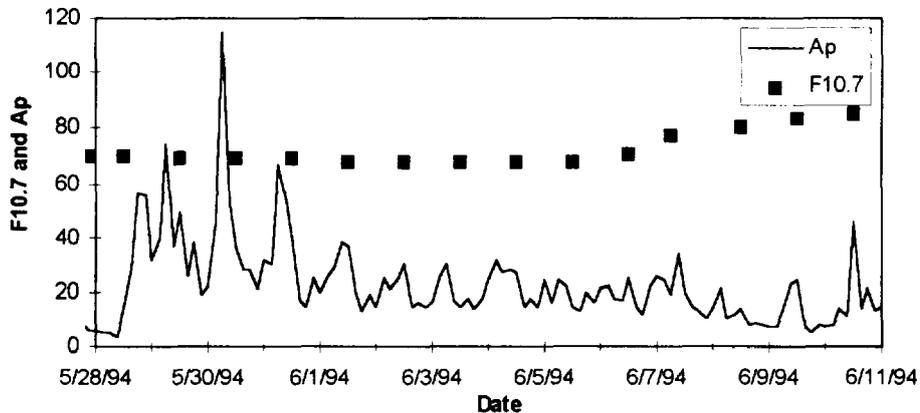
Figure 7. F10.7 and Ap indices from May 28, 1994 - Jun 11, 1994

Figure 8 shows an average error growth for up to a one week propagation for APEX. SGLS 24 hour fits were used as the truth baseline just as was done for the STEP-0 predictions. Figure 6 is composed of an average of propagation errors from seven different test cases. Each of these cases, which are referenced by the date of the actual raw data used, were produced using the fitted navigation solutions, SGLS, and angles only respectively. The average standard deviations for all seven days of navigation solution, SGLS, and angles-only predictions were 49%, 77%, and 93% of the prediction error values, respectively. Figure 9 shows the solar activity for this test period.
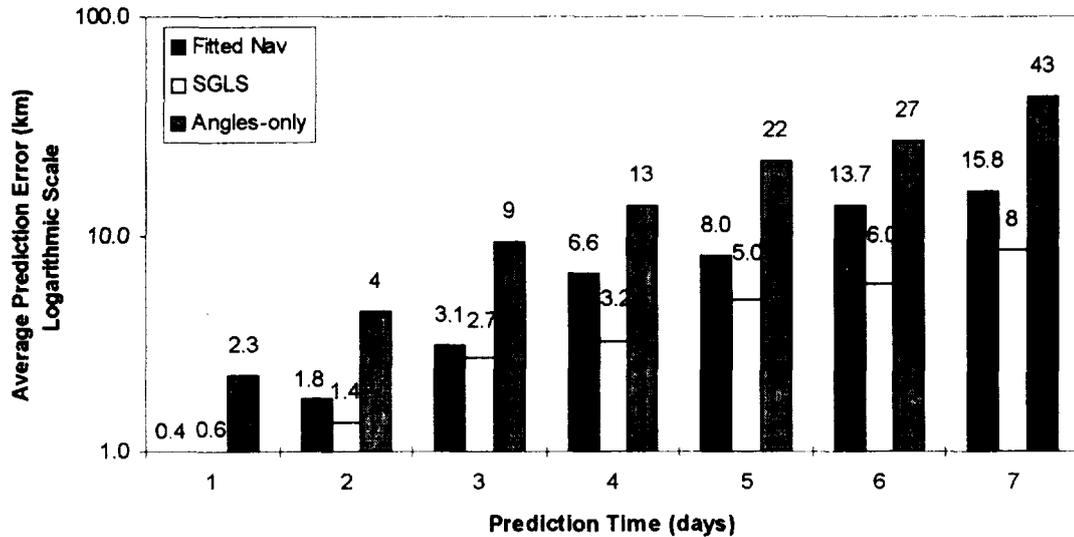
Figure 8. Propagation Error for Fitted Navigation Solutions, SGLS, and Angles-only Orbits Compared to SGLS Truth Baseline (APEX)
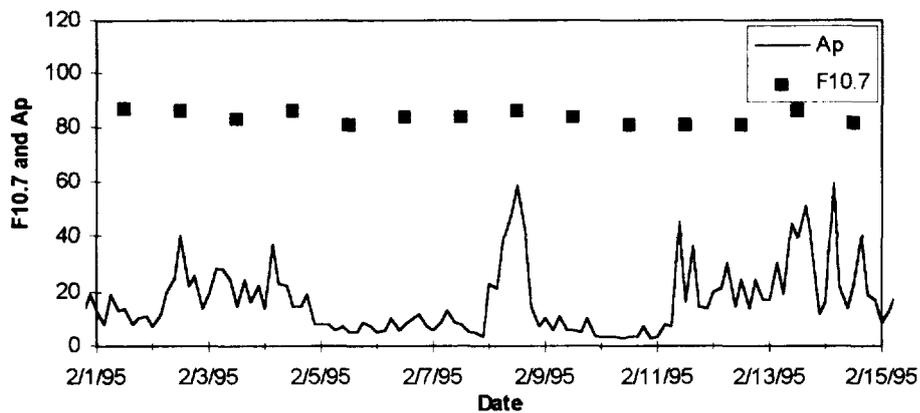
Figure 9. F10.7 and Ap indices from Feb 1, 1995 - Feb 15, 1995

Using angles-only for both one and two day fit spans provide solutions that are an order of magnitude less accurate than normal SGLS or GPS. The orbit reconstruction test cases are not optimized for prediction performance. Ideally, orbit propagations over a week should use more than one day of orbit determination data. Increasing the length of the fit span helps mitigate solar activity spikes and would improve prediction for both STEP-0 and APEX. Further study in this area should look at a variety of data spans during differing solar conditions. Also, an additive deweighting least squares fit could have been used in this study. Past TSC experience has shown additive deweighting generated orbit predictions are more sensitive to atmospheric disturbances.

Based on the STEP-0 and APEX orbit prediction results, it would appear that the TSC should encounter little problem in supporting Skipper orbit determination operations. Even if angle-only fits are used with at least a two day fit span, this would probably be sufficient to communicate with the vehicle. A problem exists: Skipper will operate at a perigee as low as 130 km and will be performing orbit maneuvers every 48 hours on its way down from 800 km to 130 km. Hence two days of orbit determination will not be available and orbit propagation will not be as accurate as STEP-0 or APEX when the Skipper orbit reaches a low perigee.

V. System Considerations

Most work in the space based GPS navigation area has focused primarily on accuracy. Tremendous results have been achieved by JPL for the Ocean Topography Experiment (TOPEX/POSEIDON) program where 3-D position accuracies of approximately 13 cm have been achieved. But does it make sense to use GPS on other types of vehicles where accuracy requirements are not so stringent.

There is a wide range of downlink bandwidth requirements required for GPS orbit determination. If only tens of meters accuracy is required then a few hundred navigation solution vectors should suffice for orbit determination. This may only amount to 100 - 200 kilobytes of data per day. The STEP-0 GPS receiver produced data at one second intervals and produced 25 MB per day of GPS data. This raw data included the pseudo-range and carrier phase, navigation solutions, and almanac data.

SGLS is the orbit determination method of choice from the TSC perspective due to the large amount of software and infrastructure that is already in place. A vehicle or mission designer may not be so constrained in this choice. Orbit determination using SGLS is a very well established process which only requires periodic software and procedural updates. Using other systems that support GPS data processing require the TSC to develop support software and integrate this with current software and hardware.

VI. Operational Considerations

An on-orbit GPS receiver is one more payload that must be managed and integrated into vehicle ground operations and on-board resources. Using a GPS receiver, rather than the traditional SGLS transponder for tracking data, has many of the same operational risks as well as benefits.

Reliability is a paramount concern, especially considering the experience the TSC has had with both the STEP-0 and APEX receivers. APEX relied on the real-time Cartesian navigation solutions from the TANS receiver for attitude and payload operations control. This implementation was terminated after receiver data problems caused attitude anomalies. There was no on-board filter that evaluated the position/velocity values or receiver time for validity. An on-board orbit propagator is probably a much more robust solution for obtaining ephemeris data for a processor even though memory errors could certainly cause the same attitude anomalies. An on-board propagator has traditionally been used for obtaining this data for other satellites.

The AST-V receiver on STEP-0 has not been capable of providing tracking data since August 1994 and had many other periods of tracking difficulty prior to this. If an operations center requires very accurate predictions, then a large data gap caused by a malfunctioning receiver could be detrimental to certain orbit operations.

A major benefit of using a GPS receiver is that it can reduce the number ground station supports. For example, a low earth vehicle could store 24 hours of GPS data and then transmit this during one station contact. For a vehicle using the traditional ground based SGLS observations, additional contacts are required to collect track data, since one contact per day is insufficient for quality orbit determination. This is an extreme example but shows that an on-board GPS receiver would negate the need for additional tracking passes. If a program wants to alleviate the concerns associated with having an orbit determination system, then SSC element sets are an option. For agencies that work with the U.S. government, SSC element sets can be made readily available and an orbit determination subsystem would not be required. This configuration does create a lack of autonomy for certain orbit related operations.

VII. GPS Orbit Determination Subsystem Evaluation Summary

A summary GPS and SGLS orbit determination options are shown in Table 6. An attempt was made to account for the different factors that should be evaluated when selecting an orbit determination methodology. This table only considers GPS orbit determination options along with SGLS and does not look at other methods such as Doppler, laser ranging, or a combination of different data types.

Table 6. Evaluation of GPS Processing Methods

Method	Accuracy	Labor	Data Volume	Comments
Single Navigation Solution	> 60 m	Light	Very Small	No drag solution. Large propagation error. Test case not run.
SGLS	> approx 50 m	Light	Small	Current TSC method
Orbit Fit over C/A code Navigation Solutions	20 - 40 m	Light	Small	STEP-0 test cases
Orbit Fit over Navigation Solutions with SA removal	5 - 15 m^4	Light	Small	RADCAL method. Used SA algorithm knowledge. Requires secure environment. Used GPS almanacs.
Orbit Fit over P code Navigation Solutions	< 5 - 15 m	Light	Small	No test cases investigated. Requires encryption keys.
Differential GPS using receiver pseudo-range only	< 10 m	Heavy	Large	Large CPU and disk usage. STEP-0 test case. Uses carrier phase data from GPS ground network
Differential GPS using pseudo-range and carrier phase.	< 1 m	Heavy	Large	Large CPU and disk usage. Current TOPEX method.

Stated accuracy values are approximate and in most cases have been achieved and documented by different agencies. No examples of performing orbit determination with P code based navigation solutions was referenced. This chart does not try to extrapolate these results to all orbit regimes and conditions. It does attempt to show different methods used in achieving different levels of on-orbit accuracy. JPL has proven differential GPS processing to the sub-meter level.

The labor ratings refer to the approximate amount of personnel hours required to complete data editing and orbit determination with current TSC methods. A labor rating of Light means less than two hours, Medium is two to four hours, and Heavy is greater than four hours. The Data Volume category includes all tracking data plus any other data necessary. For the differential case this would include such items as GPS initial orbits, NASA receiver network data, solar flux, and receiver measurands. All of the options except for differential GPS require a small amount of data, meaning less than a couple of megabytes (MB).

The differential GPS processing performed by the TSC and JPL is a very intensive computational process. To perform differential GPS processing one must obtain data from the NASA GPS ground receiver network. The TSC would use approximately 14 MB of this data for a one day fit. If continuous spans of very accurate ephemeris are needed, such as required by the TOPEX mission, then a satellite program must be willing to invest in software automation tools, hard disk storage, and trained analysts/programmers. On the other extreme, the TSC has found that fits using the receiver navigation solutions are a straight forward process that many organizations could take advantage of.

VIII. Conclusion

The orbit determination methodology used for a particular program is very dependent on required accuracies, existing infrastructure, and compatibility requirements. The TSC has determined that navigation solutions at the once per minute rate would provide better or comparable accuracy than the current SGLS system. If a spacecraft flown by the AFSCN requires greater than 10 - 20 meters accuracy, then the spacecraft program must be prepared

to invest in software development and ground processing to perform differential processing. Another option to meet these accuracies is to obtain access to the classified P code or SA removal process.

Many factors besides accuracy should be considered before deciding on GPS as an orbit determination subsystem. GPS data must be budgeted into the spacecraft telemetry.   labor and processing is required if a satellite program requires better than 10 m accuracy. Further study into the orbit determination subsystem evaluation should examine the following areas:

1) Navigation solution density relationship to orbit determination accuracy
2) Quantification of labor spent on spacecraft orbit data processing
3) Downtime of different GPS receiver models while on orbit
4) Differential GPS processing for the APEX data

IX. Acknowledgments

Special thanks to the people who have supported the Detachment 2 GPS effort. Major Jack Anthony who was the technical lead for STEP-0 and worked with the TSC in establishing STEP-0 accuracy requirements and goals. Lt Terry Wiest, Detachment 2, who initiated and coordinated a contract with JPL for transfer and modification of the MIRAGE software for use with the STEP-0 AST V receiver. To the MIRAGE team: Dr. Bobby Williams, Peter Wolff, and Joe Guinn who performed the MIRAGE software development and rehosting effort and shared their in-depth GPS processing expertise with the TSC. Thanks to Chris Bryan, formerly with the TSC, who initiated the TSC effort into GPS processing. Thanks to Warren Sue, TSC Orbit Analyst, who assisted with the TRACE orbit determination processing. Also to Mark Reynolds and Mark Frank who provided technical consulting and helped edit the paper.

X. References

[1] Trimble Navigation, "TANS QUADREX GPS Receiver Interface Control Document", 1992.

[2] Guinn, J., "TAOS Orbit Determination Results Using Global Positioning Satellites", AAS/AIAA Spaceflight Mechanics Meeting, 13-16 February, 1995.

[3] Space Test and Transportation Program Office, "Orbital Operations Handbook, Advanced Photovoltaic and Electronics Experiments Satellite", 15 June 1994.

[4] Langer, J., "RADCAL: Precision Orbit Determination with a Commercial Grade GPS   Receiver", Technical Meeting of The Institute of Navigation in San Diego, 25 January, 1994. Accuracy estimated based on Doppler comparison with GPS trajectory.

Operational Considerations of Using GPS for Spacecraft Navigation

Roger C. Hart and Kathy R. Hartman
Goddard Space Flight Center (GSFC)
Greenbelt, MD, USA

Abstract

The Flight Dynamics Facility (FDF) at the NASA Goddard Space Flight Center (GSFC) has provided operational spacecraft orbit support for many years, currently generating orbit products for about 20 satellites. To date, operational orbit determination in the FDF has been performed on the ground using data from ground-based or space-based tracking systems. Current development of spaceborne Global Positioning System (GPS) receivers is projected to have a significant effect on the support needed for operational satellite navigation. This paper identifies the functions performed in spacecraft navigation and examines and quantifies how the functions and support levels will be affected as onboard GPS receivers are implemented on spacecraft. Cases are considered spacecraft using or not using NASA ground and space networks resources.

1.0 Introduction

Interest in use of the Global Positioning System (GPS) for spacecraft navigation has grown considerably in recent years with the flight of several experiments and new spacecraft committing to the operational use of GPS. Often cited as drivers for this movement are reductions in ground operations, including elimination of traditional tracking, orbit determination, and state vector uploads to the spacecraft. Evidence is often anecdotal, focusing on only one or two issues. This paper examines the functions performed in support of spacecraft navigation and assesses the effect on ground systems.

1.1 Flight Dynamics Functions

The Flight Dynamics Facility (FDF) at the NASA Goddard Space Flight Center (GSFC) provides orbit, attitude, and TDRSS or station acquisition support for about 20 NASA and non-NASA spacecraft. FDF functions include analysis for mission planning, launch support, and routine operational support. FDF receives tracking data and telemetry and generates orbit, attitude, and acquisition products that are distributed to spacecraft control centers, scientists, and tracking networks. Figure 1 illustrates key interfaces and functions of the FDF.

FDF involvement with a spacecraft continues from the conceptual phases through the end of mission life. Support includes both analysis and operations. The following are considered as high-level navigation functions performed in the FDF:

> Mission design and orbit analysis
> Orbit determination
> Trajectory Control
> Scheduling and planning aid generation
> Acquisition data operations
> Calibration and verification of onboard system
> Onboard compute table generation
> Metric tracking data evaluation
> Anomaly resolution.
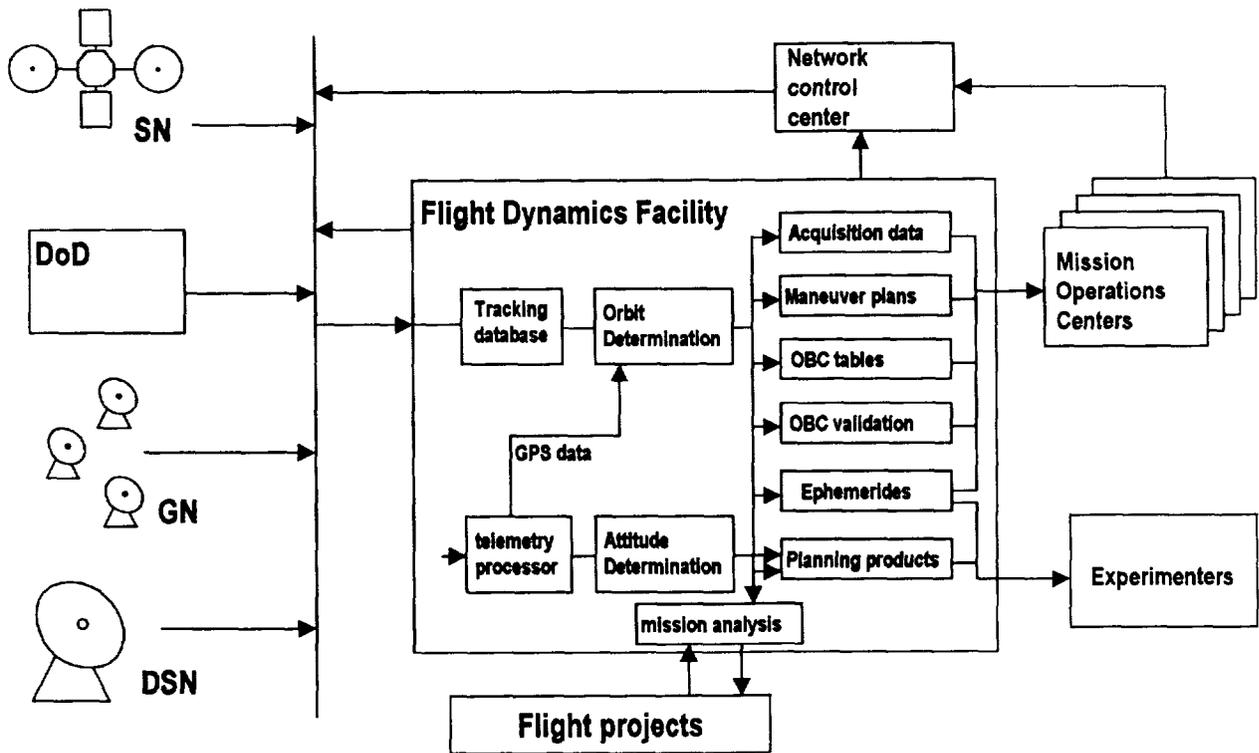
Figure 1. GSFC Flight Dynamics Facility overview

1.1.1 Mission design and orbit analysis

Given mission objectives, analysis is performed to determine an orbit that meets all requirements and constraints. Selection of the mission trajectory influences sensor placement on the spacecraft as well as power, attitude, and propulsion system design and requires close coordination between instrument developers, spacecraft designers and flight dynamics engineers in the spacecraft design phase.

Maneuver strategies must be developed for missions requiring propulsion for altitude or ground track maintenance, station keeping, rendezvous, reentry, etc. Elements of these studies may include trajectory optimization, minimization of fuel usage, orbital decay/lifetime projection, and reentry targeting. These activities continue through the mission in response to altered mission requirements or changes in spacecraft performance.

Other important considerations include error analysis to ensure that orbit accuracy requirements are met with the given tracking inputs, and analysis to determine launch windows.

1.1.2 Orbit Determination

Spacecraft trajectories may be estimated from a variety of observational types—ranges, Doppler, angles, and vectors are routinely used. As shown in Figure 1, FDF receives tracking data from NASA ground and space networks as well as Department of Defense (DOD) sites and others. Tracking data is automatically captured, pre-processed, and stored in the FDF tracking database for orbit determination by the Goddard Trajectory Determination System (GTDS).

For most FDF-supported missions routine orbit determination is performed three day per week in a largely automated process, including automated quality assurance. Orbit operations personnel are on call or provide support during launches or critical orbit maneuvers.

1.1.3 Trajectory Control

Maneuver sequences are planned to adjust an orbit to meet mission requirements. The ideal maneuver in terms of the mission orbit may conflict with communications, power, or other constraints, so the spacecraft operators are closely involved with maneuver planning and give final approval of maneuver plans. Following a maneuver, the achieved orbit is analyzed to determine actual performance of the spacecraft thrusters. Thruster calibration and bookkeeping of fuel used are important in identifying thruster malfunction and planning subsequent maneuvers, particularly for the first maneuvers following launch when the performance is not well known and may be changing. Special post-maneuver orbit determination for rapid evaluation or thruster performance is performed following critical maneuvers.

1.1.4 Scheduling and Planning Aids

Ephemerides from the definitive orbit determination process serve as the basis for generating predictive orbits and scheduling and science planning aids. Users of NASA's space network, ground network, or Deep Space Network are required to deliver projected orbits as far as two weeks in advance for network scheduling. Orbit-based products are generated to meet the requirements for spacecraft operation and science instrument management. Events such as eclipses or view periods and geometrical relations between the spacecraft and sun, for example, are computed from the predicted orbit. Attitude and orbit information are often combined to generate products for antenna pointing or scheduling viewing for instruments.

1.1.5 Acquisition Data Operation

Acquisition data are generated for the ground and space networks during launch and routine operations phases. Acquisition data are used for antenna pointing to a spacecraft.

1.1.6 Onboard system calibration

This analysis is performed during launch and routine operations to ensure the integrity of the onboard navigation algorithms. Onboard vectors returned in telemetry are compared to the ground-based orbit to validate performance.

1.1.7 Onboard Computer Support

Spacecraft typically obtain orbit information onboard from polynomial fits to a predicted orbit or an orbit propagator. Both cases require uploading information to the spacecraft onboard computer (OBC). In the first, a table of coefficients is uploaded, and, in the second, a single state vector is used.

1.1.8 Metric Tracking Data Evaluation

This work is performed during launch and routine operations phases to evaluate the tracking network integrity in support of the navigation, and to help resolve ground tracker equipment problems.

1.1.9 Anomaly Resolution

While no specific activities will be identified here, anomaly resolution is mentioned to acknowledge the need to deal with unexpected events during all phases of support.

1.2 Baseline support levels

Two missions were examined to provide representative levels of Flight Dynamics support. The Upper Atmosphere Research Satellite (UARS) and the Solar Anomalous and Magnetospheric Particle Explorer (SAMPEX) were selected because they bracket the range of products produced by FDF in number and type. UARS performs periodic restoration of its frozen orbit, is supported by Tracking and Data Relay Satellite System (TDRSS), and requires many planning products for its multiple instruments. SAMPEX is tracked from the ground, has no propulsion, and has few product deliveries. Table 1 shows Flight Dynamics support staffing for the two spacecraft in the defined classifications.

Navigation Function	UARS	SAMPEX
1. Mission design and orbit analysis	0.2	0.2
2. Orbit Determination	0.2	0.2
3. Trajectory Control	0.3	0
4. Scheduling and planning products	0.8	0.3
5. Acquisition data operations	0.1	0.1
6. Calibration and verification of onboard system	~0	~0
7. Onboard computer table generation	0.1	0.1
8. Metric tracking data evaluation	0.2	0.2
Total	1.9	1.1

Table 1. Recurring operations support levels per year of mission support (man-years)

2.0 Effects of GPS on FDF support

At this time, the first spacecraft are implementing GPS receivers for operational use. Without long-term operational history, a level of performance was assumed for this study. GPS receivers have been proposed, ranging from simple data collection devices to units capable of full orbit determination and trajectory control. The receiver assumed here produces output suitable for use by onboard control systems and of sufficient accuracy to replace the definitive ephemeris.

2.1 Flight Dynamics Functions

The following sections assess the impact of a spacecraft using GPS on functions performed within the FDF.

2.1.1 Mission design and orbit analysis

Little changes in this area for spacecraft navigating using GPS. Mission design presents unique requirements for each spacecraft. For many missions in typical low, circular orbits for which post-processing is not required, error analysis can be eliminated assuming that the receiver has been proven to meet its specifications, and the specifications satisfy mission requirements.

2.1.2 Orbit determination

GPS has the potential to eliminate the need for routine definitive orbit determination for most missions. The onboard real-time and definitive requirements are met by the GPS standard positioning service levels of performance of 100m horizontal and 156m vertical at 95% probability. For missions with tighter requirements, post-processing will still be required. While GPS positioning is adequate for most missions, the velocity accuracy

336

stated for many receivers is insufficient for ephemeris prediction and generation of long-term planning products. It is recommended that a navigation filter be included in the GPS receiver to improve the velocity solution over point solutions.

While orbit determination may be eliminated, operational savings are expected to be small given the high degree of automation in the ground support process. Orbit determination is one step in the product generation process, and its elimination amounts largely to a small reduction in CPU utilization. For facilities without orbit determination capability, this represents a greater savings in providing independence from network requirements, although orbit determination software is becoming more commonly available with commercial mission analysis software.

2.1.3 Trajectory Control

With the assumed autonomous navigation receiver, maneuver planning is still done on the ground. Again, little changes in this function except for the source of the input ephemeris. Once a labor-intensive activity, maneuver planning is recently becoming an automated process within the FDF.

The need for thruster calibration and fuel bookkeeping are not affected by GPS. Thruster calibration will require new techniques because post-maneuver orbit determination is necessary to evaluate thruster performance during a maneuver. The strength of GPS in trajectory control is that post-maneuver recovery of position knowledge is nearly instantaneous, so table uploads for post-maneuver conditions are not needed. If confidence in the propulsion system and GPS receiver are high real-time support for maneuvers may be reduced or eliminated.

The real-time nature of GPS orbit determination holds promise for completely autonomous navigation, including orbit maintenance and stationkeeping. Early development autonomous orbit control is under way.

2.1.4 Scheduling and planning Aids

Requirements for predictive products are not changed by the incorporation of GPS. Input to the process is switched from the definitive ephemeris to a GPS-derived state. It should be noted that GPS standard positioning service (SPS) performance for unfiltered, point solutions of velocity is less accurate than the traditionally determined ephemeris, and the effect on predictions should be considered against mission requirements. As a result of more capable spacecraft computers and instruments, more orbital event and pointing functions are being performed onboard, reducing ground support requirements.

2.1.5 Acquisition Data Operations

With the current NASA networks, GPS has minor impact on acquisition data operations. Again, the source of the input state vectors changes, but the generation and delivery do not. Changes to network operations designed to simplify scheduling and take advantage of GPS-derived states are under consideration.

2.1.6 Onboard System Calibration

The nature of the onboard system calibration function will change for GPS users, but the need to perform periodic check on onboard navigation performance remains. This function would migrate from the FDF to the mission operations centers.

2.1.7 Onboard computer Support

GPS can potentially eliminate some of the current table or vector uploads. The savings here will be seen in reduced system complexity, not in operations costs; with recent spacecraft, vector uploads amount to a mouse click to select from a list of available vectors. The GPS receiver represents a new spacecraft system, that requires management by the flight operators, and depending on the receiver design, the number of uploadable parameters may actually increase to accommodate initialization, modes of operation, and tuning parameters, although the

337

uploads are expected to be less frequent than current practice. Orbit propagation may still be necessary if the spacecraft cannot power the receiver continuously or as a backup capability.

2.1.8 Metric tracking data evaluation

The current function is eliminated for a GPS user spacecraft. The equivalent function would be autonomous integrity monitoring within the receiver. Depending on the level of acceptable risk, the operations center may require external information on GPS integrity.

2.2 Support Levels

Table 2 gives an update of the mission support levels from Table 1 to reflect the effects of using onboard GPS navigation with no definitive post-processing. In addition support is estimated for a mission using its own ground station and having no propulsion.

Navigation Function	UARS	SAMPEX	independent
1. Mission design and orbit analysis	0.2	0.2	0.2
2. Orbit Determination	0	0	0
3. Trajectory Control	0.3	0	0
4. Scheduling and planning products	0.3	0.3	0.3
5. Acquisition data operations	0.1	0.1	0
6. Calibration and verification of onboard system	.1	0.1	0.1
7. Onboard computer table generation	~0	~0	~0
8. Metric tracking data evaluation	~0	~0	~0
Total	1.5	0.7	0.6

Table 2. Recurring operations support levels per year of mission support (man-years)

3.0 Other considerations

This survey has focused on functions performed within the FDF, but related functions are performed within the mission operations centers. Figure 1 shows a clear separation between FDF and the mission operations centers. However, as the FDF transitions from mainframe to distributed systems, the separation is becoming less distinct, and generation of scheduling and planning aids is becoming more common within the mission operations centers, saving some overhead and special support.

Spacecraft clock maintenance has been performed by flight operations teams using data provided by the FDF. Here, too, the process has become automated, so minimal savings will be realized in terms of operator workload by a GPS-user spacecraft. The compelling argument is more in the simplification of design for spacecraft and ground support systems realized by using GPS for timing. .

Also neglected have been the FDF attitude determination functions for spacecraft using GPS as an attitude sensor. GPS attitude determination for spacecraft is in the experimental stages, so impacts on ground attitude support are not yet clear. Some missions may realize substantial reductions in hardware costs with GPS attitude determination.

4.0 Conclusions

In reviewing the functions performed in the FDF it is seen that support levels for a spacecraft using NASA network resources for communication are moderately reduced, primarily in the areas of routine orbit determination and tracking data evaluation. The trend in automation of ground-based orbit determination will reduce the degree of

savings. Generating products and planning maneuvers are larger efforts than orbit determination, and greater operations cost savings can be achieved by including the functions onboard the spacecraft or by automating the processes on the ground. Automation minimizes workload, but it does not reduce support system complexity. GPS offers the possibility of eliminating some functions and simplifying the support system.

Less capable ground stations, at university, for example, will realize the full benefit of GPS navigation, being independent of the constraints and costs of network utilization for tracking and communications scheduling. Autonomous orbit control opens the potential for automatic orbit maintenance and relative navigation, including autonomous rendezvous and formation flying.

Current methods meet the requirements of presently supported spacecraft and can meet the requirements of all but a few future missions. Substantial reductions in operations support can be realized with continued automation on the ground and improved spacecraft flight software; the more compelling arguments for GPS spacecraft navigation are, then, not in elimination of functions but in an expansion of the realm of mission possibilities.

The Global Positioning System (GPS) and Attitude Determination: Applications and Activities in the Flight Dynamics Division

Eleanor Ketchum[1]
Joe Garrick[2]

Flight Dynamics Division
Goddard Space Flight Center

Abstract

The application of GPS to spacecraft attitude determination is a new and growing field. Although the theoretical literature is extensive, space flight testing is currently sparse and inadequate. As an operations organization, the Flight Dynamics Division (FDD) has the responsibility to investigate this new technology, and determine how best to implement the innovation to provide adequate support for future missions.

This paper presents some of the current efforts within FDD with regard to GPS attitude determination. This effort specifically addresses institutional capabilities to accommodate a new type of sensor, critically evaluating the literature for recent advancements, and in examining some available -albeit crude- flight data.

Background

Originally the constellation of GPS spacecraft, currently numbering 24, was conceived to produce accurate position and time information for ground, air, and space based systems. Although the accuracy is degraded, this information would be available to anyone with a GPS receiver on a continuous basis. In addition, it was later discovered that with a pair of GPS antennas a user can determine a phase difference between signals of the antennas and consequently attitude. This phase difference is related to the angle between the line of sight to the GPS satellite and the baseline connecting the antenna pair. The method is more commonly referred to as interferometric measurement, and has been employed before in ground based receivers for the purpose of tracking a spacecraft's position.

The interferometric principle involves a passive system comprised of two antennas, separated by some baseline, receiving a signal from the same source. Antennas onboard an orbiting spacecraft uses the signals received from the individual GPS satellites as sources. From this information the direction cosine between the baseline and the line of sight to the GPS spacecraft is determined. With the use of another baseline, preferably orthogonal to the first, the direction cosines between the line of sight from that baseline to the same GPS spacecraft is obtained. Finally, the direction cosine of the third axis, orthogonal to the other baselines, is known. From these direction cosines, a unit vector to a known point in space is determined and is analogous to the use of data from typical attitude sensors for attitude determination.

The first full test using GPS data and a star tracker attitude truth (better than 1 arc min) for attitude determination and control onboard the spacecraft will be on a Spartan spacecraft (the GPS Attitude Determination And Control System, or GADACS) to be launched in the fall of 1995. Fortunately, the experimenters are in Goddard's own Guidance and Control Branch (code 712) working in conjunction with the Spartan spacecraft builders in code 740. The attitude will be determined onboard the spacecraft, but the data will be recorded and be available after the flight for ground processing. This will be the first opportunity to validate the proposed implementation

of this capability in the institutional ground based
attitude determination system used in the FDD.
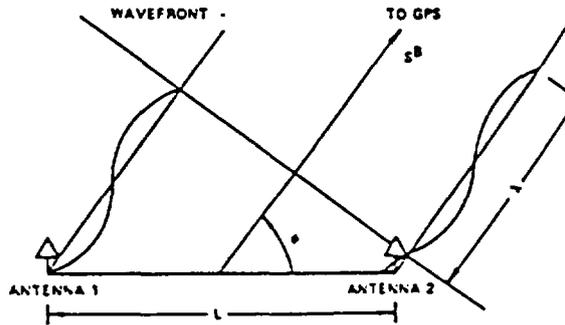
Figure 1

GPS Attitude Determination Geometry

Figure 1 illustrates the basic concept of determining a
rotation angle from phase difference. The
fundamental equation, which relates the phase
difference received from a GPS satellite to the cosine
of the angle between the baseline and line of sight to
the GPS satellite, is given by

$$\cos \alpha \approx (n + k\phi) (\lambda / b) \qquad \text{(Equation 1)}$$

where: α = angle between the baseline and line
of sight to the GPS spacecraft
n = integer number of cycles in the
phase difference between receivers
ϕ = decimal part of the phase difference
received from the GPS signal
k = scale factor which depends on ϕ's
units
λ = wavelength of the GPS signal (GPS
has two frequencies, the L1 at 1575.42
MHz., and the L2 at 1227.6 MHz. The
wavelengths are 0.19042541 meters
and 0.24437928 meters, respectively)
b = baseline length (for the Spartan
spacecraft b = 1.0 meters)

With a pair of preferably orthogonal baselines it is
possible to determine a line of sight vector to
the GPS spacecraft. The above equation relates the
direction cosines to the phase differences as follows:

$$\cos \alpha = (n_1 + k\phi_1) (\lambda/b) \qquad \text{(Equation 2)}$$

$$\cos \beta = (n_2 + k\phi_2) (\lambda/b) \qquad \text{(Equation 3)}$$

$$\cos \gamma = [1 -\cos^2\alpha - \cos^2\beta]^{1/2} \quad \text{(Equation 4)}$$

These define a unit vector in the receiver coordinate
system defined by the two orthogonal receiver

baselines fixed in the spacecraft and, therefore, the
body coordinate system frame.

$$x_r = \cos\alpha$$
$$y_r = \cos\beta$$
$$z_r = \cos\gamma$$

If the receiver coordinate system is not coaligned with
the body coordinate system then the unit vector is
converted to the body coordinate system by the
following:

$$\hat{x}_b = M^T \hat{x}_r \qquad \text{(Equation 5)}$$

where: M = rotation matrix which takes the
body coordinate system (BCS) to the
receiver system. The superscript
indicates a transpose.
$\hat{x}_r$ = unit vector to the GPS spacecraft
in receiver coordinates and
is defined as $[x_r , y_r , z_r]^T$
$\hat{x}_b$ = unit vector to the GPS spacecraft
in BCS

By combining this observed unit vector with the GPS
position unit vector, obtained from the GPS receiver
directly or analytically from previous ground
processing, the FDD institutional attitude
determination system (ADS) can use GPS data in the
same manner as it currently uses star tracker data.

The only term in equation 1 that is still unknown is n,
the integer number of cycles in the phase difference.
Because some receivers measure only the fractional
part of the phase difference, while others begin
counting cycles at randomly large negative numbers
for each locked signal so that a difference in carrier
phase between antennas contains a meaningless
number of whole cycles, the true integer number of
cycles, n, between antenna measurements is
unknown. Although there are several analytical
search algorithms to resolve this ambiguity, the fact
that the attitudes in this case are being determined on
the ground in non-real-time we have an advantage of
using a coarse idea of the attitude to determine n up
front.

Integration of GPS Observations into Institutional Systems

OPERATIONS SYSTEMS

MTASS

The FDD developed a generic attitude ground support system from the software developed for the Extreme UltraViolet Explorer (EUVE) and the Upper Atmospheric Research Satellite (UARS) missions. The motivation was to reduce errors as well as development, testing, and maintenance costs by having functions common to many missions contained within a single system. The ground support system is the Multi-mission Three-Axis Stabilized Spacecraft (MTASS) system. Since MTASS does not provide all the ground support functions needed to support each mission each mission requires some unique modules, for instance a telemetry processing system. However, MTASS does provide several generic methods to determine attitudes. These attitude determination functions are what will be addressed in subsequent sections for adaptation to using GPS observation data. The impact to the MTASS system should be minimal, with the only minor changes required for the introduction of the new GPS signal sensor. The telemetry processing as described above to turn the phase differences into observation vectors and pairing with reference vectors will be done upfront in the mission specific telemetry processing function.

Determine Real-time MACS Attitude

The real-time Modular Attitude Control System (MACS) attitude is determined using observations from a particular telemetry time frame, which is normally referred to single-frame attitude determination. The solution to the single-frame attitude problem comes from minimizing the loss function:

$$J(A) = \sum_{i=1}^{n} w_i \left| \hat{u}_B^i - A\hat{u}_R^i \right|^2$$

(Equation 6)

where: $\hat{u}_B^i$ = observations unit vectors in the body coordinate system

$\hat{u}_R^i$ = reference unit vectors in the reference coordinate system

w = weights applied to each observation/reference pairing

A = attitude matrix that relates the two coordinate systems

The popular method for finding the A which minimizes the above equation is suggested by Shuster (reference 2) and involves finding a maximum eigenvector to a modified version of the loss function:

$$J(q) = q^T Kq \qquad \text{(Equation 7)}$$

where: q = 4 element quaternion which represents the transformation between the body and reference coordinate systems; 3 elements are associated with direction, the 4th with the magnitude with the relationship:
$1 = (q_1^2 + q_2^2 + q_3^2\ q_4^2)^{1/2}$
K = 4x4 matrix derived from the observation vectors, reference vectors and weights (see reference 2 for definition)

The adaptation of GPS observations involves converting the phase differences for a particular receiver baseline into an observation vector and using a reference ephemeris for each GPS pairing them with a reference vector.

All of the changes to the current real-time system are made up front in the processing of the telemetry into engineering data (observation vectors). The user supplied parameters needed for the this telemetry processing are listed below:

- o uncertainty for the GPS position vector
- o number of possible GPS spacecraft visible at each time point
- o number of GPS sensors
- o Frequency of carrier signal
- o scale factor to convert phase difference from telemetry into a decimal number
- o baseline length

Determine Non-real-time MACS Attitude

MTASS also provides for an off-line, non-real-time attitude determination function for a better estimate of state by using batches of multiple observations and propagating those to s common (epoch) time. The procedure minimizes the loss function given by:

$$J = \frac{1}{2}([\hat{u}] - [\hat{w}])^T W([\hat{u}] - [\hat{w}])$$

(Equation 8)

343

where: $[\hat{u}]$ = set of observations in the body coordinate system

$[\hat{w}]$ = set of reference (or observation model) vectors

W = symmetric, non-negative definite matrix which weights the individual contributions of each observation or reference pair

The method used in MTASS to find the state that minimizes the above function is the batch least-squares. This method estimates a state (in our case the attitude estimate) at a particular epoch based on the a priori knowledge and sensor observations. Attitude estimates from this time point are determined by propagation using rate information.

Adapting GPS observations to the batch least-squares method is identical to the processing involved in the real-time processing defined above. The only difference is the collection of observation/reference vector pairs to be applied at a single epoch time. The weights for each of these pairs which are inversely proportional to the expected accuracy of the measurement are placed along the diagonal of the W matrix. User input parameters are similar to those for the real-time attitude determination function listed above.

Sequential Estimation of Attitude

Another method employed by MTASS is the sequential processing of observations and reference vectors, like the real-time method, but including modeling of the state and dynamics noise to improve the estimate. Batches of observations need not be stored as the "information" from all previous measurements, declining in importance over time, is propagated in the form of the covariance matrix. This method uses a Kalman Filter, which has become increasingly popular with the advances in computer technology to allow faster processing.

The equations for the Kalman Filter differ only in the type of filter employed (standard, linear or extended Kalman Filter) and the modeling for the measurement and dynamics, which depend on the state and desired estimation accuracy. Numerous papers have described implementations real-time sequential attitude estimation using GPS observations, see references 4 - 6 for some examples. Since MTASS already converts the phase differences into observation vectors in the body coordinate frame, the Kalman Filter measurement model can compute the estimated state (at this time only attitude, but will be extended to include biases and misalignments in the state at a later date) much like start tracker observations.

This Kalman Filter is an extended filter, due to its non-linearities in the differential equations, is linearized about the latest estimate of the state. Now the state being estimated is not the actual attitude, but the attitude error. At each measurement update, the state error is added to the state estimation; the state error is then reset. In between measurement updates, the state is propagated to the next step using rate information. The measurement matrix is comprised of the partial derivatives of the state differential equations with respect to each of the state error elements and evaluated with respect to the latest estimate of the state. This model for the estimation of attitude using GPS observations has been successfully tested using a realistic simulation of the GPS constellation, and a typical low-earth spacecraft with the modeling of the spacecraft dynamics.

For an 'improved' or definitive attitude solution, MTASS employs a Rauch-Tung-Streibel (RTS) backward smoother to augment the extended Kalman Filter equations. The RTS implementation can use up to twenty-four hours of data at a time. The philosophy behind the backward smoother is to make use of the knowledge of the state at the end of processing all the observation data and running backward in time to apply this knowledge to each time step, which improves the estimate. For a more detailed discussion of the RTS, and other smoothers, it is suggested that the reader find a book on optimal estimation techniques (such as reference 3).

ANALYSIS SYSTEMS

ADEAS

The Attitude Determination Error Analysis System (ADEAS) is a general-purpose linear error analysis tool for spacecraft attitude determination. ADEAS does not process sensor data but simulates the attitude determination logic and computes the resulting attitude determination accuracy. The spacecraft attitude determination scenarios that can be analyzed by ADEAS are described below:

o from low-altitude Earth orbits to International Sun-Earth Explorer (ISEE) -3 type of Earth-Sun libration point orbits

o Spin-stabilized or three-axis-stabilized spacecraft attitudes

o batch weighted-least-squares and sequential filter attitude determination methods

344

o sensor complements, which are subsets of Sun sensor, Earth sensors, star sensor, gyros, magnetometers and now GPS receivers

ADEAS' strength lies in it flexibility: it was designed to include most of the existing and anticipated Earth satellite attitude determination systems. Individual error analysis programs no longer need to be written for each spacecraft as ADEAS allows an analyst to define any (low Earth) orbit and any attitude profile, with a specified set of corrupted sensors taking measurements at a defined sampling rate.

Given that an attitude determination process necessarily involves errors-- e.g., measurement noise, sensor misalignments, gyro drifts--it is important to understand and evaluate how an estimate of the spacecraft attitude is affected by the presence of such errors. ADEAS allows an analyst to specify the type and magnitude of these errors for a particular configuration and computes the resulting uncertainties in a user-specified subset of measurement and dynamic parameters. These errors can be either "solved for" or "considered," depending on how these errors will be handled operationally; the user in effect can, through using ADEAS, assess the merits of including (or not) certain errors as states and/or solving for the errors in some other way operationally.

Adding GPS models to ADEAS not only provides a method of determining attitude errors as driven by mission unique error sources (e.g. misalignments of the baselines due to antennas mounted on deployables) but also allows the user to assess overall attitude uncertainties for systems that have additional sensors like gyroscopes or magnetometers. Fortunately, GPS observations can be modeled in ADEAS very much like the current sensors. The only exception is the observation vectors are determined from a model which produces phase differences for each GPS sensor, defined as a baseline containing a pair of GPS receivers. The model applies the expected components of the uncertainty in the measurements. The uncertainty in the measurements, or observations, is due to noise, biases and misalignments are modeled essentially as follows:

$$\Delta \vec{r} = AM(L + \delta L)\vec{e}_b + \vec{\beta} + \vec{v}$$

where: Δr = expected range difference
A = rotation matrix from misaligned body frame to inertial space
M = rotation matrix from body to misaligned body (solved for or considered)
L = baseline length

δL = baseline length error (solved for or considered)
e_b = vector from master to slave in body frame
β = line bias vector (solved for or considered)
v = noise vector

As ADEAS does not actually compute attitudes, only covariances, integer ambiguities need not be determined. The measurements are converted to observation unit vectors, as described earlier in this paper. An ephemeris file for each of the GPS satellite provides the reference unit vector modeling. From this information and user supplied parameters as to what is solved for and what is considered, as described above, a covariance analysis is done over a specified interval. For a more complete discussion on covariance analysis the reader is directed toward a book on optimal estimation (such as reference 3).

GPS Visibility Prediction Tool

To help in investigation of attitude determination using GPS observations, the second author wrote a visibility prediction software utility that gives the user flexibility in determining GPS observation times and statistics. This prediction utility provides insight into the number of observations that can be expected for a particular mission depending on such things as:

o mission altitude
o inclination
o alignment of GPS receiver baselines
o boresight of each receiver
o GPS acquisition mask for the receivers

Currently the software utility executes on an IBM compatible PC and is written in Microsoft FORTRAN. The user can adjust the configuration of the GPS or user spacecraft and the GPS receivers by means of interactive menus. This allows for greater flexibility in setting up a specific scenario. The internal modeling makes use of a two-body propagator for each of the twenty four GPS spacecraft in the constellation and for the user spacecraft. Future plans include allowing the user to read in a more accurate ephemeris file generated by an outside source. The user spacecraft attitude is modeled by propagating the attitude state to the next time step using kinematic equations. This allows for a fairly good representation of how motion affects GPS visibility. The receivers are modeled as a baseline aligned in the body coordinate system. The receivers' boresights are modeled as vectors in the body coordinate system, with a user supplied mask angle, which represents a cone around the boresight in

which GPS satellites will be visible. Simple geometric equations take into account if each of the GPS satellite are within the specified mask and not occulted by the Earth. Figure 2 shows a typical plot of GPS observations for a low Earth orbit satellite.
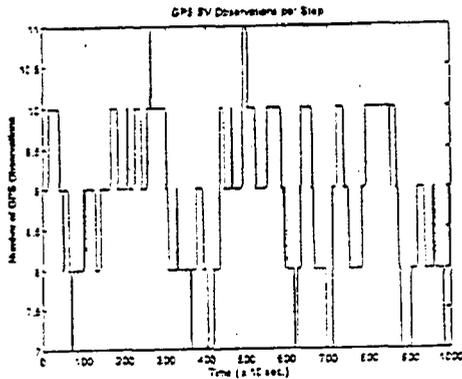
Figure 2

This utility outputs two concise report files. The first report file gives a step by step account of which individual GPS spacecraft are visible as well as the total number visible at any given time step. The second report gives a summary of the scenario's configuration, statistics for each GPS in the constellation on how often it was visible during the simulation and the percentage of time, a density table on the distribution of total GPS spacecraft visible, and the minimum and maximum time each GPS satellite is visible. The utility will be enhanced to predict the geometric dilution of precision, or GDOP, for a particular mission.

GPS Simulator

To test out the developed attitude estimation functions, a simulator would be needed to generate the GPS measurement data. A menu driven simulator was developed by the second author to execute on an IBM compatible PC and written in Microsoft FORTRAN. The simulator takes much of its modeling from the prediction utility. There were some major modifications to include more detailed and new models. The kinematics in the prediction utility were replaced by a more accurate dynamics model to allow for more precise modeling of the attitude. The GPS simulator takes the observations at each time step and processes them into realistic measurement data. The general steps involved in this process for each visible GPS at each time step are as follows:

1. Accept raw measurements, converted into whole and fractional parts of wavelengths. Imbedded in this step would be misalignments of each antenna. These are user supplied parameters.

2. Computing the phase difference for each baseline. An uncertainty is added to this quantity to account for the random properties such as noise. This is a user supplied quantity.
3. The integer portion of the phase difference is stripped off leaving only the decimal portion for processing.
4. The decimal portion of the phase difference is then adjusted for the least significant bit that may be found in the data word, that is the resolution of the data.

The next step in the simulation would be equivalent to the sensor processing normally found onboard in the flight software. The steps involved in this process are as follows for each GPS visible:

1. The input for each baseline, the final decimal phase difference, is input to a routine to determine the integer ambiguity.
2. Another routine monitors the change in phase difference to determine when the integer ambiguity needs to be updated.
3. Finally the phase differences from the two baselines are converted into observation unit vectors in the sensor coordinate system.
4. The observation unit vectors are paired with a reference vector based on GPS spacecraft id.

The output is then a set of n observation/reference unit vector pairs, where n is the number of GPS satellite visible at that time step. These pairs of data is then input into the desired attitude estimation function as was described earlier. Figures 3 and 4 show examples of the Kalman Filter and Q-method error in estimating the attitude using the GPS simulator.


Figure 3

Figure 4

346

Space Flight Data Analysis

EUVE

The EUVE spacecraft (see Figure 5), launched in 1992, is equipped with 2 Fixed Head Star Trackers (FHSTs) that provide a "true" spacecraft attitude to better than 10 arcsecs. EUVE also has a single-frequency Motorola GPS Demonstration Receiver (GPSDR) with dual antennas separated by approximately 1.8 meters. The FDD has access to all the above data since launch, providing a unique opportunity to examine the attitude determination capability of GPS with real space flight data. Unfortunately, due to a constraint in the onboard software as well as physical viewing restrictions, the GPS antennas do not stay locked on the same GPS Satellite for more than a few minutes at a time. However, even these relatively small data spans prove fruitful in the quest to properly characterize GPS data for space flight attitude determination.

Fig.5 EUVE Spacecraft

The EUVE can fly in either an inertially fixed or 3 rotations per orbit (3 RPO) about the spacecraft X axis. For data gathered during inertially fixed periods, the observed carrier phase differences matched the truth to approximately 0.1°, once a residual bias was removed, indicating at least that the noise level is of that order. However, since this bias appeared constant only for short time spans, unless properly characterized, might be difficult to solve for without truth data. In this case, the bias itself then is the real accuracy measure, and the spans examined here experienced a 0.87° error on average, with a maximum of 2°.

For the 3 RPO data, while the noise characteristics of the data were similar to those for the inertial spans, the fact that the observations of the GPS satellite came through (around) the EUVE spacecraft made for poor correlation to the truth. However, during these times, the a status flag indicated a healthy locked state and noise characteristics showed absolutely no indication of trouble. See Figures 6 and 7 for examples of differenced carrier phase as measured by the EUVE GPS receiver.

Fig. 6 3 RPO Viewing

Fig. 7 Inertial Viewing

In an attempt to find another indicator for these essentially poor measurements, the automatic gain control (AGC), which is a measure of the signal strength, was examined for each signal. Fortunately, the behavior of the AGC did seem to show, for the data examined here, when a signal was not direct. Finally, while no clear "cut off" for the AGC values differentiating healthy and poor contact spans was apparent from this data, these results indicate the merit in mapping the AGC for a mission more suitably configured for attitude determination to examine 1)repeatability in AGC based on position of a GPS satellite in body coordinates but not necessarily on particular GPS satellite and 2)correlation to the attitude bias (determined either with multiple GPS satellite viewings or with truth data). If this correlation can be found and quantified, the biases could be consequently determined directly from the AGC or some other measure of signal strength.

For more detailed discussion of the data analysis, see reference 7.

Future Work

Flight dynamics, along with operations support, traditionally performs analysis both for specific upcoming missions as well as examining existing flight data in order to improve the performance of attitude sensors and effectively save hardware costs for missions farther in the future. GPS, as it is so new, yet has created so much excitement in the era of end to end cost savings, proves fruitful for both realms of analysis.

GADACS data analysis

As stated above, the GADACS experiment is slated for launch in November 1995. As it was conceived and built at Goddard, the ability to properly process the data on the ground, checking FDD's GPS additions to the MTASS system in preparation for future support as well as provide independent verification of the experimenter's data, would be highly desirable.

TRACE data analysis

The Transition Region and Coronal Explorer (TRACE) is the 4th in the SMall Explorer series and is slated to launch in September 1997. It will fly a GPS receiver, with antennas mounted on the backs of 3 separate solar panels. The FDD ground post processed spacecraft roll angle used by scientists to correlate to their data has a 1σ goal of $0.1°$. This goal will be difficult to meet with the current hardware of a magnetometer and gyroscope. However, the GPS receiver should assist in nailing down this angle to within the goal.

The ground software to be used by TRACE will be a new modular workstation based system currently being developed. Filters similar to those for MTASS are to be implemented, as are the GPS models. The system will be able to take a quaternion output as well as raw carrier phase measurements.

The FDD hopes to provide an independent verification of the performance of the GPS receiver, one that has no space flight heritage, through several means. The scientists are providing (infrequently) several contiguous orbits of spacecraft roll angles derived from the science data. These solutions should be better than $0.1°$, and are to be used to calibrate the magnetometer and the gyroscope. This data can also be used to check the GPS determined roll angle.

Experience shows, however, that hardware systems, especially those without heritage and with extensive software, should be checked thoroughly through examining of raw measurements, in this case carrier phase. By independent checking, onboard system hardware and software errors can be decoupled and closely examined. Also, calibration parameters, such as line biases or baseline misalignments can be corrected for, as is traditionally done for other sensors.

Finally, as these antennas are on separate deployables, the issue of baseline misalignment and length uncertainty are being closely examined for TRACE both through using ADEAS as modified above, and through other studies. Once inflight, this configuration should be quite interesting to the GPS attitude community at large for study as well as for future mission planning as it is not always convenient to place GPS antennas on certain shaped spacecraft, telescopes in particular.

Conclusions

The Goddard Flight Dynamics Division is currently preparing for a completely new sensor to begin flying experimentally in late 1995, and routinely in 1997. The FDD has updated models in the current operations support and analysis software, and is preparing models for new work station based operations software to accommodate GPS measurements. Data from EUVE, although sparse for attitude by nature of the GPS configuration on the spacecraft, was examined. Finally, just as FDD has a long heritage of verifying and improving performance for traditional attitude sensors through examining flight data, preparations and studies are underway to support specific upcoming missions for GPS attitude determination.

References

1. Markley, F., Seidewitz, E., Nicholson, M.; " Attitude Determination Error Analysis System (ADEAS) Mathematical Specifications Document"; CSC/TM-88/6001, Oct. 1988.

2. Shuster, M. D., "Algorithms for Fast Optimal Attitude Computation", Computer Science Corporation, CSC/TM-78/6056, April 1978.

3. Gelb, A. (editor), " Applied Optimal Estimation", M.I.T. Press, 1989.

4. Melvin, P., and Hope, A., "Satellite Attitude Determination With GPS," *Proceedings of the*

AAS/AIAA Astrodynamics Specialist Conference,
August 1993 paper number AAS 93-556.

5. Ward, L., and Axelrad, P., "Spacecraft Attitude
Estimation Using GPS: Methodology and Results for
RADCAL," *Proceedings of the 1995 ION National
Technical Meeting*, Anaheim, CA,. January 1995.

6. Fujikawa, S., and Zimbelman, D., "Spacecraft
Attitude Determination by Kalman Filtering of
Global Positioning System Signals," to be published
in the AIAA Journal of Guidance, Control, and
Dynamics

7. Ketchum, E., and Hart, R. "Attitude
Determination of the Extreme UltraViolet Explorer
Using GPS," *Proceedings of the 1995 ION National
Technical Meeting*, Anaheim, CA,. January 1995.

Contingency Maneuver Strategies for the Total Ozone Mapping Spectrometer-Earth Probe (TOMS-EP)*

James Kestler
Computer Sciences Corporation
Lanham-Seabrook, Maryland, USA 20706

Donna Walls
National Aeronautics and Space Administration
Goddard Space Flight Center
Greenbelt, Maryland, USA 20771

Abstract

The Total Ozone Mapping Spectrometer-Earth Probe (TOMS-EP) is a polar-orbiting spacecraft designed to measure total ozone levels in the Earth's atmosphere. The nominal mission orbit is a 955-kilometer circular Sun-synchronous orbit with an ascending node mean local crossing time (MLT) between 11:02 a.m. and 11:25 a.m. These two mean local ascending node times constitute the boundaries of the MLT box for this mission. The MLT boundaries were chosen to maintain the Sun-to-Earth-to-vehicle orbit-normal (SVN) angle within a preselected set of seasonally independent boundaries. Because the SVN angle is seasonally dependent, but the MLT is not, contingency options for correcting the MLT of orbital states that fall outside of the required MLT range become time dependent.

This paper focuses on contingency orbit adjustment strategies developed at the Goddard Space Flight Center (GSFC) Flight Dynamics Division (FDD) during the mission planning phase of TOMS-EP. Time-dependent delta-V strategies are presented for correcting mission orbit states lying outside of the MLT range. Typically, passive control of the MLT drift rate can be used to restore the orbit state to the required MLT before a seasonal violation of SVN angle constraints can occur. Passive control of the MLT drift rate is obtained through adjustment of the semimajor axis and/or the inclination. The time between initial arrival on orbit at an "out-of-the box" MLT state and violation of the SVN angle constraints is always less than or equal to 1 year. The choice of which parameter(s) to adjust is dictated by the duration of this time period, the desired mission lifetime, the delta-V cost, and operational constraints

Introduction and Mission Overview

The scientific goal of the Total Ozone Mapping Spectrometer-Earth Probe (TOMS-EP) mission is to map the total ozone content of the Earth's atmosphere over a minimum period of 2 years. The original vision of the TOMS-EP project was for a 3-year nominal mission lifetime. TOMS-EP will continue the mission of the Nimbus 7 spacecraft by providing continuous total ozone coverage of the Earth. To accomplish this task, the spacecraft will be placed in a circular polar orbit of approximately 99.3-degrees inclination at an altitude of 955 kilometers (km). Figure 1 is an illustration of the TOMS-EP spacecraft. As with other Earth observing, polar orbiting missions, the need to maintain consistent back-lighting conditions requires the spacecraft to maintain an orbit that is synchronous with the motion of the Sun. Additionally, the angle between the TOMS instrument normal vector and the position vector of the Sun must be maintained within a specified range to properly calibrate the TOMS instrument. Because of the orientation of the mounted TOMS instrument, spacecraft and orbital geometry allow this requirement to be translated directly into a restriction on the angle between the orbit normal vector and the Sun's position vector. This angle is defined as the Sun-to-Earth-to-vehicle orbit-normal (SVN) angle.

Prior to assuming its station on orbit, TOMS-EP will be injected in to a 339-km × 960-km parking orbit. Table 1 gives the parking orbit parameters and 3σ errors for the parking orbit. A series of ascent maneuvers will be performed to bring the spacecraft from the parking orbit to the proper apogee and perigee altitudes and to bias the inclination to maximize the available lifetime of the mission. The propulsion system is a simple monopropellant hydrazine system with one tank and four 1-pound thrusters. Figure 2 graphically displays the nominal TOMS-EP mission lifecycle.
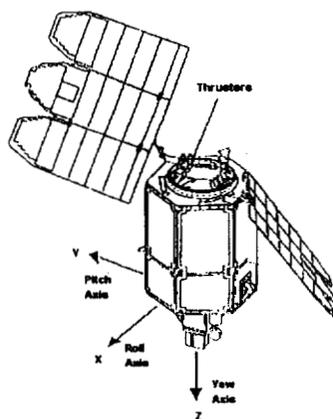
Figure 1. The TOMS-EP Spacecraft

Table 1. Nominal and 3σ Injection Parameters

Orbital Parameter	Nominal Value	3σ Error
Perigee Height (km)	339	3.5
Apogee Height (km)	960	80
Inclination (degrees)	99.3	0.22
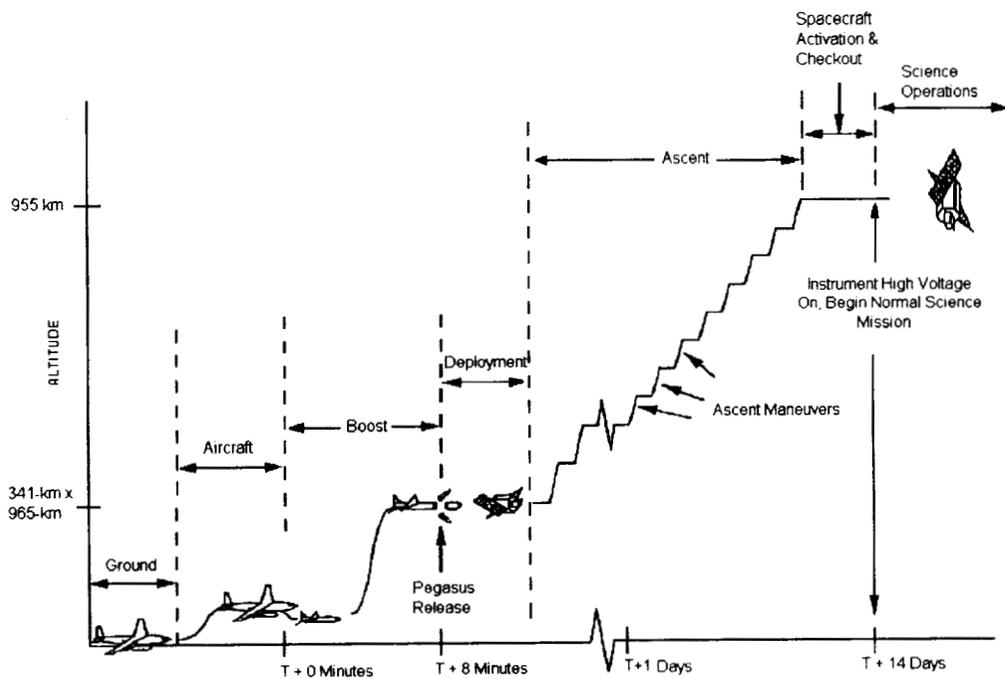
Figure 2. TOMS-EP Nominal Postlaunch Mission Phases

Design of the Nominal Mission Orbit

The nominal mission orbit for TOMS-EP was designed to ensure that the SVN angle constraints would be met, regardless of the launch date. The mission orbit has three constraints related to the mean local crossing time (MLT) of the ascending node and one constraint related to the operational altitude range of the spacecraft. These constraints are as follows:

- The MLT of the ascending node must be between 11:00 a.m. and 12:00 p.m. to satisfy the backlighting conditions required by the TOMS instrument.

- The SVN can be no greater than 107.5 degrees and no less than 91.0 degrees.

- The spacecraft can perform science operations in circular orbits in the 800-km to 1100-km altitude range, if necessary.

Because the SVN angle and MLT are both functions of the position of the Sun, it is useful to examine the dependence of the SVN angle on the MLT for mission orbits at the 99.3-degree inclination The minimum, maximum, and average SVN were determined over the course of the year as a function of ascending node MLT in the 11:00 a.m. to 12:00 p.m. range allowed by the instrument. Figure 3 shows the dependence of the SVN values on the MLT for this range. The figure shows that at approximately 11:02 a.m. the maximum SVN angle over the course of the year will be 107.5 degrees. An orbit with a fixed MLT earlier than 11:02 a.m. would violate the maximum SVN angle constraint at least once per year. Figure 3 also shows that the minimum SVN angle constraint would be violated for orbits with fixed MLTs later than 11:25 a.m. Representing the SVN angle extremes as a function of MLT in this manner provides a straightforward method of determining the MLTs at which SVN angle constraints may be violated. This allows MLT boundaries to be set for the mission, thereby defining an MLT box that guarantees no violation of the SVN angle limits. Figure 3 shows that the SVN angle limitations have, in effect, confined the available mission orbits to MLT values between 11:02 a.m. and 11:25 a.m. (Note that hh:mm in Figure 3 represents hours:minutes.)
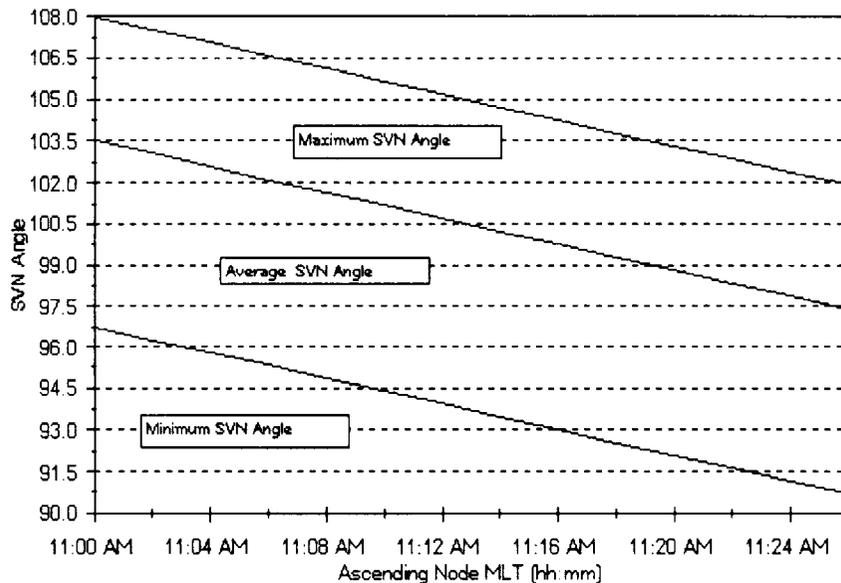
Figure 3. SVN Angle Represented as a Function of Ascending Node MLT

Representing the SVN angle variations as functions of MLT does not, however, indicate when during the year SVN angle minimums and maximums would be reached. For any allowable MLT at the 99.3-degree inclination, the SVN angle will vary over the course of a year by approximately 10 degrees. To explain this, consider the definitions of MLT and the SVN angle. MLT is based on the angle between the right ascension of the ascending node and the right ascension of the mean Sun. The right ascension of the mean Sun moves at a constant rate of approximately 0.9856 degree/day (deg/day). However, the SVN angle is defined as the angle between the orbit normal vector and the position vector of the true Sun. Because the Earth's orbit

around the Sun is inclined and not exactly circular, the right ascension of the true Sun changes at a rate that varies throughout the year. This causes a seasonal variation in the SVN angle due to the difference between the mean motion of the Earth about the Sun and the actual motion of the Earth about the Sun. Because the TOMS-EP orbit is polar, this variation in the right ascension of the true Sun has a strong effect on the SVN angle throughout the year. It therefore becomes important to keep the spacecraft orbit in an MLT range that will ensure that the SVN angle variation throughout the year does not cause a constraint violation.

To see when during the year the bounding SVN angles would be reached, the SVN angle was determined as a function of the day of the year for each of the boundary MLTs. Figure 4 shows the SVN angle as a function of the day of the year for the 11:02 a.m. and 11:25 a.m. MLT orbits. For the early boundary of the MLT box, Figure 4 shows that the SVN angle reaches a maximum of 107.5 degrees near day 210. For the late boundary of the MLT box, the SVN angle reaches the minimum limit around day 319. As the MLT of the orbit increases toward noon, the SVN angle for any given day of the year decreases.
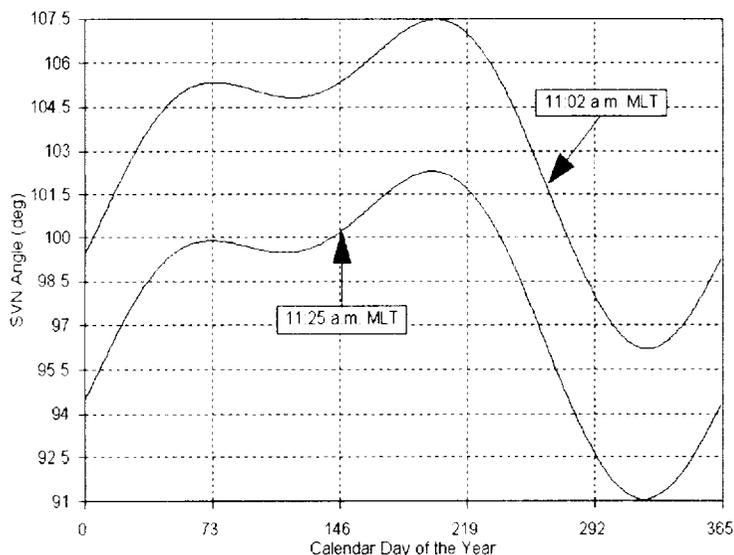
Figure 4. TOMS-EP SVN Angle Ranges Throughout The Year

Figures 3 and 4 represent the SVN angle as functions of MLT and day of the year for fixed MLTs. These figures show the effects of the Solar geometry on the angular limits. It should be noted, however, that the mission orbit MLT will change as a function of time over the course of the mission. This is partially due to drag but mainly due to the perturbative effect of the Sun's gravity on the spacecraft orbit (References 1 and 2). The solar gravitational perturbation exerts a torque on the spacecraft orbit, altering the inclination over time. This change in inclination in turn effects the rate of change of the node, causing an MLT drift rate. For orbits with MLTs earlier than noon, the Sun's gravity tends to decrease the inclination over time. To see what effect this has on the MLT of the orbit, consider the first-order equation for the nodal rate (Reference 3):

$$\frac{d\Omega}{dt} = \frac{-3\sqrt{\mu} \ J_2 \, R_e \cos(i)}{2 \, a^{7/2} (1-e^2)^2} \tag{1}$$

where Ω = right ascension of the ascending node i = orbital inclination
        a = semimajor axis e = eccentricity
        μ = gravitational constant of the Earth J_2 = coefficient of the second zonal harmonic

        R_c = equatorial radius of the Earth t = time

Because the Sun-synchronous condition relies on the nodal rate being equal to the average angular velocity of the Earth about the Sun, any change in nodal rate will cause the MLT to drift away from its initial value. Inspection of Equation (1) shows that a decrease in the inclination will cause a decrease in the drift rate when the inclination is greater than 90 degrees. For TOMS-EP, the solar perturbation decreases the inclination by approximately 0.02 degree per year. A thorough discussion of the effects of solar, lunar, and other perturbations on the evolution of MLT can be found in Reference 4.

Because MLT is not constant over the mission life, it is necessary to choose an initial inclination that will maximize the time spent in the MLT box (References 5 and 6). To determine the best choice of initial inclination for mission orbits inside the MLT box, the evolution of initial mission orbits, corresponding to the boundaries of the box, was modeled using the Goddard Mission Analysis System (GMAS). The modeling was performed using the average variation of parameters (AVGVOP) propagator with an order 21 zonal field, the Jacchia-Roberts atmospheric density model, and solar and lunar gravitational perturbations. Figures 5 and 6 display the MLT evolution for initial mission orbits with MLTs of 11:02 a.m. and 11:25 a.m., respectively. From Figure 5, it can be seen that for the 11:02 a.m. case the initial inclination would have to be set to approximately 99.37 degrees to maximize the mission lifetime. In this case, the initial nodal rate is greater than the angular rate of the mean Sun to offset the reduction of nodal rate that the Sun's gravity will affect on the orbit over time. Figure 6 shows that for the 11:25 a.m. case the initial inclination would have to be set to 99.30 degrees. In this case, there is no choice but to match the nodal rate to that of the mean Sun and accept the decrease in MLT over time. From both figures, it is clear that the available mission lifetime, without correction maneuvers, is approximately 5 to 10 years, depending on the initial MLT of the mission orbit. This is 2 to 5 times as long as called for in the mission requirements and 1.5 to 3 times as long as the originally envisioned 3-year nominal lifetime.
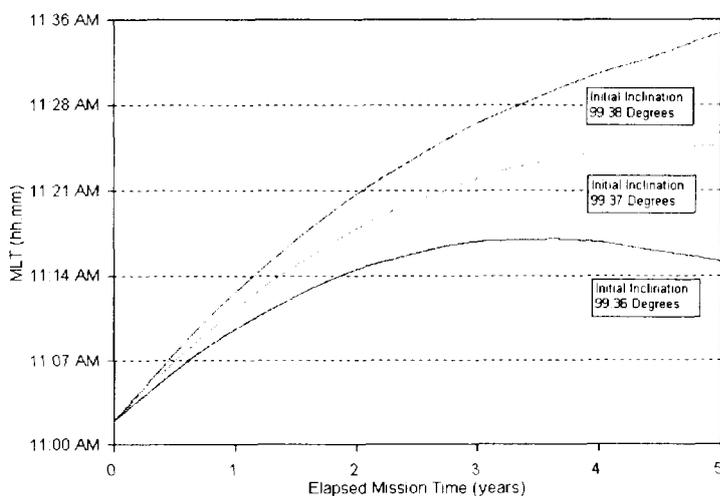
Figure 5. TOMS-EP Mission Orbit MLT Evolution for the 11:02 a.m. Initial MLT Case
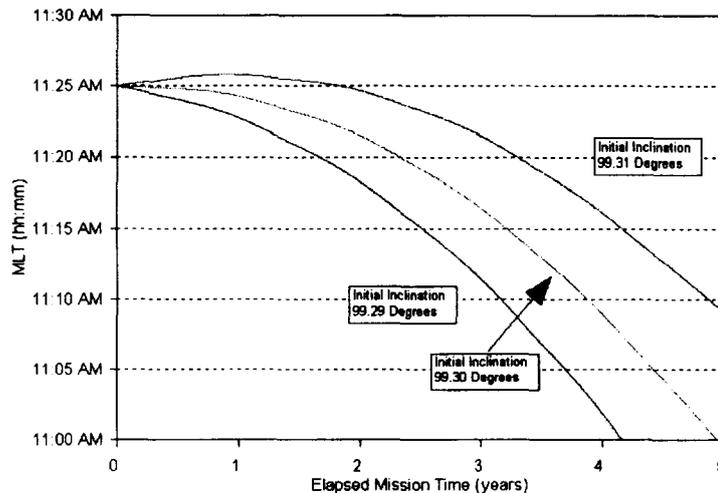
Figure 6. TOMS-EP Mission Orbit MLT Evolution for the 11:25 a.m. Initial MLT Case

Contingency ΔV Strategies for Correcting Out-of-the-Box MLT States

A contingency involving MLT will generally result from one of two things: either the MLT on arrival will be earlier than the 11:02 a.m. lower limit, or it will be later than the 11:25 a.m. upper limit. The goal in a contingency situation is to restore the spacecraft to as close to a nominal mission orbit as possible with as little interruption or delay of science data collection as possible. If the contingency is due to severely nonnominal launch vehicle performance, the insertion altitude may be significantly lower than expected, and extra fuel will be needed to bring the spacecraft up to the mission orbit. In such a case, fuel may be at a premium and the delta-V budget will also be a consideration.

For cases where the MLT will be too early, ascent maneuvers can be delayed to allow the MLT to drift noonward to an acceptable value. This is the most straightforward method of altering the MLT in a rapid manner. Figure 7 displays the MLT drift rate in minutes (min) per day relative to a Sun-synchronous orbit as a function of the semimajor axis in the low Earth regime. For TOMS-EP, the +3σ semimajor axis of the parking orbit is 7071 km. This corresponds to an average altitude of approximately 693 km. Using this strategy, even in a very extreme case where the MLT on arrival at mission orbit would be 10 minutes too early and the semimajor axis of the parking orbit is at the +3σ value, the delay would be slightly less than 3 weeks. Correction of the MLT in this manner would result in no sacrifice of available mission lifetime in the MLT box, but it could delay the start of science data collection.

However, it is possible in certain cases to avoid the delay incurred by postponing the ascent maneuver sequence. It may also be possible to avoid an interruption of science data collection. When the necessary change in MLT is small enough or the time before constraint violation would occur is long enough, it is possible to bias the inclination slightly and achieve the desired MLT drift rate. This would allow the spacecraft to drift up to the 11:02 a.m. boundary before the SVN angle constraint violation can occur. Without further correction of the nodal rate after the 11:02 a.m. boundary has been reached, the available mission lifetime in the MLT box may be impacted. To see how much the available lifetime would be impacted, the maximum possible lifetime in the MLT box was determined as a function of initial MLT. The maximum possible time in the box is, in this case, the time needed to drift noonward from the initial MLT to 11:25 a.m. and then down to 11:02 a.m. Figure 8 shows the maximum possible lifetime in the box as a function of the initial MLT in the 10:52 a.m. to 11:02 a.m. range. Using this information as a baseline, the degree to which lifetime in the MLT box will be affected can be determined.

356
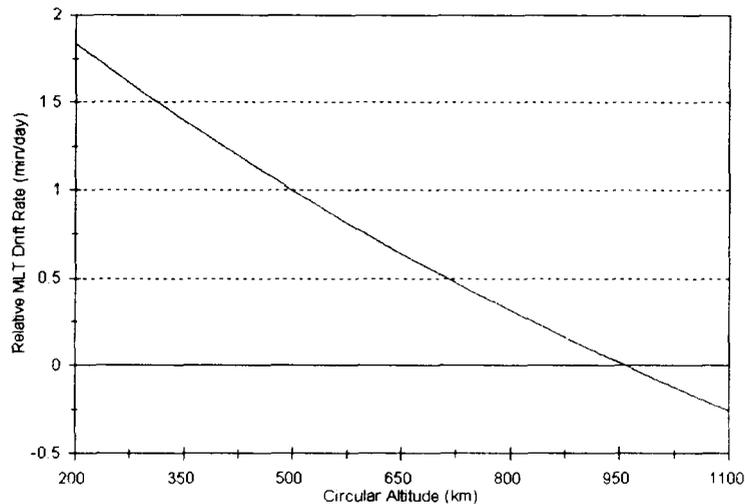
Figure 7. MLT Drift Rate Relative to a Sun-Synchronous Orbit as a Function of Circular Altitude at the 99.3- degree Inclination

Because the nodal rate is slowed by the action of solar gravity on the orbit, the MLT rate is at a maximum during the first year of the mission for orbits that must initially drift noonward. If the rate of MLT drift needed to avoid constraint violations is less than or equal to that of the maximum lifetime orbit, there will be no need to apply any correction maneuvers at all. The inclination of the initial mission orbit would merely be biased to provide the maximum lifetime in the MLT box, and no constraint violation would occur.

For an orbit with an initial MLT that is less than 11:02 a.m., the average MLT drift rate needed to avoid a constraint violation is given by

$$\frac{d(MLT)}{dt} = \left(\frac{\Delta MLT}{\tau}\right) \qquad (2)$$

where ΔMLT = (11:02 a.m. – MLT on arrival)

τ = time between arrival and constraint violation

This is illustrated in Figure 9 where the first-year MLT drift rate in minutes (min) per year is plotted versus initial the MLT for the optimum lifetime orbits at initial MLTs in the 10:52 a.m. to 11:02 a.m. range. If the MLT drift rate falls on or under the curve for the initial MLT of the orbit, then the optimum lifetime can be achieved by a simple biasing of the inclination, and no contingency correction of the MLT rate is required.

However, if the necessary MLT drift rate is greater than the slope of the curve in Figure 9, then the available lifetime in the box will be affected. Faster than optimal initial drift rates will cause the MLT to reach a maximum above the 11:25 a.m. mark if left uncorrected. This effectively reduces the maximum lifetime to less than one-half of its optimal value. The reduction of lifetime is caused by the fact that at some point the MLT will exceed 11:25 a.m. However, since even one-half of the available mission lifetime in the MLT box is still several times greater than minimum lifetime of 2 years, the impact may be acceptable. The degree to which this will be a factor can be determined by considering the MLT drift rate necessary to avoid constraint violation and the degree to which this drift rate will affect the available mission life. Figure 10 shows the inclination bias needed to ensure maximum lifetime in the MLT box for mission orbits with initial MLTs in the 10:52 a.m. to 11:02 a.m. range. The inclination values displayed are those required to maximize the time spent between 11:02 and 11:25 a.m. In each case, the maximum MLT is 11:25 a.m., providing an upper bound on the available lifetime in the MLT box.

357
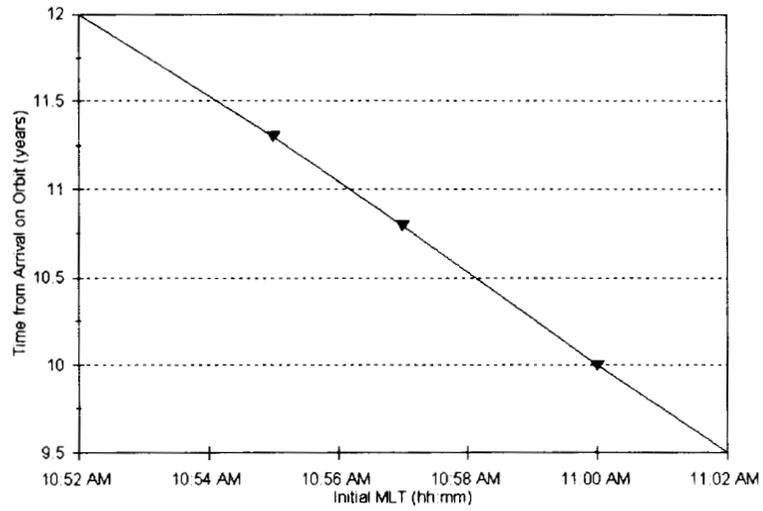
Figure 8. Maximum Possible Lifetime Versus Initial MLT on Arrival at Mission Orbit
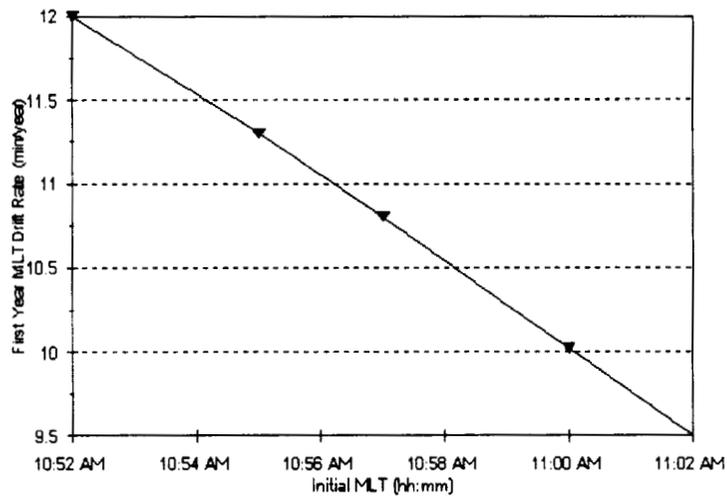

Figure 9. Average MLT Drift Rates for the First Year for Orbits With Maximum Time in the MLT Box
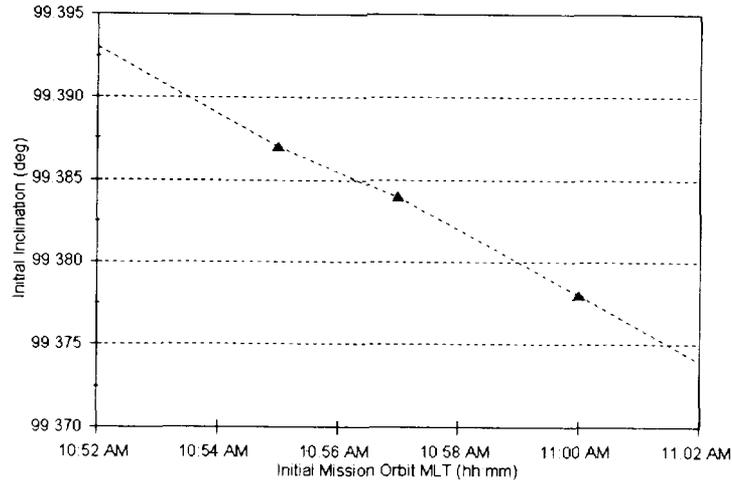
**Figure 10. Inclinations Required for Maximum Lifetime Versus Initial MLT
in the 10:52 a.m. to 11:02 a.m. Range**

To quantitatively determine the impact of faster than optimum node rate on the available lifetime in the MLT box, consider a first-order Taylor series expansion of Equation (1) about the inclination. Neglecting the effects of drag on the orbit, the nodal rate as a function of elapsed mission time is given by

$$\dot{\Omega}(t) = \dot{\Omega}(0) + \left(\frac{\partial \dot{\Omega}}{\partial i}\right)\left(\frac{d\,i}{d\,t}\right) i \tag{3}$$

Evaluating the partial derivatives of Equation (1) with respect to i yields

$$\left(\frac{\partial \dot{\Omega}}{\partial i}\right) = \tan(i)\,\dot{\Omega} \tag{4}$$

The rate of change of inclination for TOMS-EP is approximately -0.02 degree per year, and t is the elapsed mission time. The average nodal rate, $\left\langle \dot{\Omega} \right\rangle$, and the time when the 11:25 a.m. boundary is reached, λ, can be estimated using recursion formulas based on Equation (3) as follows :

$$\lambda_n = \frac{\Delta\Omega}{\left[\left\langle \dot{\Omega} \right\rangle_{n-1} - 0.9856\,\frac{\text{deg}}{\text{day}}\right]} \tag{5}$$

359

$$\left\langle \dot{\Omega} \right\rangle_n = \frac{\left(\dot{\Omega}(0) + \dot{\Omega}(\lambda_n) \right)}{2} \tag{6}$$

where $\left\langle \dot{\Omega} \right\rangle_0 = \frac{\Delta MLT}{4\tau}$ and $\Delta\Omega = \frac{\Delta MLT}{4}$.

Obviously, as λ approaches the minimum acceptable lifetime, the value of interrupting science operations for additional maneuvers after the 11:02 a.m. boundary has been reached increases.

If the MLT is late upon reaching mission orbit, the available options and strategy are essentially the same as for the early MLT case. In an extreme situation, the altitude can be raised to a higher than mission orbit value and then restored to a nominal mission orbit value at a later time. Given the maximum altitude constraint of 1100 km, the best MLT drift rate that can be achieved in this manner is approximately 15 seconds per day, which is equivalent to over 90 minutes per year. For less serious cases, the strategy is similar to that of the too-early MLT case. However, there is less flexibility for MLT correction using an inclination bias for the cases where the MLT is too late. For contingency orbits with MLTs earlier than 11:02 a.m., the solar gravitational perturbation slows the MLT drift rate over time and, in effect, stretches out the time between arrival at the initial MLT and arrival at 11:25 a.m.. However, for orbits with MLTs later than 11:25 a.m., there is no noonward drift in the MLT. Therefore, the MLT rate will decrease steadily. In effect, the solar perturbation will act to shorten the time between arrival at the initial MLT greater than 11:25 a.m. and crossing of the 11:02 a.m. boundary. In other words, when the MLT is later than 11:25 a.m., the magnitude of the average nodal rate will tend to be larger and λ will be shorter for any given ΔMLT and τ. The strategy is essentially the same as for the early MLT case except that the shorter available mission lifetime can make it necessary to perform additional adjustment(s) to the orbit once the MLT has been restored to an acceptable value.

Relative Delta-V Costs of Using Inclination or Semimajor Axis To Control Nodal Rate

Equation (1) shows that a decrease in the nodal drift rate can be accomplished by either increasing the semimajor axis or by decreasing the inclination. (Since the eccentricity is of the order 10^{-3}, its effect can safely be ignored.) The choice of which parameter to adjust will depend upon the amount of time before violation of constraints and the amount of MLT that the orbit must drift through. Also of potential interest is the relative delta-V cost of adjusting each parameter under the constraint of desired nodal rate. This not only is of interest for contingency scenarios where fuel may be at a premium but also for stationkeeping scenarios. The relative delta-V cost of performing semimajor-axis-versus-inclination adjustment can be derived from Equation (1) using a first-order Taylor series approximation for the desired change in the nodal rate. If the rate of Ω is to be altered by a semimajor axis adjustment, the change in nodal rate will be given by

$$\delta\dot{\Omega} = \left(\frac{\partial\dot{\Omega}}{\partial a} \right) \Delta a \tag{7}$$

On the other hand, the change in the nodal rate produced by a change in inclination will be given by

$$\delta\dot{\Omega} = \left(\frac{\partial\dot{\Omega}}{\partial i} \right) \Delta i \tag{8}$$

360

Evaluating the partial derivatives of Equation (1) with respect to a and i yields

$$\left(\frac{\partial \dot{\Omega}}{\partial i}\right) = \tan(i)\,\dot{\Omega} \tag{9}$$

$$\left(\frac{\partial \dot{\Omega}}{\partial a}\right) = \left(\frac{-7}{2a}\right)\dot{\Omega} \tag{10}$$

The change in the semimajor axis for a given delta-V over a simple two-impulse Hohmann transfer (Reference 7) is given by

$$\Delta a \approx \frac{2\,a^2 V}{\mu}\,\Delta V_a = \frac{2a^{1.5}\Delta V_a}{\sqrt{\mu}} \tag{11}$$

where ΔV_a is the delta-V performed to change the semimajor axis. The change in inclination for a small plane change is given by

$$\Delta i \approx \frac{\Delta V_i}{V} = \frac{\Delta V_i \sqrt{a}}{\sqrt{\mu}} \tag{12}$$

where ΔV_a is the delta-V performed to change the inclination. Substituting Equations (9) and (10) into Equations (11) and (12) and solving for the ratio of ΔV_i to ΔV_a yields

$$\varepsilon \equiv \frac{\Delta V_i}{\Delta V_a} = \frac{-7}{\tan(i)} \tag{13}$$

Equation (12) provides a means of comparing the relative efficiencies of changing the drift rate through inclination adjustment and semimajor axis adjustment when the orbits are nearly circular. Figure 11 shows the value of this ratio, defined as ε, over the range of inclinations from 90 to 120 degrees. Note that at an inclination of 99.3 degrees, the ratio is approximately 1.15. This implies that it is approximately 15 percent more expensive in terms of delta-V to alter the nodal rate for TOMS-EP using the inclination as the control variable than it is using the semimajor axis. Of possible interest to future Sun-synchronous missions is the fact that ε is less than 1 for inclinations less than 98.13 degrees. In other words, it would be more efficient in terms of delta-V to use inclination as a control parameter for the MLT drift rate when affecting small changes to the inclination.
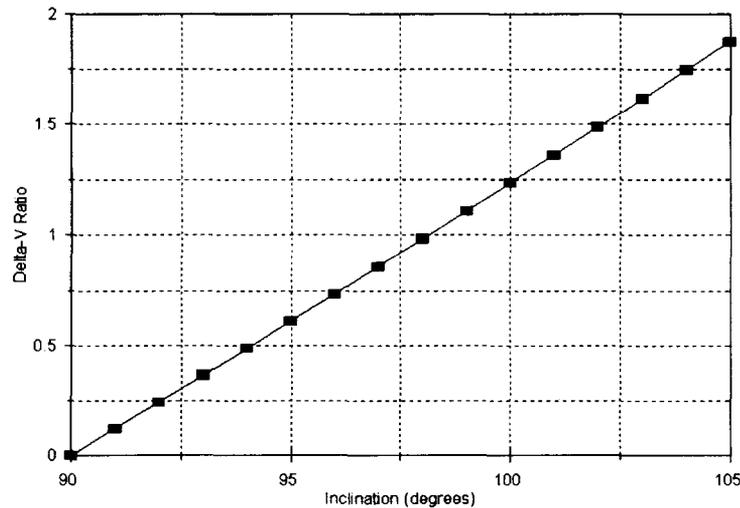
Figure 11. Delta-V Ratio as a Function of Inclination

Operational Concerns

Operational factors must be taken into account when considering the overall decision as to which control parameter to use,. To begin with, the spacecraft has a finite lifetime. Its performance, as well as that of the science instrumentation, will degrade over time. Performing maneuvers involves some measure of risk and can take time away from science operations. For example, at least four maneuvers must be executed to increase the semimajor axis, allow the node to drift down to its desired value, and then restore the semimajor axis to its nominal value. On the other hand, only half as many maneuvers are required to change the inclination, allow the node to drift back into the box, and then restore the inclination to its nominal value, provided that the adjustment to the inclination can be done in less time than the maximum maneuver duration. For TOMS-EP, the maximum maneuver duration is 35 minutes, with a nominal duty cycle of 82 percent This results in a maximum single maneuver inclination change of approximately 0.53 degree. The maximum single maneuver semimajor axis adjustment at a 955-km altitude is approximately 170 km, which would raise the circular altitude above the 1100-km limit. Since science operations cannot be conducted above 1100 km, the semimajor axis can be always be adjusted and restored to nominal in four maneuvers. If fuel is not at a premium and the necessary inclination change can be achieved in a single maneuver, it is clearly better to adjust the node rate using an inclination adjustment. This is less risky for the spacecraft and involves less operations cost and less interruption of science data collection.

Conclusions

Orbit adjustment strategies have been presented for the TOMS-EP mission for cases where the MLT of the mission orbit is outside the constraint boundaries. When the total delta-V cost is the overriding factor in the choice between the semimajor axis and the inclination as the control parameter for nodal rate adjustment, the decision can be made to first order using the ε function, which is the ratio of ΔV_i to ΔV_a. For nearly circular orbits, ε depends solely on the value of the inclination. For orbits whose inclinations are greater than 98.13 degrees, such as TOMS-EP, ε is greater than 1. However, in the case of TOMS-EP, this value is only 1.15, which is not significantly greater than 1, given the fuel budget of the mission. The choice of the semimajor axis versus the inclination as the control parameter is also dictated by operational concerns such as the maximum inclination change in a single maneuver and a desire to minimize the total number of maneuvers. Finally, it has also been shown that the size of the node rate adjustment, the available mission lifetime, and the duration prior to constraint violation are also factors in selecting a maneuver strategy.

362

References

1. Goddard Space Flight Center, Memorandum 733:5, *Analysis of Solar Gravitational Effect on Sun-Synchronous Orbit Inclination*, K. Duck, January 1973.

2. P. Jordan et al., "Analysis of the Effects of Mean Local Node-Crossing Time on the Evolution of Sun-Synchronous Orbits," *Flight Mechanics/Estimation Theory Symposium 1992*, proceedings of symposium held at Goddard Space Flight Center May 5–7, 1992, pp.177-190.

3. J. Danby, *Fundamentals of Celestial Mechanics* (2nd edition), Willmann-Bell: Richmond, Virginia, 1988.

4. Goddard Space Flight Center, Flight Dynamics Division, 553-FDD-93/016R0UD0, *Phase-A Orbit Feasibility Analysis for the National Oceanic and Atmospheric Administration (NOAA) Polar Orbiting Environmental Satellite Series O, P, Q,* (Draft), P. Jordan (CSC), prepared by Computer Sciences Corporation, February 1993.

5. Goddard Space Flight Center, Memorandum 733:73, *Inclination Biases for Sun-Synchronous Spacecraft*, K. Duck, April 1973.

6. D. Folta and L. Kraft, "Methodology for the Passive Control of Orbital Inclination and Mean Local Time to Meet Sun-Synchronous Orbit Requirements," AAS Paper No. 92-143, presented at the AAS/AIAA Spaceflight Mechanics Meeting, Colorado Springs, Colorado, February 1992.

7. R. Bate, D. Mueller, and J. White, *Fundamentals of Astrodynamics,* Dover Publications: New York, 1971.

SUMMARY OF EOS FLIGHT DYNAMICS ANALYSIS

Lauri Kraft Newman[*], David C. Folta[°]

From a flight dynamics perspective, the Earth Observing System (EOS) spacecraft present a number of challenges to mission designers. The Flight Dynamics Support Branch of NASA GSFC has examined a number of these challenges, including managing the EOS constellation, disposing of the spacecraft at the end-of-life (EOL), and achieving the appropriate mission orbit given launch vehicle and ascent propulsion constraints.

The EOS program consists of a number of spacecraft including EOS-AM, an ascending node spacecraft, EOS-PM, a descending node spacecraft, the EOS Chemistry mission (EOS-CHEM), the EOS Altimetry Laser (EOS-LALT), and the EOS-Altimetry Radar (EOS-RALT). The orbit characteristics of these missions are presented in Table 1 below. In order to assure that downlinking data from each spacecraft will be possible without interference between any two spacecraft, a careful examination of the relationships between each spacecraft and how to maintain the spacecraft in a configuration which would minimize these communications problems must be made. The FDSB has performed various analyses to determine whether the spacecraft will be in a position to interfere with each other, how the orbit dynamics will change the relative positioning of the spacecraft over their lifetimes, and how maintenance maneuvers could be performed, if needed, to minimize communications problems.

Prompted by an activity at NASA HQ to set guidelines for spacecraft regarding their end-of-life dispositions, much analysis has also been performed to determine the spacecraft lifetime of EOS-AM1 under various conditions, and to make suggestions regarding the spacecraft disposal. In performing this analysis, some general trends have been observed in lifetime calculations. The paper will present the EOS-AM1 lifetime results, comment on general reentry conclusions, and discuss how these analyses reflect on the HQ NMI.

Placing the EOS spacecraft into their respective mission orbits involves some intricate maneuver planning to assure that all mission orbit requirements are met, given the initial conditions supplied by the launch vehicle at injection. The FDSB has developed an ascent scenario to meet the mission requirements. This paper presents results of the ascent analysis.

Table 1: EOS Mission Characteristics

	EOS-AM	EOS-PM	EOS-CHEM	EOS-ALT/Laser	EOS-ALT/Radar
Mean Altitude	705 km	705 km	705 km	705 or 462 km	1336 km
Inclination	98.2	98.2	98.2	94	66
Repeat Cycle	16 days	16 days	16 days	183 days	10 days
MLT	10:30 am (desc) ± 15 min	1:30 pm (asc) ± 15 min	1:45 pm (asc) ± 15 min	N/A	N/A
Gndtrk control	± 20 km	TBD	TBD	± 800 m	± 800 m
Ground track Reference grid	WRS or previous repeat cycle track	TBD	TBD	previous repeat cycle track	TBD
Sun-Synchronous?	Y	Y	Y	N	N
Frozen?	Y	Y	Y	Y	TBD
Navigation	TONS	TONS or GN	TONS or GN	GPS	DORIS
Constraints	inc maneuvers must be performed during eclipse			No maneuvers over poles	
Other	No inc maneuvers planned	No inc maneuvers recommended	No inc maneuvers recommended	Correlate observations with MODIS w/in 10 min	
ELV	ATLAS	TBD	TBD	Delta-Lite	TBD
Launch Date	June 30, 1998	Dec. 1, 2000	Dec. 1, 2002	May 1, 2004	Dec. 1, 2003

FLIGHT MECHANICS/ESTIMATION THEORY SYMPOSIUM

MAY 16-18, 1995

SESSION 6

Geostationary Operational Environmental Satellite (GOES)-8 Mission Flight Experience*

C. H. Noonan, R. J. McIntosh, J. N. Rowe
Computer Sciences Corporation
Lanham-Seabrook, Maryland, USA 20706

R. L. DeFazio and K. F. Galal
Goddard Space Flight Center
Greenbelt, Maryland, USA 20771

Abstract

The Geostationary Operational Environmental Satellite (GOES)-8 spacecraft was launched on April 13, 1994, at 06:04:02 coordinated universal time (UTC), with separation from the Atlas-Centaur launch vehicle occurring at 06:33:05 UTC. The launch was followed by a series of complex, intense operations to maneuver the spacecraft into its geosynchronous mission orbit. The Flight Dynamics Facility (FDF) of the Goddard Space Flight Center (GSFC) Flight Dynamics Division (FDD) was responsible for GOES-8 attitude, orbit maneuver, orbit determination, and station acquisition support during the ascent phase. This paper summarizes the efforts of the FDF support teams and highlights some of the unique challenges the launch team faced during critical GOES-8 mission support.

FDF operations experience discussed includes

- The abort of apogee maneuver firing-1 (AMF-1), cancellation of AMF-3, and the subsequent replans of the maneuver profile

- The unexpectedly large temperature dependence of the digital integrating rate assembly (DIRA) and its effect on GOES-8 attitude targeting in support of perigee raising maneuvers

- The significant effect of attitude control thrusting on GOES-8 orbit determination solutions

- Adjustment of the trim tab to minimize torque due to solar radiation pressure

- Postlaunch analysis performed to estimate the GOES-8 separation attitude

The paper also discusses some key FDF GOES-8 lessons learned to be considered for the GOES-J launch, which is currently scheduled for May 19, 1995.

Introduction

The Geostationary Operational Environmental Satellite (GOES) I/M series of spacecraft (see Figure 1) are a new generation of GOES satellites containing the latest in geosynchronous weather satellite technology. The GOES program, a joint effort between the National Aeronautics and Space Administration (NASA) and the National Oceanic and Atmospheric Administration (NOAA), is designed to provide continuous weather coverage of the United States. The GOES-I/M spacecraft are built by Space Systems/Loral (SS/L) and are designed to replace the current geosynchronous meteorological satellites, of which GOES-7 is the remaining survivor. Unlike the previous series, which began with the launch of Synchronous Meteorological Satellite (SMS)-A in 1974, the new spacecraft series are three-axis stabilized. They are designed to improve the accuracy of weather data and facilitate the preparation of long- and short-range forecasts of severe weather. In addition to meteorological functions, the GOES I/M spacecraft monitor the space environment, collect data from automated terrestrial sensors, and relay aircraft and marine distress signals.
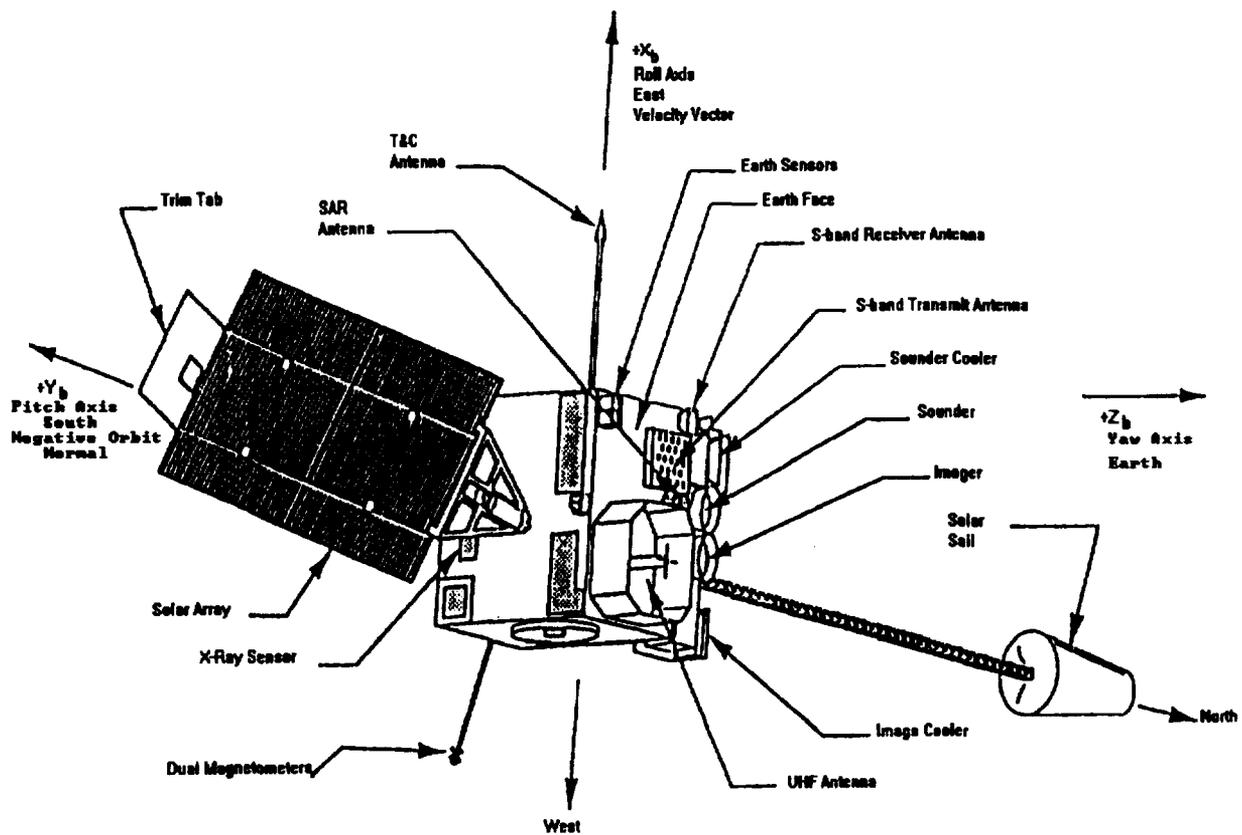

Figure 1. The GOES Spacecraft

The GOES-8 spacecraft uses an Atlas I expendable launch vehicle, which is Martin Marietta's commercially available configuration of the Atlas/Centaur. The Centaur stage inserts the spacecraft directly into a transfer orbit. The spacecraft is then maneuvered to its on-station position using its bipropellant propulsion system. Once on-station, the GOES-8 spacecraft maintains a continuous Earth-pointing attitude at a synchronous altitude of approximately 35,786 kilometers (km) and an inclination of not more than 0.5 degrees (deg).

The GOES-8 attitude and orbit control subsystem (AOCS) includes a 100-lb main satellite thruster (MST), twelve 5-lb AOCS thrusters, two momentum wheels, a reaction wheel, magnetic torquers, digital integrating rate assemblies (DIRAs), Sun and Earth sensors, and the attitude and orbit control electronics (AOCE).

GOES-8 is separated from the launch vehicle in a passive spin about the Z-axis; all appendages except the telemetry and command (T&C) antenna are stowed. After the AOCS is turned on, the Sun is captured on the -X face with a slow roll rate (0.75 degrees/second (deg/sec)) about the X-axis, when the solar array is partially deployed. During the ascent phase, GOES may be described as a zero momentum spacecraft with a closed-loop control system using thrusters as actuators. The AOCS uses a combination of sensor and gyro output to control the attitude and spacecraft body rates. Attitude maneuvers are performed by uplinking sensor offsets to the spacecraft. Following completion of the ascent phase, the GOES solar array and solar sail are fully deployed, the wheels spun up, and the spacecraft transitioned to the normal on-orbit control mode. On-station, GOES is a momentum bias spacecraft, with the attitude controlled by momentum wheels using pitch and roll data provided by the Earth sensor. A solar sail and an adjustable trim tab (on the end of the solar array) are provided to balance

370

solar radiation pressure torques about the yaw axis of the spacecraft. Magnetic torquers and thrusters are used to dump any excess yaw momentum buildup in the wheel momentum vector.

The nominal maneuver sequence (see Figure 2) required to raise GOES from its transfer orbit to a checkout orbit called for a total of six maneuvers: three Apogee Maneuver Firings (AMFs), an Apogee Adjust Maneuver (AAM), and two Trim Maneuver Firings (TMFs). The AMFs raise the perigee height (to about 255 km below geosynchronous altitude), lower the inclination to 0.5 deg, and set the final right ascension of the ascending node. In addition, the AMFs were also required to rotate the line of apsides to set up more favorable Sun-Earth-spacecraft geometry for attitude targeting operations at the time of the AAM. The AAM was designed to lower the supersynchronous transfer orbit apogee to about 255 km above geosynchronous altitude. Finally, two TMFs were planned at apogee and perigee to trim the final orbit by another 100 km and stop the drift.
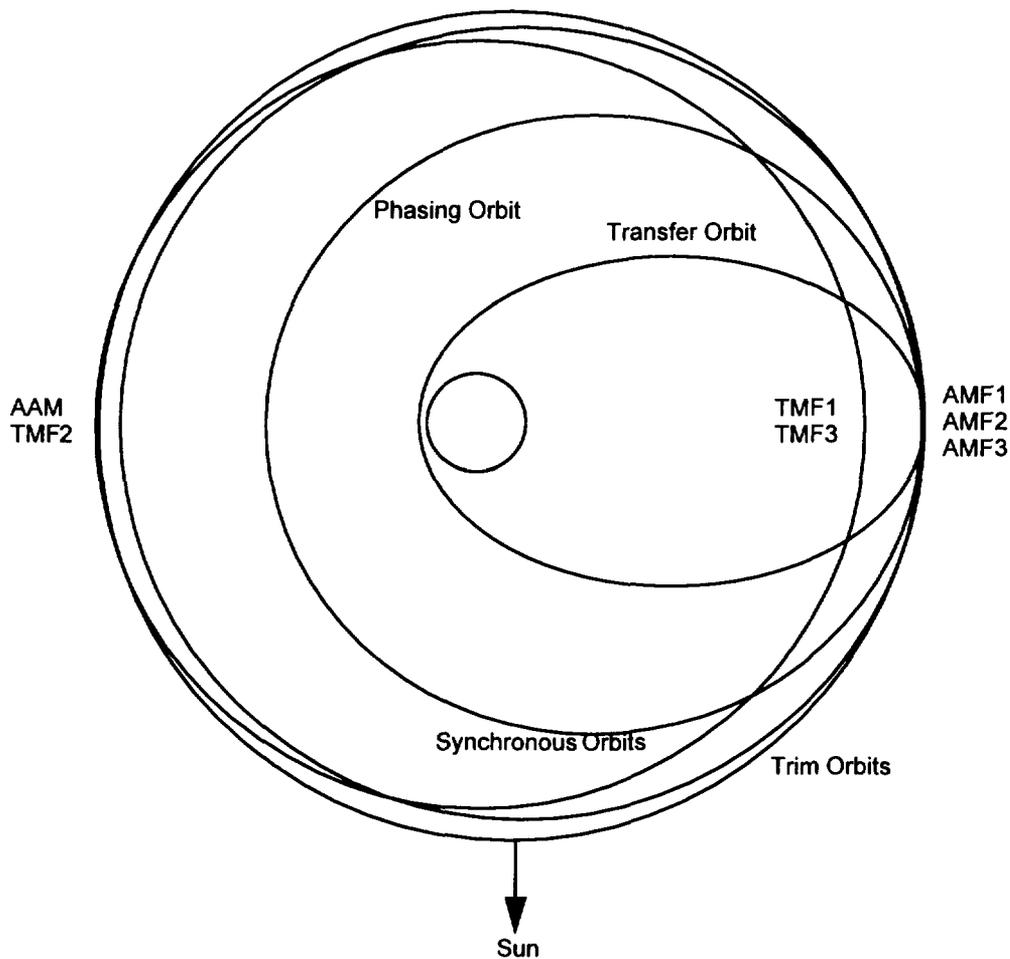
Figure 2. Nominal Maneuver Sequence

NASA's Goddard Space Flight Center (GSFC) is responsible for launch and early mission support of the GOES satellites until they are placed in geosynchronous orbit over the check-out longitude. During the ascent phase, FDF analysts work closely with the Mission Operations Support Team (MOST) in the NOAA satellite operations control center in Suitland, Maryland. After checkout, NOAA assumes full operational responsibility. The Flight Dynamics Division (FDD) has been involved with the GOES-I/M project since 1985. Software components including an attitude ground support system (AGSS), maneuver planning utilities, prediction and scheduling utilities, and dynamics/telemetry simulators were developed for the

371

GOES program to ensure safe and timely support of GOES I/M operations. High-level FDD requirements for the GOES mission are to

- Provide orbit and attitude support to achieve operational orbit
- Support the MOST and NOAA in on-orbit testing of GOES and its instruments to characterize system performance
- Hand over each GOES to NOAA for operations with sufficient onboard propellant for a minimum of 5 years of stationkeeping

Orbit Control and Mission Profile

GOES-8 was launched into an elliptical, supersynchronous transfer orbit with a 27.0 deg inclination, a 12.5 hour (hr) period, and a perigee height of 170 km. The minimum residual shutdown (MRS) option of the Atlas I launch vehicle, in which all usable propellant in the launch vehicle is expended, resulted in raising apogee by 6600 km above synchronous altitude. The decision to take advantage of the MRS option was made approximately 1 year before launch. By starting at a supersynchronous apogee, the delta-V needed to raise perigee and then lower apogee later was less than that necessary to raise perigee directly from a geosynchronous apogee height. Using the MRS scenario gained about 3- to 4 more months of spacecraft lifetime.

The desired GOES-8 checkout orbit had a geosynchronous semimajor axis with an apogee bias of 155 km above geosynchronous, a perigee bias of 155 km below geosynchronous, and a spacecraft longitude of 90 deg W. The biased orbit was chosen so that the spacecraft could later be relocated without propellant penalties. Removing the bias from either apogee or perigee allows the spacecraft to drift east or west at approximately 1 deg per day until the desired new longitude is reached.

The ascent maneuvers had to satisfy a number of constraints including the following, which were the most restrictive:

- The spacecraft had to be in view of at least two ground stations.
- The pitch angle could not exceed 3 deg, due to Earth sensor field of view considerations and associated nonlinearity affects introduced by supersynchronous altitudes.
- The burn duration for MST maneuvers lasting longer than 102.3 sec was limited to a 5-sec resolution.
- Maneuvers with the east face AOCS thrusters were limited to a maximum duration of 37 sec followed by a 15-minute (min) wait to allow the propellant management device (PMD) to refill.
- At least 30 min needed to be set aside for DIRA calibration before each burn.

AMF-1 Abort. The first maneuver, AMF-1, was performed at fourth apogee and was planned to be the largest in the sequence with a duration of 3910 sec. The maneuver started nominally on April 15, 1994, at 02:43:22 coordinated universal time (UTC). As the maneuver progressed, however, telemetry indicated that the MST flange temperature was exceeding the prescribed limits. The burn was terminated by the MOST after only 497.8 sec. The aborted AMF-1 provided about 11 percent of the planned delta-V, raising perigee by 854 km and lowering the inclination to 23.46 deg. At burn termination, the spacecraft was at a longitude of 136 deg W, with an eastward drift rate of 298 deg/day.

After reviewing AMF-1 and consulting with the MST manufacturer, the Project made the following three changes to AMF operations:

- The abort criteria were revised since it appeared that the specified limits were too conservative based on a review of the thruster flange thermal analysis.
- The DIRA calibration attitude was modified to keep the Sun off the MST and thus start the maneuver at a lower thruster flange temperature.
- The AMF sequence was increased from three to five maneuvers to reduce the length of MST firings.

The FDF replanned the rest of the ascent phase based on the above criteria.

AMF-3 Cancellation. The third maneuver, AMF-3, was originally scheduled for apogee 8, but was moved to apogee 14 after the abort of AMF-1. However, several hours before the maneuver was scheduled to begin, AMF-3 was canceled because of anomalous AOCE performance. Instantaneous spikes were observed in the gyro data, which were integrated by the AOCE

causing anomalous firings of the attitude control thrusters. The Project chose to cancel the maneuver rather than risk such anomalous attitude thruster firings during the orbit maneuver.

After careful study, it was determined that the anomalies were probably due to electrostatic discharges caused by the passage of GOES-8 through the Van Allen belts. An unusually high geomagnetic index was recorded in early April, and the increased solar activity was thought to have contributed to the anomalies in the onboard electronics. The Project switched to the backup AOCE and requested that AMF-3 be replanned for apogee 16.

The effect of the electrostatic discharges on the AOCE posed a unique paradox because of the limitation imposed on maneuver duration following the AMF-1 abort. Even though it was important to get out of the electromagnetic activity region as quickly as possible, only small maneuvers were allowed due to thruster flange temperature considerations.

Revised Maneuver Profile. Following cancellation of AMF-3, a revised maneuver sequence was computed with AMF-3 rescheduled for apogee 16. The maneuver began on April 21, 1994, at 19:38:52 UTC with a duration of 1160 sec. AMF-3 raised perigee by 4108 km and changed inclination to 11.19 deg. The maneuver ended at 36.8 deg W, with an eastward drift rate of 202 deg/day.

All subsequent burns through the AAM were performed nominally. The TMFs were slipped by 2 days in the final sequence to avoid predicted lunar interference in the Earth sensor and to adjust for small errors in longitude and drift after the AAM. Table 1 presents the four maneuver plans and gives the apogee or perigee number where each burn occurred. Apogee 1 is defined as the first apogee after spacecraft separation, and perigee 1 follows apogee 1.

Table 1. Four Maneuver Plans Including Apogee and Perigee

Maneuver	Initial Schedule	Schedule After AMF-1 Aborted	Schedule After AMF-3 Canceled	Final Schedule
AMF-1	Apogee 4	Apogee 4	Apogee 4	Apogee 4
AMF-2	Apogee 6	Apogee 11	Apogee 11	Apogee 11
AMF-3	Apogee 8	Apogee 14	Apogee 16	Apogee 16
AMF-4	not scheduled	Apogee 17	Apogee 19	Apogee 19
AMF-5	not scheduled	Apogee 19	Apogee 21	Apogee 21
AAM	Perigee 9	Perigee 20	Perigee 22	Perigee 22
TMF-1	Apogee 16	Apogee 26	Apogee 28	Apogee 30
TMF-2	Perigee 17	Perigee 27	Perigee 29	Perigee 31

Maneuver Performance

Each orbit maneuver was calibrated to assess the performance of the maneuver and make corresponding adjustments to maneuver models to improve the accuracy of subsequent maneuvers. A 3-sigma attitude error budget of 1.57 deg was allowed. The effect of AOCS thrusting between and during the burns was accounted for using telemetered counts of thruster pulses for propellant remaining purposes. Table 2 provides a summary of propellant usage, delta-V error (with respect to planned), and the yaw attitude error (see Reference 1 also).

Table 2. Summary of Propellant Usage, Delta-V Error, and Yaw Attitude Error

Event	Propellant used (kg)	Propellant remaining (kg)	Delta-V error (percent)	Yaw attitude error magnitude (deg)
AMF-1	81.52	1041.40	-0.53[1]	0.59
AMF-2	149.94	889.57	0.87	0.44
AMF-3	191.05	888.11	1.08	0.05
AMF-4	418.61	277.74	0.88	0.63
AMF-5	48.25	228.60	0.23	0.30
AAM	43.56	184.32	0.29	0.08
TMF-1	2.59	176.75	2.03	0.60
TMF-2	2.08	174.52	0.47	N/A[2]

[1] Due to AMF-1 abort, this value takes into account only the planned delta-V for the time that the motor actually fired.

[2] An attitude solution could not be computed because no Sun sensor data were available.

At the time of the GOES-8 handover from NASA to NOAA, approximately 8.6 years of propellant lifetime was remaining, considerably more than the 5-year minimum required.

DIRA Calibration and Attitude Targeting

GOES attitude maneuver targeting is a two-step process involving first calibrating the DIRA (or gyro) then using the calibrated gyro and the Earth sensor (ES) to reorient the spacecraft to place the MST in the direction of the desired orbit delta-V. During the half orbits before orbit maneuvers, the Earth is captured in roll, and the spacecraft is placed in a quasi-inertial attitude for DIRA calibration. After calibration, the computed DIRA biases are uplinked, and the spacecraft is commanded to capture the Earth in pitch, using the Earth sensor to maintain nadir pointing. From this point on through the orbit maneuver, spacecraft yaw is controlled using the integrated yaw DIRA rate.

Gyro Temperature Dependence. Upon separation of the GOES-I spacecraft from the Centaur launch vehicle, a practice DIRA calibration was performed during the first half-orbit of the mission. Its purpose was to exercise DIRA calibration spacecraft operations and get an initial estimate of the DIRA drift rate biases before the first orbit maneuver at apogee 4. This practice DIRA calibration showed that computed DIRA drift rate biases were changing with time. The DIRA yaw drift (of most concern because the yaw gyro is used for position control during orbit maneuvers) continued to increase as the spacecraft approached apogee 1. An analysis of the calibration data and temperature information obtained from the MOST indicated that the gyros were more temperature dependent than had been previously expected—the specification value on the DIRAs was 0.03 deg/hr/deg C (Reference 2). As Figure 3 shows, a least squares fit of computed yaw DIRA drift bias solutions as a function of DIRA temperature yielded a linear variation with a slope of about 0.13 deg/hr/deg C.
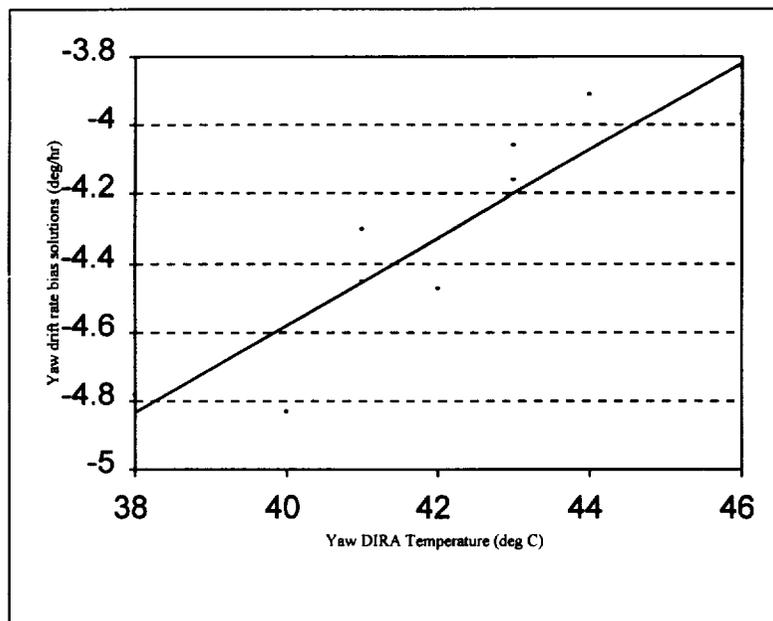
Figure 3. Yaw DIRA Rate vs. Temperature Pre-Apogee 1

Indeed, similar behavior had been observed for gyros used on the Earth Radiation Budget Satellite (ERBS), where variation of up to 0.24 deg/hr/deg C were reported (see Reference 4). The GOES I/M spacecraft use the same Northrop GIG6 gyros as those flown on ERBS.

As a result of this observed temperature dependency, a plan was devised to minimize DIRA temperature fluctuations by maintaining the spacecraft in a direct Sun-pointing attitude (0-deg yaw relative to the Sun-Earth-spacecraft plane). This approach was successful, preventing the Sun from shining on the -Y axis of the spacecraft (where the DIRAs are located), thereby keeping the DIRAs at a near constant temperature of 35 deg C; the corresponding yaw DIRA bias solved for was also

374

constant at an approximate value of -4.25 deg/hr. However, following the abort of AMF-1, where high thruster flange temperatures were observed, this attitude profile was overruled in favor of an attitude designed to keep the motor cooler. The new DIRA calibration attitude, which used the maximum allowable -27 deg DSS yaw offset to keep the spacecraft -X-axis below the orbit plane and away from the Sun, yielded an 8 to 10 deg rise in DIRA temperatures before the burn. To effectively accommodate these temperature fluctuations, sliding 20-min batch least squares solutions were computed using the average temperature at the center of the 20-min span to track the DIRA drift versus temperature. In addition, a Kalman filter was used to provide real-time estimates of attitude and DIRA biases over time. Although linear in each case, the temperature dependence of the DIRA biases (as observed during calibrations for AMFs-2, -3 and -4) was not consistent from one maneuver to the next. The temperature profiles as well as the variations in the drift rate biases with respect to DIRA temperature changed from day to day. Throughout the ascent phase, the following variations in the rate of change of DIRA drift rate biases with temperature were observed:

yaw: 0.124 deg/hr/deg C to 0.242 deg/hr/deg C

pitch: 0.031 deg/hr/deg C to 0.128 deg/hr/deg C

roll: 0.084 deg/hr/deg C to 0.143 deg/hr/deg C

Attitude Targeting Considerations. The lack of consistency in the bias rate of change from one calibration to the next made it necessary to track the drift rates in near real time before each maneuver. A history of DIRA bias solutions and temperatures observed over the course of a calibration were established; then, DIRA biases were extrapolated based on the expected temperature at the time of the burn. Nominally, initial drift biases were supplied to the MOST about 2 hours before a burn, with an opportunity to update the biases within 1 hour of the burn if the temperature or drift rates had not behaved as expected.

When calibration was complete, the spacecraft had to be reoriented to the target attitude for the delta-V maneuver. This reorientation maneuver was accomplished by uplinking an offset to the yaw DIRA, which is used for yaw attitude control. The temperature dependence of DIRA drift rate biases meant that no matter how accurately a bias was computed during calibration, a change in DIRA temperature would cause the bias to change, and consequently, the yaw attitude would drift as the yaw DIRA was used for control. In most cases, the DIRA temperatures continued to vary even throughout the burn. Therefore, the commanded yaw DIRA offset had to include an allowance for expected drift based on anticipated changes in temperature.

Beyond AMF-4, the flange temperature ceased to be a driving concern since follow-on maneuvers were shorter (less than 15 minutes). It was, therefore, possible to use a Sun-pointing premaneuver attitude, which minimized DIRA temperature fluctuations and greatly improved DIRA bias stability.

Orbit Determination

During the ascent phase, GOES-8 used NASA standard transponders for communication through ground stations—primarily Deep Space Network (DSN) 26 meter sites. Other stations used were the Indian Ocean Station (IOS) early in the mission and Santiago later in the mission. IOS, the first station to see GOES-8 after separation, was primarily used for telemetry and commanding. IOS was also used, however, for orbit determination by collecting 3-way data once the DSN site at Canberra acquired the satellite but before the uplink was switched to Canberra. After the inclination had been reduced and GOES-8 was located over the continental U. S., southern hemisphere tracking through Santiago was necessary to determine the orbit accurately enough in the time allocated.

Sensitivity to Attitude Control Thrusting. Throughout the GOES-8 NASA support period, unmodeled orbit perturbations affected orbit determination solutions just before and immediately after the delta-V maneuvers. These perturbations caused considerable difficulty in determining the orbital state near the burns and limited the effectiveness of thrust scale factor estimation. Both elements were key to determining "quick look" orbit solutions and realizing rapid postmaneuver recovery. The perturbations arose from attitude control thrusting, which occurred at a low level throughout all orbits; however, significant increases were observed during the half orbits before delta-V maneuvers. During those times, the spacecraft was maneuvered into various DIRA calibration and delta-V attitudes and commanded into tighter attitude control modes. Such perturbations yielded systematic patterns, including oscillations and ramps in the tracking residuals.

During GOES-8 real-time support, the dynamic solar radiation force modeling, which existed in FDF software, was used to absorb the effects of the autonomous attitude control thrusting. This approach worked but only because most of the AOCS thrusting turned out to be parallel to the Sun line. Current analysis is underway, however, to model the large attitude thrusting on the half-orbits before delta-V maneuvers in more detail. Once modeled, improvements in orbit determination and thrust estimation before and following GOES maneuvers should be expected.

Reference 5 contains a more detailed description of this analysis and results.

Trim Tab Support

GOES has a trim tab on the end of the solar array that is adjusted in-flight to balance solar radiation pressure torques between the solar sail and solar array. The goal is to manage yaw angular momentum using the trim tab to eliminate the need to use yaw thrusters for momentum unloading, since this activity disturbs the imaging process. The trim tab is supplemented by magnetic torquers and thrusters, which are intended to absorb excess yaw momentum if the trim tab is not set exactly right. The trim tab angle is adjusted once per day by ground command to compensate for the average solar torque expected during the next day.

Before launch, SS/L developed a table providing the theoretical value of the trim tab angle as a function of day of year, based on detailed modeling of the GOES-8 spacecraft. Once on-orbit, the initial setting of the trim tab was selected from this table. However, it was recognized before launch that predicted values would not be sufficiently accurate for operational use; thus, SS/L developed an algorithm to be used in-flight to estimate the actual torques acting on the spacecraft. The process is to look at the thruster activity, wheel speeds, and magnetic torquer activity over 24 hours, calculate the residual torque acting on the spacecraft, and calculate the trim tab angle needed to compensate this torque as well as the change in the torque that would be expected as a result of the daily change in Sun declination.

After launch, it was found that the algorithm was overly sensitive to small, short-term variations in the residual torque. The telemetry readout of the actual trim tab angle was also noisier than expected and was biased by a few tenths of a degree, causing contamination of the calculations. As a result, FDF analysts developed a simplified procedure in which the trim tab angle was adjusted every day to track the Sun, based on a theoretical calculation. Every few days, a larger or smaller adjustment was made to minimize the magnetic torquer activity. The residual torque calculation was based only on changes in trim tab angle, not the absolute angle. This approach generally worked well—no thruster firings were necessary for yaw momentum control—but was too labor intensive for routine operations and not sufficiently accurate to keep the magnetic torquer activity as low as possible. SS/L subsequently developed and implemented a new algorithm in which an empirical power series model of the trim tab angle was fit over several weeks of observations and used to predict the trim tab angle for the coming week.

The trim tab approach worked well to control the yaw angular momentum. For example, the torque due to the solar sail or solar array alone was on the order of 3×10^{-4} NM. The sum of the two without the trim tab is about an order of magnitude less and is reduced to the range of 1×10^{-6} to 1×10^{-7} NM by proper trim tab adjustment.

GOES Separation Attitude

The baseline GOES-8 separation attitude required the spacecraft Z-axis to be placed at a right ascension of 61.7 deg and a declination of -25.0 deg, with a spin rate of 7 deg/sec about that axis. Martin Marietta (then General Dynamics) had requested that FDF attempt to establish the postlaunch GOES-8 attitude using any available spacecraft data. This estimate was to help Martin Marietta verify the accuracy of the launch vehicle separation. Analysts took two approaches:

1. Attitude sensor data (DIRA, DSS, ES) were used to try to directly solve for the attitude and rate

2. Doppler tracking data were used as an indirect measurement of spacecraft nutation angle.

DIRA data available approximately 25 min after separation indicated that the spin rate was 6.2 deg/sec about the Z-axis, with average rates of -0.5 deg/sec on the X-axis and 1.7 deg/sec on the Y-axis. Based on the maximum values of the cross-axis rates, the maximum deviation of the Z-axis from the angular momentum vector was about 30 deg at that time. Meanwhile,

FDF analysts studied Doppler tracking data (References 6, 7) that suggested a spin rate of 6.86 deg about the Z-axis and a nutation amplitude of about 4 deg at the time of separation. These values are consistent with those Martin Marietta predicted prelaunch.

Additionally, Earth sensor data were obtained approximately 1.5 hr after separation, when an attitude solution was computed. Back-propagation of this attitude to the time of DIRA turn-on was attempted but was not reliable because of changing DIRA biases and the commanded high-rate mode of the DIRA (necessary to avoid saturation) that yielded a resolution of only 1.2 deg/hr.

GOES-J and Beyond

In January 1995, GOES-8 was moved from its checkout longitude at 90 deg W to its operational longitude of 75 deg W (over the east coast of the United States). On May 19, 1995, NASA intends to launch GOES-J, which will cover weather for the west coast at 135 deg W and replace GOES-7. Although the GOES-J mission should be virtually identical to GOES-8, slight modifications to both the spacecraft and operations are expected to reduce the number of complications experienced and improve spacecraft operations. The following is a summary of some of changes that have resulted from GOES-8 lessons learned:

- Fifteen kilograms of additional shielding has been added to the spacecraft to further guard against electrostatic discharges. To maintain the separation weight, the propellant will be reduced by 15 kg.

- The Santiago ground station will be scheduled in advance for tracking data support to improve accuracy and turnaround of orbit solutions.

- The GOES-J checkout orbit will not have a biased apogee and perigee. Such an orbit tended to complicate the instrument checkout for GOES-8, so a circular orbit will be targeted instead.

- GOES-J AMF abort criteria have been reviewed and revised following significant prelaunch analysis and spacecraft testing. A yaw reorientation maneuver will again be conducted to cool the MST before the delta-V maneuvers as a precaution for GOES-J. Performing a small initial calibration burn (less than 20 min) instead of a larger burn (longer than 60 min) in an attempt to characterize the thruster flange temperatures early in the ascent phase was considered. However, this idea was discarded to minimize the time spent in the transfer orbit where the possibility of electrostatic discharges poses a threat to the spacecraft.

- A quenching burn sequence will be scripted and practiced to reduce temperatures following the large MST firings. Quenching burns will be performed only as necessary.

- All FDF procedures have been updated to factor in GOES-8 lessons learned; in particular, new procedures have been implemented to streamline DIRA calibration operations and account for the DIRA drift rate dependence on temperature.

- FDF support shifts are to be streamlined and adjusted to provide quicker response to maneuver planning and product generation in support of station scheduling activities.

- Orbit determination procedures have been improved to accommodate periods of intensive AOCS thrust activity and decrease their effect on orbit solutions.

Acknowledgments

377

References

1. Computer Sciences Corporation, CSC 54814-29, "GOES-8 Propellant Remaining" (memorandum), R. McIntosh, D. Carrington, and C. Noonan, August 3, 1994

2. Space Systems/Loral, SSL-TR00570A, CCR2212, *GOES Program Spacecraft Operations Handbook DRL 503-02: Volume VI. Spacecraft Data GOES-I*, April 1994

3. Computer Sciences Corporation, "Mission Support Plan for Geostationary Operational Environmental Satellite-I (GOES-I)," S. Kirschner, March 1994

4. Computer Sciences Corporation, "Earth Radiation Budget Satellite (ERBS) Inertial Reference Unit (IRU) Performance Analysis," E. Harvie et al, February 1992

5. Computer Sciences Corporation, *Evaluation and Modeling of Autonomous Attitude Thrust Control for Orbit Determination*, W. Forcey, May 1995

6. AlliedSignal Technical Services Corporation, TSG 94-115, "Estimation of Nutation Angle from Doppler Tracking Data," S. D. Hendry, August, 1994

7. AlliedSignal Technical Services Corporation, TSG 94-97,"Analysis of Spinning Spacecraft Doppler Tracking," S. D. Hendry, July 1994

Estimation of Attitude Sensor Timetag Biases *

J. Sedlak
Computer Sciences Corporation
Lanham-Seabrook, Maryland, USA 20706

Abstract

This paper presents an extended Kalman filter for estimating attitude sensor timing errors. Spacecraft attitude is determined by finding the mean rotation from a set of reference vectors in inertial space to the corresponding observed vectors in the body frame. Any timing errors in the observations can lead to attitude errors if either the spacecraft is rotating or the reference vectors themselves vary with time.

The state vector here consists of the attitude quaternion, timetag biases, and, optionally, gyro drift rate biases. The filter models the timetags as random walk processes: their expectation values propagate as constants and white noise contributes to their covariance. Thus, this filter is applicable to cases where the true timing errors are constant or slowly varying.

The observability of the state vector is studied first through an examination of the algebraic observability condition and then through several examples with simulated star tracker timing errors. The examples use both simulated and actual flight data from the Extreme Ultraviolet Explorer (EUVE). The flight data come from times when EUVE had a constant rotation rate, while the simulated data feature large angle attitude maneuvers. The tests include cases with timetag errors on one or two sensors, both constant and time-varying, and with and without gyro bias errors.

Due to EUVE's sensor geometry, the observability of the state vector is severely limited when the spacecraft rotation rate is constant. In the absence of attitude maneuvers, the state elements are highly correlated, and the state estimate is unreliable. The estimates are particularly sensitive to filter mistuning in this case. The EUVE geometry, though, is a degenerate case having coplanar sensors and rotation vector. Observability is much improved and the filter performs well when the rate is either varying or noncoplanar with the sensors, as during a slew. Even with bad geometry and constant rates, if gyro biases are independently known, the timetag error for a single sensor can be accurately estimated as long as its boresight is not too close to the spacecraft rotation axis.

1. Introduction

One important step in spacecraft telemetry processing is assigning timetags to each sensor measurement. Errors in these timetags can occur as constant biases due to inaccurate time offsets used in the software or as possibly time-varying errors due to problems with the sensor itself or with input/output to an onboard data buffer. Timetag errors can lead to errors in the estimated attitude if either the spacecraft is rotating or the reference vectors themselves vary with time.

This work examines the feasibility of estimating attitude sensor timetag errors along with the attitude quaternion and gyro rate bias (other calibration parameters could be included as well). The timing errors are thought of as constant biases (offsets from the true observation time), but the method also applies to slowly varying errors.

The timetag biases are appended to the system state vector and estimated using an extended Kalman filter. Section 2 describes the sensitivity matrix and state transition matrix needed as input to this algorithm. Some insight into the observability of the larger state vector is obtained by examining the observability matrix in Section 3. Results of several test cases are presented in Section 4. The tests include examples with timing errors on either one or two sensors, with and without gyro rate biases, for timespans with and without attitude maneuvers. Examples where the true bias is time-varying are also considered. Conclusions are given in Section 5.

2. Theory

The extended Kalman filter theory, as applied to attitude and gyro bias estimation, is given in Reference 1. One distinguishes the full state vector consisting of the quaternion and gyro bias, from the error state consisting of a small angle rotation vector, $\vec{\alpha}$, and a correction to the gyro bias, $\Delta\vec{b}$. For each sensor measurement, the resulting error state updates the prior estimate of the full state: it rotates the attitude and additively corrects the gyro bias. Between measurements, the full state is propagated using bias-corrected gyro data.

This approach moves the normalization constraint on the attitude quaternion onto the 4th component of the error quaternion. (The error quaternion is the quaternion corresponding to the rotation vector $\vec{\alpha}$. It automatically has 4th component equal to unity, to first order in $\vec{\alpha}$.) This leaves the three components of $\vec{\alpha}$ completely unconstrained, and the normal extended Kalman filter theory then is applicable.

References 2 and 3 describe the unit vector filter (UVF) observation model used here. In this model, the actual measured quantities are converted into unit vectors in the body frame before being handed to the Kalman filter. The effective sensor noise is taken to be isotropic; that is, a single scalar parameter represents the strength of the noise, regardless of the direction of the unit vector in the actual sensor field of view.

The rest of this section expands the UVF to include timetag biases by developing the sensitivity matrix and the state transition matrix. The sensitivity matrix relates the unit vector observations to the error state. It is needed at each sensor measurement to construct the Kalman gain and estimate a new error state. The state transition matrix is used to propagate the covariance of the error state between observations.

Sensitivity Matrix

The observation of a vector quantity (*e.g.*, a star unit vector) is modeled as a reference vector, $\vec{v}$, rotated into the body frame at the true time of measurement, plus random, zero-mean sensor noise, $\vec{n}_k$. The attitude matrix, A_{true}, rotates vectors from the inertial frame to the body frame representation. The predicted observation uses the attitude estimate conditioned on the prior observations

$$true\ observation\ =\ \vec{w}_{true}\ =\ A_{true}\vec{v}_{true} + \vec{n}_k$$

$$predicted\ observation\ =\ \vec{w}_{k|k-1}\ =\ A_{k|k-1}\vec{v}_k \tag{1}$$

The $k|j$ notation indicates a quantity estimated using observation data through time t_j, and propagated (if $k \neq j$) to time t_k. Thus, in the usual parlance, $k|k-1$ indicates an a priori estimate and $k|k$ an a posteriori estimate.

The observation is assigned timetag t_k, whereas the true time of the measurement is $t_{true} = t_k - \tau$. In particular, τ is the time bias to be estimated.

The true timetag bias, its estimate, and the time bias error are related as $\tau = \tau_{k|k-1} + \Delta\tau$. At each update, one estimates $\Delta\tau$ and adds it to $\tau_{k|k-1}$ to get the a posteriori $\tau_{k|k}$. This propagates as a constant to the next update time, becoming $\tau_{k+1|k}$.

To simplify the notation, one can absorb the prior estimate $\tau_{k|k-1}$ into t_k. The reference vectors always are obtained for corrected times using the best current time bias estimate, so the subscript-k properly should indicate variables at that corrected time. Specifically, t_k is corrected and replaced hereafter by $t_k - \tau_{k|k-1}$, and the time bias *error* becomes

$$\Delta\tau\ =\ t_k - t_{true} \tag{2}$$

The advantage is that only $\Delta\tau$ (and not $\tau_{k|k-1}$) need appear in the following derivation.

380

The attitude at (corrected) time t_k is related to the attitude at the true observation time by

$$A_k = R_A(\Delta\tau)A_{true} \qquad (3)$$

where $R_A(\Delta\tau)$ is the rotation matrix for any spacecraft motion during time $\Delta\tau$. One can represent this rotation by

$$R_A(\Delta\tau) = e^{-[\vec{\omega}_k\Delta\tau\times]} \qquad (4)$$

where the true rate, $\vec{\omega}_k$, is the gyro output, $\vec{u}_k$, corrected for the gyro bias

$$\vec{\omega}_k = \vec{u}_k - \vec{b}_k \qquad (5)$$

The estimate $\vec{\omega}_{k|k-1} = \vec{u}_k - \vec{b}_{k|k-1}$ is used to approximate $\vec{\omega}_k$ in Equation (4). Also, for any vector $\vec{v}$, the "cross-product matrix" is defined

$$[\vec{v}\times] \equiv \begin{bmatrix} 0 & -v_z & v_y \\ v_z & 0 & -v_x \\ -v_y & v_x & 0 \end{bmatrix} \qquad (6)$$

The reference vector also may vary during the time interval. Its magnitude does not contribute information to the state estimate, so only rotations need be considered. Thus, the reference vector at time t_k is related to the reference at the true observation time by

$$\vec{v}_k = R_v(\Delta\tau)\vec{v}_{true} \qquad (7)$$

If the reference vector is rotating at a mean rate $\vec{r}_k$, then

$$R_v(\Delta\tau) = e^{[\vec{r}_k\Delta\tau\times]} \qquad (8)$$

The sign in the exponent here is opposite to that in Equation (4) because R_v refers to actual rotation of a vector rather than its apparent motion due to rotation of the body frame.

The sign of the attitude error angle $\vec{\alpha}$ is defined such that the true and estimated attitude matrices at time t_k are related by

$$A_k = e^{[\vec{\alpha}_k\times]}A_{k|k-1} \qquad (9)$$

The seven-component state error vector is

$$x_k = \begin{bmatrix} \vec{\alpha}_k \\ \Delta\vec{b}_k \\ \Delta\tau_k \end{bmatrix} \qquad (10)$$

The sensitivity matrix, H_k, is the derivative of the observation with respect to the state, evaluated at the prior state estimate. One can also write this as a relationship between the observation residual, $\vec{y}_k$, and the error state

$$\vec{y}_k = H_k x_k + \vec{n}_k \tag{11}$$

Note that the a priori *error* state is identically zero since it already has been used to update the *full* state vector after the previous observation (the actual error may be nonzero, but its estimate vanishes). Expanding $\vec{y}_k$ to lowest order in the error components (expanding about zero) yields

$$
\begin{aligned}
\vec{y}_k &= \vec{w}_{true} - \vec{w}_{k|k-1} \\[4pt]
&= A_{true}\vec{V}_{true} + \vec{n}_k - A_{k|k-1}\vec{v}_k \\[4pt]
&\approx \left(I + [\vec{\omega}_k \Delta \tau_k \times]\right)\left(I + [\vec{\alpha}_k \times]\right)A_{k|k-1}\left(I - [\vec{r}_k \Delta \tau_k \times]\right)\vec{v}_k - \vec{w}_{k|k-1} + \vec{n}_k \\[4pt]
&\approx -[\vec{w}_{k|k-1} \times]\vec{\alpha}_k - \vec{w}_{k|k-1} \times \vec{\omega}_{k|k-1}\Delta\tau_k - A_{k|k-1}(\vec{r}_k \times \vec{v}_k)\Delta\tau_k + \vec{n}_k \\[4pt]
&= -[\vec{w}_{k|k-1} \times]\vec{\alpha}_k - \vec{w}_{k|k-1} \times \left(\vec{\omega}_{k|k-1} - A_{k|k-1}\vec{r}_k\right)\Delta\tau_k + \vec{n}_k
\end{aligned}
\tag{12}
$$

Thus, the sensitivity matrix is

$$H_k = \begin{bmatrix} -[\vec{w}_{k|k-1} \times] & 0_{3\times3} & -\vec{w}_{k|k-1} \times \left(\vec{\omega}_{k|k-1} - A_{k|k-1}\vec{r}_k\right) \end{bmatrix} \tag{13}$$

If one simultaneously observes two vectors, $\vec{w}^1$ and $\vec{w}^2$, (*e.g.*, using two star trackers) to estimate the timetag bias of only $\vec{w}^1$, one obtains

$$H_k = \begin{bmatrix} -[\vec{w}^1 \times] & 0_{3\times3} & -\vec{w}^1 \times (\vec{\omega} - A\vec{r}) \\[6pt] -[\vec{w}^2 \times] & 0_{3\times3} & 0_{3\times1} \end{bmatrix} \tag{14}$$

where all quantities are a priori estimates $(k|k-1)$.

State Transition Matrix

The time evolution of the attitude and gyro bias parts of the error state is described in References 1 and 3. The attitude error is rotated at the rate $\vec{\omega}$, with a correction due to the gyro bias error and a noise term. The gyro and timetag biases are represented using random walk models. The timetag bias may be more properly modeled as a random constant, but the random walk leads to a somewhat more robust filter and prevents the covariance from underflowing. The evolution equation is

$$\frac{dx}{dt} = Fx + \eta$$

$$= \begin{bmatrix} -[\vec{\omega} \times] & I_{3\times3} & 0_{3\times p} \\[4pt] 0_{3\times3} & 0_{3\times3} & 0_{3\times p} \\[4pt] 0_{p\times3} & 0_{p\times3} & 0_{p\times p} \end{bmatrix} \begin{bmatrix} \vec{\alpha} \\[4pt] \Delta\vec{b} \\[4pt] \Delta\vec{\tau} \end{bmatrix} + \begin{bmatrix} \vec{n}_\alpha \\[4pt] \vec{n}_b \\[4pt] \vec{n}_\tau \end{bmatrix} \tag{15}$$

where $\Delta\vec{\tau}$ here is written more generally as a p-component vector, representing timetag bias errors for p different sensors. The vector, η, is the white noise source driving random walks in the attitude, gyro bias, and timetag bias.

Assuming the angular rates are constant during the propagation time interval, $\Delta t = t_2 - t_1$, the transition matrix is the exponential of the evolution matrix F times Δt:

$$\Phi(t_2, t_1) \equiv \Phi(\Delta t) = e^{F \Delta t} = \begin{bmatrix} \phi & \psi & 0_{3 \times p} \\ 0_{3 \times 3} & I_{3 \times 3} & 0_{3 \times p} \\ 0_{p \times 3} & 0_{p \times 3} & I_{p \times p} \end{bmatrix} \quad (16)$$

with

$$\phi(t) = \sum_{j=0}^{\infty} (-[\vec{\omega} \times])^j \frac{t^j}{j!} \quad (17)$$

and

$$\psi(t) = \sum_{j=0}^{\infty} (-[\vec{\omega} \times])^j \frac{t^{j+1}}{j+1!} \quad (18)$$

These sums collapse into well-known, finite expressions for ϕ and ψ (e.g., Reference 4). Finally, the transition matrix, along with the process noise Q-matrix obtained from η, is used to propagate the state error covariance over the time interval Δt (References 4 and 5).

3. Observability

The observability condition for an nth-order, constant coefficient, deterministic, discrete system is that the matrix

$$\mathcal{H} \equiv \begin{bmatrix} H \\ H\Phi \\ H\Phi^2 \\ \vdots \\ H\Phi^{n-1} \end{bmatrix} \quad (19)$$

be of rank n (Reference 5). If there are two vector observations (six components) per update as in Equation (14), $\mathcal{H}$ will have dimension $6n \times n$; the rank n requirement then is that there be an $n \times n$ nonsingular submatrix (i.e., its n remaining rows or columns must be independent after deleting $5n$ of its $6n$ rows).

This can be related to the batch solution for the epoch value of a state vector, x_o. The state is observable if x_o is uniquely determined by a set of n distinct observations, $\vec{y}_k$, made on x_o and the propagated states $\Phi^k x_o$. From Equations (11) and (19) one has

$$\begin{bmatrix} \vec{y}_0 \\ \vec{y}_1 \\ \vdots \\ \vec{y}_{n-1} \end{bmatrix} = \mathcal{H} x_o \quad (20)$$

383

where the noise term has been dropped (it is not usually important for observability). Left multiplication by $\mathcal{H}^T W$, where W is an arbitrary, positive-definite weight matrix, yields an $n \times n$ square matrix, $\mathcal{H}^T W \mathcal{H}$, on the right hand side. Now, if $\mathcal{H}$ has full rank, $\mathcal{H}^T W \mathcal{H}$ can be inverted to obtain

$$
x_o = \left(\mathcal{H}^T W \mathcal{H} \right)^{-1} \mathcal{H}^T W \begin{bmatrix} \vec{y}_0 \\ \vec{y}_1 \\ \vdots \\ \vec{y}_{n-1} \end{bmatrix}
\tag{21}
$$

and x_o is recovered.

When the attitude, gyro bias, and a timetag bias for a single sensor ($p = 1$) are estimated, there are $n = 7$ error state components, and one obtains from Equations (14), (16), and (19)

$$
\mathcal{H} = - \begin{bmatrix}
[\vec{w}^1 \times] & 0 & \vec{w}^1 \times \vec{\omega} \\
[\vec{w}^2 \times] & 0 & 0 \\
[\vec{w}^1 \times] \phi & [\vec{w}^1 \times] \psi & \vec{w}^1 \times \vec{\omega} \\
[\vec{w}^2 \times] \phi & [\vec{w}^2 \times] \psi & 0 \\
[\vec{w}^1 \times] \phi^2 & [\vec{w}^1 \times](\phi \psi + \psi) & \vec{w}^1 \times \vec{\omega} \\
\vdots & \vdots & \vdots \\
[\vec{w}^1 \times] \phi^{n-1} & [\vec{w}^1 \times] \sum_{j=0}^{n-2} \phi^j \psi & \vec{w}^1 \times \vec{\omega} \\
[\vec{w}^2 \times] \phi^{n-1} & [\vec{w}^2 \times] \sum_{j=0}^{n-2} \phi^j \psi & 0
\end{bmatrix}
\tag{22}
$$

where the reference vector time derivative, $\vec{r}$, has been assumed negligible.

Note that the assumption of a constant coefficient system was made to keep Equation (19) simple. Thus, the vectors $\vec{w}^1$ and $\vec{w}^2$ were taken to be the same after each propagation. But if they are constant in the body frame, they must refer to different inertial frame vectors (assuming $\phi \neq I$). So, Equation (22) represents the state observability after measuring n distinct vector pairs.

To make sense of Equation (22), evaluate it explicitly for a set of vectors with a geometry similar to that for the Extreme Ultraviolet Explorer (EUVE). Let

$$
\vec{\omega} = (\omega, 0, 0)^T
$$

$$
\vec{w}^1 = (1, 1, 0)^T / \sqrt{2}
\tag{23}
$$

$$
\vec{w}^2 = (-1, 1, 0)^T / \sqrt{2}
$$

and assume Δt is small to simplify ϕ and ψ. Then,

$$
\mathcal{H} \approx \frac{-1}{\sqrt{2}}
\begin{bmatrix}
0 & 0 & 1 & 0 & 0 & 0 & 0 \\
0 & 0 & -1 & 0 & 0 & 0 & 0 \\
-1 & 1 & 0 & 0 & 0 & 0 & -\omega \\
\\
0 & 0 & 1 & 0 & 0 & 0 & 0 \\
0 & 0 & 1 & 0 & 0 & 0 & 0 \\
-1 & -1 & 0 & 0 & 0 & 0 & 0 \\
\\
0 & -\omega\Delta t & 1 & 0 & 0 & \Delta t & 0 \\
0 & \omega\Delta t & -1 & 0 & 0 & -\Delta t & 0 \\
-1 & 1 & \omega\Delta t & -\Delta t & \Delta t & 0 & -\omega \\
\\
0 & -\omega\Delta t & 1 & 0 & 0 & \Delta t & 0 \\
0 & -\omega\Delta t & 1 & 0 & 0 & \Delta t & 0 \\
-1 & -1 & -\omega\Delta t & -\Delta t & -\Delta t & 0 & 0 \\
\\
0 & -2\omega\Delta t & 1 & 0 & 0 & 2\Delta t & 0 \\
0 & 2\omega\Delta t & -1 & 0 & 0 & -2\Delta t & 0 \\
-1 & 1 & 2\omega\Delta t & -2\Delta t & 2\Delta t & 0 & -\omega \\
\vdots & & & \vdots & & & \vdots
\end{bmatrix}
\qquad (24)
$$

Several features can be identified. First, if one is solving only for the attitude ($n = 3$), only the leftmost 18×3 submatrix applies. One can see that the first, third, and sixth rows are independent and span the three-component vector space. Thus, as expected, a single pair of vectors is adequate to determine an attitude (it is not necessary to use rows beyond the sixth, so additional observations are redundant).

Second, if one is solving for attitude and gyro bias ($n = 6$), the leftmost 36×6 submatrix applies. Again, rows 1, 3, and 6 span the attitude part of the state. Then rows 7, 9, and 12 span the gyro bias components. So this state is observable after two distinct observations of two vectors each.

Third, if one is solving for attitude and time bias ($n = 4$), the 24×4 submatrix consisting of the leftmost three columns and the rightmost column applies. One can span the first three components, with no admixture of the time bias column, by using rows 1, 6, and 7. Then, row 3 completes the set.

Finally, the entire 42×7 matrix has only rank 6. There do not exist seven independent rows. (This holds with the full ϕ and ψ, not just for the small Δt approximation.) The seven-component error state is not observable under the assumptions of a constant coefficient system and the EUVE-like geometry given in Equation (23). One can estimate the attitude and either the gyro bias or the timetag bias but not all three.

In Equation (23), the rotation rate and observed vectors in the body frame are coplanar. The unobservability of the seven-component system actually arises from this degeneracy. If they are noncoplanar, $\mathcal{H}$ does have the full rank 7. In addition, the state is observable if the system is time-dependent. Then, different rates effectively appear in subsequent rows, enabling all the components to be disentangled. Thus, for EUVE, slewing the spacecraft can improve observability both by introducing a time-dependence and by shifting the rotation vector out of the plane defined by the sensors.

4. Test Cases

This section presents test cases showing when a timetag bias can and cannot be determined, and how it affects the estimation of the rest of the state vector. Most of these results are summarized in Table 1. For all cases listed in the table, except where indicated, the state vector consists of attitude, gyro bias, and timetag bias.

The EUVE flight data cover a two-orbit timespan for December 16, 1992, when the spacecraft was in Survey Mode, rolling about the body x-axis at 3 rotations per orbit (rpo). Performance statistics reported below are obtained as mean values or root-mean-square (RMS) averages over the second orbit of the data set. The simulated EUVE data cover a 4000 sec timespan with characteristics similar to the flight data. Mean and RMS values for these cases are obtained from the second half of the timespan.

Two Timetag Biases

The UVF software was modified to solve simultaneously for separate timetag biases for the two fixed-head star trackers (FHST1 and FHST2). Simulated biases were added to the true timetags by the driver routine. Inclusion or exclusion of gyro biases in the state vector did not change these results significantly. It was found that the algorithm could not determine the time biases.

Figure 1 shows the estimated biases, their error (square root of the estimated variance), and the attitude error (root of the trace of the attitude part of the covariance matrix). The true (simulated) time biases were -0.8 and 0.0 sec. The estimates were -0.4 and 0.4 sec. The error is much larger than the estimated 1σ error of 0.06 sec. Also, the attitude error is 40 arcsec, substantially larger than the 5-arcsec errors typical of the UVF in the absence of timetag biases. In addition, the *actual* deviation between the estimated attitude and the onboard computer (OBC) estimate is 250 arcsec (RMS over the second orbit). The corresponding deviation is only 12 arcsec when no timing errors are present (Reference 4). This attitude deviation comes from the 0.4-sec average timetag error times the 3 rpo roll rate, which leads to a large roll offset. The correlation coefficients obtained from the orbit-averaged covariance matrix are near unity between the two timetags and also between the timetags and the roll angle. It is interesting that in this, and several similar test cases, the algorithm correctly obtained the difference between the FHST1 and FHST2 timetag biases to within about 0.05 sec. (This did not hold for differently placed sensors.)

Single Timetag Bias without Gyro Bias

In all subsequent tests, the filter solves for the timetag bias for only one sensor at a time. In this example, FHST2 is given a time bias of -0.3 sec. The true gyro biases are compensated using values obtained from the UVF smoother (Reference 4) and are not estimated. Figure 2 shows the estimated FHST2 timetag bias and the timetag and attitude errors derived from the covariance matrix. The time bias converges in a few hundred seconds and settles on a mean value differing from the true bias by only a few microseconds. Its estimated 1σ error is 0.005 sec (the actual standard deviation of the estimate is about 0.002 sec). The attitude estimates are very good (similar to solutions with no timing errors): estimated 1σ error is 4 arcsec, and RMS deviation from the OBC estimate is 12 arcsec. The largest correlation coefficient occurs between the timetag bias and the roll error, but its value is only 0.43. This is the only example for which the time bias estimation worked well without an attitude maneuver.

Single Timetag Bias with Gyro Bias

Figure 3 shows a case identical to that in Figure 2, except that gyro biases are also estimated. Comparison with Figure 2 indicates that the convergence is much slower, and, in fact, the time bias is moving in the wrong direction for much of the last few thousand seconds. The true simulated time bias is -0.3 sec, but the mean estimate (for the second orbit) is -0.25 sec. The estimated 1σ errors obtained from the covariance matrix are 0.02 sec, 12 arcsec, and 0.03 deg/hr

for the time bias, attitude, and gyro biases, respectively. These are significantly worse than the 5 arcsec and 0.007 deg/hr attitude and gyro bias errors obtained without timetag errors. The RMS deviation from the OBC estimate is 26 arcsec. In addition, the correlation coefficients indicate that the solution is unreliable, several being over 0.9. These results show that EUVE's attitude, gyro bias, and timetag bias together are not observable without maneuvers.

Having established that the filter can correct either the timetag or the gyro biases, but not both, iterative methods were attempted. Data with both a gyro bias and an FHST2 timetag bias were processed repeatedly, solving alternately for the gyro and the timetag bias. The results do not converge. Similarly, the iterative solution for two separate FHST timetag biases fails to converge. Thus, as expected, the observability problems that spoil the simultaneous estimation of two time biases or a timetag and gyro bias cannot be circumvented by estimating them separately and iteratively.

Timetag Bias Estimation During Maneuvers

A series of tests using simulated EUVE data were performed to show the influence of attitude maneuvers on the state observability (attitude, gyro bias, and timetag bias). The simulations include 0, 1, or 2 slews of roughly 30 deg at 0.1 deg/sec. The first slew is about the body y-axis. When there are two slews, the second is about the body z-axis. Both slews occur during the first 2000 sec.

One advantage of simulation data is that the noise characteristics are known exactly, so these tests also offer an opportunity to look briefly at the effects of filter mistuning. The filter is precisely tuned when it agrees with the simulator on the strengths of the white noise sources. These are the process noise η in Equation (15) and the sensor noise $\bar{n}$ in Equation (1). In these tests, the simulated timing error is a constant ($\eta_\tau = 0$) while the filter's timetag noise parameter is set to a small nonzero value. All other noise parameters were tuned exactly. In this case, the actual solution deviations from the true values agree very well with the expected 1σ errors. When the spacecraft undergoes maneuvers, these errors decrease in parallel. The 1σ timetag error decreases from 0.024 to 0.009 to 0.006 sec for 0, 1, and 2 slews, while the actual mean deviations go from 0.021 to 0.012 to 0.004 sec (see Table 1). The attitude errors and RMS deviations from the truth model both decrease from 14 to 7 to 5 arcsec. Most importantly, the largest correlation coefficient decreases from near unity to 0.77 for the two slew case, indicating that the separate state components have become distinguishable.

When the filter is mistuned, the 1σ errors and actual deviations no longer agree so closely. For this test, the FHST noise parameter was set to 0.005 deg rather than the true 0.01 deg used in the simulator. This causes the expected errors to decrease while the mistuning should cause the actual deviations to increase. With no maneuvers, this is exactly what is found. The timetag deviation increases to 0.032 sec and the attitude deviation increases to 18 arcsec. What is interesting is that with two slews the solution is much less sensitive to this mistuning. In this case, the actual errors revert to near their tuned values, 0.004 sec and 5 arcsec. (Some degradation is expected, but this can only be seen by averaging results from many runs using different random number sequences and initial conditions.) One concludes that state observability is an important part of filter robustness.

Estimation of Variable Timetag Bias

For the final tests, the filter is asked to solve for a single, but time-varying, timetag bias. A sawtooth function with amplitude -0.5 sec and a period of either 60 sec or 3000 sec is added to the true FHST1 timetag. Gyro biases are not estimated; the rates are corrected using the true gyro biases, determined separately.

If the filter memory time is too long, it will not be able to follow a varying time bias; it will converge instead to an average value. The process noise needs to be large enough to produce an uncertainty roughly comparable to the sawtooth amplitude in a time equal to the period. The timetag process noise is characterized by the parameter σ_τ^2, obtained from

the two-time expectation of the white noise source η_τ appearing in Equation (15):

$$E\left[\eta_\tau(t)\,\eta_\tau(t')\right] = \sigma_\tau^2\,\delta(t-t') \qquad (25)$$

A range of values for σ_τ^2 from 0.01 to 0.001 sec^2/sec leads to similar results. (All other test cases where the timetag biases were constant used $\sigma_\tau^2 = 10^{-8}$ sec^2/sec.)

Figure 4 shows the timetag bias from a typical 400-sec timespan for the more rapidly varying case. The estimate is shown as a solid line and the true timing error as a sawtooth dashed line. When the observability is good (stars available in both trackers), the estimated bias can follow the sawtooth with a residual of roughly 0.05 sec or less. However, the overall performance is not very good since the sawtooth quickly moves away from the estimated time bias between star identifications.

In spite of the rather poor timetag estimation, inclusion of the time bias in the state vector does improve the attitude determination significantly. The RMS deviation from the OBC attitude is only 11 arcsec, as good as tests with no timing errors. Without time bias estimation, the sawtooth timing error causes an RMS attitude deviation of 74 arcsec.

When the period of the sawtooth is increased to 3000 sec, the filter has much less trouble following it. Figure 5 shows the timetag bias estimate (solid) and the slowly varying true bias (dashed). The RMS deviation from the OBC is 11.5 arcsec in this case.

5. Conclusions

It has been shown that, without maneuvers, attitude sensor timing errors onboard EUVE and spacecraft with similar geometry can be solved for only for very limited circumstances. Examination of the $\mathcal{H}$-matrix shows that the attitude, gyro bias, and timetag bias are not simultaneously observable. A Kalman filter solution leads to results with large correlation coefficients. These solutions are not robust: filter mistuning changes the results and iterative methods lead to radically different estimates or diverge altogether. The timetag bias can be accurately determined only if the gyro bias is not solved for and is compensated using an accurate independent estimate.

Similarly, when there are timetag errors on two sensors, the filter algorithm cannot distinguish them. Large correlations between the individual sensors' timetag biases indicate that their estimates are unreliable. Additional tests are needed to examine cases with three or more sensors, with and without attitude maneuvers.

The observability improves dramatically when the spacecraft undergoes attitude maneuvers. The correlation coefficients decrease and the state estimates improve for each slew. This only holds, though, with fairly large maneuvers. Tests with recent EUVE flight data having a pair of 2 deg slews showed no noticeable increase in observability.

Even when the gyro bias has been compensated, the filter does not do well estimating a short-period, time-varying timetag bias. However, the problem here is probably insufficient data relative to the bias time scale (period equal to 1 minute in this test case). The filter has no trouble following the long-period variations in the final test. In either case, estimating the timetag bias improved the attitude estimates significantly. If a particular sensor has a known short-period timing problem, a better sensor model could be developed to estimate, for example, the period, amplitude, and phase as three new state vector elements, rather than trying to follow the time-variation using a single timetag bias with a large process noise.

Table 1. Timetag Bias Filter Statistics

Test Cases	Mean Timetag Deviation from True (sec)	Estimated Timetag 1σ Error (sec)	RMS Attitude Deviation from True (arcsec)	Estimated Attitude 1σ Error (arcsec)	Largest Correlation Coefficient
No Timing Error	NA	NA	11.8	5.0	0.62
One Timetag (w/o Gyro Bias)	< 5.E-06	0.005	12.0	4.2	0.43
One Timetag	0.052	0.020	25.8	12.4	0.97
Two Timetags	0.4	0.06	247	40	0.99
Simulation with No Maneuvers	0.021	0.024	13.5	13.9	0.98
Simulation with One Maneuver	0.012	0.009	6.9	6.5	0.85
Simulation with Two Maneuvers	0.004	0.006	5.1	5.1	0.77
Simulation with No Maneuver - Mistuned Filter	0.032	0.010	18.4	7.4	0.96
Simulation with Two Maneuvers - Mistuned Filter	0.004	0.004	4.8	3.6	0.65

References

1. E. J. Lefferts, F. L. Markley, and M. D. Shuster, "Kalman Filtering for Spacecraft Attitude Estimation," *J. Guidance, Control, and Dynamics*, Vol. 5, No. 5, Sept.-Oct. 1982, pp. 417-429

2. M. D. Shuster, "Kalman Filtering of Spacecraft Attitude and the QUEST Model," *J. Astronaut. Sci.*, Vol. 38, No. 3, July-Sept. 1990

3. J. Sedlak and D. Chu, "Kalman Filter Estimation of Attitude and Gyro Bias with the QUEST Observation Model," in *Proceedings, AAS/GSFC International Symposium on Space Flight Dynamics*, April 1993

4. J. Sedlak, "Comparison of Kalman Filter and Optimal Smoother Estimates of Spacecraft Attitude," in *Proceedings, Flight Mechanics/Estimation Theory Symposium*, NASA Goddard Space Flight Center, May 1994

5. A. Gelb, ed., *Applied Optimal Estimation*, MIT Press, Cambridge, MA, 1974
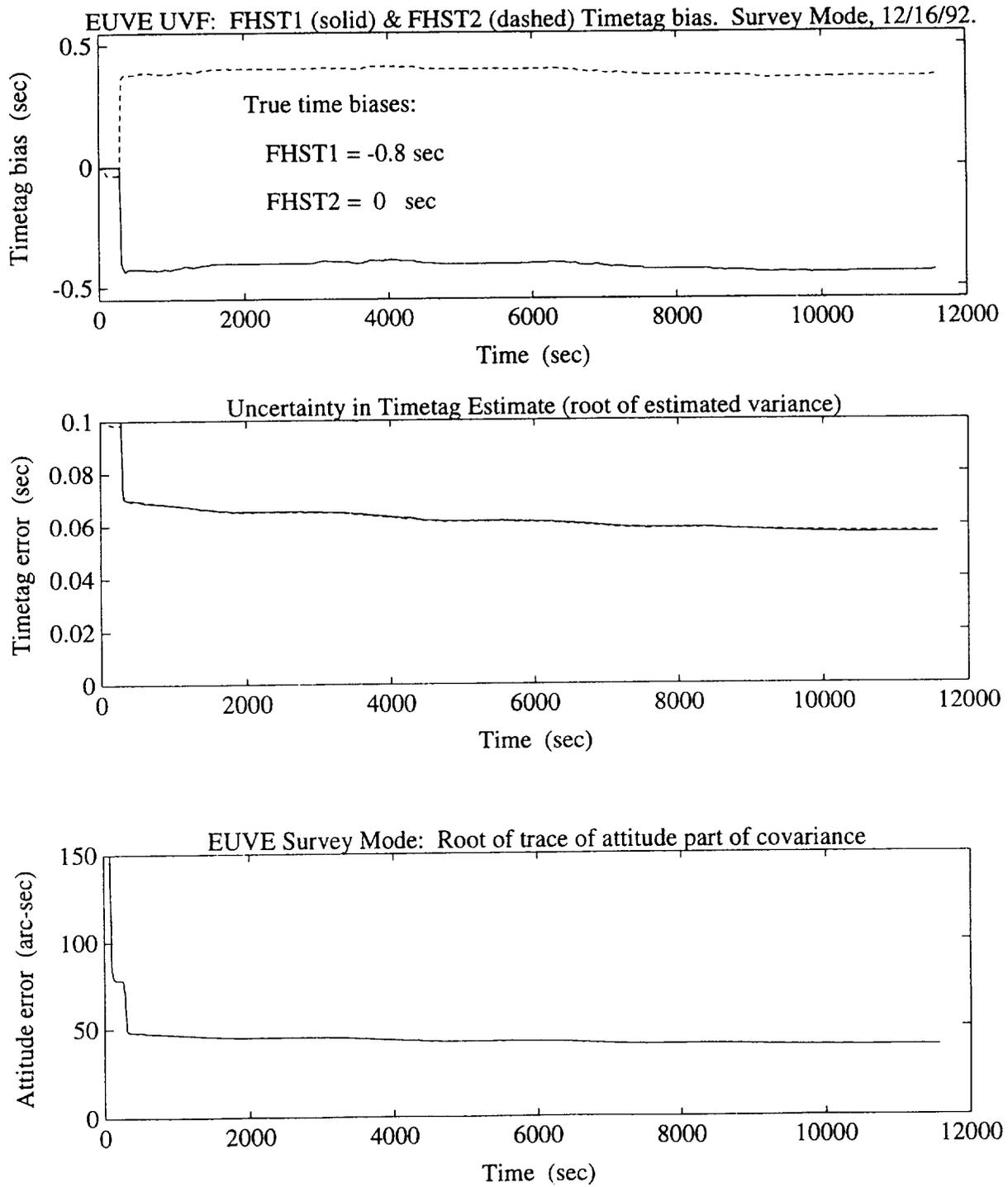
Figure 1. *Timetag Biases, Timetag Errors, and Attitude Error When Estimating Timetag Biases for Two Sensors*
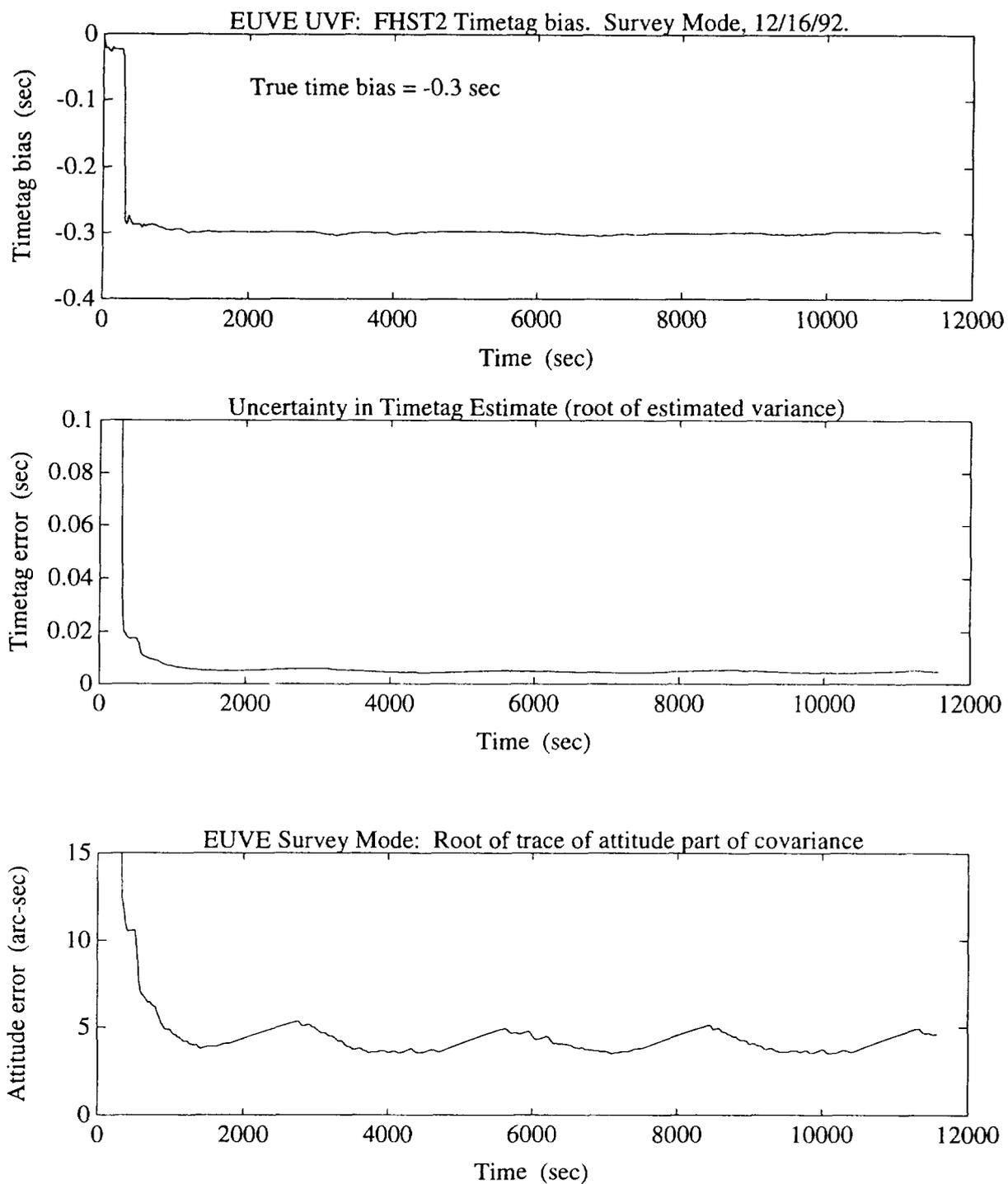
Figure 2. Timetag Bias, Timetag Error, and Attitude Error When Estimating Timetag Bias for a Single Sensor
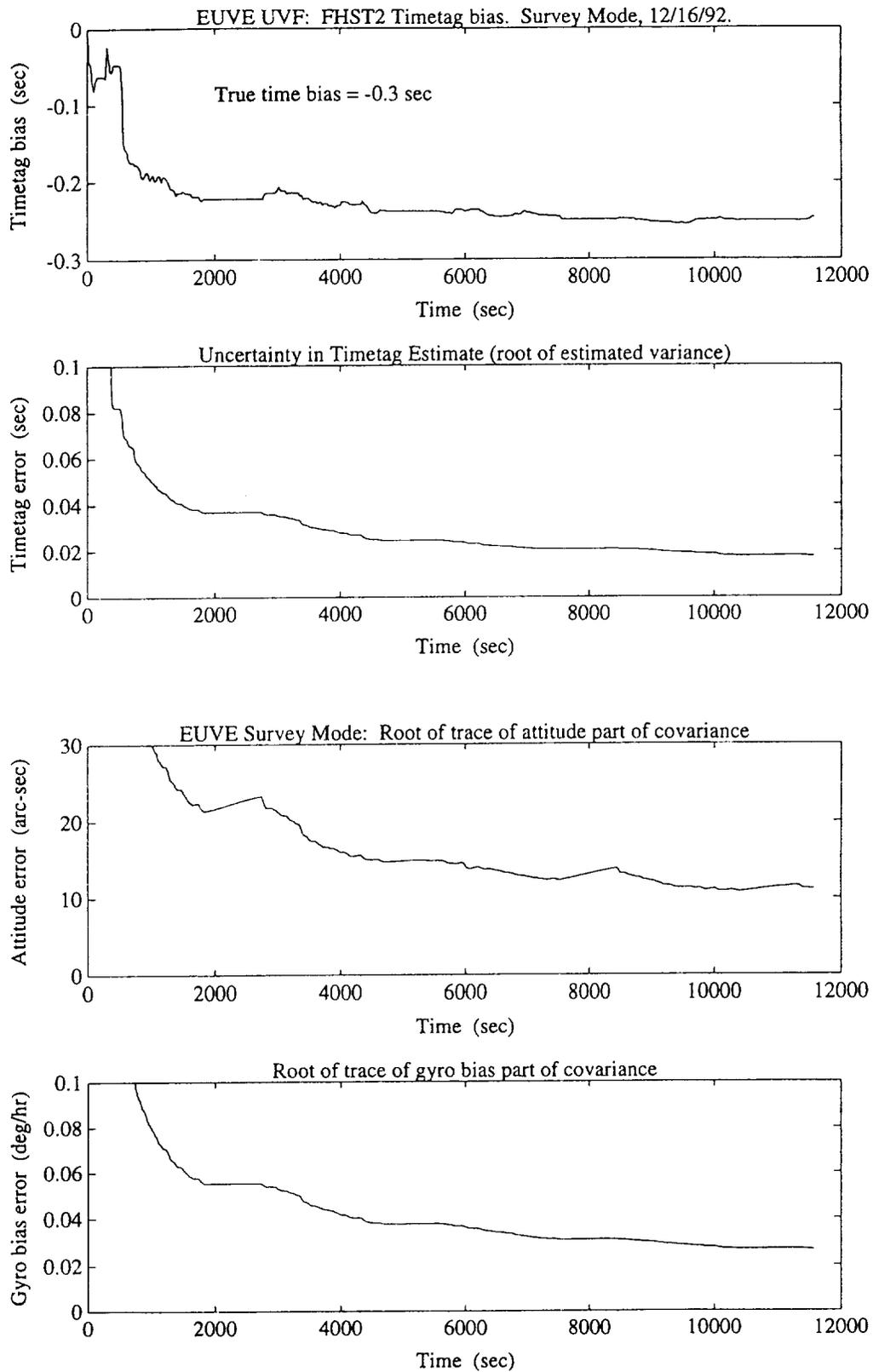
Figure 3. Timetag Bias, Timetag Error, Attitude Error, and Gyro Bias Error When Estimating Gyro Biases and Timetag Bias for a Single Sensor
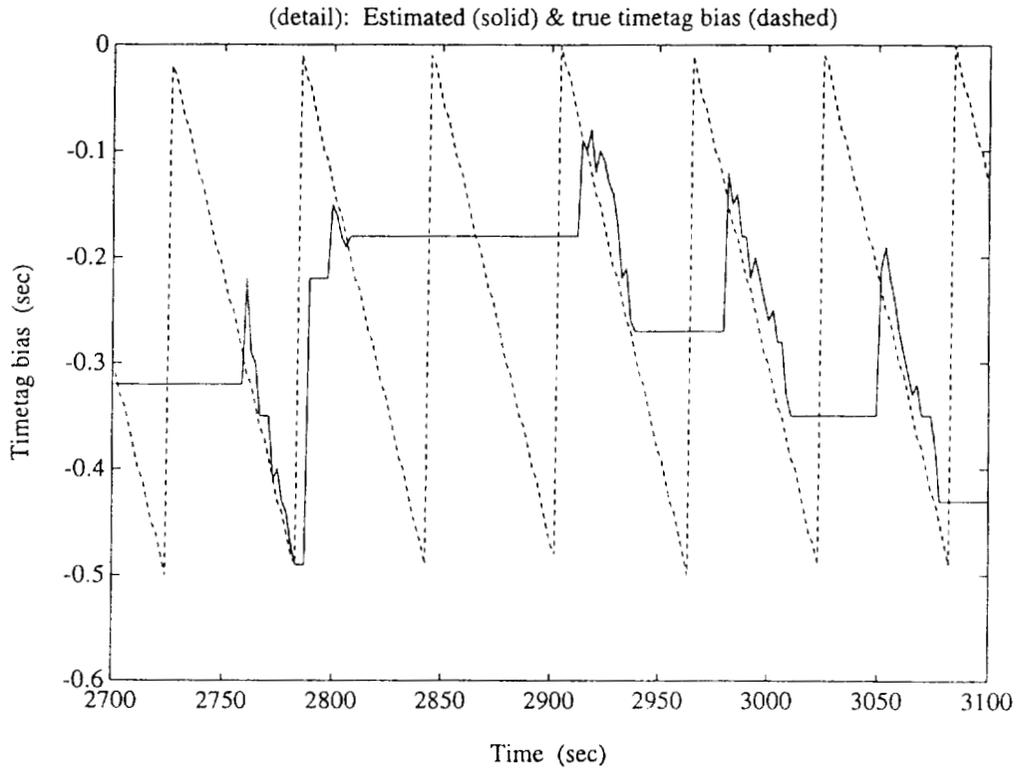
Figure 4. Estimated and True Timetag Biases When Estimating a Rapidly Varying Timetag for a Single Sensor
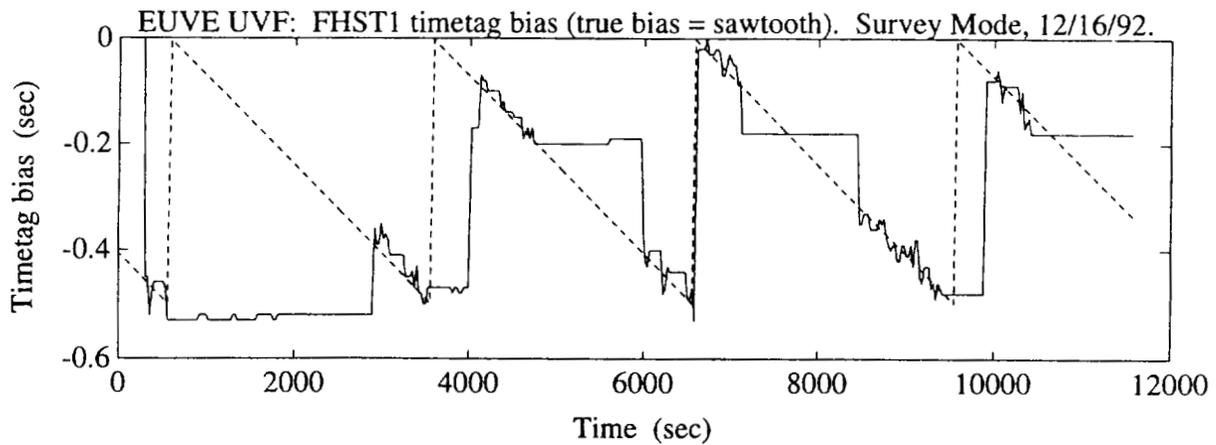
Figure 5. Estimated and True Timetag Biases When Estimating a Slowly Varying Timetag for a Single Sensor

A New Angle on the Euler Angles

F. Landis Markley
Guidance and Control Branch, Code 712
NASA Goddard Space Flight Center
Greenbelt, MD 20771
email: lmarkley@ccmail.gsfc.nasa.gov

Malcolm D. Shuster
Department of Aerospace Engineering, Mechanics & Engineering Science
University of Florida
Gainesville, FL 32611-6250
email: m.shuster@ieee.org

Abstract

We present a generalization of the Euler angles to axes beyond the twelve conventional sets. The generalized Euler axes must satisfy the constraint that the first and the third are orthogonal to the second; but the angle between the first and third is arbitrary, rather than being restricted to the values 0 and $\pi/2$, as in the conventional sets. This is the broadest generalization of the Euler angles that provides a representation of an arbitrary rotation matrix. The kinematics of the generalized Euler angles and their relation to the attitude matrix are presented. As a side benefit, the equations for the generalized Euler angles are universal in that they incorporate the equations for the twelve conventional sets of Euler angles in a natural way.

Introduction

It is well known that a rotation can be represented by a single rotation about a single axis, where the rotation axis is allowed to vary according to the rotation [1–7]. It is often more convenient to represent a general rotation as the product of three successive rotations about axes whose orientations are specified *a priori*. These parameterizations of rotations, well known as the Euler angle parameterizations [1–7], can be written

$$R(\hat{n}_1, \hat{n}_2, \hat{n}_3; \varphi, \vartheta, \psi) \equiv R(\hat{n}_3, \psi) R(\hat{n}_2, \vartheta) R(\hat{n}_1, \varphi), \tag{1}$$

where the carets denote unit vectors, and $R(\hat{n}, \varphi)$ represents a rotation by angle φ about axis $\hat{n}$. For the conventional Euler angles, the rotation axes are selected from the set $\{\hat{1}, \hat{2}, \hat{3}\}$ where

$$\hat{1} = \begin{bmatrix} 1 \\ 0 \\ 0 \end{bmatrix}, \quad \hat{2} = \begin{bmatrix} 0 \\ 1 \\ 0 \end{bmatrix}, \quad \text{and} \quad \hat{3} = \begin{bmatrix} 0 \\ 0 \\ 1 \end{bmatrix}. \tag{2}$$

The conventional Euler rotations are generally designated by the three indices, for example

$$R_{213}(\varphi, \vartheta, \psi) \equiv R(\hat{2}, \hat{1}, \hat{3}; \varphi, \vartheta, \psi) = R(\hat{3}, \psi) R(\hat{1}, \vartheta) R(\hat{2}, \varphi). \tag{3}$$

If the Euler sequence is to represent a general rotation matrix, two successive rotations cannot be about the same axis, which is to say that $\hat{n}_1 \neq \hat{n}_2$ and $\hat{n}_2 \neq \hat{n}_3$. This leaves twelve possible sets of conventional Euler axes: six symmetric sets designated 121, 232, 313, 131, 212, and 323, and six asymmetric sets designated 123, 231, 312, 132, 213, and 321.

We show in the present work that the Euler angles can be extended to a much larger set. The generalized Euler axes can be any three unit vectors such that both the first and the third are orthogonal to the second. The angle between the first and third axes is arbitrary, rather than being restricted to the values 0 and $\pi/2$ as is the case for the conventional sets. We show that this is a necessary and sufficient condition for the generalized Euler angles to provide a universal representation of rotation matrices. We derive expressions for the generalized Euler angles in terms of the rotation matrix and kinematic equations for these angles, and discuss the 'gimbal-lock' singularity of this parameterization.

Necessary Conditions for the Generalized Euler Angles

For the generalized Euler angles to represent a general rotation, it is necessary and sufficient that the rotation matrix of equation (1) be capable of mapping any unit vector $\hat{u}$ into any other unit vector $\hat{v}$. That is, there must exist angles φ, ϑ, and ψ such that the equation

$$\hat{v} = R(\hat{n}_1, \hat{n}_2, \hat{n}_3; \varphi, \vartheta, \psi)\hat{u} \tag{4}$$

has a solution for given $\hat{n}_1$, $\hat{n}_2$, $\hat{n}_3$, $\hat{u}$, and $\hat{v}$. In order to show the necessity of the conditions on the rotation axes, we can take $\hat{u}$ equal to $\hat{n}_1$ and only look at the component of this equation along $\hat{n}_3$. That is, it is certainly necessary that

$$\hat{n}_3 \bullet \hat{v} = \hat{n}_3^T R(\hat{n}_3, \psi) R(\hat{n}_2, \vartheta) R(\hat{n}_1, \varphi)\hat{n}_1 = \hat{n}_3^T R(\hat{n}_2, \vartheta)\hat{n}_1, \tag{5}$$

where we have used equation (1) and recalled that the axis of rotation is invariant under a rotation. Inserting the explicit form of the rotation matrix [5]

$$R(\hat{n}, \zeta) = \cos \zeta \, I_{3\times3} - \sin \zeta [\hat{n} \times] + (1 - \cos \zeta)\hat{n}\hat{n}^T, \tag{6}$$

with

$$[\hat{n} \times] \equiv \begin{bmatrix} 0 & -n_3 & n_2 \\ n_3 & 0 & -n_1 \\ -n_2 & n_1 & 0 \end{bmatrix}, \tag{7}$$

gives the necessary condition

$$\hat{n}_3 \bullet \hat{v} = \hat{n}_3 \bullet [\cos \vartheta \, \hat{n}_1 - \sin \vartheta(\hat{n}_2 \times \hat{n}_1) + (1 - \cos \vartheta)\hat{n}_2(\hat{n}_2 \bullet \hat{n}_1)]$$
$$= (\hat{n}_2 \bullet \hat{n}_3)(\hat{n}_2 \bullet \hat{n}_1) + \sin \vartheta[\hat{n}_3 \bullet (\hat{n}_1 \times \hat{n}_2)] + \cos \vartheta(\hat{n}_2 \times \hat{n}_3) \bullet (\hat{n}_2 \times \hat{n}_1). \tag{8}$$

Now let

$$\beta \equiv (\hat{n}_2 \bullet \hat{n}_3)(\hat{n}_2 \bullet \hat{n}_1) \tag{9}$$

and B be the positive square root of

$$B^2 \equiv [\hat{n}_3 \bullet (\hat{n}_2 \times \hat{n}_1)]^2 + [(\hat{n}_2 \times \hat{n}_3) \bullet (\hat{n}_2 \times \hat{n}_1)]^2$$

$$= \det([\hat{n}_1 \vdots \hat{n}_2 \vdots \hat{n}_3]^T [\hat{n}_1 \vdots \hat{n}_2 \vdots \hat{n}_3]) + [(\hat{n}_2 \times \hat{n}_3) \bullet (\hat{n}_2 \times \hat{n}_1)]^2 \tag{10}$$

$$= \det \begin{bmatrix} 1 & \hat{n}_1 \bullet \hat{n}_2 & \hat{n}_1 \bullet \hat{n}_3 \\ \hat{n}_2 \bullet \hat{n}_1 & 1 & \hat{n}_2 \bullet \hat{n}_3 \\ \hat{n}_3 \bullet \hat{n}_1 & \hat{n}_3 \bullet \hat{n}_2 & 1 \end{bmatrix} + [\hat{n}_1 \bullet \hat{n}_3 - (\hat{n}_2 \bullet \hat{n}_3)(\hat{n}_2 \bullet \hat{n}_1)]^2 = |\hat{n}_2 \times \hat{n}_3|^2 |\hat{n}_2 \times \hat{n}_1|^2.$$

It is clear from the final expression that $B \le 1$. Now equation (8) can be written as

$$\hat{n}_3 \bullet \hat{v} = \beta + B \cos(\vartheta - \lambda), \tag{11}$$

where

$$\lambda \equiv \text{ATAN2}[\hat{n}_3 \bullet (\hat{n}_1 \times \hat{n}_2), \ (\hat{n}_2 \times \hat{n}_3) \bullet (\hat{n}_2 \times \hat{n}_1)]. \tag{12}$$

As ϑ varies over its range, the right side of equation (12) takes only values between $\beta - B$ and $\beta + B$, so a solution will exist for ϑ only if

$$\beta - B \le \hat{n}_3 \bullet \hat{v} \le \beta + B. \tag{13}$$

However, $\hat{n}_3 \bullet \hat{v}$ can assume any value between -1 and $+1$, so it is clear from equations (9) and (10) that the coefficients β and B must have the values

$$B = 1 \quad \text{and} \quad \beta = 0 \tag{14}$$

This means that

$$\hat{n}_1 \bullet \hat{n}_2 = 0 \quad \text{and} \quad \hat{n}_2 \bullet \hat{n}_3 = 0 \tag{15}$$

or equivalently that $\hat{n}_2$ be perpendicular to both $\hat{n}_1$ and $\hat{n}_3$. With this restriction, equation (12) simplifies to

$$\lambda \equiv \text{ATAN2}[\hat{n}_3 \bullet (\hat{n}_1 \times \hat{n}_2), \ \hat{n}_3 \bullet \hat{n}_1] \tag{16}$$

and then

$$\hat{n}_3 = \cos\lambda \, \hat{n}_1 + \sin\lambda(\hat{n}_1 \times \hat{n}_2) = R(\hat{n}_2, \lambda)\hat{n}_1. \tag{17}$$

Thus λ is the angle of the rotation about $\hat{n}_2$ that takes $\hat{n}_1$ into $\hat{n}_3$.

Sufficiency of the Generalized Euler Angle Parameterization

The rotation matrix can be written as the product

$$R(\hat{n}_1, \hat{n}_2, \hat{n}_3; \varphi, \vartheta, \psi) \equiv R(\hat{n}_3, \psi)R(\hat{n}_2, \vartheta)R(\hat{n}_1, \varphi) = R(R(\hat{n}_2, \lambda)\hat{n}_1, \psi)R(\hat{n}_2, \vartheta)R(\hat{n}_1, \varphi)$$

$$= R(\hat{n}_2, \lambda)R(\hat{n}_1, \psi)R^T(\hat{n}_2, \lambda)R(\hat{n}_2, \vartheta)R(\hat{n}_1, \varphi) \tag{18}$$

$$= R(\hat{n}_2, \lambda)R(\hat{n}_1, \psi)R(\hat{n}_2, \vartheta - \lambda)R(\hat{n}_1, \varphi) = R(\hat{n}_2, \lambda)R(\hat{n}_1, \hat{n}_2, \hat{n}_1; \varphi, \vartheta - \lambda, \psi).$$

397

If this is to represent an arbitrary proper orthogonal matrix A, we must be able to find angles φ, ϑ, and ψ such that

$$A = R(\hat{n}_1, \hat{n}_2, \hat{n}_3; \varphi, \vartheta, \psi) = R(\hat{n}_2, \lambda) R(\hat{n}_1, \hat{n}_2, \hat{n}_1; \varphi, \vartheta - \lambda, \psi), \tag{19}$$

or, equivalently, to find angles φ, $\vartheta' \equiv \vartheta - \lambda$, and ψ such that

$$R(\hat{n}_1, \hat{n}_2, \hat{n}_1; \varphi, \vartheta', \psi) = R^T(\hat{n}_2, \lambda) A. \tag{20}$$

The matrix on the right side of this equation ranges over the group of proper orthogonal matrices as A ranges over this group. Thus our generalized Euler sequence can represent an arbitrary rotation if the matrix on the left side of equation (20) can represent an arbitrary rotation. To establish this fact, it is sufficient to show that this matrix can take the vectors in some orthonormal basis into an arbitrary orthonormal triad. We will take this basis to be $\{\hat{n}_1, \hat{n}_2, \hat{n}_1 \times \hat{n}_2\}$. Thus we must be able to find angles φ, ϑ', and ψ such that

$$R(\hat{n}_1, \hat{n}_2, \hat{n}_1; \varphi, \vartheta', \psi)\hat{n}_1 = \hat{v}_1, \tag{21}$$

where $\hat{v}_1$ is an arbitrary unit vector, and

$$R(\hat{n}_1, \hat{n}_2, \hat{n}_1; \varphi, \vartheta', \psi)\hat{n}_2 = \hat{v}_2, \tag{22}$$

where $\hat{v}_2$ is a unit vector in the plane perpendicular to $\hat{v}_1$, but is otherwise arbitrary. Then the proper orthogonality of $R(\hat{n}_1, \hat{n}_2, \hat{n}_1; \varphi, \vartheta', \psi)$ ensures that it will map $\hat{n}_1 \times \hat{n}_2$ into $\hat{v}_1 \times \hat{v}_2$.

Equation (21) can be written, using equations (1) and (6), as

$$\begin{aligned}
\hat{v}_1 &= R(\hat{n}_1, \psi)[\cos \vartheta' \, \hat{n}_1 - \sin \vartheta'(\hat{n}_2 \times \hat{n}_1)] \\
&= \cos \vartheta' \, \hat{n}_1 + \sin \vartheta' \sin \psi \, \hat{n}_2 + \sin \vartheta' \cos \psi (\hat{n}_1 \times \hat{n}_2).
\end{aligned} \tag{23}$$

Since $\{\hat{n}_1, \hat{n}_2, \hat{n}_1 \times \hat{n}_2\}$ is a basis, it is clear that ϑ' and ψ can be chosen so that $\hat{v}_1$ is an arbitrary vector. Equation (22) gives

$$\hat{v}_2 = R(\hat{n}_1, \psi) R(\hat{n}_2, \vartheta')[\cos \varphi \, \hat{n}_2 - \sin \varphi(\hat{n}_1 \times \hat{n}_2)] = \cos \varphi \, \hat{u}_1 + \sin \varphi \, \hat{u}_2, \tag{24}$$

where

$$\hat{u}_1 \equiv R(\hat{n}_1, \psi) R(\hat{n}_2, \vartheta')\hat{n}_2 = R(\hat{n}_1, \psi)\hat{n}_2 = \cos \psi \, \hat{n}_2 - \sin \psi(\hat{n}_1 \times \hat{n}_2), \tag{25}$$

and

$$\begin{aligned}
\hat{u}_2 &\equiv -R(\hat{n}_1, \psi) R(\hat{n}_2, \vartheta')\hat{n}_1 \times \hat{n}_2 = -R(\hat{n}_1, \psi)[\cos \vartheta'(\hat{n}_1 \times \hat{n}_2) - \sin \vartheta' \, \hat{n}_1] \\
&= \sin \vartheta' \, \hat{n}_1 - \cos \vartheta' \sin \psi \, \hat{n}_2 - \cos \vartheta' \cos \psi(\hat{n}_1 \times \hat{n}_2).
\end{aligned} \tag{26}$$

It is clear from equations (23), (25), and (26) that $\hat{u}_1$ and $\hat{u}_2$ form an orthogonal basis for the plane perpendicular to $\hat{v}_1$. Thus equation (24) shows that φ can be chosen such that $\hat{v}_2$ is any vector in this plane.

398

This completes the demonstration that the generalized Euler angles, subject to the constraint of equation (15), can represent an arbitrary rotation. Since the conventional angles are a subset of the generalized Euler angles, it incidentally provides an explicit proof that the conventional Euler angles are similarly general.

Relation to the Conventional Euler Angles

Each of the conventional Euler angle sets is a subset of the class of generalized Euler angles, characterized by a specific choice of axes and a corresponding value of the angle λ. It is easily seen from equation (12) or (17) that the symmetric sets of axes (121, 232, 313, 131, 212, and 323) have $\lambda = 0$, the even permutation asymmetric sets (123, 231, and 312) have $\lambda = \pi/2$, and the odd permutation asymmetric sets (132, 213, and 321) have $\lambda = -\pi/2$. With these substitutions, all the equations derived in this paper are applicable to the conventional Euler angles. Thus the results of this paper include universal formulas applicable to all Euler angles, conventional or generalized.

Extraction of the Generalized Euler Angles

The rotation matrix is simply defined in terms of the generalized Euler angles by equation (1). We now turn to the converse problem, the extraction of the generalized Euler angles from a rotation matrix. Equation (11), with the constraint of equation (14), gives

$$\hat{n}_3 \bullet \hat{v} = \cos(\vartheta - \lambda). \tag{27}$$

We recall from equations (4) and (5) that $\hat{v} = A\hat{n}_1$, where A is the rotation matrix that is being parameterized, so this equation can be solved for ϑ, yielding

$$\vartheta = \lambda \pm \text{ACOS}\left(\hat{n}_3^T A \hat{n}_1\right), \tag{28}$$

where ACOS denotes the principal value of the inverse cosine function, which returns a value between 0 and π. The twofold sign ambiguity in equation (28) is present in the conventional Euler angle representations as well, but it is usually avoided by restricting ϑ to the range $0 \leq \vartheta \leq \pi$ for the symmetric sets of axes or $-\pi/2 \leq \vartheta \leq \pi/2$ for the asymmetric sets. A similar resolution of the ambiguity for the generalized Euler angle case would be to take the sign of the second term in equation (28) to be positive for $\lambda \leq 0$ and negative for $\lambda > 0$. This would ensure that the values of ϑ for any particular choice of axes would always be in some interval of length π of the range $-\pi < \vartheta \leq \pi$. We will not assume that this convention has been adopted, however.

Equation (28) is analogous to the procedure for finding the second Euler angle in one of the conventional sets in terms of one of the elements of the rotation matrix. The other angles are expressed in terms of the other two elements of the same row or of the same column. This motivates us to consider the four quantities

$$\hat{n}_2^T A \hat{n}_1 = \left[\cos\psi\,\hat{n}_2 - \sin\psi(\hat{n}_2 \times \hat{n}_3)\right]^T \left[\cos\vartheta\,\hat{n}_1 + \sin\vartheta(\hat{n}_1 \times \hat{n}_2)\right] = \sin\psi\sin(\vartheta - \lambda), \tag{29}$$

$$(\hat{n}_2 \times \hat{n}_3)^T A \hat{n}_1 = \left[\cos\psi(\hat{n}_2 \times \hat{n}_3) + \sin\psi\,\hat{n}_2\right]^T \left[\cos\vartheta\,\hat{n}_1 + \sin\vartheta(\hat{n}_1 \times \hat{n}_2)\right]$$
$$= -\cos\psi\sin(\vartheta - \lambda), \tag{30}$$

$$\hat{n}_3^T A \hat{n}_2 = \left[\cos\vartheta\,\hat{n}_3 + \sin\vartheta(\hat{n}_2 \times \hat{n}_3)\right]^T \left[\cos\varphi\,\hat{n}_2 - \sin\varphi(\hat{n}_1 \times \hat{n}_2)\right] = \sin\varphi\sin(\vartheta - \lambda), \tag{31}$$

and

$$\hat{n}_3^T A(\hat{n}_1 \times \hat{n}_2) = \left[\cos\vartheta\,\hat{n}_3 + \sin\vartheta(\hat{n}_2 \times \hat{n}_3)\right]^T \left[\cos\varphi(\hat{n}_1 \times \hat{n}_2) + \sin\varphi\,\hat{n}_2\right]$$
$$= -\cos\varphi\sin(\vartheta - \lambda). \tag{32}$$

Define σ as the sign

$$\sigma \equiv \text{sign}\left[\sin(\vartheta - \lambda)\right]. \tag{33}$$

This sign is not a variable, but is fixed for any set of generalized Euler axes. It is, in fact, the same as the sign of the second term on the right side of equation (28). With this definition, we can find the other two generalized Euler angles by

$$\varphi = \text{ATAN2}\left[\sigma\,\hat{n}_3^T A \hat{n}_2, \ -\sigma\,\hat{n}_3^T A(\hat{n}_1 \times \hat{n}_2)\right] \tag{34}$$

and

$$\psi = \text{ATAN2}\left[\sigma\,\hat{n}_2^T A \hat{n}_1, \ -\sigma\,(\hat{n}_2 \times \hat{n}_3)^T A \hat{n}_1\right]. \tag{35}$$

The equations for the conventional Euler angles are, of course, special cases of these equations.

Kinematics

The kinematic equations for the generalized Euler angles are straightforward generalizations of the corresponding expressions for the conventional Euler angles. The body-referenced angular velocity vector is given by

$$\omega = \dot{\psi}\,\hat{n}_3 + \dot{\vartheta}R(\hat{n}_3, \psi)\hat{n}_2 + \dot{\varphi}R(\hat{n}_3, \psi)R(\hat{n}_2, \vartheta)\hat{n}_1 = R(\hat{n}_3, \psi)S\begin{bmatrix}\dot{\varphi} \\ \dot{\vartheta} \\ \dot{\psi}\end{bmatrix}, \tag{36}$$

where S is the 3×3 matrix

$$S \equiv \left[\hat{n}' \ \vdots \ \hat{n}_2 \ \vdots \ \hat{n}_3\right] \tag{37}$$

with

$$\hat{n}' \equiv R(\hat{n}_2, \vartheta)\hat{n}_1 = R(\hat{n}_2, \vartheta - \lambda)\hat{n}_3 = \cos(\vartheta - \lambda)\hat{n}_3 - \sin(\vartheta - \lambda)(\hat{n}_2 \times \hat{n}_3). \tag{38}$$

The second step in equation (38) makes use of equation (17). The inverse of equation (37) gives the time derivatives of the Euler angles in terms of the angular velocity:

$$\begin{bmatrix}\dot{\varphi} \\ \dot{\vartheta} \\ \dot{\psi}\end{bmatrix} = S^{-1}R^T(\hat{n}_3, \psi)\omega. \tag{39}$$

The determinant of the matrix S is given by

$$\det S = \hat{n}' \bullet (\hat{n}_2 \times \hat{n}_3) = -\sin(\vartheta - \lambda), \tag{40}$$

and its inverse is

$$S^{-1} = (\det S)^{-1}[\hat{n}_2 \times \hat{n}_3 \vdots \hat{n}_3 \times \hat{n}' \vdots \hat{n}' \times \hat{n}_2]^T$$
$$= [\sin(\vartheta - \lambda)]^{-1}[\hat{n}_3 \times \hat{n}_2 \vdots \sin(\vartheta - \lambda)\hat{n}_2 \vdots \sin(\vartheta - \lambda)\hat{n}_3 - \cos(\vartheta - \lambda)(\hat{n}_3 \times \hat{n}_2)]^T. \tag{41}$$

The kinematic equations for the conventional Euler angles are special cases of these equations.

Singularity of the Parameterization

It is clear from equations (39) and (41) that the kinematic equations for φ and ψ are singular when $\sin(\vartheta - \lambda) = 0$. It is also clear that the kinematic equation for ϑ is not singular at this or any other point. The mathematical singularity reflects the fact that the axes $\hat{n}_1$ and $\hat{n}_3$ coincide when $\sin(\vartheta - \lambda) = 0$, so the rotations about these two axes are not independent. This situation is known as gimbal lock, since it is related to the serious problem occurring in gimballed inertial reference platforms for which the Euler angles are physical gimbal angles, and the required infinite rates cannot be attained by physical actuators. It is worth mentioning, however, that the numerical errors accumulated in integration of the kinematic equations through the gimbal-lock singularity can be surprisingly small in practice [8].

It is interesting to note that the combination $\cos(\vartheta - \lambda)\dot{\varphi} + \dot{\psi}$ is nonsingular in the limit that $\sin(\vartheta - \lambda) = 0$, so that this combination of these two angular rates continues to be significant. The formulas for extracting φ and ψ from the attitude matrix, equations (34) and (35), are both undefined in this limit, however. It is possible to extract information from other elements of the rotation matrix to give a correct value to the linear combination of φ and ψ that remains well-defined, and an explicit procedure to accomplish this has been worked out for the conventional Euler angles [9]. The generalization of this procedure to the generalized Euler angles is straightforward. With a moderate amount of effort, we can derive the following relationships between the 'matrix elements' of A and the generalized Euler angles:

$$\hat{n}_2^T A \hat{n}_2 = \cos\varphi\cos\psi - \sin\varphi\sin\psi\cos(\vartheta - \lambda), \tag{42}$$

$$\hat{n}_2^T A(\hat{n}_1 \times \hat{n}_2) = \sin\varphi\cos\psi + \cos\varphi\sin\psi\cos(\vartheta - \lambda), \tag{43}$$

$$(\hat{n}_2 \times \hat{n}_3)^T A\hat{n}_2 = \cos\varphi\sin\psi + \sin\varphi\cos\psi\cos(\vartheta - \lambda), \tag{44}$$

and

$$(\hat{n}_2 \times \hat{n}_3)^T A(\hat{n}_1 \times \hat{n}_2) = \sin\varphi\sin\psi - \cos\varphi\cos\psi\cos(\vartheta - \lambda). \tag{45}$$

Now we can either find φ from equation (34) and ψ from

$$\psi = \text{ATAN2}\Big[\cos\varphi(\hat{n}_2 \times \hat{n}_3)^T A\hat{n}_2 + \sin\varphi(\hat{n}_2 \times \hat{n}_3)^T A(\hat{n}_1 \times \hat{n}_2),$$
$$\cos\varphi\, \hat{n}_2^T A\hat{n}_2 + \sin\varphi\, \hat{n}_2^T A(\hat{n}_1 \times \hat{n}_2)\Big],$$

(46)

or, alternatively, we can find ψ from equation (35) and then φ from

$$\varphi = \text{ATAN2}\Big[\cos\psi\, \hat{n}_2^T A(\hat{n}_1 \times \hat{n}_2) + \sin\psi(\hat{n}_2 \times \hat{n}_3)^T A(\hat{n}_1 \times \hat{n}_2),$$
$$\cos\psi\, \hat{n}_2^T A\hat{n}_2 + \sin\psi\,(\hat{n}_2 \times \hat{n}_3)^T A\hat{n}_2\Big].$$

(47)

Note that both equations (46) and (47) are well behaved for all values of ϑ. The use of one of these alternatives guarantees that the well-defined linear combination of φ and ψ is determined accurately even when the solution to equation (34) or (35) loses numerical significance. However, these methods are more computationally expensive than using equations (34) and (35) together, and it is best in practice to choose a set of Euler axes for which the gimbal-lock phenomenon will not be encountered.

Discussion

We have shown that the Euler angles can be generalized to encompass sequences of rotations about any three axes subject to the constraint that axes of successive rotations be perpendicular. Thus the second rotation axis must be orthogonal to both the first and the third, but the angle between the first and third axes is arbitrary. This angle, the 'new angle' promised in the title, can take on any value rather than being restricted to the values 0 or $\pm \pi/2$ as in the conventional Euler angle sequences. Kinematic equations have been derived for the generalized Euler angles, as well as equations for extracting these angles from the rotation matrix. The generalized Euler angles have the same 'gimbal lock' singularity as the conventional angle sets. Means for circumventing this problem developed for the conventional cases have been extended to the generalized Euler angles.

All the equations in this paper can be applied to the conventional Euler angle sets in a straightforward fashion, so a side benefit of this work has been to supply universal formulas applicable to all Euler angle parameterizations, conventional and generalized.

Acknowledgement

References

[1] EULER, L. "De Motu Corporum Circa Punctum Fixum Mobilium," *Commentatio 825 indicis ENESTROEMIANI, Opera posthuma,* Vol. 2, 1862, pp. 42-62, also *Leonhardi Euleri Opera Omnia, Series Secunda, Opera Mechanica et Astronomica,* Basel, Vol. 9, 1968, pp. 413-441

[2] GOLDSTEIN, H. *Classical Mechanics,* Addison-Wesley, Reading, MA 1980

[3] HUGHES, P. C. *Spacecraft Attitude Dynamics,* John Wiley & Sons, New York, 1986

[4] JUNKINS, J. L. and TURNER, J. D. *Optimal Spacecraft Rotational Maneuvers,* Elsevier, Amsterdam, 1986

[5] MARKLEY, F. L. "Parameterization of the Attitude," in *Spacecraft Attitude Determination and Control,* J. R. Wertz (ed.), Kluwer Academic Publishers, Dordrecht, 1978

[6] KANE, T.R., LIKINS, P.W., and LEVINSON, D. A. *Spacecraft Dynamics,* McGraw-Hill, New York, 1983

[7] SHUSTER, M. D. "A Survey of Attitude Representations," *Journal of the Astronautical Sciences,* Vol. 41, No. 4, pp. 439–517, October-December 1993

[8] MARKLEY, F. L. "New Dynamic Variables for Rotating Spacecraft," in *Spaceflight Dynamics 1993, Advances in the Astronautical Sciences,* Vol. 84, Part II, ed. by Jerome Teles and Mina Samii, San Diego, CA: Univelt, Inc. 1994, pp. 1149–1163, (also AAS Paper 93-330, AAS/GSFC International Symposium on Spaceflight Dynamics, Goddard Space Flight Center, Greenbelt, MD, April 1993)

[9] NICHOLSON, M., MARKLEY, F. L., and SEIDEWITZ, E. "Attitude Determination Error Analysis System (ADEAS) Release 4 Mathematical Specifications," Computer Sciences Corporation Document CSC/TM-88/6001, October 1988

A MAGNETIC HYSTERESIS MODEL

Thomas W. Flatley
NASA/GSFC Code 712
Greenbelt, MD 20771

Debra A. Henretty
NASA/GSFC Code 712
Greenbelt, MD 20771

Abstract

The Passive Aerodynamically Stabilized Magnetically Damped Satellite (PAMS) will be deployed from the Space Shuttle and used as a target for a Shuttle-mounted laser. It will be a cylindrical satellite with several corner cube reflectors on the ends. The center of mass of the cylinder will be near one end, and aerodynamic torques will tend to align the axis of the cylinder with the spacecraft velocity vector. Magnetic hysteresis rods will be used to provide passive despin and oscillation-damping torques on the cylinder.

The behavior of the hysteresis rods depends critically on the "B/H" curves for the combination of materials and rod length-to-diameter ratio ("l-over-d"). These curves are qualitatively described in most Physics textbooks in terms of major and minor "hysteresis loops".

Mathematical modeling of the functional relationship between B and H is very difficult. In this paper, the physics involved is not addressed, but an algorithm is developed which provides a close approximation to empirically-determined data with a few simple equations suitable for use in computer simulations.

I. List of Symbols

B(H)	Magnetic Flux Density (primary dependent variable)
B'(B)	Slope (dB/dH) on the "major loop" boundaries
B_r	Remanence
B_s	Saturation value of B
H	Magnetizing Field (primary independent variable)
H_c	Coercive Force
$H_L(B)$	Value of H on the left side boundary curve
f	$(H-H_L)/(2H_c)$
k	A TBD constant
q	Boundary slope multiplier
q_o	Value for q for f = 0
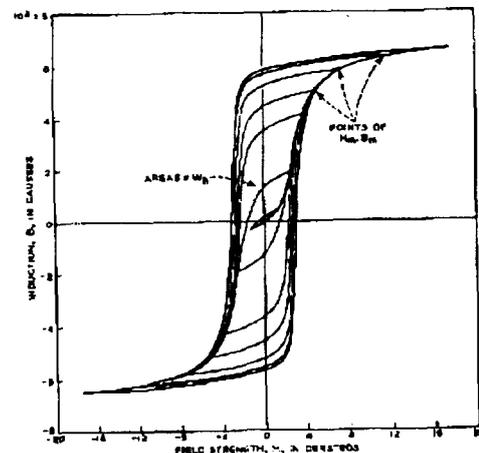
II. Motivation For Analysis

A few years ago, a proposed Gravity and Magnetic Earth Surveyor (GAMES) spacecraft design included a small, totally passive subsatellite which would be released to fly at controlled distances behind the main spacecraft. It was to carry a single laser-reflecting corner cube which ideally would be pointed directly at GAMES and provide a target for a laser-ranging experiment.

A novel subsatellite passive attitude stabilization method, using a combination of aerodynamic and magnetic torques, was proposed by Dave Skillman and Jim Abshire of the Goddard Space Flight Center (GSFC). The work reported here concerns the behavior of magnetic hysteresis rods which were to be used for subsatellite despin and oscillation control.

Although a GAMES new start did not materialize, the Project recommended, and received approval for, a Shuttle test flight of the aero/mag stabilization concept. Preparations are currently underway for the flight of the Passive Aerodynamically Stabilized Magnetically Damped Satellite (PAMS) in 1996.

## III. Development of the Boundary Curves

Magnetic hysteresis rods (long, slender, cylindrical samples of a permeable material) become magnetized when exposed to an ambient magnetic field. The "magnetizing field" (H) is the component of the external field parallel to the axis of the cylinder, and the "magnetic flux density" (B) developed in the material produces a magnetic moment parallel to the axis. The interaction of the magnetic moment and the external field produces a torque which is sometimes used to despin satellites.

For the type of materials used, there is a significant phase lag between B and H and most physics books show plots of "B/H curves" or "hysteresis loops". The function B(H) is extremely nonlinear and multi-valued.

There is no physics addressed here. The mathematical model suggested merely attempts to reproduce empirical B vs. H behavior in a form suitable for use in computer simulations of dynamic systems which employ magnetic hysteresis rods.

We begin with the familiar function y = tan(x) shown on the left below in Figure 1a. Interchanging the axes produces the not-as-familiar function y = arctan(x) as shown below in Figure 1b.
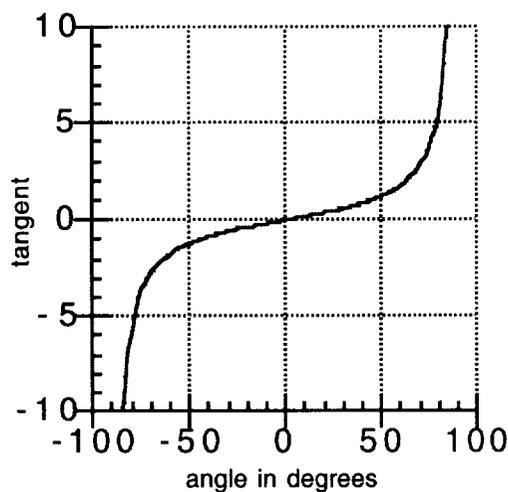
Figure 1a y=tan(x)
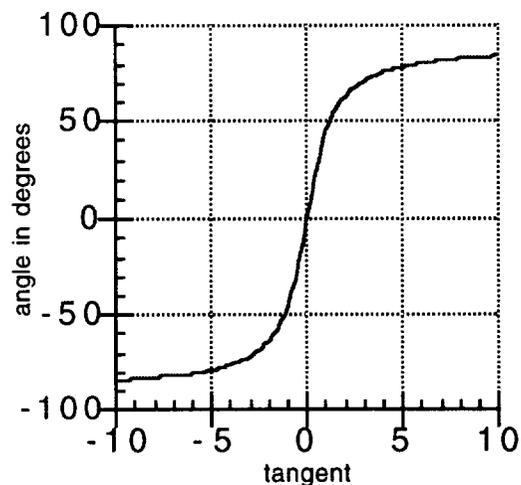
Figure 1b y=arctan(x)

We now let x = kH where k is a selectable constant and H is an independent variable. We also let y be proportional to a dependent variable (B) and wish to have the values of B limited between "saturation levels" $-B_s$ and $+B_s$. The appropriate relationship is given by

$$y = \frac{\pi}{2}\frac{B}{B_s}. \tag{1}$$

In terms of the new variables, we now have the function

$$B = \frac{2}{\pi}B_s \tan^{-1}(kH). \tag{2}$$

Figure 1c shows this function, where k has been arbitrarily set to 5.92 and B_s to 9872.
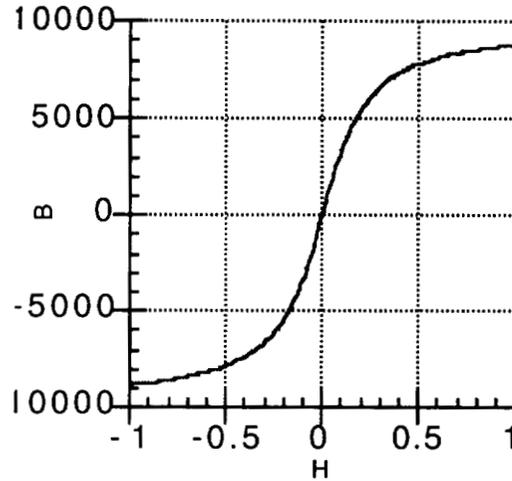
Figure 1c $B = \dfrac{2}{\pi}B_s \tan^{-1}(kH)$

Figure 1d shows the result of shifting the previous curve to the left by an amount H_c arbitrarily set to 0.135 units. Note that, where this curve crosses the ordinate axis, we let $B = B_r$. The equation for this curve is

$$B = \frac{2}{\pi}B_s \tan^{-1}\left[k(H + H_c)\right]. \tag{3}$$

For H = 0 then, we have

$$B_r = \frac{2}{\pi}B_s \tan^{-1}\left[k(H_c)\right]. \tag{4}$$

or equivalently

$$k = \frac{1}{H_c}\tan\left(\frac{\pi}{2}\frac{B_r}{B_s}\right). \tag{5}$$
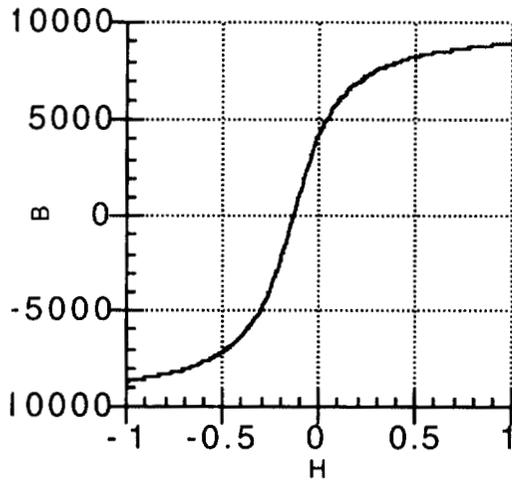
Figure 1d $B = \dfrac{2}{\pi}B_s \tan^{-1}\left[k(H + H_c)\right]$

407

Figure 1e shows the function

$$B = \frac{2}{\pi} B_s \tan^{-1}\left[k(H - H_c)\right],\qquad (6)$$

obtained by shifting the original curve to the right by the same amount H_c
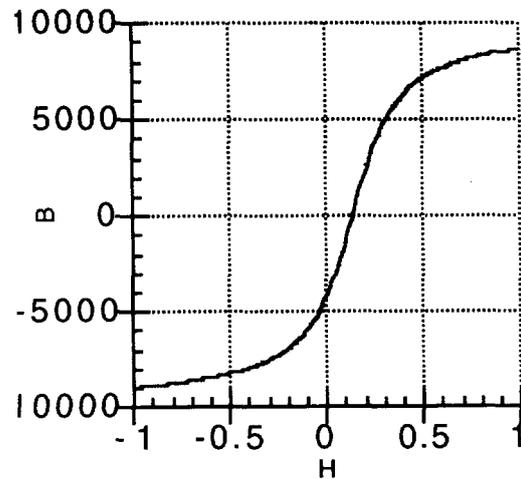
Figure 1e $\quad B = \frac{2}{\pi} B_s \tan^{-1}\left[k(H - H_c)\right]$

Finally, in this construction sequence, we superimpose the last two figures to obtain Figure 1f which bears a close resemblance to the "magnetic hysteresis loops" shown in the Electromagnetics chapter in most elementary Physics books. Usually, H is called the Magnetic Field Strength and B is called the Magnetic Induction. The units involved are discussed in an Appendix to this report. Note that the left boundary curve crosses the ordinate axis at $B=B_r$. In textbook B/H curves, this value is called the Remanence. The right boundary curve crosses the abscissa at $H=H_c$. This value is called the Coercive Force.
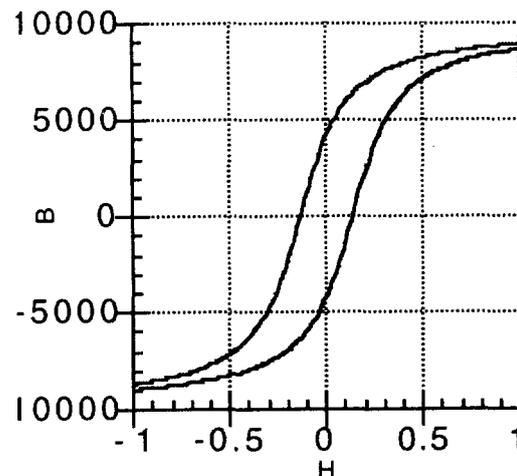
Figure 1f "Hysteresis Loop"

IV. Initial Magnetization Phase and Behavior Inside the Boundaries

Most Physics texts mention an initial magnetization phase in which $B(0)=H(0)=0$ and H is gradually increased in a positive direction. Figure 2 shows a typical "S"-shaped curve showing B first slowly increasing, then rising more sharply, then asymptotically approaching some upper limit.

Here, we assume that the slope dB/dH of this curve and that of any point within the boundary constraints depends on the horizontal distance between the current point (H,B) and the boundary curve which the point is moving away from, in this case, the left side boundary. As an example, suppose that the slope is zero coming off the left boundary and approaches the boundary slope as it approaches the right boundary. Note from the previous section that the two boundary curves are always $2H_c$ apart in the horizontal direction and define the fraction

408

$$f = \frac{H - H_L}{2H_c} \qquad (7)$$

where H_L is the value on the left boundary curve corresponding to the current value of B. Since the left side boundary is given by

$$B = \frac{2}{\pi} B_s \tan^{-1}\left[k(H_L + H_c)\right], \qquad (8)$$

then,

$$H_L = \frac{\tan\left(\frac{\pi}{2}\frac{B}{B_s}\right)}{k} - H_c. \qquad (9)$$
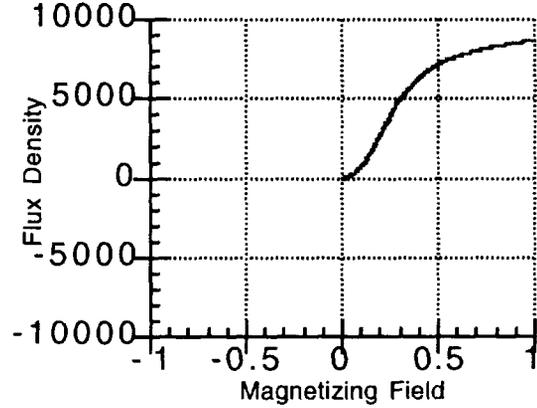
Figure 2   Initial Magnetization Phase

Now, Let B' be the boundary curve slope (either boundary) corresponding to the current value of B. Differentiating the previous equation with respect to H, we find

$$0 = \frac{\pi}{2kB_s}\sec^2\left(\frac{\pi}{2}\frac{B}{B_s}\right)B' \qquad (10)$$

or

$$B' = \frac{2}{\pi}kB_s\cos^2\left(\frac{\pi}{2}\frac{B}{B_s}\right). \qquad (11)$$

Now, a simple function providing the desired behavior could be

$$\frac{dB}{dH} = f\,B'. \qquad (12)$$

Another possibility would be

$$\frac{dB}{dH} = f^p\,B' \qquad (13)$$

where p is an exponent of the fractional distance f.

Actually, in the specific example addressed below, the slopes at the left boundary seen in the test data were small but non-zero. To account for this possibilty, a more general expression (with one more selectable constant) was used in fitting the data. We let

$$\frac{dB}{dH} = \left[q_o + (1 - q_o)f^p\right]B' \qquad (14)$$

where $q_o B'$ is the slope dB/dH near the boundary.

V. Specific Application

Some empirical B/H curve data was generously provided to the author by Frederick Mobley of the Johns Hopkins University Applied Physics Laboratory (APL). Tests were run on a long, slender rod made from AEM 4750 material, a nickel-iron alloy. The magnetizing field was oscillated between nine different peak values ranging from +/- 0.04 to +/- 0.50 units. At the higher levels, boundary curve limits were clearly achieved.

Examination of the boundary curves showed immediately that $H_c=0.135$ units and $B_r=4240$ units were reasonable approximations. Placing these values and H=0 in the left-hand boundary curve

$$B = \frac{2}{\pi} B_s \tan^{-1}\left[k(H + H_c)\right] \qquad (15)$$

409

produces an equation showing a required relationship between k and B_s, i.e.

$$4240 = \frac{2}{\pi} B_s \tan^{-1}[0.135k].$$ (16)

Another point on the left hand boundary was located at (-0.5,-7150). Using these values for H and B, respectively, produces a second requirement for k and B_s, i.e.

$$-7150 = \frac{2}{\pi} B_s \tan^{-1}[-0.365k].$$ (17)

These equations were solved numerically to find B_s=9872. With this known, we can compute k = 5.925. The resulting boundary curve then becomes

$$B = \frac{2}{\pi}(9872)\tan^{-1}[5.925(H \pm 0.135)].$$ (18)

Figure 3a shows a reproduction of some of the hysteresis rod B/H test data received from APL. The outermost contour was obtained by cycling the magnetizing field (H) between the limits of ±0.5 units and plotting the resultant steady-state B/H contour curve. The peak values of B observed were ±7150 units. Points on the left-hand boundary curve were used to determine appropriate values for k and B_s for the math model described above.
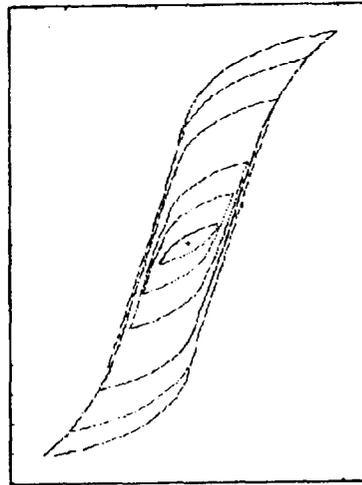
Figure 3a   Test Data

The outermost contour of Figure 3b shows the math model output for the same ±0.5 units input. Note that the test data slope appears to have a fairly large linear range compared to that produced by the model. The arctangent model shows more curvature and flattens out a little more at the extreme values of H.
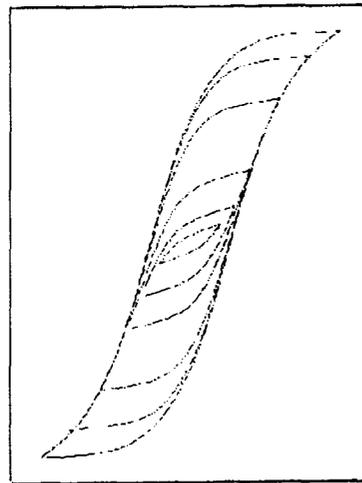

Figure 3b   Model Data

410

Figure 3c shows test data for a smaller range of H values, i.e. ±0.1 units. The outermost curve here is the same as the innermost curve of Figure 3a. This curve was used in the selection of the other two model parameters, p and q_o. Values of p = 4.75 and q_o= 0.085 were obtained by a trial-and-error iterative procedure which matched a peak value of B of 637 units and an ordinate crossing value of 275 units as observed in the test data. Figure 3d shows that a very close match was obtained.
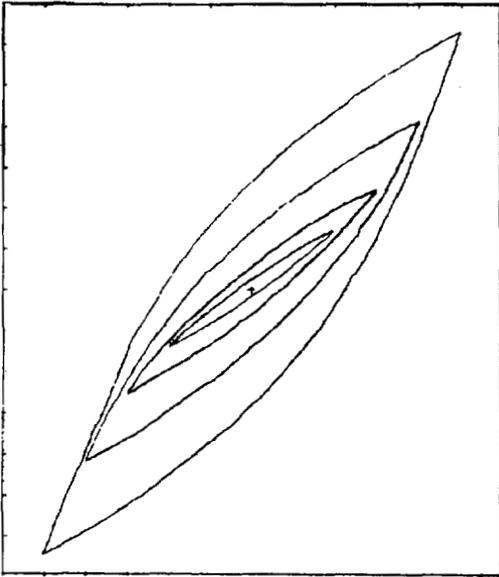

Figure 3c   Test Data

The four parameters selected above were then used in the model and B(H) contours were generated for the other ranges of H for which test data was available, i.e. ±0.4, ±0.3, ±0.2, ±0.15, ±0.08, ±0.06, and ±0.04 units. All test data and model outputs are shown in Figures 3a through 3d.
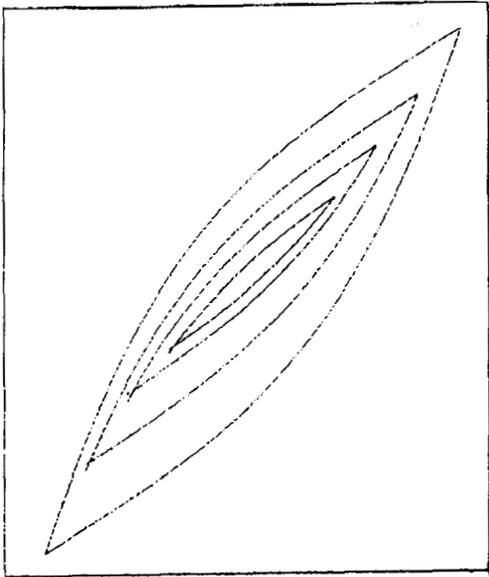

Figure 3d   Model Data

411

VI. An Algorithm for Determining dB/dt

Given B, H and dH/dt, with k, q_0, and p predetermined constants,

1. Compute H_L, the value of H on the left boundary curve corresponding to B. Since this curve is given by $B = \frac{2}{\pi} B_s \tan^{-1}\left[k\left(H_L + H_c\right)\right]$, we find

$$HL=TAN(PI*B/2/BS)/K-HC$$

2. Compute B', the boundary curve slope corresponding to the value of B. It may be shown that

$$BP=2*K*BS/PI*COS(PI*B/2/BS)**2$$

3. Find f,

$$F=(H-HL)/2/HC$$

If dH/dt is negative, measure f from the right hand boundary,

$$IF\ (DHDT.LT.0)\ F=1-F$$

4. Find q,

$$Q=Q0+(1-Q0)*F**P$$

5. Find dB/dH,

$$DBDH=Q*BP$$

6. Find dB/dt,

$$DBDT=DBDH*DHDT$$

VII. Appendix on Magnetic Units

The use of units for the variables B and H has been avoided in the body of this report. The history of magnetic units is long and sometimes contentious and it was feared that including a discussion of this subject would introduce an unnecessary distraction in the presentation of the mathematical modelling of magnetic hysteresis.

As mentioned in the body of the report, empirical B/H curves were received from Mr. Fred Mobley of The Johns Hopkins University Applied Physics Laboratory (APL) of Silver Spring, MD. The data referred to here was produced during testing of a rod made from a material known as AEM 4750 (a nickel-iron alloy) with a length of of 58 inches (1.47 meters) and a diameter of 0.1084 inches (0.00275 meters). The independent variable, the **magnetizing field H**, was expressed in **oersteds** and the dependent variable, the **flux density B** was given in **gauss.**

In modern times, people have become comfortable with **magnetic fields** in **tesla, magnetic moments** in **ampere-meters-squared** and **torques** in **newton-meters**. A magnetic hysteresis rod in space will have a certain magnetic moment M and will interact with the Earth's magnetic field B to generate a torque T, with the pertinent equation being the familiar cross product law $T = M \times B$.

In this Appendix, we attempt to bridge the gap between raw data in the form of B/H curves, with B in gauss and H in oersteds, and computer simulations of the performance of magnetic hysteresis rods in space.

An immediate possible source of confusion is the fact that the letter B is now commonly used for the external magnetic field, where historically, the letter H was used. In early-space-age literature[1] and textbooks[2], when magnetic materials were exposed to a **magnetic field strength** or magnetizing field H, a **magnetic flux density** or

magnetic induction B was developed in the material. The unit for H was oersted and the unit for B was gauss. These unit names honored two of the early researchers in the field, Hans Christian Oersted (1777-1851) and Carl Friedrich Gauss (1777-1855).

With a magnetic hysteresis rod, the magnetic moment or **dipole moment** depended on the flux density and the volume of material with the governing relationship being m = BV/4π. Here the magnetic moment m is measured in **pole-centimeters** and the volume V is in **cubic centimeters**. **Pole-cm** is a unit probably familiar to most readers and many have probably used the conversion factor of 1000 pole-cm = 1 ampere-meter-squared. Why this is so is probably not very well known.

The ampere-meter-squared unit is probably the simplest and most obvious magnetic unit. With a current in **amperes** flowing in a loop enclosing an area in **square-meters**, the magnetic moment is simply the current times the area. Now, the magnetic field in the vicinity of such a loop is of interest. The physics involved is expressed by the Biot and Savart equation

$$dH = I \, ds \times r \, / \, r^3. \tag{19}$$

In this differential equation, **H** is the magnetic field, I is the current, ds is an incremental length of coil and **r** is a vector from ds to the point of interest. Unitwise, with r and ds in centimeters, a current in **abamperes** produces a magnetic field in oersted. There are 10 amperes in one abampere.

Figure A-1 shows a circular coil of radius "a" carrying a current "i" (in amperes) and a point R in the plane of the coil at which the magnetic field is to be determined. For points far away from the coil, the following analysis shows that the magnetic field is given approximately by

$$H = \pi a^2 \, i / 10 \, R^{-3} \tag{20}$$

oersted "into the paper".
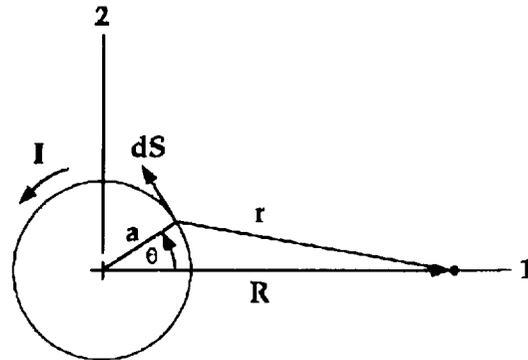
Figure A-1   Current Loop

The elemental length ds is in the 1-2 plane, with the components

$$ds_1 = - a \sin(\theta) \, d\theta \tag{21}$$
$$\text{and} \quad ds_2 = a \cos(\theta) \, d\theta. \tag{22}$$

The vector r (also in the 1-2 plane) has the components

$$r_1 = R - a \cos(\theta) \tag{23}$$
$$\text{and} \quad r_2 = - a \sin(\theta). \tag{24}$$

The vector ds x r is obviously in the 3 direction with a magnitude of a[a-R cos(θ)]dθ. The quantity r^2 is given by $R^2+a^2-2aR\cos(\theta)$. The strength of the field is then obtained by integrating (from θ = 0 to 2π) the differential equation

$$dH = i/10 \, a \, [\, a - R \cos(\theta) \,] \, d\theta \, / \, [\, R^2 + a^2 - 2 \, a \, R \cos(\theta) \,]^{3/2}. \tag{25}$$

Far from the coil. i.e., for R>>a, the denominator in this equation may be approximated by $R^3[1-3(a/R)\cos(\theta)]$ in the denominator or by $R^{-3}[1+3(a/R)\cos(\theta)]$ in the numerator. This makes the approximate differential equation

$$dH = a \, i/10 \, R^{-3} \, [\, a - R \cos(\theta) \,] \, [\, 1 + 3 \, a/R \cos(\theta) \,] \, d\theta. \tag{26}$$

413

Of the four terms here, only two will contribute to the integral, so we can let

$$dH = a \, i/10 \, R^{-3} \, [\, a - 3 \, a \, \cos^2(\theta) \,] \, d\theta. \tag{27}$$

Integrating this equation produces

$$H = a \, i/10 \, R^{-3} \, (\, 2\pi \, a - 3\pi \, a \,) = -\pi a^2 \, i/10 \, R^{-3} \, . \tag{28}$$

Now, fictitious "magnetic poles" were commonly employed in the teaching of magnetics years ago. They came in two varities, positive poles and negative poles. The force between two poles was inversely proportional to the square of the distance between them and was measured in **dynes** when the distance was in centimeters. A dyne was the force required to accelerate a mass of one gram to a level of one cm/sec^2. Forces were either repulsive or attractive, depending on whether the signs were the same or different. If a positive pole and a negative pole were placed one centimeter apart, they formed a unit dipole, with a magnetic moment of one pole-cm. Collections of "p" positive poles and "p" negative poles a distance "c" apart formed a dipole with a magnetic moment of m=pc. Now, a unit positive pole in the vicinity of this dipole would experience an attractive force toward the negative end and a repulsive force away from the positive end. The magnetic field (in oersteds) due to the dipole at this point was defined as equal in magnitude and direction to the net force vector (in dynes) acting on the unit pole.

Figure A-2 shows the dipole described above and a point **R** at which we would like to determine the magnetic field strength. It will be shown below that, for R>>c, and with **R** perpendicular to the dipole axis, the field is approximately $H = pc/R^3$. Assume now that the fields due to the coil described above and the dipole described here are equal. We then would have $\pi a^2 i/10 = pc$. Now, let A be the area of the coil in square meters. Then $a^2 = 10^4 A$, and we have 1000Ai=pc. Therefore, one ampere-meter-squared = 1000 pole-cm as stated above.
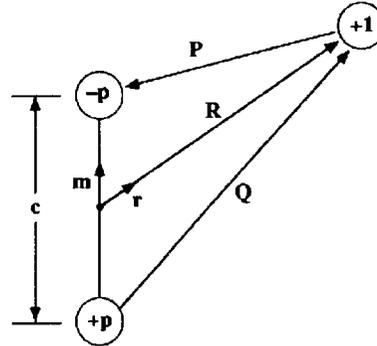
Figure A-2 Magnetic Dipole

Initially, let **R**=R**r** be a general point at a distance R from the center of the dipole, with **r** a unit vector. Let **m** be a unit vector from the positive pole to the negative pole of the dipole. Let **P** be a vector from the test point to the negative pole of the dipole and let **Q** be a vector from the positive pole to the test point as shown. We can write **R**+**P**=m**c**/2 and **Q**=m**c**/2+**R**. The force (in dynes) acting on the test pole will be p**Q**/Q³ + p**P**/P³, where P and Q are the magnitudes of the vectors **P** and **Q**.

Now, P^2=**P**dot**P**=(m**c**/2-**R**)dot(m**c**/2-**R**) or approximately, with R>>c, $P^2 = R^2 - $ c **m**dot**R**. Obviously, we have introduced the operator "dot" to indicate the scalar product between two vectors. Similarly Q^2 is approximately equal to $R^2 +$ c **m**dot**R**. The force then becomes, approximately,

$$f = p\mathbf{Q} \, [\, R^2 + c \, \mathbf{m}dot\mathbf{R} \,]^{-3/2} + p\mathbf{P} \, [\, R^2 - c \, \mathbf{m}dot\mathbf{R} \,]^{-3/2} \tag{29}$$

$$\approx (p/R^3) \, [\, \mathbf{Q} \, (\, 1 + 3/2 \, c/R \, \mathbf{m}dot\mathbf{r}) + \mathbf{P} \, (\, 1 - 3/2 \, c/R \, \mathbf{m}dot\mathbf{r}) \,]$$

$$\approx (p/R^3) \, [\, \mathbf{P+Q} - 3/2 \, c/R \, (\mathbf{P-Q}) \, \mathbf{m}dot\mathbf{r} \,]$$

$$\approx (p/R^3) \, [\, c \, \mathbf{m} - 3 \, c \, \mathbf{r} \, \mathbf{m}dot\mathbf{r} \,]$$

$$\approx (pc/R^3) \, [\, \mathbf{m} - 3 \, \mathbf{m}dot\mathbf{r} \, \mathbf{r} \,]$$

Recalling that the force in dynes is numerically equal to the magnetic field in oersteds, this equation represents a concise expression for a dipole magnetic field. It is similar to that shown in Wertz[3].

At a point on the dipole equator (which is what we were initially interested in) the field reduces to simply pc/R^3 as was stated above.

Getting back to the computer simulation of magnetic hysteresis rod behavior, we have the following rule:
<u>Given a magnetic flux density (B) in gauss , and a volume of material (V) in cubic centimeters, the magnetic moment in modern (SI) units will be M = BV/4000π ampere-meters-squared.</u>

Another perhaps familiar expression from the magnetics section of physics books is $B = \mu H$, where μ is the **permeability** of the medium. This equation converts H in oersteds to B in gauss. With the now obsolete (but still widely used) system of units, the permeability of free space was unity. Magnetic fields in space were then expressed in gauss and were numerically equal to magnetic fields in oersteds. This latter unit soon became rarely used and the Earth's magnetic field strength was stated in gauss (or milligauss) for some time. The unit **gamma** was also sometimes used in the early days of orbiting spacecraft with one gauss being equivalent to 10^5 gamma. When the emphasis on SI units arrived on the scene, "gauss" gave way to "webers per square meter" with the conversion factor of 10^4 gauss per Wb/m^2. This unit name was selected to honor Wilhelm Eduard Weber (1804-1891). Some time later, this latter unit was renamed the tesla in honor of Nikola Tesla (1856-1943). This made one gamma equal to one nanotesla.

A second rule to be followed then in dealing with B/H data in gauss and oersteds is:

<u>Working with magnetic hysteresis rods in space, the "H in oersteds" required for the math model would be obtained by multiplying the magnetic field in tesla by 10000.</u>

References:

1. Fischell, Robert E., Magnetic Damping of the Angular Motions of Earth Satellites, ARS Journal, September 1961, pages 1210-1217.

2. Lemon, Harvey Brace and Ference, Michael, Jr., Analytical Experimental Physics, The University of Chicago Press, 1947, pages 356-357.

3. James R Wertz, Spacecraft Attitude Determination and Control, D. Reidel Publishing Company, 1978, page 783.

Walter Grossman
CTA Space Systems
1521 Westbranch Drive
McLean, VA 22102
e-mail: w.grossman@ieee.org

Abstract

The Small Satellite Technology Initiative (SSTI) "CLARK" spacecraft is required to be single-failure tolerant, i.e., no failure of any single component or subsystem shall result in complete mission loss. Fault tolerance is usually achieved by implementing redundant subsystems. Fault tolerant systems are therefore heavier and cost more to build and launch than non-redundent, non fault-tolerant spacecraft.

The SSTI CLARK satellite Attitude Determination and Control System (ADACS) achieves single-fault tolerance without redundancy. The attitude determination system system uses a Kalman Filter which is inherently robust to loss of any single attitude sensor[1]. The attitude control system uses three orthogonal reaction wheels for attitude control and three magnetic dipoles for momentum control. The nominal six-actuator control system functions by projecting the attitude correction torque onto the reaction wheels while a slower momentum management outer loop removes the excess momentum in the direction normal to the local B field. The actuators are not redundant so the nominal control law cannot be implemented in the event of a loss of a single actuator (dipole or reaction wheel).

The spacecraft dynamical state (attitude, angular rate, and momentum) is *controllable* from any five-element subset of the six actuators. With loss of an actuator the *instantaneous* control authority may not span $\mathcal{R}^3$ but the controllability gramian

$$\int_0^t \Phi(t,\tau)B(\tau)B'(\tau)\Phi'(t,\tau)d\tau$$

retains full rank. Upon detection of an actuator failure the control torque is decomposed onto the remaining active axes. The attitude control torque is effected and the over-orbit momentum is controlled. The resulting control system performance approaches that of the nominal system.

---

[1] The CLARK attitude determination system is designed to test State-Of-the-Art attitude sensors by comparing performance of sensors with a star tracker-gyro precision reference. The CLARK Kalman filter estimates spacecraft attitude, angular rate, and gyro bias. These state variables are observable from any $N-1$ subset of the N attitude sensors. The system is, as such, inherently robust to loss of any single sensor.

CONTINGENCY DESIGNS FOR ATTITUDE DETERMINATION OF TRMM   N95- 27803

John L. Crassidis, Stephen F. Andrews, F. Landis Markley
Goddard Space Flight Center, Code 712
Greenbelt, MD 20771

Kong Ha

Orbital Sciences Corporation
Greenbelt, MD 20770

Abstract

In this paper, several attitude estimation designs are developed for the Tropical Rainfall Measurement Mission (TRMM) spacecraft. A contingency attitude determination mode is required in the event of a primary sensor failure. The final design utilizes a full sixth-order Kalman filter. However, due to initial software concerns, the need to investigate simpler designs was required. The algorithms presented in this paper can be utilized in place of a full Kalman filter, and require less computational burden. These algorithms are based on filtered deterministic approaches and simplified Kalman filter approaches. Comparative performances of all designs are shown by simulating the TRMM spacecraft in mission mode. Comparisons of the simulation results indicate that comparable accuracy with respect to a full Kalman filter design is possible.

Introduction

The TRMM spacecraft is due to be launched in 1997 with a nominal mission lifetime of 42 months. The main objectives of this mission include: (1) to obtain multi-year measurements of tropical and subtropical rainfall, (2) to understand how interactions between the sea, air, and land masses produce changes in global rainfall and climate, and (3) to help improve the modeling of tropical rainfall processes and their influence on global circulation.

The spacecraft is three-axis stabilized in a near circular (350 km) orbit with an inclination of 35°. The nominal Earth-pointing mission mode requires a rotation once per orbit about the spacecraft's y-axis. The attitude determination hardware consists of an Earth Sensor Assembly (ESA), Digital Sun Sensors (DSS), Coarse Sun Sensors (CSS), a Three-Axis Magnetometer (TAM), and gyroscopic rate sensors. The attitude control hardware includes three Magnetic Torquer Bars (MTB) which are used to provide magnetic momentum unloading capability, and a Reaction Wheel Assembly (RWA) which consists of four wheels in a pyramidal arrangement to maximize momentum storage capability along a preferred axis.

Primary attitude determination is accomplished using the ESA and gyroscopes. The DSS is also used twice each orbit in order to update the yaw position estimate during mission pointing. The allotted attitude knowledge accuracy is 0.18° per axis. Simulation studies indicate that the primary attitude determination system meets the knowledge requirements [1]. In the event of an ESA failure, a contingency mode is used to allow for the continuation of the scientific mission. Attitude determination for the contingency mode is accomplished using the DSS, the TAM, and gyroscopes. The allotted attitude knowledge accuracy for the contingency mode is 0.7° per axis.

The algorithm chosen for the final contingency design incorporates a sixth-order Kalman filter [2]. This filter estimates both attitude error angles and gyro drift trajectories. However, due to initial concerns in software coding size and computations, the development of simpler and less software-intensive algorithms is required. A number of algorithms is presented in this paper, including: an Isotropic Kalman Filter (IKF), a steady-state Angles-only Kalman Filter (AKF), an Enhanced TRIAD

PRECEDING PAGE BLANK NOT FILMED

Algorithm (ETA), and an Enhanced QUEST Algorithm (EQA). All of these algorithms utilize magnetic field measurements, digital sun sensor measurements (when available), and gyro measurements. The IKF is a simplified Kalman filter in which an approximation is made where the rank deficient projection matrix is replaced by the identity matrix. This leads to attitude and gyro bias covariances that are the same in all directions in space. The AKF is a steady-state Kalman filter which estimates for angles only, with no gyro bias estimation. The ETA is essentially a first-order filter on TRIAD [3] determined attitudes. During solar eclipse, the ETA relies exclusively on model propagation using gyro measurements. Also, during sensor co-alignment the filter gain is automatically adjusted so that the filter relies more on the propagated attitude. The EQA is similar to the ETA, but uses the QUEST [4] algorithm for attitude determination. This allows for weighting of individual attitude sensor measurement sets.

The organization of this paper proceeds as follows. First, a summary of the spacecraft attitude kinematics is shown. Then, a brief review of the standard Kalman filter used for attitude estimation is shown. Next, the equations and properties of the IKF, AKF, ETA, and EQA are presented. Then, these algorithms are used to estimate the attitude of a simulated TRMM spacecraft. Finally, results are shown which compare each new algorithm to the full Kalman filter. A number of factors is considered, including: telemetry requirements, on-board requirements, coding size, and attitude accuracy.

Attitude Kinematics

In this section, a brief review of the kinematic and dynamic equations of motion for a three-axis stabilized spacecraft is shown. The attitude is assumed to be represented by the quaternion vector, defined as

$$\underline{q} \equiv \begin{bmatrix} \underline{q}_{13} \\ q_4 \end{bmatrix} \tag{1}$$

with

$$\underline{q}_{13} \equiv \begin{bmatrix} q_1 \\ q_2 \\ q_3 \end{bmatrix} = \hat{\underline{n}} \sin(\theta / 2) \tag{2a}$$

$$q_4 = \cos(\theta / 2) \tag{2b}$$

where $\hat{\underline{n}}$ is a unit vector corresponding to the axis of rotation and θ is the angle of rotation. The quaternion kinematic equations of motion are derived by using the spacecraft's angular velocity ($\underline{\omega}$), given by

$$\underline{\dot{q}} = \frac{1}{2} \Omega(\underline{\omega}) \underline{q} = \frac{1}{2} \Xi(\underline{q}) \underline{\omega} \tag{3}$$

where $\Omega(\underline{\omega})$ and $\Xi(\underline{q})$ are defined as

$$\Omega(\underline{\omega}) \equiv \begin{bmatrix} -[\underline{\omega} \times] & \vdots & \underline{\omega} \\ \cdots & \vdots & \cdots \\ -\underline{\omega}^T & \vdots & 0 \end{bmatrix} \tag{4a}$$

$$\Xi(\underline{q}) \equiv \begin{bmatrix} q_4 I_{3\times3} + [\underline{q}_{13} \times] \\ \cdots \\ -\underline{q}_{13}^T \end{bmatrix} \tag{4b}$$

The 3×3 dimensional matrices $[\underline{\omega} \times]$ and $[\underline{q}_{13} \times]$ are referred to as cross product matrices since $\underline{a} \times \underline{b} = [\underline{a} \times] \underline{b}$, with

$$[\underline{a}\times] \equiv \begin{bmatrix} 0 & -a_3 & a_2 \\ a_3 & 0 & -a_1 \\ -a_2 & a_1 & 0 \end{bmatrix} \tag{5}$$

Since a three degree-of-freedom attitude system is represented by a four-dimensional vector, the quaternions cannot be independent. This condition leads to the following normalization constraint

$$\underline{q}^T \underline{q} = \underline{q}_{13}^T \underline{q}_{13} + q_4^2 = 1 \tag{6}$$

The measurement model is assumed to be of the form given by

$$\underline{B}_B = A(\underline{q})\underline{B}_I \tag{7}$$

where $\underline{B}_I$ is a 3×1 dimensional vector of some reference object (e.g., a vector to the sun or to a star, or the Earth's magnetic field vector) in a reference coordinate system, $\underline{B}_B$ is a 3×1 dimensional vector defining the components of the corresponding reference vector measured in the spacecraft body frame, and $A(\underline{q})$ is given by

$$A(\underline{q}) = \left(q_4^2 - \underline{q}_{13}^T \underline{q}_{13}\right)I_{3\times3} + 2\underline{q}_{13}\underline{q}_{13}^T - 2q_4\left[\underline{q}_{13}\times\right] \tag{8}$$

which is the 3×3 dimensional (orthogonal) attitude matrix.

Kalman Filter Review

In this section, a review of the basic principles of the Kalman filter applied to attitude estimation is shown (see [2] for more details). The state error vector has seven components consisting of a four-component error quaternion ($\delta\underline{q}$) and a three-vector gyro bias error $\Delta\underline{b}$, given by

$$\Delta\underline{x} = \begin{bmatrix} \delta\underline{q} \\ --- \\ \Delta\underline{b} \end{bmatrix} \tag{9}$$

The error quaternion is defined as

$$\delta\underline{q} = \underline{q} \otimes \hat{\underline{q}}^{-1} \tag{10}$$

where $\underline{q}$ is the true quaternion and $\hat{\underline{q}}$ is the estimated quaternion. Also, the operator $\otimes$ refers to quaternion multiplication (see [3] for details). Since the incremental quaternion corresponds to a small rotation, Equation (10) can be approximated by

$$\delta\underline{q} \approx \begin{bmatrix} \delta\underline{q}_{13} \\ 1 \end{bmatrix} \tag{11}$$

which reduces the four-component error quaternion into a three-component (half-angle) representation.

The true angular velocity is assumed to be modeled by

$$\underline{\omega} = \underline{\omega}_g - \underline{b} - \underline{\eta}_1 \tag{12}$$

where $\underline{\omega}$ is the true angular velocity, $\underline{\omega}_g$ is the gyro-determined angular velocity, and $\underline{b}$ is the gyro drift vector, which is modeled by

$$\underline{\dot{b}} = \underline{\eta}_2 \tag{13}$$

The 3×1 vectors, $\underline{\eta}_1$ and $\underline{\eta}_2$, are assumed to be modeled by a Gaussian white-noise process with

$$E\{\underline{\eta}_i(t)\} = \underline{0} \qquad i = 1, 2 \tag{14a}$$

$$E\{\underline{\eta}_i(t)\underline{\eta}_j^T(t')\} = Q_i \delta_{ij} \delta(t - t') \qquad i, j = 1, 2 \tag{14b}$$

Using the reduced error quaternion in Equation (11) and the gyro drift model in Equation (13), the state error equation may be written as [2]

$$\Delta\underline{\dot{x}} = F \Delta\underline{x} + G \underline{w} \tag{15}$$

where

$$F = \begin{bmatrix} -[\underline{\hat{\omega}} \times] & -\dfrac{1}{2} I_{3\times3} \\[2ex] 0_{3\times3} & I_{3\times3} \end{bmatrix} \tag{16a}$$

$$G = \begin{bmatrix} -\dfrac{1}{2} I_{3\times3} & 0_{3\times3} \\[2ex] 0_{3\times3} & I_{3\times3} \end{bmatrix} \tag{16b}$$

$$\underline{w} = \begin{bmatrix} \underline{\eta}_1 \\ \underline{\eta}_2 \end{bmatrix} \tag{16c}$$

$$\underline{\hat{\omega}} = \underline{\omega}_g - \underline{\hat{b}} \tag{16d}$$

State-observable discrete measurements are assumed to be modeled by

$$\underline{z}_k = h_k(\underline{x}_k) + \underline{v}_k \tag{17}$$

where

$$h_k(\underline{x}_k) = A(\underline{q}_k)\underline{B}_{I_k} \tag{18}$$

and $\underline{v}_k$ is assumed to be modeled by a zero-mean Gaussian process with

$$E\{\underline{v}_k\} = \underline{0} \tag{19a}$$

$$E\{\underline{v}_k \underline{v}_l^T\} = \delta_{kl} R_k \tag{19b}$$

The sensitivity matrix can be written as

$$H_k = \begin{bmatrix} \underline{l}_k & \vdots & 0_{3\times3} \end{bmatrix} \tag{20}$$

where

$$\underline{l}_k = 2\left[A(\underline{\hat{q}})\underline{B}_I \times\right]_k \tag{21}$$

The extended Kalman filter equations for attitude estimation are summarized by

$$\dot{P} = FP + P^T F + GQG^T \tag{22a}$$

$$\Delta \hat{\underline{x}}_k = K_k \left[\underline{z}_k - \underline{h}_k \left(\hat{\underline{q}}_k(-) \right) \right] \tag{22b}$$

$$P_k(+) = \left[I_{6\times 6} - K_k H_k \left(\hat{\underline{x}}_k(-) \right) \right] P_k(-) \tag{22c}$$

$$K_k = P_k(-) H_k^T \left[H_k P_k(-) H_k^T + R_k \right]^{-1} \tag{22d}$$

$$\hat{\underline{q}}(+) = \delta \hat{\underline{q}}(+) \otimes \hat{\underline{q}}(-) \tag{22e}$$

$$\hat{\underline{b}}(+) = \hat{\underline{b}}(-) + \Delta \hat{\underline{b}}(+) \tag{22f}$$

$$\delta \hat{\underline{q}}(+) = \begin{bmatrix} \delta \hat{\underline{q}}_{13}(+) \\ 1 \end{bmatrix} \tag{22g}$$

Isotropic Kalman Filter

In this section, the equations for the IKF are shown. The state vector consists of an incremental quaternion and gyro bias. The gyro propagation portion of the IKF is identical to the full Kalman filter shown in the previous section. However, the assumed measurement in the IKF is given by

$$\tilde{\underline{z}} = \tilde{\underline{u}} \times \hat{\underline{u}} \tag{23}$$

where $\tilde{\underline{u}}$ is the measured unit vector from either the TAM or DSS in the body frame, and $\hat{\underline{u}}$ is the corresponding expected value, obtained by mapping the inertial reference to the body-fixed coordinate system using the estimated quaternion. Also, from Equation (23) $\hat{\underline{z}} = \underline{0}$, since the cross product of a vector with itself is zero. The sensitivity matrix of the measurement model in Equation (23) is determined by using the attitude matrix of the angle error. This leads to

$$\tilde{\underline{u}} = A(\underline{\alpha}) \hat{\underline{u}} \tag{24}$$

where $\underline{\alpha}$ is an incremental error angle. Using the approximation

$$A(\underline{\alpha}) = I_{3\times 3} - [\underline{\alpha} \times] \tag{25}$$

leads to the following measurement model

$$\tilde{\underline{z}} = \left(I_{3\times 3} - \hat{\underline{u}} \hat{\underline{u}}^T \right) \underline{\alpha} \tag{26}$$

Therefore, the sensitivity matrix, which contains partials with respect to the error state, is given by

$$H = \begin{bmatrix} H_u & \vdots & 0_{3\times 3} \end{bmatrix} \tag{27}$$

where

$$H_u = I_{3\times 3} - \hat{\underline{u}} \hat{\underline{u}}^T \tag{28}$$

This matrix is the projection operator onto the space perpendicular to $\hat{\underline{u}}$, which reflects the fact that an observation of a unit vector contains no information about rotations around an axis specified by that vector. Therefore, H_u has rank two. Also, if the measurement errors for each sensor are assumed equal in all directions, then the measurement error covariance is given by

$$R = r H_u \tag{29}$$

where r is a scalar. Equation (29) indicates that there is no uncertainty in the length of the measured vector. The IKF is derived by making an approximation of replacing the rank-two sensitivity matrix in Equation (28) by the rank-three identity matrix, which leads to

$$H_u = I_{3\times3} \tag{30a}$$

$$R = r\, I_{3\times3} \tag{30b}$$

This approximation leads to attitude and gyro bias covariances which are equal in all directions in space, or *isotropic*. Therefore, the covariance matrix has the form given by

$$P = \begin{bmatrix} P_a\, I_{3\times3} & P_c\, I_{3\times3} \\ P_c\, I_{3\times3} & P_b\, I_{3\times3} \end{bmatrix} \tag{31}$$

where P_a, P_c, and P_b are scalar quantities. Also, the state transition matrix is approximated by

$$\Phi = \begin{bmatrix} I_{3\times3} & -\Delta t\, I_{3\times3} \\ 0_{3\times3} & I_{3\times3} \end{bmatrix} \tag{32}$$

where Δt is the sampling interval. Equation (32) ignores spacecraft rotation, which is irrelevant since the covariance matrix in Equation (31) is isotropic. The covariance propagation equations are now given by

$$p_{a_{k+1}}(-) = p_{a_k}(+) - 2p_{c_k}(+)\Delta t + p_{b_k}(+)\Delta t^2 + \sigma_v^2 \Delta t + \frac{1}{3}\sigma_u^2 \Delta t^3 \tag{33a}$$

$$p_{c_{k+1}}(-) = p_{c_k}(+) - p_{b_k}(+)\Delta t - \frac{1}{2}\sigma_u^2 \Delta t^2 \tag{33b}$$

$$p_{b_{k+1}}(-) = p_{b_k}(+) + \sigma_u^2 \Delta t \tag{33c}$$

where σ_u^2 and σ_v^2 are the scalar covariances of the gyro-drift ramp noise, and the gyro-drift rate measurement noise, respectively. The Kalman gain matrix is given by

$$K = \begin{bmatrix} k_a\, I_{3\times3} & \vdots & k_b\, I_{3\times3} \end{bmatrix}^T \tag{34}$$

where

$$k_a = \frac{p_{a_{k+1}}(-)}{p_{a_{k+1}}(-) + r} \tag{35a}$$

$$k_b = \frac{p_{c_{k+1}}(-)}{p_{a_{k+1}}(-) + r} \tag{35b}$$

Therefore, the Kalman covariance and state update equations are given by

$$p_{a_{k+1}}(+) = r\, k_a \tag{36a}$$

$$p_{c_{k+1}}(+) = r\, k_b \tag{36b}$$

$$p_{b_{k+1}}(+) = p_{b_{k+1}}(-) - k_b p_{c_{k+1}}(-) \tag{36c}$$

$$\underline{\hat{q}}_{k+1}(+) = \begin{bmatrix} \frac{1}{2}k_a(\tilde{u}\times\hat{u}) \\ 1 \end{bmatrix} \otimes \underline{\hat{q}}_{k+1}(-) \tag{37a}$$

$$\underline{\hat{b}}_{k+1}(+) = \underline{\hat{b}}_{k+1}(-) + k_b(\tilde{u}\times\hat{u}) \tag{37b}$$

Since, Equations (37a) and (37b) depend on the cross product measurement $(\tilde{u} \times \hat{u})$, the updates to the quaternions and biases are still perpendicular to $\hat{u}$ despite the approximation to the sensitivity matrix.

Steady-State Angles-only Kalman Filter

In this section, a simplified version of the full Kalman filter is shown. The AKF estimates only the quaternion, and not the gyro drift. The covariance and state transition matrices are the upper 3×3 blocks of the corresponding matrices in a full Kalman filter. Therefore, covariance propagation is given by

$$P_{k+1}(-) = \Phi P_k(+) \Phi + w I_{3 \times 3} \tag{38}$$

where w is the assumed scalar level of the process noise. A full angles-only Kalman filter rapidly approaches steady-state using the covariance propagation in Equation (38). Therefore, a steady-state covariance is used. An investigation of the eigenvalues of the covariance matrix shows that there is one large eigenvalue (p_{max}), and two nearly equal smaller eigenvalues (p_{min}). Also, the eigenvector corresponding to p_{max} is found to always be within 2.5 degrees of the sun vector in the body. This reflects the fact that the more accurate sun sensor cannot reduce attitude errors along the sun line, which must be estimated using the less-accurate TAM. Therefore, the covariance matrix is given by

$$P = p_{eye} I_{3 \times 3} + p_{sun} \underline{s} \underline{s}^T \tag{39}$$

where $\underline{s}$ is the sun vector in the body frame, and p_{eye} and p_{sun} are constants. The minimum eigenvalue is given by p_{eye}, and the maximum eigenvalue is given by $p_{eye} + p_{sun}$.

Sun Sensor Update

The sensitivity matrix and measurement covariance for the sun sensor are given by

$$H_s = [\hat{\underline{s}} \times] \tag{40a}$$

$$R_s = r_s I_{3 \times 3} \tag{40b}$$

where $\hat{\underline{s}}$ is the estimated sun vector in the body frame, and r_s is the scalar (isotropic) measurement covariance. The Kalman gain for the sun sensor update requires the computation of

$$\left\{ H_s P H_s^T + R_s \right\}^{-1} = \left\{ p_{eye}[\hat{\underline{s}} \times][\hat{\underline{s}} \times]^T + p_{sun}(\underline{s} \times \hat{\underline{s}})(\underline{s} \times \hat{\underline{s}})^T + R_s \right\}^{-1}$$

$$= \frac{1}{r_s + p_{eye}} \left\{ I_{3 \times 3} + \frac{p_{eye} \hat{\underline{s}} \hat{\underline{s}}^T}{r_s} \right\} \tag{41}$$

Therefore, the Kalman gain matrix is given by

$$K_s = P H_s^T \left\{ H_s P H_s^T + R_s \right\}^{-1}$$

$$= \frac{1}{r_s + p_{eye}} \left\{ p_{eye} I_{3 \times 3} + p_{sun} \hat{\underline{s}} \hat{\underline{s}}^T \right\}[\hat{\underline{s}} \times]^T \left\{ I_{3 \times 3} + \frac{p_{eye} \hat{\underline{s}} \hat{\underline{s}}^T}{r_s} \right\} \tag{42}$$

$$= \frac{p_{eye}}{r_s + p_{eye}} [\hat{\underline{s}} \times]^T$$

If the measurements are processed at a given time by accumulating an incremental error angle $\underline{\alpha}$ initialized at zero, without re-computing the quaternion between updates, the state update becomes

425

$$\underline{\alpha}(+) = \underline{\alpha}(-) + \frac{p_{eye}}{r_s + p_{eye}} \left\{ \underline{\tilde{s}} \times \hat{\underline{s}} - \left(I_{3\times3} - \hat{\underline{s}} \, \hat{\underline{s}}^T \right) \underline{\alpha}(-) \right\} \tag{43}$$

where $\underline{\tilde{s}}$ is the measured sun vector in the body frame.

TAM Update

The sensitivity matrix and measurement covariance for the TAM are given by

$$H_t = [\hat{\underline{m}} \times] \tag{44a}$$

$$R_t = r_t I_{3\times3} \tag{44b}$$

where $\hat{\underline{m}}$ is the estimated magnetic field vector in the body frame, and r_t is the scalar (isotropic) measurement covariance. The Kalman gain for the TAM update requires the computation of

$$\left\{ H_t P H_t^T + R_t \right\}^{-1} = \left\{ p_{eye}[\hat{\underline{m}} \times][\hat{\underline{m}} \times]^T + p_{sun}(\hat{\underline{m}} \times \hat{\underline{s}})(\hat{\underline{m}} \times \hat{\underline{s}})^T + R_t \right\}^{-1} \tag{45}$$

The inverse in Equation (45) is computable in closed form, but is complicated. An approximation is made which assumes r_t is much larger than both p_{eye} and p_{sun}. Therefore, Equation (45) is re-written as

$$\left\{ H_t P H_t^T + R_t \right\}^{-1} \approx \frac{1}{r_t} I_{3\times3} \tag{46}$$

The Kalman gain matrix is now given by

$$\begin{aligned} K_t &= P H_t^T \left\{ H_t P H_t^T + R_t \right\}^{-1} \\ &\approx \frac{1}{r_t} \left\{ p_{eye} I_{3\times3} + p_{sun} \hat{\underline{s}} \, \hat{\underline{s}}^T \right\} [\hat{\underline{m}} \times]^T \end{aligned} \tag{47}$$

The state update is given by

$$\underline{\alpha}(+) = \underline{\alpha}(-) + \frac{1}{r_t} \left\{ p_{eye} I_{3\times3} + p_{sun} \hat{\underline{s}} \, \hat{\underline{s}}^T \right\} \left\{ \underline{\tilde{m}} \times \hat{\underline{m}} - \left(\hat{\underline{m}}^T \hat{\underline{m}} I_{3\times3} - \hat{\underline{m}} \, \hat{\underline{m}}^T \right) \underline{\alpha}(-) \right\} \tag{48}$$

where $\underline{\tilde{m}}$ is the measured TAM vector in the body frame.

Enhanced TRIAD and QUEST Algorithms

In this section, the ETA and EQA are developed. These algorithms are essentially based on an "alpha-type" [5] filter applied to deterministic methods. The TRIAD algorithm [3] involves the construction of two triads from a pair of orthonormal vectors, $\underline{u}$ and $\underline{v}$, with basis vectors given by

$$\underline{l} = \underline{u} \tag{49a}$$

$$\underline{m} = \frac{\underline{u} \times \underline{v}}{|\underline{u} \times \underline{v}|} \tag{49b}$$

$$\underline{n} = \underline{l} \times \underline{m} \tag{49c}$$

The basis vectors are constructed for both body measured vectors $\underline{u}_B$ and $\underline{v}_B$, and for the inertial reference vectors $\underline{u}_I$ and $\underline{v}_I$. Two orthogonal 3×3 matrices are then constructed, given by

$$M_B = \begin{bmatrix} \underline{l}_B & \underline{m}_B & \underline{n}_B \end{bmatrix} \tag{50a}$$

$$M_I = \begin{bmatrix} \underline{l}_I & \underline{m}_I & \underline{n}_I \end{bmatrix} \tag{50b}$$

The attitude matrix maps the inertial reference to the body frame, and can be determined by

$$A = M_B M_I^T \tag{51}$$

An accurate method for extracting the quaternions from the attitude matrix is given in [6].

The TRIAD method (as well as all deterministic) methods requires at least two sets of vector measurements to determine the attitude matrix. This method subsequently fails when only one set of vector measurements (e.g., TAM data only) is available. Also, deterministic methods fail when vectors are co-aligned (i.e., $|\underline{u} \cdot \underline{v}| = 1$). These difficulties are overcome by combining the TRIAD determined quaternions with a gyro-propagated model and a simple first-order filter. The ETA is given by

$$\underline{q}_p(+) = \exp\left\{\frac{1}{2}\Omega\!\left(\tilde{\underline{\omega}}_g\right)\Delta t\right\}\hat{\underline{q}}(-) \tag{52a}$$

$$\hat{\underline{q}}(+) = (1-\alpha)\underline{q}_p(+) + \alpha\,\underline{q}_{triad}(+) \tag{52b}$$

where $\underline{q}_p$ is the propagated quaternion, $\hat{\underline{q}}$ is the estimated quaternion, and $\underline{q}_{triad}$ is the quaternion extracted from the TRIAD determined attitude matrix. The scalar gain variable α is given by

$$\alpha = \left(1 - |\underline{u} \times \underline{v}|^2\right)\alpha_0 \tag{53}$$

where α_0 is a constant gain. The filter gain in Equation (53) is automatically adjusted to accommodate periods of vector co-alignment (i.e., as the vectors become co-aligned, the gain approaches 0). Also, α_0 is set to zero when only one measurement set is available.

The ETA is essentially a first-order "additive" Kalman filter. In general, this approach will not maintain quaternion normalization [7]. To investigate how the ETA affects quaternion normalization, Equation (52b) may be re-written as

$$\hat{\underline{q}} = \underline{q}_p \otimes \left[I_q + \alpha\!\left(\underline{q}_p^{-1} \otimes \underline{q}_{triad} - I_q\right)\right] \tag{54}$$

where I_q is the identity quaternion. If the propagated quaternion is close to the TRIAD determined quaternion, then Equation (54) can be approximated accurately by

$$\hat{\underline{q}} \approx \underline{q}_p \otimes \begin{bmatrix} \dfrac{1}{2}\alpha\,\delta\underline{\theta} \\ 1 \end{bmatrix} \tag{55}$$

where $\delta\underline{\theta}$ is the angle vector between $\underline{q}_p$ and $\underline{q}_{triad}$. Therefore, since α_0 is very small, normalization is maintained to within first-order. For numerical precision, the quaternions are explicitly normalized.

The EQA is similar to the ETA, but uses the QUEST [4] algorithm to determine attitude. The QUEST algorithm minimizes the following cost function [8]

$$L(A) = \frac{1}{2}\sum_{k=1}^{n} a_k\left|\underline{w}_k - A\,\underline{v}_k\right|^2 \tag{56}$$

where $\underline{w}$ is a set of unit vector observations in the body-frame, $\underline{v}$ is a set of unit observations with respect to the inertial frame, and n is the total number of vector measurement sets. The constants a_k serve to weight individual sensor measurements. Shuster [4] has shown that the maximum-likelihood estimate of the attitude is obtained with weights given by

$$a_k = \frac{1}{\sigma_k^2} \tag{57}$$

where σ_k is the standard-deviation of the measurement error process for each sensor.

TRMM Simulation and Results

In order to compare the algorithms developed in this paper, a simulation study is performed using TRMM orbit parameters and performance criteria. The simulated spacecraft has a near circular orbit at 350 km, and completes an orbit in approximately 90 minutes. The nominal mission mode requires a rotation once per orbit (i.e., 236 deg/hr) about the spacecraft's y-axis while holding the remaining axis rotations near zero. The "true" magnetic field reference is modeled using a 10th order International Geomagnetic Reference Field (IGRF) model. In order to simulate magnetic field modeling error, a 6th order IGRF is used to develop "measurements." TAM sensor noise is modeled by a Gaussian white-noise process with a mean of zero and a standard deviation of 0.5 mG. The two DSS's each have a field of view of about $50° \times 50°$. The body to sensor transformations for each sensor is given by

$$T_1 = \begin{bmatrix} -0.5736 & 0 & -0.8192 \\ 0.4096 & 0.866 & -0.2868 \\ 0.7094 & -0.5 & -0.4967 \end{bmatrix} \tag{58a}$$

$$T_2 = \begin{bmatrix} -0.5736 & 0 & 0.8192 \\ -0.4096 & 0.866 & -0.2868 \\ -0.7094 & -0.5 & -0.4967 \end{bmatrix} \tag{58b}$$

Each DSS views the sun when the sensor view is greater than the cosine of $50°$. The two DSS's combine to provide sun measurements for about 2/3 of a complete orbit. The DSS sensor noise is also modeled by a Gaussian white-noise process with a mean of zero and a standard deviation of $0.05°$. The gyro "measurements" are simulated using Equations (12) and (13), with a gyro noise standard deviation of 0.062 deg/hr, a ramp noise standard deviation of 0.235 deg/hr/hr, and an initial drift of -0.1 deg/hr on each axis.

A plot of the roll, pitch, and yaw attitude errors for a typical simulation run using the full Kalman filter is shown in Figure 1. A plot of the corresponding gyro-bias estimates is shown in Figure 2. From Figure 1, the roll and yaw attitude errors show a strong dependence on orbit rate which is centered at zero, and a pitch error which is biased. This error bias may be due to non-Gaussian modeling errors in the magnetic field "measurements." These nonlinearities cause an error in inertial space which is not zero-mean and is largely along the sun line. When these errors are mapped into the body frame, sinusoidal motions occur in roll and yaw which are $90°$ out of phase from each other. Also, a biased error occurs in pitch which has the same magnitude as the sinusoidal motion, since the sun vector is $45°$ off the pitch axis. This can be shown mathematically by redefining an inertial reference fixed on the orbit plane with the x-axis tangent to the orbit plane, the z-axis pointed nadir, and the y-axis completing the triad. For a zero rotation, the inertial reference corresponds to the body frame. Therefore, from Figure 1 a starting value for the inertial reference can be chosen such that the z-axis is zero, and the remaining axes equal in magnitude. The mapping to the body frame for a rotation about the y-axis is given by

$$\underline{e} = \delta \begin{bmatrix} \cos(\mu) & 0 & \sin(\mu) \\ 0 & 1 & 0 \\ -\sin(\mu) & 0 & \cos(\mu) \end{bmatrix} \underline{s} = \frac{1}{\sqrt{2}} \begin{bmatrix} \cos(\mu) \\ 1 \\ -\sin(\mu) \end{bmatrix} \tag{59}$$

where μ is the true anomaly, δ is the magnitude of the error, and $\underline{s}$ is the direction of the sun vector, given by.

$$\underline{s} = \begin{bmatrix} 1 \\ 1 \\ 0 \end{bmatrix} \tag{60}$$

Clearly, a sinusoidal motion and constant bias is shown by Equation (59). This effect is also seen when using a Kalman filter on other spacecraft (e.g., UARS and SAMPEX). However, the full Kalman filter is able to estimate attitudes to within $0.1°$, and estimates the gyro-drift fairly accurately.

A plot of the attitude errors for a typical simulation run using the IKF is shown in Figure 3. There is no clear orbit rate dependence in roll and yaw for this algorithm, but all angle errors are now biased. This may be due to the fact that the IKF assumes that the attitude covariance is equal in all directions, so that any biased errors are translated into all axes. The gyro-bias estimates (shown in Figure 4) are estimated more accurately using the IKF, as compared to the full Kalman filter. However, comparing magnitude attitude errors in Figure 3 to Figure 1 shows that attitude accuracy is no better than the full Kalman filter.

A plot of the attitude errors using the AKF is shown in Figure 5. The errors in roll and pitch are biased, while the yaw error has a mean near zero. These errors are likely due to not correcting for gyro bias in the filter. This is further depicted in the attitude covariance matrix, which is an order of magnitude larger than the full Kalman filter attitude covariance. However, attitude accuracy is still comparable to the full Kalman filter (i.e., within 0.1°).

A plot of the attitude errors using the ETA is shown in Figure 6. The peak errors seen predominately in the pitch and yaw errors are due to periods of sun un-observability. During these periods, the filter gain (shown in Figure 7) is set to zero, so that attitude is determined from gyro-propagation solely. Also, the gain clearly shows a sinusoidal motion. This motion compensates for measurement vector co-alignment. Attitude accuracy for this simple approach is within 0.15°. Also, the EQA improves the attitude accuracy slightly, but not to any appreciable amount.

Table 1 shows a summary of telemetry requirements, on-board table (initialization) requirements, code size, and performance results for each algorithm described in this paper. Clearly, comparable performance with respect to the full Kalman filter is possible using either the IKF or AKF. Also, the AKF requires less telemetry and table values, and requires less coding size than either the full Kalman filter or the IKF. The ETA requires the least amount of telemetry and table values, and requires the least amount of coding. Even though attitude accuracy is slightly degraded as compared to the full Kalman filter, the simulation study indicates that the 0.7° attitude knowledge requirement is clearly met.

Table 1 Telemetry and Table Values, Code Size, and Performance

	Full KF	IKF	AKF	EQA	ETA
Telemetry	~40 values	~25 values	~15 values	~5 values	~5 values
Table	~30 values	~20 values	~15 values	~8 values	~5 values
Code Size	<6 K	<4K	<4 K	<2 K	<1 K
Performance	<0.1°	<0.1°	<0.1°	<0.14°	<0.15°

Conclusions

A number of alternatives to using a full Kalman filter for attitude estimation was presented in this paper. In order to quantify the performance of these proposed algorithms, a simulation study was performed for the TRMM spacecraft. The results of this simulation study indicated that comparable accuracy with respect to a full Kalman filter design is possible. In particular, the ETA was shown to be an effective attitude estimator, while at the same time dramatically decreasing coding size, and telemetry and on-board requirements. Although the full Kalman filter was chosen for the final contingency mode of TRMM, the study presented in this paper provided valuable alternatives for future attitude estimation schemes.

Acknowledgment

References

[1] *TRMM Attitude Control Subsystem Specifications*, NASA-Goddard Space Flight Center (GSFC-TRMM-712-046).

[2] Lefferts, E.J., Markley, F.L., and Shuster, M.D., "Kalman Filtering for Spacecraft Attitude Estimation," *Journal of Guidance, Control and Dynamics*, Vol. 5, No. 5, Sept.-Oct. 1982, pp. 417-429.

[3] Wertz, J.S. (ed.), *Spacecraft Attitude Determination and Control*, D. Reidel Publishing Co., Dordrecht, The Netherlands, 1984.

[4] Shuster, M.D., and Oh, S.D., "Three-Axis Attitude Determination from Vector Observations," *Journal of Guidance and Control*, Vol. 4, No. 1, Jan.-Feb. 1981, pp. 70-77.

[5] Crassidis, J.L., Mook, D.J., and McGrath, J.M., "Automatic Carrier Landing System Utilizing Aircraft Sensors," *Journal of Guidance, Dynamics and Control*, Vol. 16, No. 5, Sept.-Oct. 1993, pp. 914-921.

[6] Sheppard, S.W., "Quaternion from Rotation Matrix," *Journal of Guidance and Control*, Vol. 1, No. 3, May-June 1978, pp. 223-224.

[7] Bar-Itzhack, I.Y., and Deutschmann, J.K., "Extended Kalman Filter for Attitude Estimation of the Earth Radiation Budget Satellite," *Proceedings of the AAS Astrodynamics Conference*, Portland, OR, August 1990, AAS Paper #90-2964, pp. 786-796.

[8] Wahba, G., "A Least-Squares Estimate of Satellite Attitude," Problem 65-1, *SIAM Review*, Vol. 7, No. 3, July 1965, pg. 409.
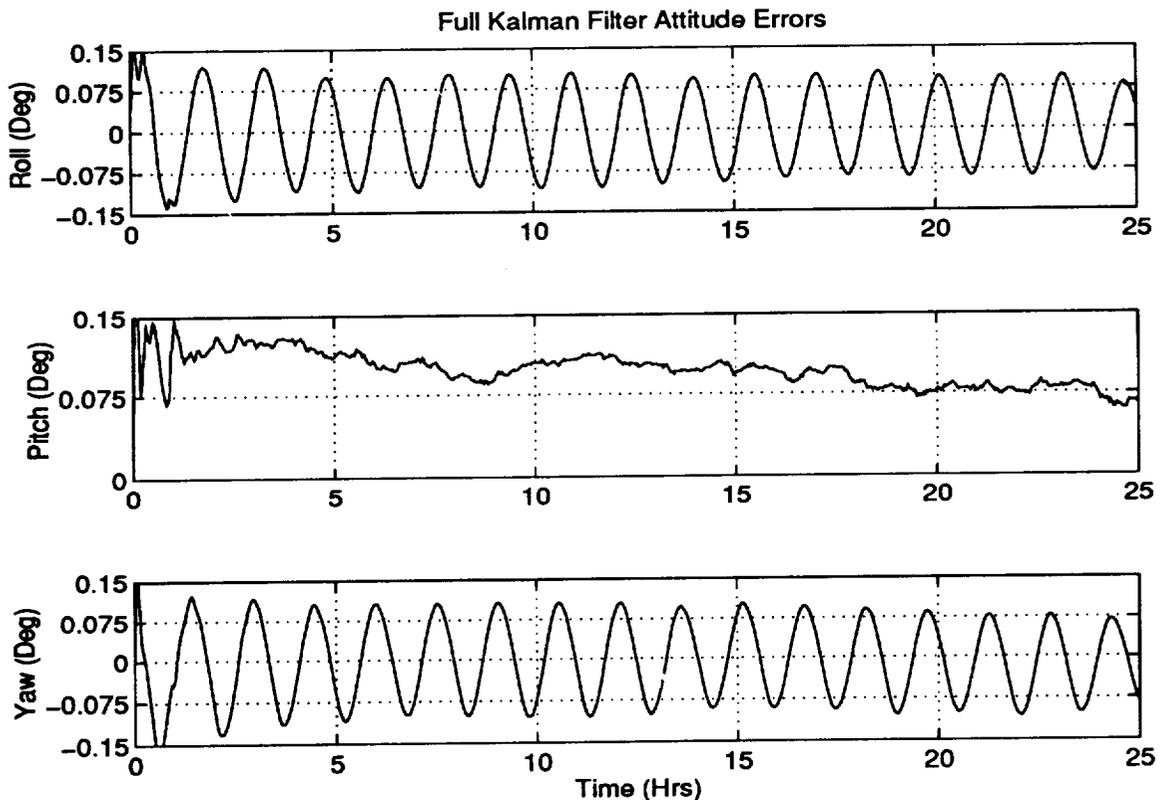
**Figure 1 Kalman Filter Attitude Errors**
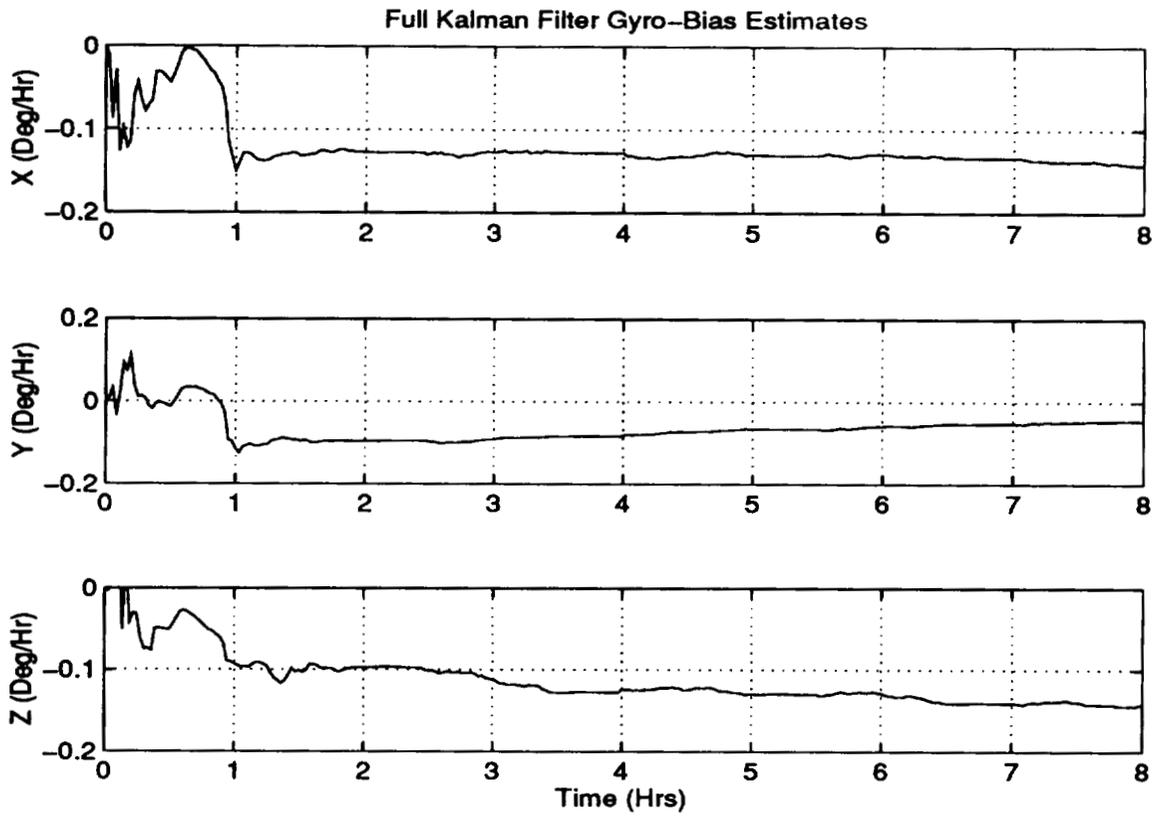
Figure 2 Kalman Filter Gyro Bias Estimates
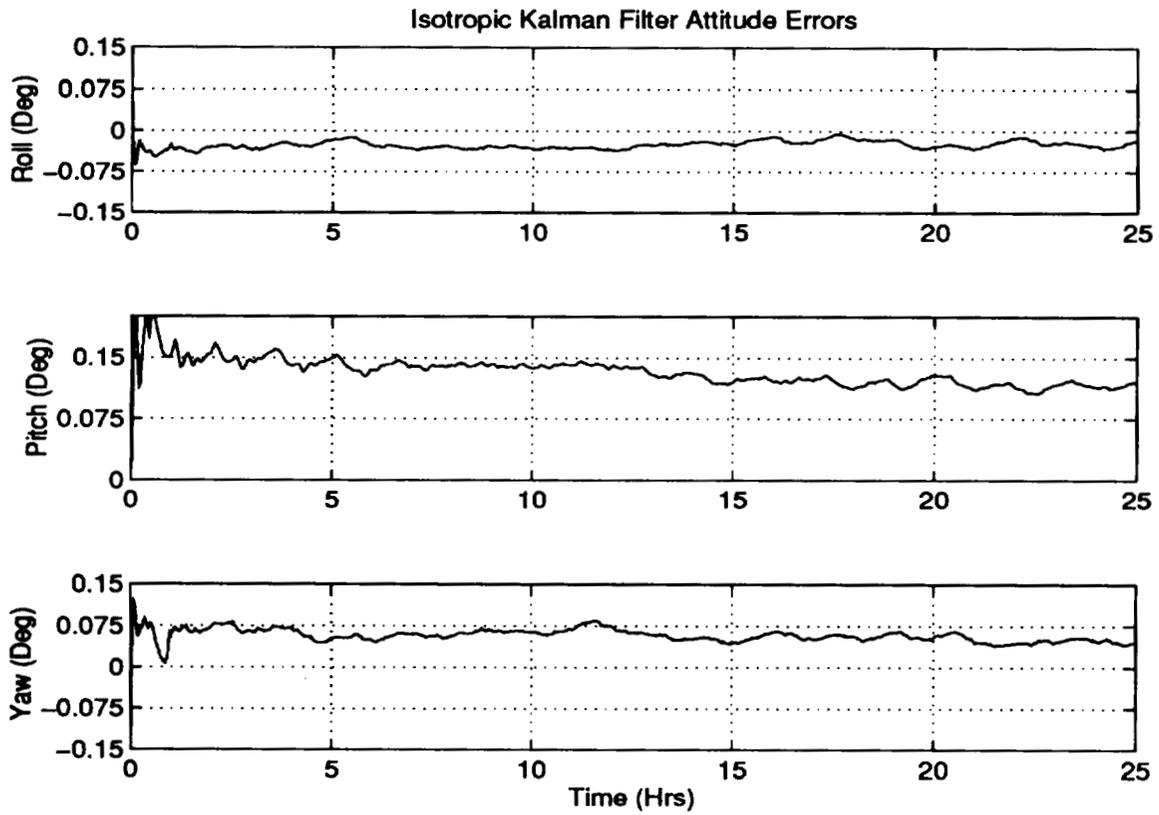
Figure 3 Isotropic Kalman Filter Attitude Errors

431

Isotropic Kalman Filter Gyro-Bias Estimates
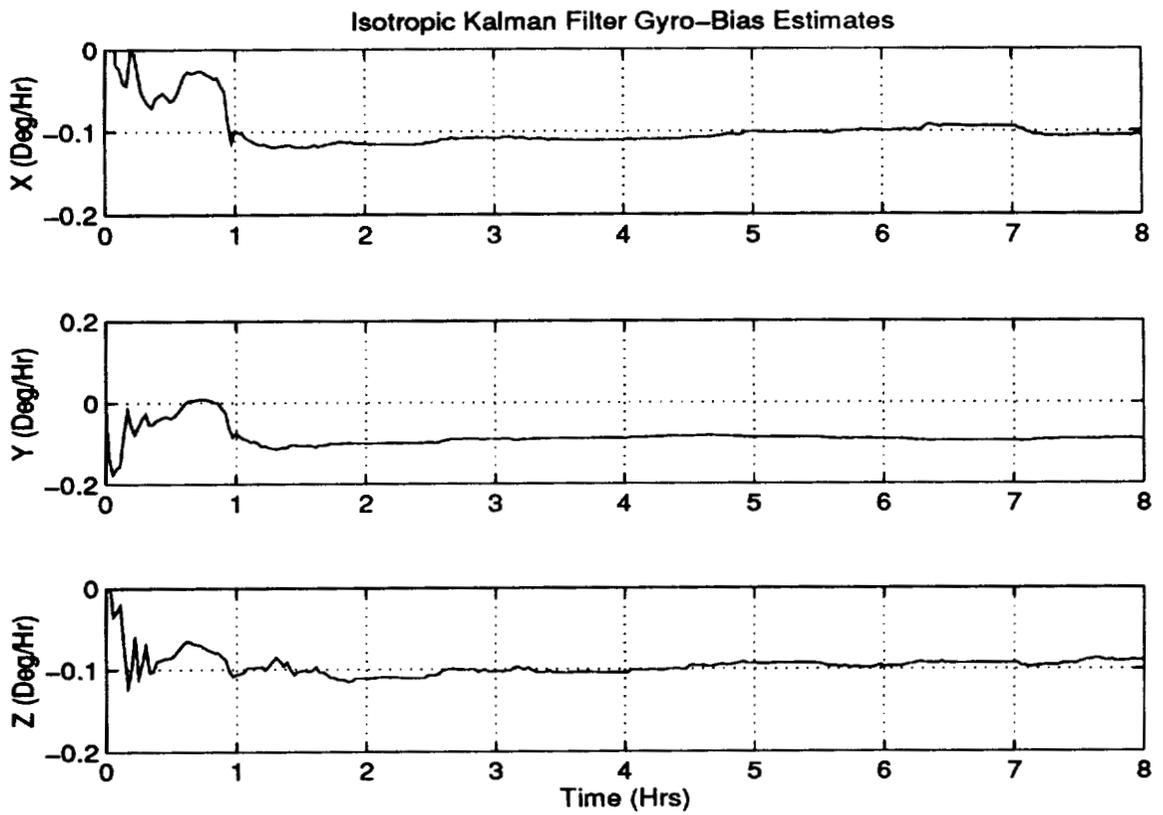
Figure 4 Isotropic Kalman Filter Gyro Bias Estimates

Angles-Only Kalman Filter Attitude Errors
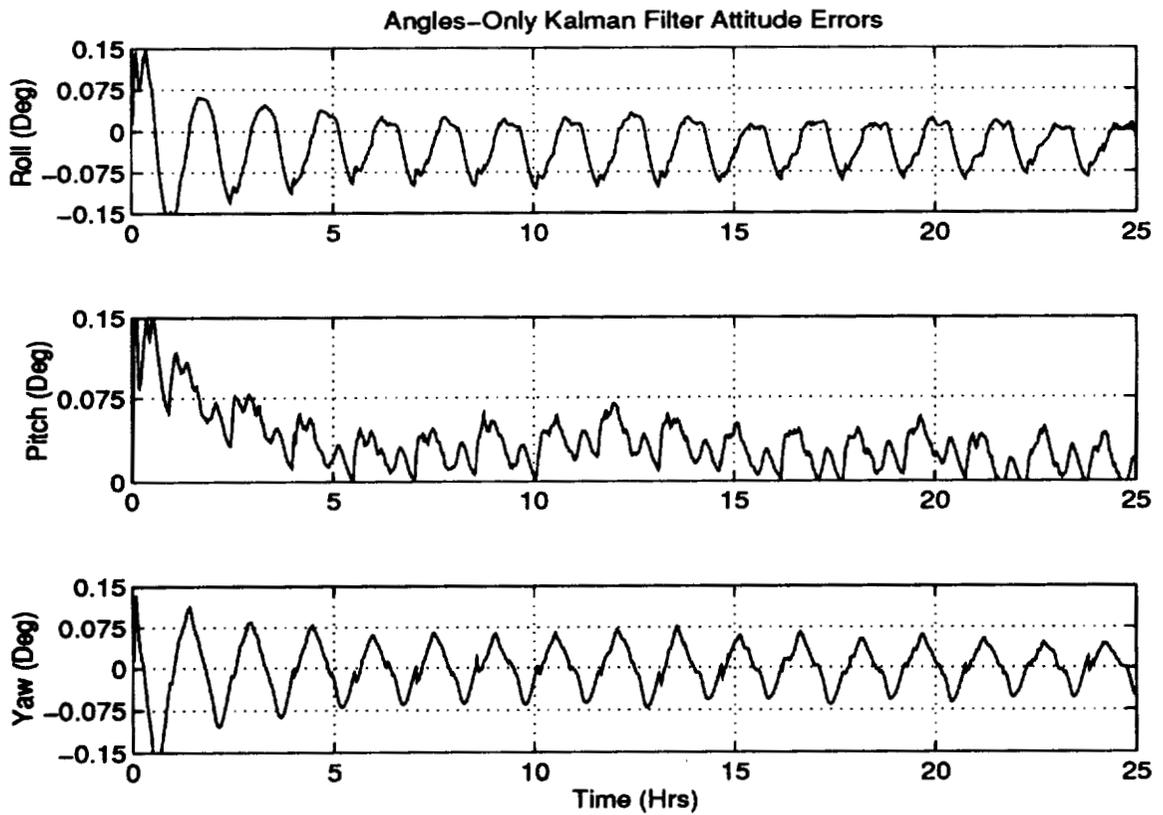
Figure 5 Angles-only Kalman Filter Attitude Errors

432
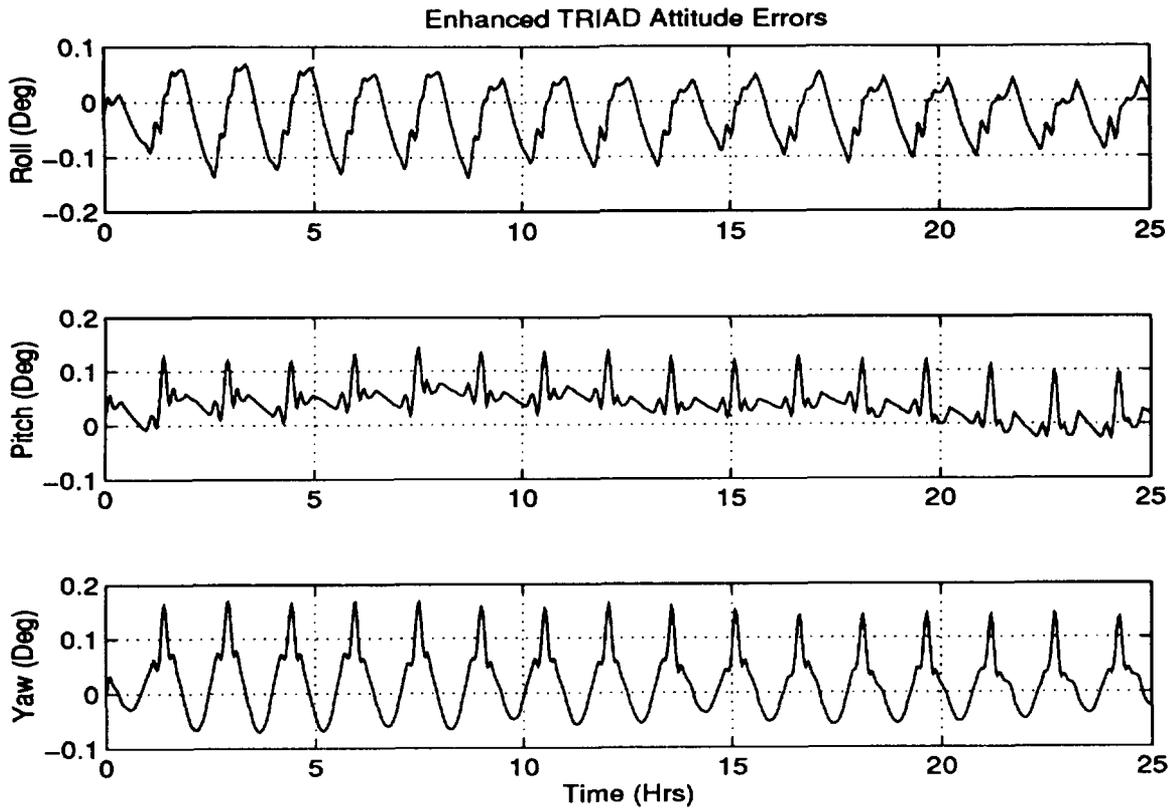
Figure 6 Enhanced TRIAD Attitude Errors
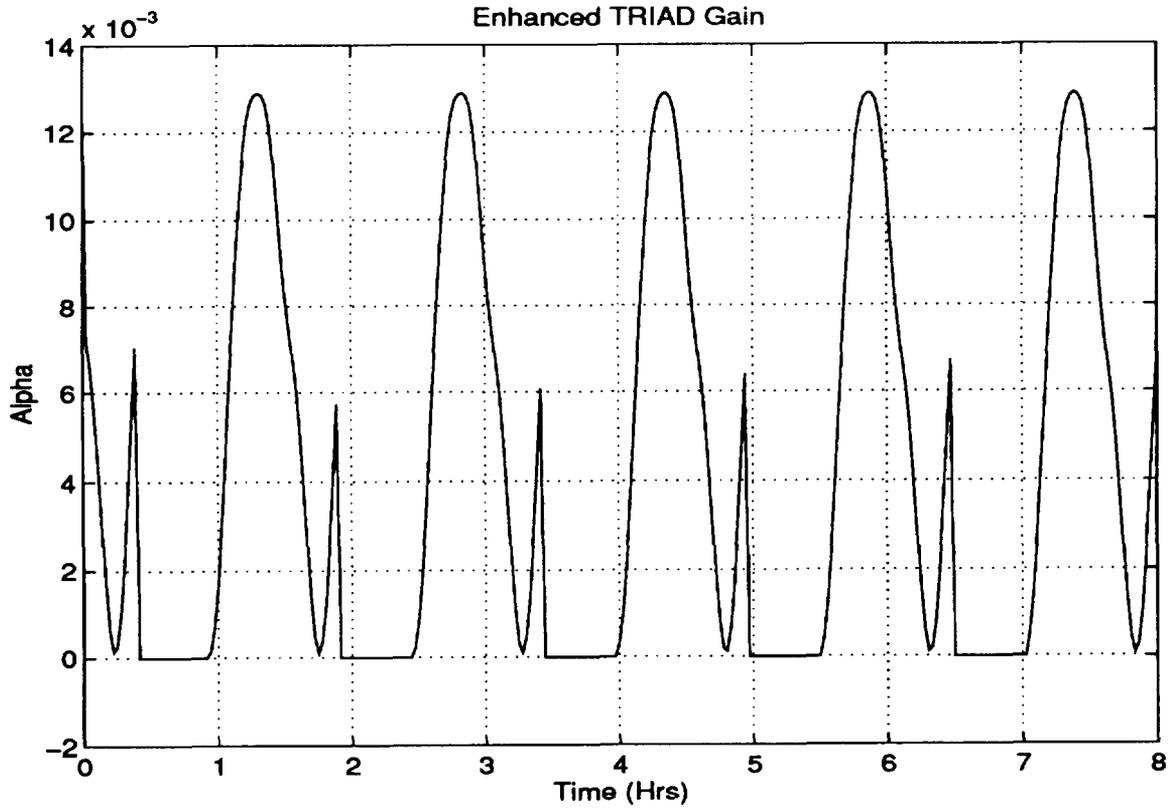
Figure 7 Enhanced TRIAD Filter Gain

ORION - A SUPERSYNCHRONOUS TRANSFER ORBIT MISSION

I M Walters,   J F Baker,   I M Shurmer*
Matra Marconi Space Systems Plc, Stevenage, UK

ORION F1 was launched on 29th November 1994 on an Atlas IIA launch vehicle. It was designed, built and delivered in-orbit by Matra Marconi Space Systems Plc and was handed over to ORION Satellite Corporation on 20th January 1995 at its on-station longitude of 37.5°W. The mission differed significantly from that of any other geostationary communications satellite in that the Transfer Orbit apogee altitude of 123,507 km was over three times geosynchronous (GEO) altitude and one third of the way to the moon.

The SuperSynchronous Transfer Orbit (SSTO) mission is significantly different from the standard Geostationary Transfer Orbit (GTO)mission in a number of ways. This paper discusses the essential features of the mission design through its evolution since 1987 and the details of the highly successful mission itself including a detailed account of the attitude determination achieved using the Galileo Earth and Sun Sensor (ESS).

THE ORION SYSTEM

The ORION Launch and Early Orbit Phase (LEOP) was the first use of the Satellite Control Centre at MMS, Stevenage. This was the first LEOP Control Centre built in the UK and was designed and built in-house in preparation for the ORION launch. All of the LEOP operations were performed by MMS staff. The Control Centre made use of the ground stations at Perth, Allan Park and Chilworth for TM/TC and tracking from the TELESAT network, and the newly built ORION station at Mt. Jackson, VA.

QUARTZ, the Flight Dynamics software used during the LEOP was written specifically for, although not limited to, the ORION F1 mission. It consists of a VAX workstation based environment with a central database and a high quality MOTIF user interface. Many of the algorithms had been well tested previously within the mission department of the company and these were brought together into an integrated suite of Flight Dynamics software.

The ORION spacecraft weighed 2361 kg at launch, 1200 kg of which was liquid propellant. Injection into the various transfer orbits was performed using a 490 N Marquardt Liquid Apogee Engine. The spacecraft was passively spin stabilised at 12 rpm during the Transfer Orbit phase. The propulsion system is combined with the

on-station thrusters so that any propellant saved during Transfer Orbit was used directly to extend life.

Because of the special nature of the super-synchronous transfer orbit, before describing the results of the LEOP itself, some of the pertinent aspects of the mission design are outlined below.

MISSION DESIGN

The following points provide the reasons and the logic behind the supersynchronous mission design.

The launch vehicle selected for the ORION mission was the Atlas IIA manufactured by Martin Marietta Commercial Launch Services. Due to the latitude of the launch site, the injection orbit would have an inclination between 23 and 27.5 degrees.

If ORION had used a standard transfer orbit (i.e. apogee at GEO altitude) with such an inclination, the propellant costs would have been prohibitive and the lifetime requirements would not have been met. Although the excess launch vehicle propellant could have been used to reduce the inclination further, the lifetime would still have been less than 7 years.

By selecting the SSTO, the propellant costs to GEO were significantly reduced. In SSTO the majority of the plane change is performed at apogee. It is most efficient at apogee because this is where the spacecraft is moving the slowest and it is close to the ascending node. The higher the apogee the lower the spacecraft velocity and hence, the more efficient the plane change.

Pushing out the apogee radius to 130,000 km, making use of excess performance available from the launch vehicle, made the plane change for ORION much more efficient - see the comparison below:

ΔV to reach Drift Orbit

Ariane standard GTO   approx. 1505 m/s
ATLAS IIA GTO   greater than 1750 m/s
ORION SSTO   1473 m/s

The SSTO mission therefore significantly decreases the ΔV required by the Liquid Apogee Engine (LAE) and thereby enabled ORION to achieve the lifetime requirement.

Figure 1 shows the SSTO relative to the geostationary orbit.
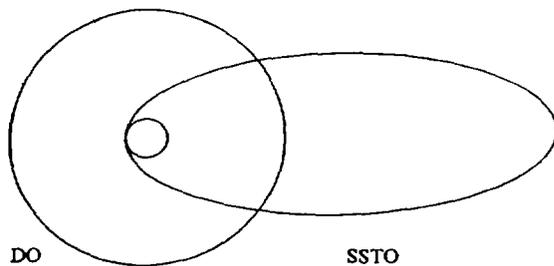
Figure 1   SSTO and GEO

The overall strategy to transfer from the SSTO to GEO is to perform a burn at apogee to raise the perigee to geosynchronous. A retrograde burn at the perigee of this Intermediate Transfer Orbit (ITO) then lowers the apogee down to geosynchronous.

To further minimise the propellant usage during LEOP, two apogee burns were selected rather than one. This improved the mission's robustness to uncertainties in the LAE performance and the attitude determination.

Two perigee burns were also selected at perigees 4 and 6 (see Table 1). The reasons behind this decision are as follows:

Table 1 Nominal LEOP Burn Strategy

Burn	Apse	Nature	ΔV (m/s)	Transfer	T - T$_0$ (hrs)
1	A1	Prograde	643.93	SSTO-ITO1	24.04
2	A2	Prograde	131.89	ITO1-ITO2	86.86
3	P4	Retrograde	329.12	ITO2-ITO3	190.17
4	P6	Retrograde	367.87	ITO3-DO	264.67

The ORION spacecraft has linearly polarised telemetry (TM) and telecommand (TC) bicone antennas with their boresights in the spacecraft XY plane. During the critical Sun and Earth Acquisition manoeuvres in Drift Orbit (DO), which involved the spacecraft rotating about its X-axis, it was necessary to have a ground station which could operate in circularly polarised mode to ensure continuous TM/TC access. There was only one ground station from the tracking network which could provide this service - Allan Park. This ground station also covered the on-station longitude.

Thus it was decided to design the nominal strategy such that in the event of having to adopt a burn back-up scenario, it would always be possible to re-target the longitude of the final perigee burn (entry into DO) to be close to on-station and hence above the horizon at Allan Park.

Various scenarios were investigated, but it was decided that two perigee burns, separated by two orbit revolutions, provided the longitude re-targeting flexibility required. By varying the proportion of the first perigee burn, the final burn longitude could be adjusted. Not only did this provide the flexibility for the burn back-up (BBU) scenarios (see Table 2), it also provided the ability to correct for any errors from the two apogee burns in the nominal scenario.

Table 2 Nominal & Burn Back-up (BBU) Strategies

Strategy	ΔV1 (m/s)	ΔV2 (m/s)	ΔV3 (m/s)	ΔV4 (m/s)	ΔV5 (m/s)	Final Longitude
Nominal	643.9	131.9	329.1	367.9	-	332.5° E
1BBU	644.4	132.0	332.1	364.8	-	332.6° E
2BBU	643.9	131.9	254.9	442.0	-	332.5° E
3BBU	643.9	131.9	303.2	393.8	-	332.6° E
4BBU	643.9	131.9	329.1	53.2	314.6	332.5° E

Note that always having to achieve a certain longitude with the final burn drove the fourth burn back-up (4BBU) strategy to have 5 burns - an extra burn was added to allow longitude re-targeting (see Table 2).

Adoption of a multiple burn super-synchronous strategy was unavoidably going to result in a transfer orbit duration much greater than ever experienced before. The impacts on the spacecraft system design were potentially significant and had to be carefully studied during the spacecraft design phase. In order to minimise the impact of the extended duration, the number of revolutions between burns was kept to a minimum.

The spacecraft Earth Elevation Sensor (EES) cant angle was carefully chosen such that, during any one transfer orbit revolution, two EES data passes (used for attitude determination) were available - one at perigee and another on the ascent to apogee (see Figure 2).
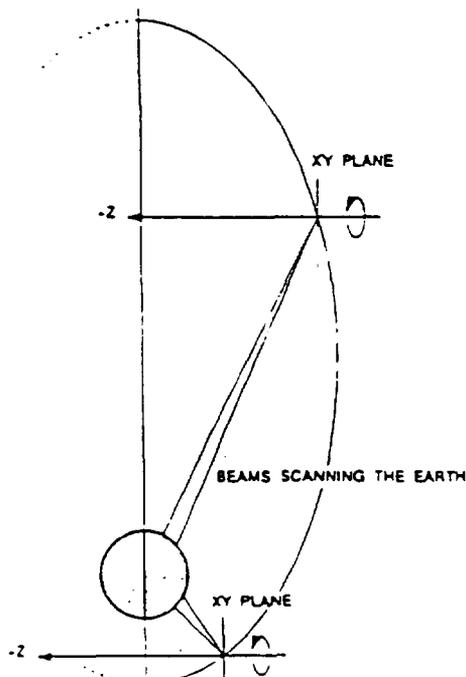
Figure 2 EES Apogee and Perigee Passes

To be able to minimise the number of orbital revolutions between burns, it was decided to use the perigee ESS data passes as well as the apogee passes. However it is not advisable to use the ESS below an altitude of 25,000 km. so the first apogee burn was sized to ensure that the perigee altitude of ITO1 was at least 25,000 km. Therefore, after the first LAE firing all perigee ESS data was deemed usable for attitude determination purposes. This resulted in a fixed 85%:15% apogee burn split.

Major Technical Issues

During the proof of concept phase of the mission a number of major technical issues. themselves a product of the

super-synchronous strategy, had to be addressed and resolved satisfactorily. The points below summarise the most significant issues:

* *Attitude Determination:* ORION was to make use of both perigee and apogee ESS data passes (see Figure 2) for attitude determination during transfer orbit. The super-synchronous strategy had raised some interesting questions that had to be answered:

The apogee ESS passes occur at altitudes in excess of 100,000 km. The sensor had never been used at such extreme altitudes before. The major effect is that the earth appears much smaller in the sensor field of view - hence the earth chords are much smaller. On the other hand, the spacecraft is moving so much slower at the high altitude that each apogee pass lasts for several hours - providing much more data that ever previously obtained.

Thus. for the apogee passes. the amount of data was not a problem. the questions to be answered were: How would the sensor behave with such small chords and how would these small chords affect the attitude determination solution ?

Thus a detailed analysis had to be performed, which involved modelling the sensor, to prove that the spacecraft attitude could be determined to sufficient accuracy for manoeuvre planning purposes.

* *TM/TC Link Margins:* The obvious effect of pushing the apogee radius out to near 130,000 km was to place considerable strain on the link margins. It was essential to guarantee adequate link margin since the critical LAE burns were to be performed when the spacecraft was at its greatest distance from the earth. Detailed analysis had to be performed, which involved calculating the link margins at every point in the orbit. to prove that links were available for these critical operations.

* *Long TM/TC Outages:* ORION's TM/TC antenna configuration consists of TM/TC +Z horns plus TM/TC bicone antennas with their boresights in the spacecraft XY plane. The resultant TM/TC nulls about the spacecraft are illustrated in Figure 3.

Due to the TM/TC null at the rear (-Z) of the spacecraft. TM/TC outages were experienced in every orbit on the descent from apogee. These outages ranged from 4 hours in SSTO up to 19 hours in ITO2.

Substantial analysis was performed to demonstrate that the spacecraft was robust to failures and had

437

sufficient autonomy to cope with such outages. An on-board applications program was developed to increase the spacecraft's autonomy during outages. This program was configured from the ground prior to outage entry. The analysis concluded that the risk presented by these outages was acceptable. Note, in the event of a spacecraft anomaly which prohibited the spacecraft being out of contact with the ground for any extended period, the back-up solution was to perform a slew manoeuvre to the orbit pole to avoid the outages.
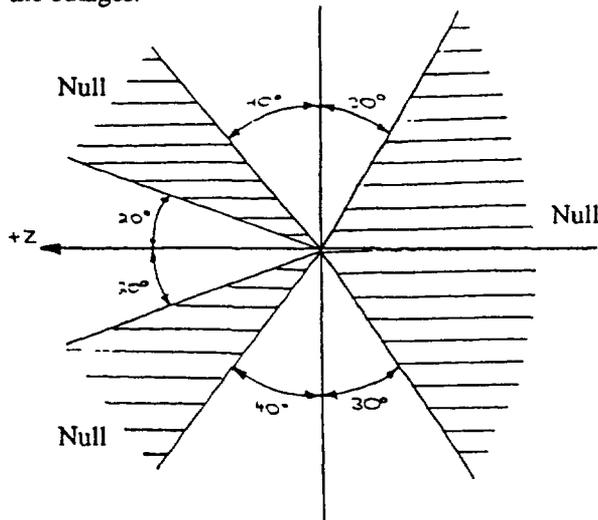

Figure 3   TM/TC Antenna Nulls

- *Orbit Determination:* The orbital geometry associated with the super-synchronous mission was significantly different to any experienced beforehand. Sufficient analysis had to be performed to confirm that the orbit could be determined to sufficient accuracy, within the time available. This was performed using an observations generator to simulate tracking data and using the QUARTZ orbit determination software to establish the attainable accuracy.

- *Launch Window:* Efforts were made to provide launch opportunities on every day of the year. As it turned out, this was not possible.

The eclipse seasons presented some interesting problems. Midday launches were ruled out, since terrestrial eclipses lasted 6 hours around apogee due to the fact that the spacecraft is moving so slowly. To achieve a midnight launch opportunity during the eclipse season, it was necessary to bias the eclipses away from perigee and hence away from the perigee burns - burning in an eclipse would have meant having no spin rate or nutation data during the burn which was not acceptable. This biasing had major

impacts on the allowable Solar Aspect Angle during LEOP.

Another consideration, unique to the super-synchronous strategy, was the effect of lunar gravity on the injection orbit. Depending on the relative positions of the moon and the spacecraft's orbit, the lunar gravity could have the effect of raising or lowering the injection orbit perigee by hundreds of kilometres. The 1BBU strategy (see Table 3) results in the spacecraft spending 1.5 revolutions in the injection orbit. Potentially, the lunar gravity could lower second perigee to an altitude below 167 km (nominal = 185 km) at which point the resultant heating effect on the spacecraft would be unacceptable. Hence, the launch window would be closed due to these lunar gravity effects.

Table 3   Nominal & BBU Strategies

Strategy	Burn Apses	Total ΔV (m/s)	Transfer Orbit Duration (hrs)
Nominal	A1,A2,P4,P6	1472.8	264.67
1BBU	A2,A3,P5,P7	1473.4	312.53
2BBU	A1,A3,P5,P7	1472.8	336.48
3BBU	A1,A2,P5,P7	1472.8	336.48
4BBU	A1,A2,P4,P7,P8	1472.8	336.47

The LAE Burn Strategy

Figure 4 shows the LAE Burn Strategy and the resultant intermediate orbits between SSTO and Drift Orbit (DO).
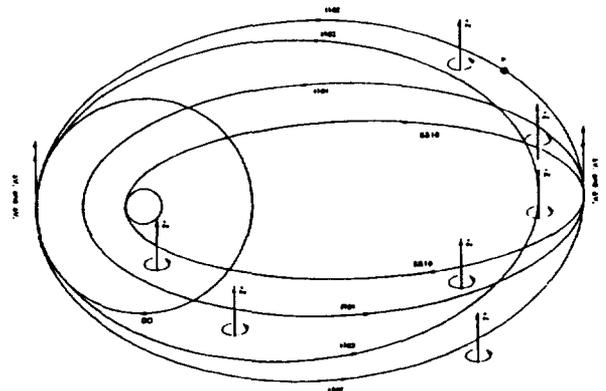

Figure 4   LEOP Nominal Burn Strategy

438

Table 4 Nominal Strategy - Orbit Details

Orbit	SemiMajor Axis (km)	Eccentricity	Inc. (deg)	Period (hrs)
SSTO	68223.95	0.9038	26.0	49.26
ITO1	80240.39	0.6005	3.12	68.83
ITO2	85296.20	0.5056	1.10	68.86
ITO3	56627.42	0.2553	0.63	37.25

The following points should be noted from the SSTO Strategy tables:

- The possibility of missing any one of the nominal burn opportunities is taken into account in the design.

- The total LAE ΔV requirement is approximately 1473 m/s.

- Going to any back-up strategy results in a negligible propellant penalty.

- The same final sub-satellite longitude is achievable regardless of the burn strategy adopted. (The on-station longitude for ORION F1 is 322.5 East).

- The sizes of the two apogee burns are effectively fixed, while those of the two perigee burns can vary significantly, from one burn strategy to another.

- Almost all the orbital plane change is performed by the two apogee burns.

- The duration of the transfer orbit can range from 265 to 337 hours, i.e. 11 to 14 days.

Once the spacecraft achieves Drift Orbit the operational activities required to achieve three-axis stabilised, Earth pointing, normal mode are relatively standard for this type of spacecraft, i.e. Sun Acquisition, followed by Earth Acquisition, entry into normal 3-axis mode and then station acquisition.

RESULTS OF THE ORION MISSION

The Atlas IIA flight designated AC110 launched at the opening edge of the 84 minute window at 10:21 UT on 29th November 1994. The first attempt on 21st November was delayed due to adverse weather and the second attempt on the 22nd was aborted four seconds before lift-off due to a launch vehicle minor mechanical fault.

The ascent phase of the Atlas and both phases of the Centaur upper stage powered flight were described as perfect by the Atlas launch team. The second Centaur burn was retargeted to reduce the Transfer Orbit inclination from 26.9° to 25.7° as the on-board computer estimated a Propellant Excess of 45 lb. due primarily to favourable winds during the Atlas phase. As the retargeted Transfer Orbit would mean the spacecraft would rise in a different place as seen by the Perth Ground Station, the Atlas launch team relayed the new targeted inclination in real-time to allow Perth to relocate their Antenna position before Acquisition.

Spacecraft separation occurred on time at 10:51. The telemetry beacon was detected by the Perth ground station twelve minutes later as it rose above the horizon, and telemetry lock was achieved at Stevenage at 11:04:08, exactly as predicted. No search pattern was required, hinting at an accurate injection by Centaur. The Atlas launch team estimated a spin rate at separation of 5.053 rpm, confirmed one hour later from the spacecraft sun sensor at 4.937 rpm.

At 11:25, the Atlas launch team provided their estimated Transfer Orbit parameters and attitude prior to separation.

The retargeted and achieved Transfer Orbit parameters were:

	Target	Achieved
ra (km)	129, 885	130, 233
rp (km)	6563.1	6563.5
i (deg.)	25.700	25.686
Ω_G (deg)	173.6	173.5
ω (deg)	179.98	179.98

After 23 hours of tracking we were able to confirm this orbit to within 4 km which was within the error of the estimate. Confirmation of the attitude had to wait until an orbit match was performed through the first apogee firing, and was found to be within 0.5° of the target, well within the 1.5° specified.

The following operations then took place in the next five hours:

- Immediately after initial acquisition by the tracking network, the spacecraft underwent a health check of all subsystems.

- The spacecraft was configured for transfer orbit by switching on the attitude control equipment and pressurising the propulsion subsystem.

- The payload reflectors were then deployed once the injection spin rate was confirmed. This decreased the

spin rate to 4.3 rpm due to the increase in spacecraft inertia.

- A spin-up manoeuvre was then performed to the nominal transfer orbit spin rate of 12 rpm required for stability during the LAE firings.

With the spacecraft now ready for its first LAE firing at Apogee 1, Flight Dynamics activities were to determine the orbit and attitude and to optimise the sequence of firings. The following sections describe the orbit and attitude determination and manoeuvre planning in more detail.

ORBIT DETERMINATION

Range, azimuth and elevation data was received from the TELESAT network via the Ottawa hub. The data was filtered and smoothed by QUARTZ before being passed to a standard Weighted Least Squares algorithm for the orbit fitting.

The software allows for azimuth, elevation and range biases to be solved, considered or fixed for up to three ground stations at once. The software can also solve for the attitude and ΔV of an LAE manoeuvre during the observations, or the Transverse, Normal and Radial components of a station-keeping manoeuvre. Solving for the attitude of the manoeuvre is referred to as orbit-matching. Pre-launch analysis showed this to be potentially very accurate and this was seen during flight. All orbit matches compared well with the attitude determined using the Earth and Sun Sensor, and in general the orbit matched attitudes were used as the attitude on which to optimise the forthcoming manoeuvre.
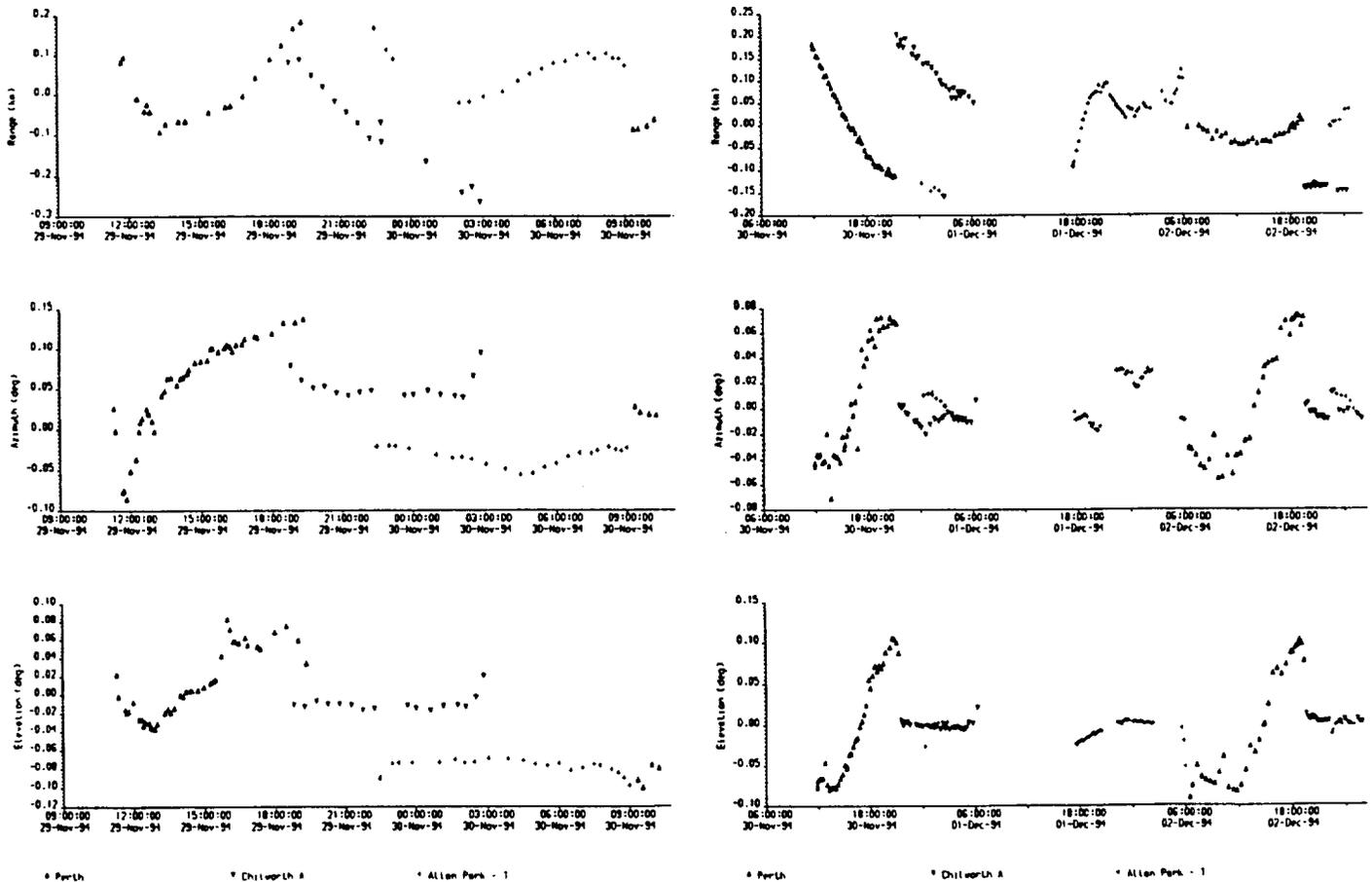

Figure 5 Range, Azimuth and Elevation Residuals prior to LAE 1 and between LAE 1 and LAE 2

440

The convergence properties during the LEOP were excellent, typically converging in three or four iterations. Various forms of weighting were available, namely:

Covariance scaling: this scales the solution covariance by the sum of the residuals divided by the number of observations, in an attempt to account for the residuals not being truly Gaussian white noise in nature. Note this does not affect the solution, only the covariance matrix.

RMS weighting: this uses the RMS of the measurement residuals from the previous iteration to weight the measurements of the current iteration. This will affect the solution, since it alters the relative weighting of the observations. It was only used once the solution had already converged as it could lead to instability if used initially.

Model weighting: this adjusts the weighting of the measurements according to the size of the correction predicted by the tropospheric model - in other words, measurements with large corrections are weighted less. This ensures that errors in the model do not significantly drive the solution.

Results obtained during the LEOP were excellent. White noise in the measurements was smaller than previously noted in GTO. Time-varying trends in the residuals were rarely greater than 300 m, again smaller than seen in GTO. Figure 5 shows the residuals obtained before and after the first LAE firing.

It was concluded that orbit determination for the SSTO mission was not significantly different from GTO.

ATTITUDE DETERMINATION

ORION F1 uses a Galileo Earth and Sun Sensor to produce sun and earth measurements for attitude determination whilst spinning. The sun sensors are the V-slit type which produce a single pulse when the sun passes through the field of view of the meridian sensor and another pulse when the sun passes through the field of view of the oblique sensor. The earth sensors are 2 pencil beams canted 4° apart and sensitive in the 14 - 16 mm wavelength range. They produce a pulse for space-earth and earth-space horizon crossings based on the derivative of the energy throughput of the detector and the value of the last threshold measured.

The ORION AOCS pre-processes these measurements before telemetering them to the ground where the QUARTZ software converts them into the basic 5 uncorrelated observations. These are: Sun Phase, the angle between the meridian and oblique sun sensor pulses; Chord Widths, the angle between the space-earth and earth-space horizon crossings for each sensor; and Separation Angles, the angle between the meridian sun pulse and the centre of the two earth pulses for each earth sensor. All angles are rotation angles measured around the spin axis.

The QUARTZ attitude determination software uses a Gauss-Newton weighted least squares algorithm to minimise the residuals between real and simulated observations and produce an updated attitude estimate. To reduce the errors on the simulated observations, both the earth sensor field of view and electronic delays caused by the components of the earth sensor are modelled. This procedure is fully described in reference 1.

The software identifies the attitude state by an inertial representation of the attitude along with biases for each of the observations and the earth sensor cant angles. Any number of these parameters can be optionally solved for, or fixed to a-priori values. (Chord width biases are not actually contained within the solution state - estimation of these values is made based upon minimising residual values still further once the WLS iteartion has been completed).

Results Summary

ORION has a small misalignment (about 1°) between the spacecraft spin-axis and the body Z axis, which also varies with propellant fill fraction. Measuring this dynamic imbalance angle (wobble angle) was particularly significant for attitude determination since the angle between the sensor and the spin axis contains a component of the wobble. With the help of apogee and perigee attitude data passes, this value was able to be refined in-flight, removing a significant error source from the Attitude Determination.

The solution method adopted was to fix only the sun phase bias and solve for all other biases (cant angle, separation angles and chord width). This method proved to be both consistent and robust.

The attitude determination results are shown in Table 5. All values are in degrees. From the table it is apparent that the attitude determination solutions are consistent with the orbit match solutions. The largest discrepancy between determined solutions and their subsequent orbit match is 0.32 degrees (AD A3 & P4 Orbit Match) for any of the data passes. It is interesting that the spin-axis right ascension seems almost as difficult to solve for as the spin-axis declination - this could be attributed to a residual wobble angle error.

Table 5 Comparison of Attitude Solutions from Attitude Determination and Orbit Matching

Solution	Attitude		Biases					
	RA	Dec.	Cant Angles		Separation Angles		Chord Widths	
			ES1	ES2	ES1	ES2	ES1	ES2
GD Injection	136.793	-15.901						
A1 AD	137.169	-15.925	0.074	0.079	0.013	0.093	-0.026	-0.014
A1 Orbit Match	137.275	-15.991						
P2 AD	137.117	-15.998	-0.149	-0.168	0.223	0.309	0.039	0.034
A2 AD	137.102	-16.083	0.191	0.185	0.043	0.115	-0.034	-0.012
A2 Orbit Match	137.230	-15.958						
Dog Leg Slew + Trim								
P3 AD	137.510	7.675	-0.100	-0.115	0.317	0.394	0.081	0.077
A3 AD	137.354	7.145	0.127	0.109	-0.103	-0.041	-0.031	-0.044
P4 AD*	137.570	7.578	0.094	0.063	0.399	0.491	0.116	0.090
P4 Orbit Match	137.491	7.436						
A4 AD	137.58	7.459	-0.012	-0.012	0.206	0.308	-0.169	-0.181
P5 AD	137.568	7.508	0.128	0.112	0.428	0.526	0.068	0.064
Trim (2 pulses)								
A5 AD	137.594	7.898	0.011	0.000	0.302	0.417	-0.090	-0.098
P6 AD*	137.516	7.769	0.297	0.289	0.505	0.627	0.061	0.059
P6 Orbit Match	137.445	7.634						

* Data incomplete due to LAE firing during data pass.

The perigee passes generated solutions which were closer (0.12-0.24 degrees) to the respective orbit match solution than the solutions generated from the apogee passes (0.24-0.32 degrees). This is consistent with pre-launch covariance analysis that predicted that the apogee pass accuracy would not be as good. This is described more fully in Reference 1.

A selection of residuals from the mission are shown in Figures 6 to 11. Only the earth sensor residuals are shown as the sun phase residuals are similar to typical GTO missions and show very well the observation quantisation (in this case 0.011 deg).
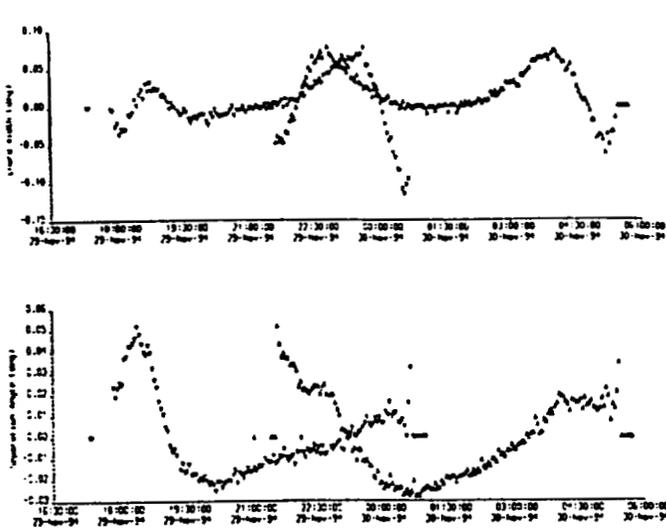
Figure 6   **A1 Earth Chord & Separation Residuals**
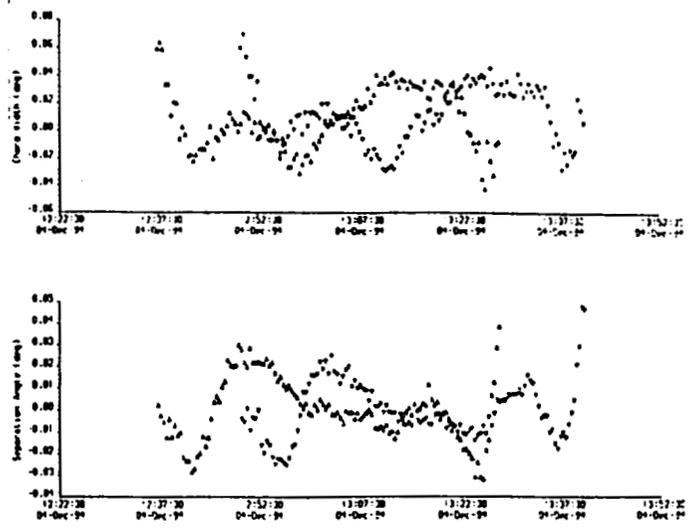
Figure 7   **P3 Earth Chord & Separation Residuals**
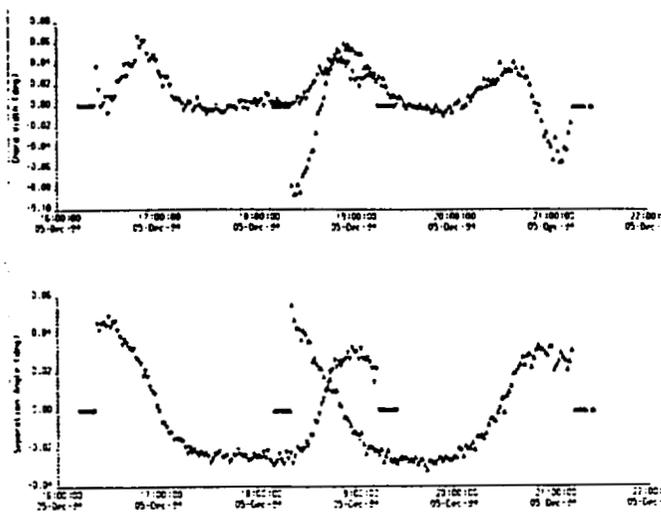
Figure 8   **A3 Earth Chord & Separation Residuals**
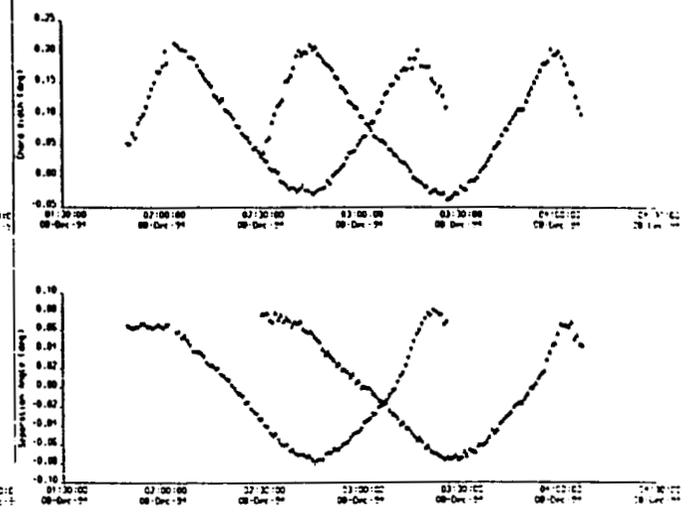
Figure 9   **A4 Earth Chord & Separation Residuals**
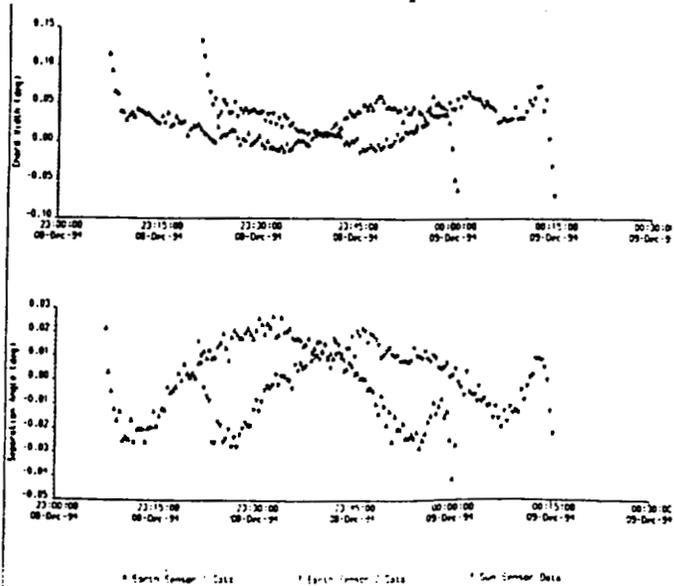
Figure 10   **P5 Earth Chord & Separation Residuals**
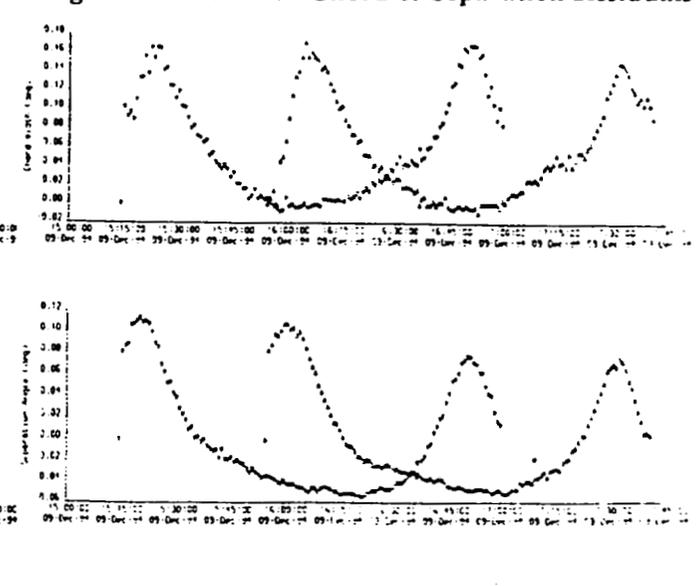
Figure 11   **A5 Earth Chord & Separation Residuals**

443

The passes shown are:

First apogee	(A1)	altitude 123,000 km
Third perigee	(P3)	altitude 25,000 km
Third apogee	(A3)	altitude 123,000 km
Fourth apogee	(A4)	altitude 65,000 km
Fifth perigee	(P5)	altitude 36,000 km
Fifth apogee	(A5)	altitude 65,000 km.

Looking at the residuals from the mission, the overwhelming first impression is of the clearly defined symmetric patterns in the SSTO, ITO apogee residuals. Their magnitudes are at least as small as GTO without the usual increase at the ends. This non-divergence at the start and end of coverage allowed the processing of all data from the apogee passes without having to cull any data. The perigee passes have less structure and are more similar to GTO but have extremely small separation angle residuals, barely exceeding 0.03 deg. The level of noise is similar for both apogee and perigee and is of the order of 0.01° and with at most 14 data points smoothed into one value the 'cleanliness' of the data has not been artificially introduced.

The patterns in the apogee data residuals are very definite and there are clear similarities between residuals patterns for data produced at similar altitudes. The patterns generated at 120,000 km (A1 & A3) have a shape very similar to that produced by the field of view and electronic delay models and therefore these patterns could be attributed to mis-modelling. It is quite significant if at super-synchronous altitudes, these modelling errors are the only significant source of error.

Discussion of Attitude Determination in SSTO

The geometry of the transfer orbit was favourable being closer to the winter solstice and avoiding sun-orbit-earth coplanarity. The large declination of the sun allowed good definition of the attitude to offset the slowly varying separation angle partial derivatives due to the low inclination.

It was thought prior to launch that diurnal earth luminance variations might produce unstable and unusable observations during the apogee passes. In fact the residual patterns are more symmetrically structured at super-synchronous altitudes which implies that the diurnal luminance variations (not simulated in QUARTZ) decrease with altitude above geosynchronous. Above geosynchronous altitudes, the relative size of the sensor field of view is larger with respect to the apparent size of the earth and the variations in the infra-red profile across the earth's surface are thus 'smoothed out'. At the highest altitude of 120,000 km, the residual patterns show virtually no random features apart from the noise at all.

Concerns were also raised that for apogee passes, very short chord data, at the beginning and end of each pass, may not be usable, and because the earth would appear smaller, it may be necessary to cull a larger percentage of data than in GTO. Pre-flight analysis had shown us that our sensor modelling ought to allow us to use all the data from each of the apogee passes, from the first chord to the last and the mission proved that this was indeed the case.

In fact, it turned out that the edge chords were extremely well behaved (compared to the simulated values) and no edge chord data had to be routinely culled, suggesting that the modelling is adequate. Modelling the electronic delays in the earth sensor reduces the errors in modelling small chords where the two horizon crossing pulses may merge, but even this is unlikely to occur at 13 rpm since the sensor transfer function is optimised up to spin rates of 90 rpm.

The chord width biases in GTO missions have tended to show a similarity between solved for values on odd revs. and even revs. It has been postulated that this is because the scanned earth longitudes are similar on alternate revs. In SSTO, two patterns emerge; there is a similarity between apogee passes (negative biases) and perigee passes (positive biases); and the biases are smaller in absolute value, when the data is produced further away from the earth. The explanation for the first pattern is not clear. The second pattern is explained as a seasonal earth luminance variation where this apparent change in earth size varies as an angular measure with distance from the earth.

GTO residuals often exhibit random patterns within themselves which vary from one pass to the next. They are thought to be due to diurnal variations in the earth's infrared profile. The general 'W' or 'U' shapes seen in the residuals are most likely caused by modelling errors increasing when the scan of the sensor crosses close to the earth limb. The SSTO apogee residuals show very pronounced patterns which are extremely symmetrical and seem to depend on altitude, the GTO-like patterns re-emerging at lower altitudes. Apart from white noise, there is virtually no random fluctuation at all. It is therefore assumed that most of the residual patterns in SSTO are due to modelling errors.

We can conclude that the methods and modelling employed for GTO can be transported wholesale to the SSTO case. The enormous amount of data produced in SSTO can be reduced to manageable proportions with an efficient smoothing process, and the representation of the

attitude state and sensor modelling are still adequate for the purpose.

The mission design of not relying on any passes of apogee data to produce an attitude solution can now be seen to be over-cautious because the solutions generated from the apogee data passes were very consistent with the solutions from the perigee passes and with the orbit matches.

MANOEUVRE OPTIMISATION

Optimisation of the four firings of the Liquid Apogee Engine required a more sophisticated approach than adopted for GTO. For each firing, the attitude, burn duration and start epoch were to be optimised, giving a maximum of sixteen optimisation variables.

The algorithm selected was the Multiple Shooting Algorithm. This divides up the Transfer Orbit into a four segments (the four coast arcs between firings) and matches the interface between segments as a set of extra internal constraints. At each interface, the six keplerian elements and the spacecraft mass must match. This leads to a total of 28 internal constraints.

Although the method is first order and progress towards the optimum slows down as the optimum is reached, it is nevertheless robust and does not rely on computing second order differentials. Progress may be slow, but it is guaranteed (given a suitable selection of the tuning constants). This turned out to be cost effective, since we were able to speed up the convergence after development by upgrading to a VAX Workstation 4000/90. The software now performs a typical convergence of 100 iterations in four minutes.

Options available were to optimise all four parameters per burn, to fix those parameters to a given value or in the case of burns 2 and 4, to set the attitude parameters to those on the previous burn. This latter option allows the optimiser to keep the attitude the same between the two apogee and the two perigee burns, thus minimising the need for an attitude manoeuvre between these firings. This strategy resulted in no trim being required between the two apogee burns, and only a 0.3° trim between the perigee burns, which in turn allowed a greater reliance to be placed on the attitude solutions achieved from the ESS and the orbit matches, since the attitude had not been altered significantly.

The manoeuvre optimisation became progressively more simple with each firing since their were less manoeuvres to optimise and less constraints to meet. Optimising the

first firing was the most intensive, and many cases were studied in the twenty four hours leading to the first firing.

The nominal cases for LAE1 were referred to as the OPOP, OOOP, FOOP and FPOP solutions. These nomenclatures refer to whether the manoeuvres were optimised, fixed or set to previous attitude, with one letter for each burn. Note that in all these cases the third firing is always optimised (since it must be slewed to anyway) but the fourth firing is assumed to be the same attitude as the third. The penalty in assuming no trim between LAE3 and LAE4 during the LAE1 optimisation was shown before launch to be negligible (< 1 gram).

FPOP represents the worst case by not trimming the attitude before the first or second firing. OOOP represents the best case by trimming before both. OPOP trims before the first firing but keeps this attitude for the second firing, whilst FOOP fixes the attitude for the first firing but trims before the second firing.

No difference was found between the OOOP and OPOP cases showing there would be no penalty in adopting a no trim between apogee burns strategy. However, there was significant uncertainty in the attitude prior to LAE1, so that trimming to an optimised attitude was not considered viable.

Given an uncertainty in attitude, the best strategy was to defer any attitude trim to before LAE2. This allows the AD solution to be compared to the orbit matched solution once the first burn has taken place.

As well as optimising the nominal case, studies around the optimum were performed by varying the attitude in Right Ascension and Declination. Grids of 7 by 7 points were performed, each point being a full optimisation of 50 iterations, so that a contour plot could be produced of the attitude sensitivity. These studies took about an hour to run on a VAX 4000/90 Work Station.

For the first firing, the following results were obtained for propellant penalties with respect to the optimum OOOP strategy:

OOOP	0 grams
OPOP	0 grams
FOOP	29 grams
FPOP	54 grams

As the maximum penalty was only 54 grams even if no trim before LAE2 was performed, then it was clear that staying in the separation attitude for both apogee burns was an acceptable strategy (54 grams of propellant is less than one day of life on-station).

This situation did not change between the first and second firing and in fact no attitude manoeuvre was performed until after the second firing, when a slew was necessary to achieve the perigee firings.

THE DOG LEG SLEW

Contrary to normal multi-burn GTO missions, a 22° slew in declination between the second and third firings is mandatory. In order to collect attitude data through perigee 3 close to the optimum LAE3 attitude, the slew was performed as two segments separated in phase by 70°. This strategy is referred to as a Dog-Leg Slew and allows the calibration of both phase angle and precession using only solar aspect angle data (Reference 4). Once both legs have been performed and the calibrations made, the final attitude can be computed and a trim back to the target attitude can be performed.

An additional tactic employed to minimise the possibility of any subsequent trim was to calibrate the phase angle only after the first segment.

The first segment of the slew was performed five hours after LAE2 and the second segment two hours later. The results of the calibration for the two segments were 0.97 for the precession calibration and 14.8 msec for the phase calibration. The required trim was 3.3° in declination to the target LAE3 attitude - this manoeuvre was performed two hours before perigee 3 and allowed the attitude determination to be performed in the LAE3 attitude.

STATION ACQUISITION

The spacecraft was eventually placed in a Drift Orbit 4° West of station with a 234 km apogee bias and a -162 km perigee bias, resulting in a drift rate of 0.3°W per day. A drift rate away from station was chosen to avoid any possibility of passing in front of TDRSS4 located 3.5°W of station, since the intense and time critical operations associated with acquiring Earth pointing may have caused RF interference with that spacecraft.

Two West manoeuvres were performed to remove the apogee bias on the 16th and 19th of December. This resulted in a drift back toward station of 1.1°E per day. Three East manoeuvres were then performed to remove the perigee bias and slow the spacecraft, on the 22nd and 23rd December. The spacecraft was finally placed in the centre of the station-keeping box with a drift rate of 0.01°E per day. This resulted in a full station-keeping cycle, with no further East-West manoeuvres required

until 6th January 1995. The eccentricity vector was correctly initialised for the sun-pointing strategy, with an eccentricity of 2.5×10^{-4} and perigee towards the sun.

CONCLUSION

The ORION SuperSynchronous Transfer Orbit mission was a complete success. The strategy of employing two apogee and two perigee burns resulted in maximum spacecraft life. A multi-burn strategy also allowed the final burn to take place at the On-Station longitude with a near zero drift rate after the final firing. This is desirable to avoid any RF interference whilst drifting past existing spacecraft in this crowded GEO sector.

The main conclusions for attitude determination are that the Galileo ESS can cope with the smaller energy throughput and smaller earth size typical in super-synchronous transfer orbits and produce sensible data. Both apogee and perigee data can be processed on the ground with no upgrade from modelling suitable for GTO to produce accurate solutions, and no data needs to be routinely culled as all the data in apogee passes is accurate enough to be used. Finally, apogee and perigee chords together allow the determination of the wobble angle, removing a significant error source from the attitude determination.

On the down side, the Transfer Orbit phase is long compared to GTO. Five and a half revolutions took just over eleven days, compared to a GTO mission of between two and five days. Although in many ways the mission was more complex than a standard GTO, the longer orbit periods did allow the intensive Flight Dynamics activities to be performed in the greater time available.

Acknowledgements

References

Baker, J.F. (1992). Study of Attitude Determination Accuracy in Super-Synchronous Transfer Orbit. Hertford: Hatfield Polytechnic.

Shurmer, I.M. and Walters I.M. (1993). ORION Mission Manual. HBK/ORN/00598/BAe Stevenage: British Aerospace Space Systems Ltd.

Fraiture L. A calibration algorithm for in-flight application to attitude slews on spinning satellites. ESOC, Darmstadt.

REPORT DOCUMENTATION PAGE

Public reporting burden for this collection of information is estimated to average 1 hour per response, including the time for reviewing instructions, searching existing data sources, gathering and maintaining the data needed, and completing and reviewing the collection of information. Send comments regarding this burden estimate or any other aspect of this collection of information, including suggestions for reducing this burden, to Washington Headquarters Services, Directorate for Information Operations and Reports, 1215 Jefferson Davis Highway, Suite 1204, Arlington, VA 22202-4302, and to the Office of Management and Budget, Paperwork Reduction Project (0704-0188), Washington, DC 20503.

1. AGENCY USE ONLY (Leave blank)	2. REPORT DATE May 1995	3. REPORT TYPE AND DATES COVERED Conference Publication - May 16-18, 1995

4. TITLE AND SUBTITLE

Flight Mechanics/Estimation Theory Symposium - 1995

5. FUNDING NUMBERS

Code 550

6. AUTHOR(S)

Kathy R. Hartman, Editor

7. PERFORMING ORGANIZATION NAME(S) AND ADDRESS (ES)

Goddard Space Flight Center
Greenbelt, Maryland

8. PEFORMING ORGANIZATION REPORT NUMBER

95B00075

9. SPONSORING / MONITORING ADGENCY NAME(S) AND ADDRESS (ES)

National Aeronautics and Space Administration
Washington, DC 20546-0001

10. SPONSORING / MONITORING ADGENCY REPORT NUMBER

NASA CP-3299

11. SUPPLEMENTARY NOTES

K. Hartman is Head, Trajectory Section, Flight Dynamics Support Branch, Goddard Space Flight Center, Greenbelt, Maryland

12a. DISTRIBUTION / AVAILABILITY STATMENT

Unclassified - Unlimited
   Subject Category 13

Availability: NASA CASI (301) 621-0390.

12b. DISTRIBUTION CODE

13. ABSTRACT (Maximum 200 words)

This conference publication includes 41 papers and abstracts presented at the Flight Mechanics/ Estimation Theory Symposium on May 16-18, 1995. Sponsored by the Flight Dynamics Division of Goddard Space Flight Center, this symposium featured technical papers on a wide range of issues related to orbit-attitude prediction, determination, and control; attitude sensor calibration; attitude determination error analysis; attitude dynamics; and orbit decay and maneuver strategy. Government, industry, and the academic community participated in the preparation and presentation of these papers.

14. SUBJECT TERMS

Flight Mechanics, Estimation Theory, Attitude Determination, Mission Analysis, Spacecraft Dynamics, Orbit Determination

15. NUMBER OF PAGES
463

16. PRICE CODE

17. SECURITY CLASSIFICATION OF REPORT Unclassified	18. SECURITY CLASSIFICATION OF THIS PAGE Unclassified	19. SECURITY CLASSIFICATION OF ABSTRACT Unclassified	20. LIMITATION OF ABSTRACT UL

NSN 7540-01-280-5500

Standard Form 298 (Rev. 2-89)
Prescribed by ANSI Std. Z39.18

National Aeronautics and
Space Administration

Goddard Space Flight Center
Greenbelt, Maryland 20771